

$2(m+1)p$

J. A. Gardner

Reproduced by
**NATIONAL TECHNICAL
INFORMATION SERVICE**
U.S. Department of Commerce
Springfield, VA. 22151

November 15, 1972



(NASA-CR-130703) SOLAR ELECTRIC
PROPULSION SYSTEM INTEGRATION TECHNOLOGY
(SEPST). VOLUME 3: SUPPORTING
ANALYSES (Jet Propulsion Lab.) 574 p HC
\$30.75 CSCL

CSCL 21C G3/28

Unclas
63173

N73-17813

NATIONAL AERONAUTICS AND SPACE ADMINISTRATION

Technical Memorandum 33-583

Volume III

*Solar Electric Propulsion System Integration
Technology (SEPSIT) Final Report*

Supporting Analyses

J. A. Gardner

**JET PROPULSION LABORATORY
CALIFORNIA INSTITUTE OF TECHNOLOGY
PASADENA, CALIFORNIA**

November 15, 1972

JPL Technical Memorandum 33-583, Vol. III

**Prepared Under Contract No. NAS 7-100
National Aeronautics and Space Administration**

ACKNOWLEDGMENTS

The cooperation and contributions of the people who supported the Solar Electric Propulsion Systems Integration Technology study are greatly appreciated. The following people were primarily responsible for the technical analyses: G. L. Anenberg, J. C. Arnett, K. L. Atkins, M. H. Bantell, Jr., A. Bratenahl, E. R. Bunker, Jr., P. O. Chelson, E. N. Costogue, R. H. Dawe, J. A. Gardner, H. H. Gernandt, E. Greenberg, R. W. Gulizia, W. Irace, R. A. Jacobson, D. J. Kerrisk, D. B. Kubly, T. W. Macie, M. L. MacMedan, E. L. Marsh, R. A. McCreary, J. P. McDanell, M. J. Olsasky, E. V. Pawlik, R. A. Proud, R. G. Ross, D. B. Smith, W. J. Weber III, J. R. Womack, C. W. Yen, B. Zeldin, and, for documentation, L. Pottage.

Preceding page blank

CONTENTS

SECTION

I.	INTRODUCTION	I-1
II.	MISSION STUDIES	II-A-1
A.	SEP THRUST SUBSYSTEM PERFORMANCE SENSITIVITY ANALYSIS	II-A-1
1.	Study Background	II-A-1
2.	Summary of Results	II-A-4
3.	Conclusions	II-A-5
4.	Approach	II-A-6
5.	Analysis	II-A-13
B.	NAVIGATION STUDIES	II-B-1
1.	The Low-thrust Navigation Problem	II-B-1
2.	Summary of NDT Study Results	II-B-7
3.	SEP Thrust Subsystem Statistical Error Model	II-B-18
4.	Orbit Determination	II-B-44
5.	Approach Navigation	II-B-72
6.	Physical/Photometric Model of Encke and Imaging Considerations for Approach Guidance	II-B-88
C.	SEP MISSION RISK ANALYSIS	II-C-1
1.	Risk Factor Analysis	II-C-2
2.	1980 Encke Rendezvous Mission and Risk Factors	II-C-18
3.	1980 Encke Rendezvous Mission Risk Assessment	II-C-24
4.	Future Development	II-C-32
III.	SEP MODULE AND THRUST SUBSYSTEM STUDIES	III-A-1
A.	POWER CONDITIONER SELECTION AND SEP MODULE INTEGRATION STUDY	III-A-1
1.	General Functional Requirements	III-A-1
2.	Electrical Design	III-A-2

PRECEDING PAGE BLANK NOT FILMED

CONTENTS (Contd)

SECTION

3.	Packaging Design and SEP Module Integration	III-A-10
4.	Conclusions.	III-A-39
B.	SWITCHING MATRIX TRADEOFF STUDY.	III-B-1
1.	Alternate Connection Methods.	III-B-1
2.	Encke Rendezvous Mission Requirements	III-B-7
3.	Mission Reliability Analysis.	III-B-12
4.	Weight Analysis	III-B-29
5.	Conclusions.	III-B-35
C.	SWITCHING MATRIX AND ROTARY SWITCH DESIGN AND ANALYSIS	III-C-1
1.	Rotary Switch Design	III-C-1
2.	Switching Matrix Assembly Design	III-C-10
3.	Conclusions and Recommendations	III-C-20
D.	THRUSTER ARRAY THERMAL ANALYSIS	III-D-1
1.	Design Guidelines.	III-D-1
2.	Preliminary Thermal Constraints	III-D-2
3.	Approach	III-D-4
4.	Results and Discussions	III-D-7
5.	Conclusions.	III-D-18
E.	THRUST VECTOR CONTROL TRADEOFF STUDY	III-E-1
1.	Introduction.	III-E-1
2.	Conclusions.	III-E-2
3.	Description of TVC Concepts.	III-E-2
4.	Detailed Comparison of Designs	III-E-16
5.	Analytical Expression for Total Thrust and Attitude Control Moment	III-E-21
IV.	SEP MODULE POWER SUBSYSTEM STUDIES.	IV-A-1
A.	POWER SUBSYSTEM OPERATING VOLTAGE SELECTION	IV-A-1

CONTENTS (Contd)

1.	Power Subsystem Description.	IV-A-2
2.	Solar Array Study.	IV-A-7
3.	Power Distribution Study.	IV-A-32
4.	Pre-regulator and SEP Module House-keeping Power Inverter Study.	IV-A-42
5.	Results and Conclusions	IV-A-48
6.	Recommendations.	IV-A-50
B.	SOLAR ARRAY STUDIES.	IV-B-1
1.	Dynamic Interactions With Attitude Control.	IV-B-1
2.	Structural Interface With SEP Module.	IV-B-49
3.	Solar Array Temperature Analysis	IV-B-61
C.	MAXIMUM POWER POINT DETECTOR CONCEPT SURVEY	IV-C-1
1.	Maximum Power Point Operating Problem.	IV-C-1
2.	Closed-loop Systems.	IV-C-4
3.	Open-loop Systems	IV-C-9
4.	Comparison of Closed-loop and Open-loop Systems	IV-C-14
5.	Recommendations for Further Development	IV-C-14
V.	SEP MODULE SUPPORT SUBSYSTEMS STUDIES	V-A-1
A.	DATA HANDLING	V-A-1
1.	SEP Module Data System Requirements	V-A-2
2.	Data System Candidates.	V-A-10
3.	Preferred Data System Characteristics	V-A-17
4.	Areas Requiring Further Study.	V-A-36
5.	Summary and Recommendations	V-A-38
B.	TELECOMMUNICATIONS/SEP INTERACTION STUDIES	V-B-1
1.	Spacecraft Ion Beam Noise Effects	V-B-1
2.	Effects of Dispersive Media on Coherent Communications	V-B-11

CONTENTS (Contd)

REFERENCES

SECTION II-A	II-A-33
SECTION II-B	II-B-112
SECTION II-C	II-C-33
SECTION III-A	III-A-42
SECTION III-D	III-D-21
SECTION IV-A	IV-A-52
SECTION IV-B	IV-B-70
SECTION IV-C	IV-C-17
SECTION V-A	V-A-41
SECTION V-B	V-B-39

TABLES

I-1.	Relationship of Supporting Analyses to SEPSIT Study Goals	I-3
II-A-1.	Summary of Mission Boundaries	II-A-13
II-A-2.	Available Contingencies and Controls	II-A-16
II-A-3.	Space Vehicle Parameters	II-A-24
II-B-1.	Thruster Performance and Uncertainty Standard-deviation Summary Data	II-B-33
II-B-2.	Summary of Estimated Sun-sensor and Star-tracker Errors	II-B-37
II-B-3.	Effects of Actuator Backlash	II-B-37
II-B-4.	Thrust-subsystem Parameter Effects on Thrust Magnitude Error	II-B-47
II-B-5.	Process Noise Standard Deviations for Multiple Thrusters	II-B-48
II-B-6.	Effect of Station Location Errors	II-B-71
II-B-7.	Nomenclature	II-B-92
II-B-8.	Approach Guidance Vidicon Optics Requirements	II-B-96
II-C-1.	Mathematical Models and Parameters	II-C-6
II-C-2.	General Mission Characteristics	II-C-19
II-C-3.	Forbidden Thruster Combinations	II-C-22
II-C-4.	A Computer Output for a Failure History Simulation and the Associated Probability, Least-switching Policy	II-C-25

CONTENTS (Contd)

TABLES

II-C-5.	A Computer Output for a Failure History Simulation and the Associated Probability, Equal-burn Policy.	II-C-26
II-C-6.	Probability of Success for a 1980 Encke Rendezvous Mission	II-C-27
III-A-1.	Electromagnetic Compatibility/Magnetic Control Requirement Summary	III-A-4
III-A-2.	Selected Power Conditioner Electrical Design Characteristics	III-A-5
III-A-3.	Solar Array Heat Load on PCs	III-A-33
III-B-1.	Combinations of Thrusters Which Satisfy the Attitude Control Symmetry Requirements	III-B-11
III-B-2.	Operating Thrusters Required for Optimum and Degraded (Class II) Missions	III-B-19
III-B-3.	Monte Carlo Mission Simulation Case Summary.	III-B-20
III-B-4.	Component Masses	III-B-30
III-B-5.	Thrust Subsystem Component Masses	III-B-30
III-C-1.	Circuit Grouping for Switching Matrix Assembly	III-C-13
III-D-1.	Estimated Additional Weight for Thermal Control Arrangements.	III-D-19
III-E-1.	Comparisons Based on the Basic TVC Attitude Control Function	III-E-3
III-E-2.	Comparisons Based on the TVC Actuator Designs	III-E-4
III-E-3.	Comparisons Based on the TVC Electronic Design	III-E-5
IV-A-1.	Solar Array Size, Weight and Power Estimates	IV-A-9
IV-A-2.	Circuit Switching and Estimated Available Power for an Array of 20 kW	IV-A-17
IV-A-3.	Circuit Switching and Estimated Available Power for an Array of 10 kW	IV-A-18
IV-A-4.	Circuit Switching and Estimated Available Power for an Array of 5 kW.	IV-A-19
IV-A-5.	Maximum Current in Relation to Wire Gage	IV-A-35
IV-A-6.	Maximum Current in Relation to Contact Size	IV-A-36
IV-A-7.	Least Weight Case	IV-A-39
IV-A-8.	Least Power Loss Case	IV-A-40

CONTENTS (Contd)

TABLES

IV-A-9.	Power Loss and Cable Weights at Three Operating Voltage Ranges	IV-A-41
IV-A-10.	Design Data for Pre-regulator and Propulsion Housekeeping Inverter.	IV-A-42
IV-A-11.	Summary of Efficiency Calculations for Pre-regulator.	IV-A-48
IV-A-12.	Specific Power Density, 2.5-kW Solar Array	IV-A-49
IV-A-13.	Least Weight and Power Loss.	IV-A-50
IV-B-1.	Mode Frequencies For 20-kW Array, Aspect Ratio = 7.38 Lowest Natural Frequency = 0.03 Hz	IV-B-13
IV-B-2.	First Six Hybrid Elastic Modes and Frequencies (Hz), 20-kW Array, Aspect Ratio = 7.38	IV-B-14
IV-B-3.	Rigid Elastic Coupling Terms for First Six Modes, 20-kW Array, Aspect Ratio = 7.38	IV-B-15
IV-B-4.	Mass-Inertia Properties, 20-kW Array, Aspect Ratio = 7.38	IV-B-16
IV-B-5.	Solar Array Configurations	IV-B-19
IV-B-6.	Computer Input Data	IV-B-30
IV-B-7.	$K_{sy} = 100$, $K_{sz} = 250$	IV-B-32
IV-B-8.	$K_{sz} = 250$, $K_{sx} = 295$	IV-B-33
IV-B-9.	$K_{sy} = 100$, $K_{sx} = 295$	IV-B-34
IV-B-10.	SEPSIT Spacecraft Natural Frequency and Ratio of Bearing-assembly Stress to Failure Stress for Three Solar-panel Configurations	IV-B-60
IV-C-1.	Summary of Open-loop and Closed-loop Systems	IV-C-15
V-A-1.	SEP Thrust Subsystem Commands	V-A-5
V-A-2.	Thrust Subsystem Measurements	V-A-7
V-A-3.	Subsystem Software	V-A-11
V-A-4.	Comparison of an Autonomous SEP Module with a Ground-Dependent Module	V-A-14

CONTENTS (Contd)

FIGURES

II-A-1.	Launch Speed, Acceleration, and Tradeoffs for 950-day Encke Rendezvous Mission	II-A-9
II-A-2.	Data for Selection of Flight Time, 1980 Encke Rendezvous Mission	II-A-10
II-A-3.	Example of Mission Contingency in Launch-period Adjustment	II-A-19
II-A-4.	Mission Contingencies in Arrival and Propellant Adjustments	II-A-20
II-A-5.	Mission Contingencies Available in Launch Periods	II-A-22
II-A-6.	Mass and Propellant Ratios as Functions of I_{sp}	II-A-25
II-A-7.	Effect of Off-nominal Double Ion Content for 0-and 10-deg Beam Divergence Angles, Θ	II-A-27
II-A-8.	Mission Constraint on Subsystem Parameters	II-A-28
II-A-9.	Limit Combinations of Double Ion Content and Beam Divergence Angles	II-A-29
II-A-10.	Constraint Boundaries and Nominal Expected Performance for Thrust-subsystem Efficiency, η_{tss}	II-A-31
II-B-1.	Mission Options Versus Navigation Technology	II-B-2
II-B-2.	Mk II Navigation System	II-B-4
II-B-3.	Comparison of Batch and Sequential Filter Performance	II-B-5
II-B-4.	Fundamental System Functions	II-B-21
II-B-5.	Celestial and Vehicle Coordinate System Relationships and Celestial Sensor Error Definition	II-B-34
II B-6.	Definition of Reference Star Cone Angle in Vehicle XYZ	II-B-35
II-B-7.	Thrust Covariance in Y Caused by Sun-sensor Errors	II-B-39
II-B-8.	Summary of Standard Deviations of Thrust Pointing	II-B-41
II-B-9.	Effect of Batch Size on Computed and Actual rms Position Error After 10 days of Tracking	II-B-52
II-B-10.	Typical Multistation Tracking Pattern	II-B-54
II B-11.	Baseline Navigation Performance for Various Tracking Strategies	II-B-56
II-B-12.	Sensitivity of Optimal Filter Performance to Thrust Magnitude Standard Deviation for Various Tracking Strategies	II-B-58

(CONTENTS (Contd))

FIGURES

II-B-13.	Sensitivity of Optimal Filter Performance to Orientation Angle Standard Deviation for Various Tracking Strategies	II-B-59
II-B-14.	Sensitivity of Optimal Filter Performance to Thrust Magnitude Correlation Time for Various Tracking Strategies	II-B-60
II-B-15.	Sensitivity of Optimal Filter Performance to Orientation Angle Correlation Time for Various Tracking Strategies	II-B-61
II-B-16.	Simulated Filter Performance with Mismodeled Thrust Magnitude Standard Deviation	II-B-63
II-B-17.	Simulated Filter Performance with Mismodeled Orientation Angle Standard Deviation	II-B-64
II-B-18.	Simulated Filter Performance with Mismodeled Thrust Magnitude Correlation Time	II-B-65
II-B-19.	Simulated Filter Performance with Mismodeled Orientation Angle Correlation Time	II-B-66
II-B-20.	Time History of rms Position Error with Data Every Day	II-B-68
II-B-21.	Time History of rms Position Error with Data Every Day	II-B-69
II-B-22.	SEP Guidance Procedure	II-B-74
II-B-23.	The rms Final State Errors Versus Flight Time and Weighting Parameters	II-B-77
II-B-24.	The rms Final State Errors Versus Process Noise Level	II-B-79
II-B-25.	Orbit Determination Uncertainties for Straight Approach without Ranging	II-B-80
II-B-26.	Orbit Determination Uncertainties for Straight Approach without Ranging and with Offset	II-B-81
II-B-27.	Orbit Determination Uncertainties for Straight Approach with Ranging and Offset	II-B-82
II-B-28.	Guidance Results for Straight Approach without Ranging and with Offset	II-B-83
II-B-29.	Orbit Determination Uncertainties for Curved Approach without Ranging	II-B-84

CONTENTS (Contd)

FIGURES

II-B-30.	Orbit Determination Uncertainties for Curved Approach with Ranging	II-B-85
II-B-31.	Curved Approach Trajectory	II-B-87
II-B-32.	Optics Design Curves for $r_1 = 100$ km	II-B-93
II-B-33.	Optics Design Curves for $r_1 = 2500$ km.	II-B-94
II-B-34.	Photometric Models of Encke	II-B-95
II-B-35.	Guidance Performance Imposed by Unmodeled Errors in the Photometric Model	II-B-98
II-B-36.	Photometric Geometry for a Point Source.	II-B-101
II-B-37.	Comet Morphology and Surface Brightness Model.	II-B-107
II-B-38.	Imaging an Extended Source	II-B-108
II-B-39.	Mariner Vidicon Transfer Characteristics	II-B-109
II-C-1.	Risk Factors	II-C-3
II-C-2.	Thruster Mortality Curve	II-C-7
II-C-3.	Thruster Reliability Curve	II-C-8
II-C-4.	Power History Change Caused by Failure	II-C-10
II-C-5.	Example of an Equal-burn Policy	II-C-12
II-C-6.	Power Profile, 1980 Encke Rendezvous Mission	II-C-13
II-C-7.	Admissible Trajectory Alternatives for Imperfect Thrust Subsystem.	II-C-16
II-C-8.	Geometric Configuration of Seven-thruster System.	II-C-21
II-C-9.	Constant-risk Contour Map for 1980 Encke Rendezvous Mission, Class II Mission Goal	II-C-28
II-C-10.	Constant-risk Contour Map for 1980 Encke Rendezvous Mission, Class I Mission Goal	II-C-31
III-A-1.	Selected PC Functional Block Diagram.	III-A-6
III-A-2.	Power Transistor Derating Curve	III-A-8
III-A-3.	PC Assembly within the SEP Module	III-A-12
III-A-4.	Detailed View of Two Opposing PCs within the SEP Module.	III-A-14
III-A-5.	HAC Prototype PC, Component Side	III-A-24
III-A-6.	Thermal Analysis Model of PC Assembly	III-A-29
III-A-7.	PC Structural Mounting Concept	III-A-35

CONTENTS (Contd)

FIGURES

III-A-8.	PC/SEP Structural Model	III-A-36
III-A-9.	First Mode Natural Frequency of PC	III-A-37
III-A-10.	Combined Structural Mass of PC Frame plus Spacecraft PC-bay Rim	III-A-38
III-B-1.	Hard-wired Connection Approach	III-B-3
III-B-2.	Complete or Partial Switching Approach.	III-B-4
III-B-3.	JPL SEPST III Switching Matrix	III-B-5
III-B-4.	Thrust Subsystem Power Profile for Encke Mission	III-B-8
III-B-5.	Thruster-Array Configuration	III-B-9
III-B-6.	Typical Acceptable Thruster Arrangements	III-B-10
III-B-7.	Thruster Reliability Versus Time	III-B-13
III-B-8.	JPL SEPST III Power Conditioner - Thruster Connecting Switch.	III-B-15
III-B-9.	Thruster Operation Sequence for Near Equal Thruster Burn Time	III-B-18
III-B-10.	Encke Comet Mission Reliability Versus Thruster Failure Rate, Monte Carlo Simulation, Case 1	III-B-21
III-B-11.	Encke Comet Mission Reliability Versus Thruster Failure Rate, Monte Carlo Simulation, Case 2	III-B-22
III-B-12.	Encke Comet Mission Reliability Versus Thruster Failure Rate, Monte Carlo Simulation, Case 3	III-B-23
III-B-13.	Encke Comet Mission Reliability Versus Thruster Random Failure Rate, New Thrust Subsystem Configurations, Case 3	III-B-24
III-B-14.	Encke Comet Mission Reliability Versus Thruster Random Failure Rate at Various Switch Failure Rates, Monte Carlo Simulation, Case 4	III-B-25
III-B-15.	Encke Comet Mission Reliability Versus Thruster Failure Rate, Monte Carlo Simulation, Location of a Spare Thruster, Case 5	III-B-26
III-B-16.	Encke Comet Mission Reliability Versus Thrust- Subsystem Weight.	III-B-31
III-B-17.	Encke Comet Mission Reliability Versus Thrust- Subsystem Weight.	III-B-32
III-B-18.	Encke Comet Mission Reliability Versus Thrust- Subsystem Weight.	III-B-33
III-B-19.	Encke Comet Mission Reliability Versus Thrust- Subsystem Weight.	III-B-34

CONTENTS (Contd)

FIGURES

III-C-1.	Photograph of Hermetically Sealed Five-Deck, Ten-contact Switch	III-C-2
III-C-2.	Typical Four-circuit Wafer	III-C-5
III-C-3.	Wafer/Rotor Interface	III-C-6
III-C-4.	Switch Assembly	III-C-8
III-C-5.	Switch, Top View	III-C-9
III-C-6.	Cutaway View of Switching Matrix	III-C-15
III-C-7.	Edge-board Connection Concept	III-C-18
III-C-8.	Crimp-splice Matrix Connection Concept	III-C-19
III-D-1.	Baseline 30-cm Thruster	III-D-5
III-D-2.	Bare Thruster Array with Solid Ground Shells	III-D-8
III-D-3.	Sunshade Arrangement with Solid Ground Shell	III-D-9
III-D-4.	Sunshade Arrangement with Perforated Ground Shell	III-D-10
III-D-5.	Thruster Array with Baffle Separator and Shading Frame with Solid Thruster Ground Shell	III-D-11
III-D-6.	Thruster Array with Baffle Separator and Shading Frame with a Perforated Thruster Ground Shell	III-D-12
III-D-7.	Basic Thruster-array Configuration	III-D-14
III-D-8.	Thrusters A, B, C, D, and G Operating at Full Power	III-D-15
III-D-9.	Thrusters A, B, C, D, and G Operating at Full Power, Heat Pipe Application	III-D-16
III-D-10.	Thruster B Operated at One-half Power, No Solar Heating	III-D-17
III-E-1.	SEP Spacecraft	III-E-6
III-E-2.	Thruster Array	III-E-8
III-E-3.	TRW Electric Propulsion Module	III-E-9
III-E-4.	TRW Thrust Vector Control Actuator System and Retention Mechanism	III-E-10
III-E-5.	Pitch Control	III-E-12
III-E-6.	JPL Thruster Configuration	III-E-13
III-E-7a.	Gimbal Actuator	III-E-15
III-E-7b.	Translator Actuator	III-E-15

CONTENTS (Contd)

FIGURES

III-E-8.	Thruster Array	III-E-17
III-E-9.	Reorientation Schemes	III-E-19
III-E-10.	Twist Geometry for TRW Design	III-E-22
IV-A-1.	SEP Module Power Subsystem with Mariner/Viking Spacecraft.	IV-A-3
IV-A-2.	Flexible Substrate in a Planar Configuration	IV-A-5
IV-A-3.	Solar Cell Circuit Design for One Sector	IV-A-10
IV-A-4.	Typical Locations of Electrical Bus Bars	IV-A-12
IV-A-5.	Available Power, 20-kW Solar Array Configuration	IV-A-14
IV-A-6.	Available Power, 10-kW Solar Array	IV-A-15
IV-A-7.	Available Power, 5-kW Solar Array	IV-A-16
IV-A-8.	Effect of Open-circuit Cell Failure and Back- biasing of Remaining Cells in Parallel	IV-A-22
IV-A-9.	Module Failure (Bypass) Rate as a Function of the Number of Cells in Parallel	IV-A-24
IV-A-10.	Expected Percentage of Cell Module Failure Versus Cells in Series Per Bypass Diode After Five-year Operation in Space	IV-A-25
IV-A-11.	Module Failure as a Function of the Number of Cells in Series Per Bypass Diode After Five- year Operation in Space	IV-A-27
IV-A-12.	Power Distribution Subsystem (PDM).	IV-A-33
IV-A-13.	Alternate Approaches for Delivering Regulated Power to Propulsion Housekeeping and Spacecraft	IV-A-43
IV-A-14.	Housekeeping Power Conditioning Units (Input Voltage from 50 to 100 V).	IV-A-45
IV-A-15.	Housekeeping Power Conditioning Units (Input Voltage from 100 to 200 V)	IV-A-46
IV-A-16.	Housekeeping Power Conditioning Units (Input Voltage from 200 to 400 V)	IV-A-47
IV-B-1.	Control System Block Diagram	IV-B-6
IV-B-2.	Solar Array Model	IV-B-11
IV-B-3.	Array Configurations Considered in Study.	IV-B-17
IV-B-4.	Array Rotation Configurations	IV-B-18

CONTENTS (Contd)

FIGURES

IV-B-5.	Mode Type 1.	IV-B-21
IV-B-6.	Mode Type 2.	IV-B-22
IV-B-7.	Mode Type 3.	IV-B-23
IV-B-8.	Mode Type 4.	IV-B-24
IV-B-9.	Mode Type 5.	IV-B-25
IV-B-10.	Mode Type 6.	IV-B-26
IV-B-11.	Mode Type 7.	IV-B-27
IV-B-12.	Mode Type 8.	IV-B-28
IV-B-13.	Simulation Analysis, Case a	IV-B-37
IV-B-14.	Simulation Analysis, Case b	IV-B-38
IV-B-15.	Simulation Analysis, Case c	IV-B-39
IV-B-16.	Simulation Analysis, Case d	IV-B-40
IV-B-17.	Simulation Analysis, Case e	IV-B-41
IV-B-18.	Simulation Analysis, Case f	IV-B-42
IV-B-19.	Simulation Analysis, Case g	IV-B-43
IV-B-20.	Simulation Analysis, Case h	IV-B-44
IV-B-21.	Simulation Analysis, Case i	IV-B-45
IV-B-22.	Simulation Analysis, Solar Array Tip Deflections	IV-B-50
IV-B-23.	Rollup Solar-Panel Structural Model	IV-B-54
IV-B-24.	SEPSIT Spacecraft Structural Model	IV-B-56
IV-B-25.	SEPSIT Spacecraft Mode Shapes	IV-B-58
IV-B-26.	Thermal Model of Solar Array	IV-B-64
IV-B-27.	Solar-array Sensitivity to Heliocentric Distance	IV-B-68
IV-B-28.	Effect of Edge Curl on Solar-array Temperature	IV-B-69
IV-C-1.	Block Diagram of a Solar Electric Propulsion Spacecraft	IV-C-2
IV-C-2.	Solar Array - Converting Operating Points	IV-C-3
IV-C-3.	Series MPPT Configuration.	IV-C-5
IV-C-4.	Parallel MPPT Configuration	IV-C-6
IV-C-5.	Extremum Regulator Functional Block Diagram.	IV-C-7
IV-C-6.	Solar Array Dynamic Resistance Measurement	IV-C-12

CONTENTS (Contd)

FIGURES

V-A-1.	Thrust Subsystem Components	V-A-3
V-A-2.	SEP Module Power Subsystem Components	V-A-9
V-A-3.	Typical Ballistic-Trajectory, Unmanned Spacecraft (Based on MVM 73 and Viking Orbiter 75).	V-A-15
V-A-4.	SEP Spacecraft with CCS and FDS Interface Lines Between the Spacecraft and the SEP Module	V-A-16
V-A-5.	Candidate SEP Spacecraft Showing Effects of Signal Conversion and Multiplexing on the SEP Module	V-A-18
V-A-6.	Candidate SEP Spacecraft Showing Preferred Data System Configuration	V-A-19
V-A-7.	Preferred Data Subsystem	V-A-20
V-A-8.	Typical Bus Receiver	V-A-25
V-A-9.	FDS Slave, Basic Components	V-A-28
V-A-10.	Analog Receiver with Common Mode Suppression.	V-A-31
V-A-11.	Differential Analog Summing Amplifier with Common Mode Suppression	V-A-31
V-A-12.	Methods of Inductive Spike Suppression	V-A-32
V-A-13.	Typical Interface Output Circuits	V-A-33
V-B-1.	Spacecraft Antenna/Exhaust Beam Configuration	V-B-2
V-B-2.	Integration Limits of Conical Beam	V-B-5
V-B-3.	Results of Antenna Noise vs Antenna Pointing Angle	V-B-10
V-B-4.	Critical Ranges	V-B-12
V-B-5.	Critical Range vs Normalized Spacecraft Antenna Distance to Beam Radius	V-B-13
V-B-6.	Phase-locked Loop	V-B-16
V-B-7.	Geometric Configuration of Signals and Phase Angles	V-B-20
V-B-8.	White Gaussian Noise Filters	V-B-21
V-B-9.	Slow Fading (Received Signal Power the Same in Each Case)	V-B-27

SECTION I

INTRODUCTION

This volume describes in detail those analyses which were performed in support of the design-point selection for the SEP module thrust-subsystem as embodied in the thrust-subsystem functional description document, which appears in Appendix A, Volume II, of this report. Each of these analyses had at least one of the following objectives:

- (1) To aid in the specification of parameters which affect the performance of elements within the thrust subsystem.
- (2) To improve understanding of thrust subsystem interface requirements with the goal of optimizing interfaces wherever possible.
- (3) To assure feasibility of some of the more critical technological aspects of SEP application.

Table I-1 summarizes the relationship of each of the analyses contained in this volume to the above objectives. The table, as well as this volume, is subdivided into studies which are related directly to the Encke rendezvous mission application, thrust-subsystem studies, power-subsystem studies, and other supporting subsystem studies. Specific output goals of each analyses are contained within the body of Table I-1.

All studies which required a mission and/or space vehicle design were based, for the most part, on the SEP module/Viking-based-spacecraft applied to the 1980 Encke rendezvous mission, as described in Volume II of this report. Deviations from this rule are caused by the initiation of some studies before the baseline design was made final. In all cases, however, these deviations are minor in nature and do not affect the conclusions of the studies.

Preceding page blank

Table I-1. Relationship of Supporting Analyses to SEPSIT Study Goals

SEPSIT STUDY SUPPORTING ANALYSES		SEPSIT STUDY GOALS		
		Specify Thrust-subsystem Element Characteristics	Identify and Define Thrust-subsystem Interface Requirements	Establish Feasibility of Key SEP Technology Requirements
Mission Studies	SEP Thrust-subsystem performance sensitivity analysis	Examine the sensitivity of trajectory performance to variations in power level, specific impulse, thrust-subsystem efficiency, thruster-beam divergence, thrust-beam double ion content, and establish tolerance limits for these parameters.		
	Navigation studies	Develop a time-dependent model of thrust-subsystem performance dispersions, as determined by variations in thruster-beam voltage, current, divergence angle, single and double ion content, thruster grid alignment and erosion, celestial-sensor performance and thrust-vector control actuator performance, and establish tolerance limits for these parameters consistent with acceptable navigation accuracies.		Evaluate the feasibility of advanced orbit-determination methods which would permit successful navigation in spite of the unusually large random accelerations attendant to low-thrust systems. Develop a feasible terminal navigation scheme and investigate the requirements imposed on spacecraft imaging instruments.
	SEP mission risk-factor analysis	Evaluate the impact of thrust-subsystem size, reliability and operational strategy on the probability of mission success, thereby providing a data base to aid in the allocation of thrust-subsystem reliability.		
Thrust-Subsystem Studies	Power-conditioner selection and SEP-module integration study	Define size, electrical, thermal, and structural characteristics of thrust-subsystem power conditioners.	Determine optimum thermal and structural interfaces of multiple power-conditioner assembly with SEP module configuration.	
	Switching-matrix tradeoff study	Select best power-conditioner-to-thruster-connection method based on weight and probability of mission success tradeoffs, and supply data which would aid in allocating power conditioner, connecting switch, and thruster reliability.		
	Switching matrix development analyses	Provide a preliminary design of selected power-conditioner-to-thruster switch as determined by the switching matrix tradeoff study.		
	Thruster-array thermal analysis	Determine impact of thruster thermal control methods such as thermal coatings, shields, and heat pipes on maintaining thruster components within acceptable temperature limits, and specify a preferred thermal control approach.	Evaluate the thermal interface requirements imposed on thrusters by surrounding SEP module elements such as thrust vector control actuators, propellant lines, and power conditioner assemblies.	
	Thrust-vector-control tradeoff study	Compare the merits of the JPL gimbal-translator with the TRW collar-gimbal thrust-vector control approaches, and select tentative best method for future thrust-subsystem applications.		
Power-Subsystem Studies	Power-subsystem operating-voltage selection	Specify thrust-subsystem input voltage range.	Select power-subsystem operating-voltage range based on consideration of solar array, power conditioning, and distribution benefits.	
	Solar Array Analyses	Dynamic interactions with attitude control		Develop a linear dynamic attitude-control simulation of a space vehicle with large, flexible solar arrays. Evaluate the feasibility of using a SEP thrust-vector control system as an attitude-control device for various solar-array sizes and dynamic characteristics.
		Structural interface with SEP module		Identify the feasibility and specify means of structurally integrating large flexible solar arrays into a SEP module. Special attention is given to the interaction of the arrays with the SEP module during large displacement, low frequency, launch vibration modes.
		Thermal Analyses		Evaluate the combined effects of solar-array edge-cool and high solar intensity environment (.34 AU) on the feasibility of maintaining solar arrays within acceptable temperature limits.
	Maximum power-point detector concept survey			Examine closed and open loop methods of operating solar arrays at or near their maximum power output; list advantages of each method.
Support-Subsystem Studies	Data handling		Determine the command, control, and sequencing requirements of a SEP thrust subsystem, including the response times required, parameters to be measured, failures to be handled (both transient and permanent), parameters to be controlled, data storage, and data transmission. Evaluate the various hardware implementations in relation to: complexity, cost effectiveness in satisfying the requirements, reliability, noise tolerance [electromagnetic interference (EMI) and radio frequency interference (RFI)], and weight, and, from the evaluation, to arrive at a preferred data system configuration.	
	Telecommunications - SEP interaction studies		Provide data whereby thruster ion-beam effect on telecommunications performance might be understood and possibly minimized.	Evaluate the effects of "Bremsstrahlung radiation" generated by the ion-thruster exhaust beam on telecommunications uplink performance; and develop a model to evaluate the effect of a general dispersive media, e.g., solar corona or ion beam, on telecommunications performance.

SECTION II

MISSION STUDIES

A. SEP THRUST SUBSYSTEM PERFORMANCE SENSITIVITY ANALYSIS

1. Study Background

a. The Hardware Problem

A low-thrust trajectory is a radical departure from the traditional ballistic trajectory in propulsion system operations. The SEP hardware will be in operation for months, rather than minutes; and trajectory energy is imparted in an integral fashion over a significant time period. Achievement of the desired final state vector (mission success), however, is still dependent on the ability to predict and control the hardware performance over the increased operation time.

Because the propellant is expended on the atomic scale, control must be exercised in an indirect manner. For instance, because no direct measurement of mass flow rate is available, the flow rate must be controlled from some a priori calibration. Present control schemes utilize the relationship between the discharge power and the mass utilization efficiency, as indicated by the ion beam current, to regulate propellant flow. Calibrations are made for the individual thrusters, and these calibrations are assumed to be accurate in flight. The difficulty with this scheme is in the sensitivity of the calibration to a number of thruster parameters, including thruster geometry, magnetic field strength and shape, division of flow between main and cathode vaporizers, etc. These calibrations will also vary in time as a function of component aging, line and load variations, and subsystem random perturbations.

The effective specific impulse (I_{sp}) and overall efficiency (η_{TSS}) of a SEP thrust subsystem are subject not only to calibration uncertainties, but to variations with input power and time. The effects of these

JPL Technical Memorandum 33-583, Vol. III

uncertainties and variations on the trajectory must be understood and the knowledge used to set hardware limits which ensure mission success. These limits must be the development standards for thrust subsystem hardware.

I_{sp} and η_{TSS} are related to thrust subsystem parameters as follows:

$$I_{sp} = \frac{1}{\dot{m}g} \sqrt{\frac{2e}{M}} \sum_{i=1}^N \dot{m}_i (\eta_{1i} + \sqrt{2} \eta_{2i}) \sqrt{V_{Bi}} \overline{\cos \theta_i} \cos \alpha_i \cos \beta_i \zeta_i \quad (1)$$

$$\eta_{TSS} = \frac{1}{N} \sum_{i,j=1}^N \eta_{c_j} \eta_{PC_j} \frac{(\eta_{1i} + \sqrt{2} \eta_{2i})^2 V_{Bi} I_{Bi}}{(\eta_{1i} + 2\eta_{2i})^2 \overline{\cos^2 \theta_i} \cos^2 \alpha_i \cos^2 \beta_i \zeta_i^2} \quad (2)$$

The summations are carried out over each operating thruster, i , and each power conditioner, j . The various terms are defined as follows:

- F = thrust level delivered by the subsystem, N
- \dot{m} = propellant mass flowrate, kg/sec
- g = 9.78 m/sec^2
- e = electronic charge = $1.6 \times 10^{-19} \text{ C}$
- M = mass of the propellant atom = $3.34 \times 10^{-25} \text{ kg (mercury)}$
- η_1 = fraction of \dot{m} exiting as singly ionized mercury atoms
- η_2 = fraction of \dot{m} exiting as doubly ionized mercury atoms
- V_B = net potential through which ions are accelerated
- I_B = ion current in the exhaust beam = $(\eta_1 + 2\eta_2) \frac{e}{M} \dot{m}$
- P = power available to the thrust subsystem for conversion to thrust
- η_c = cabling efficiency

η_{PC} = power conditioner efficiency

N = number of operating thrusters

P_{TH} = power available to an individual thruster $\approx \eta_c \eta_{PC} \frac{P}{N}$

$\overline{\cos \theta}$ = beam divergence factor

α = gimbal angle

β = thrust vector misalignment angle

ζ = factor for thrust recovery from charge exchange, deposition, etc.

In the ideal case, each of these parameters would be held rigidly constant with the exception of P , P_{TH} , \dot{m} and I_B , and the latter three would vary in a known and predictable manner with P . In practice, none of these parameters are constant.

Through equations (1) and (2) the individual parameter uncertainties are combined. The combined parameters, I_{sp} and η_{TSS} , directly enter the equations of motion and characterize the subsystem for trajectory performance. Thus, examination of the effects of variances in these combined parameters on the trajectory and a subsequent setting of acceptable variance limits are the first step in defining specifications for the individual subsystem parameters.

b. Mission Interfaces

The magnitude of the instantaneous thrust acceleration supplied by the SEP system is related to the parameters I_{sp} and η_{TSS} by

$$a = \frac{2\eta_{TSS}P}{mI_{sp}g} \quad (3)$$

where m is the instantaneous mass being accelerated. The acceleration couples the system hardware parameters to the trajectory performance through the equation of motion,

$$\ddot{\underline{r}} + K \frac{\underline{r}}{r^3} = \underline{a} = \frac{2\eta_{TSS} P(r)}{m I_{sp} g} \underline{u} \quad (4)$$

where \underline{r} is the position vector, K represents the gravitational constant, and \underline{u} is the unit vector of the applied acceleration. $P(r)$ gives the available power from the solar arrays as a function of position.

A successful trajectory has three important constituents:

(1) reaching the desired position and velocity, (2) with the required amount of hardware, (3) in a specified amount of time. Prediction of success is achieved when the equation of motion has been integrated over the trajectory to reach the desired final position and velocity. A determination of mass is implied, but it is an additional unknown in equation (4). The relationship for the mass flow rate in terms of the system parameters is obtained by

$$\dot{m} = \frac{2\eta_{TSS} P(r)}{I_{sp}^2 g^2} \quad (5)$$

Equations (4) and (5) thus allow the study of trajectory sensitivity to the combined hardware parameters, I_{sp} and η_{TSS} .

2. Summary of Results

A 1261-kg spacecraft with 20 kW of installed power at 1 AU and 16 kW delivered to the thrust subsystem was considered. The thrust-subsystem nominal I_{sp} was 3000 sec and the efficiency was 65%. For this case, the hardware constraints were a minimum delivered I_{sp} of 2910 sec and a minimum efficiency of 61.5%. To provide for these tolerances, the propellant reserve would have to be 56 kg.

The nominal subsystem efficiency was based on the assumption that the parameters η_1 , η_2 , $\overline{\cos \theta}$, $\cos \alpha$, $\cos \beta$, and ζ in equations (1) and (2) have values of $\eta_1 = .9$, $\eta_2 = 0$, $\overline{\cos \theta} = \cos \alpha = \cos \beta = \zeta = 1$. As these

parameters are varied, both specific impulse and efficiency vary. Variation of $\bar{\theta}$ and η_2 were specifically examined to determine limits caused by the trajectory. The results indicated that only small variations in these parameters could be tolerated. For example, for $\bar{\theta} = 5$ deg, the maximum allowable value of η_2 is about 0.035.

The study also showed that constraints on the hardware performance could be relaxed by the addition of more power. Increasing the power level to the thrust subsystem by 1 kW, for example, drops the minimum acceptable efficiency at 3000 sec to 60.2%, and at 2900 sec to 58.6%. Thus, the power level significantly influences hardware constraints. Since power, however, is a major cost item, there could be a strong motivation to hold to the least possible power level. To do this requires (1) a good knowledge of the true performance of the thrust subsystem at the time the power level is selected, and (2) tight constraints thereafter to meet that performance.

3. Conclusions

The major conclusions reached in the study are:

- (a) Uncertainties in achievable thrust-subsystem performance must be considered in selecting both the power level of the spacecraft and the ion-beam voltage.
- (b) Any reasonable variance in the thrust-subsystem performance can be accommodated by increasing the power level.
- (c) Once the power level and beam voltage have been selected, hard limits are set on thrust subsystem performance. Violation of these limits will make the mission unattainable.
- (d) On the basis of the above, an accurate knowledge of true subsystem performance is essential prior to the final selection of a design power level and beam voltage; otherwise, the final selection of the power level must be based on worst-case assumptions of thrust-subsystem performance.

4. Approacha. Study Guidelines

The equations of motion are subject to the hardware controls available in the thrust acceleration term. In addition to the combined subsystem parameters under investigation, I_{sp} and η_{TSS} , the controls include the amount of time the system is operated, the initial mass which must be accelerated; and the time history of the thrust pointing vector, \underline{u} . To perform a detailed or total study of trajectory sensitivity to the hardware parameters, variances in the additional controls should be included. Each control should be optimized in the sense that histories (e.g., thrust-coast times and pointing vector) which ensure a successful trajectory as defined in Section II-A-2, but which, at the same time, place the least restriction on the thrust-subsystem operating specifications, would be selected. The objective should be to determine the set of paths over a desired launch opportunity which exhibit these features:

- (1) A relatively low amount of thrust time, thereby increasing reliability through a reduction of hardware operation time.
- (2) Placement of coasts, which could be used as thrust periods to increase trajectory tolerance to substandard hardware performance.
- (3) A thrust pointing history minimizing the number of vehicle inertial attitude changes.
- (4) Trajectory success over a wide range of I_{sp} and η_{TSS} .

The above features are parametric constraints in the mathematical formulation to determine these paths. Because the equation of motion is nonlinear and because of the number of controls, simulation and study of the constraints are difficult and time-consuming, even on the fastest computers. Bounding the controls significantly increases the complexity and over-constrains the problem. Current trajectory analysis programs have, therefore, been formulated as optimizers of the final mass with freedom from constraints, which allows

adequate preliminary analysis with increased computational speed, while keeping analyses costs relatively low. As a result, only limited capability exists for any detailed simulation of constraints. For these reasons, the results of this analysis study are classed as preliminary.

The study guideline enforced by the analysis tools and the available study time was to determine the set of paths exhibiting feature (4) under the constraint of feature (1). Thus, trajectories were required to have coast phases, but accurate quantitative thrust times were not determined. Further, it was not possible to examine the effects of thrust-period placement or constrained thrust angles on the tolerances for the collective parameters, I_{sp} and η_{TSS} . Note that the omission of features (2) and (3) leaves the probability of significant future changes in the acceptable hardware performance limit. The importance of early tolerance specifications for hardware development raises the priority for securing fast, accurate, flexible, and inexpensive hardware simulation programs to alleviate the guideline restrictions of this study.

b. Trajectory Analysis

A large number of trajectories displaying the effects of hardware parameter changes must be studied to determine how much variation the trajectory can tolerate without jeopardizing mission success. The basic data can then be analyzed with selected mission success standards, and the boundaries for the hardware parameters can then be determined. The unavailability of the simulation tool described previously forced utilization of a recently developed optimization program (Ref. II-A-1), which features fast trajectory computations through approximation techniques, to perform a sensitivity analysis of a 1980 Encke rendezvous mission. Trajectories were determined for a range of launch dates consistent with this mission opportunity. Because of the large number of interacting hardware and mission parameters, the initial approach was to reduce the total number of parameters to be considered in detail. A range of launch energies was selected. All masses were normalized and fixed trajectories generated for a spectrum of launch energies. Parameters

were mission time and I_{sp} . The initial acceleration, a_0 for each path was examined as a function of the launch-energy spectrum, as shown in Fig. II-A-1. Initial acceleration, in a heuristic sense, is indicative of the amount of energy to be supplied by the thrust subsystem. As launch speed increases, the required initial acceleration decreases up to a certain point. Over the range above 4 km/sec, the amount of launch excess speed has little effect. A speed typical of this range (8 km/sec) was selected for use in detailed analysis, thus reducing the energy parameters under consideration to a single representative value in a manner completely independent of launch vehicle capabilities.

The mission times were also quickly reduced, as shown in Fig. II-A-2. At times below about 950 days, the selected optimization quantity, the ratio of final mass to initial jet power, rapidly decreases. The reasons for selection of ratios like this as optimization functions have been discussed in the open literature (Ref. II-A-2), and the reasons for the particular choice made during the study is discussed in part 5a of this section. An allowance was made for auxiliary spacecraft power, ΔP , through inclusion of a $\Delta P/P_j$ of .02 divided by efficiency.

After the parameters were reduced, the study could be focussed on the generation of detailed data. Before this could take place, however, mission success boundaries had to be defined.

c. Trajectory Success Boundaries

1) Hardware and Science Considerations. The acceptable final state of the vehicle is strongly influenced by the science objectives. Because of the emphasis in FY 1972 on hardware technology, the science role was minimized; authoritative science boundaries for the mission were not set; and arbitrary assumptions were made. For example, the closer to perihelion that rendezvous occurs, the larger the masses that can be delivered by a given thrust subsystem. Thus, from a hardware standpoint, it is desirable to arrive as close to perihelion as possible. However, arrivals close to perihelion may leave insufficient time for scientific analysis; and communications

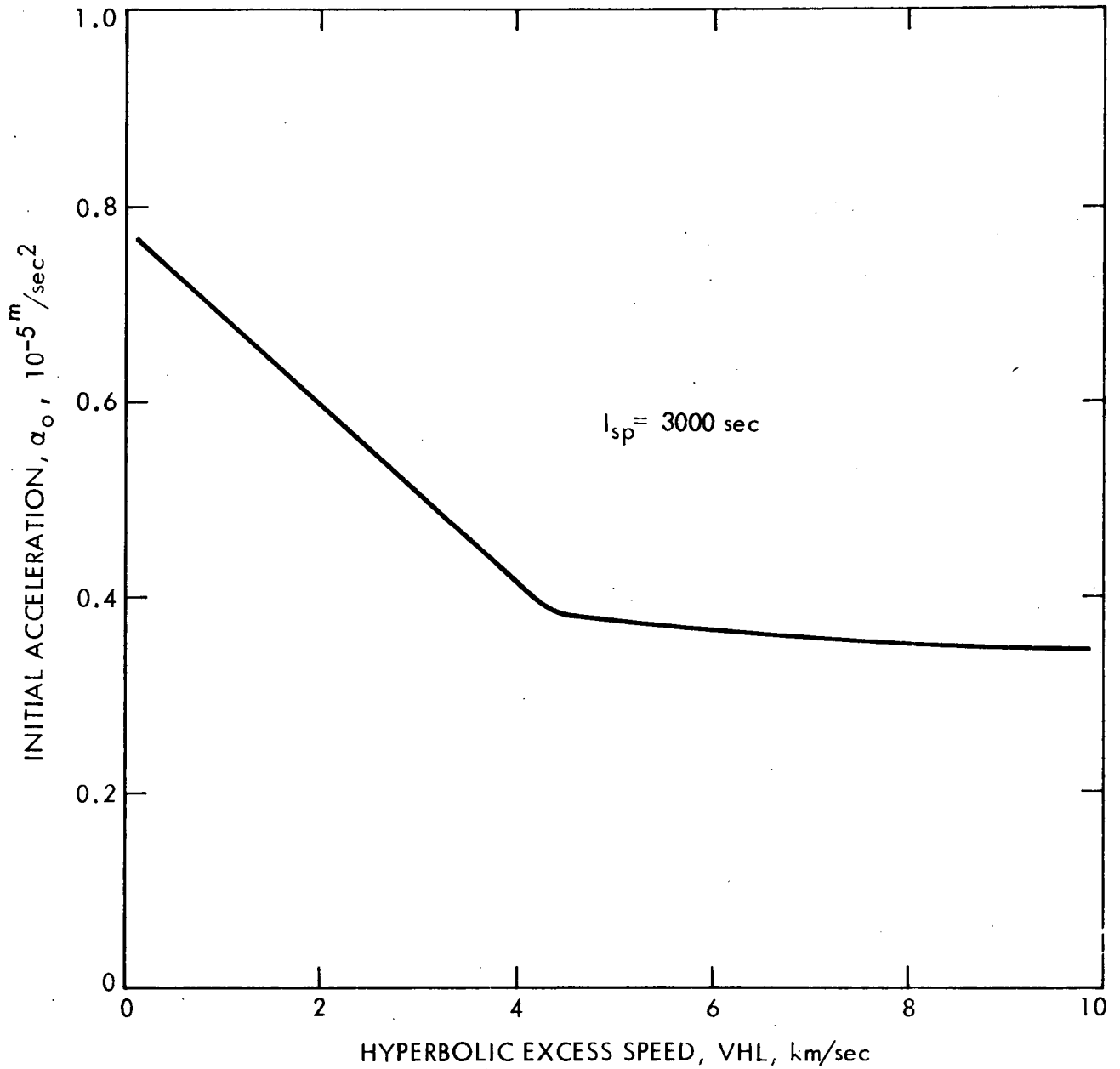


Fig. II-A-1. Launch Speed, Acceleration, and Tradeoffs for 950-day Encke Rendezvous Mission

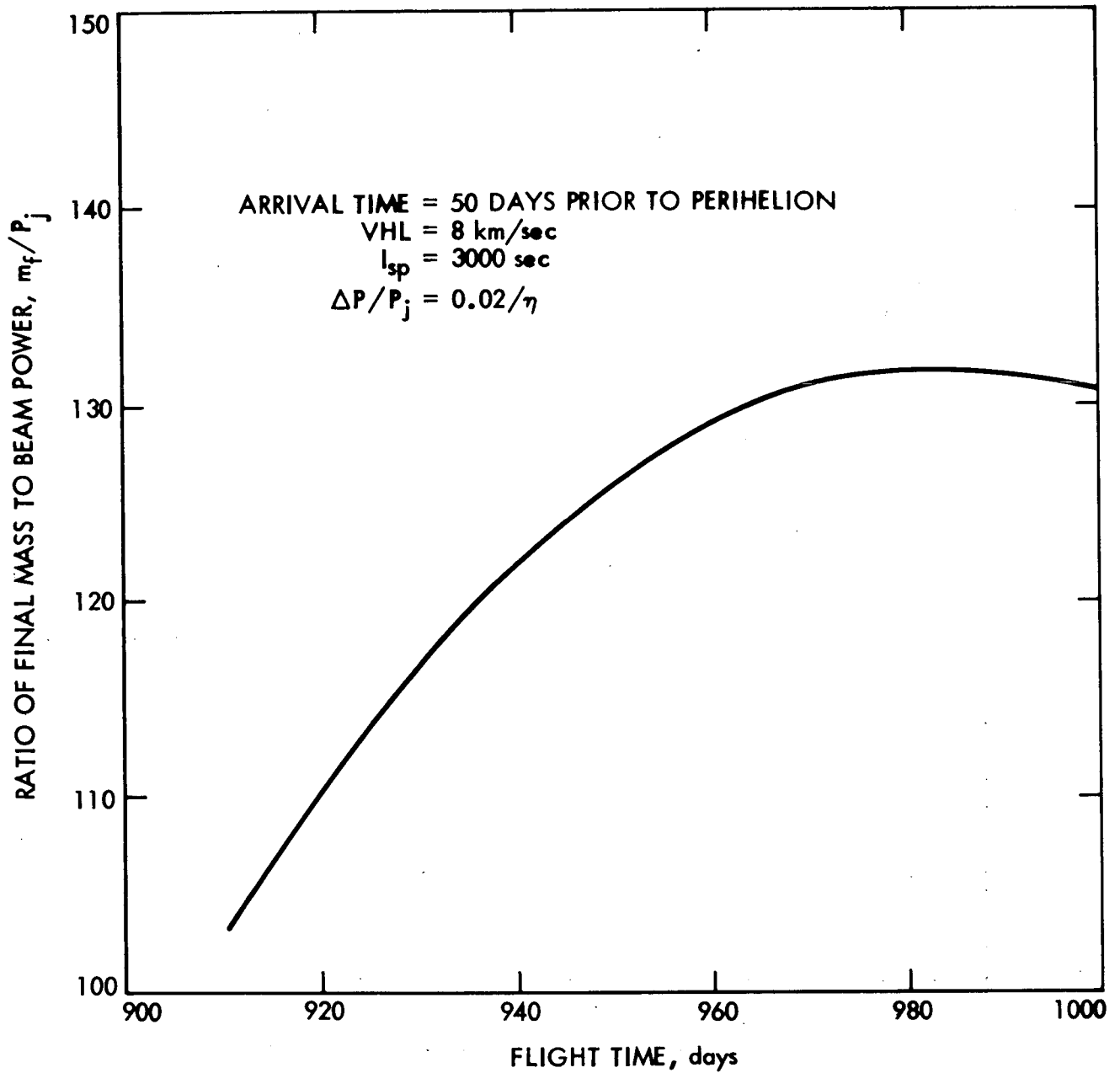


Fig. II-A-2. Data for Selection of Flight Time, 1980 Encke Rendezvous Mission

and earth-based observations of the comet become more difficult because of the effective conjunction, as the comet passes behind the sun. Thus, science considerations most likely favor early arrival. A preliminary investigation examined the tradeoff between early arrival and mass delivery capability. The minimum acceptable mass performance appeared to exclude missions intercepting the comet earlier than 50 days prior to perihelion. This time was accepted as a mission boundary, although no definitive statement from scientists qualifies it as totally acceptable.

Setting the acceptable mission boundary at 50 days before perihelion defines the final state vector for the vehicle and sets the limit for trajectory tolerance to performance. Once this point is set as the limit for acceptable performance, it is possible to determine acceptable values for hardware performance parameters.

Late arrivals, to the extent allowed by science, thermal, and communication constraints, become contingency options and increase the mass delivery performance.

2) Rendezvous Condition. The second element in the definition of mission success is the rendezvous condition. The selection of a 50-day pre-perihelion arrival point determines the position elements of the final state vector at the comet. For purposes of this sensitivity study, an acceptable rendezvous, which determines the velocity elements of the final state vector, is taken as that which results in zero relative velocity between the comet and the vehicle. This occurs when the SEP thrust subsystem reduces the hyperbolic approach speed, VHP, to zero. Minimum performance capability is associated with the $VHP = 0$ state. Relaxation of the relative velocity to a slow flyby condition represents a contingency. Again, the definition of the lowest acceptable relative velocity depends on the availability of authoritative science objectives and understanding of instrument and navigation capabilities. In the interim, the FY 72 development resulted in defining the exact rendezvous ($VHP = 0$) as the acceptable mission boundary for hardware specifications.

3) Launch Period. A third major element in defining acceptable mission boundaries is the launch period. Although the approach was to obtain basic data which is independent of launch vehicle specifications, it is practical in developing hardware tolerances to consider launch vehicle and mission operational requirements. Flight project plans for early launches to the outer planets originally required a minimum of 21 days for dual-launch missions employing the Titan launch vehicle. Later, this was relaxed slightly to a demand of 15 days for a single launch program. Eventually, the actual period selected will reflect the confidence of project management in handling unforeseen problems in launch operations. To ensure compatibility with worst-case conditions and dual-launch programs, the mission boundary was conservatively set at 30 days.

4) Thrusting Periods. Finally, a qualitative objective was set for thrusting periods. The lack of sophisticated mission simulation precluded detailed analysis to determine the acceptable coast and thrust periods. However, preliminary work showed that better mass capability was achieved over the most probable range of hardware operation, on trajectories having no coast periods. In studies of the coasting options, coast periods were automatically placed by the computer to minimize performance loss. The study guidelines eliminated definitive statements regarding coast trajectories. However, it was recognized that mission boundaries used in selecting hardware limits should include, to the extent allowable, the minimum acceptable conditions. For this reason, some consideration of coast periods was necessary because, realistically, there will be a "reasonable" amount of coast during the flight. Therefore, the hardware tolerance results include undesignated coast periods.

A summary of mission boundaries is given in

Table II-A-1.

Table II-A-1. Summary of Mission Boundaries

Parameter	Boundary
Arrival	50 days prior to comet perihelion
Velocity	Matching at the comet (VHP = 0)
Launch Operations	Any time during a 30-day opportunity
Coast Periods	A reasonable amount of coast time
Thrust Vector Pointing	No limitations placed on thrust pointing history for this study

5. Analysis

a. Important Parameter Combinations

Because of the close interaction of hardware and trajectory over a long period of time, more parameters must be analyzed for a low-thrust than for a ballistic trajectory. Data must be carefully handled so that the displays show the relationships consistent with the approach discussed in part 4 above.

The most important parameter which relates thrust-subsystem hardware technology development to performance is the final mass, m_f (the space vehicle mass at the trajectory end-point). Using final mass as a trajectory success criteria facilitates reallocation of mass between the thrust subsystem and the other subsystems, including the science payload.

The force which delivers the final mass is embodied in the kinetic energy contained in the thrust exhaust beam. Beam power is the effective power remaining after all the elemental losses defined in Section II-A-1-a have occurred. In the equations of motion (Section II-A-1-b), beam power

enters as the combination of the elemental losses and the input power, $P(r)$, through the relationship,

$$P_j(r) = \eta_{TSS} P(r) \quad (6)$$

Equation (6) is the instantaneous value of the beam power resulting from the instantaneous values of η_{TSS} and $P(r)$. The objective of the study was to determine the minimum acceptable value of the collective parameter, η_{TSS} .

The value of η_{TSS} could change during the trajectory. Because the system may operate at nominal efficiency over only part of the trajectory, the design limit on efficiency must be based on the entire trajectory. Thus, the conditions for setting the minimum acceptable value were selected as those at the poorest anticipated operating point. If the design is based on such minimum performance limits, then nominal or superior performance on any part of the trajectory will increase the probability of success.

Mass and beam power occur as a ratio in the equation for instantaneous acceleration, equation (3). For determination of each trajectory, this equation is integrated between initial and final values, after substitution in the equation of motion, (4). If the other control parameters in equation (4), specific impulse, (I_{sp}), and pointing vector, (\underline{u}), are given, then a spectrum of trajectories can be represented by the associated ratios of final mass to initial beam power where beam power includes the value of efficiency (η_{TSS}) at $t = 0$ for a given input power (P) at $t = 0$. With this ratio as the objective function, the values required for setting hardware boundaries can be combined and displayed for each trajectory. The use of this ratio as the objective function, instead of mass alone, does not affect the trajectory optimization in the range of beam powers considered in this study (Ref. II-A-2).

A similar parameter combination was used to account for propellant requirements. The instantaneous mass appearing in the vehicle

acceleration term of equation (4) includes both hardware and propellant. The objective function ratio, m_f/P_j , is related to the mass at any time by

$$m/P_j = (m_f + m_p)/P_j \quad (7)$$

Thus, the propellant specific mass with respect to initial beam power, m_p/P_j , is an integral part of the trajectory calculation; and the value at $t = 0$ determines the allowable initial mass for each trajectory and thrust-subsystem beam-power combination.

The other control explicitly considered was I_{sp} . The study objective included determination of an acceptable design value, which was accomplished by treating it as a parameter in the calculations so that its effects on the objective ratio, m_f/P_j , could be determined.

As mentioned in Section II-A-4-a, no control was imposed through the thrust pointing history. The trajectory computations allowed the thrust vector to follow any pointing history which maximized the objective function. Similarly, although coasting trajectories are required, no control was set on placement or duration of the coast periods. These features were beyond the capabilities of the analysis tools.

b. Available Contingencies

Setting limits or specifications for thrust-subsystem design and operations requires understanding all available mission contingencies or controls, such as arrival time, launch period, and coast periods. For arrival times and launch periods, contingency is added to a system meeting the success boundaries, if the mission boundary definition is altered to allow later arrival times and shorter launch periods. Decisions about the contingency effect of coast periods are dependent upon further study.

Other contingencies, not considered as mission success criteria, are important as controls indirectly affecting mission success. In

general, the ability to change the controls, which define the low-thrust mission mode, is available during three pre-target phases: (1) the initial design, (2) post-hardware delivery, and (3) post-launch. The number of controls available for respecification diminishes with each phase. Table II-A-2 summarizes the controls available during each phase, including those discussed in Section II-A-4-a. Criteria have been set for launch excess capability and launch

Table II-A-2. Available Contingencies and Controls

Controls	Initial Design Phase	Post Hardware Delivery	Post Launch
Launch Excess Capability	X	X	
Launch Period	X	X	
Arrival Date	X	X	X
Coast Periods	X	X	X
Vehicle Design Mass (de-fueled)	X		
Solar Power Reserve	X	X	X
Propellant Mass (reserve)	X	X	
Thrust Pointing Capability	X	X	X

period in Section II-A-4-b. To a lesser extent, the arrival date is also set insofar as vehicle design mass requirements can be anticipated. The vehicle design mass is considered to be an outside input for this study, and is based on preliminary configuration studies. The control, solar power reserve, can be considered as part of the assumed 18% array-degradation. If the degradation is not as severe as anticipated, the reserve or excess power is available to the thrusters. Specification of the propellant reserve is intimately connected with the coast-period design and must be such that launch can be made within

the 30-day launch period and such that additional thrusting can be provided, if coast periods are shortened. The control, thrust pointing history, can be tailored during the design phase for the expected reference path. If a fairly narrow constraint is imposed because of look-angle requirements of other subsystems, then the adjustment flexibility in the post-hardware delivery and the post-launch phases is limited.

Table II-A-2 shows that during the initial design and construction phase, limits can be set and tradeoffs can be made among mission and hardware parameters to define mission success and set hardware specifications. Once the hardware which meets those specifications is delivered, adjustments can still be made should late considerations demand redefinition of mission goals. After launch, however, thrust subsystem anomalies can only be handled by adjusting the planned coasting periods, accepting later arrival at the target, using the planned solar power reserve, and altering the path with a new thrust-pointing profile.

1) Adjusting the Coasting Periods. As discussed previously, launch energy can be treated independently of the launch vehicle. The low-thrust trajectories of interest are determined by the behavior of the initial acceleration (a_0) as a function of launch excess speed (VHL). For any a_0 and VHL combination, launch excess capability may exist for a given launch vehicle in that it can deliver more mass at the selected launch excess speed, or more speed for a given mass. The SEP module, sized in the design phase, will be expected to have a predicted mass and beam power. If no limits are imposed on these characteristics, the actual module delivered may be more massive than anticipated, while the available beam power could be exactly as expected. The result, as seen in equation (3), would be the reduction in the actual a_0 achievable by the thrust subsystem. Without some adjustment of the trajectory, the resulting final state would not be the desired one. If the launch vehicle selected has the additional capability, the first alternative might be to raise the amount of launch energy supplied to compensate for the lower-than-planned contribution of the SEP module. For the Encke rendezvous mission, this alternative is available only over a very limited range. Figure II-A-1

shows that if SEP module initial acceleration goes below about 0.36, increases in VHL have no effect in saving mission success. Thus, VHL has limited value for electric systems and has low threshold values of initial acceleration for this mission.

The contingency in reduction of the required launch period has a similar behavior. Figure II-A-3 shows the behavior for several combinations of thrust subsystems and propellant specific masses, defined in relation to initial beam power. Final acceleration is plotted on the abscissa introducing the reciprocal of the objective function discussed in Section II-A-5-a, (m_f/P_j) . The plot indicates the sensitivity of the required launch period to acceleration reductions. A delivered hardware system which is heavier than expected or which has a substandard beam power, can be compensated for, within limits, by reducing the 30-day launch period. For example, contingency for post-hardware delivery adjustments for a thrust subsystem with a specific propellant load of 49 kg/kW and $I_{sp} = 3,000$ secs can be included by specifying a delivered hardware mass, m_f , and beam power, P_j , which results in a calculated a_f of 5.44×10^{-4} m/sec². The lowest value which could be accepted without violation of the 30-day constraint would be 5.36×10^{-4} m/sec².

As seen in Fig. II-A-2, the best performance returns are realized for flight times of approximately 950 days. Shorter times drastically reduce performance, whereas longer times provide only modest gains. Figure II-A-4 illustrates the mission contingency available by allowing arrival nearer perihelion. If the actual final mass is greater than expected, or the delivered beam power less than expected, the ratio of the mass and beam power which must be delivered, m_f/P_j , is increased. Such an unexpected increase may make arrival at 50 days before perihelion impossible. However, the figure shows that contingency is available for increases in m_f/P_j , if the acceptable mission boundary is redefined, and, furthermore, that it is possible to readjust the propellant load specific mass ratio, m_p/P_j , to the appropriate value to maintain the 50-day point. This readjustment is required to impart the necessary energy increase through additional thrust time. The result of this adjustment is the probable decrease in the amount of coast time available for in-flight contingency.

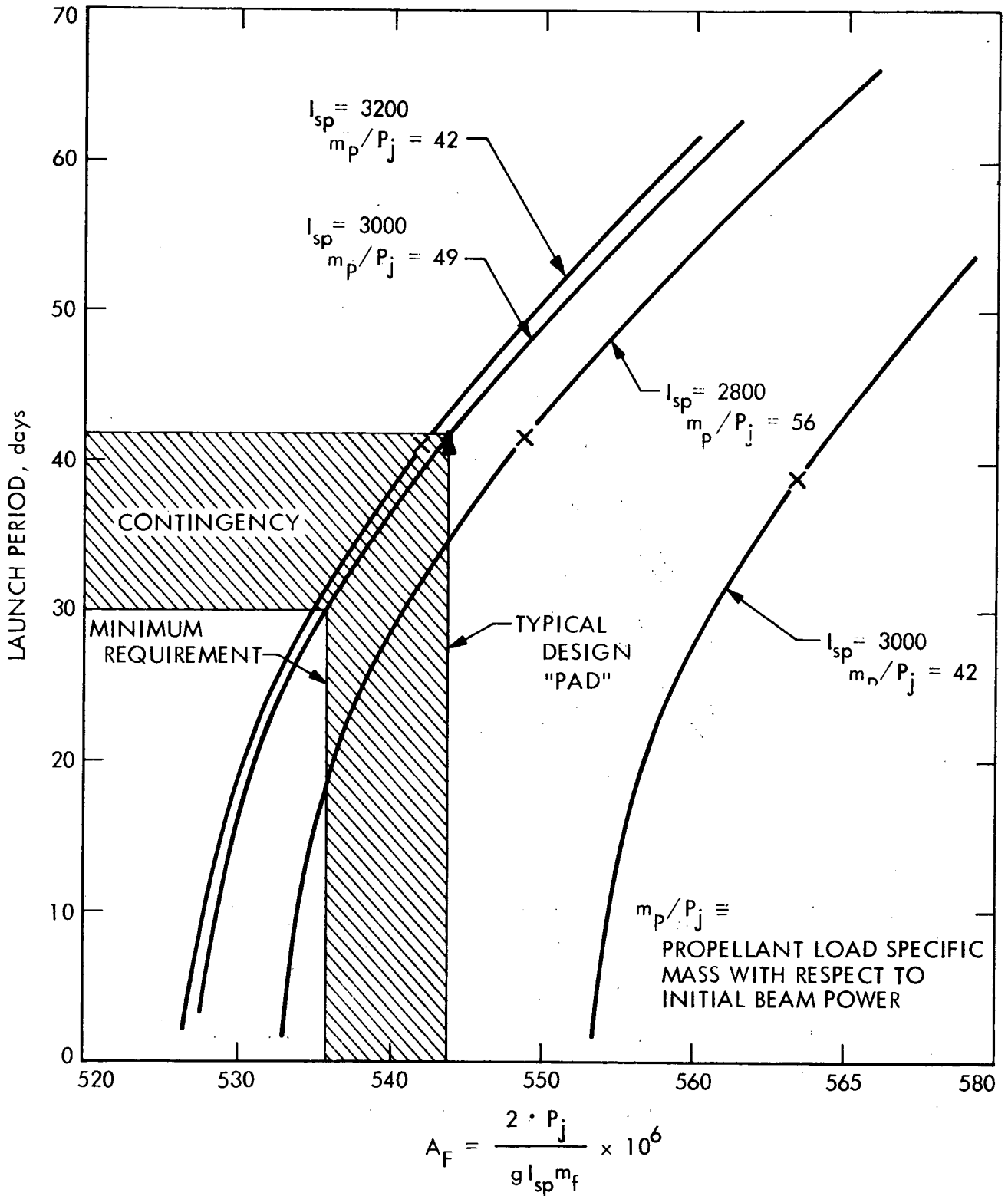


Fig. II-A-3. Example of Mission Contingency in Launch-period Adjustment

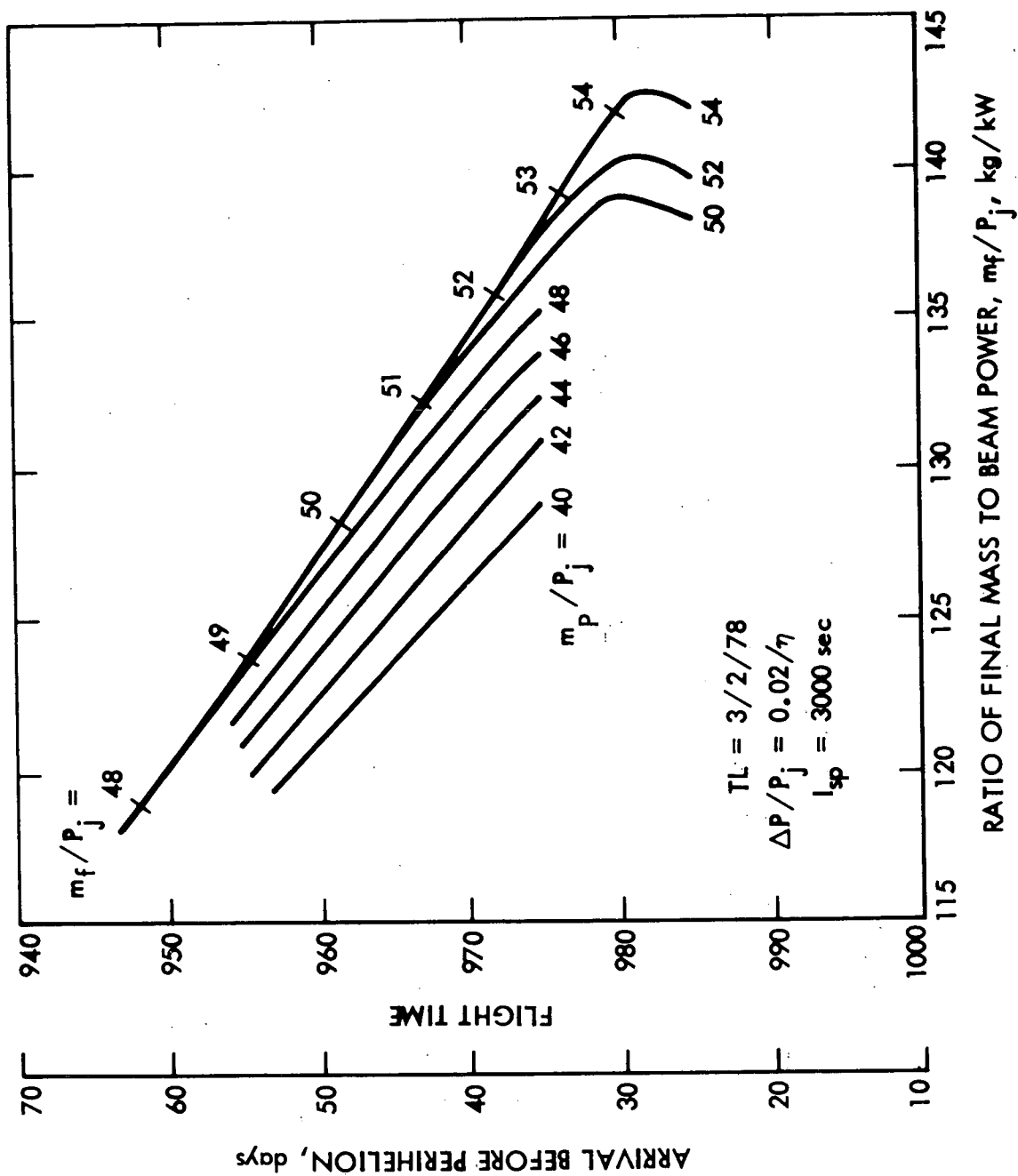


Fig. II-A-4. Mission Contingencies in Arrival and Propellant Adjustments

As stated previously, the use of coast time as a control for setting hardware specifications was treated in this study in a qualitative manner only because of the non-availability of an appropriate simulation program. The approach used, illustrated in Fig. II-A-5, typifies the basic data used for the operational analysis of the hardware sensitivity (Section II-A-5-c). The figure is based on the 50-day arrival time and illustrates a delivered thrust subsystem with an I_{sp} of 3,000 secs. The auxiliary power allowance is given as a ratio which includes the thrust-subsystem efficiency, η_{TSS} . The solid lines represent various values of the objective function, m_f/P_j . Each point is a possible trajectory for the vehicle with that specific m_f/P_j . The path flown depends on the launch date. All the displayed trajectories include some amount of coast, except those connected by the dotted line, which denotes the continuous thrust boundary. The paths farthest to the left of this boundary have the largest amount of coast. Allowance for use of planned coasts as contingency is accomplished by constraining the allowed launch dates with the second dotted line denoted "launch period closed". This line is arbitrarily placed to provide a reasonable allowance of coast time and to reserve available paths for in-flight contingency use (post-launch phase). The propellant load ratio must be based on using this contingency. For example, if the actual delivered hardware has an m_f/P_j of 125 kg/kW, a propellant reserve ratio, which theoretically allows thrusting through the planned coasts and up to the boundary, is $m_p/P_j \approx 47$ kg/kW. Selection of this value would include some contingency for in-flight performance loss. The rationale for use would be as follows: Suppose launch occurs on 1 March, with $m_f/P_j = 125$ kg/kW and a propellant load ratio of $m_p/P_j = 47$ kg/kW. These values are based on a 30-day launch period, plus reserve. All the available contingency paths lie on the vertical line shown in Fig. II-A-5. A failure reducing the in-flight P_j would instantly increase the required objective function, m_f/P_j . Concurrently, the propellant load ratio, m_p/P_j , would increase. The result would place the spacecraft at a contingency trajectory point on the vertical line. The mission would still be possible provided that the new pointing history can be met and the new value of m_p/P_j is consistent with the m_f/P_j ; i.e., sufficient propellant reserve is carried. As shown, the new trajectory is much closer to the continuous thrust boundary, and the coast contingency is reduced.

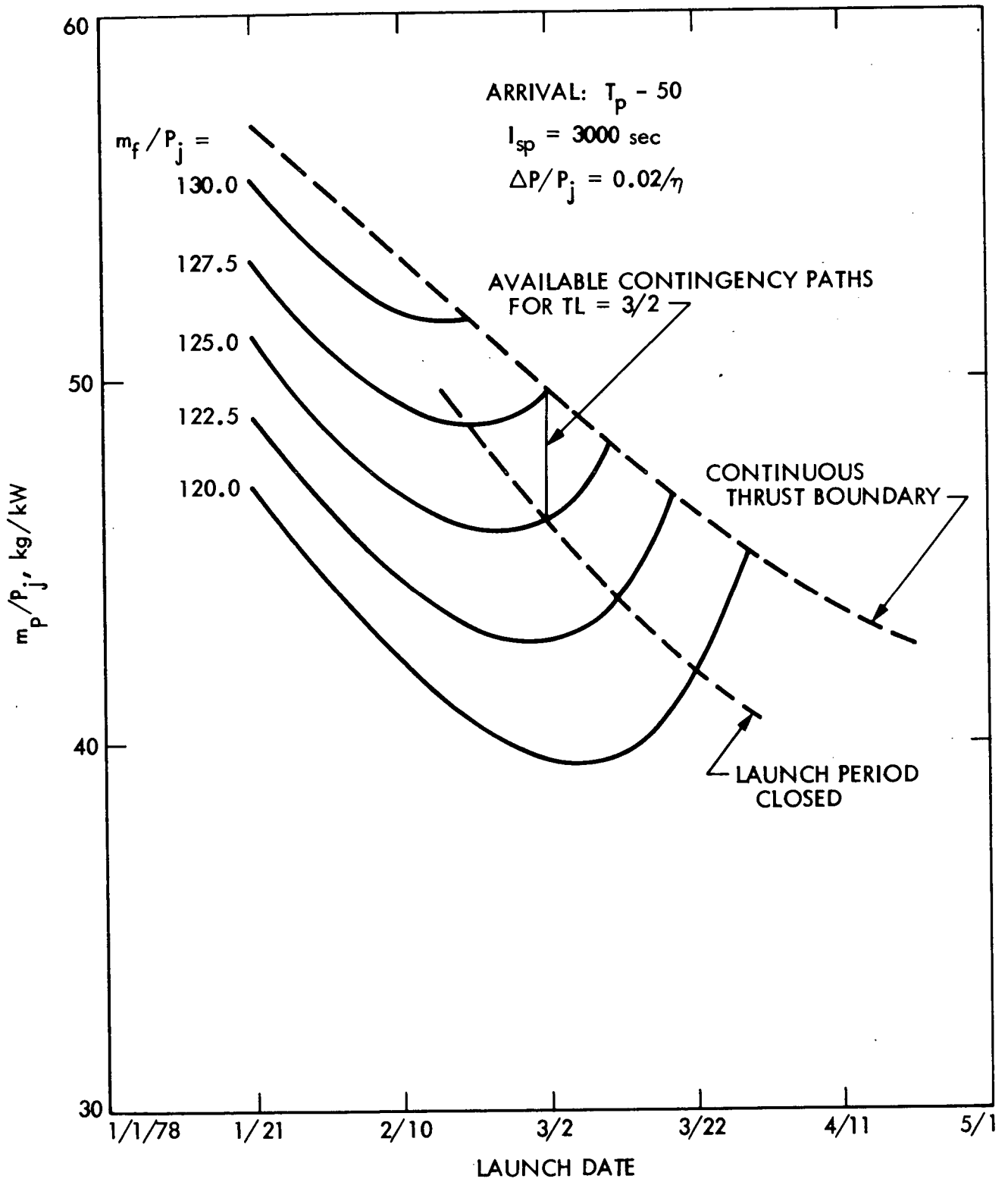


Fig. II-A-5. Mission Contingencies Available in Launch Periods

2) Using the Solar Power Reserve. Solar power reserve was not investigated in this study. The large uncertainty in the amount of solar-array degradation, which can be expected, makes meaningful analysis difficult at present. It was recognized, however, that the profile for $P(r)$ in equation (4) determines P_j , and therefore, the number of paths available to the hardware system. As a result, a conservative approach must be taken; and the additional power which may be available, if the degradation or auxiliary power requirement is not as expected, can not be relied on in setting pre-flight development specifications. Even so, a requirement less than expected will provide contingency for in-flight adjustments even though an a priori quantitative prediction appears unlikely.

3) New Thrust-pointing Profile. Thrust-pointing capability and its interaction with planned contingency coast periods remains as an important and relatively unstudied control. Only with the availability of detailed targeting simulation programs can the capability to alter the mission through a changed pointing program and/or coast profile be evaluated.

c. Hardware Sensitivity Analysis

The objective of this portion of the study was to examine the sensitivity of mission performance to the combined subsystem parameters, η_{TSS} and I_{sp} as defined in equations (1) and (2), and thereby derive the constraints, which should be imposed on the thrust-subsystem hardware delivered. The approach taken was (1) to sequentially examine each of the contingency factors available and their impact on necessary thrust-subsystem performance, starting from an assumed nominal mission and spacecraft preliminary design; (2) to examine the effect of variations of η_{TSS} and I_{sp} on these contingencies and the constraint boundaries for subsystem performance; and (3) to determine the effect of design changes on these boundaries.

To implement this approach, the status of the spacecraft after launch was examined. The vehicle then has a fixed propellant mass, a fixed dry mass, a fixed solar-array area, a fixed thruster array, and a fixed beam voltage. The variables still available are: time-of-arrival, coast arc lengths,

thrust-pointing history, and possible additional power available from the reserve allocation for solar-array degradation. Of these, only thrust pointing history is considered a free variable. To take advantage of any of the others, some contingency planning must have been previously incorporated, such as inclusion of sufficient reserve in the propellant load to permit thrusting during designed coast arcs to compensate for lower-than-nominal thrust-subsystem performance.

The nominal space vehicle considered has the parameters given in Table II-A-3. In the event of subnormal thrust subsystem performance,

Table II-A-3. Space Vehicle Parameters

Parameter	Nominal Value
Dry Mass	1261 kg
Propellant Load	480 kg
Power to Thrust Subsystem	16 kW at 1 AU
Thrust Subsystem I_{sp}	3000 sec
Thrust Subsystem Efficiency	65% (at full power)

the contingency path(s) selected will depend upon the type of off-nominal behavior experienced. The curves shown in Fig. II-A-6 depict the ratio of the maximum allowable final mass to initial jet-power ratio based on the selected mission success boundaries, and the corresponding ratio of required propellant mass to initial jet power as functions of I_{sp} . For the assumed nominal space vehicle, the actual values are $m_f/P_j = 122.5 \text{ kg/kW}$, and $m_p/P_j = 47 \text{ kg/kW}_j$, which are well within the constraint boundaries.

The effect of finding, after launch, that the thrust-subsystem performance was less than anticipated was then investigated. As a starting

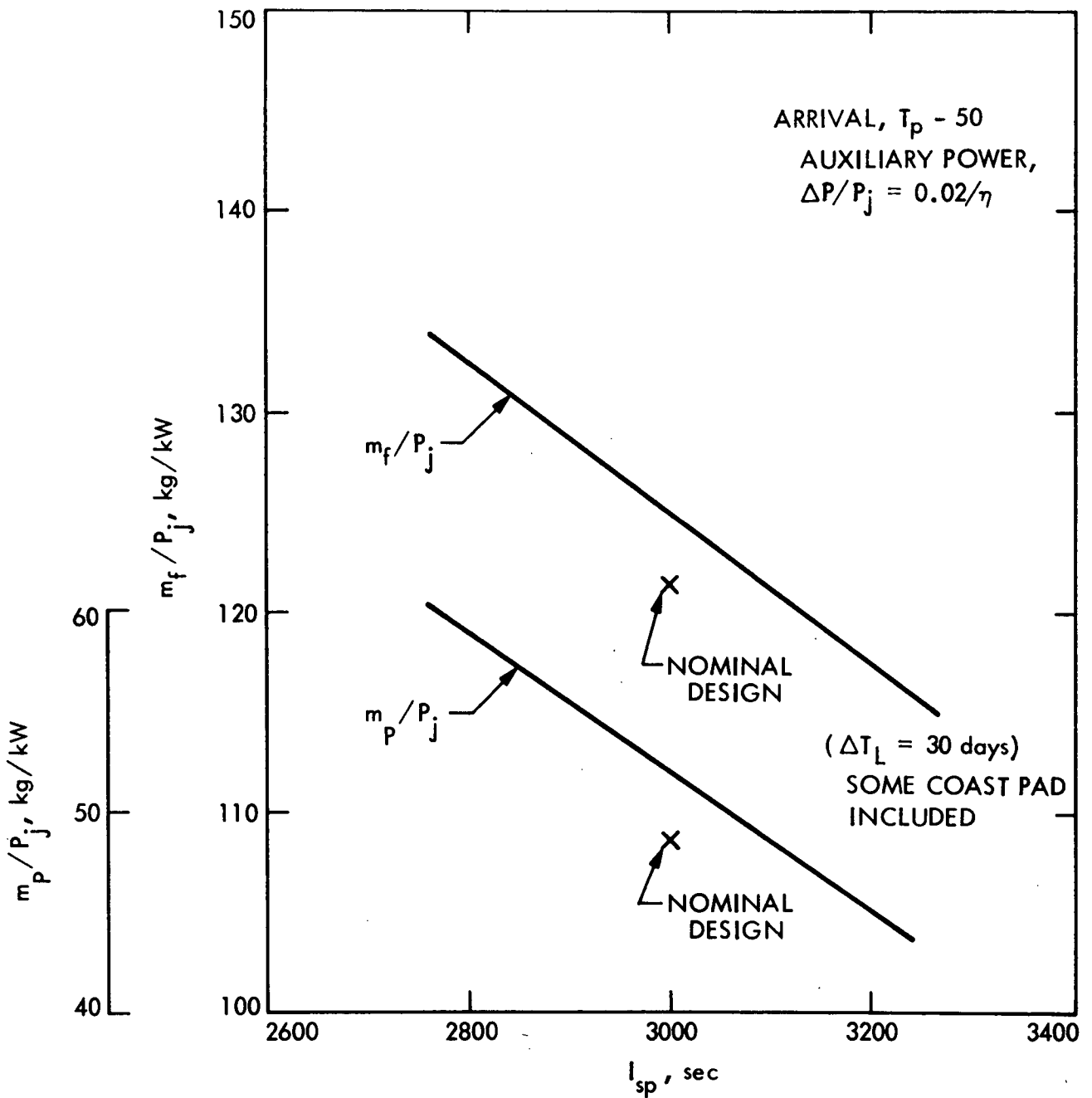


Fig. II-A-6. Mass and Propellant Ratios as Functions of I_{sp}

point, nominal values were assigned for $\eta_2 = 0$, $\eta_1 = 0.9$, and $\cos \theta = \cos \alpha = \cos \zeta = 1$ in equations (1) and (2). The effect on η_{TSS} and I_{sp} was plotted as these parameters varied from nominal. One such case is shown in Fig. II-A-7, where, for $\eta_1 + 2\eta_2$ held constant at 0.9, the effect of $\eta_2 \neq 0$ is shown for the cases of $\bar{\theta} = 0$ and $\bar{\theta} = 10$ deg. (It is assumed that beam voltage and, hence, power efficiency is fixed.) The data from Fig. II-A-7 was then used to determine "actual" values of m_f/P_j as a function of I_{sp} (Fig. II-A-8). By superimposing the curves of Fig. II-A-6, it can be seen that the constraint boundary is violated for I_{sp} values less than 2910 sec; i.e., the thrust-subsystem performance is too low to deliver the 1261-kg spacecraft to the destination, even with the continuous thrusting. More significant, even at 2910 sec, 536 kg of propellant are required to deliver the 1261-kg spacecraft, i.e., 56 kg more than the nominal amount. To provide this reserve propellant, the planned coast periods must be reduced; i.e., if the subsystem performed nominally, it would still require thrusting through a substantial portion of the planned coast periods in the nominal missions. The exact effect of this was not calculated because of the limitations of the trajectory program used. The limiting case was taken as the 2910-sec point, which in turn sets limits on the allowable variations of η_2 and $\bar{\theta}$ from their nominal values of zero, as shown in Fig. II-A-9, wherein η_2 is plotted as a function of $\bar{\theta}$. For $\bar{\theta} = 0$, the maximum allowable value of η_2 is 0.040, decreasing to 0.028 for $\bar{\theta} = 10$ deg.

The contingencies available after the delivery of the hardware, but prior to launch, were considered next. For this case, the solar-array area, beam voltage, spacecraft dry mass, and thruster array size are fixed, but propellant loading is still an available variable. If thrust subsystem performance is off-nominal and is discovered at this point, then propellant loading can be changed to accommodate the lower performance, assuming adequate tankage. The additional variable here, as opposed to the preceding case, is the launch date. If, however, the launch period can not be violated, i.e., a launch window of less than 30 days is not acceptable, then the two cases are identical, and no relaxation of the above mentioned constraints is possible. The significance of this case is that it can be used to redefine the propellant load and the nominal mission in a controlled manner.

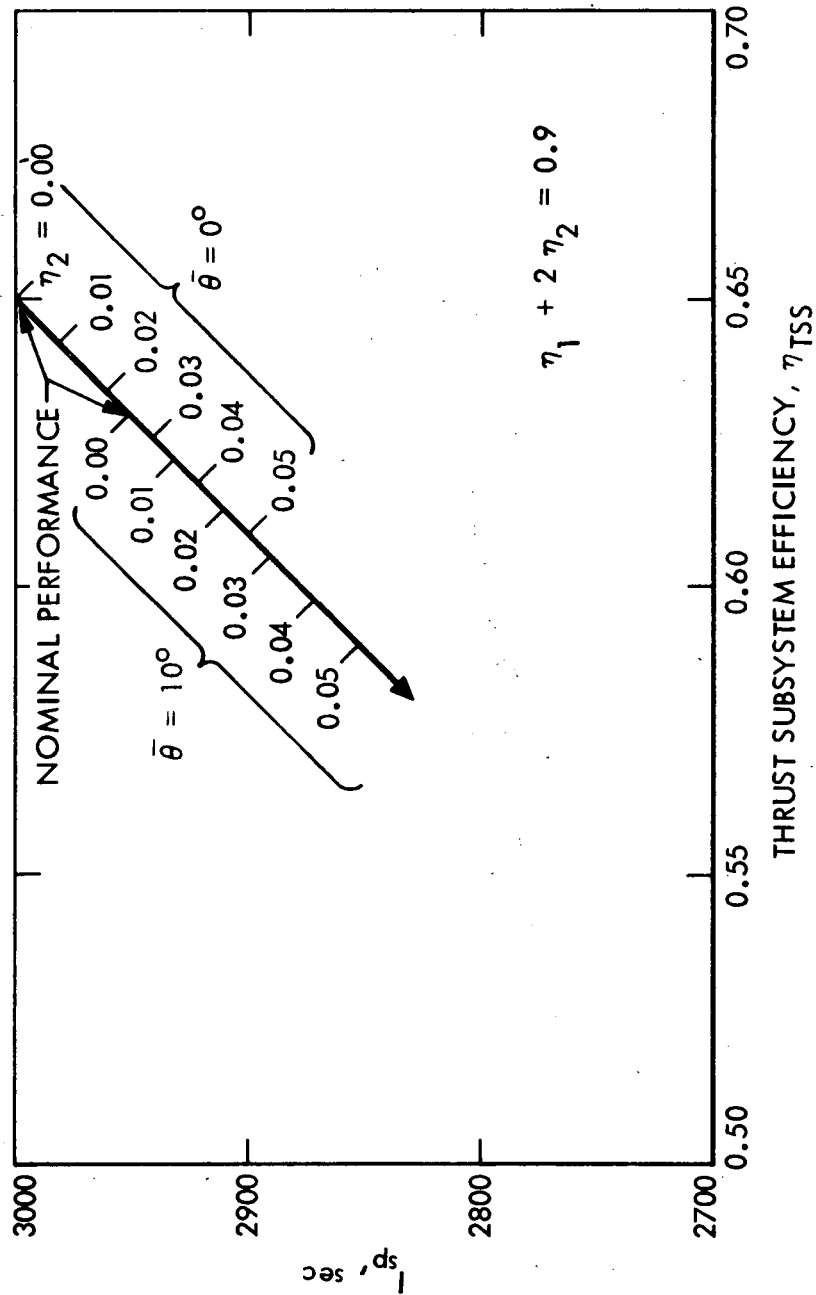


Fig. II-A-7. Effect of Off-nominal Double Ion Content for 0-and 10-deg Beam Divergence Angles, $\bar{\theta}$

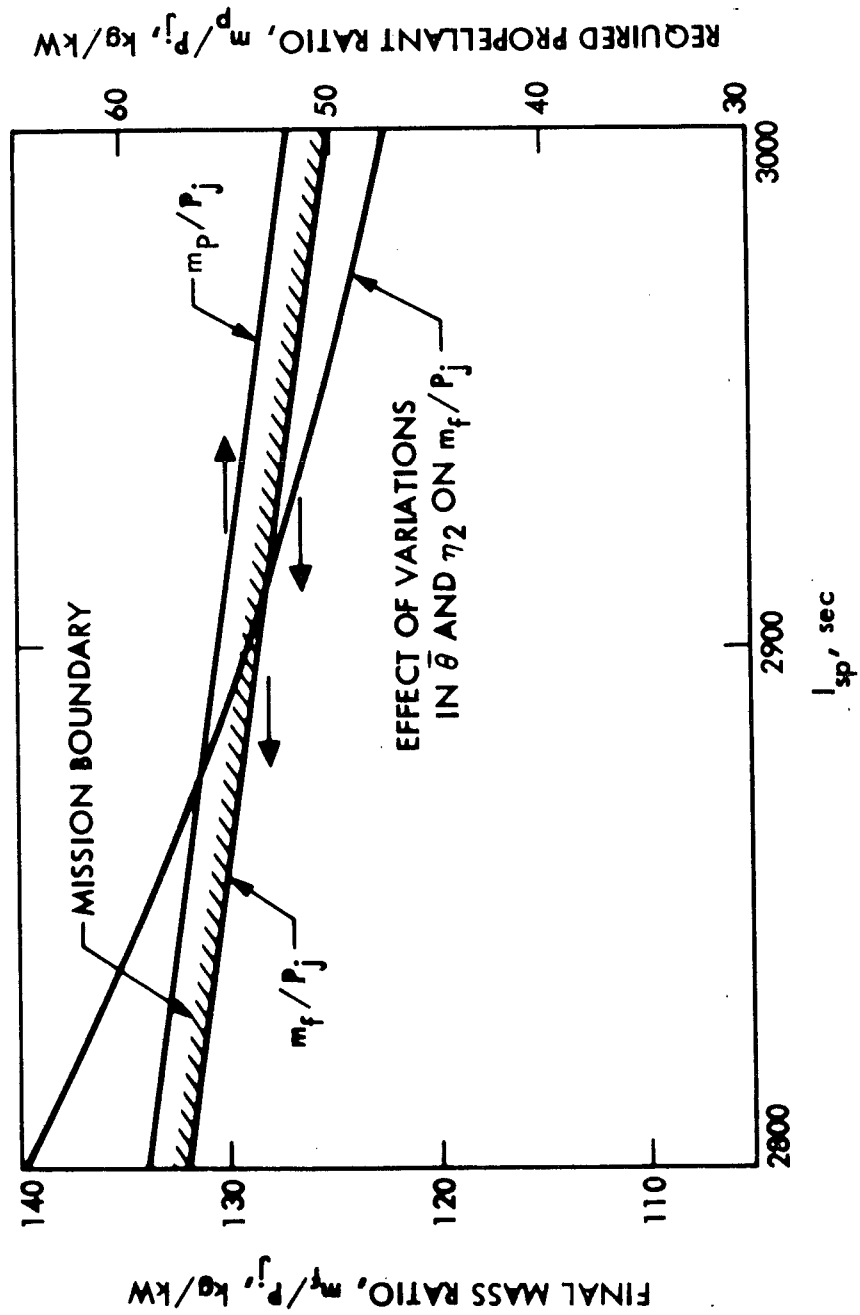


Fig. II-A-8. Mission Constraint on Subsystem Parameters

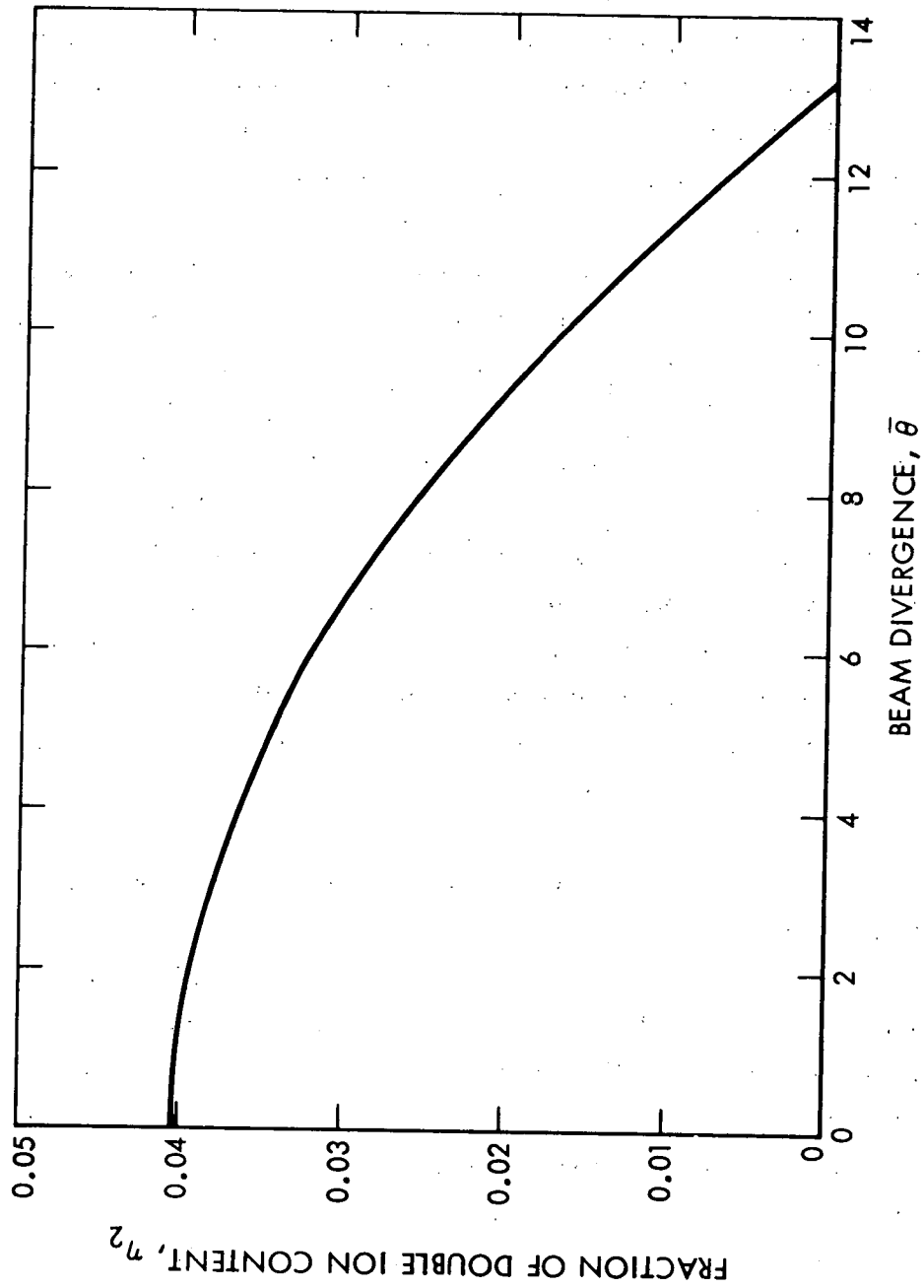


Fig. II-A-9. Limit Combinations of Double Ion Content and Beam Divergence Angles

The situation changes significantly, if possible variations are considered during the preliminary design phase, when such fixed hardware parameters as beam voltage and solar-array area can still be varied. Because the range of power levels of interest is far below the optimum value, in terms of mass delivery capability, for the launch vehicles being considered, significant increases in propellant reserves and mass-delivery capability can be obtained by increasing the power level. This is illustrated in Fig. II-A-10, wherein constraint boundaries on η_{TSS} at several values of I_{sp} have been plotted for various power levels. These curves indicate that spacecraft dry masses of 1261, 1281, and 1301 kg, respectively, can be delivered for 16-, 17-, and 18-kW initial power to the thrust subsystem. These mission boundaries inherently include a given I_{sp} versus η_{TSS} relationship. They must be updated for inclusion of variable I_{sp} systems. Also shown is a band which covers the nominal subsystem performance over its expected operating range. The band accounts for efficiency and I_{sp} variations with power level. It can be deduced from this figure that, as long as the path of the thrust-subsystem operation from the nominal point, A, to some other point, B, does not cross the appropriate mission success boundary, then success, as measured by the delivered final mass for the selected power level, will be achieved. Such a path could result from throttling, etc. If, however, the path crosses the boundary, as typically shown at C, then mission failure occurs.

The figure shows that the operational range and, consequently, the interaction with mission success boundaries is strongly influenced by $\bar{\theta}$ and η_2 . For example, suppose point C is reached by some throttling function which maintains $\bar{\theta}$ and η_2 at zero. Several possibilities are then added, which can translate C as shown. If constant I_{sp} is maintained, the dotted path results. This path reduces the effects of $\bar{\theta}$ and η_2 , showing that a system of 17 kW and $M_f = 1281$ kg is still successful at full throttling with $\bar{\theta} = 10^\circ$ and $\eta_2 = .04$. However, if constant I_{sp} is not maintained, the same values of $\bar{\theta}$ and η_2 result in mission failure for the 17-kW system. From this data, it can be seen that by initially designing for 18 kW, substantial variations in the various parameters can be tolerated within the corresponding mission-success boundary. Further, if the true values of $\bar{\theta}$ and η_2 are known, the

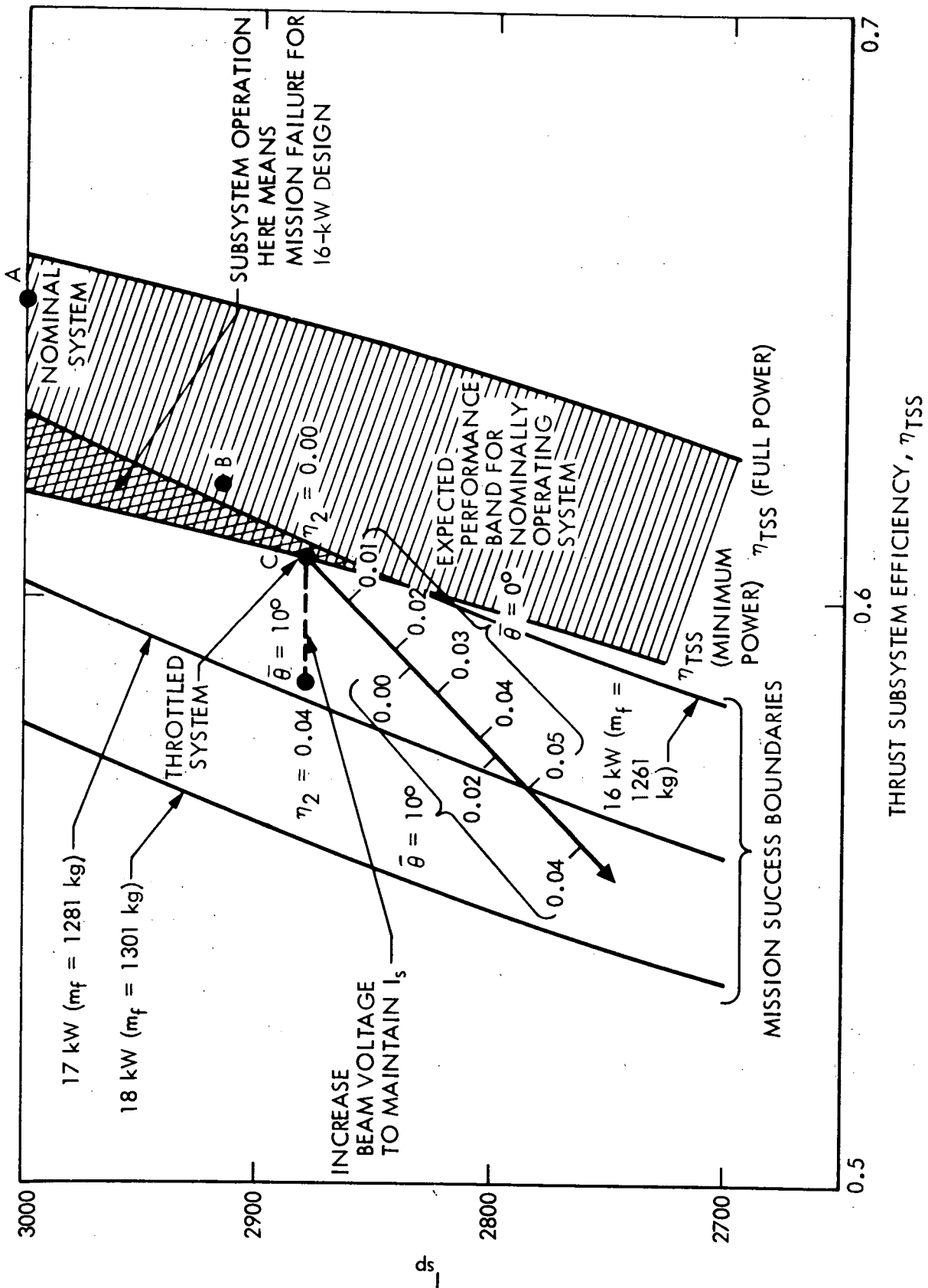


Fig. II-A-10. Constraint Boundaries and Nominal Expected Performance for Thrust-subsystem Efficiency, η_{TSS}

dotted line shows that the design power level can be reduced to 17 kW; and the corresponding success boundary is not violated, provided that the beam voltage is increased to maintain constant I_{sp} .

The conclusion to be drawn from this is the importance of knowing, at the time of preliminary design, the exact values of such parameters as η_2 and $\bar{\theta}$. Unplanned values for these parameters can, however, be accommodated by increasing the design-power level. Since this directly affects cost, the cost of minimizing allowable variances in subsystem parameters must be traded off against the cost of the additional power required to accommodate them.

A direct quantitative cost analysis was beyond the scope of this investigation. However, off-nominal subsystem performance during the various phases of the program has certain qualitative effects on cost. If off-nominal performance is detected during the preliminary design phase, or if provision for worst-case performance is made, the only cost increase is for the additional power required, which amounts to a few hundred thousand dollars. If such performance is detected after hardware delivery and it is necessary to change either the power level, the power conditioner, and/or the propellant loading, as well as flight software and mission operations, the cost goes up by an order of magnitude. If it is not detected until after launch and the mission constraint boundaries are violated, the result is mission failure, which costs on the order of one hundred million dollars. Therefore, the most cost effective approach is to take the most pessimistic performance values, based on available data, for the mission design. Because the degree of pessimism depends upon the quality of data available, the real tradeoff is between the cost of reducing pessimism by better calibration and the cost of increased power for overly pessimistic assumptions. This tradeoff remains to be performed.

REFERENCES

- II-A-1. D. W. Hahn, F. T. Johnson and B. F. Itzen, Chebychev Trajectory Optimization Program (CHEBYTOP) Final Report No. D2-121308-1, The Boeing Co., July 1969.
- II-A-2. T. A. Barber, J. Horsewood, and H. Meissinger, Basic Parameters for Low Thrust Mission and System Analysis, AIAA Paper No. 72-426 presented at the 9th Electric Propulsion Conference, Bethesda, Md., April 17-19, 1972.

B. NAVIGATION STUDIES

A navigation development team (NDT) was formed to investigate in depth the requirements and feasibility of a solar electric propulsion Encke Rendezvous Mission. This section includes the general background of low-thrust navigation and the results of the specific studies undertaken by the NDT. Summary results of the thrust subsystem error modeling study and the orbit determination studies are presented. Also, the new error modeling developments are described because they are fundamental to the orbit determination and guidance studies. These studies lead to the definition of a feasible navigation scheme for a low thrust rendezvous mission to Encke.

In addition, the terminal maneuver strategy also has an important impact on thrust-subsystem tolerance specifications. This viewpoint was investigated by the NDT and it was proven that it is feasible to accomplish terminal guidance using a practical optical imaging design, in the presence of random acceleration errors as large as five percent.

1. The Low-thrust Navigation Problem

Navigation, in the broader sense, describes a multifunctional system comprised of three integrated areas: orbit determination, maneuver strategies, and guidance. The interfaces binding these operations are even stronger for low-thrust missions than for ballistic missions, so that a low-thrust navigation system must be designed as an entity.

Current navigation methods rely totally on an earth-based command and control system. Feedback control of the spacecraft depends entirely on an earth-based tracking system, known as Mark I (Mk I), which employs conventional doppler and range data. Mk I navigation has been improved by reducing the data-error sources to a point where planetary excursions to the terrestrial planets are well within the capability of the system.

Although earth-based navigation will continue to improve, most missions over the next two decades will require some additional navigational support from the spacecraft itself. Figure II-B-1 illustrates the evolution of

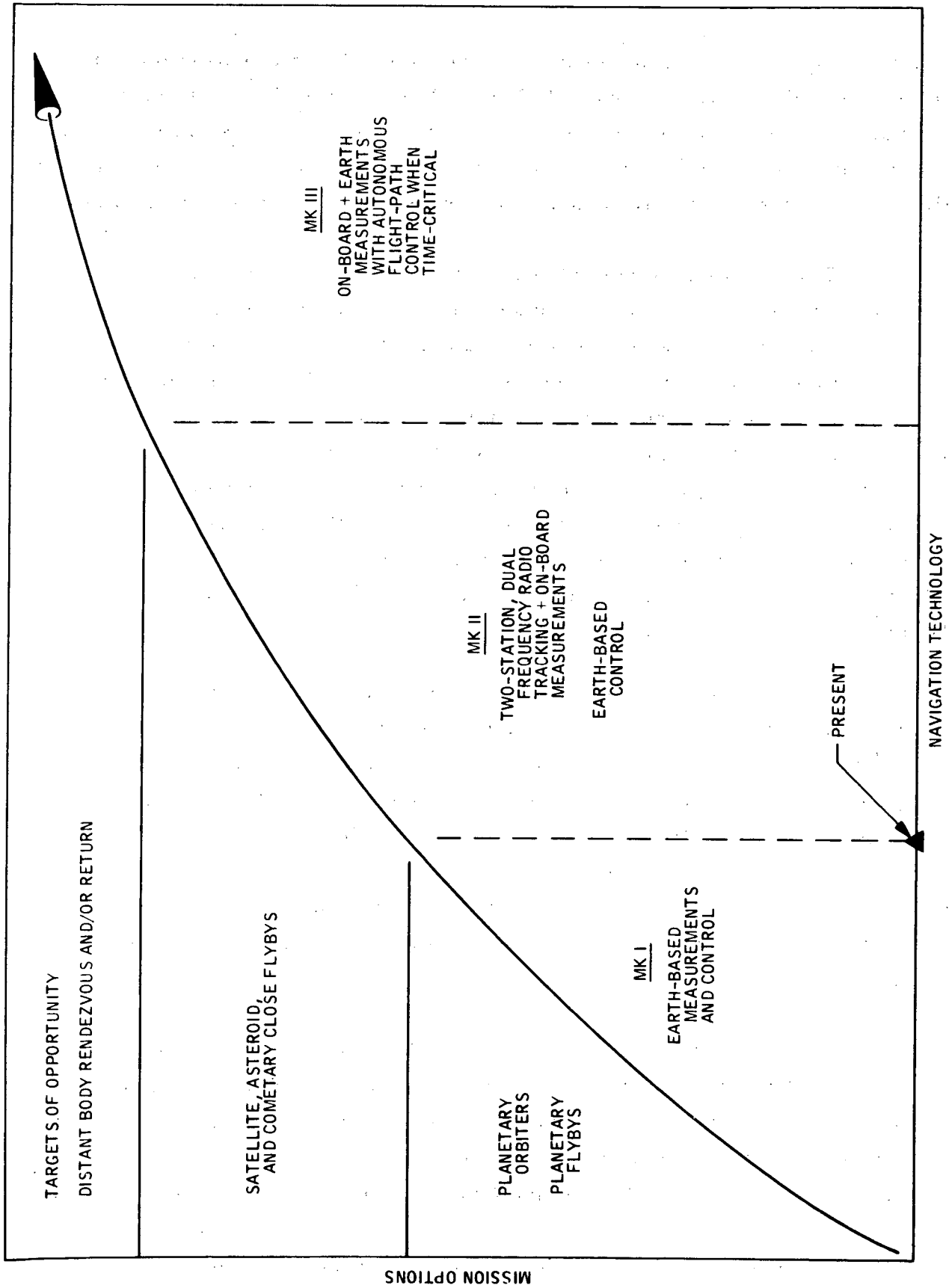


Fig. II-B-1. Mission Options Versus Navigation Technology

navigation against a "timeline" of mission options. The navigation technology represented by the systems in Fig. II-B-1 apply equally well to both ballistic and low-thrust missions except that the low-thrust system requires Mk II for the planetary missions. However, it is worthy to note the general commonality, a duality that is most beneficial to the low-thrust technology development program.

Current studies have shown that low thrust is very attractive for small-body and comet missions. Consequently, a low-thrust rendezvous mission to Encke in 1980 was selected as a definitive means of focusing low-thrust technology development. The low-thrust navigation system to be developed for this mission clearly falls within a Mk II class of system. The ephemerides for small-body and comets are the major source of error or uncertainty. Physical properties of these targets limit the capability to improve their ephemerides by earth-based tracking. But earth-based data, supplemented with spacecraft-based data, dramatically reduces ephemeral errors from a dominate source to a level commensurate with platform-error sources, such as DSN station-location errors.

Figure II-B-2 conceptualizes a Mk II navigation system (Ref. II-B-1). Development of a particular navigation system begins with these basic ideas and then transforms each of the block concepts into a working process with compatible interfaces. This transformation is not routine, even for a mission needing only well developed existing technology, for there are many design options to be considered in each area. For example, for orbit estimation, the best combination of available types of data must be selected according to a set of overall systems requirements, of which accuracy would certainly be a prime factor.

Not all technology for navigating a low-thrust spacecraft is fully developed. A SEP thrust system has unpredictable variations in accelerations, which dominate the navigational problem. These continual random acceleration dispersions (process noise) are typically three orders of magnitude larger than the nongravitational acceleration dispersions encountered on ballistic missions.

The comparison shown in Fig. II-B-3 illustrates the effect of process noise on conventional doppler data. The degrading effect in estimating

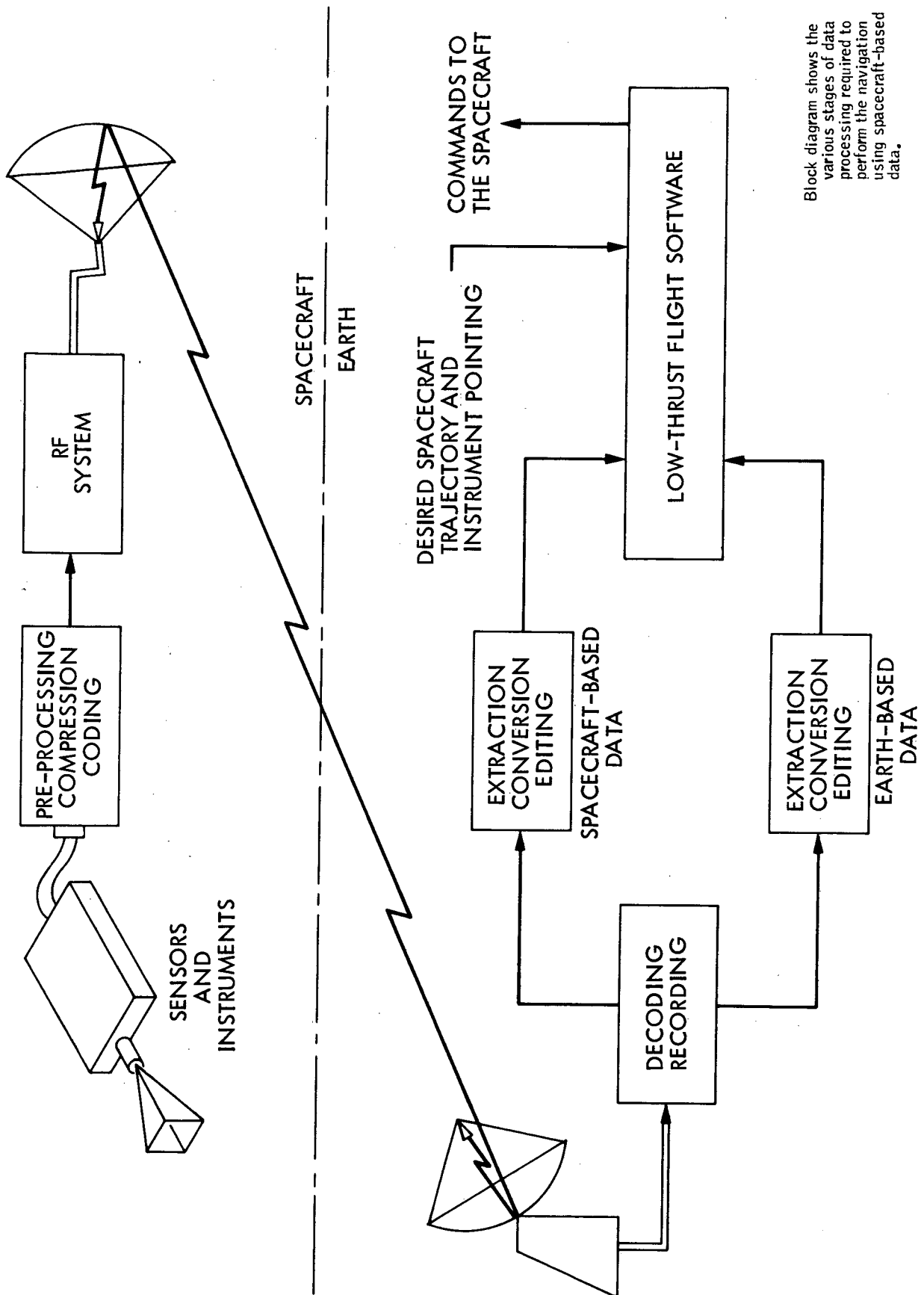


Fig. II-B-2. Mk II Navigation System

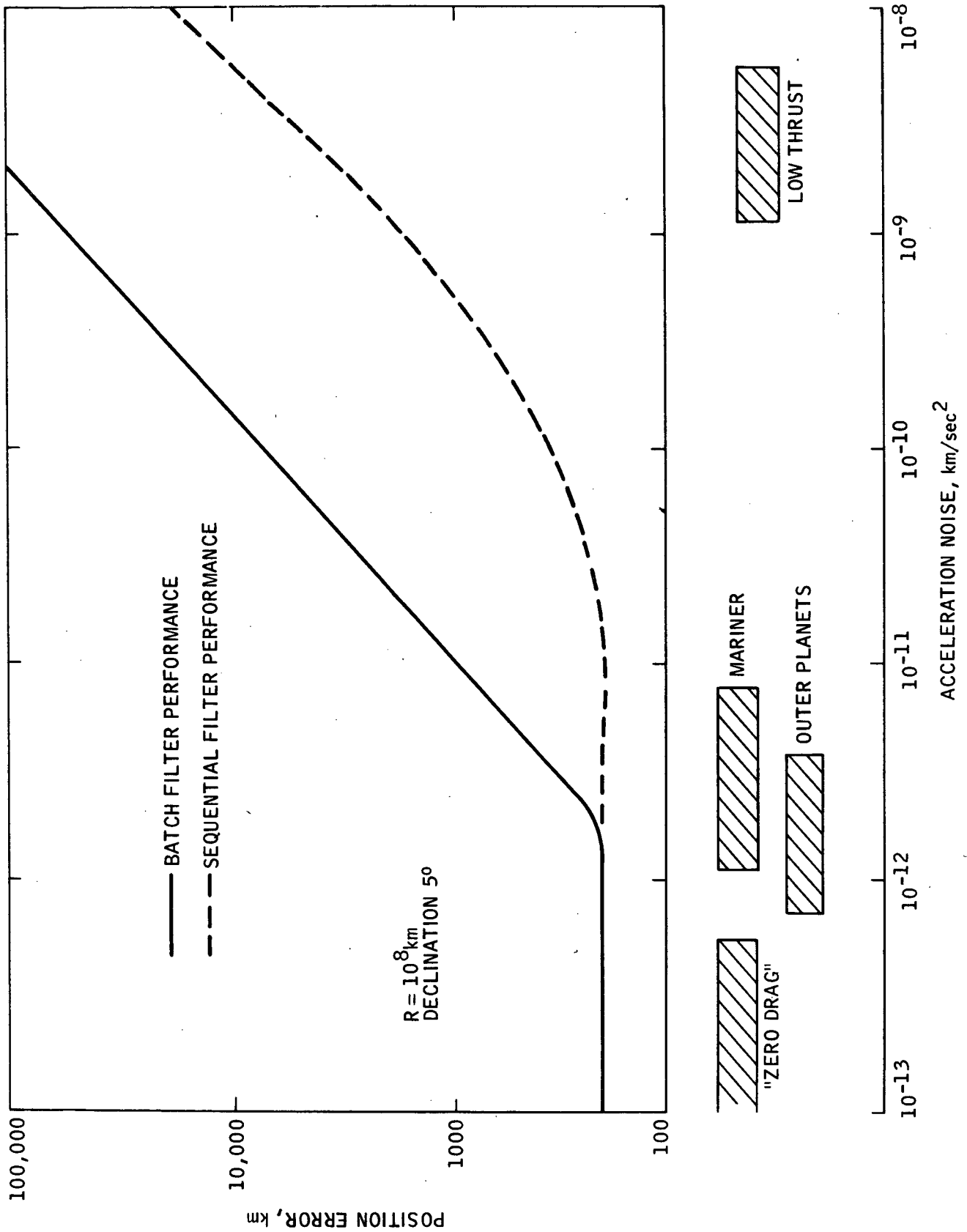


Fig. II-B-3. Comparison of Batch and Sequential Filter Performance

position accuracy as acceleration noise is increased can be seen. Two popular orbit estimation techniques are illustrated. Because the current system is expected to produce acceleration errors up to 10^{-8} km/sec² in magnitude, innovations are necessary to reduce the impact of noise on accuracy, with an ultimate goal of approaching the accuracies of ballistic missions.

Batch processing of low thrust data is not appropriate. Sequential estimation is more promising, but current filters are far from adequate. Better filters can be devised, but this may require better models of the random noise process; this is difficult. The best filter would possibly be an adaptive type, second-order filter which can approach "ideal" performance even in a changing environment, although even this may not be good enough.

Another approach would be an attempt to directly measure the acceleration disturbance, instead of trying to model its behavior. Still another approach would be to find some unique data type (other than conventional doppler) which would be insensitive to this kind of disturbance. Because all of these possibilities, and others, may have some merit, technology studies are necessary for the design of a low-thrust navigation system.

In addition to the acceleration noise problem, there are other problems caused by the level of available propulsive acceleration: (a) control with a low continuous acceleration precludes conventional ballistic maneuver strategies and (2) large corrections are often required near comet rendezvous because of dramatic improvements in ephemeris information; thus, control problems may be encountered.

After a feasible low-thrust navigation system is defined and developed, sensitivity studies can be performed to investigate the parameter effects on navigation performance. The most significant parameters are those used to model the random acceleration dispersions of the thrust subsystem. Studies of this kind not only solidify the navigation system design, but the results can also be used in a reverse role by thrust designers, who, on the basis of navigation performance, can determine the best set of thrust subsystem tolerances for design criteria.

2. Summary of NDT Study Results

Four main task areas need to be studied for Mk II navigation: (a) error modeling, (b) orbit estimation, (c) maneuver strategies, and (d) guidance. These tasks are related in pairs, respectively. An initial task for study of (a) and (b) is to model the unpredictable random accelerations dispersions of the thrust subsystem.

Modeling may or may not enhance the filter design; however, complete models are required for a total sensitivity analysis of hardware. Further, the orbit determination problem must be studied as an integral part of the navigation system. The ultimate lower level of accuracy (theoretical) is determined by the orbit estimation procedure employed.

The other pair of tasks, (c) and (d), are related in that adequate maneuver strategies and feasible guidance schemes to implement them must be determined. Because of Encke's dominate ephemeris uncertainty, navigation is separated into a cruise phase and a terminal phase. Cruise navigation of the spacecraft to within the ephemeris uncertainty of the comet is routine. However, once the spacecraft is in the vicinity of the comet, terminal navigation becomes critical in that rendezvous accuracies of ≤ 1000 km must be achieved within a very short period, typically, less than 20% of the cruise time. Therefore, controllability may be a serious navigational problem, depending largely on how soon spacecraft optics can acquire the comet.

a. Thrust-subsystem Error Model

Previous low-thrust studies have modeled the low-thrust subsystem acceleration errors as purely random stationary processes, with equal components in all three body axes (spherically distributed). No biases were assumed to exist in acceleration errors. There are arguments that this approach is conservative; however, it does not lend itself readily to relating accuracy sensitivities to specific hardware parameter sensitivities. As

mentioned earlier, a more complete model is needed to provide data for specifications of acceptable tolerances, useful for both operational design and manufacturing.

The basic approach is to first obtain parametric models of the thrust subsystem. Analytical parameter models are then converted to statistical models, with only those parameters which contribute significantly to eventual acceleration errors retained. Next, time-varying statistics are mapped into tractable random processes along both a principle thrust direction and perpendicular cross-axis components. These random processes are assumed to be stationary, unbiased, and time correlated (exponential, autocorrelated processes). Biases in these components are treated by superposition of a time-varying, first-order random process onto a similar process, whose time correlation value is infinite.

Unlike previous models, the major error sources were found to be basically dual in nature: those which are statistically independent (do not share a common error source), and those which are dependent, (common errors).

Thrust subsystem parameters such as beam current, beam voltage, mass utilization efficiencies, and beam-angle divergence can be treated as independent error sources. These error sources are rss proportional to the square root of the number of engines on the basis of total thrust. Dependent error sources occur because of errors introduced through a common source such as the celestial sensor-attitude reference system, or the thrust-vector control system. In contrast to statistically independent errors, common errors increase in proportion to the number of engines. Consequently, the current model yields acceleration errors which are not symmetrical about the thrust axis.

The independent error sources and their standard deviations are discussed in Section 3. The rss value of these errors (except the angle, β) represents the total time-varying standard deviation in acceleration error along

the principle thrust axis caused by one engine. This value is calculated as 3.5% (6.35% is the maximum value, i.e., when the errors are summed). Correspondingly, the rss of the biases is 2.2%.

Cross-axis acceleration errors result from both independent and dependent error sources. The independent errors, such as plate warpage, $\bar{\beta}$, do not actually vary with time, since plate warpage attains a permanent set. The long correlation time reflects the bias nature of this quantity. A 1- σ value of this component was estimated at 1.2%.

The dependent error contribution, caused by pointing errors, is much less significant. A time-varying drift in the celestial reference system produced acceleration errors less than 1%, with a bias contribution less than 0.1%. Also, a candidate thrust-vector control system was examined as a dependent contributor to the cross-axis acceleration errors. It is shown that, if a closed loop control system, such as the translating system proposed at JPL, is used, maximum acceleration errors are produced on the order of only 0.5%; these errors are quite negligible. However, there are other systems currently being proposed, which produce significantly larger errors, on the order of one radian. Consequently, to cover all possibilities, conservative estimates of this component, which amount to 1%, are used in the orbit determination analysis.

Lastly, statistical independence of the parameter vectors was assumed. This assumption is justified under normal operations; however, operation in certain failure modes could invalidate this model. Notwithstanding the degree of sophistication, the error model still serves adequately as a basis for a much needed sensitivity analysis, which relates hardware parameter errors to orbit estimation performances.

b. Orbit Determination

An integrated program was undertaken whereby a software development program and a mission navigation study were merged. From the outset, design of orbit estimation processes to resolve the ambiguities caused by the presence of unpredictable acceleration dispersions dominated the early activities of the NDT.

As discussed previously, the spacecraft can remain in cruise configuration, navigating within the earth-based ephemeris uncertainty of the comet up to the terminal phase, when a Mk II navigation system is required. This fact establishes the framework for the design of the orbit determination software, consisting of filter models and tracking strategies. Proper filter design and tracking strategies can be adequately designed through accuracy comparisons of steady-state orbit parameter estimates (position and velocity at some epoch), and by the rate at which the estimation filter attains steady-state values. Steady-state values can be obtained from a single data arc, strategically located, so that the results are representative of all such data arcs. A typical 30-day arc, which can be used for both the cruise and terminal phases, was selected to be located near the end of the mission.

The following possible solutions to the "process noise" problem (unpredictable random acceleration errors) were considered:

- (1) Precise error modeling (second order models).
- (2) Adaptive filtering (real time identification of process noise statistics).
- (3) Inertial (accelerometer) data.
- (4) Types of data insensitive to process noise (optical and radio).

It would be logical to analyze types of data first, although the reasons for this choice are not obvious. For example, consider approach number three. Concurrent studies by the University of Texas (Ref. II-B-2) have shown that the use of inertial accelerometer data is not feasible unless "precise gyro platform alignment (within .01 deg) and very low noise-to-signal ratios (.07) in the accelerometers are maintained." However, this type of data could still be effective in combination with one or more of the alternative schemes. Furthermore, first-order error models may be sufficient for the first two solutions, and the improvements of various types of data should be studied before more complex software with second-order error models, and adaptive filtering are investigated. Consequently, the fourth proposition was initially selected for further detailed orbit determination studies.

Orbit estimation processes are often characterized by the filter model and the baseline standard deviations assumed. A batch-sequential (discrete sequential filter), square-root filter design was developed to effectively utilize as much of the ballistic batch software as possible. Companion orbit estimation algorithms were constructed with filter models compatible with the error modeling discussed in Section II-B-3. Baseline standard deviations for thrust-axis errors were used. These deviations correspond to a configuration for four thrusters assumed operating over the entire 30-day data arc. Assumptions for the baseline values in the cross-axis directions were conservative compared to the model estimates indicated in Section II-B-3. The estimates were representative of worst-case spacecraft designs. Assessments of the cross-axis standard deviations of better designs appear to be approximately equal to one third of the baseline values used. However, since one of the primary study-objectives involves a sensitivity analysis, baseline selections can be somewhat arbitrary.

Several tracking strategies, representative of the cruise portion of the mission, were compared. Tracking strategies for the cruise phase consist of using various configurations and operations of earth-based tracking stations, from single-station tracking to multiple-station configurations. However, the actual measurements to be taken by each station still consist of standard doppler and range data. Projected 1980 data-measurement accuracies were taken to be 3 m and 1 mm/sec for two-way range and doppler data, respectively.

The orbit determination results were not totally unexpected. An 'optimal' filter model (theoretically, the best that can be done) with a multi-station configuration, representing a type of combined data consisting of two-way and three-way data processed simultaneously, virtually eliminates the process noise problem. Steady state rms position accuracies are on the order of 35 km. QVLBI is a similar type of data, except that the two-way and three-way data are explicitly differenced. This type of data yields even better values of position accuracy (24 km). On the other hand, there is a severe order of magnitude degradation in accuracy, if only single-station conventional doppler is used.

The precise accuracies obtainable from the multistation types of data are not required for cruise in the Encke mission because the ephemeris uncertainty is on the order of 30,000 km before recovery. According to the optimal filter results, single station doppler with range yields accuracies well within Encke's ephemeris uncertainty. A preliminary conclusion would indicate the use of single-station tracking during cruise, and multiple stations during the terminal phase.

However, the optimal filter approach assumed the modeling to be perfect, and this will certainly not be the case. Some indication of the impact of less perfect knowledge on the accuracy can be observed from the batch filter results, which indicate the accuracies when almost the worst model is used instead of the best (see Section II-B-4). The batch filter models only the bias effects. The multistation type of data, QVLBI, degrades 2680 km, while the other data types are orders of magnitude larger. It is through these magnification effects produced by modeling errors that the real advantages of the QVLBI data are realized.

However, in reality, our knowledge of modeling errors is expected to be considerably better, although some uncertainty is expected. For example, if needed, second-order models (or other conventional filter techniques) can always be used to reduce model error effects to some degree. Since the worst-case results can be tempered, preliminary conclusions can still be valid, even if model errors degrade optimal accuracies by one order of magnitude.

Realistic answers to these modeling error effects are important to the practical operation of the DSN tracking facilities. Daily tracking with multiple stations for 900 days is unrealistic, but it is feasible over short periods, such as the 60-day terminal phase, when it is really needed. Even this may be an inordinate requirement. However, during the terminal phase, additional optical data, which is also insensitive to process noise, will be available to compensate for the effects of tracking less frequently with the DSN.

However, the more important question to assess is the cruise-tracking DSN duty requirements over approximately 80% of mission time. As mentioned earlier, even with a one order of magnitude degradation in accuracy, cruise tracking can still be accomplished by conventional, single-station techniques. Tracking frequency analysis indicates that a tracking data pass taken only once per week is a reasonable DSN duty cycle to provide the needed cruise-accuracy requirements.

Orbit determination analysis provided several other results, such as the effect of station location errors, SEP thrust-subsystem parameter sensitivity analysis, and rudimentary simulation results to enhance existing knowledge of the realistic impact of imperfect modeling. Sensitivity studies were made to investigate the impact of the optimal filter performance caused by fluctuations in the baseline standard error deviations of the thrust-subsystem parameter error model. The sensitivity studies show that the multistation data, MS3W and QVLBI, are generally less sensitive to baseline changes of the thrust-subsystem error model than other tracking strategies. Of the other strategies, single-station accuracy sensitivities indicate that these types of data are more sensitive to changes in the model error assumptions related to orientation angles than to changes in the expected errors of the thrust magnitude parameters.

c. Maneuver Strategies

Orbit determination provides the current-state estimate required as input to any control guidance scheme employing any one of a variety of possible maneuver strategies. The control policy will usually depend on the current estimate of the vehicular state and the definition of the performance criteria. Admissible control corrections will in all probability be subject to one or more control constraints. Maneuver strategies employing a feedback control system can either be linear or nonlinear, depending upon the model assumed for the transfer function. A linear system described in Section II-B-5 was selected as the initial basis upon which a more general software design can be adapted, if needed.

It is well documented that the low thrust spacecraft can be navigated during the cruise portion of the mission, to within Encke's large

ephemeris uncertainties. Typically, only a single continuous correction less than 100 m/sec near the midpoint of the cruise phase is sufficient to maintain accuracies well within these ephemeris uncertainties, requiring almost a negligible amount of fuel. However, as the spacecraft nears encounter, the ephemeris uncertainty can suddenly improve after acquisition by the onboard optical sensors; however, the spacecraft may not have enough time to obtain the required orbit correction using only the low thrust system, and the question of controllability could become critical. In any case, the terminal guidance problem has significantly more impact on the low thrust navigation design, especially since final rendezvous accuracy will be uniquely determined by the performance of the terminal guidance system.

A linear terminal maneuvering strategy was constructed to study the accuracy limitations associated with terminal guidance. In particular, guidance accuracy sensitivities to the level of the process noise (acceleration errors) can be determined as a means of determining thrust-subsystem tolerance limitations on various model parameters. By using both the QVLBI and optical data as the means of performing the orbit estimation, some limiting steady-state accuracy can be achieved, virtually independent of the level of process noise present. However, the spacecraft can never achieve this accuracy because random acceleration errors continually inhibit its ability to completely make the necessary orbit corrections. Unlike the orbit estimation problem, an increase in the process noise can degrade the terminal accuracies achievable because of an increased guidance inefficiency. As a supplement to this important study, the effectiveness of onboard ranging, as an additional device to improve accuracy, can be evaluated in conjunction with the effects of various approach geometrics.

The guidance scheme simulated attempts to control state deviations from a reference path, using at most only three control parameters. The scheme is general enough to consider hardware bounds on the control parameters and weight certain state deviations over others. The control policy is devised to avoid the possibility of controllability problems which characterize many standard terminal controllers. This new policy requires that the current

control effort must minimize the projected terminal errors without regard to future control opportunities, so that every effort is put forth in reducing terminal errors as soon as possible.

For purposes of numerical studies, in particular, the thrust-subsystem sensitivity study, conservative estimates were assumed wherever numerical values were needed. The initial ephemeris uncertainty in the position of Encke was assumed to 30,000 km, a value representative of Encke's ephemeris uncertainty before earth recovery. The velocity uncertainty was on the order of tens of meters per second. In the various studies discussed, the standard deviations of the angle measurement error were taken to be 100 arc sec, 10 and 1 km, respectively. Control bounds of $u_{\max} \cong 10 \text{ deg } (3\sigma)$ were imposed to limit the possible thrust vector angle deviations. An acceleration percentage of $\sim 18\%$ (four thrusters), spherically distributed, was assumed for a process noise baseline value.

The guidance scheme itself possesses several unique and desirable features which avoid the controllability problems associated with conventional terminal regulators. As such, a scheme based on these principles is a feasible candidate for a low-thrust guidance breadboard program.

Numerical results presented in Section II-B-5 contain a complete set of parametric data, relating all possible terminal velocity accuracies obtainable to all possible terminal position accuracies obtainable, given a terminal guidance time to rendezvous for several possible choices of weighting factors. Regions of feasible rendezvous and flyby possibilities are superimposed to indicate areas of probable interest.

The strategy discussed is the conventional, but more demanding, maneuver of reaching rendezvous accuracies without delay. There are other, less stringent strategies proposed which employ a series of delayed maneuvers, permitting ample time for corrections to be made.

The following conclusions were reached:

- (1) In spite of the large ephemeris uncertainties of Encke, rendezvous is possible if onboard navigation is initiated no later than 40 days prior to nominal encounter.
- (2) The reduction of terminal state errors becomes more difficult as the process noise levels are increased. At levels above 5% of the nominal thrust acceleration, rendezvous cannot be achieved if terminal navigation begins later than 50 days prior to encounter.

The last important result of this study concerns the design of a feasible navigation system. Optical data contains no range information, so that, in lieu of an onboard ranging device, many previous studies have included an offset bias during the final approach so that range information can be inferred from the optical data. It is shown in Section II-B-5 that the use of a curved nominal approach trajectory permits orbit determination without relative range measurements and without the use of an artificially imposed bias.

d. Guidance Analysis

Section II-B-5 develops the necessary maneuver strategies applicable to the terminal rendezvous phase. However, maneuver strategies are only part of an overall guidance system which must execute the maneuvers. For this low-thrust mission, the chief design problem critical to successful execution of the corrective maneuvers is the onboard optical system. Therefore, a guidance study was performed to investigate potential problem areas.

To begin with, a candidate optical system must be able to see the comet before executing any terminal maneuvers. In addition, guidance considerations fix a lower bound on the time to execute the maneuvers, given a certain level of process noise. On the other hand, the earlier the comet can be detected, the less stringent the requirements on thruster-subsystem tolerances and guidance effort. For example, if the comet can be detected before

JPL Technical Memorandum 33-583, Vol. III

encounter time minus fifty days (E-50 days), the terminal maneuver analysis indicates that a 5% level of process noise is still acceptable for a successful mission. With these design tradeoffs in mind, it is easy to see the importance of an optical sensor analysis.

The only real data available on the performance of an imaging system is the experimentally derived detectability data for the Mariner Mars 71 B (telephoto) camera. The source of the data was the Mariner Mars 71 optical navigation demonstration (OND). Everything else is pure hypothesis. However, the impact of various hypothesis can be assessed by synthesizing the postulated photometric characteristics of the comet in terms of Mariner camera nominal parameters.

More specifically, the fundamental approach used in the optics analysis for guidance was to combine the suggested comet brightness models and integrated photometric data with the experimentally derived detectability data.

For a 100% confidence level, a star detectivity threshold of 7.5^m was used as the reference for visual magnitude comparisons, with integrated surface brightness assumed to be imaged over a single picture element. In this manner, different surface brightness models can be compared to assess the impact of imprecise comet photometric knowledge on the design of a practical optics system.

Basically, magnitude curves for the brightness of the pertinent components of the comet model are generated as a function of comet geocentric distance with time to encounter. Given a set of optical parameters, nominal integration times can be determined for both point source and central halo radii of 100 km to 2500 km, respectively. Nominal recovery is assumed to occur at E-60 days to account for uncertainties in the photometric model.

The results contained in Section II-B-6 are most significant. If an ample margin of integration time is designed into the optics system to

allow for brightness variations (exposure time or shutter speed), optical recovery can be made as early as E-60 days regardless of whether the comet appears as a point source or an extended source. If factors are weighted toward the extended source models, the design margin on the integration time amounts to about 11 sec on the average. The extra integration time amounts to an additional 20%, but it provides for a detectability range in terms of visual magnitude of 2 about a reference of 7.5^m . If the probable uncertainty in visual magnitude is assumed to be larger, longer integration times should be designed into the system.

In Section II-B-6, these results are shown to hold true for a range of Mariner camera designs, ranging from a maximum sensitivity design, having a focal length of 150 mm (aperture diameter was assumed to be 20 cm) to a much less sensitive design having a focal length of 400 mm.

3. SEP Thrust Subsystem Statistical Error Model

The principle objective of the thrust subsystem sensitivity task under the NDT is to evaluate the impact of electric engine parameter uncertainties on navigation accuracy, assuming the baseline mission to be a rendezvous with the comet, Encke, in the early 1980s. It is anticipated that this study will identify all significant thruster parameter sensitivities to encounter accuracy. The resulting data will permit the specification of acceptable tolerances in both manufacturing and thrust-subsystem operational performance.

The SEP thrust subsystem statistical error model was developed as a tool for investigating the effects of thrust subsystem parameter uncertainties on navigation accuracy. The data presented here is unique because it represents the first attempt to establish a navigation/thrust subsystem interface through hardware considerations and constraints.

a. Introduction

The use of continuous thrust for deep space missions presents navigation problems that are ordinarily non-existent in ballistic missions.

These problems arise from the presence of proportionately large random accelerations resulting from uncertainties in the direction and magnitude of the thrust vector. Therefore, a consideration of principal concern to the study of thrust tolerance relative to navigational accuracy is the construction of a realistically adequate model and statistics for the expected behavior of the random accelerations. Current navigation analyses consider the stochastic process for the random accelerations (process noise) to be stationary and spherically distributed with exponential autocovariance,

$$R(t, \tau) = \sigma^2 e^{-\frac{|t-\tau|}{\alpha}} [I] \quad (3 \times 3) \quad (1)$$

where σ is the process variance and α is the correlation time. The specification of acceptable tolerances in thrust subsystem operational performance can be achieved only if the variations in the parameters which affect thrust production are properly accounted for.

Although the simplified model given by (1) is tractable and possesses a certain degree of physical justification (Ref. II-B-3), it fails to correlate uncertainties in thrust to uncertainties in the dominant thrust subsystem parameters and the factors that contribute to them. To meet this deficiency, knowledge of the dominant error sources and their interactions is obtained by investigating the composition of the component parts of the thrust system and all related subsystems, e. g., attitude and thrust vector control.

A realistic model is therefore achieved by meeting the following general objectives:

- (1) Define a hardware model for the thrust system and all related system functions.
- (2) Derive a perturbation model relating changes in thrust in terms of engine parameter and related errors.
- (3) Translate expected random behavior of parameter variations into statistical variables.

- (4) Map statistics of parameter variations into statistics for thrust variations using the thrust perturbation model.

b. Definition of Fundamental System Functions

The fundamental system of related functions chosen for analysis is shown in Fig. II-B-4. The thrust system receives conditioned solar power from N power conditioner units. The thruster array is composed of N operating thrusters and M spares (a five-thruster array, one spare are shown without loss of generality). The switching network couples the power conditioner units to the thrusters so that all operating thrusters are connected to separate power conditioner units.

Attitude and thrust vector control (TVC) are achieved simultaneously by means of a two-degree-of-freedom translator mechanism. Control about the third axis normal to the plane of translation is achieved by differentially gimbaling two of the engines. The TVC mechanism is actuated in discrete steps by means of a stepper motor. Attitude control is maintained by celestial references, traditionally, the sun, and a convenient reference star. Sensors used to implement the celestial reference system are two single-axis sun sensors and a star tracker.

c. The Generalized System Covariance Model

Variations in the net thrust vector with respect to set of reference body coordinates are considered to occur from two processes: (a) changes in the nominal thrust in body coordinates and (b) rotations of the body coordinate system. Further classification of the error sources in a statistical sense provides data concerning the correlation of random variables. Errors of a specific type (i.e., voltage, current, etc.) which do not share a common source will be independent in a statistical sense, resulting in a root-sum-square net contribution. Conversely, an error that shares a common source will be perfectly correlated in a statistical sense, resulting in a summation of the

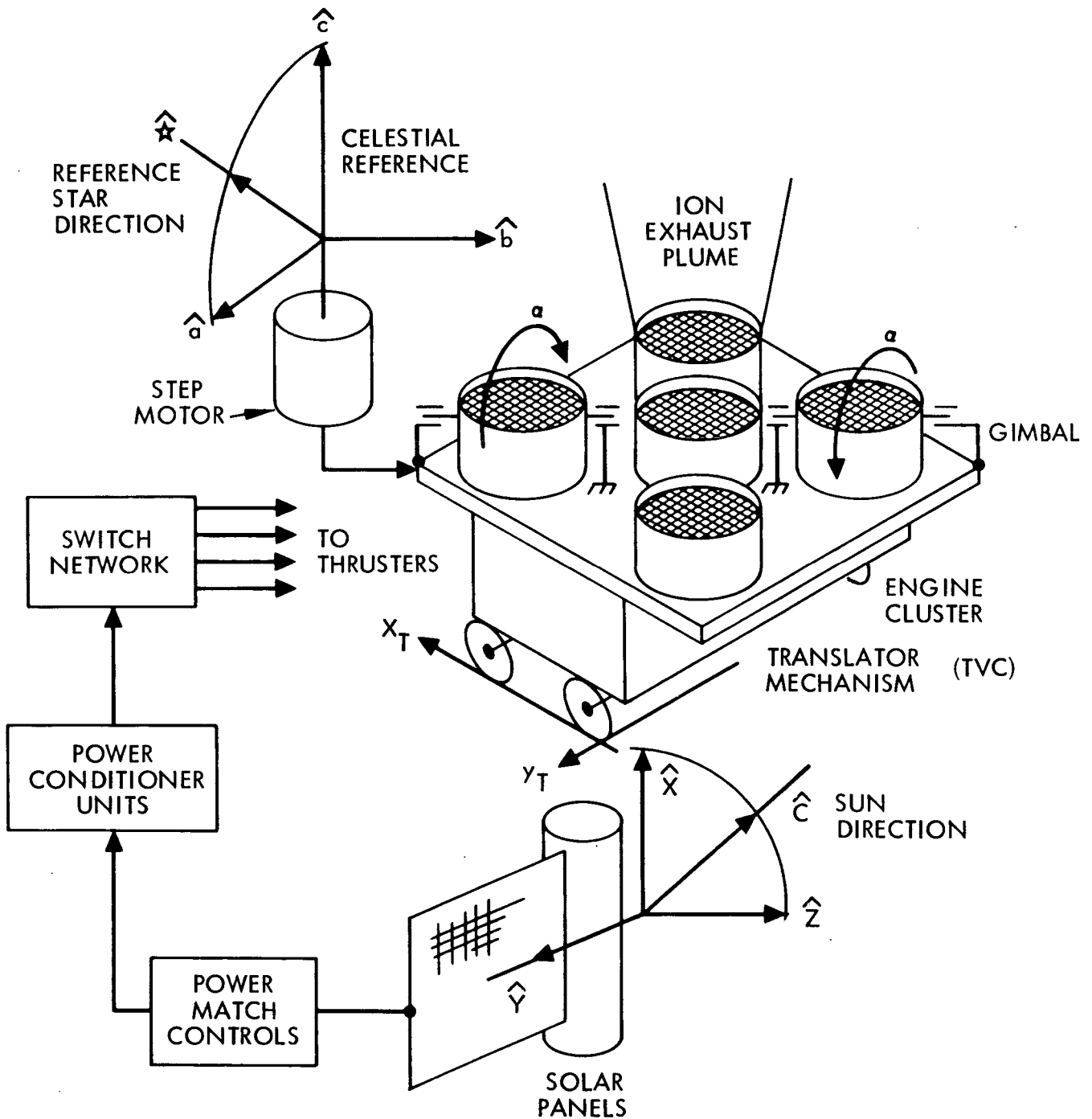


Fig. II-B-4. Fundamental System Functions

contributions of the errors individually. However, the collection of all thrust parameter variables is assumed to be statistically independent to first order.

Symbolically,

$$W_i = \sum_{k=1}^N \sum_{j=1}^M A_{ijk} \lambda_{jk} + \sum_{k=1}^N \sum_{j=1}^L B_{ijk} \gamma_j$$

for each component W_i of the normalized thrust⁽¹⁾ error vector in the reference coordinate system. The summations are carried out over the total number of operating thrusters N , the number M of independent errors, λ_j , and the number L of common errors, γ_j . In vector formulation, the thrust error is

$$\bar{W} = \sum_{i=1}^N A_i \bar{\lambda}_i + \sum_{i=1}^N B_i \bar{\gamma} \quad (2)$$

where to first order in the errors, $A = \frac{1}{T_o} \frac{\partial \bar{T}}{\partial \bar{\lambda}}$, $B = \frac{1}{T_o} \frac{\partial \bar{T}}{\partial \bar{\gamma}}$

$\bar{T}(t)$ is the nominal thrust vector per thruster and T_o is the total thrust.

Normalized random errors $\bar{\lambda}$ and $\bar{\gamma}$ assume the general form

$$\bar{\lambda}_i = \bar{\lambda}_{o_i} + \bar{\lambda}_i(t)$$

$$\bar{\gamma}_i = \bar{\gamma}_{o_i} + \bar{\gamma}_i(t)$$

where $\bar{\lambda}_{o_i}$, $\bar{\gamma}_{o_i}$ are biases, and $\bar{\lambda}_i(t)$, $\bar{\gamma}_i(t)$ are time varying components. It is assumed that the magnitude of the error is not a function of thrust, and that bias and time varying components are independent.

(1) Normalized variable = $\frac{X}{X_o}$, where X_o is the nominal value.

JPL Technical Memorandum 33-583, Vol. III

It has been assumed that the probable behavior of a single engine is representative of the engine cluster as a whole. This assumption provides a great computational savings because only the average response of the navigation process to a representative set of uncertainties in the thrust process need be investigated.

The assumption of statistical independence for the elements of the random parameter vectors $\bar{\lambda}$ and $\bar{\gamma}$ is entirely justifiable for normal operating conditions. However, operation in certain failure modes could induce correlation between parameters; e.g., if the control loop regulating the main beam were opened, drifts in the accelerator, screen and anode power supplies would induce drifts in beam current.

The autocovariance matrix is the expected value of (2) at arbitrary times t_1 and t_2

$$\begin{aligned} R_w(t_1, t_2) = & \sum_{i=1}^N A_i E [\bar{\lambda}_i(t_1) \bar{\lambda}_i^T(t_2)] A_i^T \\ & + \sum_{i=1}^N B_i E [\bar{\gamma}(t_1) \bar{\gamma}^T(t_2)] \sum_{i=1}^N B_i^T \end{aligned} \quad (3)$$

Define

$$\Lambda_i(t_1, t_2) = E [\bar{\lambda}_i(t_1), \bar{\lambda}_i^T(t_2)]$$

$$\Gamma(t_1, t_2) = E [\bar{\gamma}(t_1), \bar{\gamma}^T(t_2)]$$

where,

$$E[\lambda_{ij} \lambda_{ik}^T] = 0, \quad j \neq k$$

$$E[\gamma_i \gamma_j] = 0, \quad i \neq j$$

Equal throttling of all operating thrusters is assumed so that the mapping matrices A, and B remain invariant from thruster to thruster ($T_o = NT$).

Finally, it is assumed that the autocovariance for the λ_{ij} are identical in agreement with a previous assumption, so that

$$\Lambda_i = \begin{bmatrix} R_{\lambda_1}(t_1, t_2) & (0) \\ \vdots & \vdots \\ (0) & R_{\lambda_M}(t_1, t_2) \end{bmatrix} \quad \text{all } i = 1 \dots N$$

Similarly, the autocovariance for the correlated error sources is

$$\Gamma = \begin{bmatrix} R_{\gamma_1}(t_1, t_2) & (0) \\ \vdots & \vdots \\ (0) & R_{\gamma_L}(t_1, t_2) \end{bmatrix}$$

Equation (3) takes the form

$$\underline{R_w(t_1, t_2)} = \frac{1}{N} A \Lambda(t_1, t_2) A^T + B \Gamma(t_1, t_2) B^T \quad (4)$$

The preceding calculations indicate that all independently derived error sources ($\bar{\lambda}$) rss proportional to \sqrt{N} on the basis of total thrust (ΔT) and decrease in proportional $\frac{\sqrt{N}}{N} = \frac{1}{\sqrt{N}}$ on the basis of percentage change in total thrust ($\frac{\Delta T}{T_o}$). Common errors ($\bar{\gamma}$) add in proportion to N on the basis of total thrust and contribute the same amount on the basis of percentage change.

d. Stochastic Process Considerations

Choosing a random process to adequately represent the stochastic behavior of the thrust and related system parameters is difficult because of the lack of any statistical data derived by experimentation. Meaningful experiments are virtually impossible because of the long correlation times involved. In lieu of this data, some intuitive assumptions about $\lambda_i(t)$ must be made. It is desirable that $\lambda_i(t)$, $\gamma_i(t)$ process the following properties (Ref. II-B-4):

- (1) The process should possess a unimodal probability density function. This implies that small values of the noise are expected to occur more often than large values.
- (2) The process should be unbiased, i.e., the statistical average of the noise should tend to zero.
- (3) The process should be autocorrelated in time. This is necessary because dominant variations in the process behavior are expected to occur at frequencies within the bandwidth defined by the characteristic frequency of the spacecraft dynamics.
- (4) The process should be stationary. This implies that the variance of the noise is expected to remain constant in time.

A process which fits the preceding description was introduced by Ornstein and Uhlenbeck (Ref. II-B-5) as a model for the velocity of a particle undergoing a Brownian motion. The statistical properties of the Ornstein-Uhlenbeck (O.U.) process are defined by the following relations:

- (1) The probability density function is unimodal

$$f [x(t)] = \frac{1}{\sqrt{2\pi} \sigma_x} e^{-\frac{1}{2} \left[\frac{x(t)}{\sigma} \right]^2}$$

where σ_x is the standard deviation of the process.

- (2) The O.U. process is unbiased

$$E [x(t)] = 0$$

- (3) The O.U. process is exponentially autocorrelated in time

$$R_x(t_1, t_2) = \sigma_x^2 e^{-\alpha |t_2 - t_1|} \quad (5)$$

where $1/\alpha$ is the correlation time of the process and, since $R_x(t_1, t_2)$ depends only on the time difference $(t_2 - t_1)$, $x(t)$ is stationary.

There exists a duality between the continuous Markov process characterized by the "random walk" and the O.U. process because both processes satisfy a Langevin equation of the form

$$\dot{x}(t) = -\alpha X(t) + u(t) \quad (6)$$

where $u(t)$ is Gaussian white noise, i.e.,

$$E[u(t)] = 0$$

$$R_u(t_1, t_2) = Q \delta(t_2 - t_1)$$

The definition of the process given by (6) is particularly useful when formulating problems in state space. The noise is conveniently represented by adjoining the state vector with the stochastic vector \bar{X} .

e. Thrust System Error Model

The nominal thrust from a single thruster is given by the relation

$$T = K \left(\frac{\eta_1 + \sqrt{2} \eta_2}{\eta_1 + 2\eta_2} \right) I_B \sqrt{V_B} (\overline{\cos \theta} \cos \beta) \zeta$$

where

$$K = \sqrt{\frac{2m_o}{e}}; \quad m_o = \text{mass of atomic mercury } (3.34 \times 10^{-25} \text{ kg})$$

$$e = \text{electronic charge unit } (1.6 \times 10^{-19} \text{ coul})$$

$$I_B = \text{Ion current in the exhaust beam, } = (\eta_1 + 2\eta_2) \frac{e}{m_o} \dot{m}$$

$$\dot{m} = \text{Mass flow rate (kg/sec)}$$

$$V_B = \text{Net ion acceleration potential}$$

$$\eta_1 \eta_2 = \text{Mass fraction of the total flow rate in existing as singly and doubly charge mercury atoms, respectively.}$$

$$\overline{\cos \theta} = \text{Exhaust beam divergence factor, abbreviated } \overline{C\theta}$$

$$\zeta = \text{Thrust recovery tolerance factor} = 1 + \epsilon$$

Normalized perturbations in the thrust vector \bar{T} along T is written generally as

$$\left. \frac{\Delta \bar{T}}{T} \right|_x = \sum_{i=1}^N \frac{1}{T} \frac{\partial T_x}{\partial \left(\frac{x}{x_o} \right)_i} \Delta \left(\frac{x}{x_o} \right)_i \quad (7)$$

Define

$$a_i = \frac{1}{T} \frac{\partial T_x}{\partial (\frac{x}{x_o})_i} = [1, \frac{1}{2}, k \frac{\eta_2}{\eta_1}, -k \frac{\eta_2}{\eta_1}, 1, \epsilon_o] \quad (7a)$$

$$-k = 2 - \sqrt{2}$$

and

$$\bar{x}_{x_o} = [\frac{\Delta I_B}{I_B}, \frac{\Delta V_B}{V_B}, \frac{\Delta \eta_1}{\eta_1}, \frac{\Delta \eta_2}{\eta_2}, \frac{\Delta \bar{C}_\theta}{C_\theta}, \frac{\Delta \epsilon}{\epsilon}]^T \quad (7b)$$

Perturbations normal to \bar{T} are written

$$\Delta T_{y,z} = -[Tx] \bar{\beta}$$

where

$$-[Tx] = \begin{bmatrix} 0 & -T_x \\ T_x & 0 \end{bmatrix} = \frac{\partial \bar{T}}{\partial \bar{\beta}} \Big|_{y,z}$$

$$\bar{\beta} = \beta_y \hat{Y} + \beta_z \hat{Z}$$

where β_x, β_y are the accelerator and/or screen warpage and misalignment angles, and \hat{Y}, \hat{Z} are unit vectors in vehicle coordinates*.

Perturbations in \bar{T} normal to \bar{T} are therefore given by

$$\frac{\Delta T}{T}_{y,z} = \begin{bmatrix} 0 & 1 \\ -1 & 0 \end{bmatrix} \begin{bmatrix} \beta_y \\ \beta_z \end{bmatrix} = \frac{1}{T} \frac{\partial \bar{T}}{\partial \bar{\beta}} \bar{\beta} \quad (8)$$

where $\bar{\beta}$ has the dimension of radians.

* $\hat{X}, \hat{Y}, \hat{Z}$ are the vehicle-body-axis coordinate system of unit vectors where X is aligned with the net nominal thrust and Y is aligned with the solar panels.

The following summary data (Ref. II-B-6) represents current knowledge of the uncertainties and contributing factors concerning the parameters given in equations (7):

- (1) V_B is the net potential difference experienced by the ions formed in the thruster from their point of formation to their point of departure from the spacecraft field of influence. This voltage will be uncertain to within about 4 V because of varying line drops and uncertainties in the thruster plasma potential and the ion beam exit potential. An additional voltage uncertainty is caused by the regulation of the main beam power supply. For the present units, this is 1%, or 20 V. The combination of these two factors gives an uncertainty of about 0.5% in the thrust and the specific impulse.
- (2) I_B is the difference between the currents drawn by the main beam and accelerator power supplies and is the main control parameter for regulating thrust. Uncertainties in I_B arise primarily from the gain of the control loop, which regulates I_B , and from the drift in the reference that sets I_B . Present regulation schemes use type 0 controllers. The uncertainty introduced by the finite gain of the control loop coupled with the uncertainty in main vaporizer characteristics is on the order of 0.5 to 1%. Also, I_B is set by an analog reference signal against which the measured value of I_B is compared. Electronic components used to generate such analog signals, B, are subject to thermal and time-dependent drifts, which, if uncompensated, can result in an error of several percent. With reasonable compensation schemes, it is felt that this reference drift can be held to about 1%. Thus the total uncertainty in I_B is estimated to be on the order of 1.5% rss.

- (3) The electrostatic and mechanical geometries of the accelerating structure produce an ion beam composed of many hundreds of small, diverging beamlets. The angle of divergence of the individual beamlets varies across the exit grid and also varies in time as a function of the beam current density. Because of the difficulty in measuring an individual beamlet, no precise information is available on the true average beam-divergence loss. Faraday probe measurements in the ion beam are generally used to estimate the angle of divergence, but the errors in translating these measurements into a value of $\cos \theta$ are probably large. Current estimates of Faraday probe data will not give the divergence angle to better than ± 5 deg. The error or uncertainty that this introduces is obviously a function of the angle, which, in turn, is dependent on the electrostatic geometry. In general, divergence will increase with reduced specific impulse; it could vary from about 15 deg at 2 kV screen potential to up to 20 deg at 1 kV. It is estimated that, at 3000 sec, the inherent uncertainty in the value of $\cos \theta$ will be about $\pm 3\%$ around a base value of 0.96, and that $\cos \theta$ will vary with I_B , with the magnitude of this variation at present unknown.
- (4) The factor ζ is introduced to account for charge exchange and erosion effects. Examination of thruster accelerator grids indicates that most charge exchange ions originate downstream of the accelerator grid. The fast neutrals formed in the process then exit with a velocity higher than that of the ions, because they have not been decelerated through the full decel potential. This represents a slight thrust enhancement. A further small thrust enhancement is obtained by the release of material from the accelerator grid because of the charge exchange ion impact.

- (5) By far the most important factors contributing to subsystem performance uncertainties are those affecting the mass flow rate. Because at present no direct measurement of mass flow rate is available, it must be controlled from some a priori calibration. Present control schemes utilize the relationship between the discharge power and the mass utilization efficiency (as indicated by the ion beam) at constant flow rate to regulate propellant flow. This implies that an a priori calibration of $(\eta_1 + \eta_2)$ versus P_{TH} (conditioned power delivered to the input terminals of a single thruster) and a subsidiary calibration of η_2 versus V_4 (arc discharge voltage) are made. In flight, P_{TH} and V_4 are controlled, and η_1 and η_2 are assumed to follow the calibration curves. The difficulty with this scheme is the sensitivity of the calibration to a number of thruster parameters, including thruster geometry, magnetic field strength and geometry, division of flow between main and cathode vaporizers, cathode-keeper potential, total extraction voltage, and neutralizer coupling potential. These parameters will vary in time as a function of component aging, line and load variations, and subsystem random perturbations. Using present control schemes, the uncertainty in the initial calibration is probably on the order of 1%, and the variation in time on the order of $\pm 5\%$.
- (6) The angle β represents the achievable alignment accuracy of the thrust vector to the nominal thrust direction. This accuracy is a function of mechanical tolerances and the thermal load unbalance on the accelerating grids. No accurate measurements of β are available. However, a careful design should render β less than 2 deg (3σ). Current data indicates that β is time invariant, implying that the grid plates warp to

some maximum angles and attain a permanent set over the power profile. For the purpose of this study, β is considered time varying with long correlation time.

- (7) Thrust vectoring (gimballing) two of the thrusters (see Fig. II-B-4) reduces the net thrust in proportion to the cosine of the gimbal angle α ; the maximum gimballing angle is ± 10 deg. Because the thrusters are used to achieve closed loop attitude control, no a priori prediction of the vectoring loss can be made. However, α is not modeled as a random variable in the thrust error equation because it is assumed that the gimbal angles will be calibrated and measured to an accuracy such that the resulting error in thrust will be less than 0.10%. Table II-B-1 summarizes the current best estimates of the various error sources and their expected behavior as a function of time in accordance with the assumed O.U. process noise model.

f. Celestial Sensor Error Model

Thrust pointing error caused by errors induced in mechanization of the celestial reference system can only be estimated in an order-of-magnitude sense at this time because sensor mechanization and strategy for obtaining the celestial reference has not been established. However, the following considerations indicate a probable approach to be taken.

Ballistic missions in the ecliptic plane require a star tracker with aperture-center axis normal to the vehicle roll axis. Consequently this axis is directed toward the south ecliptic pole. Since Canopus is the brightest star near this location, it is used for roll reference. However, for deviations from ecliptic flight the large solar arrays can inhibit the field of view because the axis of the solar panels is constrained to be normal to the sun line for the chosen baseline mission; gross rotations of the vehicle about an axis tangent to the plane of the orbit thus renders Canopus viewing impossible during certain

Table II-B-1. Thruster Performance and Uncertainty Standard-deviation Summary Data

Parameter	Nominal Value	Calibration Accuracy (% Nominal)	A Priori Process Standard Deviation	Correlation Time	Contribution to $\Delta T/T$		
					Bias, %	Time Varying Component, %	
I_B	Programmed	± 0.5	$\pm 1.5\%$	weeks	0.5	1.5	
V_B	1 - 2 kV	± 0.5	$\pm 1.0\%$	weeks	0.25	0.5	
$\cos \theta$	0.96	± 2.0	$\pm 3.0\%$	weeks	2.0	3.0	
η_1	0.8 - 0.85	± 1.0	$\pm 5.0\%$	days-weeks	0.02 - 0.05	0.1 - 0.2	
η_2	0.04 - 0.07	± 20.0	$\pm 25.0\%$	days-weeks	0.5 - 1.25	0.5 - 1.0	
ϵ	0.005	± 30.0	$\pm 30.0\%$	days-weeks	0.15	0.15	
\bar{p}	0.0	--	$\pm \frac{2^\circ}{3}$	months	--	1.2 cross axis	
Note: Maximum at E -450 Minimum at E -0					2.0	.812	3.50
					0.0	0.0	1.20
					0.0	0.0	1.50
					Max	Min	Max
							Min

portions of the trajectory. The solution of the attitude reference problem will possibly involve any one or all of the following considerations: electrical and/or mechanical gimbaling of the star tracker, use of multiple reference stars, and sun-sensor gimbaling because of the need for solar-panel articulation. A simplified analysis of thrust pointing error caused by celestial reference mechanization is presented here in lieu of any design data concerning the above technique(s).

It is assumed that the celestial reference system is the sun and a convenient reference star. The sun sensors collectively have the equivalence of a two-axis sensor. Consequently, uncertainties in the sun-sensor output trace a solid angle as shown in Fig. II-B-5. The star tracker is sensitive to motion about or out of a plane. Therefore, uncertainties in the star-tracker output trace a wedge.

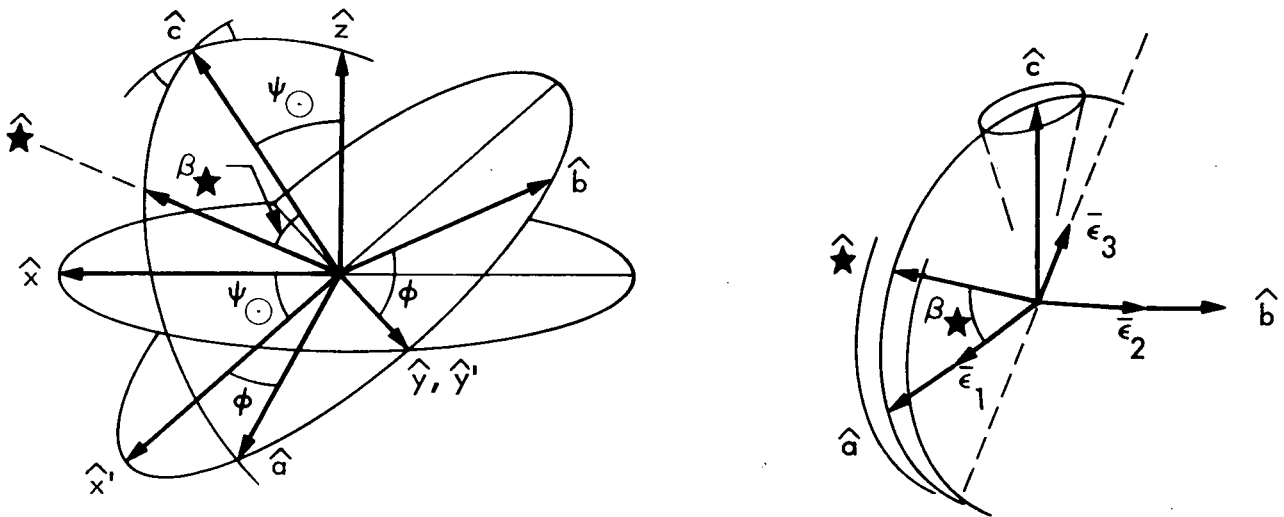


Fig. II-B-5. Celestial and Vehicle Coordinate System Relationships and Celestial Sensor Error Definition

It is assumed that $\bar{\epsilon}_1$, $\bar{\epsilon}_2$ and $\bar{\epsilon}_3$ represent small rotation vector derived from errors in the sun sensor, and star tracker respectively. Resolution of these errors into the celestial reference a, b, c gives equivalent errors \bar{e}_a , \bar{e}_b and \bar{e} .

$$\begin{bmatrix} \epsilon_a \\ \epsilon_b \\ \epsilon_c \end{bmatrix} = \begin{bmatrix} 1 & 0 & -\cos \beta_* \\ 0 & 1 & 0 \\ 0 & 0 & \sin \beta_* \end{bmatrix} \begin{bmatrix} \epsilon_1 \\ \epsilon_2 \\ \epsilon_3 \end{bmatrix}$$

The transformation from celestial to vehicle coordinates is specified as T_v^c and given by the relation

$$\begin{bmatrix} \hat{X} \\ \hat{Y} \\ \hat{Z} \end{bmatrix} = [\hat{a}; \hat{b}; \hat{c}]_{XYZ} \begin{bmatrix} \hat{a} \\ \hat{b} \\ \hat{c} \end{bmatrix}$$

where

$$\hat{b} \triangleq \frac{\hat{C} \times \hat{a}}{\sin \beta_*} \Big|_{XYZ}$$

$$\text{and } \hat{a} \triangleq \hat{b} \times \hat{c} \Big|_{XYZ}$$

as shown and noted in Fig. II-B-6*.

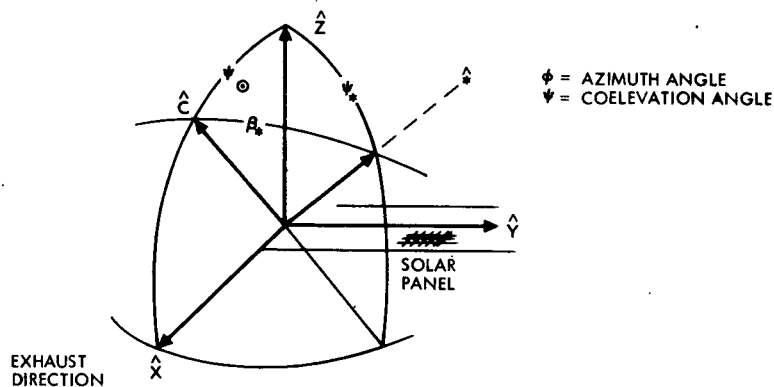


Fig. II-B-6. Definition of Reference Star Cone Angle in Vehicle XYZ

*The basis $\hat{a}, \hat{b}, \hat{c}$ is specified in the basis system $\hat{X}, \hat{Y}, \hat{Z}$.

The resulting mapping of celestial sensor errors $\bar{\epsilon}_{1,2,3}$ into equivalent errors in body coordinates is given by

$$\bar{\epsilon}_{XYZ} = [T_v^c E] \bar{\epsilon}_{123}$$

where

$$\bar{\epsilon}_{abc} \triangleq E \bar{\epsilon}_{123}$$

Contribution to cross-axis thrust uncertainties are given by

$$\Delta T_{y,z} = \bar{T} \times \bar{\epsilon}_{YZ}$$

In terms of percentage change in total thrust normal to \bar{T}

$$\left. \frac{\Delta T}{T} \right|_{y,z} = \begin{bmatrix} 0 & -1 \\ 1 & 0 \end{bmatrix} \begin{bmatrix} \epsilon_y \\ \epsilon_z \end{bmatrix} = \frac{1}{T} \frac{\partial \bar{T}}{\partial \bar{\epsilon}} \bar{\epsilon}_{yz} \quad (9)$$

Pointing error ϵ_y, ϵ_z was determined using sun-sensor errors only because the drift represents the dominant component of the angular uncertainty from a statistical point of view. Sensor biases and/or null offsets can be estimated in flight quite easily. However, the increase in knowledge of the average behavior of the random-time varying component is very slight. Nevertheless, the ability to estimate the state of the random process is increased as the correlation time becomes large.

Table II-B-2 summarizes current estimates of sun-sensor and star-tracker errors and their expected behavior as a function of time.

Table II-B-2. Summary of Estimated Sun-sensor and Star-tracker Errors

Sensor	Bias	Drift	
		Standard* Deviation	Correlation Time
(ϵ_1, ϵ_2) Sun Sensors	$\leq .08^\circ$	$.17^\circ$	days - weeks
(ϵ_3) Star Tracker	$\leq .05^\circ$	negligible	—

*Assumes a zero mean uniform distribution between $\pm .30^\circ$.

g. Thrust Vector Control

It has been shown that closed loop operation of the thrust vector control system results in a low-frequency, low-amplitude, limit cycle in each axis of the control system. This oscillation is a function of the electronic compensation time constants and the amount of backlash in the gimbal and translator actuators.

Tests have been run to show the effects of actuator backlash on the system. Table II-B-3 summarizes the results (see Ref. II-B-8).

Table II-B-3. Effects of Actuator Backlash

Actuator	Backlash, steps	Limit Cycle Period, min	Limit Cycle Amplitude, deg
Translator	1	30	0.002
Gimbal 1	0.6	30	0.003
Gimbal 2	6	30	0.03

However, the gimbal actuator with large backlash, as shown in the table above, will not meet the mission requirements because the margin is too small to allow for acquisitions, ion thruster changeovers, variations in external torques upon the spacecraft, and variations in the engine thrust profile. Reduced actuator backlash will promote a corresponding reduction in limit cycle amplitude. Using the worse case condition given in Table II-B-3, six-step actuator backlash yields a thrust pointing error of 0.5 mrad or 0.05% variation in the cross-axis thrust component. On the basis of the preceding data, it is concluded that thrust pointing error caused by thrust-vector-control mechanization errors is negligible.

h. Covariance Mapping

Covariance data for the thrust system and celestial sensors are mapped into covariance for percentage change in thrust $\Delta T/T$ by equation (4). The scalar autocorrelation function for the process noise is given by equation (5). The parameter transformation matrices A and B are

$$A = \begin{bmatrix} \frac{1}{T} \begin{bmatrix} \frac{\partial \bar{T}}{\partial x} \\ x_o \end{bmatrix} & (0) \\ \hline (0) & \frac{1}{T} \begin{bmatrix} \frac{\partial \bar{T}}{\partial \beta} \end{bmatrix} \end{bmatrix}_{3 \times 8} \quad B = \begin{bmatrix} 0 & 0 \\ 0 & \frac{1}{T} \begin{bmatrix} \frac{\partial \bar{T}}{\partial \epsilon} \end{bmatrix} \end{bmatrix}_{3 \times 3}$$

where the elements of the partitions are specified by equations (7), (8) and (9). All thrust parameter errors are assumed to be independently derived; thrust-pointing error caused by celestial sensor errors must appear as a common source to all thrusters. The mapping of the autocovariance of vector $\bar{\epsilon}_{yz}$ into component thrust autocovariance is

$$-\frac{1}{T^2} \begin{bmatrix} \frac{\partial \bar{T}}{\partial \epsilon} \end{bmatrix} E \left[\bar{\epsilon}_{yz} \bar{\epsilon}_{yz}^T \right] \frac{\partial \bar{T}}{\partial \epsilon} = \begin{bmatrix} \sin^2 \psi_o & 0 \\ 0 & 1 \end{bmatrix} \sigma_{ss}^2 e^{-\alpha_\epsilon |t-\tau|} \quad (10)$$

where σ_{ss}^2 is the sun-sensor error variance and the components ϵ_y , ϵ_z are assumed circularly distributed with the same correlation times. Sun-sensor errors are specified in the coordinate system defined by x' , y' , z , as shown in Fig. II-B-5. The inclusion of star-tracker errors in the model gives rise to thrust cross-correlation terms in y and z . However, the effect is probably negligible under the given set of assumptions concerning star-tracker drift. Figure II-B-7 indicates the relationship between the coelevation angle of the sun and the mapping of the sun-sensor variance. Parameter covariance matrices in normalized form are given by the following relations where subscripts b, t represent bias and time-varying components, respectively and, e.g.,

$$\text{diag} \begin{bmatrix} 2 & -\alpha_\epsilon & |t-\tau| \\ \sigma_{\epsilon_t}^2 & & \end{bmatrix} = \begin{bmatrix} \sigma_{w_y}^2 & 0 \\ 0 & \sigma_{w_z}^2 \end{bmatrix} e^{-\alpha_\epsilon |t-\tau|}$$

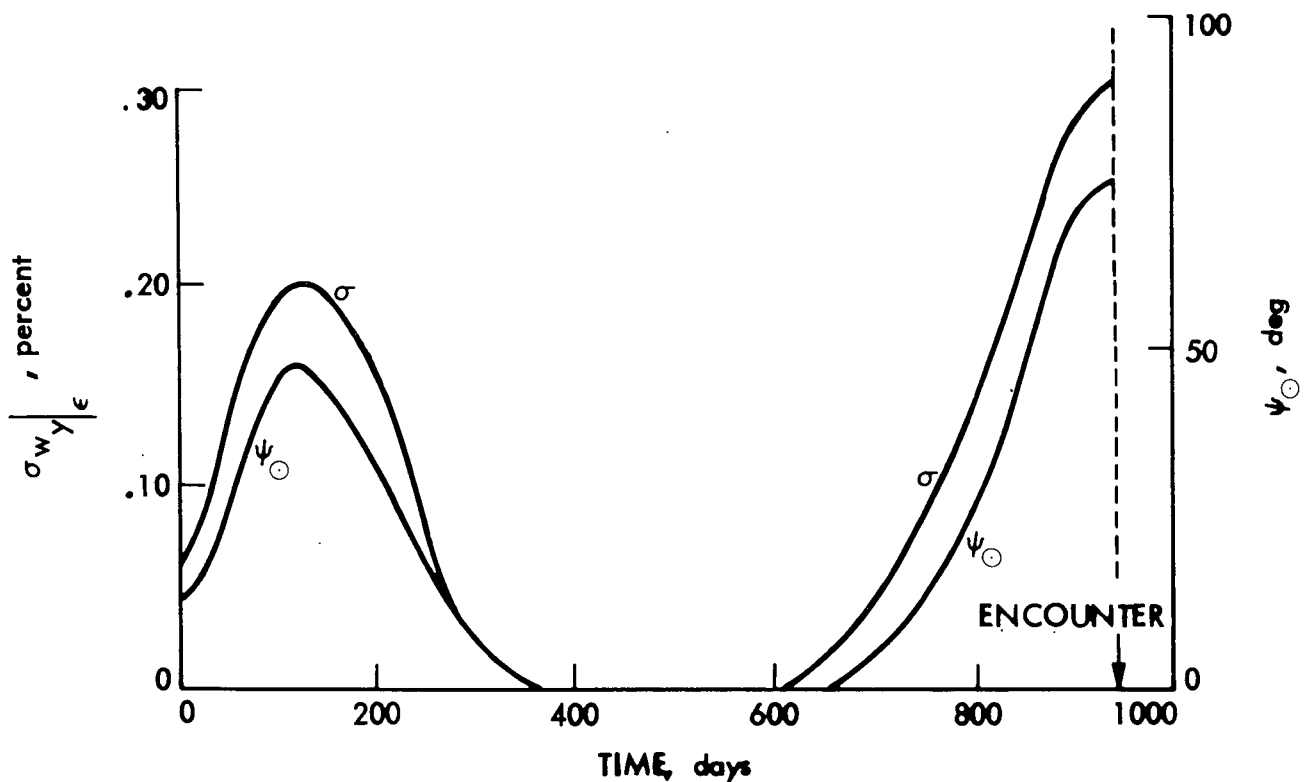


Fig. II-B-7. Thrust Covariance in Y Caused by Sun-sensor Errors

$$\frac{\Lambda}{N}(t, \tau) = \frac{1}{N} \begin{bmatrix} \text{diag} [\sigma_{x_b}^2 + \sigma_{x_t}^2 e^{-\alpha_x |t-\tau|}]_{6 \times 6} & 0 \\ 0 & \text{diag} [\sigma_{\beta_t}^2 e^{-\alpha_\beta |t-\tau|}]_{2 \times 2} \end{bmatrix}$$

$$\Gamma(t, \tau) = \begin{bmatrix} 0 & (0) \\ (0) & \text{diag} [\sigma_{\epsilon_t}^2 e^{-\alpha_\epsilon |t-\tau|}]_{2 \times 2} \end{bmatrix}$$

Mapping $\frac{\Lambda}{N}$ and Γ by A and B gives the autocovariance for the percentage change in total thrust in each of the three axes.

$$R_w(t, \tau) = \begin{bmatrix} \frac{1}{N} \sum_i a_i^2 \Lambda_{x_i}(t, \tau) & 0 & 0 \\ 0 & \frac{1}{N} \Lambda_{\beta_z}(t, \tau) + \Gamma_{\epsilon_z}(t, \tau) & 0 \\ 0 & 0 & \frac{1}{N} \Lambda_{\beta_y}(t, \tau) + \Gamma_{\epsilon_y}(t, \tau) \end{bmatrix}$$

The behavior of the standard deviations for the components of $R_w(t, \tau)$ as a function of time is shown in Fig. II-B-8. This summary data is a compilation of Table II-B-1 and Fig. II-B-7. The comparison is facilitated

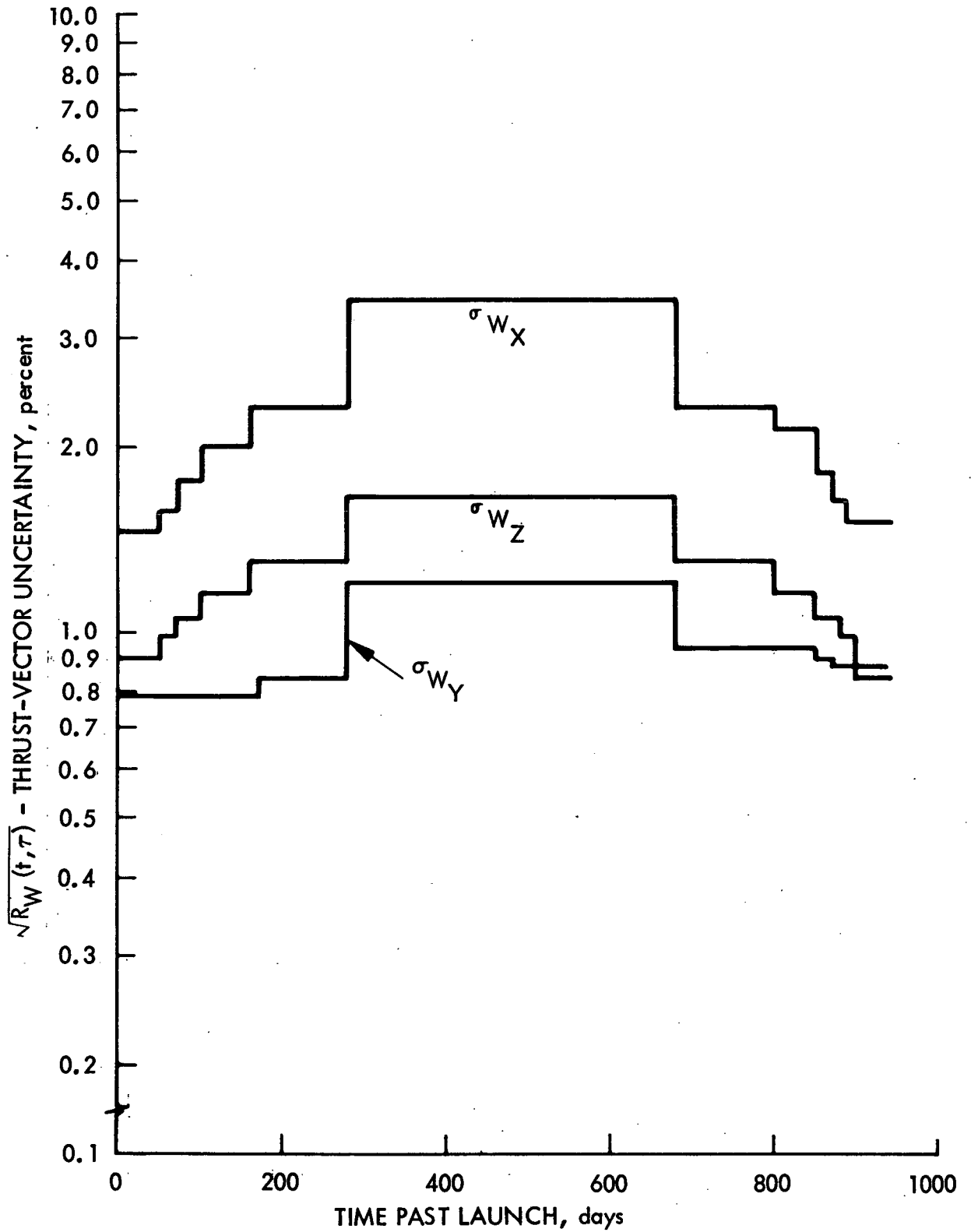


Fig. II-B-8. Summary of Standard Deviations of Thrust Pointing

without loss of generality by assuming that the correlation times for each of the random processes associated with individual components of $R_w(t, \tau)$ are identical, viz,

$$R_{w_x}(t, \tau) = \frac{1}{N} \left[\sigma_{I_B}^2 + \sigma_{c\theta}^2 + \frac{1}{4} \sigma_{V_B}^2 + \frac{1}{400} (\sigma_{\eta_1}^2 + \sigma_{\eta_2}^2) + \frac{1}{40000} \sigma_{\epsilon}^2 \right] e^{-\alpha_x |t-\tau|}$$

$$R_{w_y} = \left[\frac{1}{N} \sigma_{\beta_z}^2 + \sin^2 \psi_{\theta} \sigma_{ss}^2 \right] e^{-\alpha_y |t-\tau|}$$

$$R_{w_z} = \left[\frac{1}{N} \sigma_{\beta_y}^2 + \sigma_{ss}^2 \right] e^{-\alpha_z |t-\tau|}$$

In reduced form:

$$R_{w_x}(t, \tau) = \sigma_{w_x}^2 e^{-\alpha_x |t-\tau|}$$

$$R_{w_y}(t, \tau) = \sigma_{w_y}^2 e^{-\alpha_y |t-\tau|}$$

$$R_{w_z}(t, \tau) = \sigma_{w_z}^2 e^{-\alpha_z |t-\tau|}$$

The standard deviations, $\sqrt{R_{w_{x,y,z}}(t, \tau)}$, are plotted in Fig. II-B-8. Standard deviation, σ_{w_x} , is directly proportional to $1/\sqrt{N}$ and hence, follows the power curve. Switching points were calculated based on an 18-kW thrust system with six operating thrusters. Standard deviations $\sigma_{w_{y,z}}$ do not follow the $1/\sqrt{N}$ law directly because of the contributions from $\sigma_{\epsilon_{y,z}}$.

without loss of generality by assuming that the correlation times for each of the random processes associated with individual components of $R_w(t, \tau)$ are identical, viz,

$$R_{w_x}(t, \tau) = \frac{1}{N} [\sigma_{I_B}^2 + \sigma_{\frac{2}{c\theta}}^2 + \frac{1}{4} \sigma_{V_B}^2 + \frac{1}{400} (\sigma_{\eta_1}^2 + \sigma_{\eta_2}^2) + \frac{1}{40000} \sigma_{\epsilon}^2] e^{-\alpha_x |t-\tau|}$$

$$R_{w_y} = [\frac{1}{N} \sigma_{\beta_z}^2 + \sigma_{\epsilon_2}^2] e^{-\alpha_y |t-\tau|}$$

$$R_{w_z} = [\frac{1}{N} \sigma_{\beta_y}^2 + \sigma_{\epsilon_1}^2] e^{-\alpha_z |t-\tau|}$$

In reduced form:

$$R_{w_x}(t, \tau) = \sigma_{w_x}^2 e^{-\alpha_x |t-\tau|}$$

$$R_{w_y}(t, \tau) = \sigma_{w_y}^2 e^{-\alpha_y |t-\tau|}$$

$$R_{w_z}(t, \tau) = \sigma_{w_z}^2 e^{-\alpha_z |t-\tau|}$$

The standard deviations, $\sqrt{R_w(t, t)}$, are plotted in Fig. II-B-8. Standard deviation, σ_{w_x} , is directly proportional to $1/\sqrt{N}$ and hence, follows the power curve. Switching points were calculated based on an 18-kW thrust system with six operating thrusters. Standard deviations $\sigma_{w_{y,z}}$ do not follow the $1/\sqrt{N}$ law directly because of the contributions from $\sigma_{\epsilon_{y,z}}$. Reference star, Canopus, was used, and values of $\sigma_{\epsilon_{y,z}}$ were averaged between thruster switching times.

4. Orbit Determination

Solar electric propulsion is characterized by high-level, stochastic, nongravitational accelerations resulting from random variations in the thrust process. The random accelerations are roughly three orders of magnitude larger than those caused by gas leaks, solar pressure, etc. on ballistic missions and, at such levels, constitute the dominant error source for earth-based interplanetary navigation of SEP spacecraft (Ref. II-B-3).

Because reduction of thrust subsystem errors to the level of ballistic errors does not appear to be feasible, the successful navigation of SEP missions depends upon making the orbit determination process more tolerant of stochastic forces. At the very least, this requires the application of stochastic error modeling and sequential filtering techniques which are presently optional for most ballistic missions. Beyond this, one must look for types of data less sensitive to acceleration effects than conventional two-way radio data, or attempt to measure accelerations in real time with precision, onboard inertial measurement devices, or consider some form of adaptive filtering.

Most promising among the various proposed alternatives is the use of differenced multistation data, QVLBI. Preliminary studies (Refs. II-B-9 and 10) indicate that QVLBI can effectively recover the right-ascension and declination information lost from the two-way doppler signal, thus restoring a near-ballistic orbit determination capability to SEP missions. The damaging effects of random accelerations are then caused more by the actual orbit degradation than by the loss of information from the data.

Despite substantial progress in SEP orbit determination capability, the fundamental question of what error tolerances are acceptable for the SEP thrust subsystem is yet unanswered. Clearly, the answer depends upon particular mission requirements, mission geometry, and tracking strategy, and, especially, upon whether or not QVLBI is employed. If it is, it is necessary to know whether or not its potential capabilities are fully realized in practice, since it has not yet been proved in an actual mission demonstration. QVLBI has some disadvantages. To be effective, it requires stable interstation

frequency standards, precise clock synchronization, and charged-particle calibration. Furthermore, the cost of operating the DSN in a multistation configuration over long flight times must be considered and weighed against the possibility of using sufficiently tight tolerances on thrust subsystem parameters to allow single station tracking, at least during the interplanetary, or cruise, portion of the mission.

The results of the orbit determination studies undertaken in FY 1972 are presented herein. The primary purpose of the studies was to support SEPSIT with specific data concerning the effect of thrust-subsystem parameter errors on the orbit determination capability for the 1980 Encke rendezvous mission. The effectiveness of various single station and multistation tracking modes, including QVLBI, is determined and compared. In each case, the sensitivity of the optimal filter to variations in thrust-subsystem parameters is determined using the best available thrust-subsystem error model for a baseline point. The effects of modeling errors, tracking frequency, and station location errors are also investigated, but in less detail. This study does not presume to specify error-tolerance requirements for thrust-subsystem parameters, but some useful guidelines toward this end are developed. Although the specific numerical results are for the Encke mission, the general observations and conclusions should apply to a wide class of SEP missions.

These results are the first to be obtained using the new SEP version of the accuracy analysis program ATHENA, (Ref. II-B-11) which became operational in February, 1972. This study would not have been possible with earlier SEP software.

a. Thrust Subsystem Error Model

The results of any SEP orbit determination study depend strongly upon the assumptions made about the stochastic nongravitational accelerations. Some studies have been rendered virtually worthless by unrealistic error model assumptions (Refs. II-B-12 and 13). For this reason, an effort has been made by the NDT and thrust subsystem personnel during the past two years to identify the major thrust-subsystem error sources and to develop a

satisfactory error model. The resulting "process noise model" is the basis for the present study. The basic characteristics of this model will be outlined in this section. Detailed analysis and justification are given in Refs. II-B-6 and 14, and Section II-B-3.

The stochastic accelerations are assumed to be caused solely by variations in the thrust vector, which is represented by its magnitude (T) and two orientation angles (ϕ_1 and ϕ_2). Errors in each of the quantities T , ϕ_1 , and ϕ_2 are assumed to be independent and to consist of a zero-mean, time-varying, random component superimposed upon a bias. Each time-varying component is modeled as a first order Gauss-Markov random process characterized by two parameters: (1) the standard deviation, which is a measure of uncertainty, and (2) the correlation time, which is a measure of transience. The following system of notation is used: σ_{Tb} , σ_T , and τ_T denote the standard deviation of the bias, standard deviation of the time-varying component, and correlation time, respectively, for the thrust magnitude error; $\sigma_{\phi b}$, σ_ϕ , τ_ϕ are the corresponding parameters for the thrust orientation angles. The two angles are assumed to have identical statistical properties so that a single set of parameters applies to both.

To obtain baseline values for the standard deviations of the process noise model, it was necessary to identify the contributing thrust-subsystem error sources, determine the expected error in each parameter, and compute the corresponding effect on the thrust process. The bias in the orientation angles is caused mainly by grid warpage and is typically about 2 deg (.035 radian). The time-varying component of ϕ_1 and ϕ_2 represents the pointing error of the spacecraft within the deadband of the attitude control sensors. This is expected to be less than 1 deg, or approximately .01 radian.

Analysis of thrust magnitude errors is somewhat more complicated, as there are at least six significant thrust-subsystem parameters contributing to the overall magnitude error, namely,

$$\begin{aligned} I_B &= \text{beam current} \\ V_B &= \text{net accelerating potential} \end{aligned}$$

$\overline{\cos \theta}$ = beam divergence factor

η_1 = singly ionized fraction of mass flow

η_2 = doubly ionized fraction of mass flow

ϵ = charge exchange parameter

The contribution of each parameter to the relative thrust magnitude error ($\Delta T/T$) is determined from a linear expansion of the basic thrust equation about nominal parameter values, i.e.,

$$\frac{\Delta T}{T} = \frac{\Delta I_B}{I_B} + \frac{1}{2} \frac{\Delta V_B}{V_B} + (2 - \sqrt{2}) \frac{\eta_2}{\eta_1} \left[\frac{\Delta \eta_1}{\eta_1} + \frac{\Delta \eta_2}{\eta_2} \right] + \frac{\Delta \overline{\cos \theta}}{\overline{\cos \theta}} + \frac{\epsilon}{1-\epsilon} \frac{\Delta \epsilon}{\epsilon} \quad (8)$$

and from available information about the range of parameter variations. This information is summarized in Table II-B-4. Only the total thrust magnitude standard deviations (σ_T and σ_{Tb}) are needed for orbit determination purposes, but eq (8) and Table II-B-4 are included here to relate orbit determination results to fundamental thrust-subsystem parameters over which control may be exercised.

Table II-B-4. Thrust-subsystem Parameter Effects on Thrust Magnitude Error.

Parameter	Nominal Value	Assumed Calibration Accuracy, %	Assumed Variation with Time, %	Contribution to Thrust Error	
				σ_{Tb} , %	σ_T , %
I_B	Programmed	± 5	± 1.5	.5	1.5
V_B	1500 kV	$\pm .5$	± 1	.25	.5
$\overline{\cos \theta}$.96	± 2	± 3	2.0	3.0
η_1	.80 - .85	± 1	± 5	.02 - .05	.10 - .25
η_2	.04 - .07	± 20	± 25	.5 - 1.0	.50 - 1.25
ϵ	.005	± 30	± 30	.15	.15
Total (rms)				2.2	3.5

The discussion of error modeling thus far applies to a single thruster. In multi-thruster operation, the combined effect of those error sources that are statistically independent between thrusters is an rms average. This is the case for all the relevant error sources affecting the process noise model except the pointing error caused by the attitude control sensors, which is independent of the number of thrusters. These relationships are reflected in Table II-B-5, which gives the effective standard deviations of the process noise model as a function of the number of thrusters operating.

Table II-B-5. Process Noise Standard Deviations for Multiple Thrusters

Number of Operating Thrusters	Thrust Magnitude (% of Nominal Thrust)		Orientation Angles (radian)	
	σ_T	σ_{Tb}	σ_ϕ	$\sigma_{\phi b}$
1	3.5	2.2	.010	.035
2	2.5	1.6	.010	.025
3	2.0	1.3	.010	.020
4	1.75	1.1	.010	.0175
5	1.6	1.0	.010	.016

From Table II-B-5, it may appear that the stochastic accelerations will be smaller, and, therefore, less damaging, in a multiple-thruster configuration. Actually, for a fixed thruster size, the opposite is true. The number of thrusters operating must be matched to the available power derived from the solar arrays, but the total thrust produced by the thruster array is also proportional to power, so the nominal thrust level is approximately a linear function of the number of thrusters operating. Thus, if there are N thrusters operating, the error as a percentage of nominal thrust is reduced by \sqrt{N} , but the nominal thrust is larger by a factor of N ; consequently, the thrust

(and acceleration) errors are larger (by \sqrt{N}) than at single-thruster power levels. The present study is based on the last 30 days of the 950-day Encke rendezvous mission. During this time, power matching requirements dictate that there will be three thrusters operating for 10 days, four thrusters for 14 days, and five thrusters for the final 6 days. Since the four-thruster configuration is dominant, the standard deviations from Table II-B-5 corresponding to four thrusters were used as baseline values. The indicated thrust magnitude error of 1.75% represents acceleration errors of $.5$ to $.9 \times 10^{-8}$ km/sec² during this particular mission segment.

The correlation times required for the error model are somewhat more nebulous than the standard deviations. Observed variations in the quantities contributing to the thrust magnitude error indicate relatively long correlation times, on the order of days to weeks (Ref. II-B-6). Because the longer correlation times in this range approach a bias effect of which the orbit determination process is relatively tolerant, a value for τ_T toward the lower end of this spectrum, namely, 5 days, was selected as the baseline value in the interest of conservative modeling. Pointing errors are higher in frequency and more transient than the thrust magnitude fluctuations. Correlation times on the order of hours appear to be appropriate. Accordingly, a baseline value of 3 hr was selected for τ_ϕ .

Conspicuously absent from this error model is any mention of mass variations, which, if present, also contribute to the stochastic acceleration. The fundamental thrust-subsystem parameters do not affect mass directly, but three of them, namely, I_B , η_1 and η_2 , ultimately affect mass through variations in the mass flowrate \dot{m} . Indeed, a linear expansion for \dot{m} analogous to eq (8) indicates that the time-varying error component in \dot{m} may be as large as $\pm 5\%$. This seemingly large error is actually negligible for the following reasons: first, the variations in fuel, i.e., mass, expended over the 30-day period of a typical tracking interval is a small portion of the total fuel for the 950-day mission, which, in turn, is a relatively small portion (about 30%) of the total spacecraft mass; e.g., for the particular 30-day period of interest in this study, a 5% variation in mass flowrate represents a maximum

of .17% variation in the total mass, which is clearly negligible with respect to the thrust magnitude errors. Furthermore, since the mass variation is the integral of the error in \dot{m} , higher frequency components are attenuated, and the slowly varying components, even if they are not of negligible magnitude, could be adequately represented as a bias over a short tracking interval. The foregoing observations do not preclude the possibility of a large initial uncertainty in mass caused by the cumulative effect of mass-flowrate errors over a long period of time preceding the data arc. In this study, an initial uncertainty of 100 kg (out of a total spacecraft mass of 1200 kg) was assumed.

b. The Batch-sequential Filter and Batch Size

The navigation filter used for this study was a batch-sequential, square root filter, JEWEL (Ref. II-B-16), operating on REGRES and VARY files generated by the new SEP version of ATHENA. The distinguishing feature of the batch-sequential filter is that all time-varying stochastic quantities included among the estimated and/or considered parameters are represented as piecewise constant functions; i.e., they are treated as constants within specified time intervals called "batches". For example, the thrust-subsystem error model parameters in this study, though ostensibly modeled as continuously varying random processes, were actually represented in the filter as discreet Gauss-Markov sequences, taking on different constant values within each batch. There are at least two significant advantages of such a filter. The first is computational efficiency, which results from the use of rapid, reliable batch processing algorithms and from the fact that the propagation of the estimate and covariance takes place between batches rather than between individual data points. However, this advantage is largely lost if the batch size is very small (which was necessarily the case in this study for reasons to be made clear presently). The second advantage is one of flexibility. A variety of functions can be represented in the filter without the necessity for integrating a new set of variational equations and recomputing data partials; e.g., to determine the effect of a change in correlation time for the first order Gauss-Markov process in the study was a very simple matter.

The performance of the batch-sequential filter depends upon the choice of batch size. The smaller the batch size, the better the piecewise constant function represents its continuous counterpart, but larger batches effect more efficient computation. Furthermore, the sensitivity of the filter to batch size depends upon the level and functional form of the stochastic forces involved. Some useful guidelines for batch size selection as a function of acceleration standard deviation and correlation time have been derived by Russell and Curkendall (Ref. II-B-15). Their criteria would allow batches of at least one day for stochastic accelerations at the ballistic level (10^{-12} km/sec²), but would restrict the batch size to less than an hour for accelerations at the SEP level (10^{-9} km/sec²). The necessity for such a small batch size was verified empirically in this study. The results are given in Fig. II-B-9. The solid curves represent the formal, computed rms position error after 10 days of single-station tracking with conventional radio data (doppler and range) as a function of batch size. The upper solid curve is for thrust-subsystem parameter standard deviations and correlation times at their baseline SEP values. The lower curve is for standard deviations three orders of magnitude smaller, representing a typical ballistic case. To faithfully represent the intended process noise model, the batch size must be sufficiently small that further reduction would have negligible effect. This implies a maximum batch size on the order of 1 hr for the SEP case, and that was the value used in this study. The ballistic case is much less sensitive to batch size. Although the abscissa in Fig. II-B-9 only goes to 12 hr, batch sizes up to 5 days were investigated for the ballistic case with resulting variations in the computed rms position error of only about 2 km (i.e., 10%). Thus, the batch size is rather arbitrary in the ballistic case, but one day appears to be a reasonable choice.

From the solid curve in Fig. II-B-9, it might appear at first glance that smaller errors result from the use of larger batches. The opposite is true, as indicated by the dashed curve, which shows the actual error in the estimate obtained in several simulations, using the same data in each case, but varying the filter batch size. The filter performance is relatively consistent for batch sizes up to 1 hr, but degrades rapidly beyond that point. The apparent discrepancy between the computed error statistics and actual errors

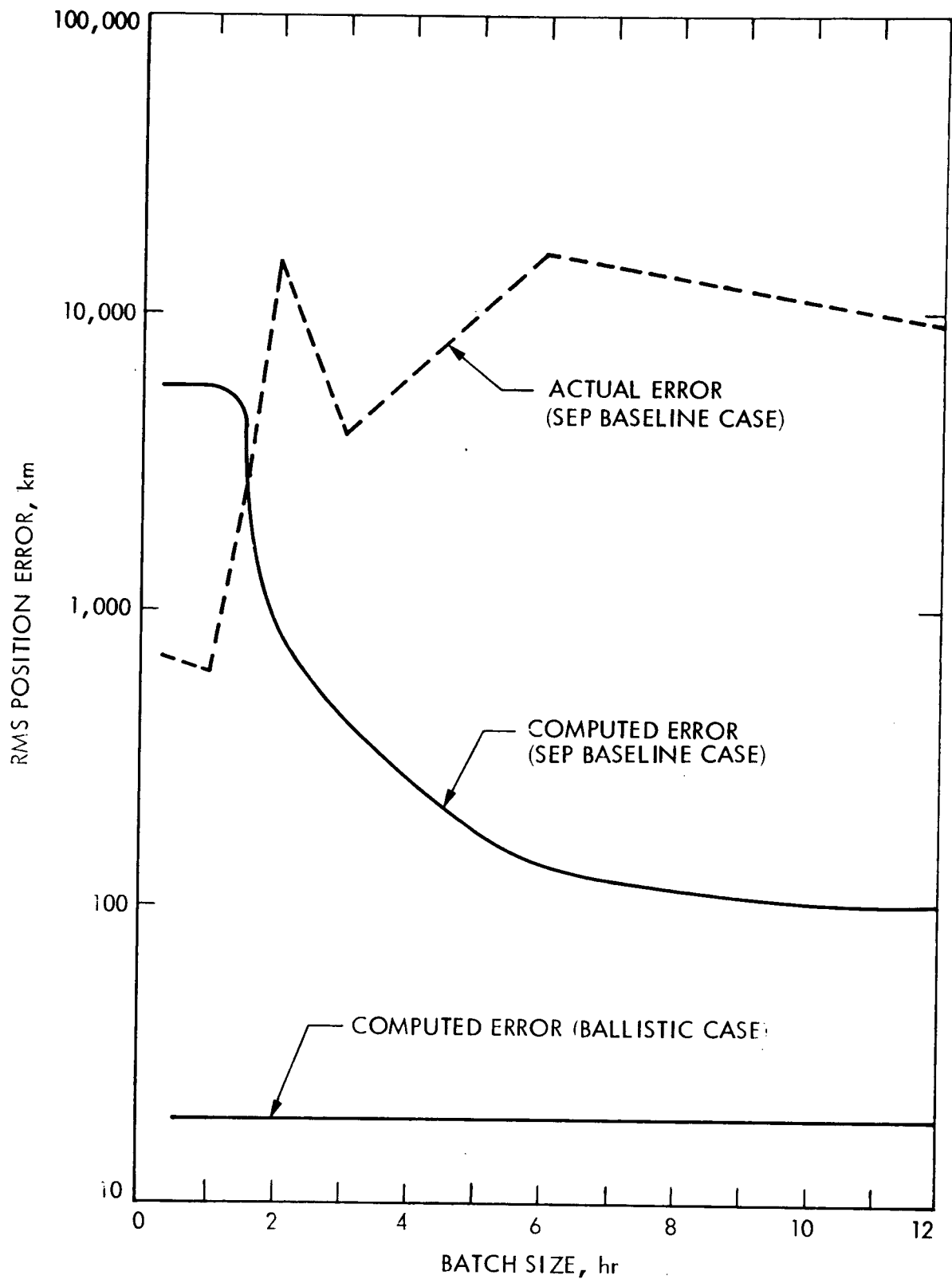


Fig. II-B-9. Effect of Batch Size on Computed and Actual rms Position Error After 10 days of Tracking

is the natural consequence of a modeling error. When the batch size becomes too large, the filter model is no longer accurate, and the formal, computed error statistics become deceptively optimistic.

Qualitatively, the effects demonstrated here are exactly as one should expect, but it is perhaps surprising (and disconcerting) that such complete and disastrous degradation of performance should result from a seemingly small change in a supposedly arbitrary filter parameter; e.g., a discrepancy of two orders of magnitude between actual and computed errors results if the batch size is set at 6 hr, rather than 1 hr. Therefore, the user of batch-sequential software must beware, especially when stochastic accelerations at the SEP level are involved.

c. Filter Configuration and Tracking Strategies

The batch size for the filter as discussed above, was set at 1 hr, and all parameters of interest were explicitly estimated; i.e., there was no "consider" option. The estimated parameters, in addition to the spacecraft state, were the initial mass, the biases and stochastic components of the two thrust vector orientation angles, ϕ_1 and ϕ_2 , and the stochastic component of the relative thrust magnitude $\Delta T/T$. The bias in relative thrust magnitude was not estimated because, if it is assumed that the nominal mass is constant during the tracking interval (it actually decreases 3.4% in this case), the effect of a bias in relative thrust magnitude is indistinguishable from that of a bias in the mass, i.e., they are perfectly correlated. Therefore, it is redundant for the filter to explicitly estimate both quantities. The large initial mass uncertainty assumed for this study (100 kg) effectively absorbs the bias component in thrust magnitude so that the latter may be neglected.

Five different tracking strategies were investigated in this study:

- (1) Single-station, doppler data only.
- (2) Single-station, doppler and range.

- (3) Multistation, two-way doppler and range (no simultaneous or three-way data).
- (4) Multistation, two-way and three-way doppler and range, including simultaneous, but not explicitly differenced, data.
- (5) Multistation, explicitly differenced (two-way minus three-way) simultaneous doppler and range plus de-weighted conventional two-way data.

For the sake of brevity, the strategies described above will be called SSDO, SSDR, MS2W, MS3W, and QVLBI, respectively. The last two strategies use exactly the same data, but in different ways. The MS3W strategy processes all the data routinely, whereas QVLBI does not use the three-way data directly, but, rather, uses the difference between simultaneous two-way and three-way data (Ref. II-B-9). All the two-way data is retained in QVLBI, but it is de-weighted so that the filter extracts as much information as possible from the explicitly differenced data, depending on the two-way data for geocentric range and range-rate information only, for which purpose it is most reliable. The basic two-way range and doppler measurements were assumed to be accurate to 3 m and 1 mm/sec (for a 1-min sample), respectively; but the measurements were weighted at 1 km and 250 mm/sec for the QVLBI strategy.

DSN Station 14 (Goldstone) was used for all single-station tracking. Stations 61 (Madrid) and 51 (Johannesburg) were added for the multistation strategies. These stations were selected because of their favorably overlapping view periods to provide the simultaneous two-way and three-way data required for QVLBI, as illustrated in Fig. II-B-10. The basic tracking

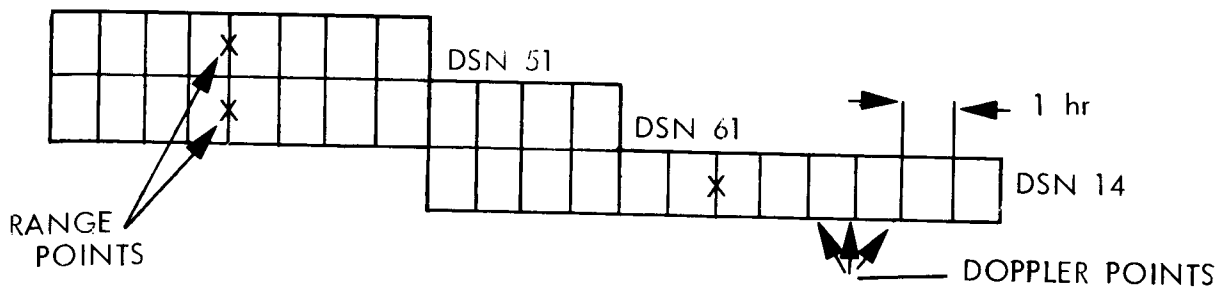


Fig. II-B-10. Typical Multistation Tracking Pattern

pattern was repeated once each day. The view period from the southern hemisphere, i.e., Station 51 was relatively short, and became even shorter as the mission progressed because of the high declination of the trajectory, which approaches 60 deg at the time of encounter. Both simultaneous range and doppler are available between Stations 51 and 61 (the north-south baseline), but only simultaneous doppler between Stations 61 and 14 (the east-west baseline).

d. Baseline Performance

A proper interpretation of the results requires a clear understanding of what is meant by an optimal* filter. As the term is used in this report, an optimal filter is one which accounts for all error sources and properly models their dynamic behavior and statistical properties; i.e., the filter model faithfully represents the real-world situation. This means, for example, that whatever stochastic accelerations may be experienced by the SEP spacecraft are in fact sample functions of the random process assumed by the filter, with standard deviations and correlations as assumed.

The optimal sequential filter performance for each of the five tracking strategies with the thrust-subsystem-parameter standard deviations and correlation times at their baseline values is indicated by the shaded bars in Fig. II-B-11. The performance criterion is rms position error one half day before encounter. There is about an order of magnitude improvement with each change of tracking strategy as one proceeds from SSDO to SSDR, MS2W, and MS3W, respectively, but the additional improvement of QVLBI over the MS3W performance is relatively insignificant. To fully appreciate the power of QVLBI tracking strategy, one must look at something other than optimal filter performance. The batch filter bars shown in Fig. II-B-11 represent the rms position error in the initial state estimate resulting from a batch filter solution in the presence of unmodeled SEP stochastic accelerations as generated by the program HUMBUG. These are the errors which would result if the real-world stochastic accelerations were actually as represented by our baseline thrust-subsystem error model, but only the bias components were taken into account

*It is taken for granted that the filter is an unbiased, minimum variance estimator for its model.

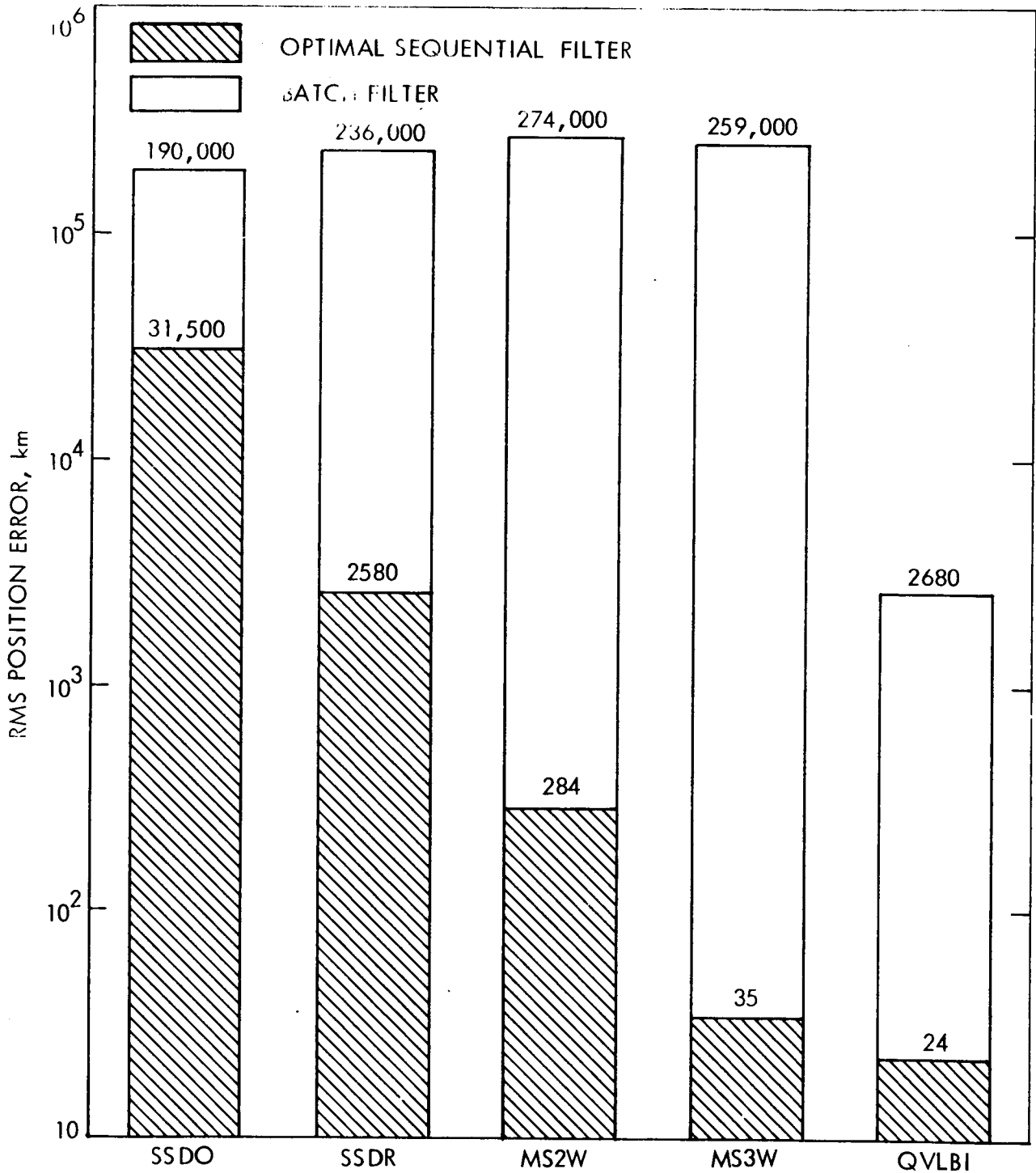


Fig. II-B-11. Baseline Navigation Performance for Various Tracking Strategies

by the filter model. It is not intended to suggest orbit determination for an SEP mission would ever be attempted using a batch filter, but, instead, to demonstrate the relative sensitivity of the various tracking strategies to modeling errors by assuming a very bad model, i.e., a simple bias. In this evaluation, QVLBI is clearly superior, its performance being nearly two orders of magnitude better than any of the other tracking strategies and about equal to the SSDR performance with an optimal filter.

e. Sensitivity of Optimal Filter to Thrust-subsystem Error Model Parameters

The sensitivity of the optimal filter performance to changes in the standard deviations and correlation times of the thrust-subsystem error model for the various tracking strategies is given in Figs. II-B-12 through 15. As before, the performance is evaluated in terms of the rms position error one half day before encounter; however, to display the results for the various tracking strategies concurrently, the curves are plotted in terms of percent of baseline performance (Fig. II-B-11). Each figure shows the effect of changing one parameter (standard deviation or correlation time) with all others held constant at their baseline values.

A cursory examination of Figs. II-B-12 through 15 leads to the following observations:

- (1) For values near the baseline values, the position error varies almost linearly with the standard deviations for all tracking strategies.
- (2) The MS3W and QVLBI strategies have almost identical optimal filter performance and are generally less sensitive to parameter variations than the other three strategies.
- (3) The remaining three strategies are much more sensitive to changes in orientation angle parameters (both σ_ϕ and τ_ϕ) than in thrust magnitude parameters. (Because

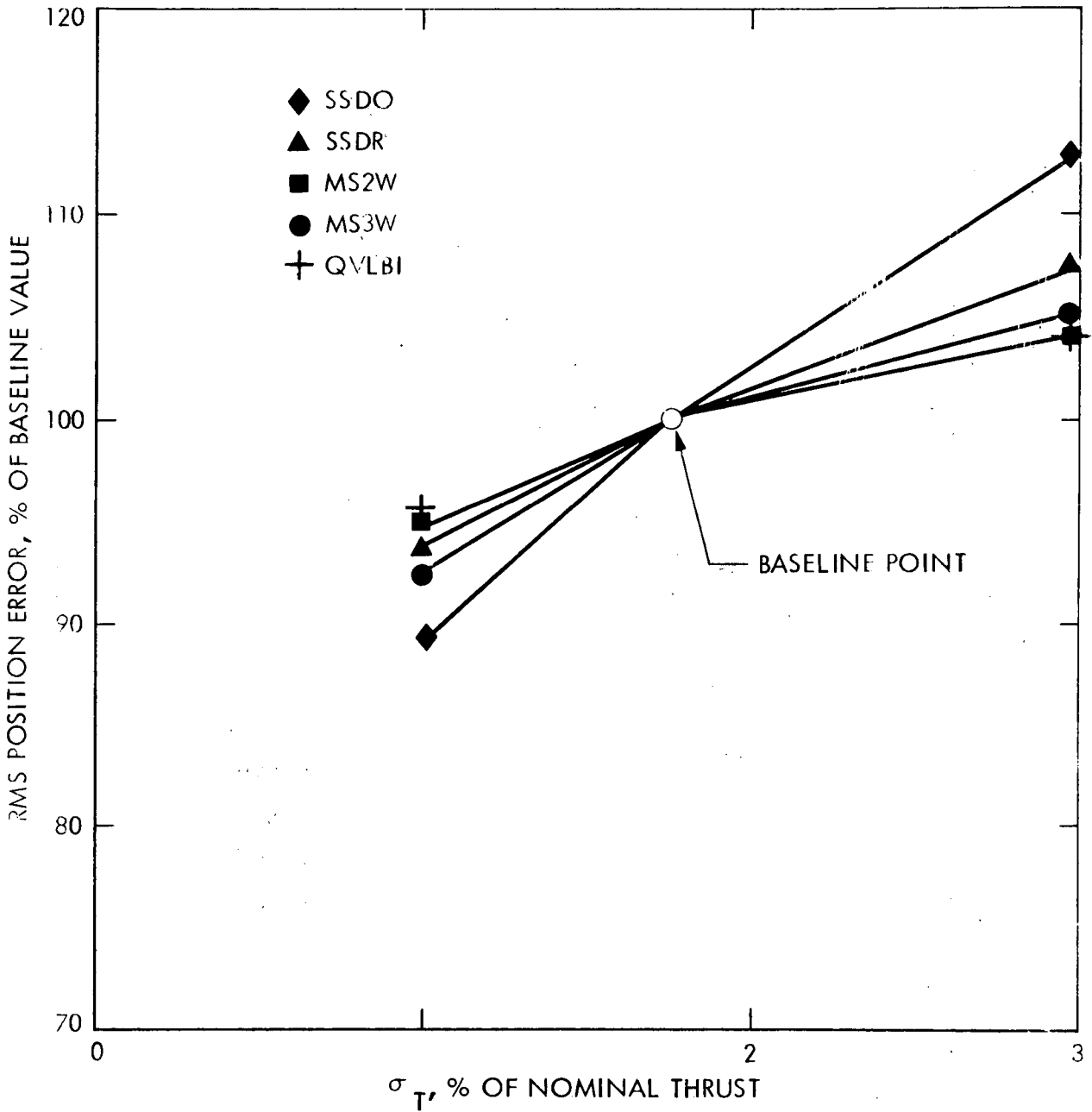


Fig. II-B-12. Sensitivity of Optimal Filter Performance to Thrust Magnitude Standard Deviation for Various Tracking Strategies

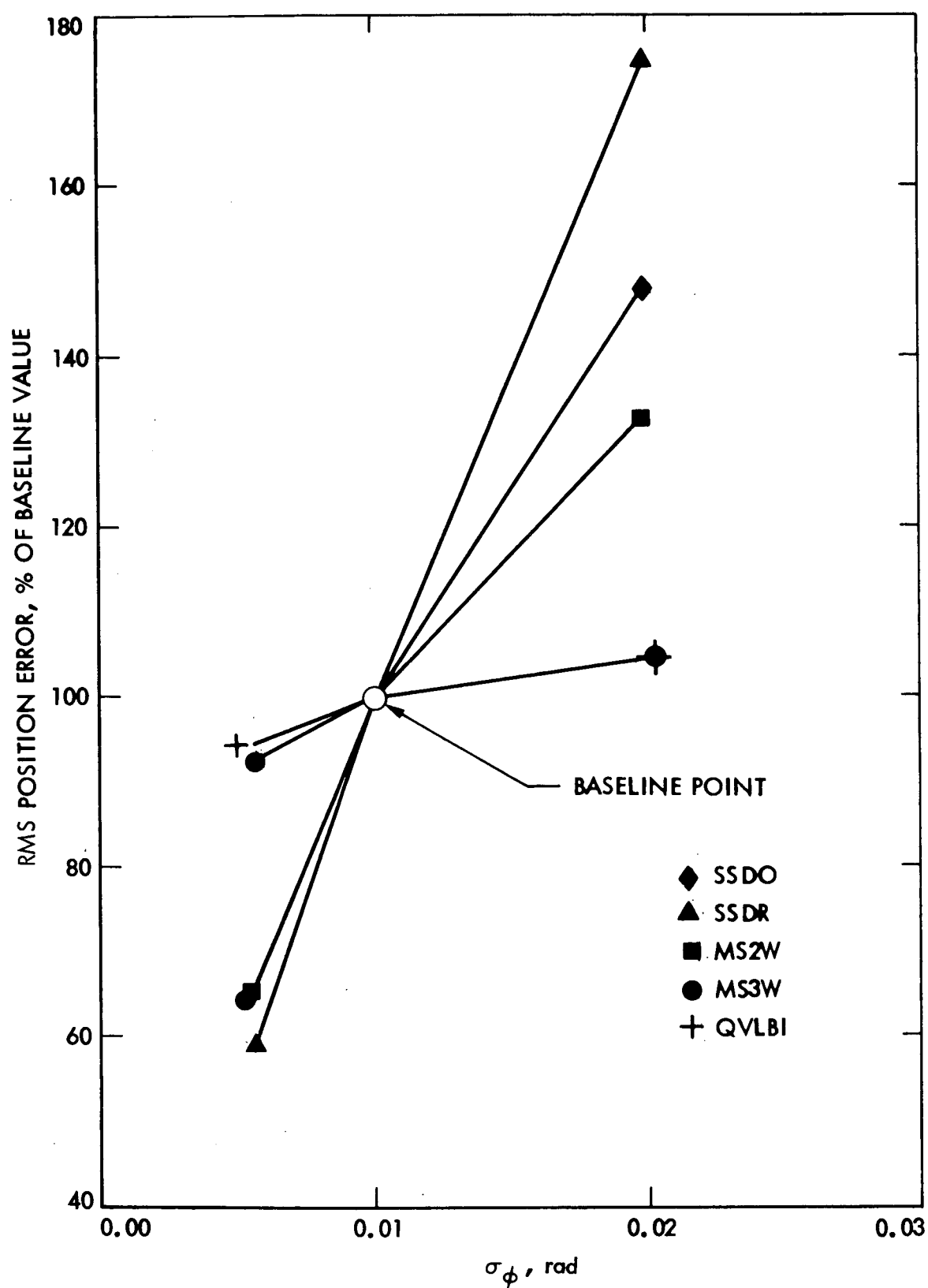


Fig. II-B-13. Sensitivity of Optimal Filter Performance to Orientation Angle Standard Deviation for Various Tracking Strategies

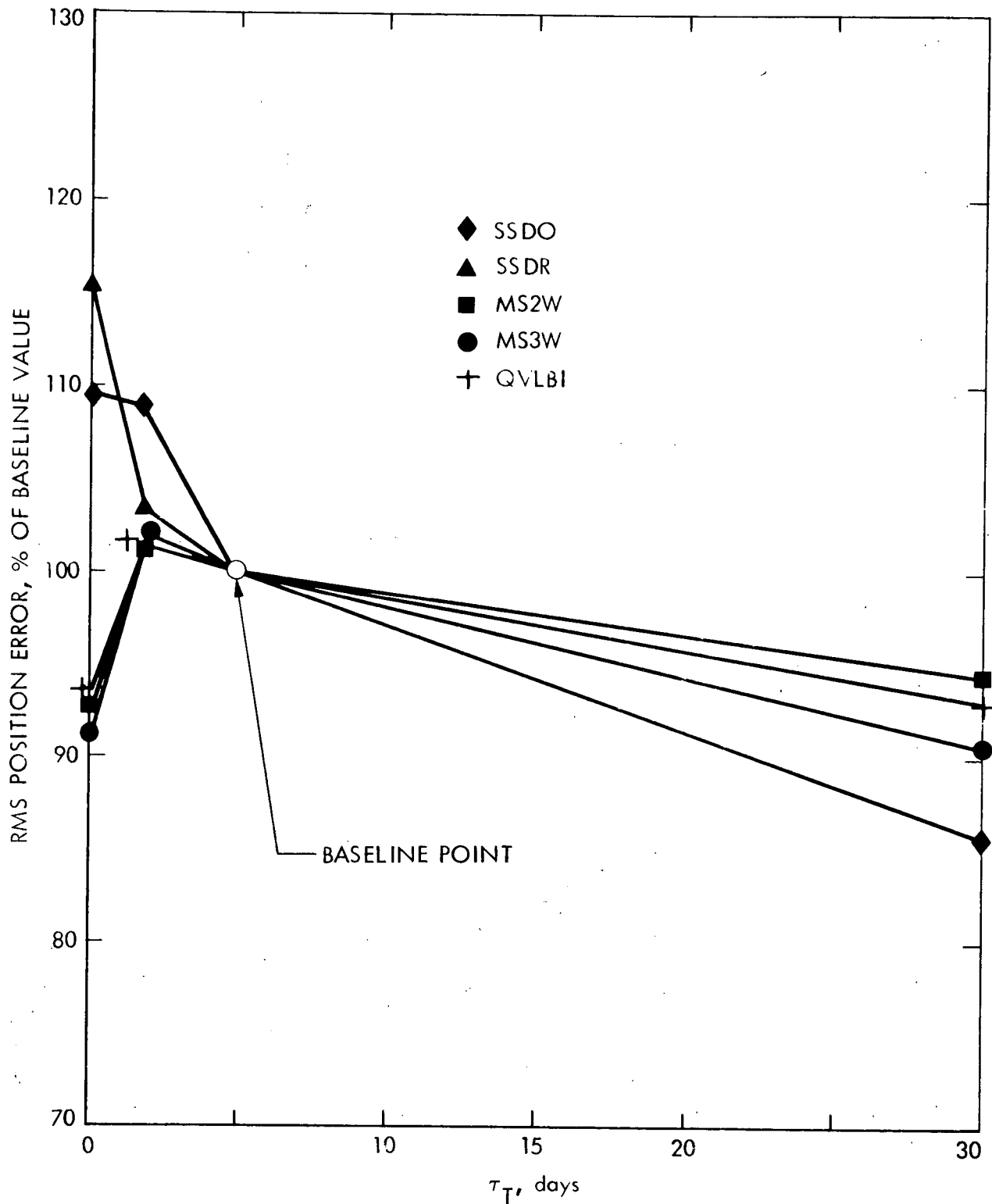


Fig. II-B-14. Sensitivity of Optimal Filter Performance to Thrust Magnitude Correlation Time for Various Tracking Strategies

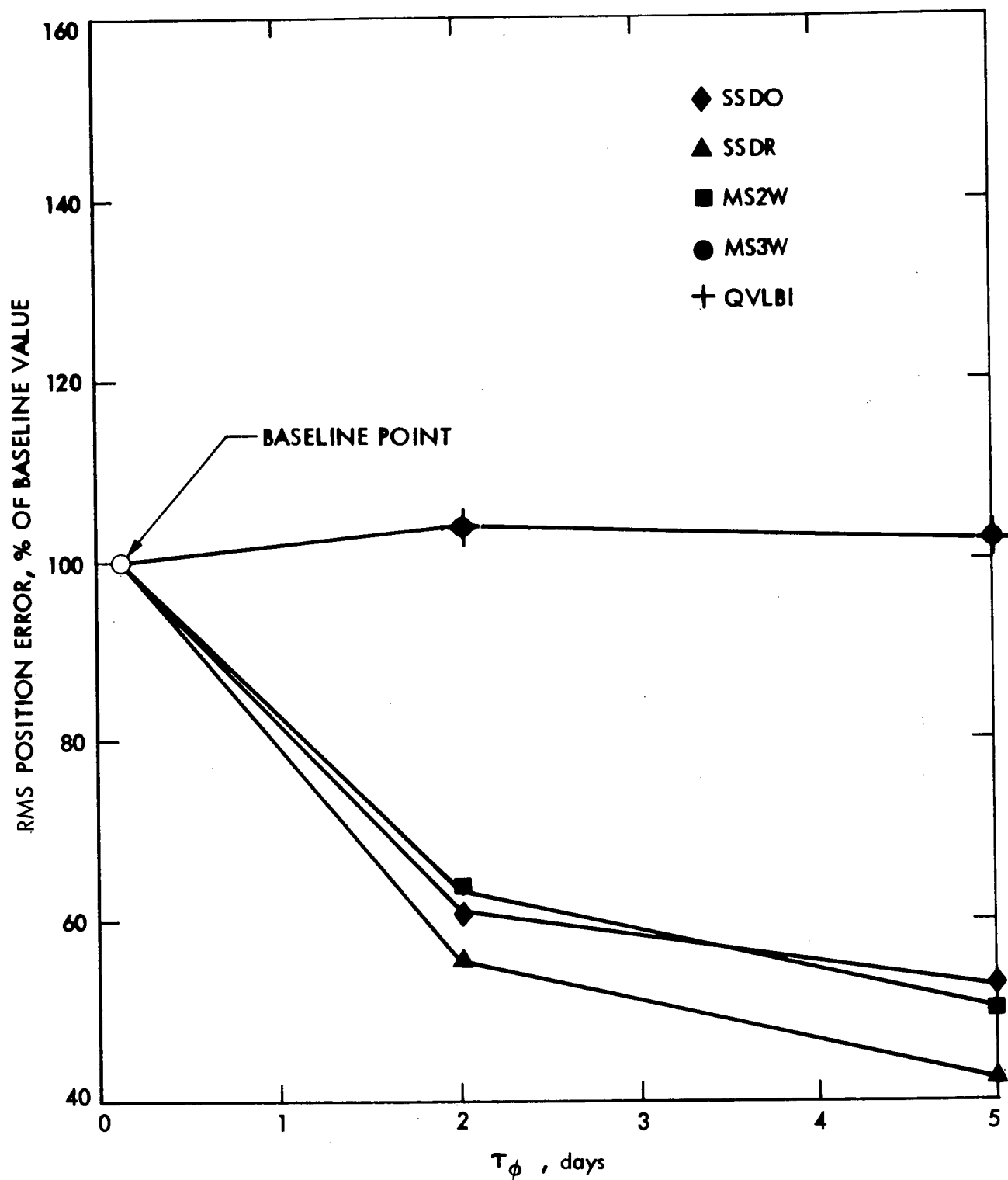


Fig. II-B-15. Sensitivity of Optimal Filter Performance to Orientation Angle Correlation Time for Various Tracking Strategies

Figs. II-B-13 and 15 are plotted on a different scale than Figs. II-B-12 and 14, the difference is greater than may appear at first glance.)

- (4) For the MS3W and QVLBI strategies the "worst" correlation time is about two days, whereas the single-station performance is monotonic with correlation time (at least for the range of the parameter values investigated). Inexplicably, the MS2W performance follows that of the other multistation strategies with respect to τ_T , but follows the single-station performance with respect to τ_ϕ .

f. Simulated Suboptimal Filter Performance

A study was initiated to investigate how, given a particular stochastic environment, the filter performance is affected by parameter variations in the stochastic model; i.e., the effect of mismodeling. Because, at the time, simulation was the only means available for investigating this question, the scope of this phase of the study is limited. The simulated state errors were generated by the computer program, RANDOM, using a particular thrust-error profile selected randomly from the stochastic process represented by the baseline thrust-subsystem error model. The resulting errors in the state estimate for various assumed values of the thrust-subsystem error model parameters are given in Figs. II-B-16 through 19 for all but the SSDO strategy, which was not of sufficient interest to be included.

Perhaps the most striking characteristic evident in the figures is the absence of any severe degradation of performance, especially for the multistation strategies. More often than not, the multistation performance was better when parameters were mismodeled than when modeled correctly. On the other hand, the single-station performance, in 8 suboptimal simulations out of 9, was consistently degraded by mismodeling; but the largest error, which resulted from assuming too low a value for the thrust-magnitude correlation time, was only a factor of four worse than the optimal filter performance

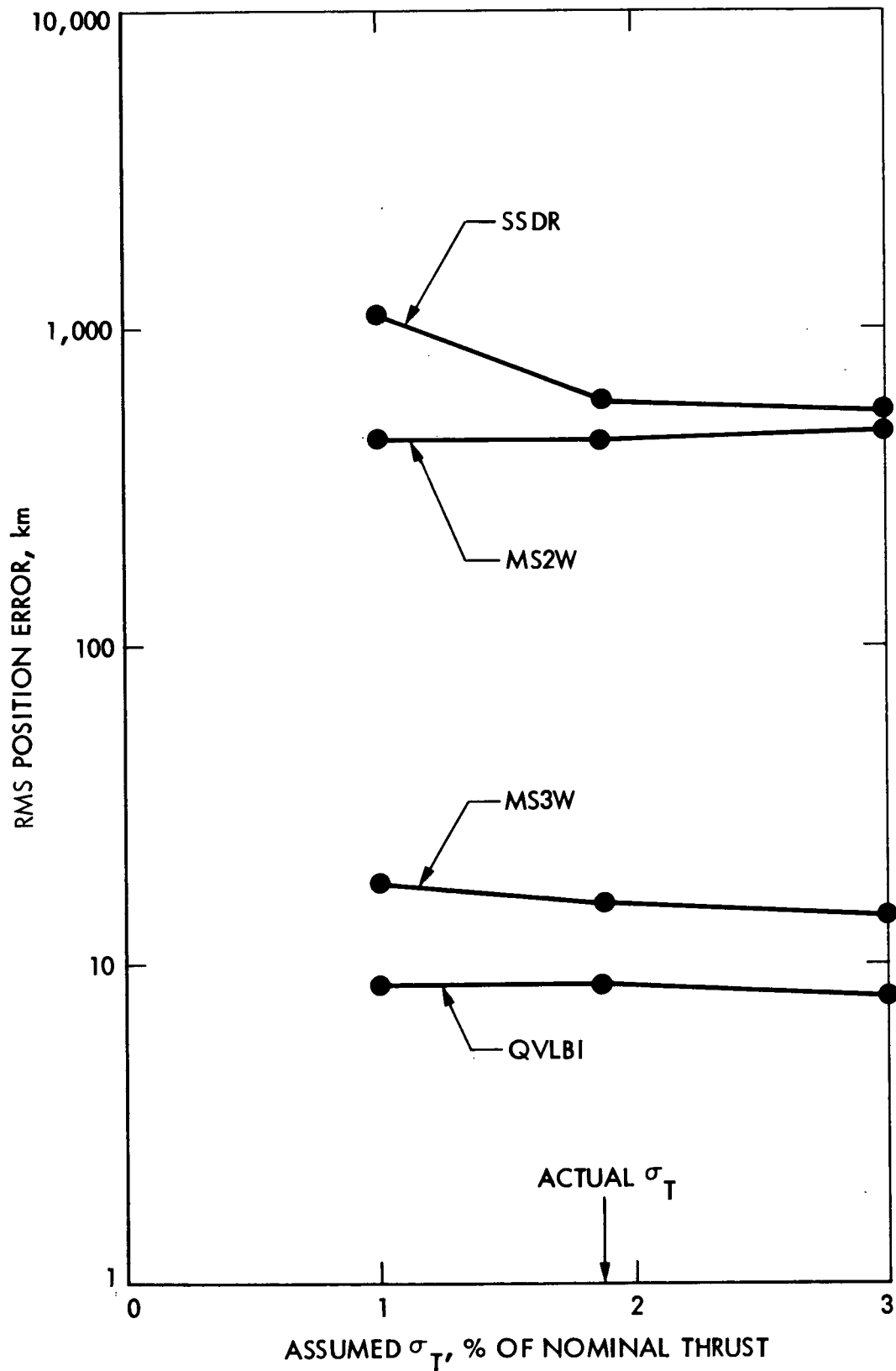


Fig. II-B-16. Simulated Filter Performance with Mismodeled Thrust Magnitude Standard Deviation

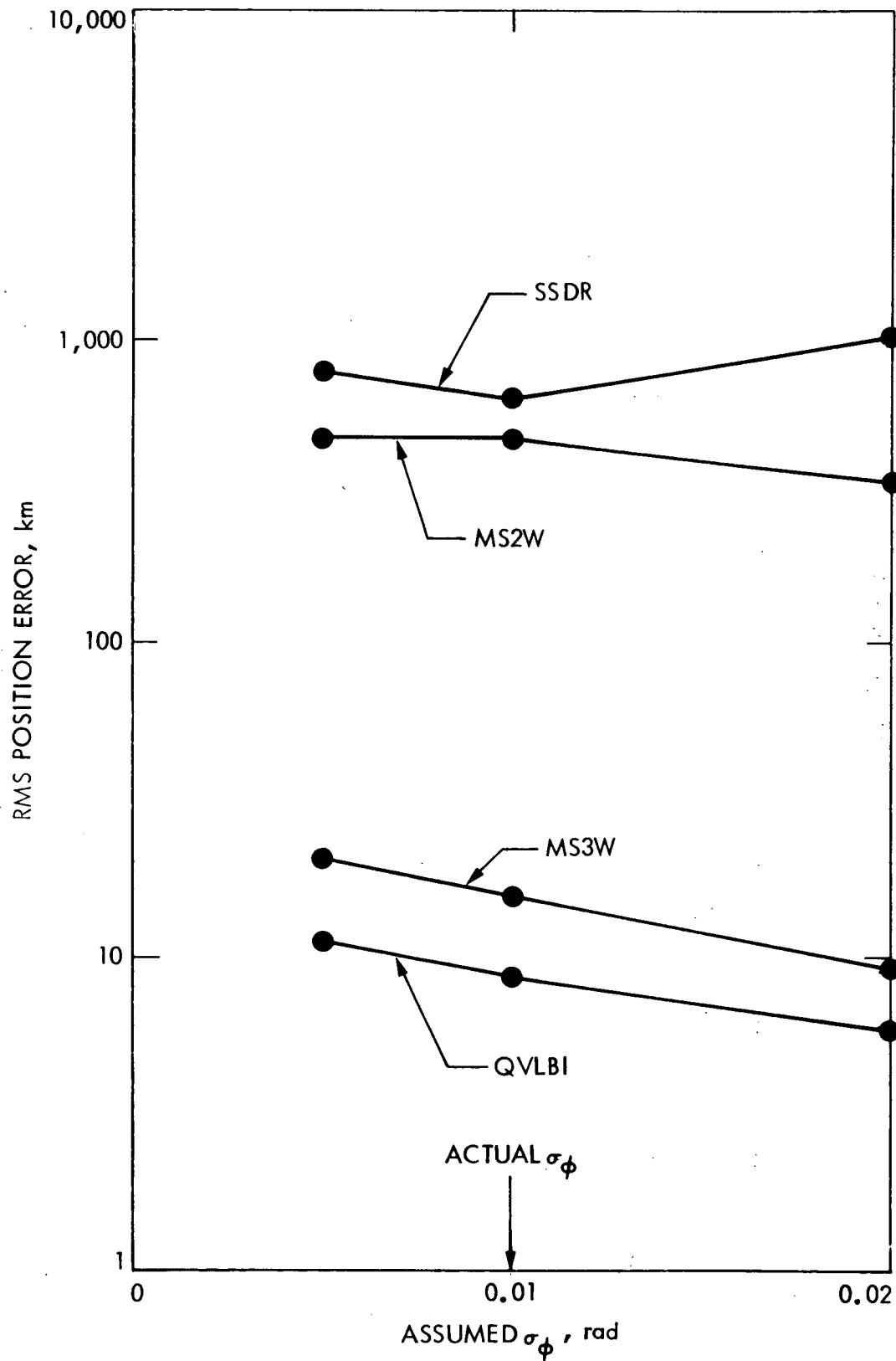


Fig. II-B-17. Simulated Filter Performance with Mismodeled Orientation Angle Standard Deviation

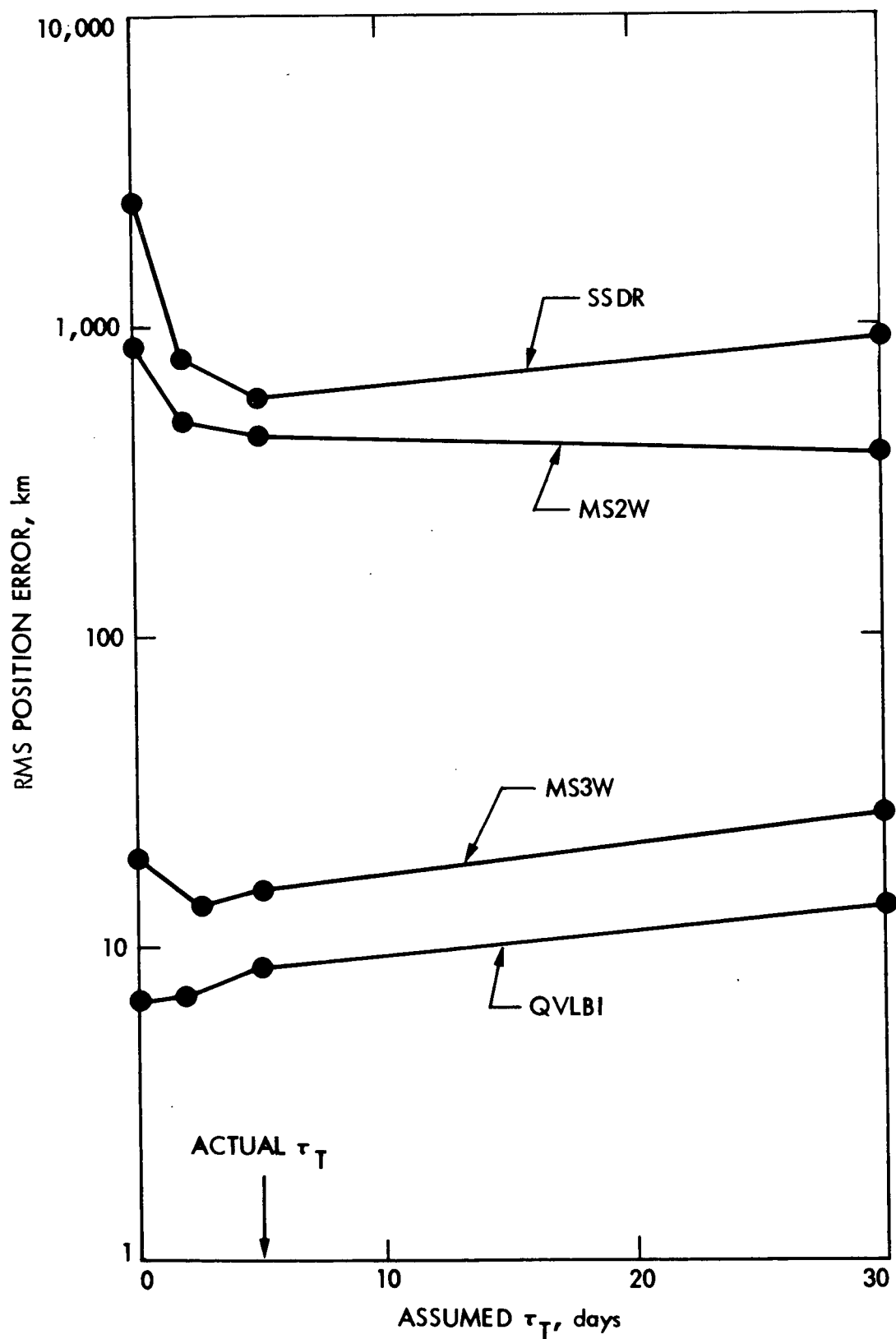


Fig. II-B-18. Simulated Filter Performance with Mismodeled Thrust Magnitude Correlation Time

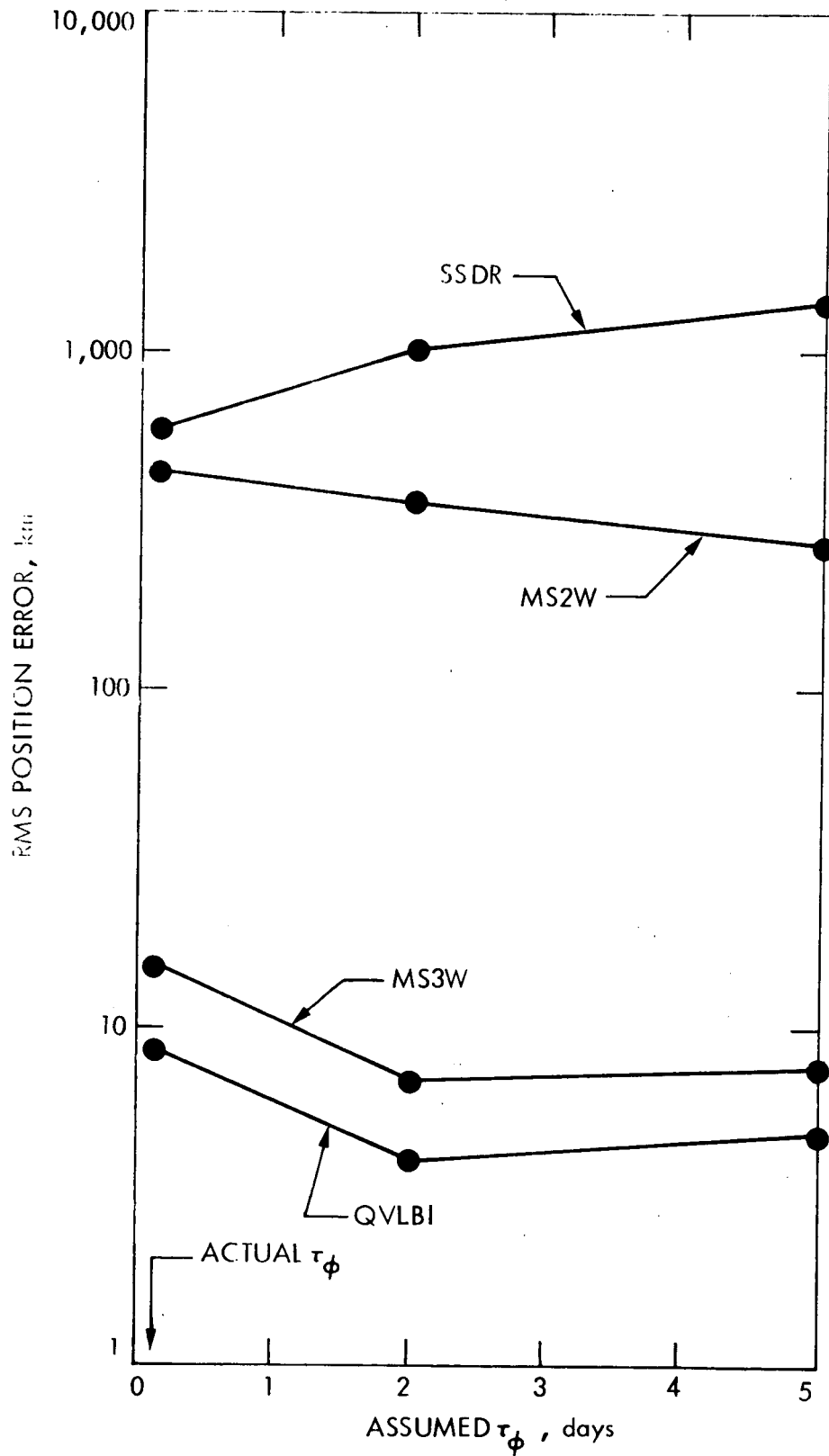


Fig. II-B-19. Simulated Filter Performance with Mismodeled Orientation Angle Correlation Time

for this particular thrust-error history. The MS3W performance almost exactly parallels that of QVLBI for the range of parameters investigated. This appears to be inconsistent with the earlier observation, based on the batch filter results shown in Fig. II-B-11, that MS3W should be much more sensitive to modeling errors than QVLBI. However, these results are not necessarily in conflict nor even surprising when one considers that the modeling errors simulated herein are minor. The basic structure of the model is always the same; only certain parameter values are changed, and these are changed one at a time; i. e., three of the four parameters are always correctly modeled. The batch filter solution, however, represents a gross modeling error in terms of structure. The sequential filter may be sufficiently robust to tolerate minor errors in its model but may be vulnerable to more basic model discrepancies.

It is, of course, risky to draw conclusions about ensemble behavior from a few simulations based on a single sample function. In addition, the filter performance in the presence of multiple error sources (including a priori state errors and errors in biases and station locations) may be quite different from that given here, in which the random thrust process is the sole source of the simulated state errors. For example, setting the standard deviations too high in the process noise model of the filter causes the filter to expect larger accelerations. Consequently, state errors actually caused by other sources may be erroneously attributed to the random accelerations. No harm can come from this, if the random accelerations are in fact the only error source, as in these simulations. However, because a more complete and careful study of modeling-error effects is needed, such a study, using better analysis tools, which have recently become available, will be undertaken in FY 73.

g. Data Rate Impact

Thus far, performance has been evaluated in terms of rms position error at a selected point. The rate of orbit determination is also of interest, particularly as it relates to the data rate. This information is shown in Figs. II-B-20 and 21. Figure II-B-20 gives the rms position error for each

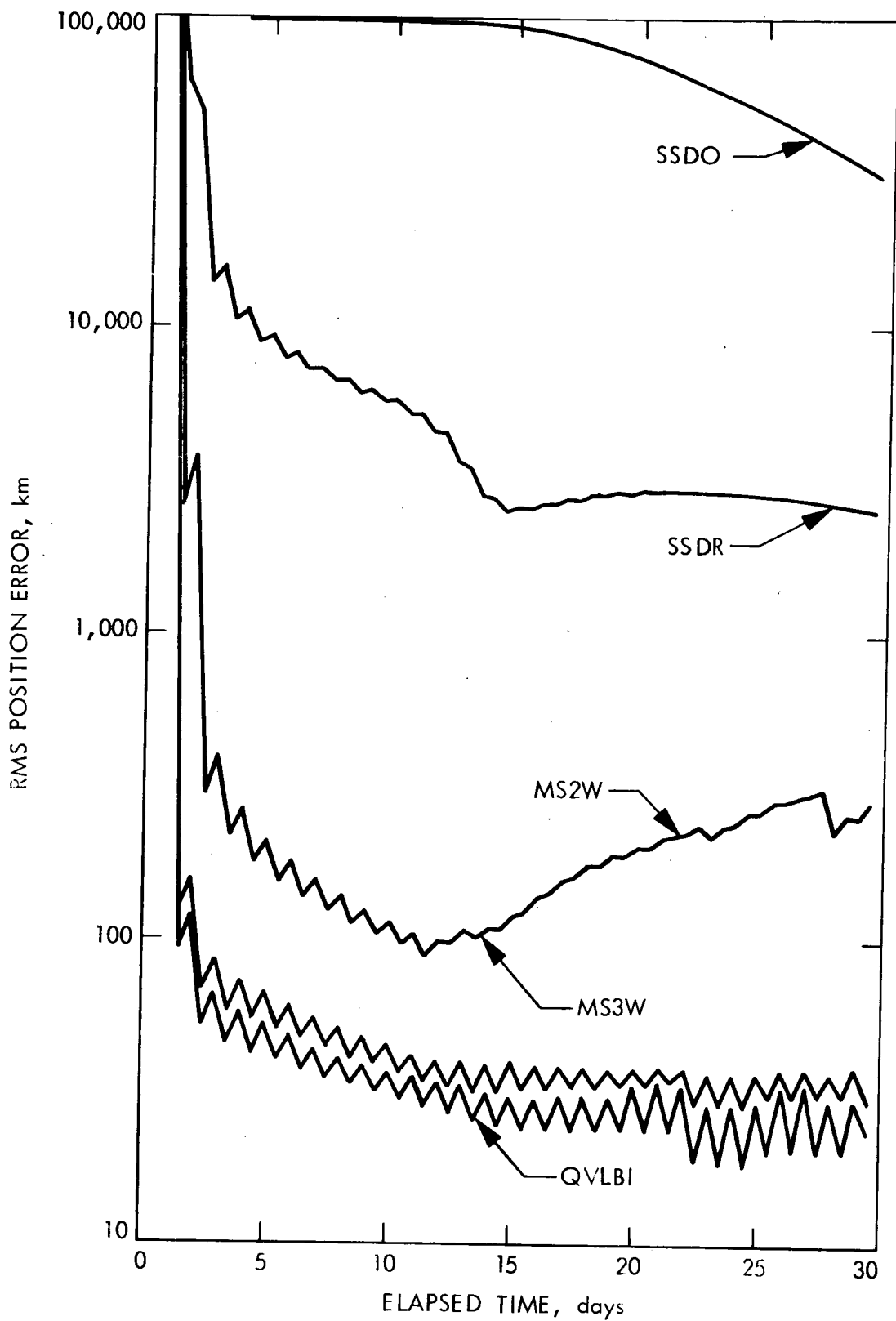


Fig. II-B-20. Time History of rms Position Error with Data Every Day

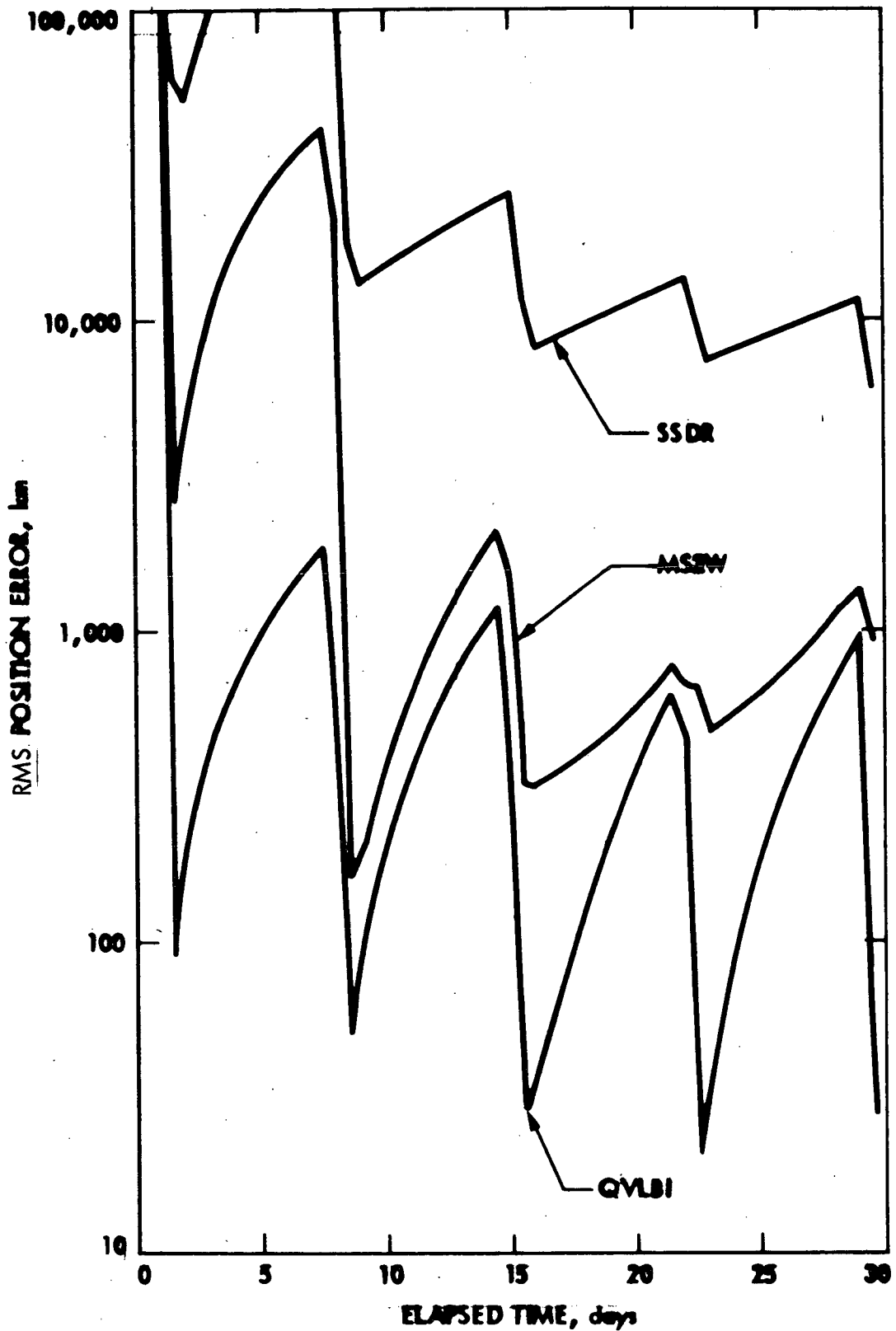


Fig. II-B-21. Time History of rms Position Error with Data Every Day

tracking strategy as a function of time over the 30-day tracking interval for the baseline case, wherein data is taken every day, beginning with the second day. Figure II-B-21 repeats this information for three of the five tracking strategies with data every seven days (five passes during the 30-day period). The a priori state errors were assumed to be arbitrarily large, 10^5 km in each position component and 1 km/sec in velocities.

The rapid degradation of orbit information between passes of data, caused by stochastic accelerations, is apparent in both figures, but especially in Fig. II-B-21, wherein the data is more widely spaced. However, the capability of QVLBI to re-determine the orbit from a single pass of data is equally dramatic. (MS3W performance is not included in Fig. II-B-21 because it is almost indistinguishable from QVLBI.) With data every day, a steady-state level of performance is reached within 15 days by all tracking strategies except SSDO. The apparent deterioration of MS2W performance beyond 15 days is not readily explained, but is probably because the nominal thrust level (and, therefore, the level of stochastic accelerations) is increasing during this time period.

h. Effect of Station Location Errors

Station location errors are not included in any of the performance data presented thus far, under the tacit assumption that they would be negligible with respect to the stochastic acceleration effects. This is a valid assumption for the single-station and MS2W tracking strategies, but not for MS3W and QVLBI, wherein errors in the estimate of spacecraft position are on the order of tens of kilometers. Consequently, the effect of "considering" station location errors was computed separately for each tracking strategy. These results are given in Table II-B-6. The indicated rms position errors are those resulting from expected (conservative) 1980-level station location errors of 1.5 m in spin radius, 3 m in longitude, and 5 m parallel to the spin axis of the earth. The station location effect is small because the geometry of the Encke mission is favorable in relation to earth. At the time of encounter, the distance from the earth is .3 AU, and the declination is 60 deg. These results were

obtained with batch-filter software, but the effect on the optimal sequential filter should be comparable.

Table II-B-6. Effect of Station Location Errors

Tracking Strategy	RMS Position Error From Station Locations, km	Total RMS Position Error for Baseline Optimal Filter Including Station Locations, km
SSDO	16.5	31,500
SSDR	15.1	2580
MS2W	16.6	284
MS3W	12.7	38
QVLBI	10.5	26

i. Concluding Remarks

The results of this study indicate that QVLBI is consistently the best tracking strategy, reducing orbit uncertainties to the order of 100 km with a single pass of data. However, if a reasonably accurate process noise model is available, explicit differencing of the two-way and three-way data is not required. Furthermore, if position errors on the order of several thousand kilometers are acceptable, single station tracking may be feasible with thrust-subsystem parameter errors at their present level. Improved single-station performance will result from reducing thrust-subsystem errors. On the other hand, much larger thrust-subsystem errors may be tolerated by the more sophisticated multistation tracking strategies without sacrificing orbit determination capability beyond the 1000-km level, providing that near-optimal filter performance can be achieved. A follow-up study will be required to fully assess the impact of mismodeling.

5. Approach Navigation

The term, navigation, in this report is used in its broad sense to include both the orbit determination and guidance functions. In the approach phase, the orbit of the spacecraft must be determined relative to the target body. When the target is a small body with large ephemeris uncertainty, e.g., a comet, onboard measurements, usually angular position measurements, possibly supplemented by onboard ranging, must be used. Orbit determination provides the state estimate required to implement guidance, i.e., the real-time generation of a control policy which provides the desired trajectory. Control depends upon the current estimate of the state of the vehicle, the definition of mission completion or success, and upon any constraints which are imposed on the control variables and/or the trajectory. For low thrust, the simplest approach to the development of a guidance scheme is to employ linear perturbation theory in which the guidance equations are based upon the linear terms in the expansion of the vehicle equations of motion about a reference or nominal trajectory. The guidance scheme seeks to control state deviations from that reference by generating corrections to the reference control program. Depending on the particular form of the linear algorithm, the vehicle is directed either back to the nominal, or along a new trajectory which is near the nominal and which also satisfies the mission.

This section is concerned primarily with the guidance problem for a SEP spacecraft. A simplified linear algorithm is developed and applied to the approach phase of a rendezvous mission to Encke. The terminal navigation accuracy is investigated and displayed as a function of the guidance interval and weighting parameters associated with the guidance algorithm. In addition, the effects of various factors which influence navigation performance through degradation or enhancement of the orbit determination process are investigated. These include the effect of various levels of process noise (stochastic nongravitational accelerations) and the effectiveness of onboard ranging in conjunction with various approach geometries.

a. Simplified Test Model Guidance Program

The present SEP guidance scheme is a simplified test model for the breadboard guidance program now under development. In this linear scheme, the reference trajectory is subdivided into a sequence of time intervals, and constant control corrections of limited magnitude are computed for each interval. The corrections are designed so that, at the time of nominal mission completion, the actual trajectory deviates from the nominal by as little as possible. The mathematical formulation of the scheme is based on the solution of the following optimal control problem:

The quantity

$$J = \sum_{i=1}^n \xi_{i, j+1}^2 A_i$$

is minimized subject to

$$\xi_{i, j+1} = \xi_{i, j} + \sum_{k=1}^m \Gamma_{kj} U_{kj}$$

and

$$|U_{kj}| \leq \alpha_{kj}, \quad k = 1 \text{ to } m$$

where

$\xi_{i, j}$ = the projected final error in state i caused by the state deviations at the start of interval j

$\xi_{i, j+1}$ = the projected final error in state i caused by the state deviations at the end of interval j

U_{kj} = control variable k in interval j

α_{kj} = bound on U_{kj}

Γ_{kj} = control coefficient for U_{kj}

A_i = weighting coefficient for $\xi_{i,i+1}$

Figure II-B-22 shows the general guidance procedure. The final error, $\xi_{i,j}$, results, if deviations X_j are permitted to propagate uncorrected to nominal final time t_f ; however, if X_j is reduced to X_{j+1} , the final error can be reduced to $\xi_{i,j+1}$; i.e., U_{kj} maps X_j into X_{j+1} which, when propagated uncorrected to t_f , yields the smallest final error.

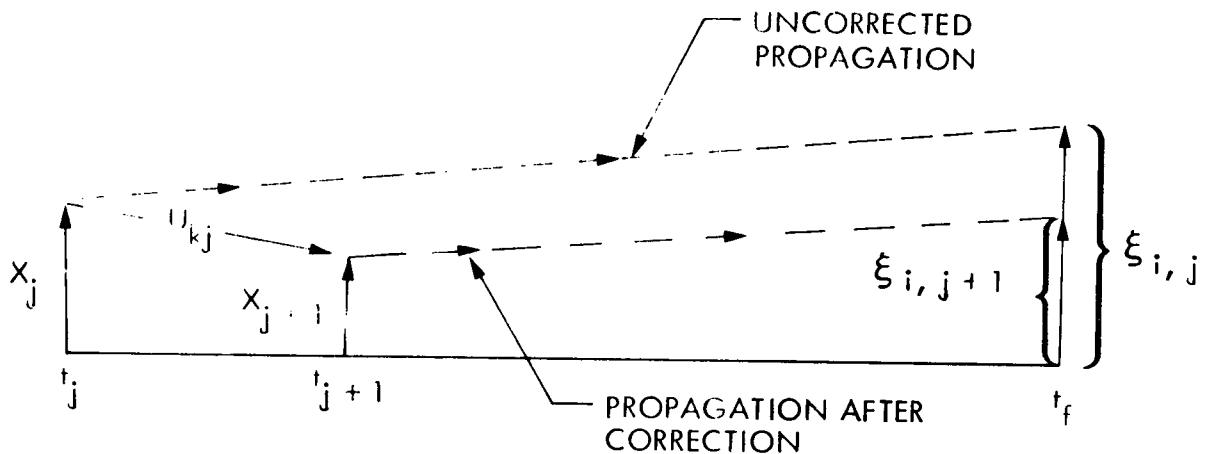


Fig. II-B-22. SEP Guidance Procedure

An obvious defect in the test model guidance scheme is that, at any time, only three constant control corrections are available to modify the trajectory. Consequently, the scheme can not, in general, null out the final deviations in more than three state variables; however, for more than three states, it will give the smallest final errors attainable with three controls. A more flexible guidance technique can overcome this limitation, but its development is beyond the scope of the simplified test model because any improvement increases complexity in both the computation and implementation of the control corrections.

The primary reasons for the formulation selected for the test model are:

- (1) By requiring the control corrections in the current time interval to minimize the final miss without considering the possibility of future corrections, the test model seeks to correct the trajectory as soon as possible. A guidance scheme with this characteristic of early correction is desirable because of the time needed for trajectory modification by a low thrust vehicle.
- (2) Simple corrections are best for reliability and ease of implementation; consequently, only constant control changes are employed.
- (3) The control determination algorithm must be computationally tractable, and constant changes in a single interval satisfy this requirement.
- (4) Hardware considerations limit the available control effort, and the bounds on the control variables explicitly account for this limitation.

This scheme does not explicitly require that state deviations prior to encounter be kept small, as do "state regulator" algorithms. To do so, would direct the control effort away from the primary goal of minimizing the terminal error. On the other hand, the large early state excursions and last-minute control corrections characteristic of conventional terminal controllers are eliminated by the requirement that the current control effort must minimize the projected terminal error without regard to future control opportunities. Thus, the undesirable features of both popular approaches are avoided. The underlying philosophy here is to do as much as possible toward reducing terminal errors as soon and as simply as possible.

b. Application of the Guidance Scheme to the Encke Rendezvous Mission

The test model guidance scheme has been applied to the approach phase of the Encke mission. In this mission, one of the major

difficulties is the lack of adequate knowledge of the comet ephemeris, which has uncertainties of about 30,000 km and tens of meters per second (Refs. II-B-17 and 18). The final approach navigation will use onboard optical tracking to determine the comet/spacecraft relative motion, and trajectory corrections will be made on the basis of the measured relative errors. Because of the time required to effect trajectory modifications, it is imperative that the comet be acquired and tracked prior to encounter for a period of time sufficient to permit any necessary corrections. It is then important to ascertain the latest time at which approach navigation can be initiated and still achieve a rendezvous. Because the guidance equations contain a set of unspecified weighting coefficients, it is also necessary to determine the best settings for these coefficients and to study the effect of changes in the settings on guidance system performance.

Figure II-B-23 is a plot of terminal miss in position and velocity versus initiation time and coefficient values. The intersection of a solid and a dashed line gives the final position and velocity errors, which will occur if guidance is initiated at the specified time with the specified weights (W_p for position, W_v for velocity). Initial $1-\sigma$ errors are taken to be 30,000 km and 11.57 m/sec (1000 km/day). Successful rendezvous is defined as final errors of less than 1000 km and 4 m/sec. It can be seen that approach navigation must be initiated no later than 40 days prior to nominal encounter, and that the best set of parameters is approximately $W_p = 1$, $W_v = 2$. As the duration of the navigation period increases, the values of the parameters become less critical, and the final state errors decrease.

For alternate mission studies, Fig. II-B-23 also contains a flyby region. All trajectories with terminal position errors of less than 1000 km lie within this region. It may be seen, for example, that if the comet were not acquired until 20 days prior to encounter, a flyby with a relative velocity of less than 20 m/sec is still possible.

All of the results given in the figure are based on an assumed process noise level of 1.8% of the nominal thrust acceleration. For

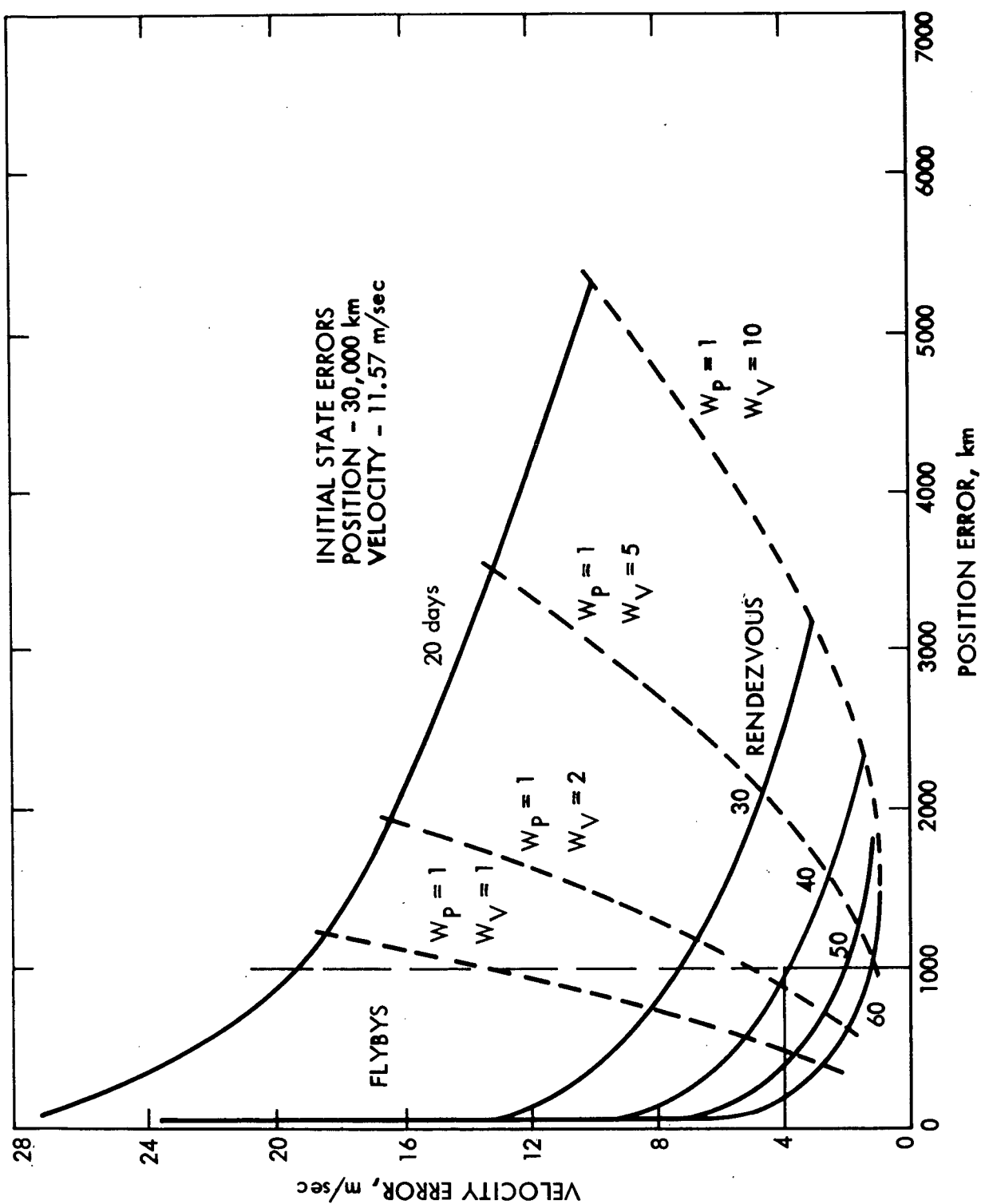


Fig. II-B-23. The rms Final State Errors Versus Flight Time and Weighting Parameters

hardware design specifications, it is important to know if successful missions are possible at higher levels. To answer that question, the 50-day rendezvous with parameters $W_p = 1$, $W_v = 2$, was selected as a baseline, and simulations were made with noise levels of 1.8, 4, 6, 7, and 8%. The results are given in Fig. II-B-24. It is clear that rendezvous is possible in the 4% case, and a slow flyby in the 6% case. However, at higher noise levels, the approach navigation scheme is unable to reduce the terminal state errors to acceptable values.

c. Approach Orbit Determination for the Encke Rendezvous Mission

All of the guidance results in the previous section are based on state deviations which were determined with both angle and range measurements. To reduce onboard hardware requirements, it is important to know if ranging is indeed necessary, or whether navigation is possible with angle measurements alone. For the latter possibility, the reference trajectory must be shaped so that deviations from the nominal angle measurements contain sufficient information to completely determine the state deviations. From a study of three different nominal approaches for the Encke mission, it was found that the unique ability of a low-thrust vehicle to shape its trajectory can be used to remove the need for onboard range measurements. In this study, the standard deviations of the angle measurement error, target-center-finding error, and the range-measurement error were taken as 100 arc sec, 10 and 1 km, respectively. Measurements were taken, and control corrections were implemented once each day. The vehicle was assumed to be experiencing a random acceleration which was spherically distributed with a $1-\sigma$ value of 1.8% of the nominal thrust acceleration and a correlation time of 5 days. Figures II-B-25 through 30 present the main results of the study.

The position uncertainty for a straight approach without ranging is shown in Fig. II-B-25. Although the crosstrack uncertainty drops off rapidly at first and then continues to decrease at a moderate rate, the down-track uncertainty is never reduced and, in fact, increases because of the presence of the process noise. The uncertainties for a straight approach to a point offset

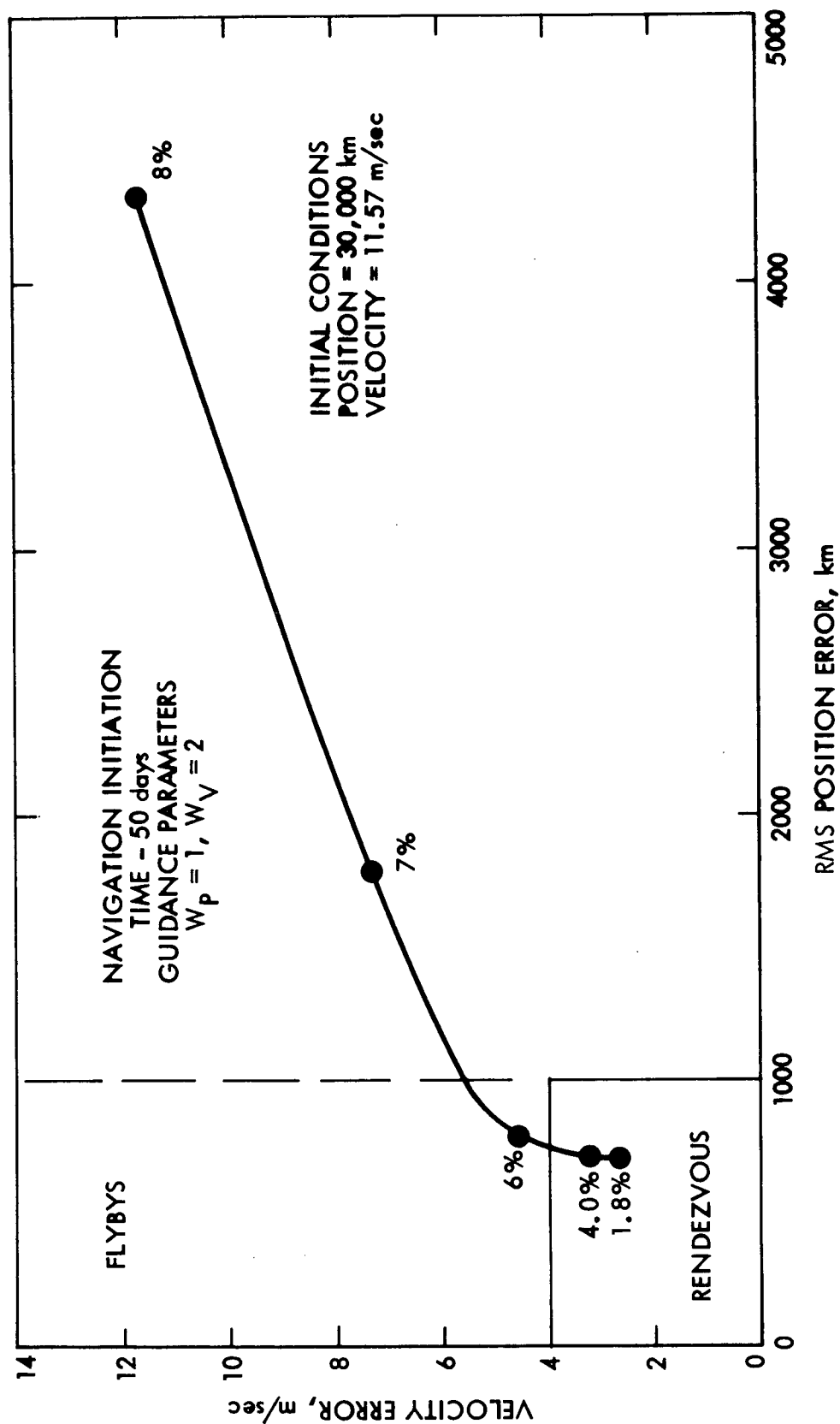


Fig. II-B-24. The rms Final State Errors Versus Process Noise Level

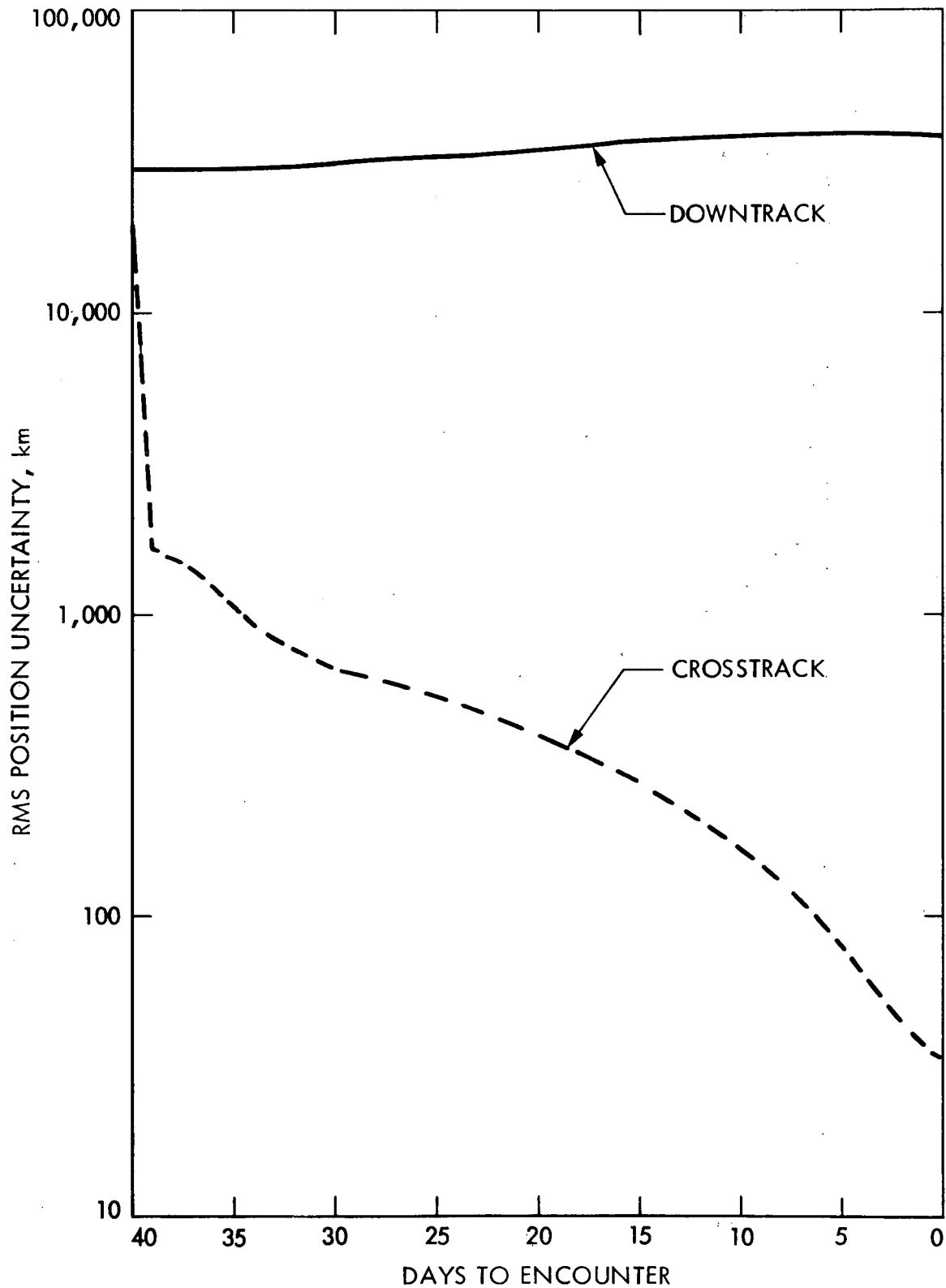


Fig. II-B-25. Orbit Determination Uncertainties for Straight Approach without Ranging

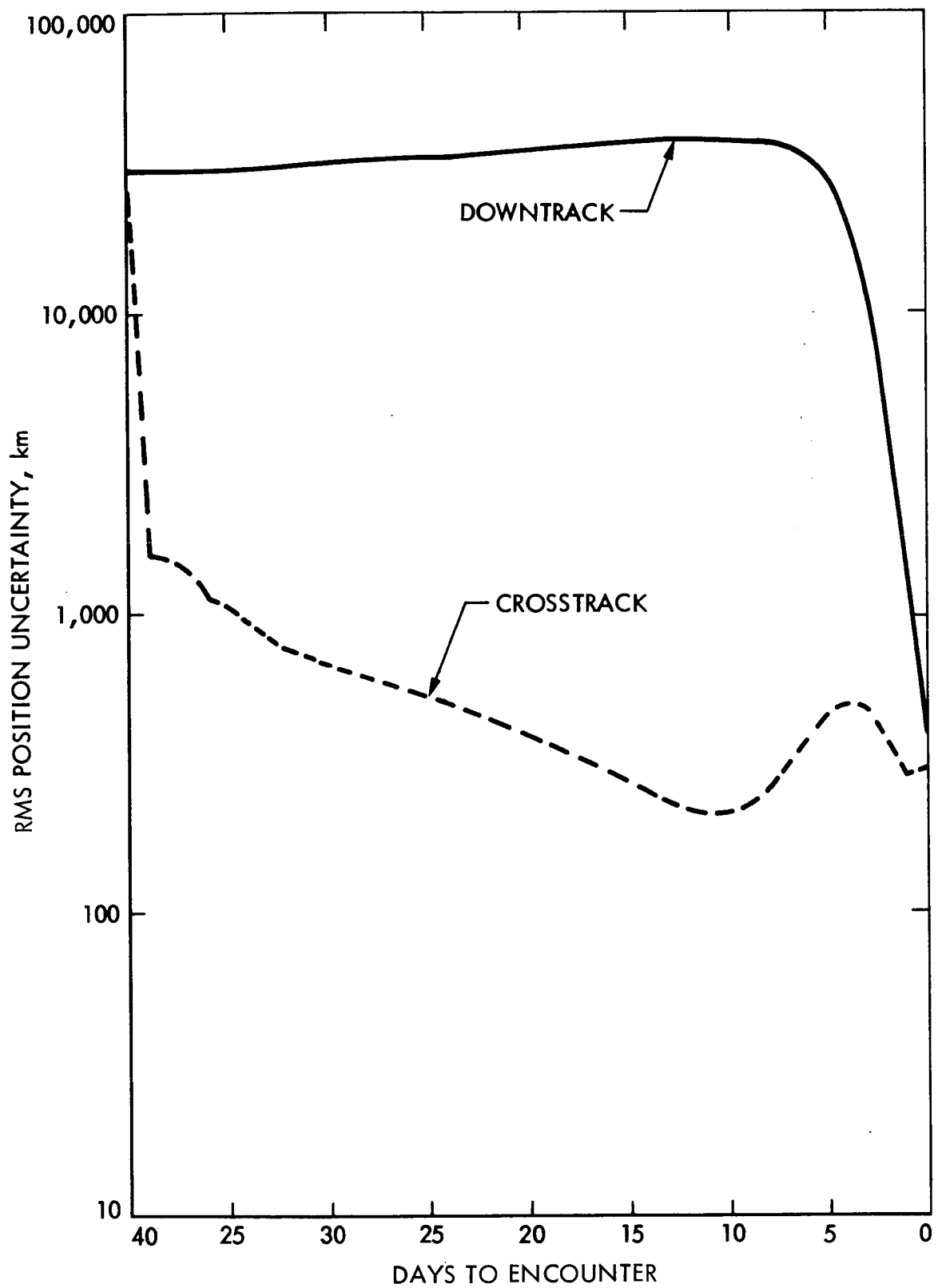


Fig. II-B-26. Orbit Determination Uncertainties for Straight Approach without Ranging and with Offset

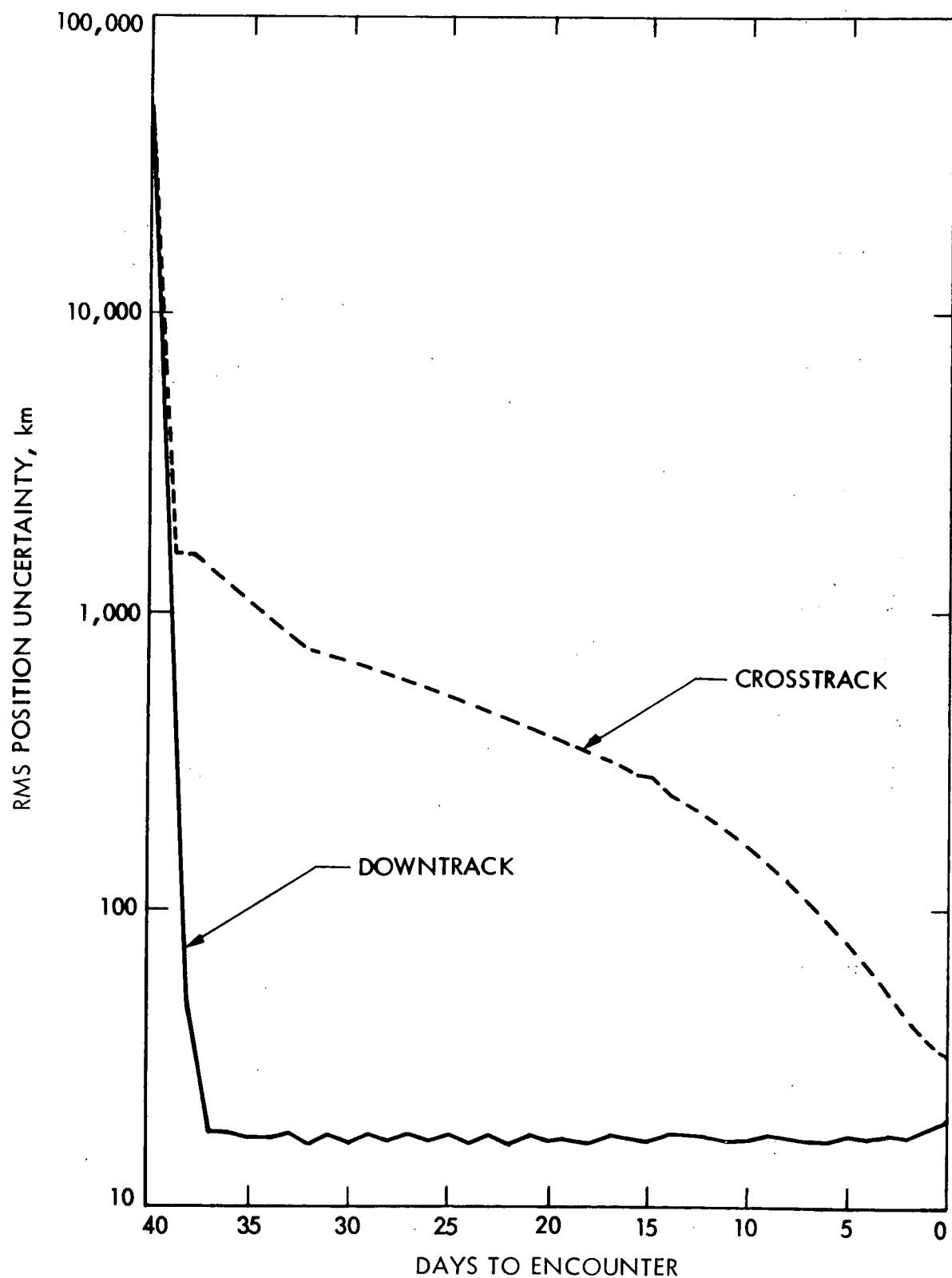


Fig. II-B-27. Orbit Determination Uncertainties for Straight Approach with Ranging and Offset

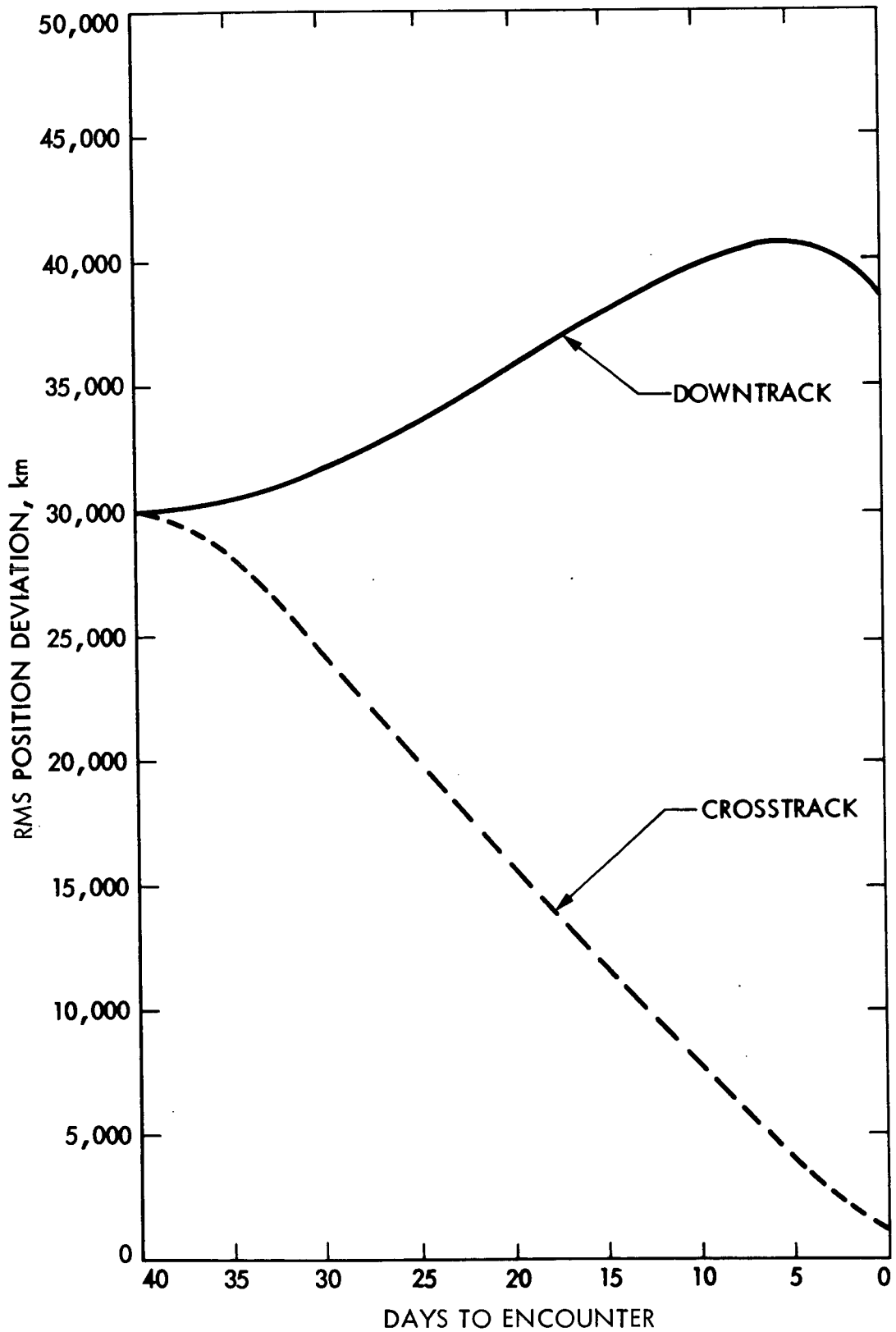


Fig. II-B-28. Guidance Results for Straight Approach without Ranging and with Offset

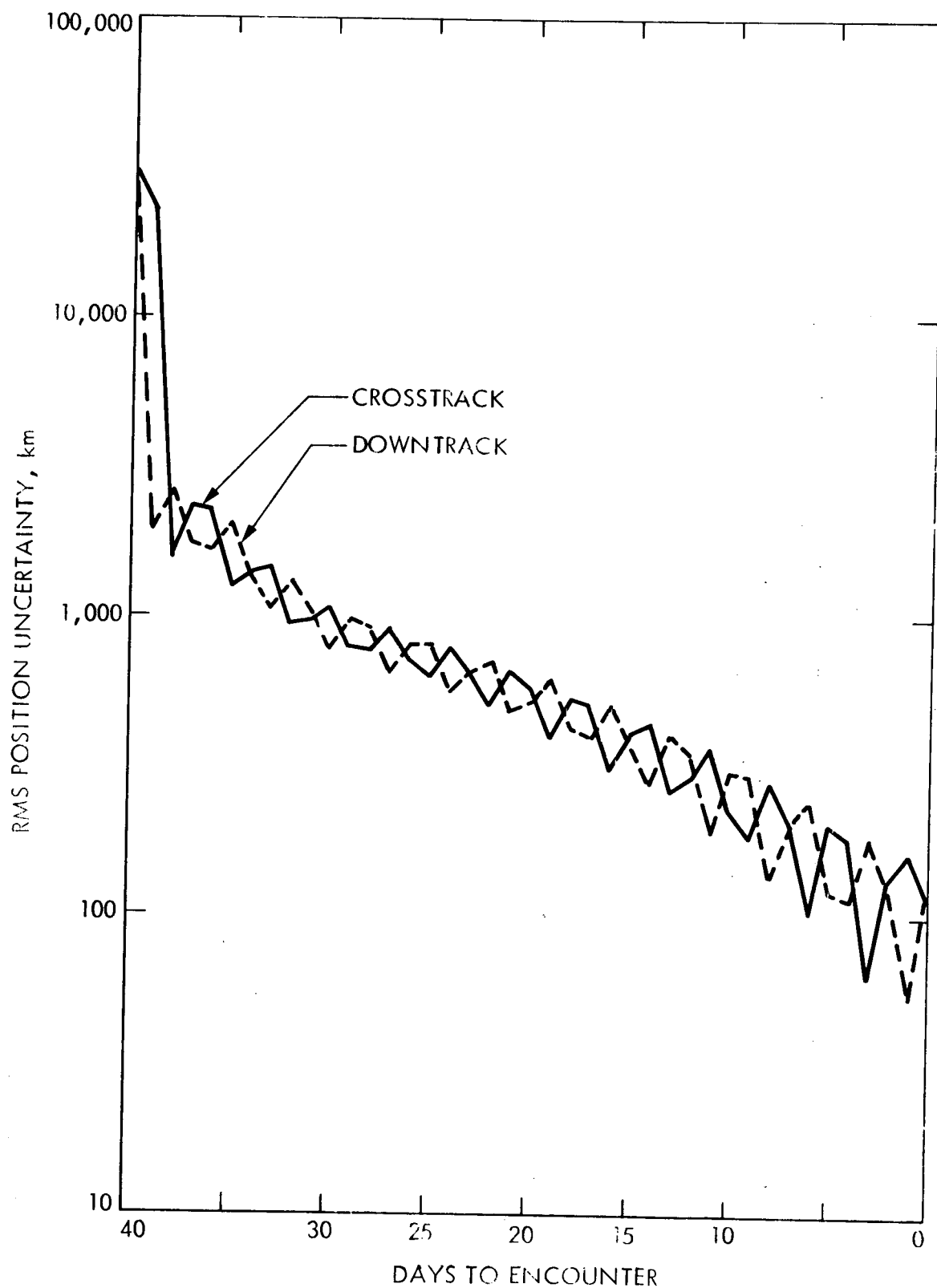


Fig. II-B-29. Orbit Determination Uncertainties for Curved Approach without Ranging

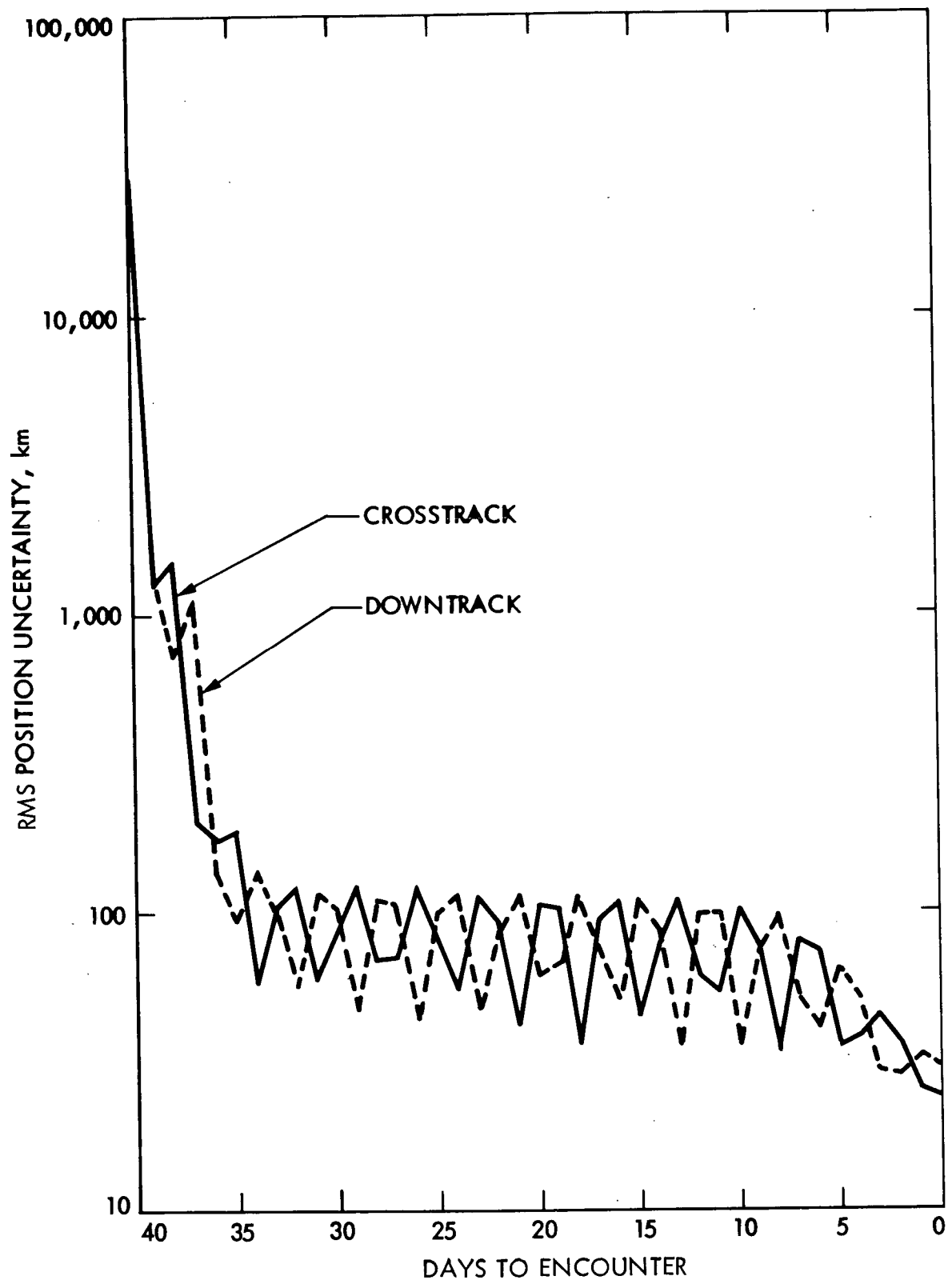


Fig. II-B-30. Orbit Determination Uncertainties for Curved Approach with Ranging

from the comet by about 1000 km are given in Fig. II-B-26 and 27 for cases without and with ranging, respectively. Although the final crosstrack and down-track positions are determined within acceptable limits, it is clear that including range measurements gives an order of magnitude improvement. More important, however, is the fact that, in the absence of ranging, the downtrack uncertainty is removed too late; and the guidance scheme is unable to correct the trajectory. This effect is demonstrated by a plot of the state deviations in Fig. II-B-28. During the first 35 days of the approach, downtrack errors can not be removed because of the position uncertainty, and in the last 5 days, when the uncertainty decreases, insufficient time remains for the large position error to be substantially reduced.

Figures II-B-29 and 30 give the position uncertainties associated with the curved approach shown in Fig. II-B-31. The results of Fig. II-B-29 were obtained without ranging; those of Fig. II-B-30 included range measurements. It can be seen that, with the curved nominal trajectory, accurate position determination is possible with angle measurements alone. Although the addition of ranging produces an improvement by a factor of four to five in orbit determination capability, the uncertainties are already at such a low level that the additional reduction has little effect on overall navigation performance. For example, for the case under investigation, the final down-track and crosstrack errors are reduced from 866 and 922 km to 837 and 896 km, respectively, when the range measurements are included.

d. Conclusion

This report has presented a simple linear test model guidance scheme for the SEP spacecraft and employed it in an analysis of terminal navigation for a rendezvous mission with Encke. It can be concluded from the analysis that:

- (1) In spite of the large ephemeris uncertainty of Encke, rendezvous is possible if onboard navigation is initiated earlier than 40 days prior to encounter.

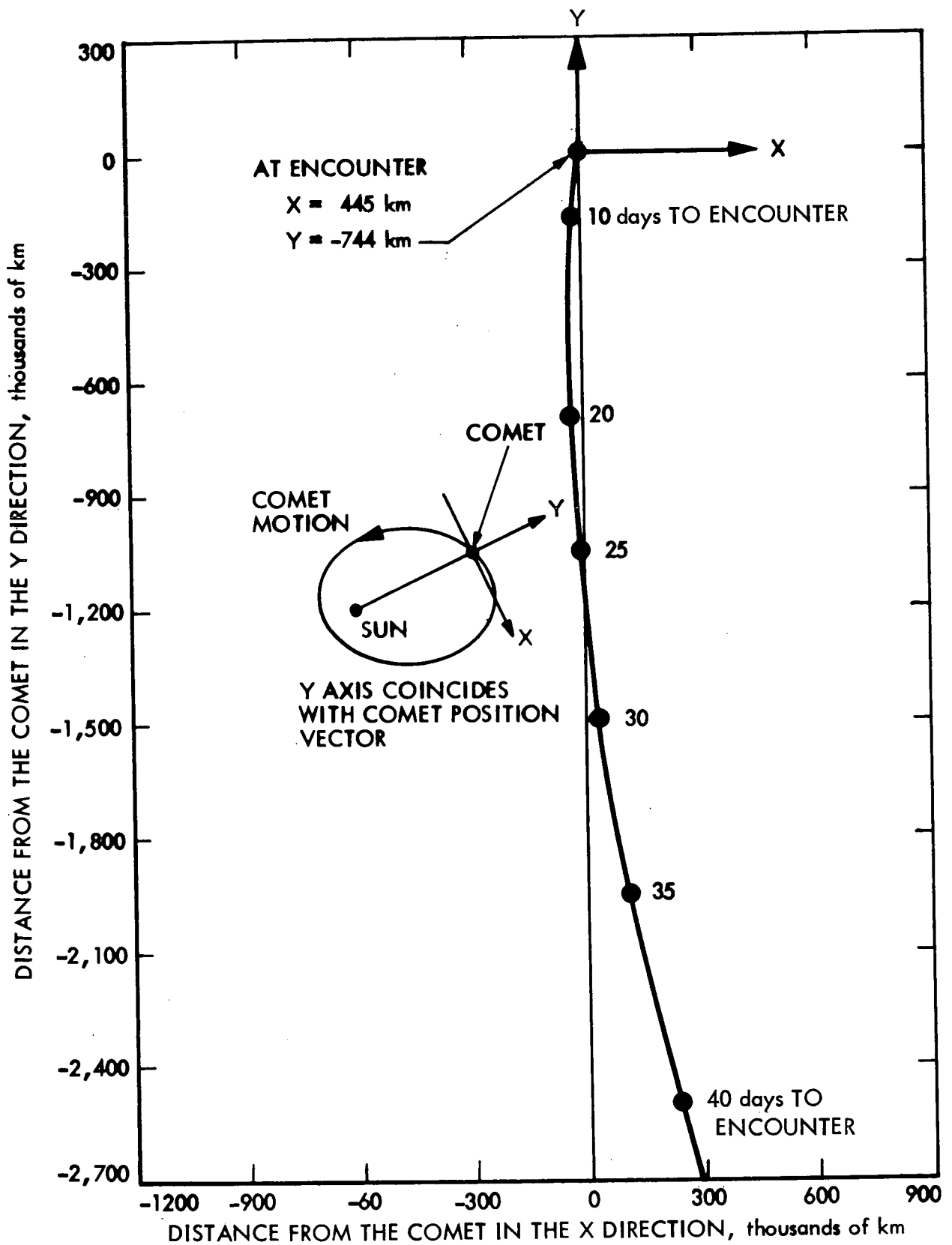


Fig. II-B-31. Curved Approach Trajectory

- (2) The reduction of terminal state errors becomes more difficult as process noise levels increase. At levels above 5% of the nominal thrust acceleration, rendezvous can not be achieved if terminal navigation begins later than 50 days prior to encounter.
- (3) The use of a curved nominal approach trajectory permits orbit determination without relative range measurements and, consequently, reduces the onboard hardware requirements.

6. Physical/Photometric Model of Encke and Imaging Considerations for Approach Guidance

a. Introduction

Accurate navigation and guidance⁽¹⁾ of an electrically propelled spacecraft near an ephemeral target such as a comet or an asteroid is a challenging task. Discerning an adequate approach-guidance strategy to achieve the required terminal state can be difficult under certain adverse conditions concerning the absolute state of the spacecraft and spacecraft state relative to the target. The following considerations pertinent to these adverse effects are introduced in brief to motivate the need for accurate physical and photometric models of the target body, here assumed to be the short period comet, Encke.

Comet ephemerides are notoriously poor, primarily because of unmodeled secular forces (thrust) produced by ejection of material at the nuclear surface. However, recent advances in cometary physics and orbit determination by Delsemme, Whipple, Marsden, et al, (Ref. II-B-18) have reduced ephemeris uncertainties considerably. These uncertainties still remain large in a relative sense to the extent that the uncertainty along the line of sight may be on the order of 10,000 to 30,000 km, even after recovery by

⁽¹⁾Henceforth collectively referred to as approach guidance.

earth-based telescope some hundreds of days before perihelion and assuming additional knowledge based on previous passages. State uncertainties normal to the line of sight may be on the order of hundreds to a few thousands of kilometers. Approach guidance difficulties arise when the approach asymptote is nearly colinear with the axis of maximum ephemeris uncertainty. Without direct range measurements, range determination depends entirely upon derived observations from the imaging sensor, which is autonomously insensitive to range variations. If the approach trajectory is biased or has significant curvature, range data can be extracted by observing cross-track motion. However, the process of indirect range determination requires a comparatively large number of optical measurements over a long period of time, especially if the approach cross-axis dynamics are slow, as in a rendezvous encounter. The range ephemeris problem is further aggravated by limited control effort (tens of μg availability) and the presence of relatively high levels of process noise caused by thrust-parameter uncertainties, which map into an uncertainty in the application of control effort. As a direct consequence of these adverse effects, it is concluded that successful approach guidance could depend upon the earliest possible detection of the target body by the imaging system. For the mission currently under study, guidance considerations indicate that a rendezvous condition can be achieved if the comet is acquired no less than 40 days prior to encounter (E - 40). However, nominal recovery is assumed to occur at E - 60 days to account for uncertainties in the photometric model.

To assess the severity of this requirement on the imaging system, it is necessary to acquire physical and photometric data for the comet. The procedure adopted here is to employ the data compiled in Ref. II-B-18. A generalized set of optics design curves were derived in terms of the defined photometric data. These design curves are subsequently used to synthesize optical parameters for a specified approach-guidance strategy. Vidicon sensor/electronics and raster size/resolution are assumed to be of the Mariner class.

b. Summary of Results

The principal concern of this imaging study was the investigation of the factors and tradeoffs involved in optics selection for guidance

considerations alone. Optics design was based on considering the pseudo point-source sensitivity to be valid, if the majority of the flux from the coma, as an extended source, is contained within a single picture element, as imaged. A conclusion of the survey made of Ref. II-B-18 indicates that the generalized icy-halo model of coma formation suggested by Delsemme and Miller is applicable to Encke. In its basic conception, the nucleus is surrounded by a dense shroud of highly reflective sublimating ice crystals. The radius of the halo is subject to conjecture. However, expected values are bounded between $r_1 = 100$ and $r_2 = 2500$ km.

The fundamental ploy used in optics synthesis for guidance was to combine the suggested surface brightness model and integrated photometric data with experimentally derived detectability data for the Mariner narrow-angle (telephoto) camera as obtained from the Mariner Mars 71 optical navigation demonstration (OND). Results of the OND experiment indicated that a star of 7.5^m could be recovered from the video data and identified with virtually 100% confidence. Star detectivity threshold of 7.5^m was subsequently used as the reference for visual magnitude comparisons with the integrated surface brightness as imaged over a single picture element. Optical parameters were synthesized from the visual magnitude estimates by comparison with the nominal parameters of the narrow-angle camera.

Optical parameter synthesis was accomplished by the following method. The optics synthesis model in terms of the reduced quantities of the lens speed, N , focal length, F , and integration time, T , is given by

$$N = F T^{\frac{1}{4}} 10^{-\Delta V(f)/10} \quad (1)$$

where

$$\Delta V(f) = V(f) - V_r$$

$V(f)$ is the visual magnitude of the coma integrated over the central picture element for the specified surface radiation pattern, and V_r is the reference threshold

visual magnitude of 7.5^m (see Table II-B-7 for nomenclature). Figures II-B-32 and 33 are plots of equation (1) for two surface radiation patterns and the Mariner reference optics data, as indicated. Point source data was calculated from (1) the assumption that the visual magnitude of the central coma (here assumed to be the halo-nucleus combination), as imaged, is not a function of focal length. Magnitude curves for the brightness of the pertinent components as a function of cometocentric distance, with time to encounter as a parameter, are plotted in Fig. II-B-34. The data for the coma, as imaged, represents an example of a specific set of optics to demonstrate the pertinent considerations. Optical parameters are focal length $f = 200$ mm, lens speed $n = .75$ with aperture diameter $d = 26.7$ cm. Nominal integration times are 9.0 and 31.3 sec for central halo radii of 100 and 2500 km, respectively. A 2^m error in the photometric model shifts the recovery time to E - 35 and E - 30 days, respectively, if additional integration time (9 sec, 11 sec) is not allotted.

Optical parameters were chosen by the following means. Requirements for changes in N and errors in the brightness model $V(f)$ induce a requirement for change in integration time according to the sensitivity relation

$$\Delta T = \left. \frac{\partial T}{\partial N} \right|_{\Delta V, F} \Delta N + \left. \frac{\partial T}{\partial V(f)} \right|_{N, F} \Delta V(f) \quad (2)$$

An $n = .75$ ($N = .3$) aperture is assumed to be the smallest that can be practically realized in terms of design and construction. An $n = 2$ ($N = .8$) aperture is assumed to be the largest that will provide the point source resolution (diffraction limit of $10\text{-}\mu\text{m}$, $25\text{-}\mu\text{m}$ spot size) similar to Mariner Mars 71 (Ref. II-B-18). It is assumed that aperture diameter $d = 20$ cm so that the constraint $N = F$ is established as shown in Fig. II-B-32 and 33. Table II-B-8 summarizes the values of n and f necessary for $N = F$ and the required integration times for both point-source and central-halo radii of 100 and 2500 km, respectively. Also tabulated is the contingency increase in integration time required for a 2^m error in the value of $V(f)$, assuming the surface brightness model is correct, and the penalty in later recover date ΔE for not allowing for the extended integration time because of an error in $V(f)$.

Table II-B-7. Nomenclature

A	Areal density, dimensionless
a	Aperture
a_N	Nucleus cross sectional area
d	Aperture diameter, cm
f	Optical focal length, mm
t	Integration time for the imaging system, sec
n	Lens speed = f/d
η	Lens system transmission efficiency, dimensionless
F	Reduced focal length relative to the reference sensor, f/f_r
N	Reduced lens speed n/n_r
T	Reduced integration time (shutter speed), t/t_r
$I(r)$	Source luminous intensity or radiation pattern, cd (lm/sr)
I_\odot	Luminous intensity of the sun
F	Total flux (power) absorbed (lm)
Ω	Solid angle, steradians
r	Distance from the nucleus at the source
R	Distance from the center of the lens at the raster surface
ρ	Comet-observer distance, AU
Δ	Comet-sun distance, AU
V	Visual magnitude, dimensionless
α	Albedo or reflectance factor
$\phi(\theta)$	Phase function
θ	Phase angle, deg

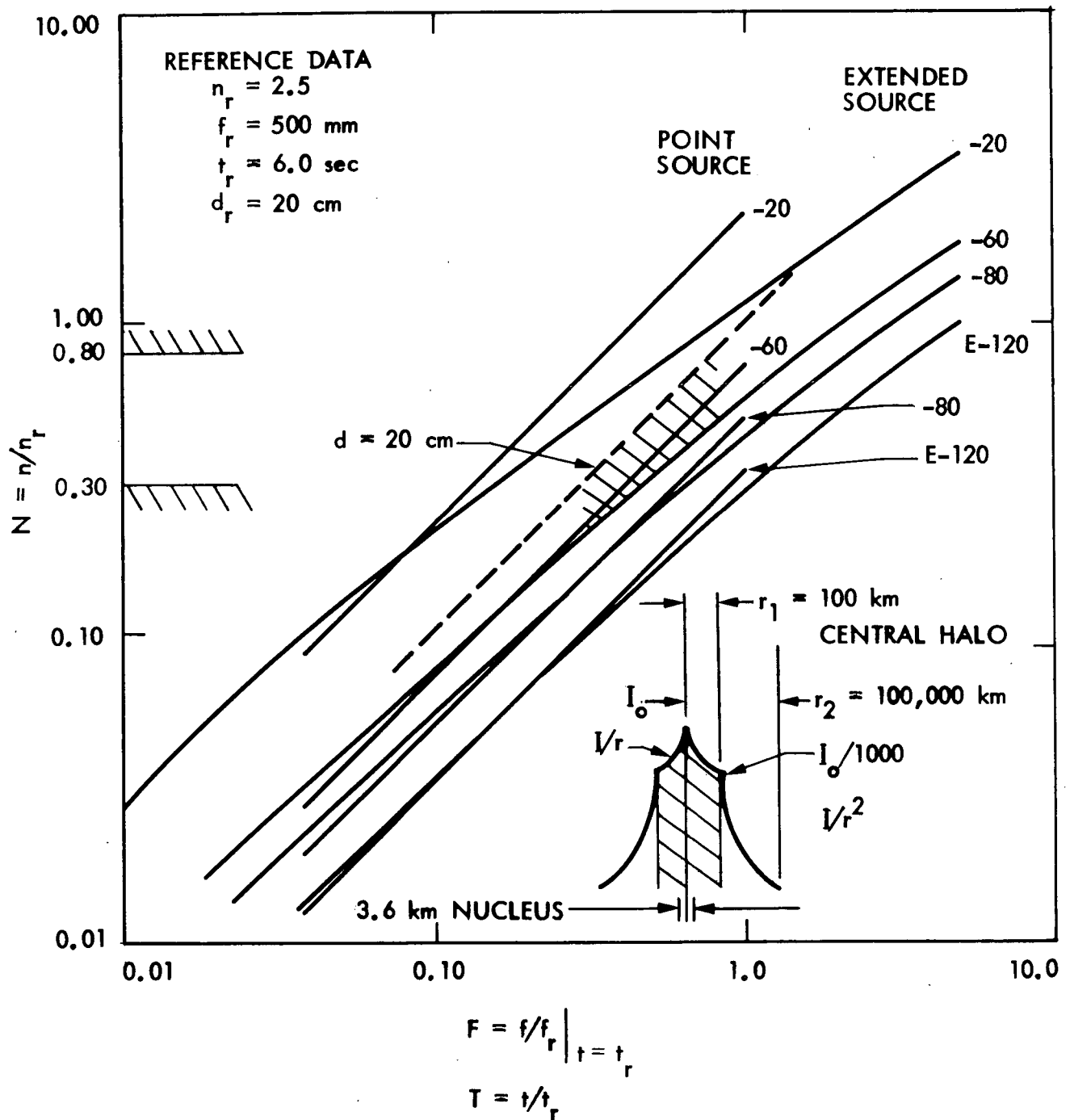


Fig. II-B-32. Optics Design Curves for $r_1 = 100 \text{ km}$

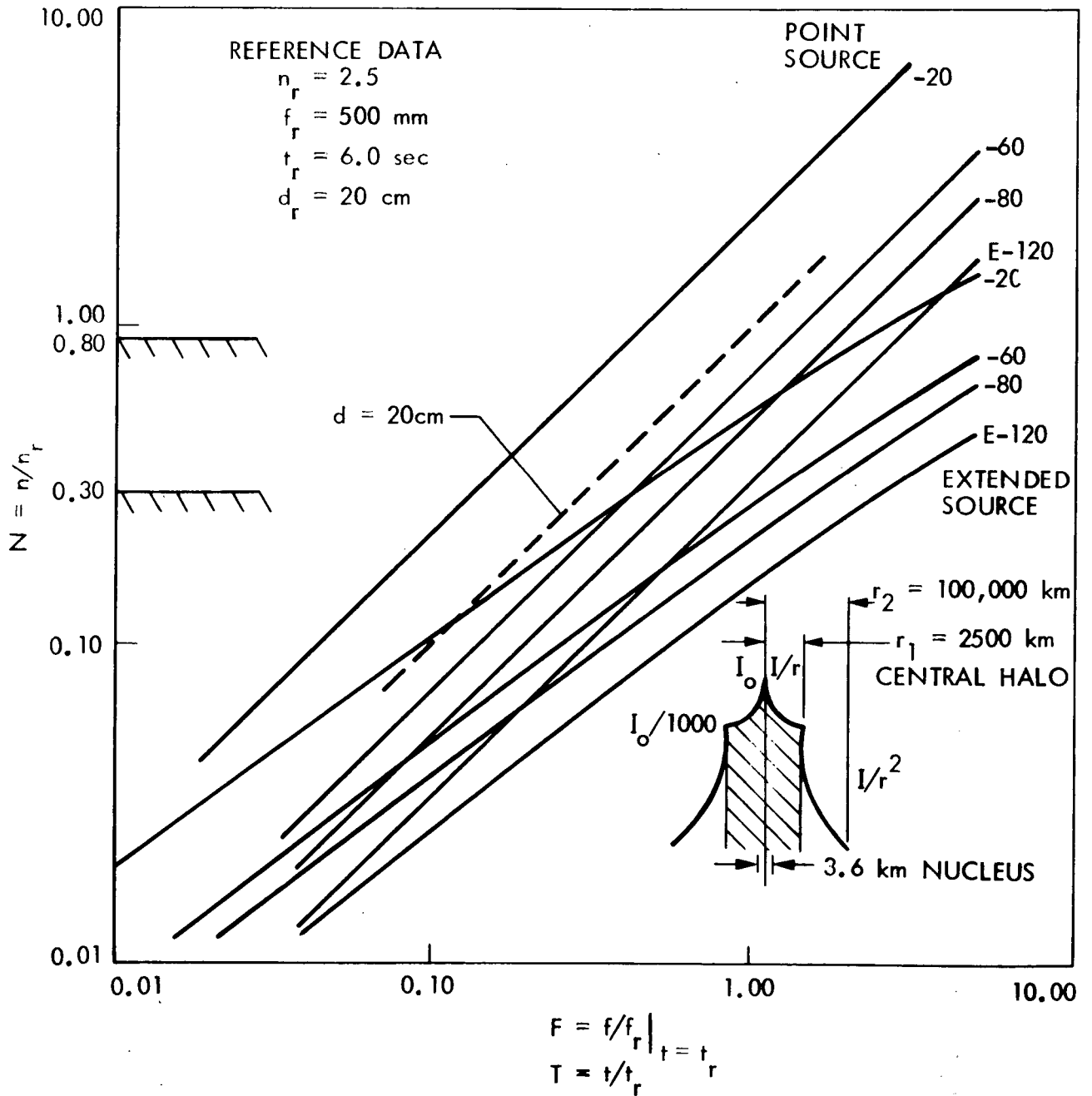


Fig. II-B-33. Optics Design Curves for $r_1 = 2500 \text{ km}$

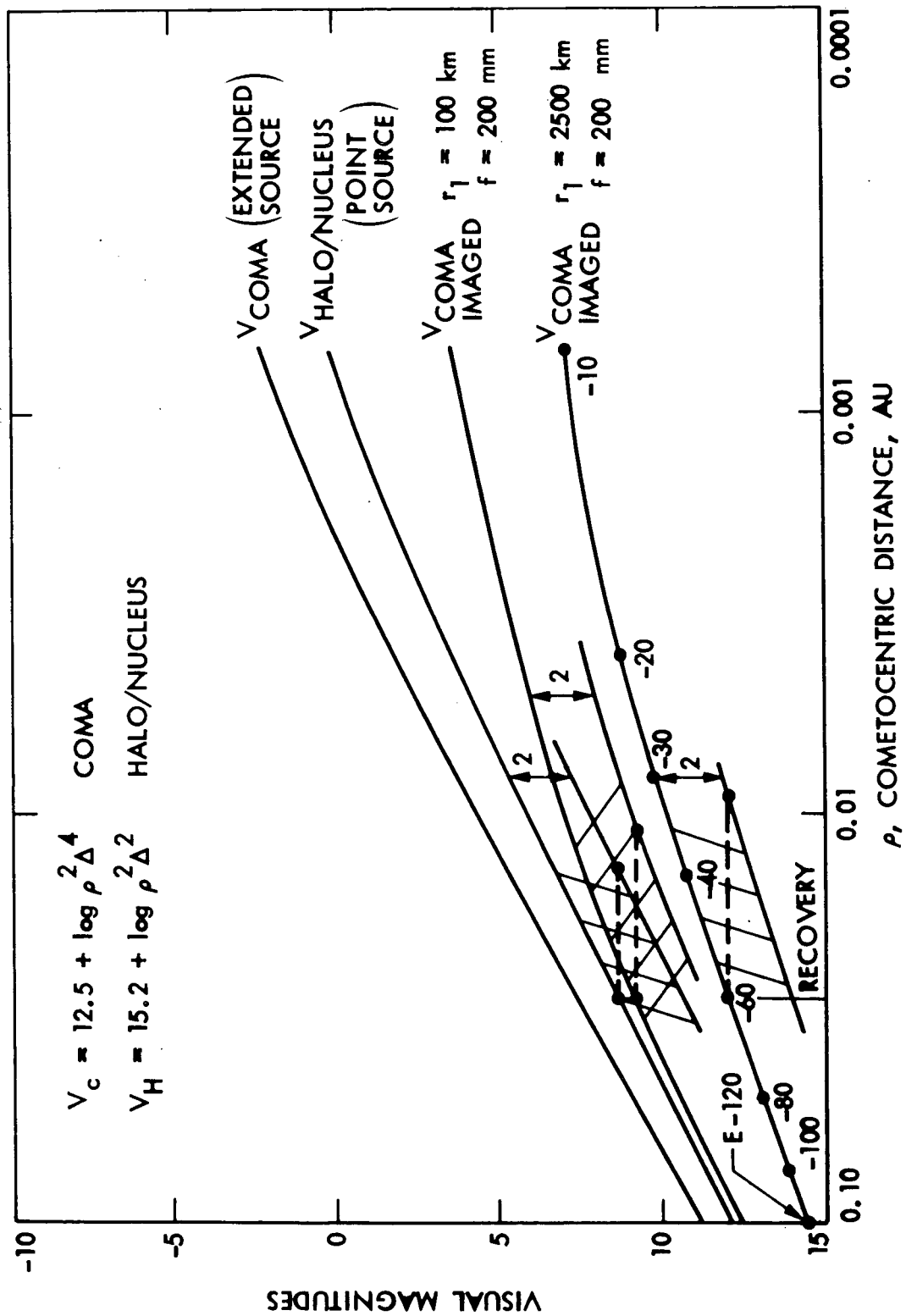


Fig. II-B-34. Photometric Models of Encke

Table II-B-8. Approach Guidance Vidicon Optics Requirements

Optics Parameters		Point Source	Extended Source		$\Delta V_m = 2^m$					
F, reduced	f, mm	t_p , sec V_m	$t_{100'}$, sec V_m	$t_{2500'}$, sec V_m	Δt_p	Δt_{100}	Δt_{2500}	ΔE_p , days	$\Delta E_{100'}$, days	$\Delta E_{2500'}$, days
.30	150	14.7 8.85	17.2 9.03	46.8 11.77	12	9	11	20	25	30
.45	225	14.7 8.85	19.5 9.25	53.2 12.15	12	10	10	20	27	30
.55	275	14.7 8.85	19.7 9.45	60.5 12.45	12	10	9	20	28	30
.65	325	14.7 8.85	20.9 9.60	60.3 12.65	12	12	12	20	29	30
.80	400	14.7 8.85	23.5 9.86	64.7 12.90	12	9	12	20	30	30

Approach Guidance Assumptions

Mariner sensor electronics

Miss distance, 0.0

Reference $V_m = 7.5^m$ Target maximum velocity, .30 μ r/sec

Aperture diameter, d = 20 cm

Surface brightness models $r_1 = 100$ km, $r_1 = 2500$ km

Nominal recovery, E - 60 days

Imaging impact on approach guidance is shown in Fig. II-B-35. This data indicates the performance of a particular optimal guidance algorithm as described in Ref. II-B-19. Performance is shown in terms of rms final state errors in position/velocity with time-to-go and position/velocity weighting indices as variable parameters. A rendezvous is considered to be achieved if $\sigma_V \leq 4$ m/sec and $\sigma_p \leq 1000$ km. The shaded areas indicate expected guidance performance with imposed imaging constraints from Table II-B-8, assuming no contingency allotment in integration time for a maximum expected 2^m error in the photometric model. For maximum sensitivity (shortest focal length/largest aperture), $n = .75$ so that $f = 150$ mm. From Table II-B-8, the maximum expected integration time is 58 sec. Assuming a worse case target velocity of $0.30 \mu\text{rad/sec}$, the central halo image could be smeared over $.30 (58) (150) (60) (10^{-6}) = .157$ picture elements with the raster scale factor assumed to be 60 picture elements/mm. The resulting field of view is $5.5 \text{ deg} \times 4.6 \text{ deg}$, which is more than adequate for imaging a star field containing a number (greater than two) of 8^m stars.

Recovery from the video data was assessed by the following considerations. If a $25\text{-}\mu\text{m}$ spot size and a $10\text{-}\mu\text{m}$ point source diffraction pattern are assumed, a point source would form an image on the raster surface in accordance with the convolution of the spot and diffraction patterns with a distributed adjustment in magnitude caused by smear velocity. The physical dimension of a picture element is $1/60 = 16 \mu\text{m}$. Neglecting target motion, the image would be contained within two picture elements. If it is assumed that the majority of the radiation from the central halo as an extended source is contained with a single picture element, the resulting image usable for identification would be contained within two to three picture elements, as imaged. Because of the very sharp peak on the coma radiation pattern, the resulting video image might very well simulate a noise spike. However, a camera modification to include a peak detection scheme, as outlined in Ref. II-B-18, and/or a multiple picture sequence would greatly enhance identification.

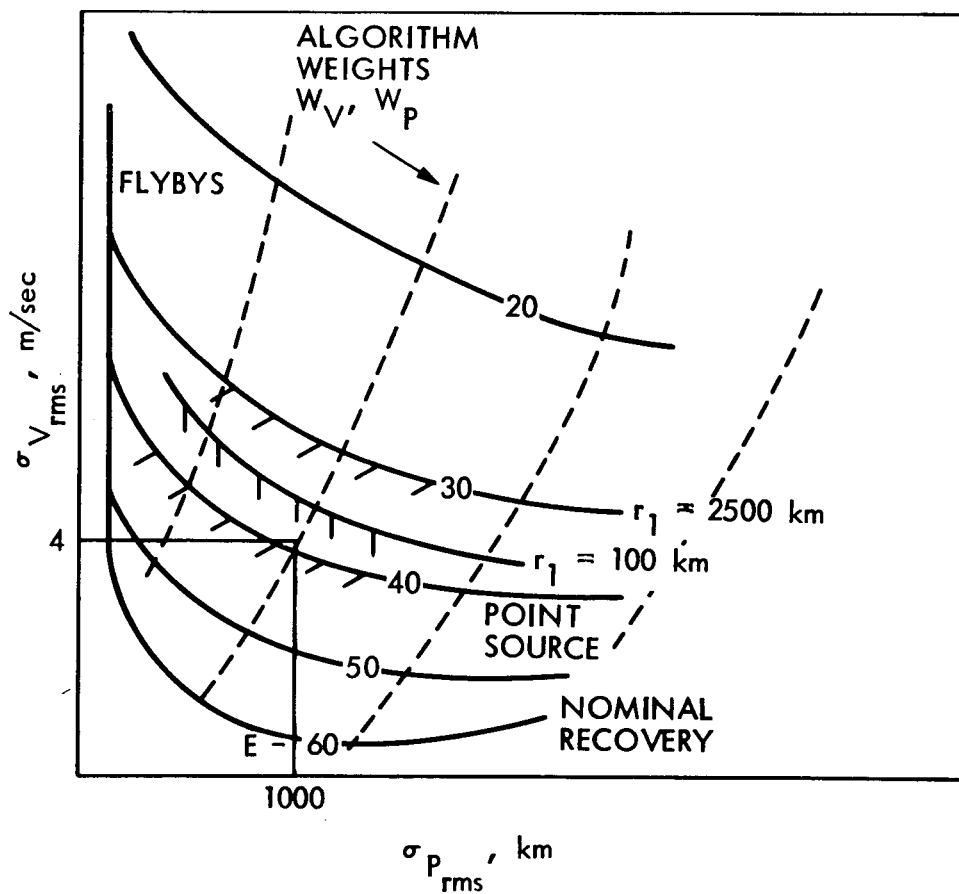


Fig. II-B-35. Guidance Performance Imposed by Unmodeled Errors in the Photometric Model

c. Physical Model of Encke's Coma

To draw some inferences concerning the extended source photometrics of Encke, a model of the coma in terms of its dimensions and physical constituents is presented. This data is a very brief summary of Section 2.4 in Ref. II-B-18.

It is reasonably assumed that the bulk of desorbed gas escaping from the nucleus is H_2O because large quantities of OH and H are associated with Encke. The gas is presumed to leave the nuclear surface at nearly Mach 1 and, a few nuclear radii removed, is accelerated to approximately 1 km/sec. Number densities of parent H_2O and molecules (CO_2 , CH_4 , N_2 , H_2 , He) decrease in proportion to $1/r^2$ from the nucleus to a distance of roughly 10^4 km. The radial region in which the gas exists as parent molecules must be on the order of τ/V where τ is the characteristic time for photodissociation by sunlight and V is the expansion speed for the undissociated gas. Since $\tau \sim 10^4, 10^5$ sec at 1 AU for most molecules, the characteristic size of the molecular region is about 10^4 to 10^5 km at 1 AU. The previous arguments are not applicable ad hoc because the state of the nucleus is essentially independent of any chemical and/or gas dynamical generalities.

Delsemme and Miller proposed a more far reaching theory of coma formation predicated primarily on the objection that photodissociation alone was insufficient over a 10^3 -to 10^4 -km cross section to account for the supply of material required to explain the observed features in the coma. In the proposed model, condensates of H_2O form a nuclear mantle of a snowy lattice-like substance at large heliocentric distances. Radiation caused by solar flux accelerates desorbed gas from the icy surface. The desorbed gas dislodge small icy grains of the snow. The grains contain additional trapped volatiles, which are released by solar radiation as they move outward. The gas molecules are subsequently dissociated and ionized. The resulting halo thus provides a partial shroud of ice crystals of high albedo which are accelerated away from the nucleus along with primary neutral gas. The grains are linearly reduced in size because of sublimation and disintegration by secondary

desorption of trapped gas. According to Delsemme and Miller, laboratory results indicate that approximately 90% of the grains would not be propagated to distances exceeding 4000 km from the nucleus at 1 AU heliocentric distance. The dependence of average halo radius on heliocentric distance is empirically derived to be about

$$r_H = 3200 \Delta^{1.22} \text{ km}$$

Based on this calculation, it can be concluded that the halo might occupy the same area as the neutral inner coma in prehalo models of coma formation.

Target acquisition and approach guidance will occur at heliocentric distances between 1 and 2 AU so that the average halo radius during the approach phase will be about

$$r_H = 3200 (1.5)^{1.22} = 5250 \text{ km}$$

d. Photometrics of Encke

1) Geometric Nucleus. The light flux density (brightness) of a cometary head emitted solely by reflectance will be represented by an asteroidal relation of the form

$$F = \frac{F_o(\alpha, r_N)}{\rho^2 \Delta^2} \phi(\theta) \quad (3)$$

The constant of proportionality F_o is readily derived by some rather simple photometric considerations. A comparison is made of the flux (power) received by the observer on earth, as shown in Fig. II-B-36.

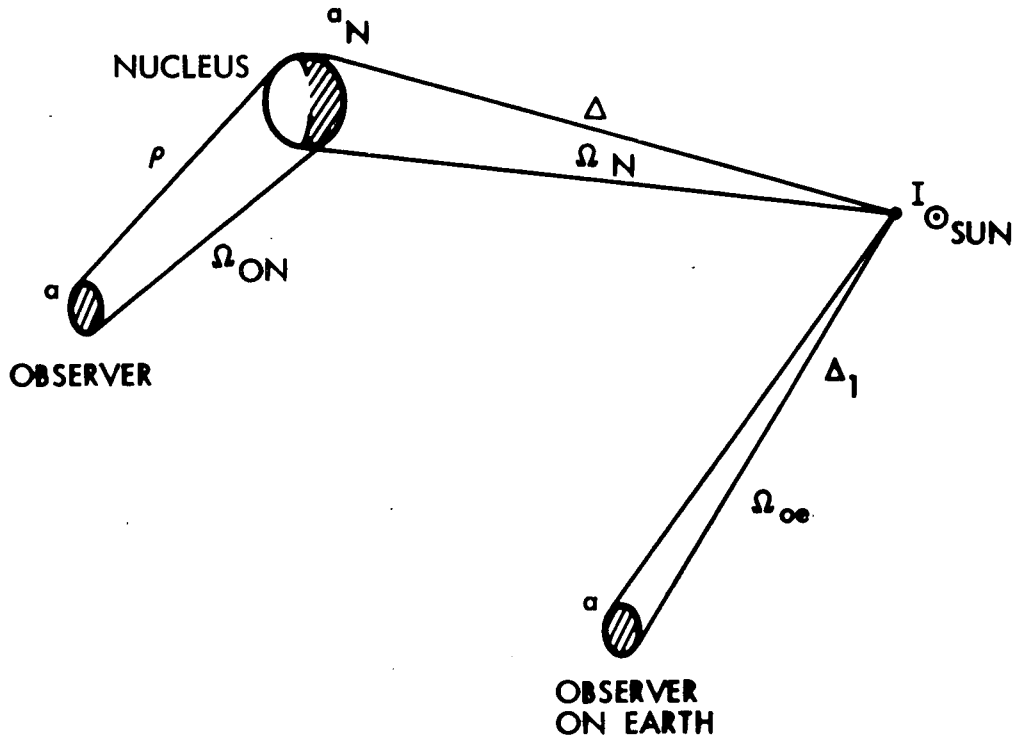


Fig. II-B-36. Photometric Geometry for a Point Source

Flux from the sun received by the target is

$$F_N = \int I_{\odot} d\Omega_N = I_{\odot} \frac{a_N^2}{\Delta^2}$$

Flux from the sun received by an observer on earth is

$$F_{oe} = \int I_{\odot} d\Omega_{oe} = I_{\odot} \frac{a^2}{\Delta_1^2}$$

Flux from the sun reflected by the target to the observer on board the spacecraft is

$$F_o = F_N \frac{a/\rho^2}{4\pi} \Psi(\theta) \alpha$$

Combination of the above relations allows solution of F_o in terms of F_{oe}

$$F_o = F_{oe} \frac{\Delta_1^2 r_N^2}{\rho^2 \Delta^2} \alpha \phi(\theta) \quad (4)$$

where $\phi(\theta) = \Psi(\theta)/4 = 1.0$ @ $\theta = 0^\circ$

Comparing (3) with (4)

$$F_o (\alpha_1 r_N) = F_{oe} \Delta_1^2 r_N^2 \alpha$$

Visual magnitude equivalence of (4) by the relation

$$\frac{F}{F_{oe}} = 10^{-(V_m - V_{m_{oe}})/2.5} \quad \text{gives}$$

$$V_{m_N} = V_{m_{oe}} - \log_{10} \frac{\alpha \phi r_N^2}{\rho^2 \Delta^2}, \quad \Delta_1 = 1 \text{ AU},$$

where the sun, as seen from earth, is -26.72^m . Roemer (Ref. II-B-20) computed the nuclear radius of Encke using 13 independent magnitude observations for the 1957 and 1960 apparitions with the following results:

$$r_N = 3.5 \text{ km, assuming } \alpha = 0.02$$

$$r_N = 0.6 \text{ km, assuming } \alpha = 0.70$$

The probable range of r_N is $1.8 \leq r_N \leq 4.5$ and is based on the concept that the nucleus of Encke is a dying asteroidal object of very low albedo; $\alpha = .02$ corresponds to the reflectivity of the blackest asteroids. The value $\alpha = .70$ represents the reflectivity of H_2O solids and of Venus.

Using the former values of αr_N yields the magnitude relation for the geometric nucleus of Encke,

$$V_{m_N} = 13.2 - \log \frac{\emptyset}{\rho^2 \Delta^2} \quad (5)$$

Experimental data has shown that only very rarely does the total (integrated) brightness behave in the straightforward manner predicted by (5). The inverse power law for heliocentric distance is usually considerably greater than two; the deviation from pure reflectance is commonly deduced by means of the relation

$$F = \frac{F_o}{\rho^2 \Delta^n} \quad (6)$$

where the parameters F_o , n are estimated in a least squares sense by observations of the comet over a broad arc of the orbit. Departure from an inverse square law indicates that the light from a comet must be caused largely by emitted energy. Spectroscopic results indicate that the energy source is caused by emission by excited gases. Thus n provides a measure of cometary activity. Visual magnitude equivalence of (6) gives

$$V_{m_c} = V_{m_{oc}} + 2.5 \log \rho^2 \Delta^4 \quad (7)$$

2) Coma. The equation used for the 1980 apparition is from (7),

$$V_{m_c} = 12.5 + 2.5 \log \rho^2 \Delta^4 \quad (8)$$

The value of $V_{m_{oc}} = 12.5$ was obtained by extrapolating the 1961 value of 10.5 under the assumption that Encke will lose two magnitudes in brightness by 1980. Traditionally, values of $n = 6$ are quoted. However, in accordance with

Ref. II-B-20, a " Δ^{-4} dependence is used for simplicity and in deference to tradition". This reasoning is not contrary to intuition, since the results derived from (8) would not be severely altered by other choices.

e. Photometric Halo/Nucleus and Delsemme's Model

According to Delsemme's hypothetical model of coma formation, a shroud of sublimating ice crystals or halo surrounds a solid nucleus of monolithic vesicular structure. The ice particles are presumably formed when a clathrate type of icy surface is blown away from the nuclear surface by gases escaping at velocities near the speed of sound. The halo thus represents a conglomerate of grains graded in size; all sizes are assumed present near the nucleus, giving the central halo a comparatively dense, highly reflective center. Halo-particle density is assumed proportional to $\Delta^{-2.1}$ whereas gas production at the surface would be at Δ^{-2} , depending directly upon solar radiation. Coma formation in accordance with the Delsemme model would depend directly on the secondary production of neutral and radical gases trapped in the grain particles and would vary as the product $\Delta^{-2} \Delta^{-2.1} = \Delta^{-4.1}$. A third factor (Δ^{-2}) is added because of the release of hydrogen and hydroxyl radicals (H^+ , OH^-) from the expelled grains. Following Delsemme, the model for the variation of coma formation with heliocentric distance is $\Delta^{-6.2}$, which seems to be in closer agreement with traditionally quoted values for Encke. However, the Δ^{-4} law is used here for reasons previously given.

Assuming the central halo obeys a $\Delta^{-2.1}$ brightness law, light from the nucleus and central region of the halo should be virtually undistinguishable. Additionally, if the dense shroud of ice crystals shielding the nucleus is optically thick, then the central region of the halo is the "photometric nucleus" and should obey an asteroidal brightness law of the form given by (3). The constant of proportionality $V_{m_{oh}}$ is deduced by adding two magnitudes to the value $V_{m_{on}} = 13.2$ in (5) to account for secular decline in grain production by 1980, in accordance with previous assumptions regarding secular

decline in brightness. The resulting expression for the brightness of the central halo is

$$V_{m_H} = 15.2 + \log \frac{\emptyset}{\rho^2 \Delta^{2.1}} \quad (9)$$

where the phase function \emptyset is not necessarily the same as previously described in (5).

f. Model for Surface Brightness and Instrument Considerations

Surface brightness considerations for the current study were based on Delsemme's model of coma formation, as previously described. Presuming that material ejected from the nuclear surface within the central halo is fragmented at a uniform rate, the occupied surface area of the fragments will be proportional to the distance from the nucleus, i.e., $a_o \propto r$. Consequently, the areal density A (occupied area per unit area) will vary as $1/r$, assuming a spherical expansion, $A \propto r/4\pi r^2 \propto 1/r$. However, the areal density of fine solid material and gas in the outer halo and gas coma will vary as $1/r^2$ because it is assumed that there is no further significant particle fragmentation, i.e., that the occupied area is constant. If angular symmetry about the line of sight is assumed, the intensity in the direction of an observer far removed from the target varies with r according to

$$I(r) = I_o \left(\frac{r_o}{r_o + r} \right) \quad r_1 \geq r \geq 0 \text{ km}$$

$$I(r) = I_1 \left(\frac{r_1}{r} \right)^2 \quad 10^5 \geq r \geq r_1 \text{ km}$$

and

$$I_1 = \left(\frac{r_o}{r_o + r_1} \right) I_o \quad 10^2 \leq r_1 \leq 25(10)^2 \text{ km}$$

The constant r_0 was chosen such that the brightness is diminished by 7.5^m at r_1 and by 20^m at r_2 , in accordance with the suggested profiles set forth in Ref. II-B-18. The assumed distribution of radiation intensity along the line of sight is shown in Fig. II-B-37.

The power absorbing capability of the lens system is determined by the following considerations. Let $I(r)$ represent the luminous intensity/unit solid angle per unit area at the source as shown in Fig. II-B-38. If it is assumed that the lens is far removed from the source, the flux in area ds collected by the lens in solid angle Ω is given by

$$dF = I(r) \frac{a}{r^2} ds$$

From solid angle considerations (see Fig. II-B-38),

$$dF = \frac{I(R) dS}{r^2}$$

Lens speed is defined as $N \triangleq \frac{f}{d}$ so that, over some finite area S in the image plane (raster surface), the power absorbed is given by

$$F = \frac{\pi}{4} \frac{1}{n^2} \int I(\rho, f, R) dS(R) \quad (10)$$

Inspection of (10) indicates that the amount of incident power collected by the lens system aperture is a function of the source radiation field $I(r)$ and the lens speed, which completely define the optics. Knowledge of the noise and transfer characteristics of the sensor (photomultiplier, etc.) and the associated electronics, in addition to apparent target motion, allows the synthesis of a complete optical instrument to meet a specific set of approach-guidance requirements. However, a fundamental constraint is the use of the Mariner class of vidicon and electronics.

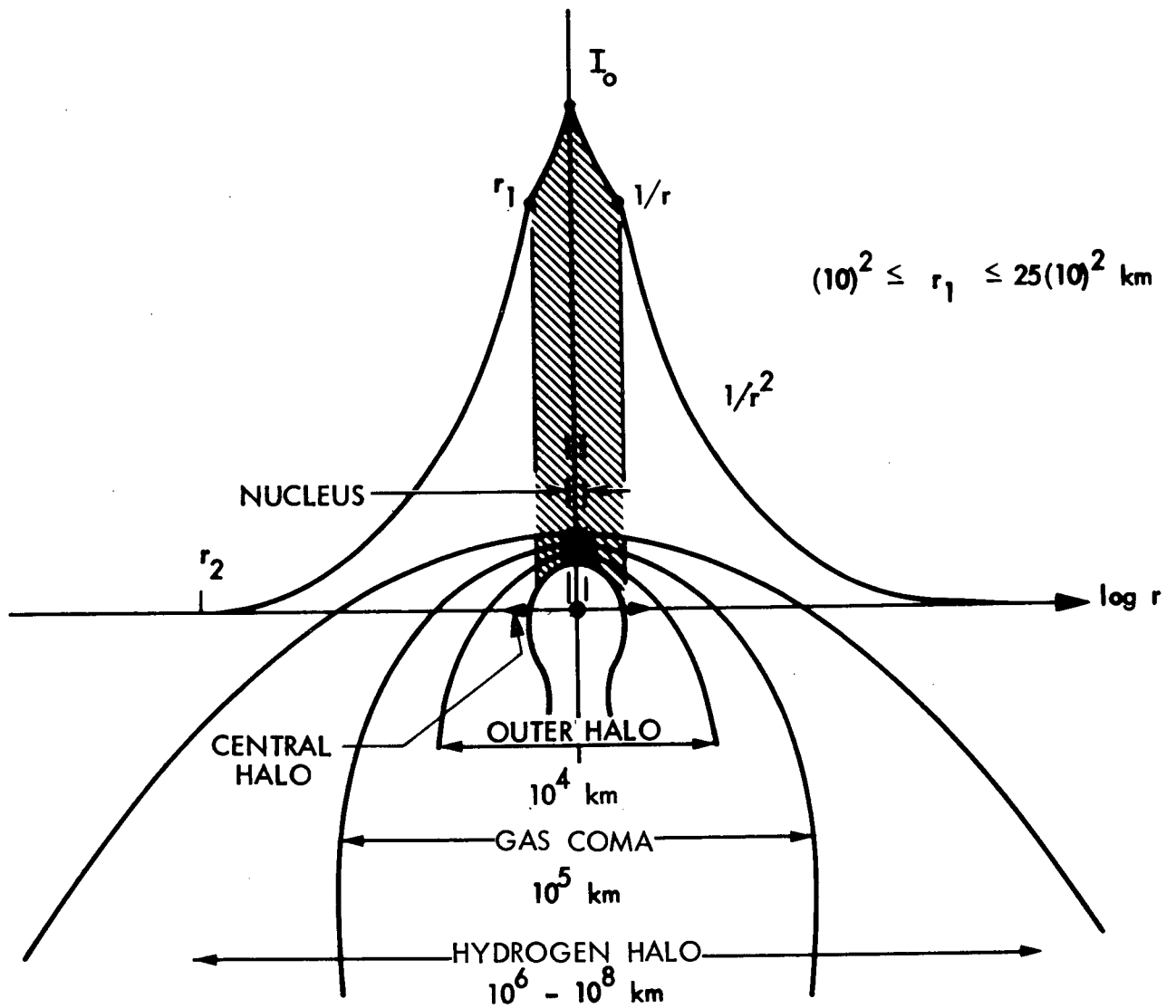


Fig. II-B-37. Comet Morphology and Surface Brightness Model

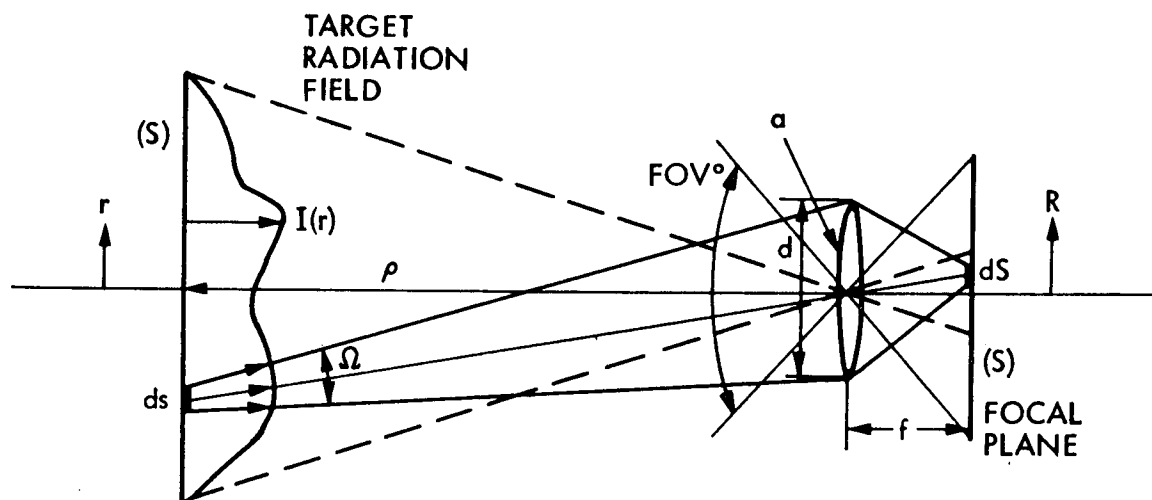


Fig. II-B-38. Imaging an Extended Source

The stellar-source transfer characteristic for Mariner Mars 71 narrow-angle camera is shown in Fig. II-B-39. This data represents information compiled during the Mariner Mars 71 OND. Visual magnitude reference data was taken from the Smithsonian Astrophysical Observatory (SAO) catalog. Symbols indicate picture identification (i.e., orbit no., camera, picture no.) and the vertical lines connecting the symbols designate that the same star appeared in the indicated pictures. Output digitization is nine bits full scale (DN = 512 maximum) with an rms background of approximately 15 DN.

The pronounced discontinuity in Fig. II-B-39 near $V_r = 8^m$ aids in establishing a lower bound on detectability. It was determined that of all stars, $V_r \geq 8^m$, only 50% were recovered from the video data. However, the DN values failed to correspond with expected values as indicated in Fig. II-B-38. Possible explanations are (a) that SAO visual magnitude data is not accurate at low energy levels, (b) that detector magnitude was

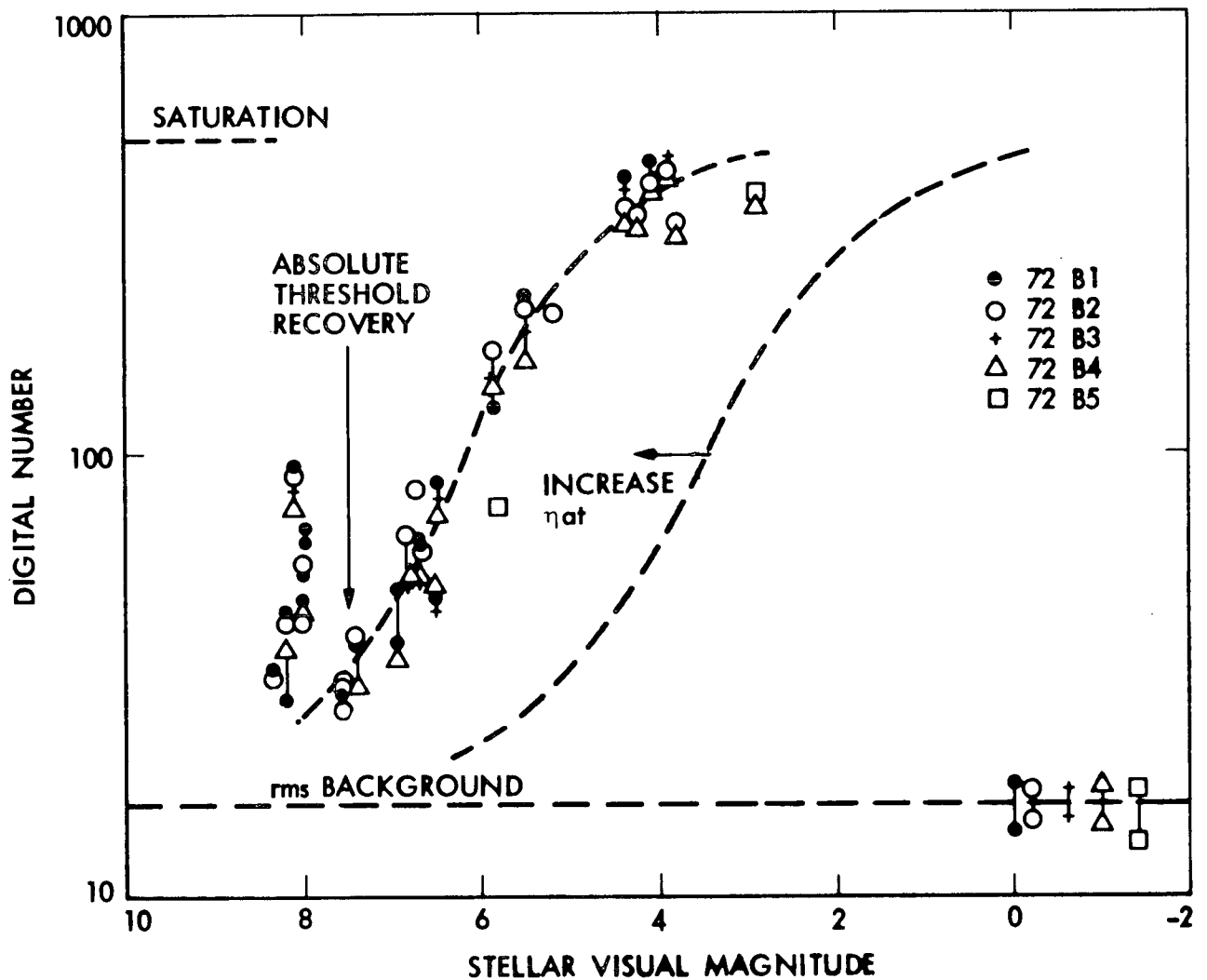


Fig. II-B-39. Mariner Vidicon Transfer Characteristic

proportionately lower than the visual magnitude, implying a possible color inconsistency. Stars of $V_r \geq 8^m$ not recovered were probably below the detectability threshold for the software and/or sensor. However, nearly 100% of stars $V_r \leq 7.5^m$ were recovered from the video data and identified relative to expected DN values.

A typical vidicon transfer curve is indicated by the dashed trend line as shown in Fig. II-B-39. The output current in the region of low flux density is assumed to be of the form

$$i = K\eta a (Ft)^{\frac{1}{2}} + i_o \quad (11)$$

where the one-half power associated with the energy absorbed (Ft) accounts for the "shot effect" and i_o is an rms output caused by electronic noise and dark current. Thus, for a specified sensitivity factor K and input flux F , an increase in the output current must be because of a proportional increase in the product ηa . The flux density required to induce the DN output at the level of detectability for the Mariner Mars 71 narrow-angle camera, here assumed to be $V_r = 7.5^m$ magnitude, is represented by F_r . By comparing the reference sensor to the desired sensor at the same output (i_r), one obtains from (11)

$$\left. \frac{F}{F_r} \right|_d = \left(\frac{\eta_r}{\eta} \right)^2 \left(\frac{f_r}{f} \right)^4 \left(\frac{n}{n_r} \right)^4 \frac{t_r}{t} \quad (12)$$

where the subscript (d) indicates that the comparison is to be made at the level of detectability.

In terms of surface brightness at the source

$$\frac{F}{F_t} = \frac{\int_{s_p} I(\rho, f, R) dS(R)}{\int_S I(\rho, f, R) dS(R)} = \frac{\left[\begin{array}{c} \text{energy absorbed by the} \\ \text{central picture element} \end{array} \right]}{\left[\begin{array}{c} \text{total energy} \end{array} \right]} \quad (13)$$

where s_p represents the area of one picture element.

Equation (12) is then converted to visual magnitudes to obtain

$$\frac{n}{n_r} = \frac{f}{f_r} \left(\frac{\eta}{\eta_r}\right)^{\frac{1}{2}} \left(\frac{T}{T_r}\right)^{\frac{1}{4}} 10^{-(V(f) - V_r)/10} \quad (14)$$

where $V(f)$ is the integrated brightness of that portion of the source subtended by one picture element. For nucleus imaging

$$\frac{F}{F_t} = 1 \quad \text{so that}$$

$$\frac{n}{n_r} = \frac{f}{f_r} \left(\frac{\eta}{\eta_r}\right)^{\frac{1}{2}} \left(\frac{T}{T_r}\right)^{\frac{1}{4}} 10^{-(V_t - V_r)/10} \quad (15)$$

where V_t is the brightness of the photometric nucleus as given by (9). The log of (14) and (15) is obtained so that for $\frac{\eta}{\eta_r} = 1$,

$$\log \frac{n}{n_r} = \log \frac{f}{f_r} + \left[\frac{1}{4} \log \frac{T}{T_r} - \frac{(V(f) - V_r)}{10} \right] (V=V_t, \text{ point source}) \quad (16)$$

The visual magnitude reference $V(f)$ for the integrated brightness is given by

$$V(f) = V_t - 2.5 \log \frac{F(f)}{F_t}$$

where the flux ratio F/F_t is calculated from (13), and the brightness of the coma V_t is calculated from (8). Equation (16) is plotted in Fig. II-B-32 and 33 with recovery and integration times as parameters, i.e., $V(f)$ is assumed to establish the recovery based on the integrated brightness at that time, and the optical parameters are varied with $V(f)$ and integration time ratio T/T_r held constant.

REFERENCES

- II-B-1. William G. Breckenridge and Thomas C. Duxbury, "Defining a Spacecraft-Based Navigation System", Astronautics and Aeronautics, pp. 44 to 49, May 1970.
- II-B-2. B. D. Tapley, and H. Hagar, Jr., Navigation Strategy and Filter Design for Solar Electric Missions, University of Texas, TR AMRL-1040, May, 1970.
- II-B-3. J. F. Jordan, "Orbit Determination for Powered Flight Space Vehicles on Deep Space Missions", Journal of Spacecraft and Rockets, Vol. 6, No. 5, May 1969, pp. 545-550.
- II-B-4. J. F. Jordan, "Optimal Stochastic Control Theory Applied to Interplanetary Guidance", Ph.D. Thesis, 1966.
- II-B-5. Selected Papers on Noise and Stochastic Processes, Nelson Wax, ed., Dover Publications, Inc. N. Y., 1954.
- II-B-6. D. J. Kerrisk, Electric Thrust Subsystem Performance Uncertainties, JPL Interoffice Memorandum to K. L. Atkins/D. B. Smith, November 22, 1971 (JPL internal document).
- II-B-7. J. M. Driver, Graphical Mission Analysis Data for an Encke Rendezvous, JPL Interoffice Memorandum 393.1-113, 1971 (JPL internal document).
- II-B-8. W. E. Crawford, "Undisturbed Limit Cycle Behavior of the Solar Electric Thrust Vector Control System", JPL Engineering Memorandum, E.M. 344-287 WEC, October 13, 1970 (JPL internal document).
- II-B-9. V. J. Ondrasik, and K. H. Rourke, Applications of Quasi-VLBI Tracking Data Types to the Zero Declination and Process Noise Problems, AAS Paper No. 71-399, AIAA/AAS Astrodynamics Conference, Ft. Lauderdale, Fla., August 17-19, 1971.
- II-B-10. V. J. Ondrasik, and K. H. Rourke, "Application of New Radio Tracking Data Types to Critical Spacecraft Navigation Problems", JPL Quarterly Technical Review, Vol. 1, No. 4, January 1972, pp. 116-132.

REFERENCES (Contd)

- II-B-11. V. J. Ondrasik, M. W. Nead, T. Nishimura, K. H. Rourke, ATHENA: Formulation Memo Number I, Trajectory, Variational Equations, Partial Derivatives, and Simulated Data Times, JPL Interoffice Memorandum 391.2-119, December 31, 1970 (JPL internal document).
- II-B-12. Guidance and Navigation Requirements for Unmanned Flyby and Swingby Missions to the Outer Planets, Vol. III: Low Thrust Missions, MIT Charles Stark Draper Laboratory, R-678, June 1970.
- II-B-13. J. P. McDanell, and L. D. Friedman, Comments on "Guidance and Navigation Requirements for Unmanned Flyby and Swingby Missions to the Outer Planets" by the MIT Draper Lab., JPL Interoffice Memorandum 391.2-120, January 19, 1971 (JPL internal document).
- II-B-14. M. H. Bantell, Electric Thrust Subsystem Error Model, JPL Interoffice Memorandum 343-4-72-075, January 26, 1972 (JPL internal document).
- II-B-15. R. K. Russell, and D. W. Curkendall, On Modeling Continuous Accelerations as Piecewise Constant Functions, JPL Technical Memorandum, TM 391-288, Feb. 21, 1972 (JPL internal document).
- II-B-16. C. L. Thornton, EVA - A Sequential Process Noise Filter with Accompanying Evaluation Algorithm, JPL Technical Memorandum TM 391-335, July 17, 1972 (JPL internal document).
- II-B-17. Alan L. Friedlander, William C. Wells, Comet Rendezvous Mission Study, IIT Research Institute Report No. M-28, October 1971.
- II-B-18. Study of a Comet Rendezvous Mission, TRW Systems Report No. 20513-6005-R0-00, April 12, 1972.
- II-B-19. R. A. Jacobson, Approach Navigation for Solar Electric Spacecraft with Application to a Comet Encke Rendezvous Mission, JPL Technical Memorandum, TM 391.347, August 1, 1972 (JPL internal document).
- II-B-20. E. Roemer, "Cometary Nuclei - Introductory Report", Mémoires de la Société Royale des Sciences de Liège, Liège, France, 1966.

C. SEP MISSION RISK ANALYSIS

This section presents the results of a study conducted to develop a method to realistically assess the risks involved in performing a solar electric mission and to provide effective ways of designing low-risk, low-thrust missions. For low-thrust missions, as long as the energy source (the solar array, for SEP) is intact, the failures of some energy conversion devices or thrusters resulting in partial thrust-subsystem failures do not immediately destroy the chance of achieving the mission goal. Because the low-thrust mode is inherently flexible, if a thruster should fail, an alternate mode can be used to attain an acceptable mission objective. Redundant hardware may be used as an alternate mode or the subsequent thrust program may be modified to alter the trajectory by various means, such as cancellation of coast phases or an extension of flight time. Such modifications recover the energy loss by extending the burn time should the thruster failures induce a power shortage. As long as the mission constraints are not violated, mission reliability may be increased significantly, if trajectories are designed with more options in case of failures. Essentially, this procedure uses operational tactics to compensate for imperfect hardware.

Therefore, in assessing risk, not only the reliability of the hardware, but also the design and the mode of execution of the thrust program must be considered. In the following discussion, mission risk is estimated within these guidelines. The extent to which this concept may be applied to enhance SEP mission success has yet to be explored. At present, methodology is emphasized, rather than the full implication of the approach. However, the method was applied to a 1980 Encke Rendezvous Mission, and the results were used to evaluate the sensitivity of mission success to the hardware failure statistics. In turn, the evaluation was used to provide rational thrust-subsystem design requirements for the mission. The inclusion of mission operational factors made a substantial difference in the predicted risk, thus determining that the risk factor must be considered during the mission design.

1. Risk Factor Analysis

Mission risk factors include hardware aspects and the mission operational modes. The risk prediction processes used perform simulation of probable thruster failures, measurements of failure effects on the mission goal, and associated probability computations. Figure II-C-1 shows the pertinent risk factors considered and their relationships to the predicted risks.

a. Hardware Risk Factors

1) Thruster Power Rating and Number of Thrusters.

Prior to an actual thrust-subsystem design, a thrust subsystem specific mass is assumed and used to determine a trajectory which optimizes the payload while satisfying certain selected constraints.

Once a desired mission and the reference trajectory is chosen, the required power profile as a function of time is determined, i. e., the solar array output power available for conversion into mechanical energy. Because the thrust mode presupposes full utilization of this solar-array power output, the thrust subsystem must be designed to operate with such a power history. This process is called power matching. The general practice of power matching is to provide, for each mission phase, enough numbers of thrusters, N_i , of given power rating, P_i , (power input to power conditioner) such that $(\sum_i N_i P_i)$ is at least equal to the maximum power yield of the solar array during the entire mission. A number of redundant thrusters can be provided for added reliability. Variations in the power profile are matched by adjusting the number of thrusters in operation and, at the same time, relying on the ability of the thrusters to throttle in the range of about 2 to 1.

The thruster power rating affects the mission reliability mainly through its impact on the trajectory reshaping possibilities. It is correct to assume that smaller thrusters are more favorable than larger thrusters because a failure results in a smaller power loss, thus leaving more opportunity to complete the mission in another mode. However, there is a weight penalty

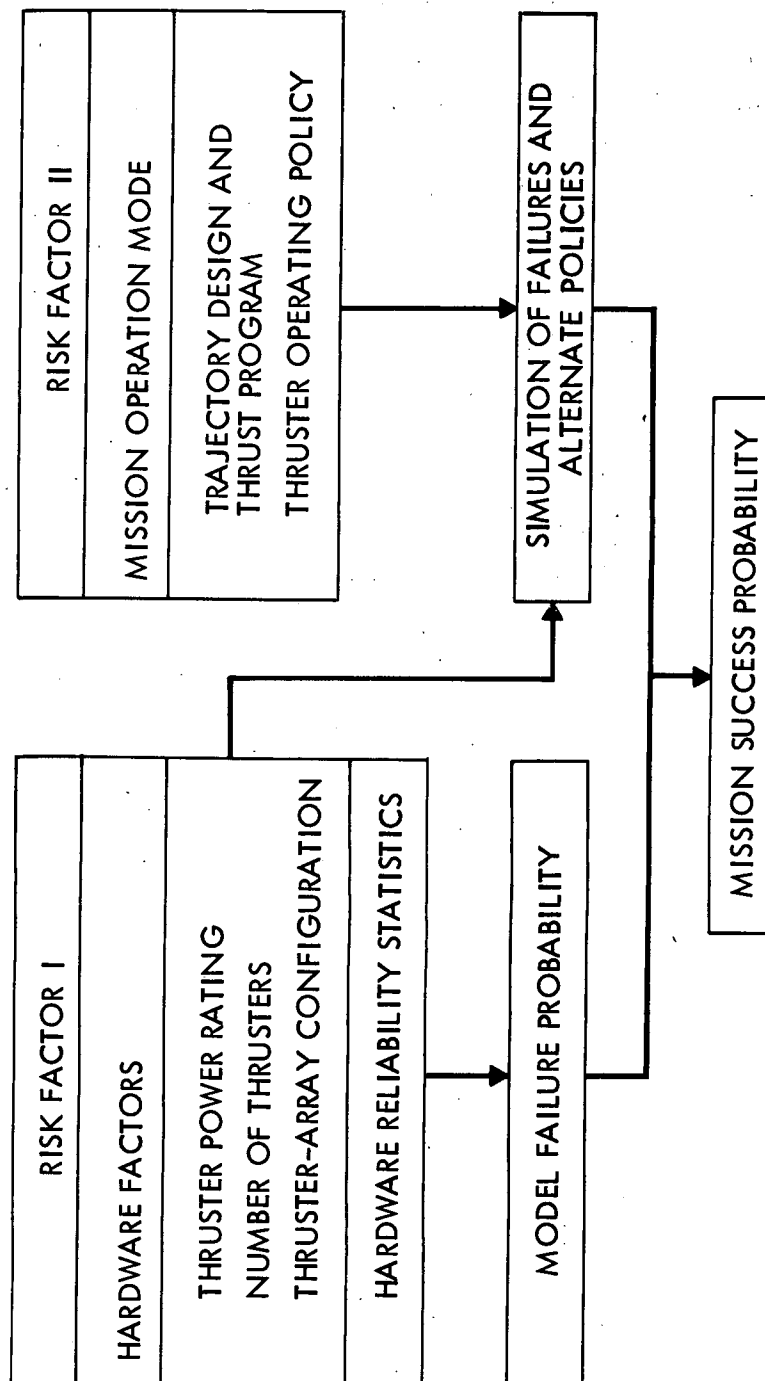


Fig. II-C-1. Risk Factors

because the thrust-subsystem specific mass increases as the power rating per thruster is decreased.

Provision of spare thrusters always increases mission reliability. The required number of spares to attain a certain reliability depends upon the power rating for reasons presented above. Assuming that the thruster failure statistics are independent of the size, a desired mission reliability can be achieved for various feasible combinations of (P-N) design points. Such information should be obtained prior to an actual subsystem design to expedite the selection of the design point which is most cost-effective, and which satisfies design constraints within the required confidence level.

2) Thruster Failure Modes and Failure Statistics. The key constituents of reliability in the thrust-subsystem must be identified for a failure analysis. The mathematical models of failures must be established to allow a quantitative description of the failure probabilities. Systematic testing programs are needed to obtain actual failure distributions in the time domain and in the operating environment extremes. At present, the data available are of a preliminary and speculative nature. However, these preliminary data can be used to carry out parametric studies wherein the parameters cover the entire possible range.

The key failure modes considered are:

- (a) Thruster life. Thruster life is limited by grid wear-out or by depletion of the cathode emissive material.
- (b) Thruster or power conditioner component failure. According to standard reliability engineering procedure, such failure could be considered to have a Poisson distribution.
- (c) Thruster restart failure. The risks involved in restarting a thruster can be modeled by binomial form.

- (d) Delivery or infant failure. Conventional modeling of this type of failure can be made. However, in this study, it is assumed that thrusters would be tested thoroughly and that this type of failure can be ignored.

Table II-C-1 summarizes the explicit mathematical models and the range of parameters used in this study. (See Ref. II-C-1 for the primary data source used.) Computer plots of failure distribution and the reliability curve are shown in Figs. II-C-2 and II-C-3.

3) Power Conditioner and Thruster Switching Matrix. The use of switching mechanisms to allow interconnection of a power conditioner (PC) to many thrusters may add to system reliability. To include this factor in the analysis, in addition to the modeling of the switching logic, the switching mechanism reliability data must be given. Because this was beyond the scope of the study, the simulation of independent PC failures was not performed. One to one PC-thruster connections were assumed; thus failure statistics used represent the PC-plus-thruster unit. (See Section II-B for a detailed treatment of the effect of the switching mechanism on mission risks.)

4) Thruster Array Geometry. Because of spacecraft attitude stabilization requirements, the simultaneous operation of thrusters in some combinations are forbidden. Such is the case for the thruster system assumed for the JPL design for a 1980 Encke Rendezvous Mission. The constraints reduce the possible alternatives in thruster burn in case of failures, and the burn strategy simulation must exclude such combinations.

b. Operational Mode Factors

The impact of a failure on the mission goal depends on the time and type of failures (failure modes). Fatal failure modes can be identified by systematic trajectory error analysis. The probability of occurrence of such failure events depends not only on the nature of the hardware but also on the

Table II-C-1. Mathematical Models and Parameters

Failure Type	Failure Distribution Model	Reliability	Parameter Value
Delivery (infant)	Binomial	S	1
Start-up	Binomial	q	10^{-5}
Thruster, normal operating	Exponential	$R_1(t) = e^{-\lambda t}$	$\lambda = (6 \sim 50)/10^6 \text{ hr}$
Thruster wear-out	Log-normal	$R_2(t) = \int_t^{\infty} \left[\frac{1}{\sigma \sqrt{2\pi}} e^{-(\lg \tau - \mu)^2 / 2\sigma^2} \right] d\tau$ $R(t) = R_1(t) R_2(t)$ $T = e^{\mu} + \sigma^2/2$ $\Delta T = \sqrt{e^{2\mu + 2\sigma^2} - e^{2\mu + \sigma^2}}$	$T = 300 \sim 450 \text{ days}$ $\Delta T = 50 \text{ days}$
Power conditioner	Same as thruster	<p>Since one to one PC-thruster switching is assumed, it is not necessary to model the PC failure separately. For PC+thruster system, the failure rates are additive, and the wear-out life should be the shorter one of the two components.</p>	
<p>Note: t = Elapsed thruster burn time R = Total reliability λ = Thruster failure rates T = Thruster wear-out life (mean) ΔT = Thruster wear-out life (standard deviation)</p> <p>It is assumed that all thrusters have identical failure statistics and mutually independent failures.</p>			

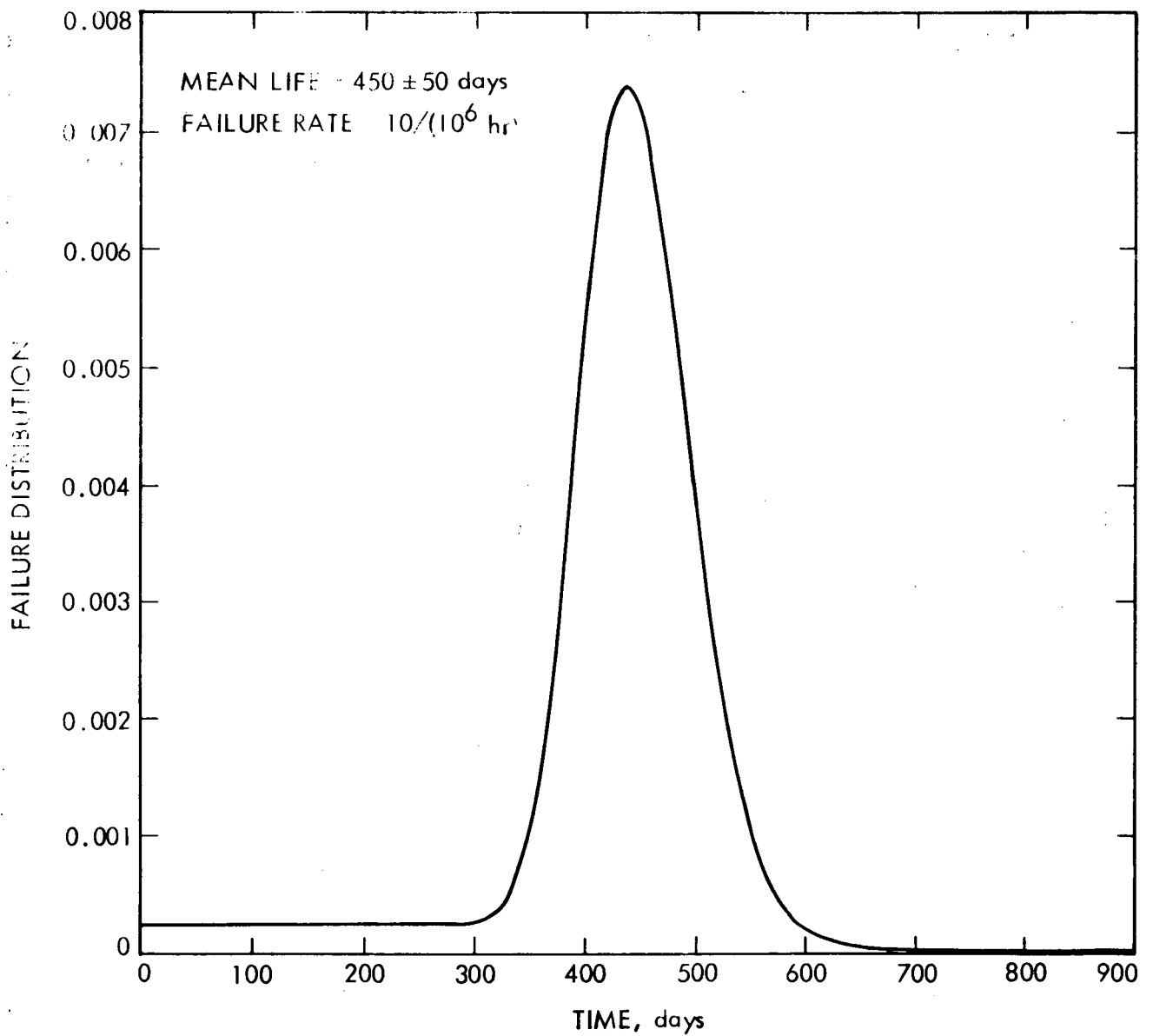


Fig. II-C-2. Thruster Mortality Curve

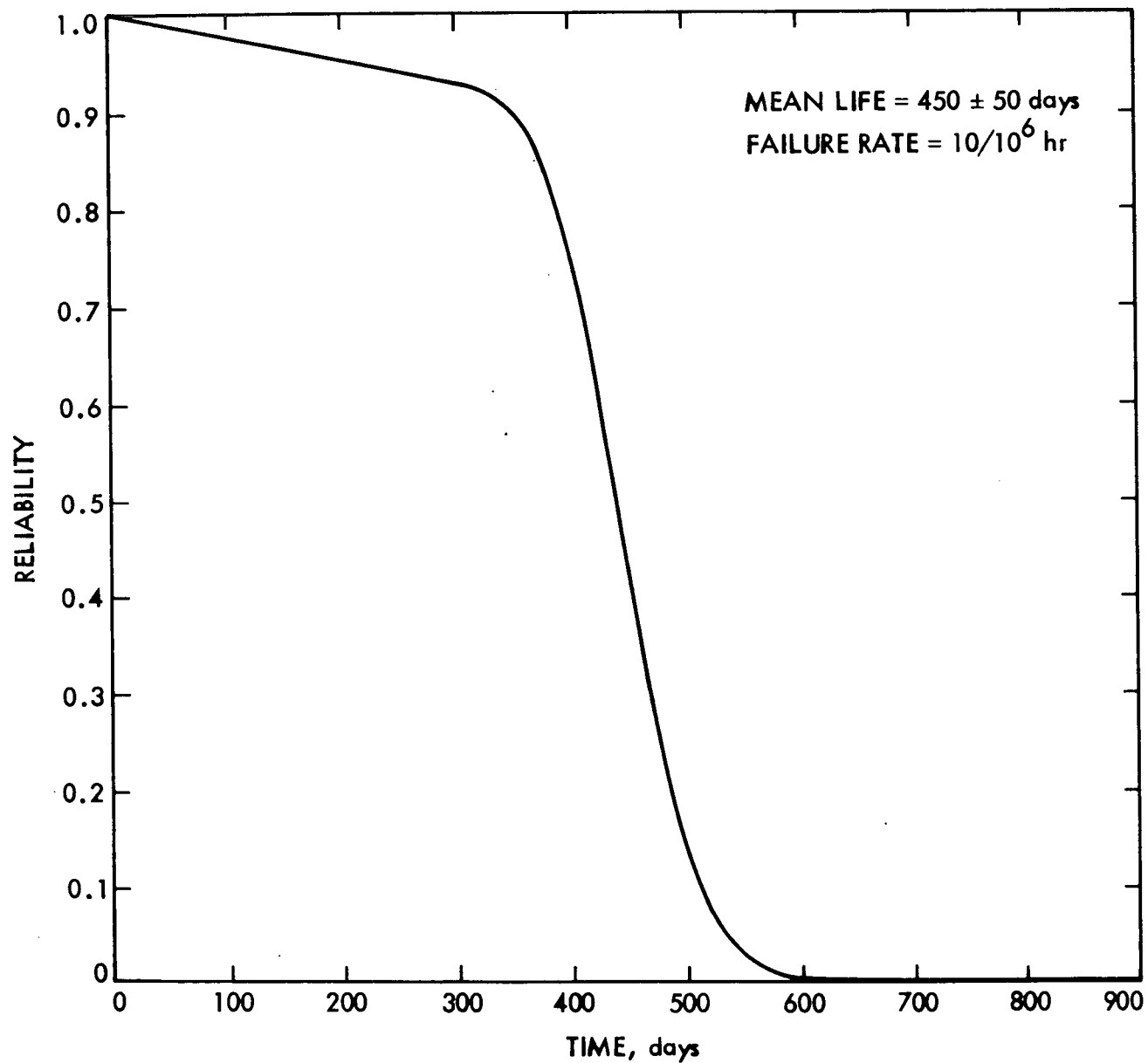


Fig. II-C-3. Thruster Reliability Curve

strategy used in operating the available thrusters (burn policy). In planning a mission, careful trajectory design may ease the impact of most probable failures on the mission goal. At the same time, a well planned burn policy may considerably reduce the probability of fatal errors.

1) Trajectory Design and Trajectory Error Analysis.

Mission goals can be attained in more than one way for a given mission. This is particularly true of a continuously propelled, solar-electric mission. Alternate thrust programs, rather than redundant components, may be used to compensate for partial power failures caused by component malfunction. If the initial trajectory design permits such maneuvers, mission risk can be reduced. For example, a planned coast phase and/or a wide target encounter time window can be provided. The acceptable range of such provisions depends upon the overall mission constraints, including design philosophy and cost factors. In this study it was not possible to fully explore and construct such trajectories. However, the effects of such considerations were demonstrated in the 1980 Encke Rendezvous Mission risk analysis.

Trajectory error analysis consists of identifying non-fatal (admissible) failure modes and providing corresponding alternate thrust modes. Failures which can be compensated for by redundant thrusters require no additional trajectory analysis. Further failures require modification of the planned trajectory, thus requiring trajectory reoptimization. An example of a modified thrust program (mainly, the power profile) is shown in Fig. II-C-4, wherein the spacecraft for the Encke Rendezvous Mission, requiring five 3.228 kW thrusters, was left with three thrusters at $t = 930$ days. The key aspect to be noted in thrust modification for risk prediction is the power profile change, which affects the burn-policy and the probability of mission completion in that mode.

The trajectory optimization program, CHEBYTOP, was used for this analysis. The JPL Low-Thrust Trajectory-Optimization Program (EPITOP) was used, whenever appropriate, for spot checking. Because of the approximate nature of CHEBYTOP, some differences in results were noted when it was compared with the EPITOP. However, the differences in required

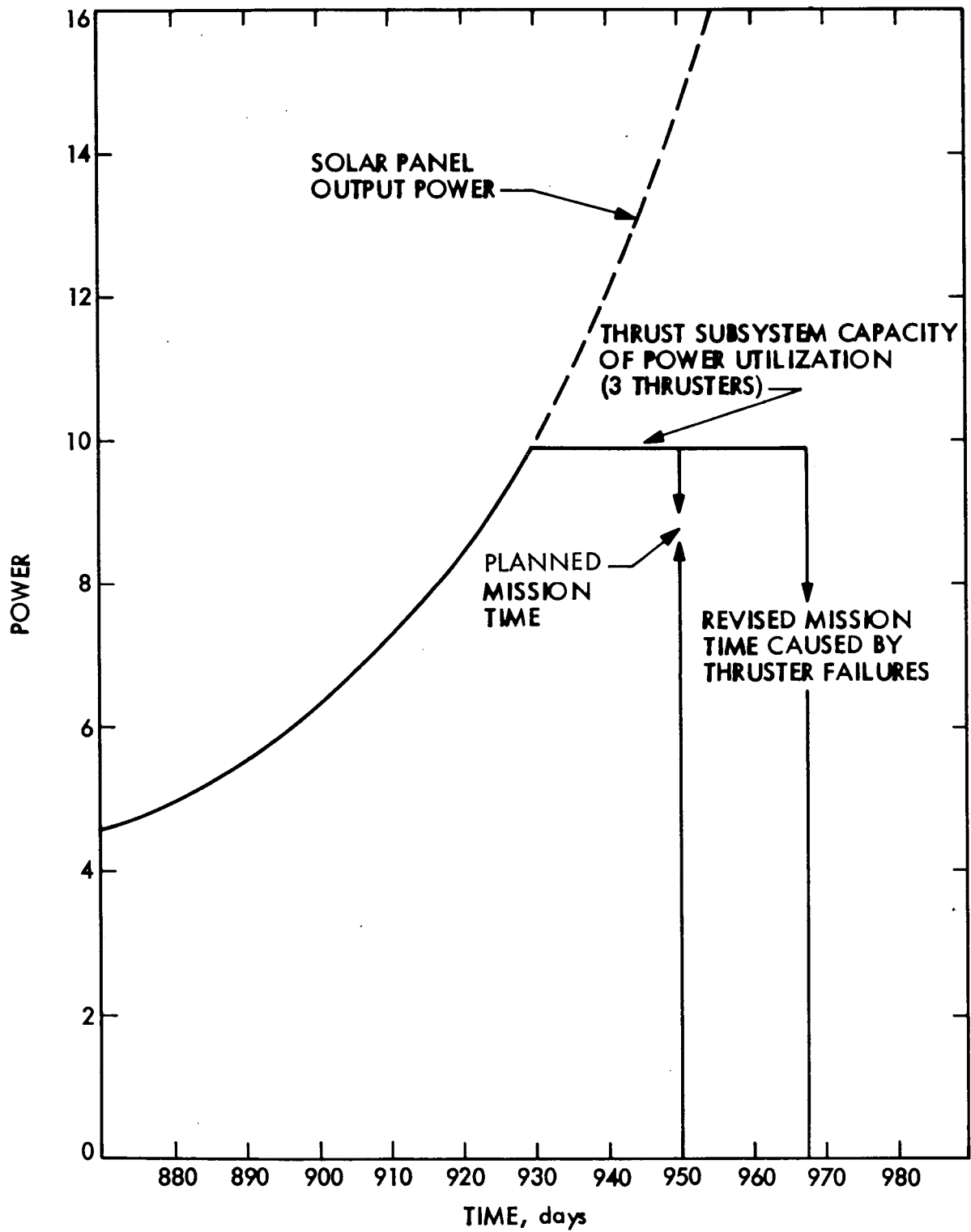


Fig. II-C-4. Power History Change Caused by Failure

thrust history or burn time (~ 2 or 3 days) are insignificant for the purpose of success probability calculations or for the diagnosis of mission feasibility.

2) Thruster Burn Policy. At a given time of the mission, the thrust-subsystem state is given. Be it perfect or degraded by failures, the desired thrust program must be executed according to some kind of a policy. A given policy controls the choice of thrusters and duration of burn allocation. An example of the thruster burn profile based on a burn-policy is shown in Fig. II-C-5, wherein each of seven thrusters is allocated equal amounts of burn time to perform a Encke Rendezvous Mission. Each time a failure occurs, the subsequent burn profile must be revised. The criteria for choosing a burn policy is, again, the reliability. Given a thrust history without incident, the required total burn time, T_B can be obtained simply by adding the product of the number of thrusters and the burn time for different phases of the mission (see Fig. II-C-6). If T_i is the assigned burn time for i^{th} thruster, the reliability, R , of such a burn policy would be

$$R = R(T_1) R(T_2) \dots R(T_N) \quad (1)$$

with the constraint

$$T_1 + T_2 + \dots + T_N = T_B$$

where

R = (PC + Thruster) system reliability

N = Number of thrusters used

If the life time of the thrusters were very long and $R(T_i)$ were essentially of exponential type,

$$R(T_i) = e^{-\lambda T_i}$$

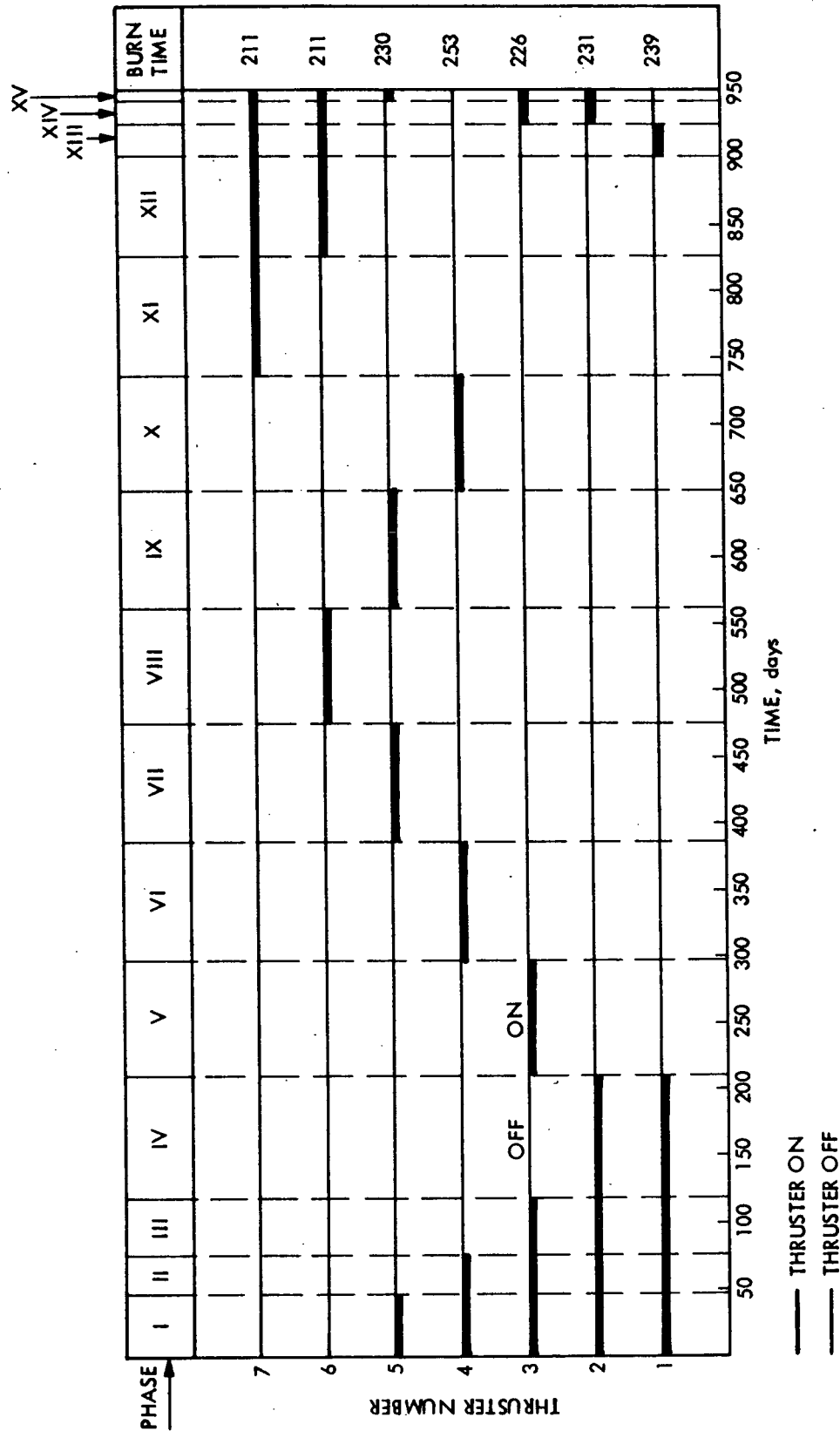


Fig. II-C-5. Example of an Equal-burn Policy

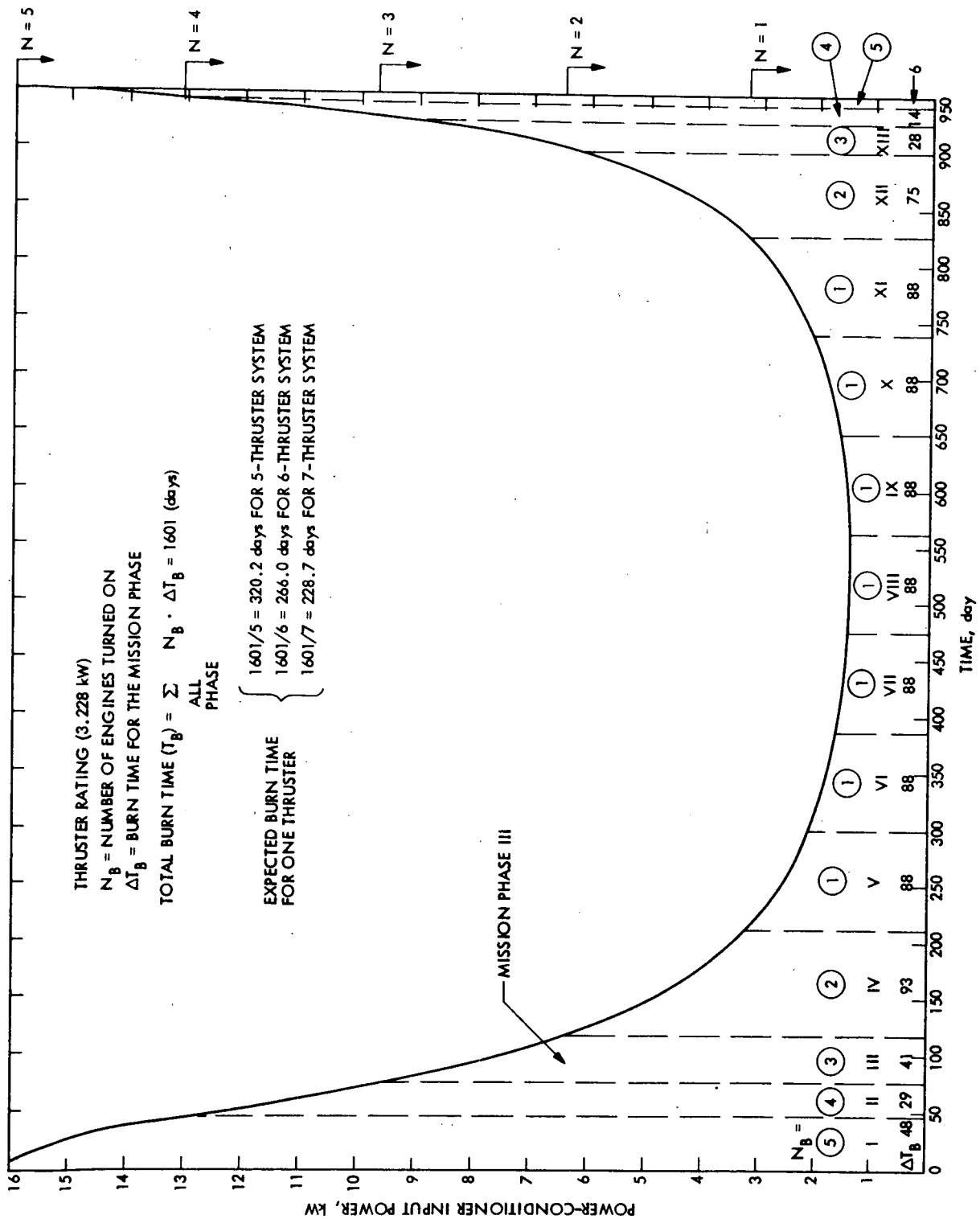


Fig. II-C-6. Power Profile, 1980 Encke Rendezvous Mission

then

$$R = e^{-\lambda T_B}$$

is independent of the burn policy as long as the existing number of thrusters meets the minimum requirement. However, in reality, thruster life is of finite duration and can be considerably shorter than the mission flight time. Because $R(T_i) \rightarrow 0$ as T_i approaches the lifetime, leading to complete failure, an arbitrary burn policy must be avoided. Since failure rates are monotonically increasing functions of elapsed burn time under the assumed reliability model, it can readily be proven that equal distribution of burn time to the existing thrusters would be the minimum risk policy (equal-burn policy).

Minimization of R with constraint $\sum_i T_i = T_B$ requires that

$$\frac{\dot{R}(T_1)}{R(T_1)} = \frac{\dot{R}(T_2)}{R(T_2)} \cdots \frac{\dot{R}(T_N)}{R(T_N)} = -\text{failure rates}$$

which can be satisfied if $T_1 = T_2 = \dots T_N = T_B/N$. The above argument disregards the risks associated with thruster restart. In actual operation, it is perhaps more convenient to operate thrusters continuously as long as the operating condition is good and the switching of thrusters takes place only as a result of failures or as the number of thrusters burning is to be changed. Without sufficient spares, such policy would have little chance of success in a mission with nominal operation, but the probabilities of attaining the mission objectives in alternate modes would be greater. This procedure is termed the "least-switching policy". In this study, the equal-burn policy is emphasized, but the least-switching policy was also used in a few cases to illustrate its implications.

c. Risk Prediction Method

Low thrust trajectories are expensive and difficult to generate. To predict the risks involved in performing a solar electric mission, it is impractical to attempt a Monte-Carlo type of analysis where numerous random failures are simulated, and retargeting or reoptimization of the trajectory is performed as the failures occur. The method proposed here is intended to minimize the labor of numerous trajectory computations by concentrating on a finite number of trajectory alternatives which can be used to approximate any of the actual alternative trajectories. The main purpose of the analysis is to investigate the mission feasibility and the probability of mission success. It is not mandatory to have very accurate trajectory profiles to perform this type of study. In the following, a step-by-step description of the risk prediction method is given:

- (1) Step 1. A finite number of trajectory points is systematically chosen to divide sequentially the entire mission into M different phases. The division can be based on the time interval during which the desirable number of thrusters on is constant. However, the size of a phase interval should not be too large.
- (2) Step 2. The admissible failures at the beginning of each phase are identified. The alternative trajectory corresponding to each failure mode is constructed. This establishes correspondences between a trajectory mode and thrust subsystem state (i.e., the number of surviving thrusters). In general, the correspondence is one trajectory to many thrust system states. This procedure forms a trajectory tree, exhibiting the branching of the flight path as the failures occur. Figure II-C-7 is an illustration of such a trajectory branching map made for the 1980 Encke Rendezvous Mission.

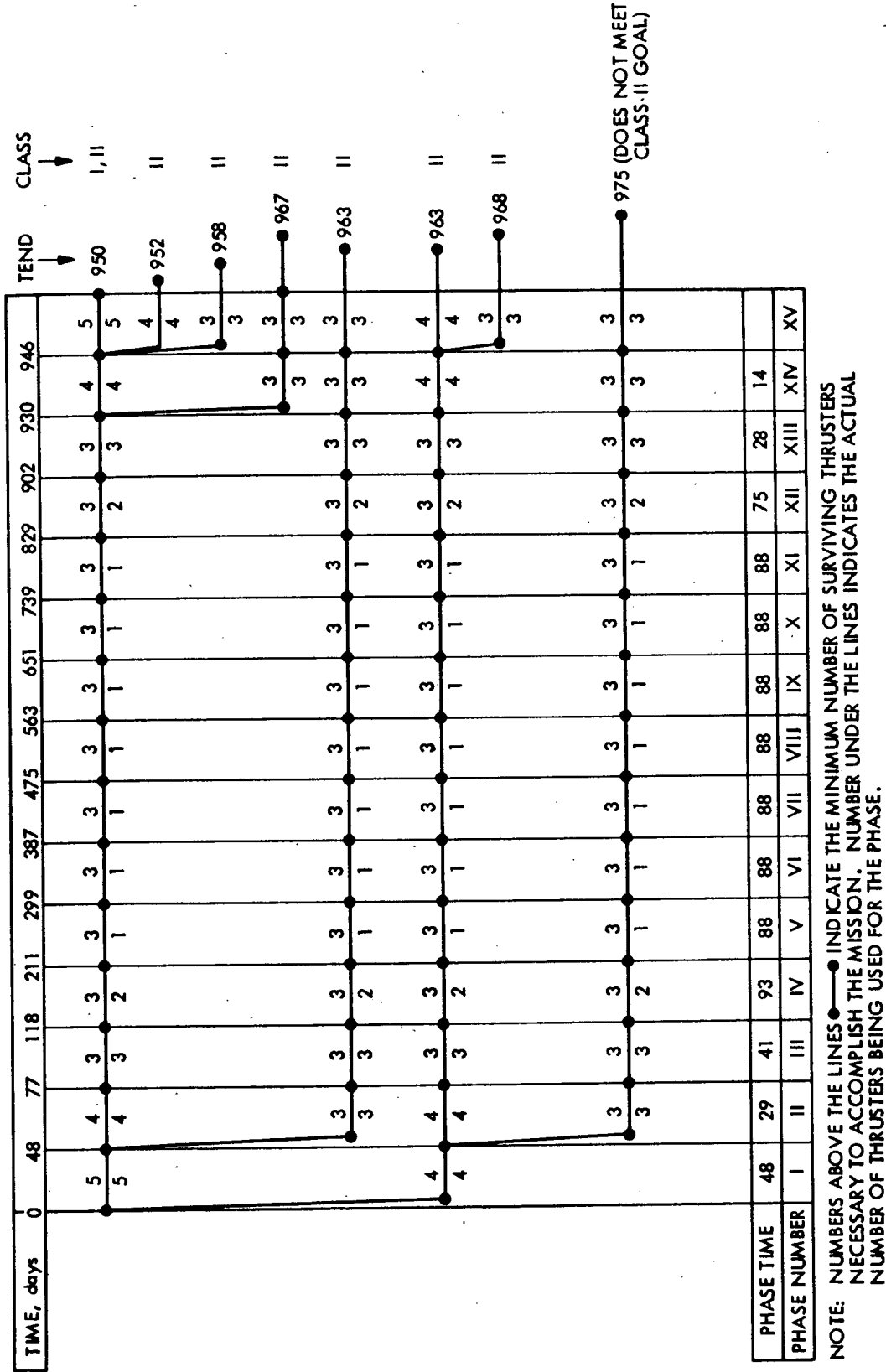


Fig. II-C-7. Admissible Trajectory Alternatives for Imperfect Thrust Subsystem

- (3) Step 3. Thruster reliability data is obtained by using assumed models, and the data is stored in a tabular form.
- (4) Step 4. The engine burn is started in accordance with a burn-policy and a planned thrust program at the beginning of i^{th} phase.
- (5) Step 5. A failure mode I_i , which may occur during the i^{th} phase if Step 4 were executed, is simulated. If it is assumed that N_i -thrusters are functioning at the end of the last stage, there are $\sum_{j=1}^{n_i} C_j^{n_i}$ modes in which the thrust subsystem could fail. The probability of this I_i^{th} failure mode can be computed. Considerations of failure modes which have zero probabilities (or less than 10^{-6}) are discarded.
- (6) Step 6. If the failures are not fatal, the required thrust mode modification based on Step 2 is examined; the program is changed; the engine burn allocation is revised; and the i^{th} phase is completed. The probability of the i^{th} phase completion $[p_{I_i}(i)]$ in this revised mode is then computed.

No random number generating schemes are used to assign an exact time of failure. It is assumed that the impact of a failure occurring any time within the phase is approximately the same as if it were occurring at the beginning of the phase. Thus, revision of burn allocation always starts at the beginning of the phase (conservative estimates).

- (7) Step 7. In the next phase, Steps 4 to 6 are repeated until the last phase of the mission is completed. Probability of mission completion with a failure history, I (sequential failure modes I_i constitute a failure history), is

$$P_I = \prod_{i=1}^M p_{I_i}(i)$$

- (8) Step 8. Steps 3 to 7 are repeated for all possible failure histories, giving a total success probability of

$$P = \sum_I P_I$$

The justification and advantage of the above procedure can be argued as follows:

- (1) In the limit, where the number of phases chosen becomes infinitely large and the interval infinitely small, the method of prediction is mathematically exact.
- (2) By a convenient choice of phases, an approximate trajectory prediction can be made, which in turn greatly reduces the labor of trajectory reoptimization.
- (3) The inaccuracies in prediction made by the finite interval procedure can actually be measured only if one experiments with the size of the interval. This procedure is impractical from a computational point of view, at least, in the case of the Encke risk analysis, because the required number of failure history simulations increase almost exponentially as the number of phases increased. However, the estimate is pessimistic, and it is believed that the error can not be large. At most, four failures were involved for the Encke seven-thruster system throughout the mission. Penalty measurement errors made in a few such events probably are insignificant compared with whatever error was committed in modeling of the hardware reliabilities.

2. 1980 Encke Rendezvous Mission and Risk Factors

a. General Mission Profile

A mission with the characteristics shown in Table II-C-2 was selected for analysis.

Table II-C-2. General Mission Characteristics

Event	Characteristics
Launch date	March 16, 1978
Arrival date	October 21, 1980 (-47 days to T_P^*)
Solar panel size	$P_O = 16.6 \text{ kW}$
Housekeeping power	$P_A = 0.6 \text{ kW}$
Specific impulse	$I_{SP} = 3000 \text{ sec}$
Injected mass	$M_O = 1630 \text{ kg}$
Injection C_3	$C_3 = 54.2 \text{ (km/sec)}^2$
Nominal final mass	$M_f = 1163 \text{ kg}$
Propellant mass	$M_p = 457 \text{ kg}$

* T_P = Time of Encke perihelion

b. Definition of Mission Success

Three different class of success are:

- (1) Class I, the selected mission mode. In this mode, rendezvous with Encke occurs at the desired rendezvous time of -47 d to T_P .
- (2) Class II, a degraded but acceptable rendezvous mode. Herein, the mission goals are considered attained, if the spacecraft can achieve rendezvous with Encke any time before -27 days to T_P . This time also ensures

that the heliocentric radius of the spacecraft is larger than 0.7 AU at encounter.

- (3) Class III, flybys, if relative velocities are less than 1 km/sec.

As explained in paragraph 1-b, Class II and Class III are used to explore the effects of trajectory design on the predicted risk.

c. Power Time History

The available solar panel output power as a function of time for the given selected mission mode and along the desired trajectory constitutes the basis for thrust-subsystem design and the power matching policy (see Fig. II-C-6). The minimum number of thrusters required at various phases of the mission is given for a 3.228-kW thruster plus PC. An estimate of engine burn time required for one thruster based on equal-burn time policy is also shown for thrust subsystems with five, six, and seven PC-plus-thruster arrays. In case of failures wherein the solar panel output power can not be matched, trajectory reoptimization using a limited maximum power curve, as shown in Fig. II-C-4, is performed.

d. Hardware Parameters and Reliability Data

- 1) Power Rating. It is assumed that the maximum allowable power input to a PC-plus-thruster system is 3.228 kW with a throttling ratio of 2 to 1. The 3.228-kW number is assigned arbitrarily to match the expected maximum solar array output power of 16.14 kW during the mission, using five thrusters. However, this number is compatible with a 30-cm thruster being considered at JPL.

- 2) Number of Thrusters. Thrust-subsystems with five, six, and seven thrusters were analyzed in this study.

- 3) Symmetry Requirements on Thruster Firing. A seven-thruster system, tentatively considered for design, has the geometrical

configuration shown in Fig. II-C-8. The combinations of thrusters which are prohibited are summarized in Table II-C-3.

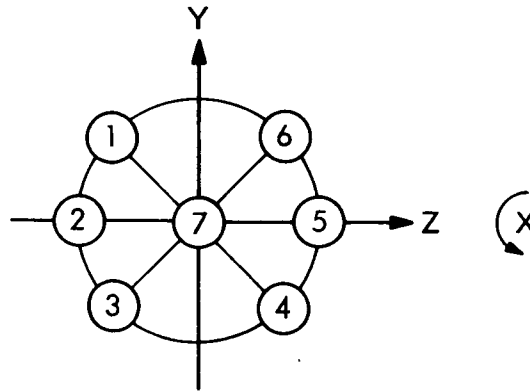


Fig. II-C-8. Geometric Configuration of Seven-thruster System

4) Hardware Failure Parameters. No hard data could be obtained regarding the thrust-subsystem reliability. However, based on the content of Ref. II-C-1, the following assumptions were made:

- (a) Thruster life in the range of 300 to 450 days was assumed. In practice, thruster life is measured in terms of ampere-hours. In modeling the wear-out failure, the independent parameter should be the elapsed burn time in ampere-hour units (defined as effective elapsed burn-time). At a fractional-power-level operation, such as Phase VIII, where a thruster is to operate at about the 50% level, the effective burn time should be 44 days instead of 88 days. The conversion of simple burn-time into effective burn-time was not carried out in this study.

Table II-C-3. Forbidden Thruster Combinations

Number of Thrusters to be Fired	Forbidden Combinations
5	None
4	2347, 3457, 4567, 1567, 1267, 1237, 2467, 1357
3	237, 347, 457, 567, 167, 127, 247, 357, 467, 157, 267, 137, 234, 345, 456, 156, 123, 246, 135
2	25, 36, 47*
1	None

*Allowed combinations

For six-thruster system, thruster ⑦ is removed.

For five-thruster system, ② and ⑤ is removed.

Forbidden combinations for six-thruster system and five-thruster system can be inferred from the above table.

- (b) For thrusters, failure rates of $(6 \sim 10)/10^6$ hr are conjectured. For PCs, roughly the same number has been quoted. Allowing an error with a factor of 2, failure rates in the range $(6 \sim 50)/10^6$ hr were considered for the thruster plus PC.
- (c) A somewhat arbitrary number of 10^{-5} was assigned for thruster restart failure.

e. Trajectory Error Analysis

In accordance with the method described in paragraph 1-c, Steps 1 and 2, the entire mission duration is divided into 15 different mission phases. The division of mission phases and phase intervals coincide with the times where the number of burning thrusters require changing. The long phase of about 620 days for one thruster is further divided into 7 phases for failure simulation purposes. The results of trajectory error analysis are summarized in the trajectory map for the Class II goal, shown in Fig. II-C-7. The seven branches of thrust modes appearing in the map can be used to approximate any of the actual alternate thrust modes that may be used in case of admissible failures. The straight line between neighboring circles represents one segment of a spacecraft path. Branching of trajectories appears as failures of different degrees occur. The time of Encke encounter (T_{end}) differs for different thrust modes as is indicated in the figure. However, the engine number switching points change insignificantly as the trajectories branched. This is fortunate in that the computer algorithm for the simulation of failure and burn-revision becomes much simpler to implement.

f. Thruster-Burn Policy

Both equal-burn policy and minimum-switching policies were considered. Given a failure history, the associated burn history must be

simulated following a policy. Examples of computer outputs simulating such burn histories are shown in Tables II-C-4 and II-C-5. The probability of success associated with the same failure history and the burn history is also given in the tables, illustrating Steps 4 to 7 of paragraph 1-c.

3. 1980 Encke Rendezvous Mission Risk Assessment

The predicted success probabilities for 1980 Encke Rendezvous Mission are summarized in Table II-C-6. The probabilities are shown as a function of thrust-subsystem failure parameter sets (i.e., thruster life and failure rate), and mission class. An equal-burn policy is used to assign thruster firing sequence. Effects of symmetry requirements and least-switching-policy were examined for one set of hardware failure parameters. Conversion of the data of Table II-C-6 into a constant risk contour map (see Fig. II-C-9) revealed some useful information regarding the hardware design requirements. The following conclusions were made from the data obtained:

a. Effects of Hardware Reliability on the Thrust-subsystem Design

As assumed previously, if 3.2 kW were a convenient thruster power level for design, then the five-thruster system is obviously not satisfactory. It does not guarantee 90% reliability even when using very optimistic hardware-failure data. For six-thruster and seven-thruster systems, constant risk contours for the Class II mission goal are plotted on a failure parameter plane (Fig. II-C-9). The failure domain within the shaded area represents the currently conjectured failure data bounds. If less than 1% risk is desired for a N=6 or N=7 system, the design effort must be made to shift the hardware failure data domain to the left of the 1% curve. (See Fig. II-C-8 for the asymptotic behavior of constant risk curves.) As the thruster-life

Table II-C-4. A Computer Output for a Failure History Simulation and the Associated Probability, Least-switching Policy

Phase Number	I	II	III	IV	V	VI	VII	VIII	IX	X	XI	XII	XIII	XIV	XV
Failure History	7*	7	7	7	7	7	7	7	6	6	5	4	4	4	4
Burn-time History, Least-switching policy															
Thruster Number															
1	48**	-	-	-	-	-	-	-	-	-	-	123	151	165	172
2	48	77	118	211	-	-	-	-	-	-	-	-	-	225	232
3	48	77	-	-	-	-	-	-	-	-	-	-	105	119	126
4	48	77	118	-	-	-	-	-	-	-	-	193	221	235	242
5	48	77	118	211	299	387	475	563	x	x	x	x	x	x	563
6	0	-	-	-	-	-	-	-	-	-	88	x	x	x	88
7	0	-	-	-	-	-	-	-	88	176	x	x	x	x	176
Probabilities of Success	0.944	0.973	0.971	0.956	0.979	0.884	0.319	0.064	0.961	0.979	0.020	0.017	0.980	0.987	0.993

$$P = \prod_i P(i) = 0.477 \times 10^{-5}$$

Note: Life = 450 ± 50 days; Failure rates = $6/10^6$ hr; Restart risk = 10^{-5}

* Number of surviving engines.

** Elapsed burn time of the thruster at the end of the phase.

x Thruster failed.

- Thruster off.

Table II-C-5. A Computer Output for a Failure History Simulation and the Associated Probability, Equal-burn Policy

Phase Number	I	II	III	IV	V	VI	VII	VIII	IX	X	XI	XII	XIII	XIV	XV
Failure History	7*	7	7	7	7	6	6	6	5	5	5	4	4	4	4
Burn-time History, Equal-burn policy															
Thruster Number															
1	48**	77	118	211	-	-	-	-	x	x	x	x	x	x	211
2	48	77	118	211	-	-	-	-	-	-	-	-	239	253	260
3	48	77	118	-	-	206	-	-	-	-	-	-	234	248	255
4	48	77	-	-	-	x	x	x	x	x	x	x	x	x	x
5	48	-	-	-	-	136	-	224	-	-	-	299	-	313	319
6	0	-	-	-	-	-	88	-	176	-	-	x	x	x	x
7	0	-	-	-	-	-	-	-	-	88	176	251	279	293	300
Probabilities of Success	0.966	0.983	0.982	0.974	0.987	0.124	0.987	0.987	0.126	0.987	0.987	0.105	0.988	0.991	0.996

Note: Life = 450 ± 50 days; Failure rates = 6/10⁶ hr; Restart risk = 10⁻⁵P = 0.137 x 10⁻⁵

* Number of surviving engines.

** Elapsed burn time of the thruster at the end of the phase.

x Thruster failed.

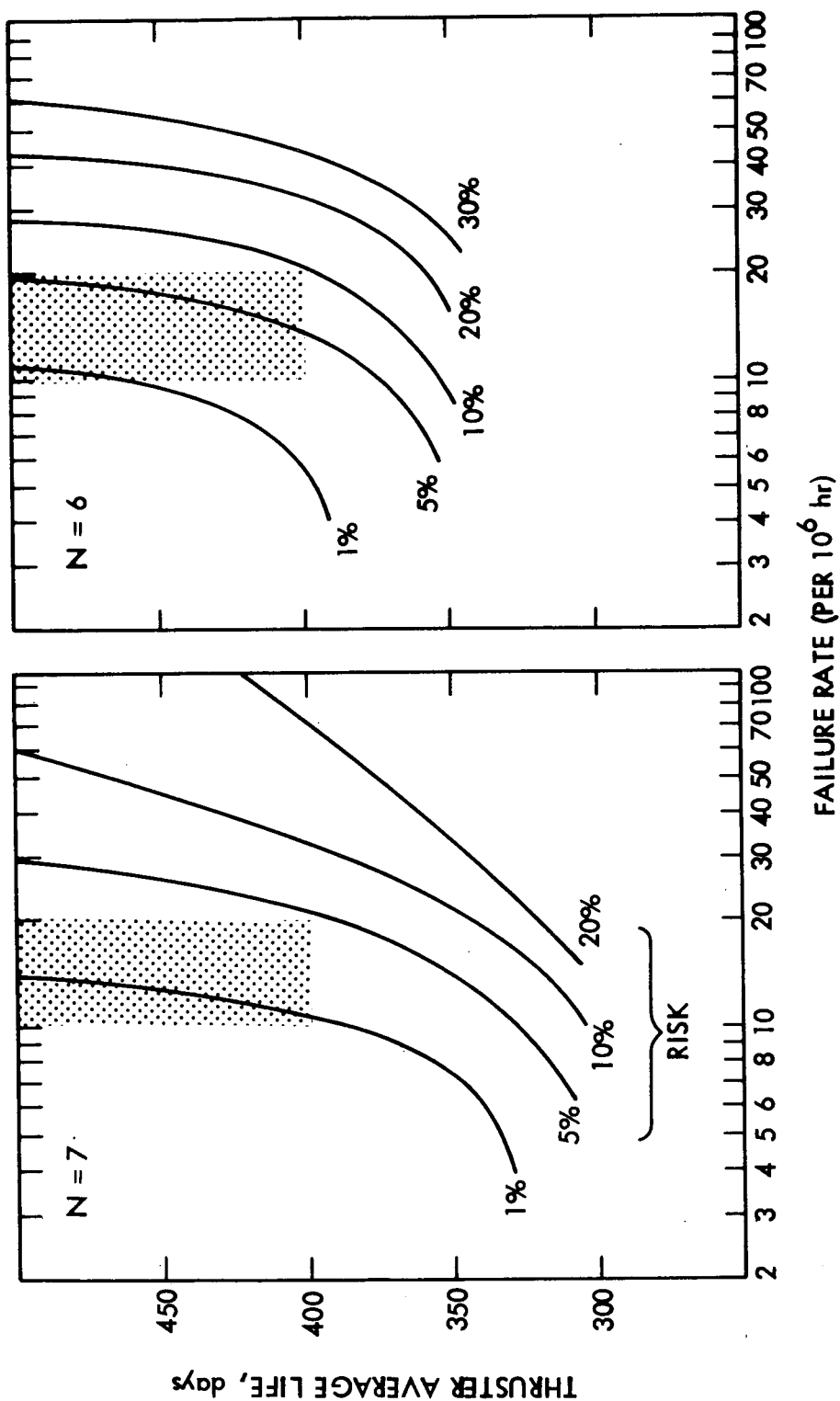
- Thruster off.

Table II-C-6. Probability of Success for a 1980 Encke Rendezvous Mission

N ↓	Life (days) → Failure Rate ($\lambda/10^6$ hr) →	450 ± 50			400 ± 50			350 ± 50			300 ± 50		
		6	10	50	6	10	50	6	10	50	6	10	50
5	Class I	78.2 77.8* 0. **	67.1 66.7* 0. **	14.4 14.3* 0. **	59.1	50.6	10.9	12.1	10.4	2.2	0.22	0.19	0.04
	Class II	93.5 87.7* 81.0**	87.7 80.8* 71.0**	39.9 28.1* 18.9**	85.0	77.5	27.3	42.0	36.8	9.61	1.92	1.71	0.40
6	Class I	97.5 96.6* 8.7**	93.9 92.6* 7.5**	41.5 40.2* 1.6**	95.2	90.7	38.2	80.3	72.6	23.4	23.5	20.4	4.9
	Class II	99.6 98.9* 98.2**	98.9 97.3* 95.6**	73.3 61.4* 51.3**	98.9	97.5	62.6	93.4	88.7	41.7	47.3	42.0	12.3
7	Class I	99.8 99.5* 84.7**	99.2 98.5* 75.7**	67.8 64.3* 22.9**	99.6	98.8	66.1	98.1	95.8	54.5	81.1	74.5	27.9
	Class II	99.9 99.7* 99.8**	99.8 99.2* 99.5**	89.5 75.6 78.0**	99.8	99.5	84.1	99.1	98.1	71.3	92.0	87.1	42.5

* Success probability with symmetry maintained in the thruster burns.

** Success probability using least-switching policy.



NOTE: CLASS II MISSION GOAL

N = NUMBER OF THRUSTERS

FAILURE RATES INDICATED ARE CAUSED BY PC PLUS THRUSTER

Fig. II-C-9. Constant-risk Contour Map for 1980 Encke Rendezvous Mission, Class II Mission Goal

parameter increases, the constant risk curve approaches asymptotically to a constant failure-rate line. At the other extreme, it tends to coincide with a constant thruster-life line as the failure rate approaches zero. This implies that, with a fixed number of thrusters and a given failure rate, improvement in thruster-life beyond a point does not contribute to the reduction of mission risks. For the same reason, given a fixed thruster life, design efforts beyond a point to reduce hardware failure rate is ineffective.

With the current design baseline, Fig. II-C-9 indicates that thruster life is not the key risk factor in controlling the Encke mission if a six-or seven-thruster system is desired. The low-risk contours are approaching the constant failure-rate lines at the current thruster-life expectancy. To reduce the mission risk, it is more effective and desirable to control the failure rate to less than the asymptotic value. For a seven-thruster system, the desirable 1% risk curve tends to approach the failure rate ≈ 15 line after thruster life ≈ 500 days. Thus, unless one is fairly sure of controlling the failure rate to less than 15 per 10^6 hrs, a seven-thruster system cannot attain a 99% chance of success, even with very long lasting thrusters. In this case, an eight-thruster system will be required, or the advantage of multichannel PC to thruster switching must be investigated. If a thruster failure rate of six and a PC failure rate of seven, as predicted by the hardware technicians, were reliable, then a seven-thruster system can be considered to be adequate because, by all indications, thrusters lasting 450 ~ 500 days are within reach with present technology.

b. Effects of Symmetry Requirements

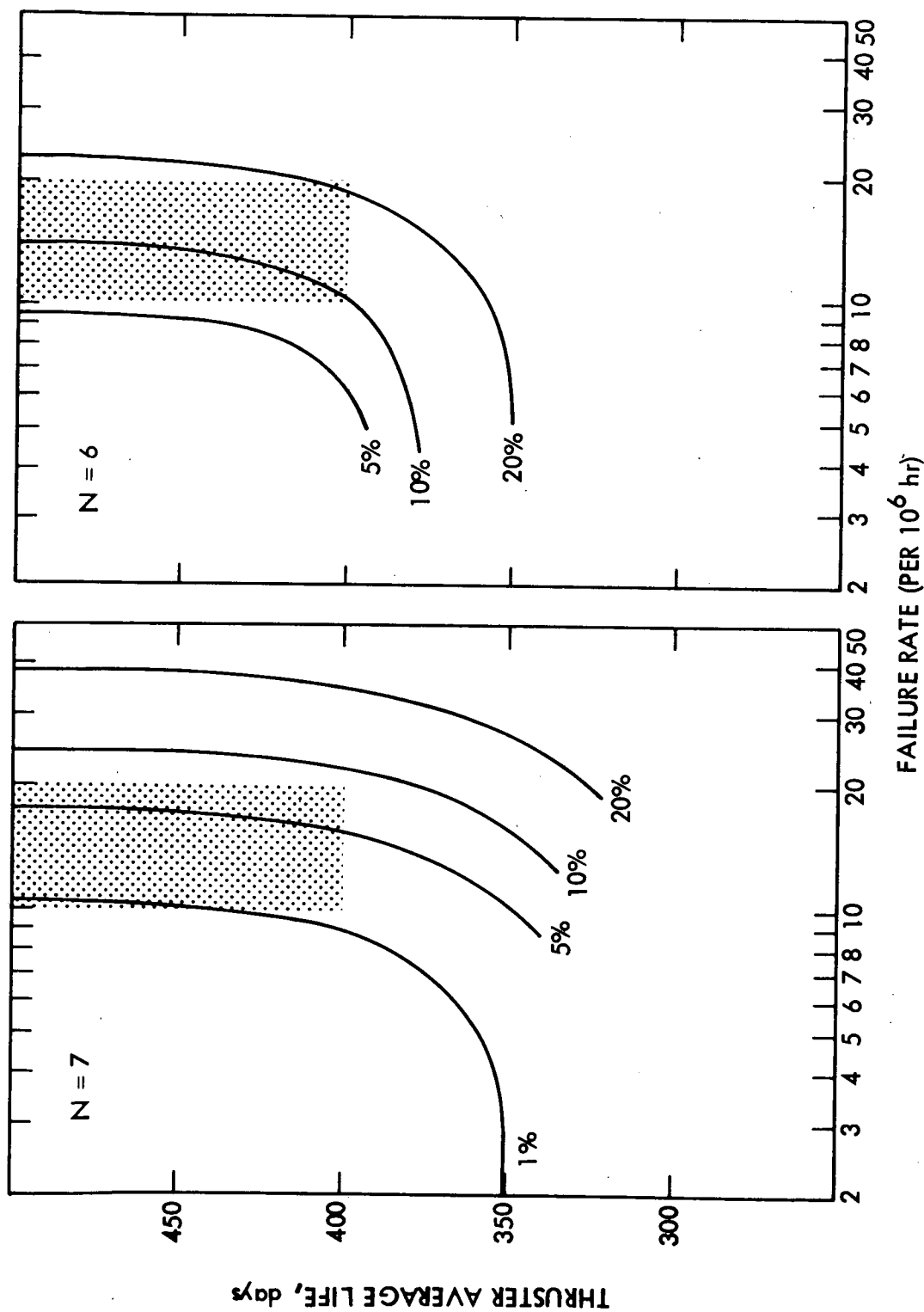
In view of the conclusions reached in paragraph a, only the seven-thruster system must be considered. Even though the data obtained are not exhaustive, it is expected that, within the current failure data domain, the symmetry constraint can degrade the mission reliability by no more than 1%.

c. Effects of Trajectory Design

The data in Table II-C-6 show significantly greater success probabilities for the Class II mission goal as compared to the Class I goal, which means that a mission design which allows up to a 20-day encounter time delay helps to ease the mission risk considerably. This fact, in turn, eliminates the possibility of over-designing the thrust-subsystem. The risk contour plots for the Class I mission goal, shown in Fig. II-C-10, illustrate this point. The confidence levels exhibited for a seven-thruster system appear similar to that of the six-thruster system shown in Fig. II-C-9. Thus, if the possibility of a Class II type of achievement were disregarded and the design point were chosen in the manner discussed in paragraph 3-a, an eight-thruster system would be recommended, which is one thruster too many.

d. Class III Mission Goal

Consideration of the Class III mission goal and the chances of success have not been investigated in as much detail as the Class II mission goal. The main difficulty in analyzing this class of mission is in forming the trajectory tree. Because there is no software which will generate a minimum flyby velocity (V_{hp}) and the associated trajectory simultaneously, it is necessary to scan over many V_{hp} s until a possible minimum is reached, which requires many trajectory searches. In addition to the freedom in the choice of $V_{hp} < 1$ km/sec, there is a degree of freedom in the encounter time (T_{end}) in establishing the failure-mode to alternate thrust-mode correspondence. This added degree of freedom in the choice of available trajectories demands another law (criterion) to single out one point in the acceptable ($V_{hp} - T_{end}$) domain and the corresponding thrust-mode. In this particular study, wherein the rendezvous mission is the main interest, no extra effort was made to solve the problem of flyby-class goal in an exact manner. However, a preliminary study of the possibility of flyby missions ($V_{hp} < 1$ km/sec) in case of severe failures was made. An arbitrarily selected, but valid, failure to flyby-mode correspondence was set up and the risks evaluated for a five-thruster system. The results show that, for median failure parameters, the probability of success for the Class III



NOTE: CLASS I MISSION GOAL

N = NUMBER OF THRUSTERS

FAILURE RATES INDICATED ARE CAUSED BY PC PLUS THRUSTER

Fig. II-C-10. Constant-risk Contour Map for 1980 Encke Rendezvous Mission, Class I Mission Goal

mission goal is 94% compared with 87% for the Class II mission goal. This number indicates that uncertainties (2 ~ 3% risks) in the recommended seven-thruster system can be completely erased if the Class III mission goal is considered acceptable.

e. Effects of Burn-policy

As expected, the least-switching policy is inferior when compared to the equal-burn policy in achieving either Class I or Class II mission goals. This is particularly true for a Class I mission objective because thruster life is limited and only a limited number of thrusters are available. As the assumed wear-out life becomes long and the number of available thrusters becomes large, normal failure dominates and the risk becomes insensitive to the policy (see paragraph 1-b-2). Such appears to be the case for the recommended seven-thruster system in achieving a Class II mission goal. For currently estimated failure statistics, the difference in predicted risk between the least-switching and the equal-burn policies is not expected to be more than 1 to 2%.

4. Future Development

Future studies will be concentrated on the applications of this technique. Further analysis of the 1980 Encke Rendezvous Mission will be made to explore the possibility of designing a better mission mode, better in the sense that mission risk aspect is considered in the mission-mode selection as well as in satisfying the hardware and mission constraints. Investigation into the risks associated with various thruster power-number combinations will be made. With this type of information, thrust-subsystem reliability and mass trade-off studies can be conducted to allow selection of an optimal design point.

Refinements to the algorithm of simulating failures and subsequent burn allocation will be investigated, so that the predicted results will not be altogether on the pessimistic side.

REFERENCES

- II-C-1. JPL Conference Report, March 27, 1972, Reliability Data and Failure Modes of 30-cm Thrusters (JPL internal document).

SECTION III

SEP MODULE AND THRUST SUBSYSTEM STUDIES

A. POWER CONDITIONER SELECTION AND SEP MODULE INTEGRATION STUDY

This study was conducted to assess the applicability of the SEPST III power conditioner (PC) to a 1980 Encke rendezvous mission using the JPL proposed SEP module attached to a Viking based spacecraft, and, if necessary, to recommend modifications for that mission application. Because the Encke rendezvous mission provides the most severe environmental and performance requirements of all proposed SEP missions, the PC design recommendations which emerge should be an appropriate basis for PC design for any foreseeable SEP mission.

At the start of this study, the state of the art of the thruster power conditioning was represented by the SEPST III PC units (Ref. III-A-1). These units are designed to operate a mercury ion thruster with an anode 20 cm in diameter at an input voltage level of 53 to 80 V. At an output of 2.5 kW, the units have a specific mass of 4.9 kg/kW and an operating efficiency of 89.5% at full power. Two such units have operated in thermal vacuum for more than 4500 hr.

1. General Functional Requirements

The PCs must perform the following functions:

- (a) Generate regulated voltage and currents for the operation of the ion thruster.
- (b) Control the operation of the thruster at the desired thrust level via several control loops.
- (c) Neutralize the spacecraft potential relative to the local space plasma by providing electrons at a controlled bias voltage.
- (d) Provide telemetry signals to evaluate the performance of the thruster and the status of the PC.

To perform the above functions, the PC electrically interfaces with:

- (a) The power subsystem to receive unregulated solar array power.
- (b) A command system to receive signals which initiate and control its operation.
- (c) A data system to condition telemetry signals which denote its status.

In addition to the electrical interfaces, there are a number of mechanical and thermal control interfaces.

The PC must be capable of surviving the launch and mission environment. The performance of the PC depends upon an efficient power dissipation scheme. Because the ultimate dissipation mode is thermal radiation, radiative surface characteristics are vital not only during the time the PC is in operation, but also during the time it is dormant.

Finally, the PC must be compatible with the electromagnetic requirements of other spacecraft subsystems and, especially, the science instruments. Suppression techniques must be used to control electromagnetic interference (EMI), which is caused by high frequency switching of high power electrical energy.

2. Electrical Design

a. SEPSIT Design Requirements

1) Input Requirements. Unregulated voltage to the PC is supplied from a solar array which is a fixed polarity, current-limited source. To be compatible with this solar array, certain requirements need to be defined:

- (a) The PC must not, under any circumstances, supply current of reverse polarity to the solar array.

- (b) The input voltage range is expected to be 200 to 400 V based on the power-subsystem operating voltage tradeoff study (Section IV-A).
- (c) The current ripple (peak to peak) into the PC should be limited to 1% of the operating current value under all conditions, including transients. This will allow the operation of the PC to vary approximately 1% off the maximum power point of the solar-array source.

It is anticipated that limits will be imposed on input voltage ripple and transients; the determination of acceptable limits is still under study. The impact of these transients and ripple on the PC design were not studied.

2) Output Requirements. The electrical output requirements, the regulation, and the range of control loops are dictated by the thruster design and mission constraints. The output will be compatible with the Lewis Research Center (LeRC) 30-cm thruster.

3) Command and Telemetry Requirements. A number of commands and telemetry signals will be required to operate, to control the operation, and to define the status and performance of the unit. The type of commands will be digital coded or digital discrete depending on the control and functions required.

4) Electromagnetic Interference. The design must meet the electromagnetic compatibility/magnetic control requirements summarized in Table III-A-1. These requirements are based on Viking Orbiter specifications.

b. Selected Design

Major characteristics of the selected design are shown in Table III-A-2. A functional block diagram of the design is shown in Fig. III-A-1. It closely follows the SEPST III design concept. The major deviations proposed

Table III-A-1. Electromagnetic Compatibility/Magnetic Control Requirement Summary

Environment	Requirements
<u>Conducted Noise Generation</u> Intersubsystem Quiet Circuits Intersubsystem Noisy Circuits Direct Access or Umbilical Circuit Common to Chassis ¹	300 mV (peak to peak) none 1000 mV (peak to peak) 1000 mV (peak to peak)
<u>Radiated Noise Generation (Measured at 1 m)</u> <u>Magnetic Fields</u> 1 Hz to 10 Hz 10 Hz to 1 Hz <u>Electric Fields</u> 30 Hz to 200 kHz (BB) 15 kHz to 40 MHz 200 kHz to 40 MHz (BB) 350 MHz to 450 MHz 2.1 GHz to 2.3 GHz 5.5 GHz to 5.8 GHz	none none none none none -9 dB $\mu\text{m V/m}$ < -24 dB $\mu\text{m V/m}$ < 76 dB $\mu\text{m V/m}$
<u>Conducted Transient Noise Immunity</u> Intersubsystem Interfaces (Centaur) Intersubsystem Interfaces Direct Access or Umbilical Circuit Common to Chassis ²	none < ± 1 V or ± 100 mamp < ± 3 V or ± 300 mamp < ± 3 V or ± 5 mamp
<u>Radiated RF Power Immunity</u> 350 - 450 MHz 2.1 - 2.3 GHz 5.5 - 5.8 GHz 8.3 - 8.5 GHz	3 W/m ² average 10 W/m ² average 600 W/m ² peak 0.5 W/m ² average
<u>Maximum Radial Magnetic Field^{3, 5}</u> Bus Mounted Subsystems Scan Platform Instruments All Other Assemblies	5000 nT 5000 nT at surface ⁴

- Notes: 1. Two meters of #24 AWG wire.
2. Not commonly connected to chassis.
3. Hardware demagnetized by 4 nT (maximum).
4. Science instruments within about 1/3 m from surface.
5. A 16-m boom to magnetometer with an 0.03 nT sensitivity is assumed.

Table III-A-2. Selected Power Conditioner Electrical Design Characteristics

Power Supply	Module Type	Power Output per Supply, W		Number of Modules		Power Output per Module, W		Efficiency, %	Power Dissipation per Module, W	
		Maximum Design Rating	Normal Operating	Normal	Operating Minimum	Maximum	Normal Operating		Maximum	Normal Operating
<u>Power Supply Output Modules</u>										
Screen	Inverter	3000	2000	8	6 ¹	340	250	93.5	24 ¹	17.6 x 8 = 141
Arc	Inverter Transformer Rectifier/Filter	630	555	2 1 1 1	1 1 1 1	630	566 557 555	93.5 98.4 99.6		39.3 9.2 2.2 51.7
Accelerator	Inverter	300	20	1	1	300	20	82.0		4.0
Main Vaporizer		20	6							
Cathode Vaporizer		20	3.5							
Neutralizer Heater		50	4							
Neutralizer Keeper	Low voltage	45	24	1	1	175	91.52 /45.5	86.0	1 ³	6.8
Isolator Heater		20	4.5							
Neutralizer Vaporizer		20	3.5							
Cathode Keeper		60	6				96 ²			
Cathode Heater	High voltage	90	4 2630.5	1	1	150	/10	82.0	21.0 ³	1.2
Total Output										
<u>Supporting Modules</u>										
Screen/Accelerator Filters	Filter	3300	2020	1	1	—	2020	99.6		8.0
Screen	Staggered Generator	—	—	1	1					3
Control	Control	—	—	1	1					3
Line Regulator	Regulator	264	100	1	1	26 ²	100	93.0	20 ³	7.5
5-kHz Inverter	Inverter	243	87.5	1	1	243 ²	87.5	94.0	15 ³	5.5
Total Power Dissipation										230.7

¹ Power sharing mode. Minimum modules capable of supplying power.² Power during startup.³ Dissipation during startup.

$$\text{Overall Efficiency} = \frac{2630.5}{2630.5 + 230.7} = .92$$

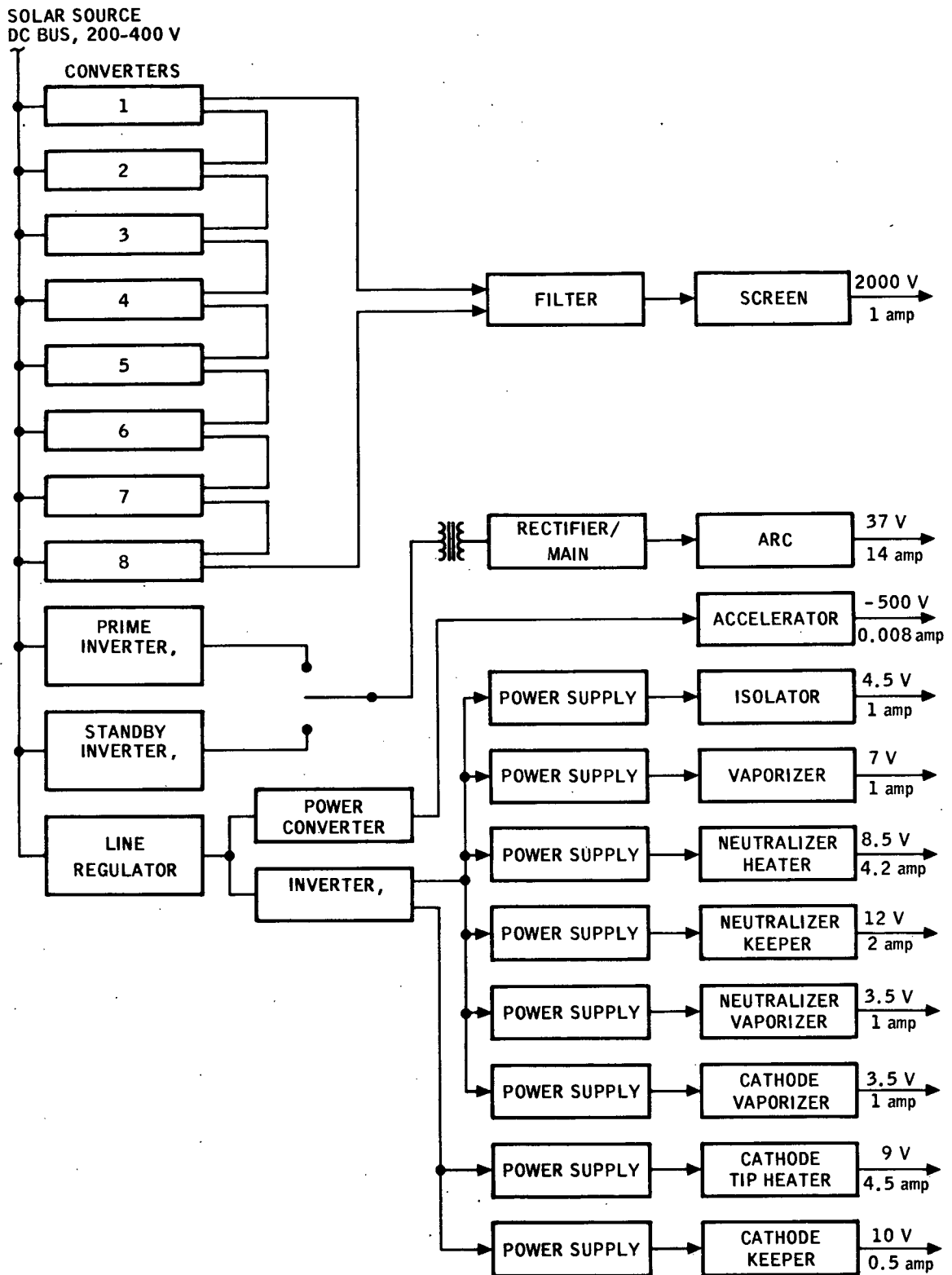


Fig. III-A-1. Selected PC Functional Block Diagram

for the SEPSIT design are (1) to raise the input voltage range from 53 to 80 V to 200 to 400 V, (2) to modify the output characteristics to accommodate the LeRC 30-cm thruster design, (3) to raise the power-transistor junction temperature from 55°C to 110°C, and (4) to modify circuit designs, cabling, and circuit locations to minimize EMI effects.

1) Input Voltage Increase. The increase of input voltage from a range of 53 to 80 V to 200 to 400 V will reduce the input current to the SEPST III PC and power producing inverters and modules. This current reduction suggests higher power-producing inverters than the SEPST III inverters of 300 W. However, since the efficiency of the medium voltage design is expected to be 92 to 93%, only 1 to 2% higher, the high power-producing inverter will result in higher power dissipative modules and will utilize bulkier power transformers.

Because the power losses of these modules are high compared to other spacecraft packages, large radiating surfaces are required. For this reason and because of the thermal performance and reliability estimates of the SEPST III design, it is recommended that the medium voltage design utilize the same low power inverter concept.

2) 30-cm Thruster Application. The 30-cm thruster developed by LeRC requires power from eleven supplies. The nominal operating power of the thruster is 2630.5 W (Ref. III-A-2). The design ratings, normal operating power output of each supply, the additional supporting modules, and the design characteristics of the electrical design based on a 92% efficiency are shown in Table III-A-1.

3) Power Transistor Junction Temperature. The SEPST III unit was designed to satisfy a reliability requirement of .95 for 10,000 hr of operation. To meet the requirement, the electronic components were derated below the manufacturers' ratings. The power transistors, among the most critical components, were operated at a junction temperature of $50 \pm 5^\circ\text{C}$, which established the component mounting radiation base-plate temperature.

According to the Stefan-Boltzmann law, heat is radiated by a body at a rate proportional to the product of the radiating surface area and the fourth power of its absolute temperature. On this basis, it was recognized that, if it were possible to reliably operate the transistor function at a higher temperature, the maximum shearplate temperature would be correspondingly increased, and the PC would require less radiating surface area, i.e., shearplate surface area. It was clear that this approach could potentially lead to a smaller, lighter PC. Furthermore, a smaller radiating area requires less heater power for maintaining a minimum temperature for a dormant PC. Therefore, a review of the reliability analyses, failure rate, and derating of electronic components (especially of the power transistor) was performed. It was concluded that the $50 \pm 5^\circ\text{C}$ function temperature was based on very conservative reliability estimates of the Hughes Aircraft Company.

The power transistor selected for the proposed design is an experimental device developed by Solitron, Inc. Figure III-A-2 shows

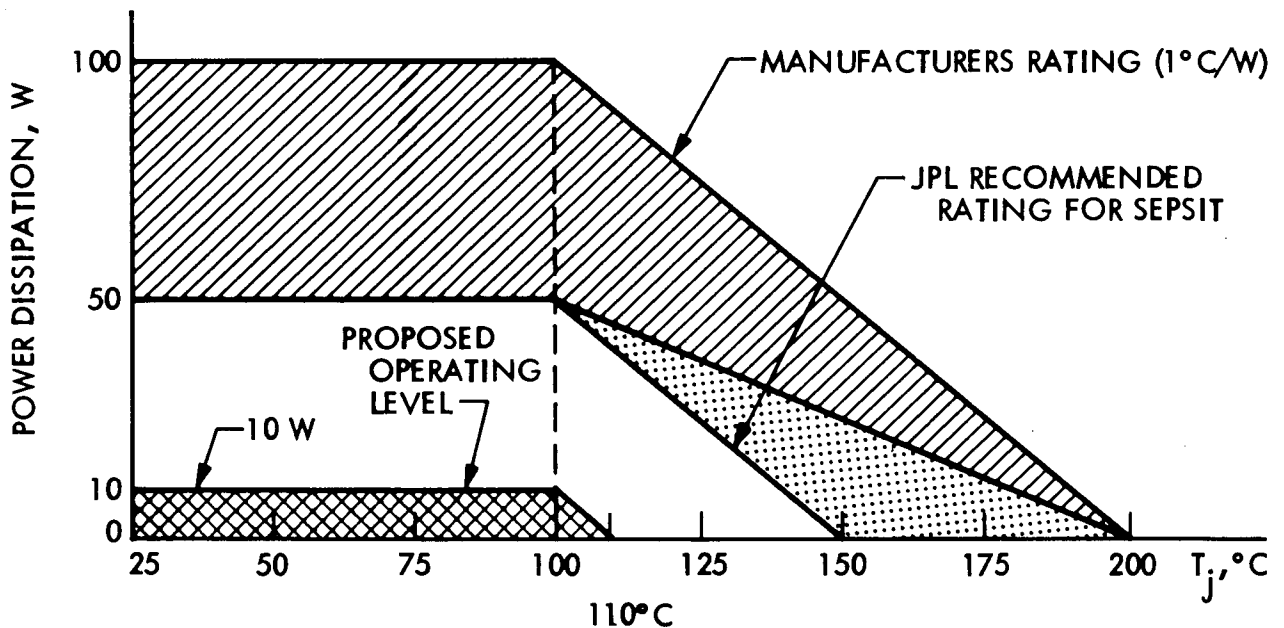


Fig. III-A-2. Power Transistor Derating Curve

the rating proposed by industry based on maximum power dissipation of a transistor of 100 W at the case temperature of 25 to 100°C , then derating at the rate

of $1^{\circ}\text{C}/\text{W}$ until 0 power at 200°C junction temperature is reached. The JPL electronic parts engineering group recommends a 50% derating for reliability. The actual power dissipation of the transistor, as applied in the design, is expected to be about 10 W. As can be seen, the 10-W dissipation for 100-W power transistor is minimal. It is felt that the case temperature of the power transistors can be raised to 110°C safely without degrading the reliability of the part and of the design. A minimum start-up radiator temperature of -20°C , a minimum storage temperature of -40°C , and a minimum steady-state operating temperature of 0°C , are considered realistic for the electrical design.

4) EMI Reduction. To evaluate the magnitude of the EMI problem, the SEPST III units were tested for conducted and radiated EMI in an ambient environment (Ref. III-A-3). It was concluded that the following design techniques would be used to insure compliance with the SEPSIT EMI requirements listed in Table III-A-1:

- (a) Reduction of nonfunctional rise times, such as spikes common to the square wave inverter waveforms, or even modification of the waveform.
- (b) Elimination of common impedances. Transformer coupling should be employed, and telemetry pick-offs and operational amplifier-telemetry outputs should be removed from common impedance points.
- (c) Promotion of isolation between circuitry, especially circuits sharing internal control and circuits generating outputs.

Additional isolation can be achieved through the incorporation of suppression techniques or components. These are:

- (a) Compartmentation of circuits, especially circuits that generate steep current and voltage wavefronts. Confinement can be accomplished through the use

of shielding, i. e., shielding of individual modules and/or the entire PC, and filtering.

- (b) Utilization of devices which can slow collapse of magnetic fields at turn-off.
- (c) Separation of cable harness into compatible groups. The groups to be separated are: power input, signal, telemetry, and power output. In addition to separate cables, it is advisable to provide separate connectors.

3. Packaging Design and SEP Module Integration

Packaging design refers to the task of assembling an electrical design into a configuration which satisfies both electrical design requirements and those requirements which are imposed by the electronic parts, packaging techniques, materials, processes, spacecraft configuration, and mission design. This design task requires the inputs of several highly related technical disciplines: configuration definition, temperature control, structure, and cabling. This section describes the impact of each of these disciplines on the packaging design which best suits the previously described preferred electrical design and Encke rendezvous mission requirements. The design which follows must depart from the SEPST III design for several reasons: (a) the preferred electrical design differs from that of the SEPST III units in both total power output (and resulting dissipated power) and maximum allowable power-transistor-junction temperatures, (b) recent dynamic tests of the SEPST III units (Ref. III-A-4) indicated that the design was inadequate to survive expected launch loads, and (c) heater power required to maintain dormant PCs at minimum design temperatures was deemed excessive for past SEP module/PC integration schemes.

a. Configuration Evolution and Description

The SEPSIT space vehicle will be exposed to great variations in solar irradiance during the course of the Encke rendezvous mission, from 110 W/m^2 at 3.5 AU to $12,000 \text{ W/m}^2$ at .34 AU. It is clear that the exposed

surfaces of the PCs must not be directly exposed to such extremes. One of the early approaches considered involved placing all the PCs on the anti-sun side of the space vehicle with the sun-side insulated. This approach, while thermally acceptable, would present the following problems:

- (1) The space-vehicle center of gravity would tend to shift toward the anti-sun side.
- (2) Such a PC location would make the space vehicle long.
- (3) This configuration would lead to a comparatively heavy space vehicle because the structural capabilities of the PCs themselves could not be efficiently utilized.
- (4) While going through the asteroid belt, the PC shearplates would be nearly normal to the plane of the paths of the highest probability of micrometeoroids.
- (5) A large micrometeoroid shield would be required on the sun side.

Because of these deficiencies, alternate approaches were considered. The scheme ultimately adopted is far superior to the one described above in all five problem areas. In addition, it, too, satisfies the thermal requirement for avoidance of solar illumination of PC shearplates. Figure III-A-3 illustrates the proposed SEP module/PC integration scheme. The six PCs required for the Encke rendezvous mission are shown, with variable-emittance louver assemblies attached, mounted back-to-back with their shearplates perpendicular to the solar array axis of rotation. By maintaining an angle of 90 deg between this axis and the sun-space vehicle line, direct solar illumination of the louvered PC surfaces is avoided.

The proposed PC configuration utilizes the SEPST III flat-pack design concept for high power dissipation modules in which components are mounted directly to radiator/shearplate modules, which, in turn, are mounted to the PC chassis. Individual modules are mounted from the rear of the PC chassis to allow module removal for post assembly repairs without requiring removal of the delicate louver assembly. The two-module width provides

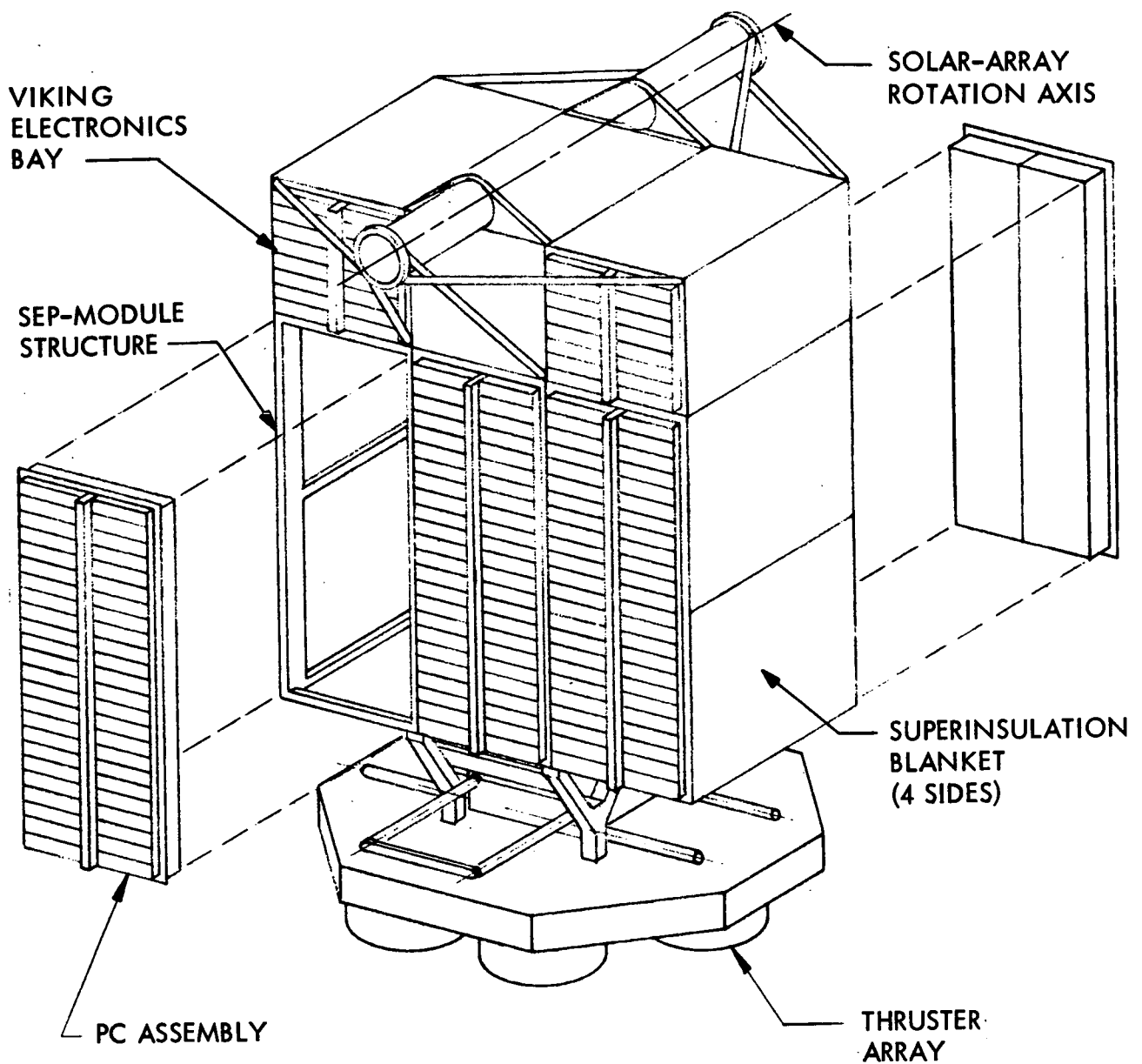


Fig. III-A-3. PC Assembly within the SEP Module

compatibility with SEPST III module component layouts. Module rows are separated by a cabling support on which are mounted individual module plug-in connectors and the primary PC input and output connectors. Figure III-A-4 shows some of the details of two opposing PCs.

b. Configuration Sizing

The criteria for determining the 75°C temperature control surface for sizing the PC radiating/shearplate area was the junction temperature of the power transistors. Using the 110°C value justified in part 2 of this section, the 75°C surface temperature was established by allocating a 35°C temperature gradient for the thermal resistance from the transistor junction to the shearplate. This provided for the thermal resistance from the transistor junction to the transistor case; the transistor mounting on the shearplate, including the thermal dispersion factors; and the worst case condition when only six out of eight screen inverter modules are operating.

The thermal analysis discussed in part 4-c following was performed on the basis of a 75°C, isothermal, PC shearplate/radiator with no PC to PC conductive heat transfer. As expected, the maximum area sizing condition was all six of the PCs operating at closest solar approach; the recommended area is 6451.60 cm² (1000 in.²) per PC. For a total PC dissipated power of 1384 W (230.7 W per PC), as specified in Table III-A-2, the overall PC power density is 1.48 W/cm² (.23 W/in.²). The assumption of no conductive heat transfer is quite valid in the case of all PCs operating, whereas the validity of the isothermal radiator assumption depends on the adequacy of individual module circuit arrangements and module arrangements on the PC chassis.

The PC size would be the same as that of the minimum required radiation area 6451.60 cm² (1000 in.²), if the shearplate/radiator area of each module could maintain the required power density. A larger shearplate than the minimum radiation area is required as a result of maintaining SEPST III module similarity, existing SEPST III part sizes, a practical physical minimum module size 5.08 cm (2 in.) for the selected configuration, and use of a standby arc inverter module.

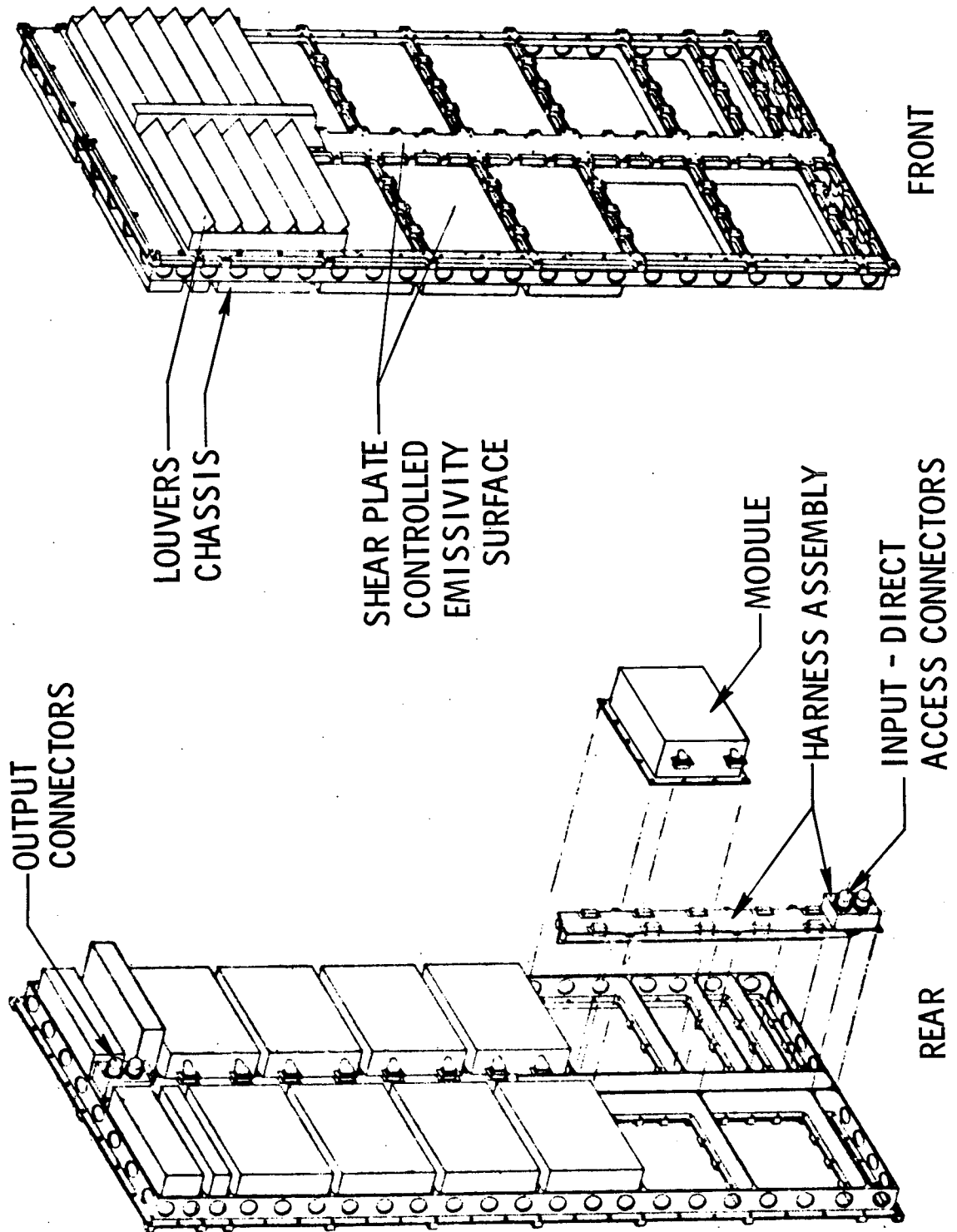


Fig. III-A-4. Detailed View of Two Opposing PCs within the SEP Module

The width of the proposed PC was initially selected during SEPSIT configuration studies to provide structural continuity with the SEP module. This nominal 50.80-cm (20-in.) width (similar to the Mariner assembly chassis) satisfied several criteria and was used in sizing the selected PC design. Some of these criteria are:

- (1) PC width should be minimized to raise the natural frequency and hence lower structural mass.
- (2) Conductive heat transfer between PCs is enhanced by minimizing PC width, thus aiding the process of passive heating of dormant PCs.
- (3) A width was required that could provide for a two-module-wide assembly with a center cable-way for the electrical connect harness and support that would accommodate the SEPST III power-dissipating module layouts with minimum changes.
- (4) A width that was compatible with the Mariner temperature-control louver technology, including adequate conduction to the louver blade control mechanism, was required. Louver assemblies from 40.6 to 55.9 cm (16-to 22-in.) widths are available. Development costs and mission risk can be minimized by the use of existing louver assembly technology and hardware.

A width that would provide a ratio of a 2.5 to 3.0 length to a 1.0 width provides a reasonable compromise between the minimum length SEP structure, the minimum width PC, and the overall length and width of the PC supporting structure.

The specification of individual module dimensions is not required at this stage of the PC development; however, using the following ground rules and the criteria listed above, the range of module widths can be calculated permitting the specification of preliminary overall PC dimensions for the selected configuration. These ground rules are:

- (1) SEPST III electronic module similarity must be maintained.
- (2) All modules are to be the same length. This length for thermal sizing purposes is equal to one half the PC width.
- (3) Maximum power transistor junction temperature is 110°C .
- (4) The average power density of 1.48 W/cm^2 ($.23 \text{ W/in.}^2$) (for a shearplate/radiator surface temperature of 750°C) is to be used.
- (5) The low power dissipating modules must be packaged with techniques to achieve the smallest module shearplate/radiator area consistent with part sizes.
- (6) The minimum width module required for maintaining physical integrity is to be two inches.
- (7) At least four structural elements are to be provided as beams across the width of the PC.

The preliminary PC size based on the stated ground rules and criteria is $50.80 \times 139.7 \text{ cm}$ ($20 \times 55 \text{ in.}$). It should be emphasized that these dimensions are flexible within the limits of minimum area and other criteria stated above, and they should be reviewed as other SEP missions and configuration applications are defined.

c. Thermal Analysis

The performance of any electronic device, a PC, in particular, depends, among other things, upon its temperature level and distribution. This is a consequence of the inescapable fact that the electrical characteristics of virtually all electronic parts are, to some degree, temperature-dependent. Moreover, irreversible damage may occur to certain components, if their established temperature limits are exceeded.

The problem of controlling the temperature of each individual part can, by clever application of packaging techniques, be reduced to the

temperature control of a single heat-sink surface. Because of its secondary use as a structural member in shear, this surface is commonly referred to as the shearplate/radiator. To ensure good electrical performance and reliability, the following shearplate temperature limits were established in parts 3 and 4 of this section.

- (1) Minimum temperature during shutdown, -40°C .
- (2) Minimum start-up temperature, -20°C .
- (3) Minimum steady-state operating temperature, 0°C .
- (4) Maximum operating temperature, $+75^{\circ}\text{C}$.

The selected PC/SEP module integration scheme can be seen in Fig. III-A-3. The super-insulation blanket which covers the four otherwise open sides isolates all PC surfaces, excluding the shearplates, from the external thermal environment, but not from each other. This configuration has the advantage of strong infrared radiation coupling between the units. Conductive coupling is desirable, but it is not an absolute necessity.

The PC shearplates, which are placed normal to the space vehicle Y axis*, are exposed to a significant fraction of the energy re-radiated by the solar arrays. This additional heating, unfortunately, increases monotonically as the PC-compartment dissipation increases and results in a tendency toward higher PC temperatures. Additionally, wide variations in total PC compartment heat dissipation will be experienced during the course of the mission. Based on the selected PC design, the total dissipation could vary from as little as 179.4 W (one PC at half normal output of 1315.25 W with efficiency of 88%) to as much as 1384.2 W (6 PCs at full output power). If the additional heat load from the solar arrays is ignored, and the PC thermal coupling is assumed to be strong, then a simple relationship between the maximum and minimum shearplate/radiator temperature can be obtained. That is,

*The spacecraft vehicle Y axis is parallel to the solar-array axis of rotation.

$$t_{\min} = \left(\frac{P_{\min}}{P_{\max}} \right)^{1/4} (t_{\max} + 273.15) - 273.15$$

where t is temperature in $^{\circ}\text{C}$, and P is the power dissipation. For $t_{\max} = 75^{\circ}\text{C}$, $P_{\min} = 179.4 \text{ W}$, and $P_{\max} = 1384.2 \text{ W}$, t_{\min} would be -64.3°C . This temperature is much too low. To estimate how much additional heater power must be added to the 179.4 W to maintain the required minimum operating temperature of 0°C , the above equation can be used by specifying $t_{\min} = -20^{\circ}\text{C}$ and solving for P_{\min} . The result is $P_{\min} = 524.5 \text{ W}$. Therefore, $524.5 - 179.4 = 345.1 \text{ W}$ must be supplied as heater power. Considering that the difference between the total space vehicle power and the propulsion power is only about 500 W at the trajectory aphelion, it is unacceptable to provide that much heater power. Fortunately, the problem can be remedied by supplying each shearplate with a variable-emittance louver assembly.

A conservative estimate of the effective emittances for fully open and fully closed louvers is .76 and .12, respectively (based on the louver control area). Louvers, typically, have a control range of about 15°C and can be adjusted to be fully closed for all temperatures at or below some preselected temperature. If the maximum expected PC temperature for heliocentric distances of 2 AU and greater is selected as the fully closed, set-point temperature, the louvers will be fully closed during the passage of the space vehicle through the asteroid belt. Thus, the louvers, in addition to performing a temperature control function, can also provide effective micrometeoroid protection for the PC shearplates.

A mathematical analog of the thermal characteristics of the PC compartment was formulated for the purpose of determining certain design parameters, e.g., required shearplate area, and for subsequent prediction of thermal performance. The model assumes that (1) there is no direct solar incidence on any louvered surface, (2) the superinsulated compartment walls are adiabatic, (3) conductive coupling between PCs is negligible, (4) the louvered shearplates are externally irradiated only by the solar arrays, and (5) solar array temperature is independent of the PC-compartment temperature

level or distribution. Details of the analysis are contained in part f of this section. Some of the more important conclusions follow:

- (1) About $.6452 \text{ m}^2$ (1000 in.^2) of shearplate/radiator area are required for each PC. A significantly larger area would reduce PC temperatures too much at large heliocentric distances, where the dissipation could be as low as 179.4 W, and the availability of heater power, which could correct the situation, is at its lowest level. Conversely, a significantly smaller area would cause the PCs to overheat when the power dissipation increases to the maximum of 1384.2 W.
- (2) Little or no heater power will be required to maintain minimum shearplate/radiator temperature limits, even at trajectory aphelion. Present day louver and super-insulation application technology can be used to achieve this goal with only one PC operating at one-half normal output power (179.4 W dissipation).
- (3) PC shearplate/Radiator temperature will not exceed 75°C during the portion of the mission from space vehicle launch to Encke rendezvous. With six PCs operating at full normal output power (1384.2-W dissipation), the 75°C limit will be exceeded only at heliocentric distances less than 1 AU. At this dissipation level, the temperature of the hottest PC at perihelion is presently estimated as 82°C . If it were certain that there would be some conductive coupling, five PCs could be operated at full normal power through perihelion without exceeding 75°C .
- (4) The back-to-back spacing distance can be varied between .3 and .9 m with only minor deviations in PC operating temperature.
- (5) Conductive coupling between PCs, although neglected in the analysis, can only enhance the expected thermal

performance by making the PC compartment more nearly isothermal.

The thermal design and analysis makes use of assumptions which imply ideal conditions. For example, the superinsulation blanket is considered a perfect thermal insulator. Of course, no perfect insulation exists so that allowances must be made for some heat leakage. But, perfect or imperfect, the blanket must be able to survive a multitude of hazards such as extremes of temperature, micrometeoroid impacts, ultraviolet degradation, and proton bombardment. There are indications that developing a low-weight, low-cost insulation system, which, in addition to performing its thermal function, must provide micrometeoroid protection, may not be a simple task. Tests conducted at the Boeing Radiation Effects Laboratory (BREL) have shown that a widely used superinsulation material, goldized Kapton, is reduced to char when the Kapton side is irradiated with a 10 earth-sun solar simulator. An Encke rendezvous spacecraft will be exposed to this kind of environment at perihelion. Naturally, steps must be taken to avoid such a catastrophic failure.

Another implied assumption is that heat leaks to or from the PC compartment, although structural members or other penetrations are negligible. By careful design and material selection, such leaks can be reduced, at least in principle, to an acceptable level.

Finally, the condition that the space vehicle Y axis is always maintained normal to solar rays can not be met except within some error band of about plus or minus one-four degree. To compound the problem, even if perpendicularity could be exactly maintained, the louver blades could still be illuminated whenever they are not in the fully closed position. Because of the high ratio of solar absorptance to emittance of the blade material (polished aluminum), high solar irradiation could produce a temperature great enough to cause melting. One possible solution to both problems would be to provide parapets around the periphery of each of the two sets of louvered shearplates. These would provide the shading necessary to prevent solar illumination.

d. Structural Design

The structural design of a SEP thruster PC is governed by a number of design objectives and functional requirements. These requirements to a large extent control the ease and manner with which a PC can be integrated into a spacecraft structure. Because of the large size of the PCs (over 0.64 m^2), the ease and manner with which they integrate into the spacecraft structure can have a significant impact on spacecraft configuration and total mass. For this reason a study was undertaken to identify and explore the requirements relating to the structural design and integration of the thruster PCs.

The study determined a number of important structural design requirements, which are discussed in the following subsection, as are the degree to which a preliminary PC design meets these requirements and ways of improving upon the preliminary design. Based on these improvements an alternate PC structural design was devised, and a structural analysis of the combined spacecraft/PC structural system was made. The results of this study indicate the importance of the stiffness of the spacecraft structure supporting the PC. The conclusions drawn, which pertain to the structural design of thruster PCs, are presented at the end of this section.

1) PC Structural Design Requirements. Because the ease of integration can significantly influence the configuration and mass of the spacecraft itself, considerable emphasis was placed on identifying and exploring design requirements which influence the integration of the PCs into the spacecraft structure. Five major structural design requirements and design objectives for the PC were defined. The PC structure should:

- (a) Support PC electronics, cabling, and thermal control components and maintain an acceptable dynamic environment during launch.
- (b) Provide a clean structural interface for a SEP module structure integration.
- (c) Provide a convenient format for ground handling and testing.

- (d) Be capable of meeting meteoroid shielding, EMI shielding, and other similar environmental requirements.
- (e) Minimize total spacecraft weight, not just the weight of the PC.

Besides maintaining its own integrity, the structure is generally called upon to limit the PC deformation amplitudes which are critical to the survival of the electronic modules and thermal louver assemblies. A general rule of thumb is that the lowest natural frequency of the complete PC assembly should be maintained around or above 200 Hz, when mounted on the spacecraft. It is also important that the spacecraft structure, to which the PC attaches, not deform to the extent of warping or applying excessive loads to the PCs.

Meeting the above minimum frequency and spacecraft structural warpage criteria places requirements on the stiffness and strength of the spacecraft structure. Additional requirements are placed on the spacecraft structure by the PC method of attachment and interface load reaction requirements. An important decision in the design of a PC is the tradeoff between stiffening or strengthening the PC versus stiffening or strengthening the spacecraft structure, or increasing the number of spacecraft/PC attachment points. Such decisions should be based on improving the degree to which the previously stated design objectives are met with emphasis on minimizing total spacecraft weight, versus minimizing just the weight of the PCs. A decision which reduces the PC weight, but substantially increases the weight of the interfacing spacecraft structure is a false economy.

An important objective from the point of view of minimizing total spacecraft weight is the elimination of redundant structural elements. For this reason, the PC should be constructed to serve as a member of the spacecraft structure and to carry any loads which would require the addition of redundant structural members, if the loads were not carried by the PCs. Specifically, the parallelogramming of large rectangular bays can only be efficiently eliminated by providing shearplates or diagonal members which carry

the shear loads which tend to collapse the bay. Because the PC mounts into a rectangular bay, it is important from a spacecraft-weight standpoint that the PC carry the shear loads and eliminate the need for additional redundant shear stiffening. This implies that the structure of the PC should be designed to carry spacecraft shear loads, and that the method of attachment to the spacecraft must be capable of transferring the shear loads between the spacecraft and the PC.

2) Structural Design Deficiencies of the SEPST III PC.

During recent years the development of solar electric PC units has centered on the electrical design and integration of the units into the overall solar electric thrust subsystem. One design which has progressed to the flight prototype stage is the Hughes Aircraft Company (HAC) PC for the 20-cm SEP thruster (Ref. III-A-1). This design consists of 20 rectangular electronic modules assembled into a large rectangular assembly, as shown in Fig. III-A-5. Each module is attached around its periphery to the planar frame which provides the system stiffness. The frame is composed of a rectangular network of I-beams surrounded by a channel, and it attaches to the spacecraft structure around its periphery and at one interior point. The general design was based on minimizing the weight of the PC structure and providing adequate surface area for temperature control purposes.

During the attempt to integrate the HAC design into SEPSIT spacecraft configurations a number of deficiencies were noted:

- (a) The HAC structural design is based on an infinitely rigid spacecraft and on an unrealistic clamped-boundary condition at the PC/spacecraft attachment. Even in a test which used an extremely stiff vibration test fixture, the flexibility of the foundation and attachment led to a reduction in the first mode natural frequency from the predicted value of 159 Hz to the measured value of about 70 Hz (Ref. III-A-3). The 70-Hz

Reproduced from
best available copy.

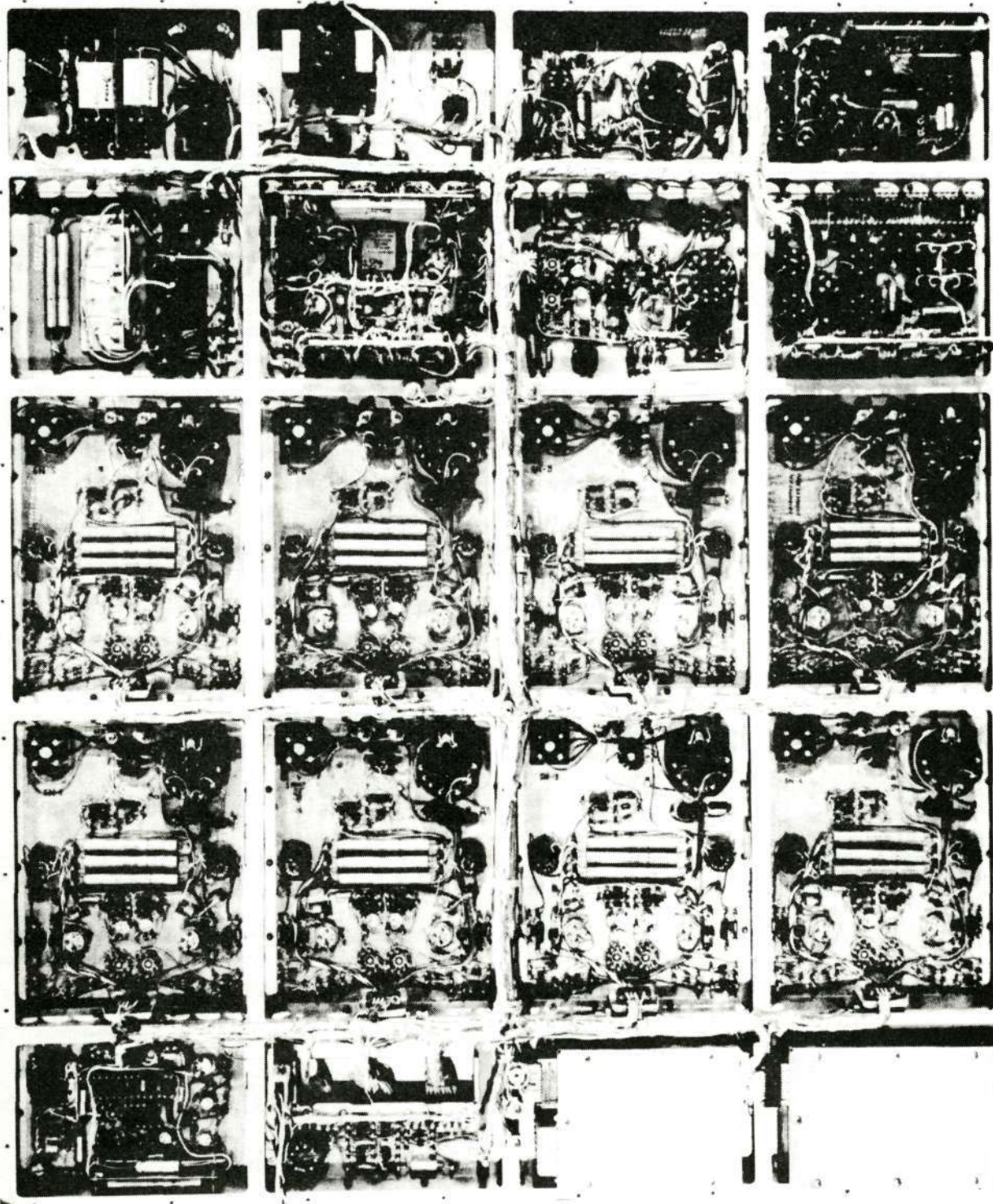


Fig. III-A-5. HAC Prototype PC, Component Side

value is dangerously low compared to the nominal 200-Hz requirement previously discussed.

- (b) The design uses an attachment point in the middle of the I-beam frame (Fig. III-A-5). It is assumed that the spacecraft structure at this point is significantly stiffer than the PC structure. Because this is not a natural location for spacecraft structure, redundant structure would have to be added to support this point. Obtaining the high stiffness required by the PC could result in a very heavy structure, possibly weighing more than the entire PC structure. From a weight standpoint, it is much more efficient to strengthen the PC and eliminate the center support point.
- (c) Although the PC itself has considerable shear strength in plane, the method of attachment to the spacecraft is not capable of transmitting shear loads in the plane of the PC. Therefore, redundant spacecraft structure would have to be supplied to prevent the PC bay from parallelograming. It is much more efficient in terms of weight to design the PC to carry the necessary in-plane shear loads.
- (d) The HAC PC was not designed to provide a structural interface for the thermal louver assemblies.

From the above, it is clear that, as spacecraft and mission constraints are defined and prototype designs are reduced to flight hardware, it is important to place increased emphasis on thermal and mechanical integration of the PCs with the spacecraft.

3) Means of Improving PC Structural Design. As part of the SEPSIT effort, means for improving the PC structural, electronic packaging, and cabling designs were devised and an improved PC-mechanical design was generated. The primary structural changes were as follows:

- (a) The width of the PC was decreased from .75 to .5 m (30 to 20 in.) to allow for better integration with the spacecraft structure, improved integration with available thermal louver assemblies, and decreased structural weight. Because the stiffness of the frame members is inversely proportional to the cube of their length, the decreased width significantly increased the stiffness of the transverse members. These members were designed as the primary structural members, and only a single longitudinal member was used to support the cabling.
- (b) Based on a realistic stiffness for the spacecraft structure and on a pinned edge boundary condition, instead of a clamped edge condition, the natural frequency of the PC was increased to around 200 Hz. Various spacecraft structural stiffnesses were assumed and results are presented in part 2 of this section.
- (c) The PC/spacecraft attachment method was designed to carry in-plane shearloads, and the PC as a whole was designed to serve as a shearplate in the spacecraft structure.
- (d) Provisions were made for mounting the thermal louver assemblies and meeting their interface requirements.

Early in the study, it was determined that the ease and manner with which the thruster PCs integrate into the spacecraft structure has a significant impact on spacecraft configuration and total mass. Study of current PC designs indicates that past development has centered on the electrical design and integration of the units into the solar-electric thrust subsystem. Several structural design deficiencies were noted in the study and design improvements are recommended. As spacecraft and mission constraints are defined, and prototype designs are

upgraded to flight hardware, it is important that increased emphasis be placed on the structural integration of the PC with the spacecraft.

e. Cabling

Cabling arrangement for the HAC flatpack design presented several problems. These include:

- (1) Wire lengths to chassis ground connections were excessive.
- (2) High voltage cable separation was inadequate.
- (3) The electrical interface terminals were placed on the radiating surface, thus exposing the connections and wiring directly to space.
- (4) The module-mounting technique prevented the use of hard-mounted, plug-in connectors.
- (5) Wire routing did not utilize optimum path-determination techniques.
- (6) Cabling support and routing bracketing were not designed concurrently with structure and, thus, resulted in weight penalties.
- (7) Inadequate EMI protection was provided.
- (8) The internal connectors used did not provide EMI shielding.
- (9) Because of the use of terminals, many conductors were not 100% insulated.
- (10) Location of power input/output connections were not related to the configuration constraints for PC mounting on the spacecraft and thus resulted in longer power flow paths and, hence, potentially higher power losses.

While a detailed review of the PC harness connection requirements has not been performed, it is apparent that wire runs will be inherently shorter by the use of a central harness with inputs from the power

subsystem located on the PC structure at one end and the outputs to the thrusters at the other end. Connection of the modules can be accomplished by connectors mounted within a few centimeters of either side of the central wiring runs. Separation of signals can be readily accomplished by mounting cables on opposite sides of the central cable support. Such cables can be readily fabricated on standard tooling and would be interchangeable from PC to PC. Appropriate grounding, shielding and twisting of conductors, and adequate cable separation will result in reduction of EMI.

From a high voltage protection standpoint, it is desirable to separate high from low voltage outputs. This separation can be accomplished by the use of two output connectors; one, a 5000-V rated connector for the high voltages, and the other, a standard 14-19 connector for the low voltages. The 14-19 connector uses the center contact for the -1000-V, 5-spacer contacts around the center for voltage-stress gradient reduction and uses the outer ring for low voltage outputs. In general, high voltage design should conform to JPL Specification DM 505139.*

f. Design Analyses

1) Thermal Analysis. A mathematical analog of the thermal characteristics of the PC compartment was formulated for the purpose of determining certain design parameters, e.g., required shearplate area, and for subsequent prediction of thermal performance. Figure III-A-6 shows the PC assembly and parameters used in this analysis. The model assumes that (a) there is no direct solar incidence on any louvered surface, (b) the super-insulated compartment walls are adiabatic, (c) conductive coupling between PCs is negligible, (d) the louvered shearplates are externally irradiated only by the solar arrays, and (e) solar array temperature is independent of the PC-compartment temperature level or distribution. Described mathematically, the model used is a system of seven non-linear equations. These equations, in fact, merely represent heat balances on each of the six PCs (nodes 1 through 6) and on the interior adiabatic walls (represented as node 7).

* JPL internal document.

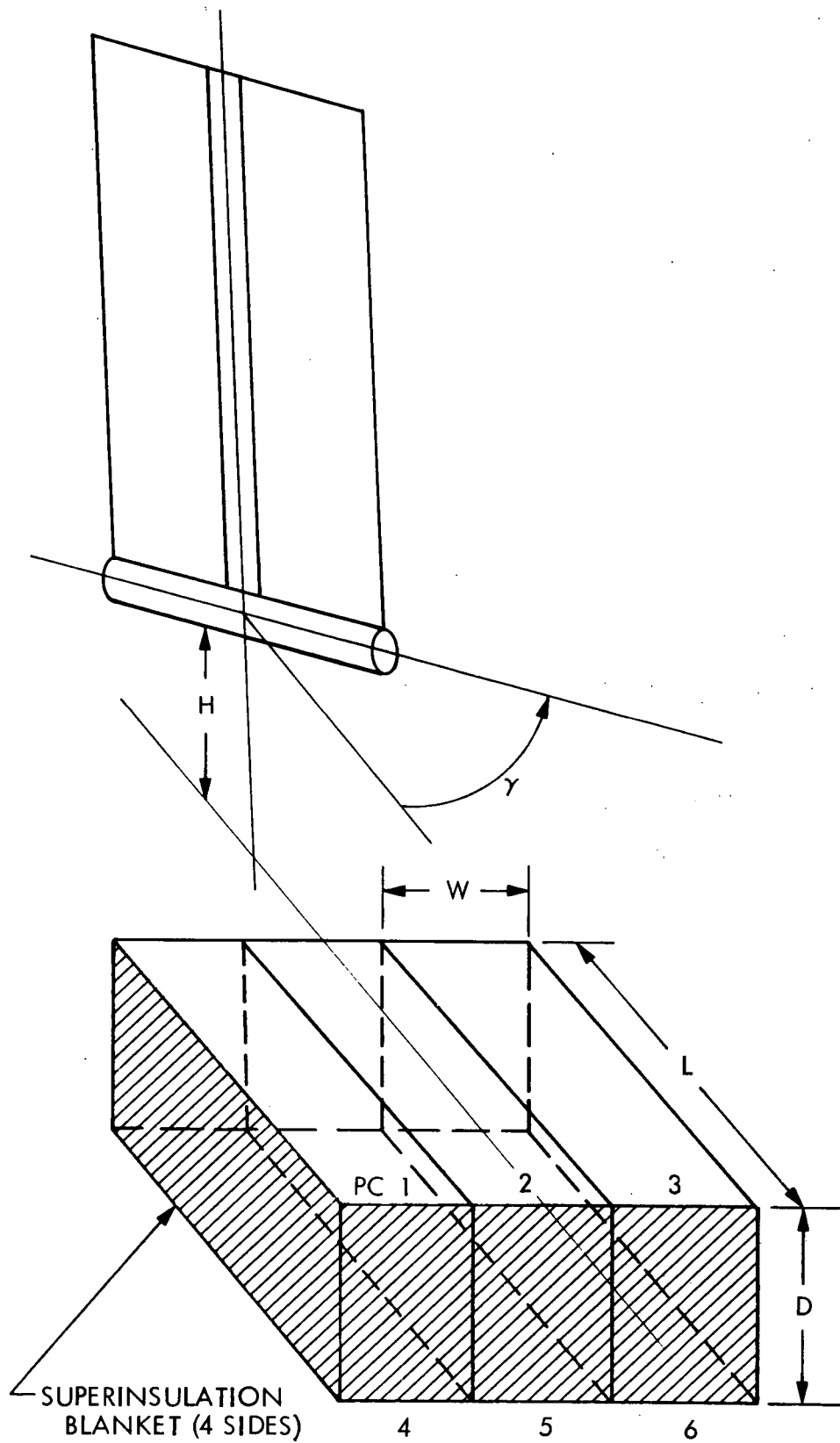


Fig. III-A-6. Thermal Analysis Model of PC Assembly

For nodes $i = 1, 2, \dots, 6$,

$$\sigma A_i \hat{\epsilon}_L (T_i) T_i^4 = P_i + \sum_{j=1}^7 \sigma A_i \mathfrak{F}_{i,j} (T_j^4 - T_i^4) + \sigma A_i \mathfrak{F}_{i,s} T_s^4 \quad (1)$$

and for node 7,

$$0 = \sum_{j=1}^7 \sigma A_7 \mathfrak{F}_{7,j} (T_j^4 - T_7^4)$$

where

A = shear plate surface area or area of adiabatic wall

$\hat{\epsilon}_L$ = effective emittance of louvered shear plate

\mathfrak{F} = Hottel radiation exchange factor

P = PC power dissipation

T = absolute temperature

σ = Stefan-Boltzmann constant

and subscripts i , j , and s denote node i , node j , and solar array, respectively.

The effective emittance of the area actually controlled by the louvers ϵ_L and the effective emittance of the louvered shearplate $\hat{\epsilon}_L$ are related by

$$\hat{\epsilon}_L (T_i) = f \epsilon_L [\beta(T_i)] + (1-f) \epsilon_b$$

where f is the fraction of area A_i controlled by the louvers, assumed here to be 0.8, and ϵ_b , the effective emittance of the border area, i.e., the non-controlled fraction of A_i , is taken to be about 0.1. As the form of the term $\epsilon_L [\beta(T_i)]$ suggests, ϵ_L is a function of the louver blade angle, β , which, in

turn, depends upon the shearplate temperature for fully closed louver blades T_{fc} and the control range $\Delta T_c = 15^\circ\text{C}$ are parameters in the equation for the blade angle

$$\beta = \begin{cases} 0 & T_i \leq T_{fc} \\ \frac{\pi}{2} \left(\frac{T_i - T_{fc}}{\Delta T_c} \right) & T_{fc} < T_i < T_{fc} + \Delta T_c \\ \frac{\pi}{2} & T_i \geq T_{fc} + \Delta T_c \end{cases}$$

where β is expressed in radians. Based on Mariner louver performance, a conservative model of ϵ_L versus β was constructed. This led to the relationship:

$$\epsilon_L = \begin{cases} .12 & \beta = 0 \\ \phi(\beta) & 0 < \beta < \frac{\pi}{2} \\ .76 & \beta = \frac{\pi}{2} \end{cases}$$

The function ϕ is the second degree polynomial which fits the points

$$\epsilon_L(0) = .12, \epsilon_L\left(\frac{\pi}{4}\right) = .53, \text{ and } \epsilon_L\left(\frac{\pi}{2}\right) = .76.$$

Hottel's radiation exchange factors $\mathfrak{F}_{i,j}$ for the surfaces interior to the PC compartment can be expressed in matrix notation as

$$[\mathfrak{F}_{i,j}] = [(\delta_{i,j} - \rho_j \mathfrak{F}_{j,i})/\epsilon_j]^{-1} [\epsilon_j A_j F_{j,i}]$$

where $\delta_{i,j}$ = Kronecker delta

$F_{j,i}$ = form factor from node j to i

ϵ_j = emittance of interior compartment node j

and ρ_j = reflectance of interior compartment node $j = 1 - \epsilon_j$.

Since strong radiation interchange within the PC compartment is desirable, it was assumed that $\epsilon_i = .87$, $i = 1, 2, \dots, 7$ corresponding to Cat-A-Lac flat black paint, a well-known thermal control coating. In reference to Fig. III-A-6, $A_i = WL$, $i = 1, 2, \dots, 6$ and $A_7 = 2D(3W + L)$. The elements $F_{i,j}$ of the form factor matrix were computed using a combination of form factor algebra and the equation for configuration A-1 of NACA TN-2836, (Ref. III-A-4), which gives an analytical expression for the form factor between directly opposed, parallel rectangles as a function of L/D and W/D .

A conservative estimate of $\mathcal{F}_{i,s}$ was used, which neglects inter reflection and assumes fully open louvers. That is,

$$\mathcal{F}_{i,s} = (\max \hat{\epsilon}_L) \epsilon_s F_{i,s}$$

where

$$\max \hat{\epsilon}_L = 0.8(0.76) + 0.2(0.1) = 0.628$$

and $\epsilon_s = 0.78$, assuming an array with 2 Ω -cm cells with blue filters (Ref. III-A-5).

Because of the complex geometry involved, no attempt was made to determine $F_{i,s}$ by an exact method. JPL's version of VUFACT (one of the NASA-MSFC LOHARP programs), which utilizes a numerical integration algorithm, was used instead. A range of $F_{i,s}$ was computed for various values of the solar array drum/thrust beam angle, γ , and the array drum height, H . Both γ and H are illustrated in Fig. III-A-6. The term $\sigma \mathcal{F}_i T_s^4$, the heat absorbed by PC_i per unit area, is tabulated in Table III-A-3 as a function of H and γ , and for $T_s = 323$ K (50°C) and 413 K (140°C). These are the solar array temperatures expected just beyond Encke rendezvous (1 AU) and at perihelion, respectively.

Equations (1) were solved for T_i ($i = 1, 2, \dots, 7$) with the aid of a digital computer by means of an iterative technique. Some of

Table III-A-3. Solar Array Heat Load on PCs

H, m	γ , deg	$\sigma \mathcal{F}_{i,s} T_s^4$, W/m ²					
		$T_s = 323 \text{ K } (50^\circ\text{C})$			$T_s = 413 \text{ K } (140^\circ\text{C})$		
		i = 1 or 4	2 or 5	3 or 6	1 or 4	2 or 5	3 or 6
.6	0	70.4	54.6	70.4	188.2	145.7	188.2
.6	30	84.9	77.4	58.6	226.8	206.7	156.4
.6	60	84.9	85.7	79.7	226.8	228.9	212.8
.6	90	84.3	85.8	84.3	225.2	229.3	225.2
.9	0	51.5	36.9	51.5	137.6	98.6	137.6
.9	30	71.2	58.3	40.9	190.2	155.8	109.3
.9	60	74.3	71.5	63.8	198.6	191.1	170.5
.9	90	71.2	72.6	71.2	190.3	193.9	190.3

the parameters varied were heliocentric distance, total power dissipation of the PC compartment, power distribution within the PC compartment, D, L, γ , H. The results and conclusions of this analysis were discussed in part 3-c of this section.

2) An Analysis of PC/Spacecraft Rigidity Requirements.

To explore PC structure and structural interface requirements, an improved PC configuration was visualized by incorporating the recommended structural modifications into the low-voltage PC design shown in Fig. III-A-5. A finite element dynamic model was made for the general PC configuration and the SEP module structure near the PC. These structures were then sized together to provide minimum weight and minimum PC deflections, as required by the electronic modules and louver assemblies.

To account for the SEP module stiffness at the PC interface, it was necessary to assume a representative SEP module structure. Two structural configurations were considered. They are noted by the left and right side of the composite SEP module/PC bay in Fig. III-A-7. The structural model used to analyze the combined SEP module/PC structure is shown in Fig. III-A-8. The rim of the SEP module/PC bay is included in the model, and its possible attachments to the rest of the SEP module structure are modeled by the 10 pinned-to-ground conditions shown in Fig. III-A-8. All analyses pinned the first six boundary points; some analyses also pinned points 7 and eight; and some pinned all ten. It was assumed that each of the PC members was pinned directly to the spacecraft-bay rim, and the stiffness of the PC rim was neglected. A primary function of the PC rim is to support the internal members during ground handling.

From the analyses, it was determined that the spacecraft weight could be minimized by supporting the PC-bay rim at six points. For this configuration, a parametric study was made to determine the relationship between PC-and SEP-module structural-member parameters versus PC natural frequency. The results of this study are presented in Fig. III-A-9 and 10. Figure III-A-9 describes the first mode natural frequency of the

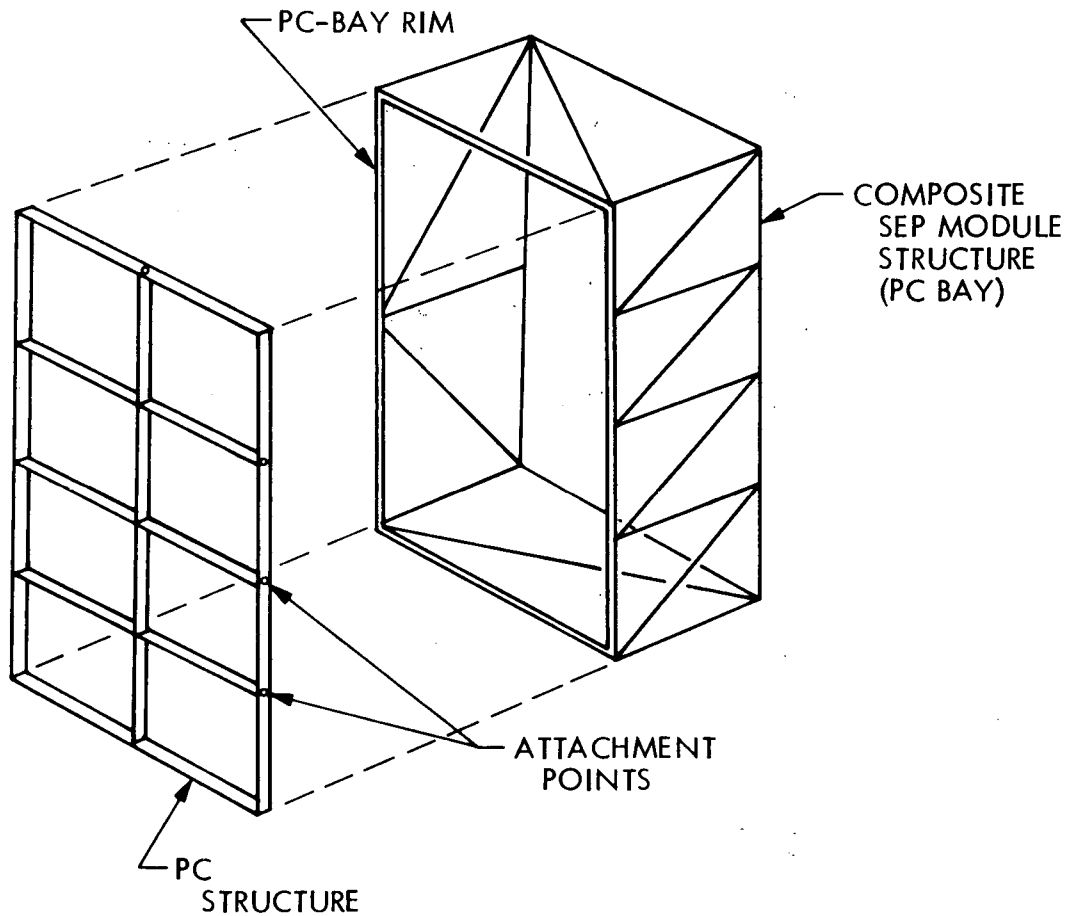


Fig. III-A-7. PC Structural Mounting Concept

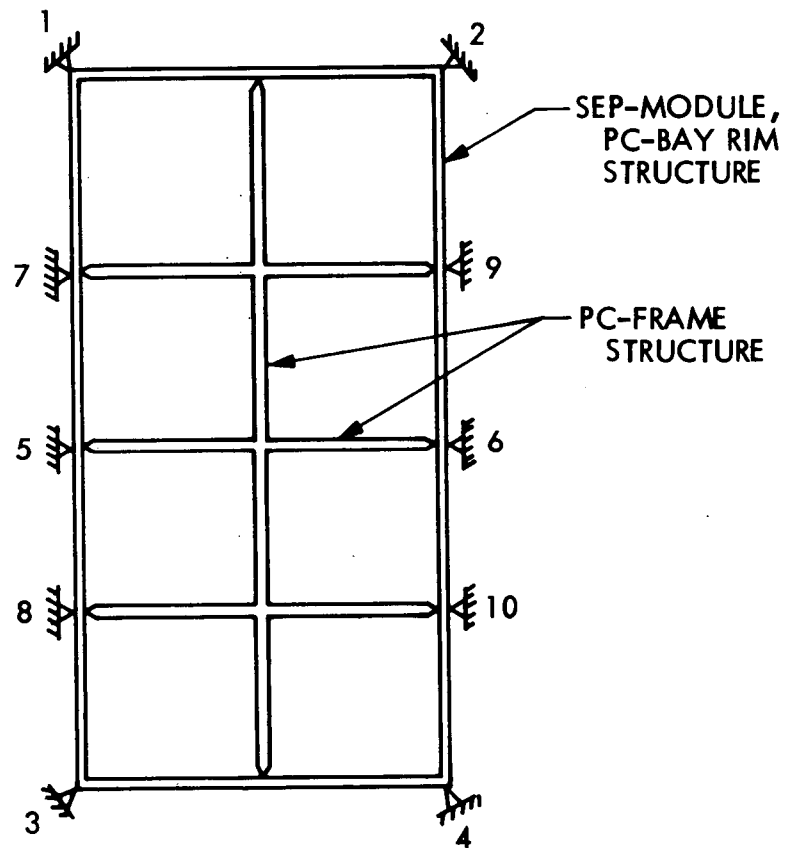


Fig. III-A-8. PC/SEP Structural Model

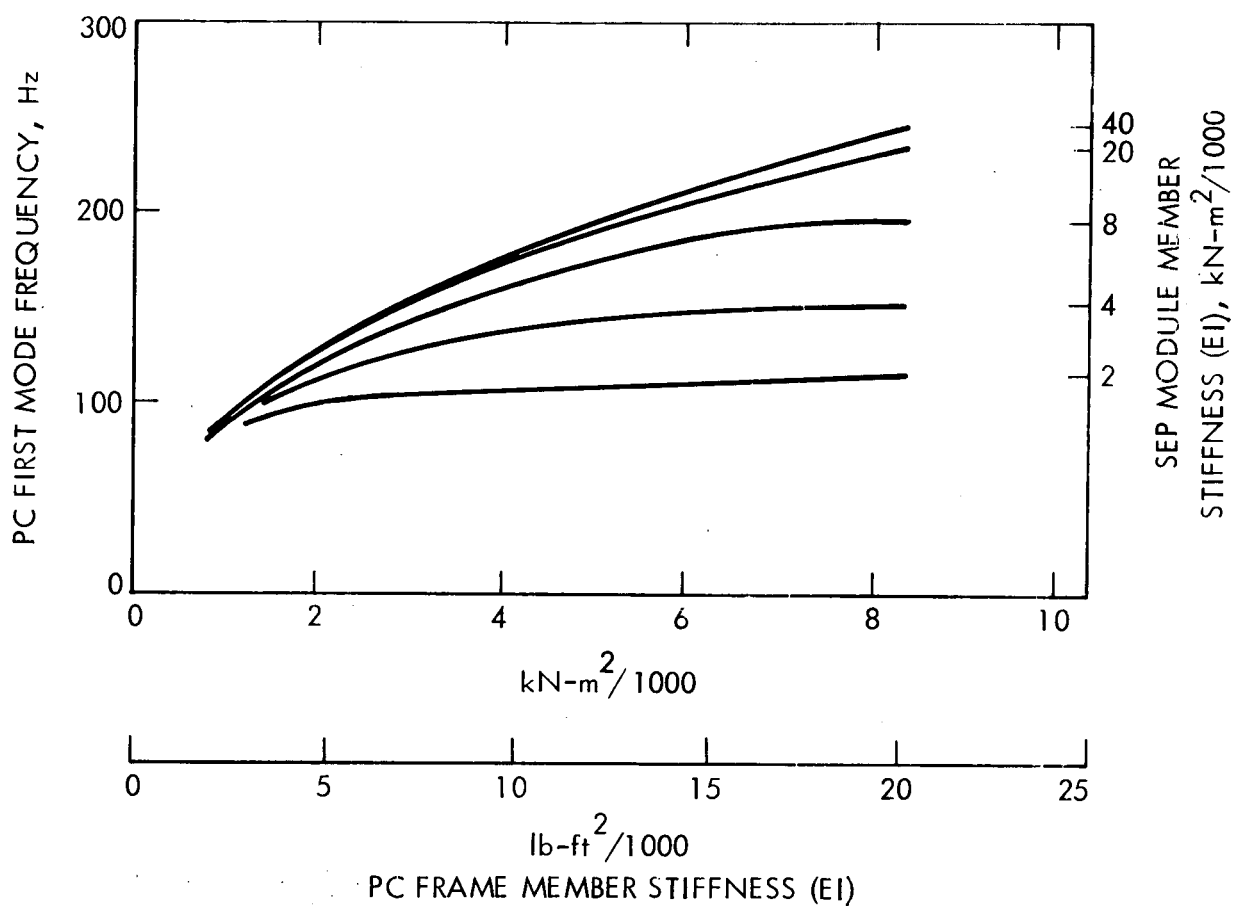


Fig. III-A-9. First Mode Natural Frequency of PC

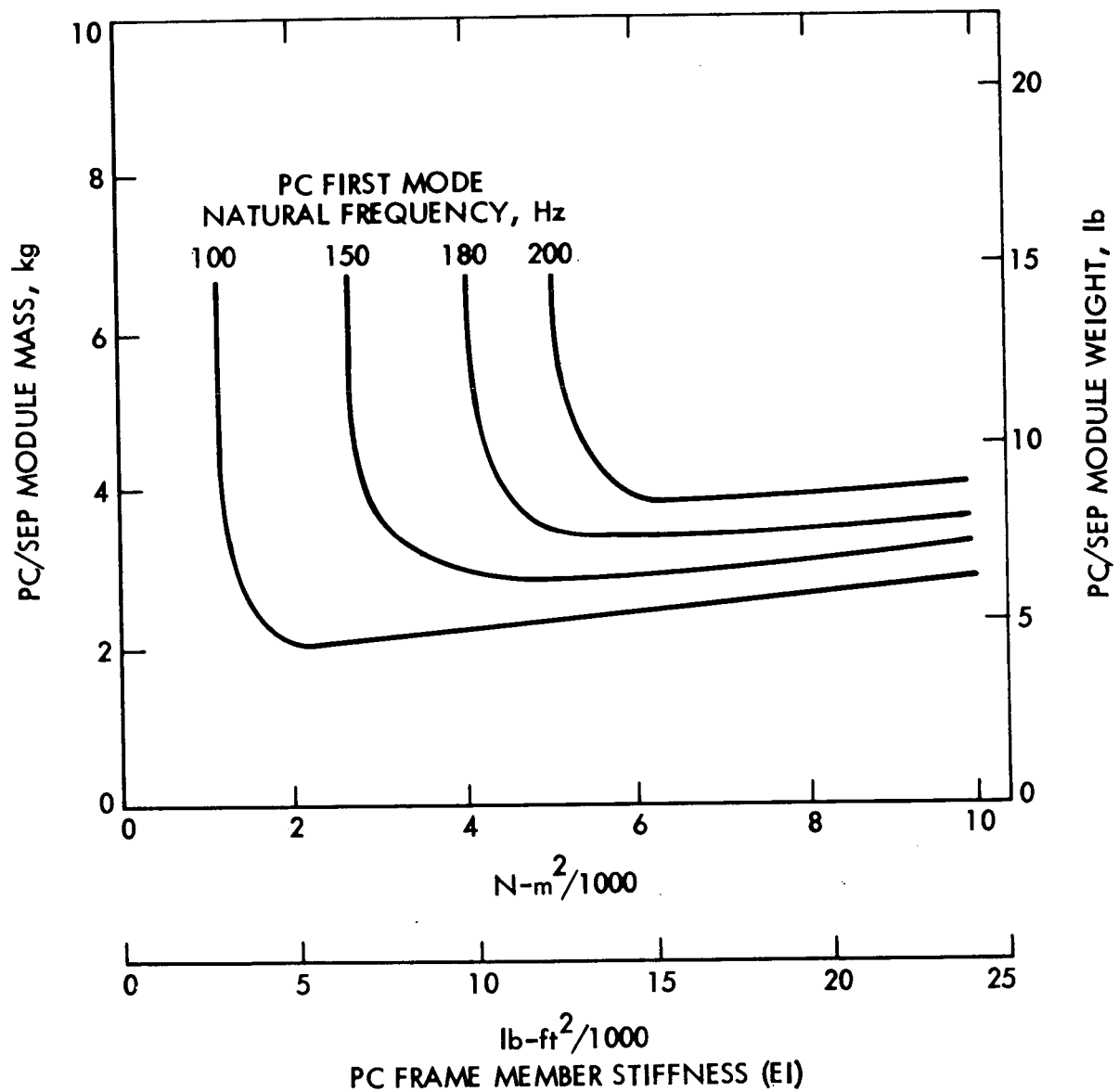


Fig. III-A-10. Combined Structural Mass of PC Frame plus Spacecraft PC-bay Rim

PC/SEP-module combination as a function of the cross-sectional stiffness of the PC-and SEP-bay rim members. The PC members must have a stiffness greater than about 5000 N-m^2 ($12,000 \text{ lb-ft}^2$) to achieve a PC first mode natural frequency greater than 200 Hz.

Figure III-A-10 uses the data in Fig. III-A-9 along with typical weights for frame members to estimate the total weight of the PC structure plus SEP-module bay rim as a function of PC member stiffness and lowest natural frequency. The optimum stiffness of PC structural members for each particular minimum natural frequency is indicated by the lowest weight point on each curve. As indicated in Fig. III-A-10, for a minimum first mode natural frequency of 200 Hz, considerable weight can be saved by increasing the PC frame stiffness from 5000 N-m^2 to about 6000 N-m^2 ($15,000 \text{ lb-ft}^2$). This change increases the weight of the PC structure by 0.1 kg (0.2 lb) but substantially decreases the required stiffness and weight of the SEP module structure.

Although the final structural configuration of the improved PC design is still to be defined, the above described study represents a method for solving the combined PC/SEP-module structural problem and stiffness of required structural members. Similar analyses will have to be conducted, when the final PC configuration is defined, to more accurately estimate the PC/SEP-module structural parameters.

4. Conclusions

A PC concept which employs a modular, integrated electronic-packaging/structure approach is not only feasible but provides significant weight and operational improvements over the SEPST III design. It is apparent that, in addition to being influenced by the electrical requirements of providing voltages, currents, and closed loop control of a thruster, the PC design is strongly influenced by thermal and structural interfaces with the remainder of the space vehicle. Although the preferred design size, which has emerged, is specifically suited to a JPL SEP module for application to Encke rendezvous, the design concept and criteria which it reflects are considered appropriate for all

forseen applications. With this in mind, the following preliminary design requirements for a thruster PC are offered:

- (a) The PC should operate over an input voltage range of 200-400 V using high voltage transistors in the screen power supplies*.
- (b) Output characteristics should be compatible with the LeRC 30-cm thruster.
- (c) Reverse currents should not be imposed on the solar-array bus.
- (d) To allow for maximum solar-array power utilization, the input current ripple should be limited to 1% of peak-to-peak value of the operating current under all conditions including transients.
- (e) The circuit design will provide required voltages and currents within specification for operation at shearplate/radiator temperatures between +75°C and 0°C and will be capable of start-up at -20°C and of surviving in a dormant state at -40°C.
- (f) The power transistor junction temperature shall not exceed 110°C operating at maximum power with a 75°C shearplate/radiator temperature.
- (g) All electrical parts, packaging parts, and materials used in the PC will be properly derated to meet reliability requirements while operating within the specified temperature range.
- (h) Effective EMI protection and suppression techniques should be considered and included in the design.
- (i) Cable routing lengths should be minimized by proper connector placement, application of power-flow concept to module placement, and connector assignments.
- (j) Provisions for cable routing and support will be included in the structural design.
- (k) Input and output connectors should be located to minimize cable lengths within the SEP module.

*The merits of silicon controlled rectifier (SCR) power circuitry should be investigated as more data become available.

- (l) The PC structure will be designed for a minimum resonant frequency of 200 Hz.
- (m) The module shearplate/radiator surface shall carry in-plane shearloads and provide meteorite protection.
- (n) The PC structure will provide a mounting surface and interface attachment for a specified louver assembly to cover at least 80% of the surface area.
- (o) The minimum area for the PC shearplate/radiator surface will be 6451.60 cm^2 (1000 in.^2) and have an integrated surface emittance greater than .85.
- (p) The assembly will be packaged with electronic functional, removable, and replaceable modules. The flatpack planar approach is recommended for high power dissipators, and approved efficient techniques must be used to minimize shearplate/radiator area for low dissipation modules.
- (q) High voltage cabling design shall meet requirements of JPL Specification DM505139.*
- (r) The PC will be installed as a complete assembly with only mechanical fasteners and connector mating required.
- (s) Preliminary analyses indicates that the selected PC should be packaged within a 50.80×139.7 -cm (20×55 -in.) rectangular frame.

*JPL internal document.

REFERENCES

- III-A-1. T. M. Masek, Integration of a Flight Prototype Power Conditioner with a 20-cm Ion Thruster. AAIA Paper No. 71-159, presented in the 9th Aerospace Sciences Meeting January 25-27, 1971.
- III-A-2. H. Kaufman, 30-cm Thruster PC Requirement, Message Number 358 from NASA Headquarters, Washington, D. C., Sept. 21, 1972.
- III-A-3. D. T. Frankos, Electromagnetic Interference status of the SEPST III Power Conditioner for the Solar Electric Propulsion System, JPL Interoffice Memorandum, July 21, 1972 (JPL internal document).
- III-A-4. D. C. Hamilton and W. R. Morgan, Radiant-Interchange Configuration Factors, Purdue University, December 1952.
- III-A-5. Ronald G. Ross, et al, Measured Performance of Silicon Solar Cells Assemblies Designed for Use at High Solar Intensities, JPL Technical Memorandum, TM 33-473, pp. 134, Fig. 141, March 15, 1971.
- III-A-6. J. R. Womack, and J. C. Chen, Structural Evaluations and Dynamic Testing of Solar Electric Propulsion Components, AAIA Paper 72-442, presented at AAIA 9th Electric Propulsion Conference, Bethesda, Maryland, April, 1972.

B. SWITCHING MATRIX TRADEOFF STUDY

This study examines alternate methods of connecting power conditioners (PCs) to thrusters in the context of a 1980 Encke rendezvous mission with an SEP module/Viking spacecraft. The objectives of the study are to (1) select the preferred connection method, and (2) to supply data which would aid in selecting the preferred number of PCs and thrusters for the Encke mission. Probability of mission success and SEP thrust subsystem mass are key factors in the selection process.

A study with objectives similar to this study was performed by the General Dynamics Corporation, Pomona Division, in 1968 (Ref. III-B-1). From this study, it was derived that mission reliability is a function of PC and thruster-failure rates. Both complete and partial switching connections were considered. The study results were not applicable to this study because:

- (1) There were no switching failures; the switches used were assumed to be perfect.
- (2) The attitude-control, thruster-symmetry operational requirements were ignored.
- (3) The thruster wear-out failure mode was ignored (i.e., it was assumed that wear-out did not set in until the mission was completed).
- (4) The mission had a decreasing power profile, quite different from the Encke Rendezvous Mission, which requires that the same number of thrusters be in operation at the end of mission as at the beginning. The study concluded that some form of switching was necessary. Partial switching was favored based on a qualitative estimate of the undesirable intricacies of a complete switching matrix.

1. Alternate Connection Methods

Three methods of connecting PCs to ion thrusters were investigated:

- (1) The hard-wired method.
- (2) The complete switching method.
- (3) The partial switching method.

a. Hard-wired Connection

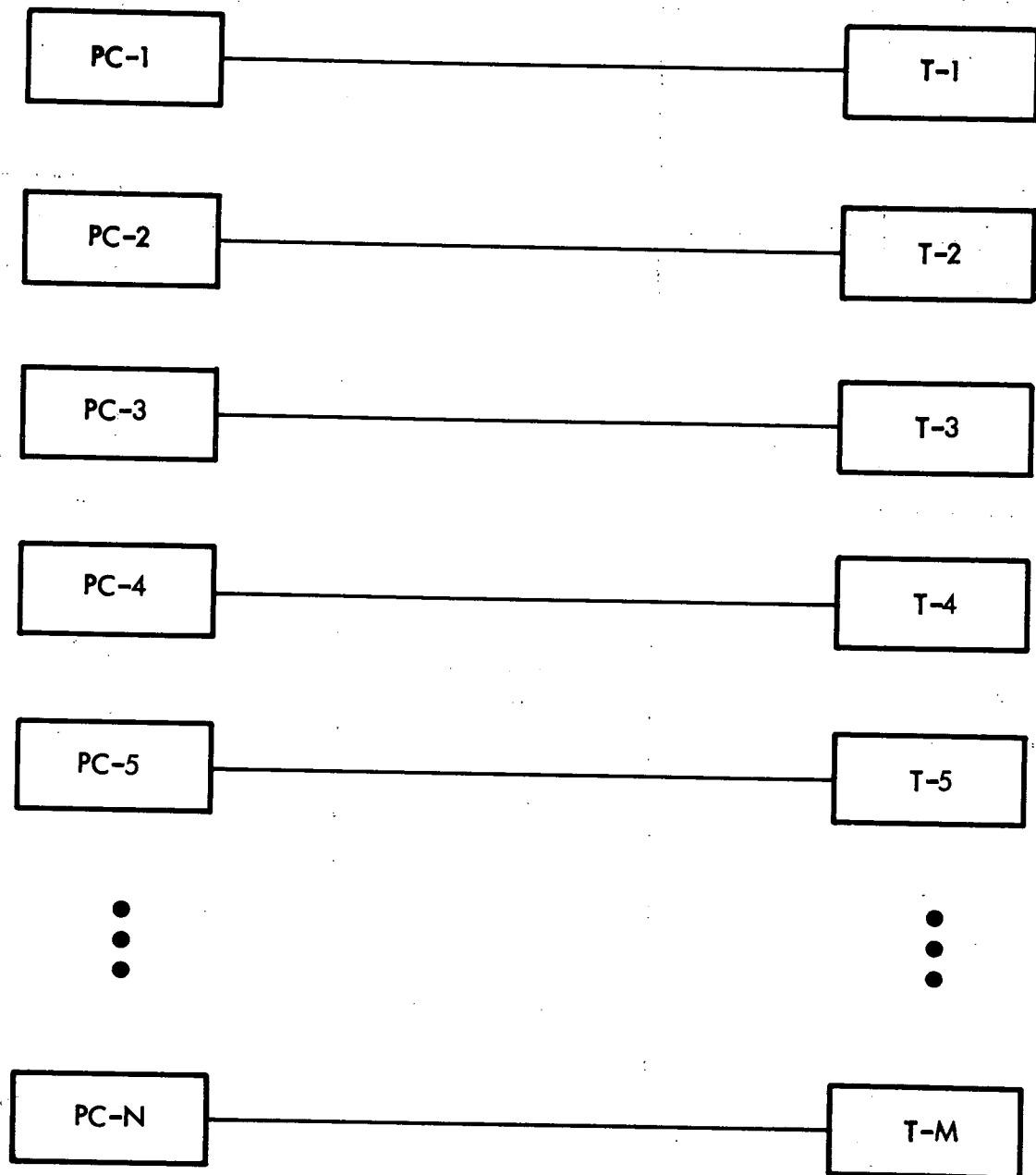
The hard-wired connection of PCs to thrusters is shown schematically in Fig. III-B-1. In this approach, each PC is directly connected to one thruster. Spares are in the form of sets, a PC with its thruster. Some of the characteristics of the hard-wired approach are:

- (1) No switching circuitry exists between a PC and a thruster which can inhibit the operation of either component in case of a switch failure.
- (2) A failure of one of the units of the set, PC or thruster, removes both units.
- (3) Spares must be in the form of sets, a PC and the connecting thruster.

b. Complete Switching

A schematic of the complete switching approach is shown in Fig. III-B-2. The complete switching approach permits the connecting of any PC to any thruster. This is accomplished with a rotary multiposition switch for each PC. A logic circuit is required to ensure the proper connection between a PC and an available thruster.

A switching matrix capable of providing the required connections was developed at JPL (see Ref. III-B-2). It consists of the logic unit, which receives commands from the control computer and drives the switches to the required positions. A schematic of this switching matrix, shown in Fig. III-B-3, illustrates how the input of one PC is switched to any of the five thrusters or dummy load as described in Ref. III-B-2. Some of the characteristics of the complete switching approach are:



PC - POWER CONDITIONER

T - THRUSTER

N - NUMBER OF PCs

M - NUMBER OF Ts

Fig. III-B-1. Hard-wired Connection Approach

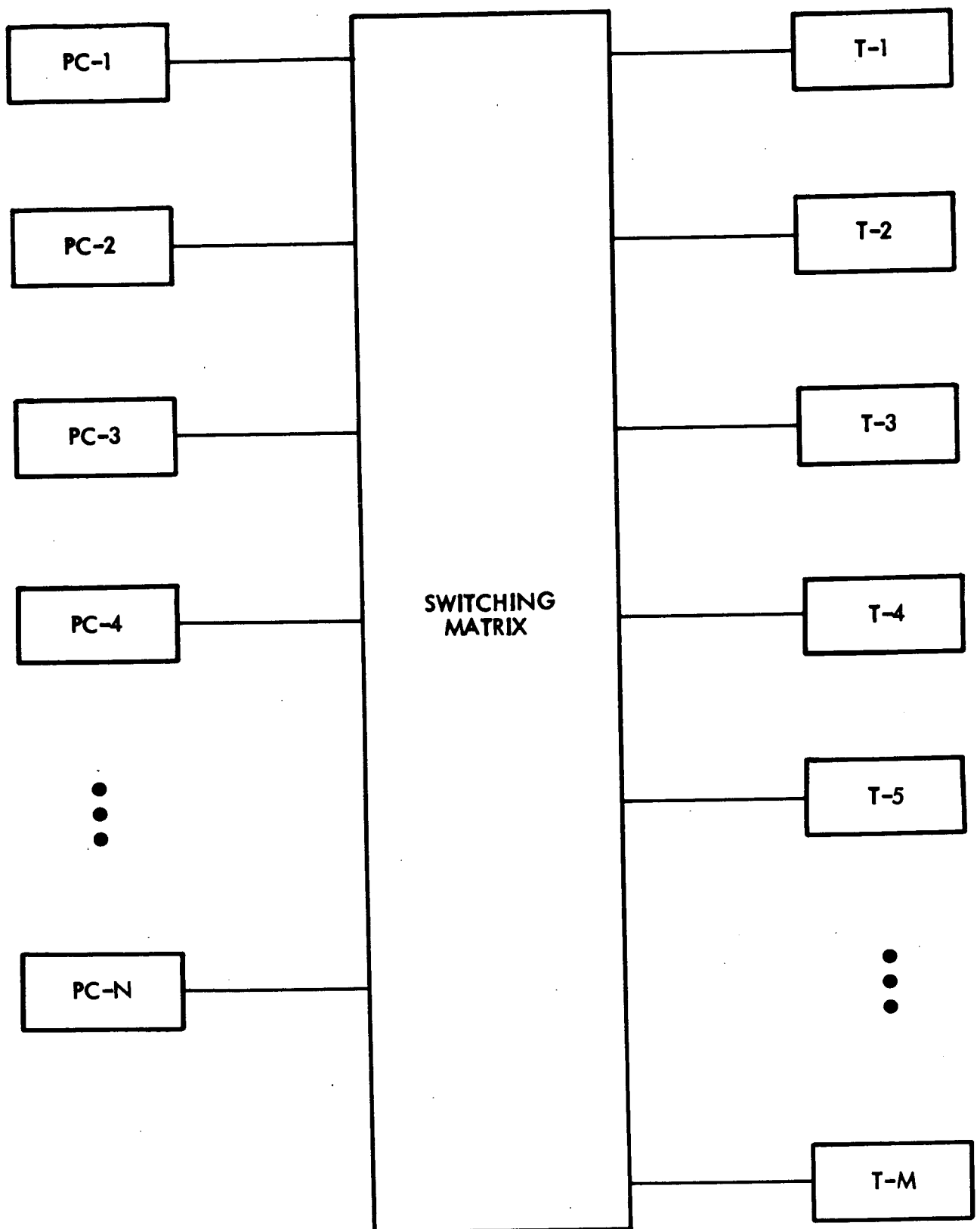


Fig. III-B-2. Complete or Partial Switching Approach

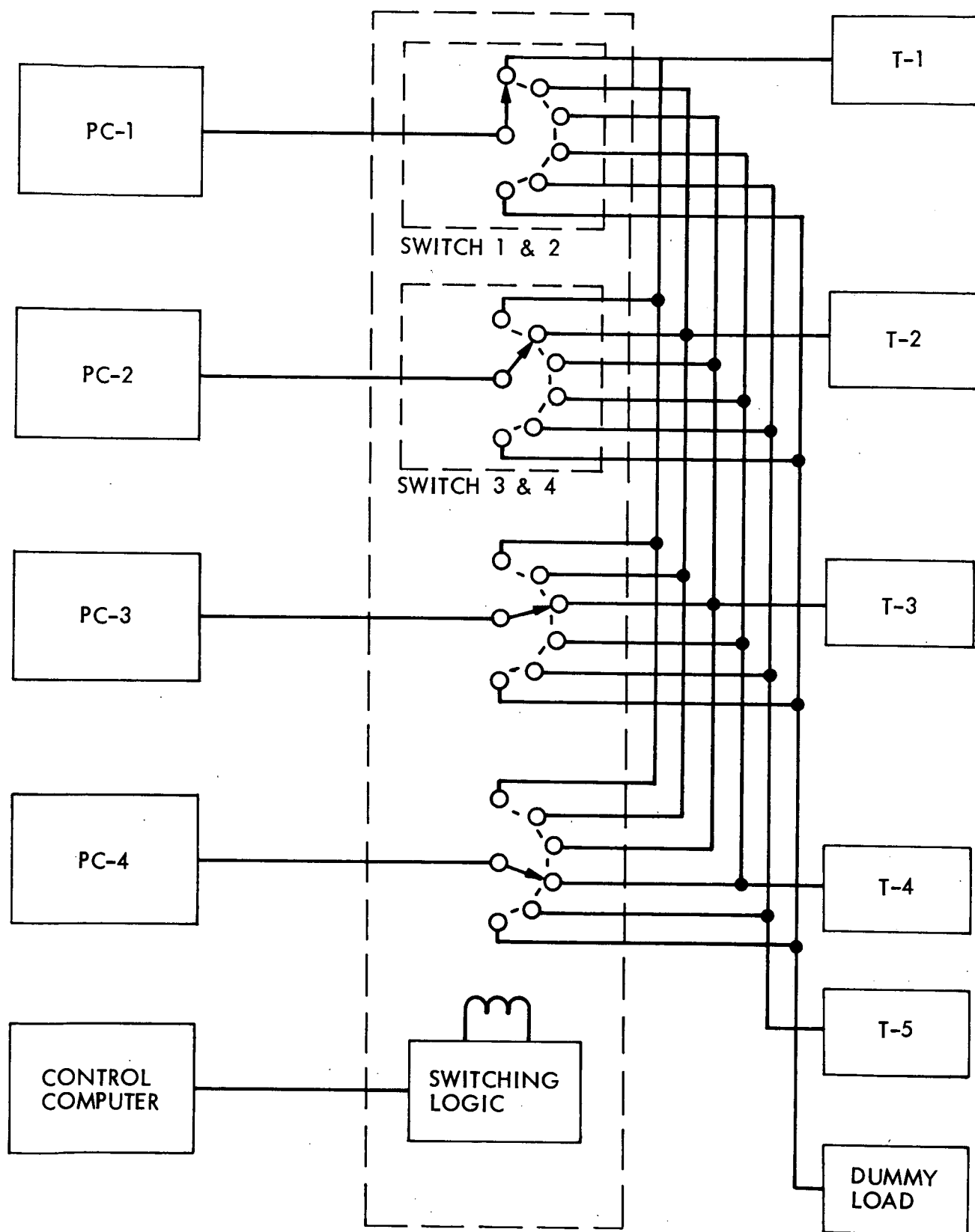


Fig. III-B-3. JPL SEPST III Switching Matrix

- (1) Spares of either PCs or thrusters can be added depending on the probability of the mission success as influenced by the reliability of each component.
- (2) Attitude-control, thruster-symmetry requirements may be satisfied more easily because all thrusters are available even if a PC fails.
- (3) A switch failure is added as a possible failure mode.

c. Partial Switching

The partial switching approach is schematically identical to that shown in Fig. III-B-3. In this approach, only designated spare thrusters are connected to any PC. A switch, which will be used to complete the connection, will have one position more than the number of spare thrusters. With one spare thruster, a two-position switch is required for each PC. One position will connect a PC to its normally assigned thruster; the second position will connect a PC to the spare thruster. The number of positions of the switch will increase as the number of spare thrusters increases.

In the study of partial switching between PCs and thrusters, the following combinations have been examined:

- (1) Five PCs/six thrusters, one spare thruster.
- (2) Five PCs/seven thrusters, two spare thrusters.
- (3) Six PCs/seven thrusters, two spare thrusters and one spare PC.

Some characteristics of the partial switching approach are:

- (1) Thruster symmetry requirements are more difficult to achieve than with the complete switching approach.
- (2) A smaller switch than for the complete approach can be used (two or three positions versus six to seven positions) for the same number of operating thrusters.

2. Encke Rendezvous Mission Requirements

a. Power

The Encke mission requires that the thrust subsystem provide thrust during the entire mission for a trajectory which extends from earth (1.0 AU) to 3.3 AU and which returns to 1.0 AU for rendezvous with the comet. Figure III-B-4 shows the thrust subsystem power profile. At the beginning of the mission, the solar-array power available is sufficient to operate five 30-cm thrusters*. As the solar-array power output decays, throttling of the thrusters (reducing of thrust output) is initiated to remain within the solar array power available. Throttling continues until the solar array power available is sufficient to operate four thrusters at full thrust. At this point, one thruster is shut down and the four-thruster output is readjusted to full thrust. The same approach of thruster throttling and shutdown is employed through the outbound portion of the mission so that the solar power source available will not be exceeded. The reverse process is employed during the inbound portion of the mission.

b. Thrust Vector Control

The thruster arrays considered in this study are shown in Fig. III-B-5. Translation in orthogonal directions within the plane of the array is used for continuous attitude control about two spacecraft axes. Control about the third axis (perpendicular to the array) is achieved by gimbaling opposite thruster pairs. During portions of the mission, when two or more thrusters are operating, an operating opposite pair must be available for third-axis control. Figure III-B-6 shows a typical acceptable arrangement of thrusters for the three arrays examined. All acceptable arrangements are shown in Table III-B-1. Spare thruster availability, in the event of a failure, is governed by these acceptable arrangements.

*Assuming the input to the PCs is 3.1 kW each.

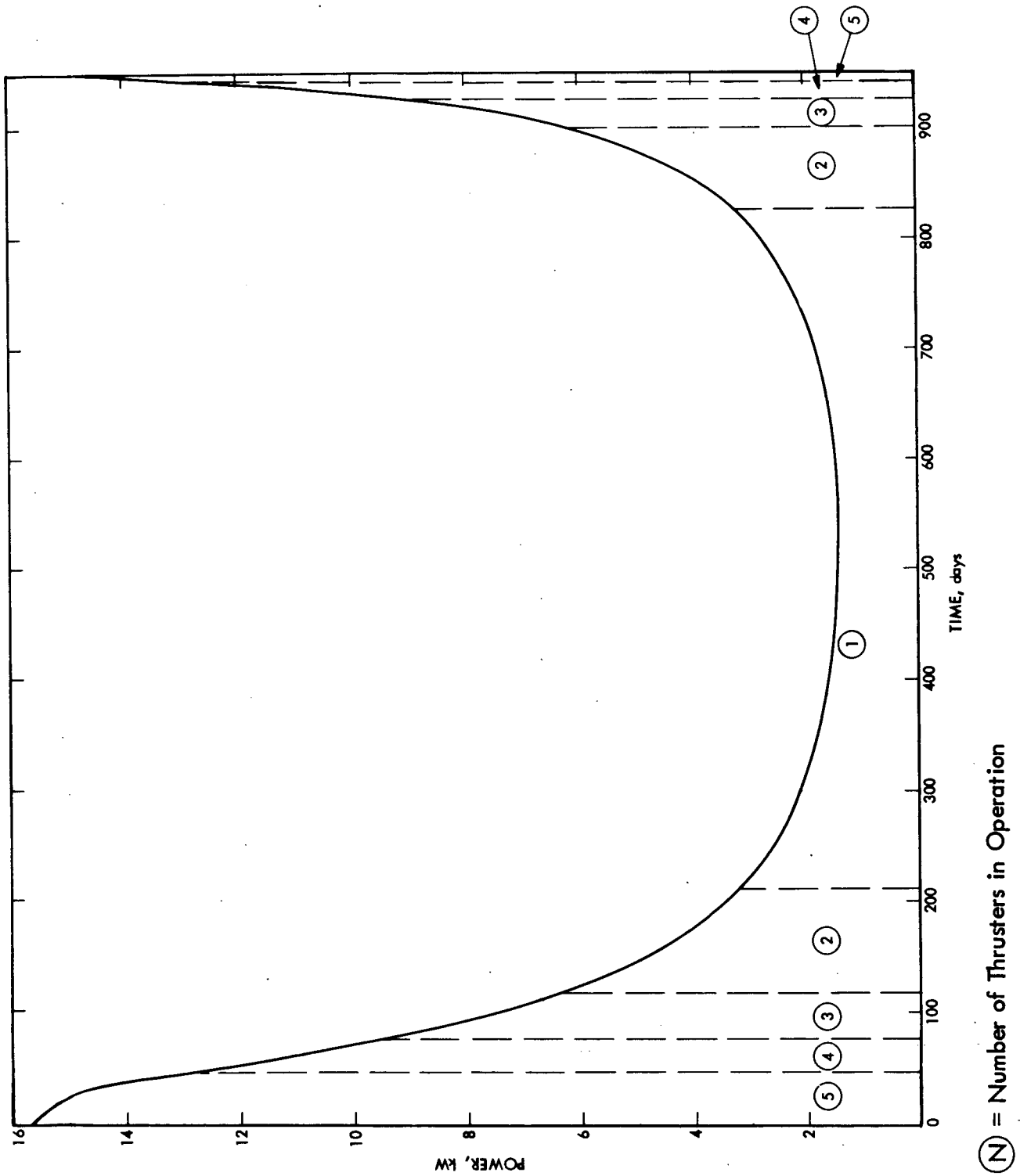
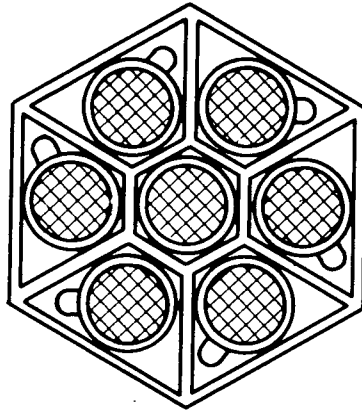
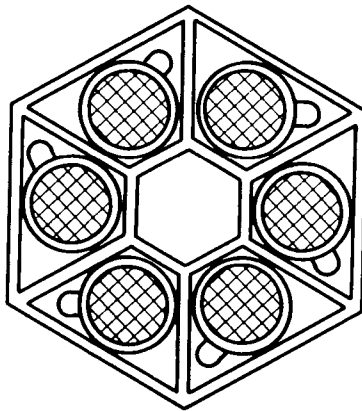


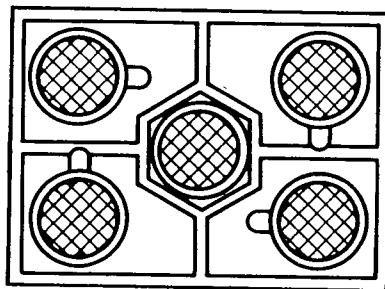
Fig. III-B-4. Thrust Subsystem Power Profile for Encke Mission



a) 7-THRUSTER ARRAY



b) 6-THRUSTER ARRAY



c) 5-THRUSTER ARRAY

Fig. III-B-5. Thruster-Array Configuration

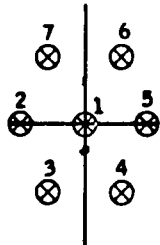
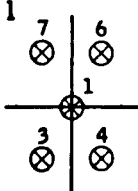
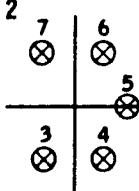
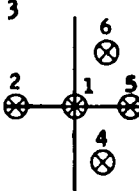
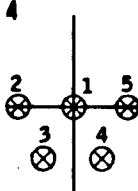
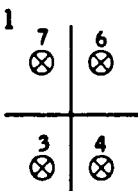
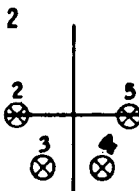
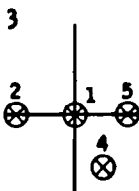
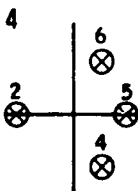
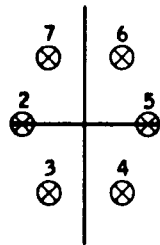
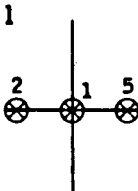
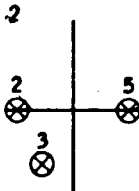
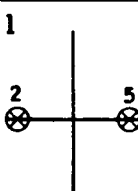
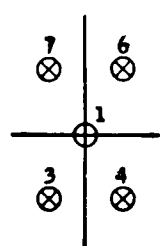
THRUSTER ARRAY CONFIGURATION (SEE FIG. 1)	NUMBER OF THRUSTERS IN OPERATION	ACCEPTABLE ARRANGEMENTS			
7 THRUSTERS 	5 THRUSTERS	1 	2 	3 	4 
	4 THRUSTERS	1 	2 	3 	4 
6 THRUSTERS 	3 THRUSTERS	1 	2 		
	2 THRUSTERS	1 			
5 THRUSTERS 	1 THRUSTER	EVERY THRUSTER, WITH TRANSLATION			

Fig. III-B-6. Typical Acceptable Thruster Arrangements

Table III-B-1. Combinations of Thrusters Which Satisfy the Attitude Control Symmetry Requirements

Number of Thrusters in Operation	5	5	5	5	4	4	4	4	3	3	2
Arrangement	1	2	3	4	1	2	3	4	1	2	1
Acceptable Combinations	1, 3, 4, 6, 7*	3, 4, 5, 6, 7*	1, 2, 4, 5, 6*	1, 2, 3, 4, 5*	3, 4, 6, 7*	2, 3, 4, 5*	1, 2, 4, 5*	2, 4, 5, 6*	1, 2, 5*	2, 3, 5*	2, 5*
	1, 2, 3, 5, 6	2, 3, 4, 5, 6	1, 2, 3, 5, 7	1, 3, 4, 5, 6	2, 3, 5, 6	3, 4, 5, 6	1, 2, 3, 5	2, 3, 4, 6	1, 3, 6	2, 4, 5	3, 6
	1, 3, 4, 6, 7	2, 3, 5, 6, 7	1, 2, 3, 4, 6	1, 4, 5, 6, 7	2, 4, 5, 7	4, 5, 6, 7	1, 3, 4, 6	3, 4, 5, 7	1, 4, 7	3, 5, 6	4, 7
		2, 4, 5, 6, 7	1, 3, 4, 5, 7	1, 2, 5, 6, 7		2, 5, 6, 7	1, 4, 5, 7	3, 5, 6, 7		4, 6, 7	
		2, 3, 4, 6, 7	1, 3, 5, 6, 7	1, 2, 3, 6, 7		2, 3, 6, 7	1, 2, 5, 6	2, 4, 6, 7		2, 5, 7	
		2, 3, 4, 5, 7	1, 2, 4, 6, 7	1, 2, 3, 4, 7		2, 3, 4, 7	1, 3, 6, 7	2, 3, 5, 7		2, 3, 6	
							1, 2, 4, 7			3, 4, 7	
							1, 3, 5, 6			2, 5, 6	
							1, 4, 6, 7			3, 6, 7	
							1, 2, 5, 7			2, 4, 7	
							1, 2, 3, 6			3, 4, 6	
							1, 3, 4, 7			3, 4, 7	

*Shown in Fig. III-B-6.

3. Mission Reliability Analysis

A Monte Carlo analysis with 5000 simulations per data point was selected as the basis for this reliability analysis, because the number of possible thrust subsystem states and failure modes combined preclude an exact analysis. The exact analysis described in Section II-C of this volume was possible because the thrust subsystem was reduced to only one reliability element, i.e., the thruster.

a. Component Failure Rate Data

The failure rates of the components considered in the study have been derived from data and information available from manufacturers, experts in the field, and from JPL component-part failure rates based on previous spacecraft experience. Because the data obtained are only best estimates, all the important failure-rate parameters were varied to some extent to determine their effect on the mission reliability.

1) Thruster. There are two important failure modes with the thruster that need to be considered; one is random failure, and the other is wear-out failure. At present there are insufficient test data to obtain good data for either.

Exact estimates of wear-out life are difficult to obtain. Discussions with an expert at LeRC (Ref. III-B-3) indicated that, by proper grid and cathode design, a 30-cm thruster can be fabricated with a mean wear-out life of at least 14,000 hr and, possibly, up to 20,000 hr. Two thruster wear-out curves were used to temper these estimates with currently planned thruster lifetime goals (see Ref. III-B-4). The curves are shown in Fig. III-B-7. The early wear-out curve shows wear-out starting after about 6000 hr with a mean wear-out life of about 10,000 hr. The late wear-out curve shows wear-out starting after about 8000 hr with a mean life of about 12,000 hr. A random failure rate of $6/10^6$ hr is assumed for these curves. Both curves are more pessimistic than the estimates obtained from LeRC. In this study, thruster wear-out life was considered a parameter, and both curves were used.

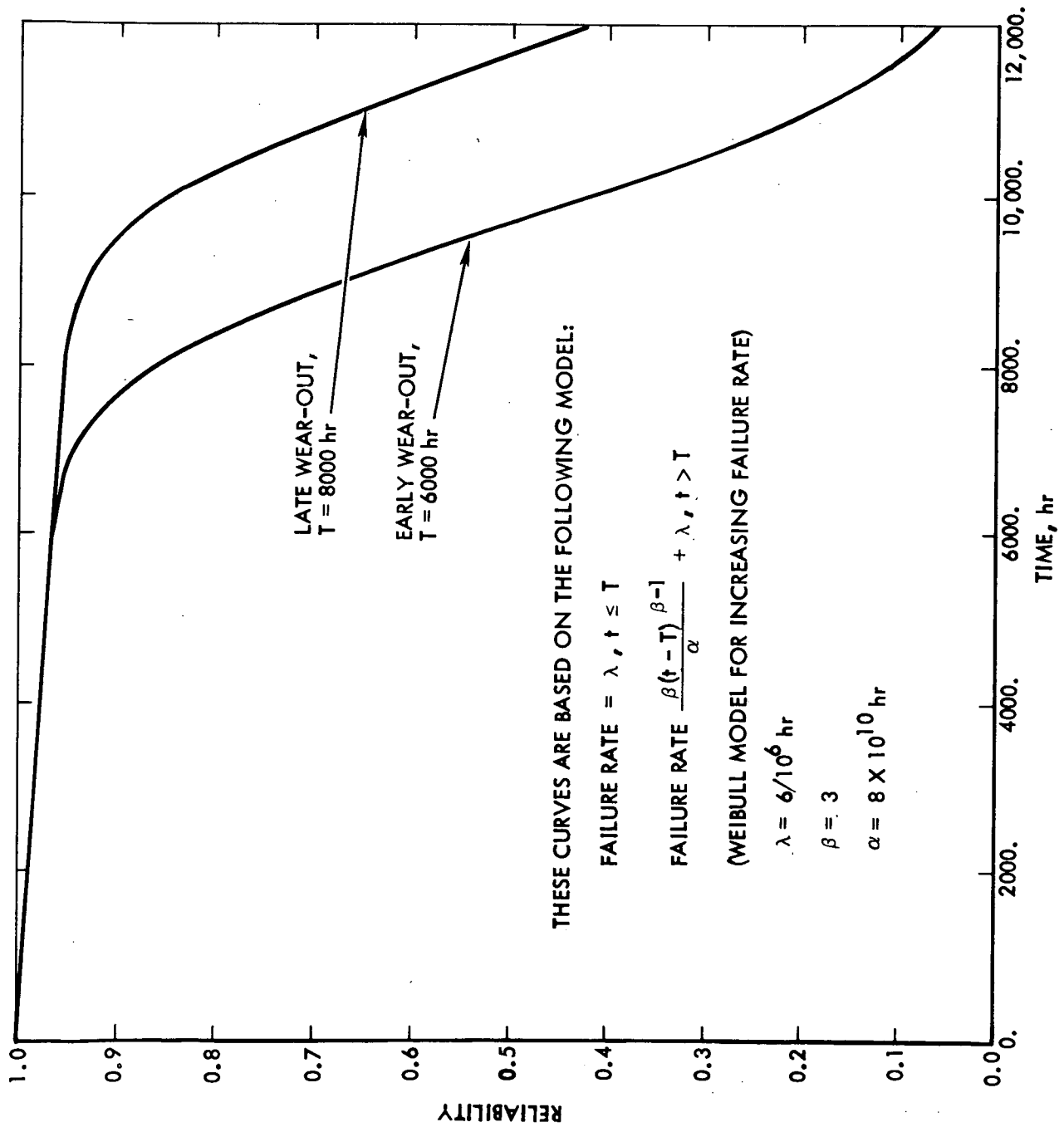


Fig. III-B-7. Thruster Reliability Versus Time

Random failure rate was computed using both the Hughes and TRW thruster reliability models (Refs. III-B-5 and 6). The TRW model is based on a comparison of the thrusters to a traveling wave tube with the similarities in functions and parts noted. The Hughes Aircraft Company model assigns a failure rate on each component of the thruster based on mechanical and electronic parts experience and then adds the results. When the Hughes model was used, the calculated random failure rate was $4.66/10^6$ hr. With the TRW model, the calculated random failure rate was $5.91/10^6$ hr. Although experts at LeRC felt that random failure rate could be ignored, a range of $1/10^6$ hr to $50/10^6$ hr was evaluated for completeness.

2) Power Conditioner. It was assumed that the PCs have random failure modes only. Hughes Aircraft Company, supplier of a prototype PC to JPL, completed a reliability analysis and derived a failure rate of $3.29/10^6$ hr for the unit. Using the Hughes reliability model and applying component failure rates used on some current JPL programs, the PC-failure rate was re-computed as $7.35/10^6$ hr. A failure rate of $5./10^6$ hr was selected for this reliability analysis, a value between the Hughes and the JPL calculations. A PC-failure rate of $10/10^6$ hr was also examined to determine the effect of this parameter on mission reliability. An 0.1-dormancy factor was used for the PCs. In the dormant, or turned-off state, the failure rate for a dormant PC is 0.1 of the failure rate for an active PC.

3) Switch

A switch typical of the type considered in this study is shown in Fig. III-B-8. Because JPL experience with this type of switch is limited, a reliability model of the switch was developed, using information in Ref. III-B-7 as a base, to obtain an estimate of the failure rate. This model produced a failure rate estimated at $20/10^6$ hr for the complete switch. Seven thruster-contact positions were used per switch. Using the same approach, an estimate for the failure rate of the switches for the limited switching method was obtained. For the switch with three positions capable of connecting two spare thrusters to any PC, a failure rate of $11/10^6$ hr was computed. For

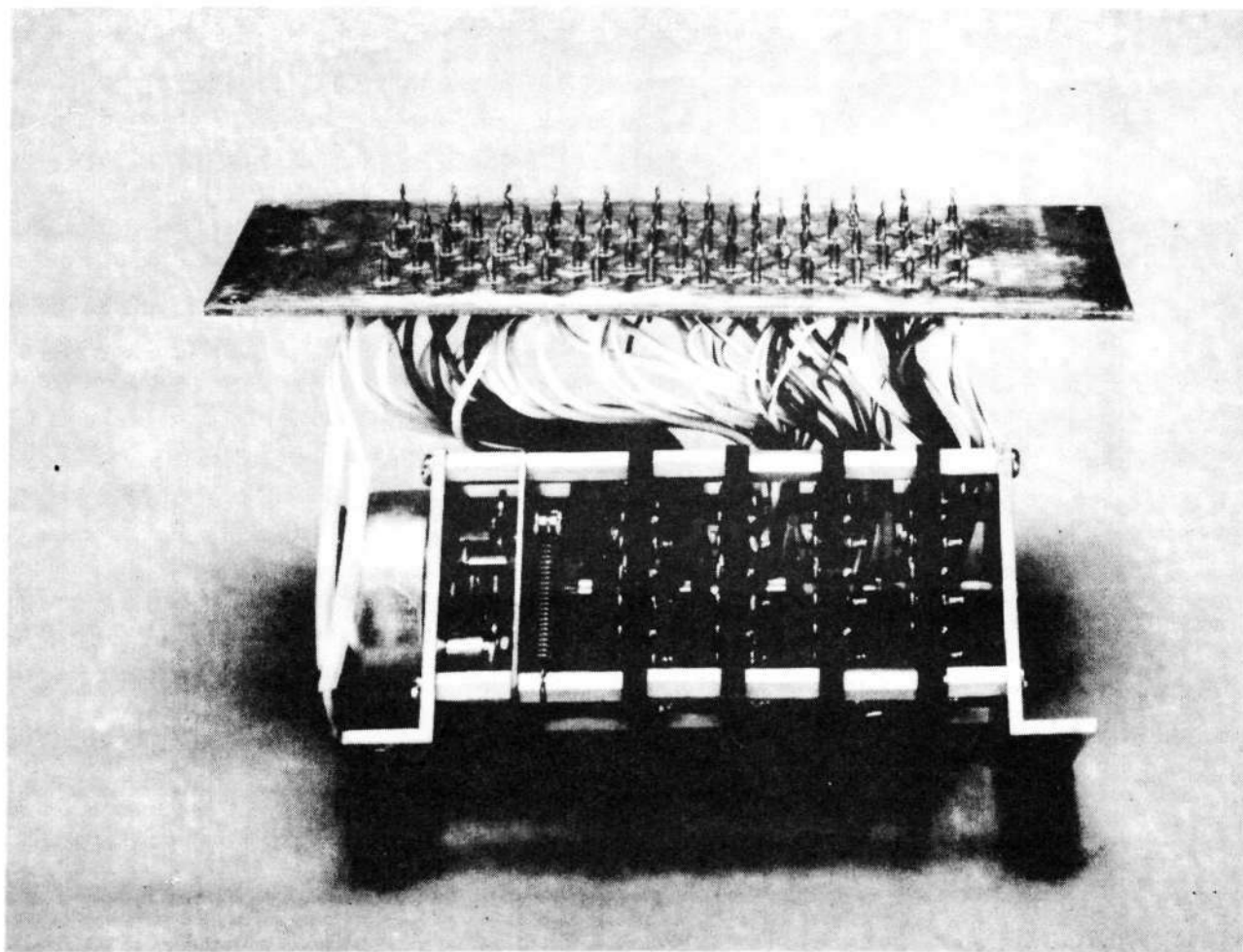


Fig. III-B-8. JPL SEPST III Power Conditioner - Thruster Connecting Switch

the switch with two positions capable of connecting one spare thruster to any PC, a failure rate of $3/10^6$ hr was computed.

Three switch failure modes were considered:

- (a) A "stuck-at" failure, wherein a PC remains connected to a particular thruster and can not be switched to any other thruster. This could occur, for example, if the switch motor failed.
- (b) An "open" failure, wherein a contact to one of the thrusters has opened, thus preventing the PC from operating that particular thruster. This could occur because a wire or contact is broken or because a switch terminal is contaminated.
- (c) A "complete" failure, wherein the PC assigned to the switch can not be switched to any thruster; it is totally disabled. This failure mode is equivalent to a PC-failure, and it could occur, for example, if one of the switch wafers should crack.

The probability that any of the above failures can occur is based on test data and previous experience with rotary switches. From the information available, the following conditional probabilities apply:

- (a) "Stuck at" failure, 0.35.
- (b) "Open" failure, 0.5.
- (c) "Complete failure, 0.15.

b. Mission Model

Mission success is defined in Section II-C of this volume.

Two classes of success are:

- 1) Class I. A Class I success is obtained when the spacecraft follows a trajectory which rendezvous with the comet at least 40 days before Encke perihelion.

2) Class II. A Class II success is a slightly degraded success in which rendezvous occurs at least 27 days before Encke perihelion.

In the simulation, the mission was started with the desired parameters and, as failures appeared, continued as long as the degraded operations could be performed. If the degraded operations achieved a Class II success in the simulation, the mission was considered as successful. The mission reliability (mission probability of success) was then obtained by taking the ratio of mission success to the total number of missions simulated.

A thruster operation sequence chart can be drawn from the mission profile (see Fig. III-B-4). Figure III-B-9 shows this chart for a mission with five thrusters available and no failures occurring. In the simulation model, this operational sequence was followed prior to a failure. If a failure occurred, a spare thruster, if available, was switched in and symmetry requirements were checked. Switch and PC-status were also checked to see whether or not PCs were available to drive the thrusters chosen for operation. If the number of operating thrusters per phase called for were not available (either because of failures or a combination of failures and symmetry requirements), then fewer thrusters were operated as long as the conditions of a Class II success were achievable. Table III-B-2 shows the operating thrusters required for a Class II success. If this minimum was not maintained, then that simulation was considered a failure. The mission simulation gives a probability of obtaining at least a Class II success.

Any simulation introduces statistical errors because it is based on random numbers. For this study, 5000 simulations were used for each data point. This number was a compromise between getting as much accuracy as possible while using a reasonable amount of computer time. With this number of simulations, inaccuracy caused by statistical error appears to be reduced to about ± 0.005 (i.e., a reliability of .910 means that .905 and .915 are good bounds on .910).

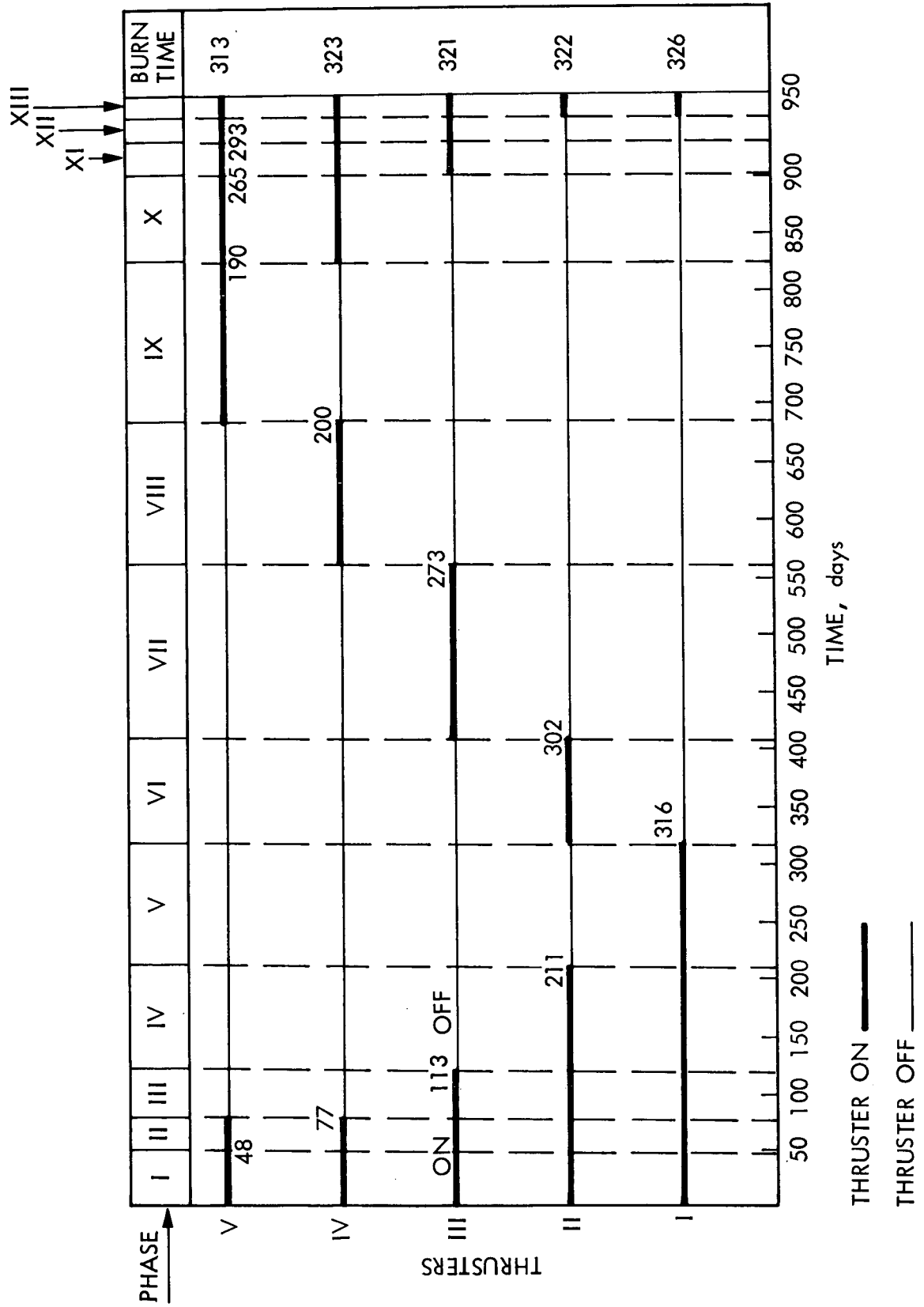


Fig. III-B-9. Thruster Operation Sequence for Near Equal Thruster Burn Time

Table III-B-2. Operating Thrusters Required for Optimum and Degraded (Class II) Missions

Phase Number	Operation Time Per Phase, days	Optimum Number of Thrusters in Operation	Minimum Number of Thrusters in Operation for Class II Success
1	48	5	4
2	29	4	3
3	41	3	3
4	93	2	2
5	105	1	1
6	91	1	1
7	155	1	1
8	123	1	1
9	142	1	1
10	75	2	2
11	28	3	3
12	14	4	3
13	6	5	2

c. Results

Several cases which covered the range of parameters selected for this study were investigated using the Monte Carlo simulation technique. The cases investigated are listed in Table III-B-3, and the results are shown in Figs. III-B-10 through III-B-15.

The following observations can be made from the data presented in Figs. III-B-10 through III-B-15:

- (1) The combination of six PCs connected to seven thrusters by the complete switching method is the most reliable of the combinations studied, regardless of the wear-out and random failures of the thrusters.

Table III-B-3. Monte Carlo Mission Simulation Case Summary

Case Number	Reliability Parameters			Configurations Investigated					
	Thruster Mean Wear-out Life, hr	PC Failure Rate Per 10^6 hr	Switch Failure Rate Per 10^6 hr		Hardwired		Limited Switching		Complete Switching
			Partial	Complete	PCs	Thrusters	PCs	Thrusters	
1	10,000	5.0	3.0*	20.0	5 6 7	5 6 7	5 5 6	6 7 7	5 6 7 7
2	10,000	10.0	3.0* 11.0**	20.0	Same as case 1 except 5-5 hardwired excluded				
3	12,000	5.0	3.0* 11.0**	20.0	4	4 4	4 4	5 6	5
4	10,000	5.0	5.5** 16.0**	10.0 30.0	Plus all case 1 configurations				
5	10,000	5.0	3.0*	—			6	7	
Position of spare thruster in seven-thruster array varied									

* One spare thruster.

**Two spare thrusters.

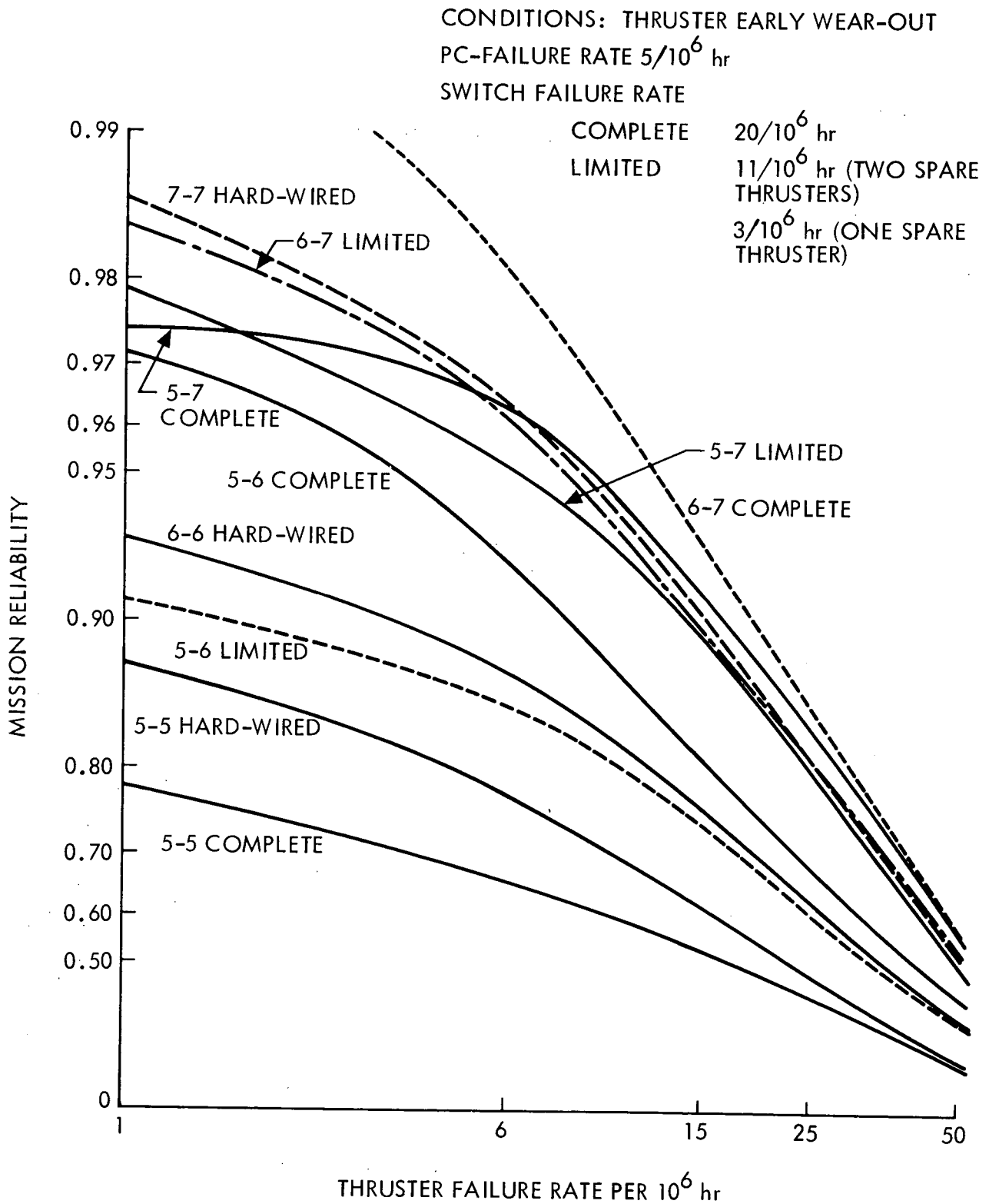


Fig. III-B-10. Encke Comet Mission Reliability Versus Thruster Failure Rate, Monte Carlo Simulation, Case 1

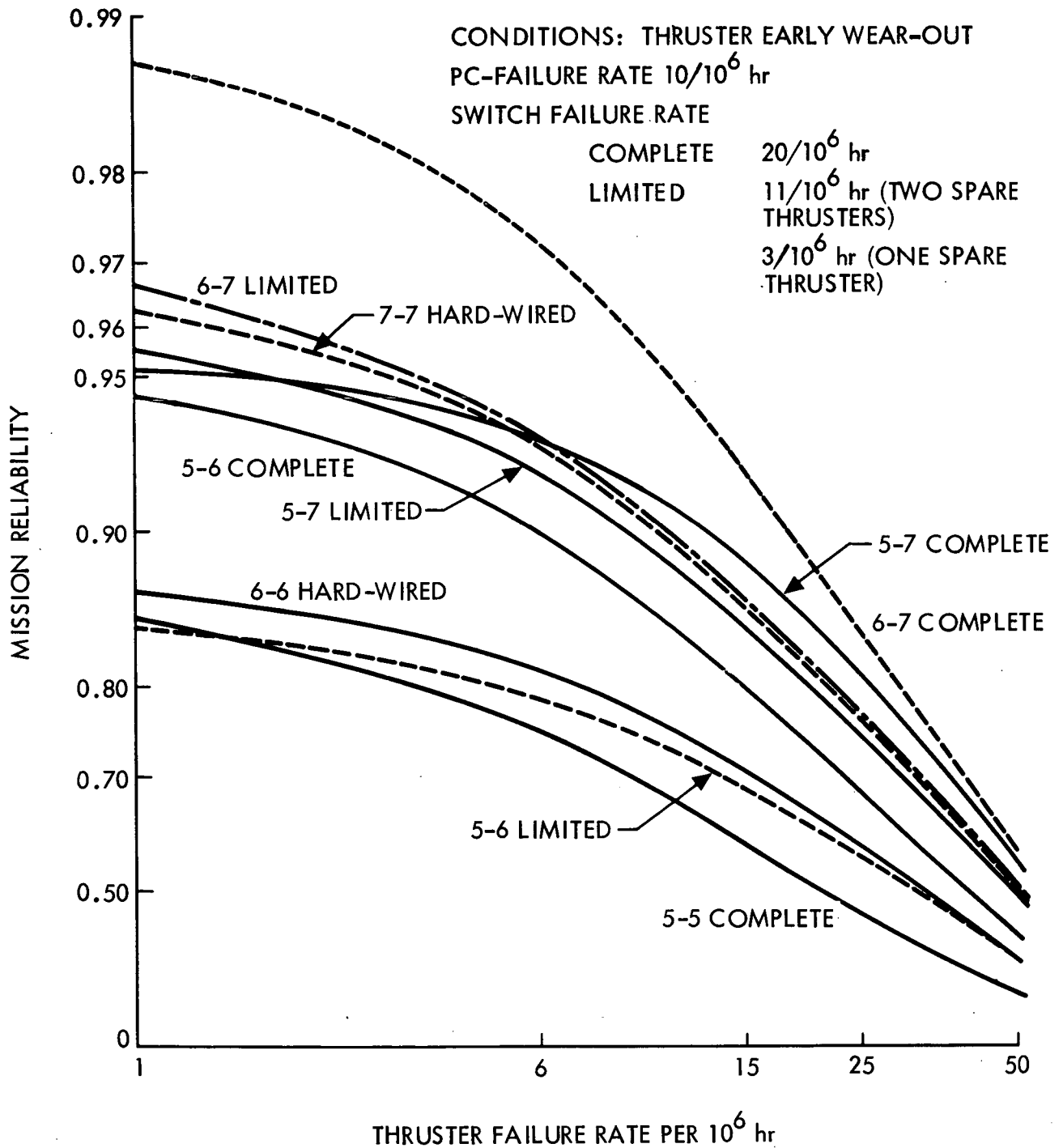


Fig. III-B-11. Encke Comet Mission Reliability Versus Thruster Failure Rate, Monte Carlo Simulation, Case 2

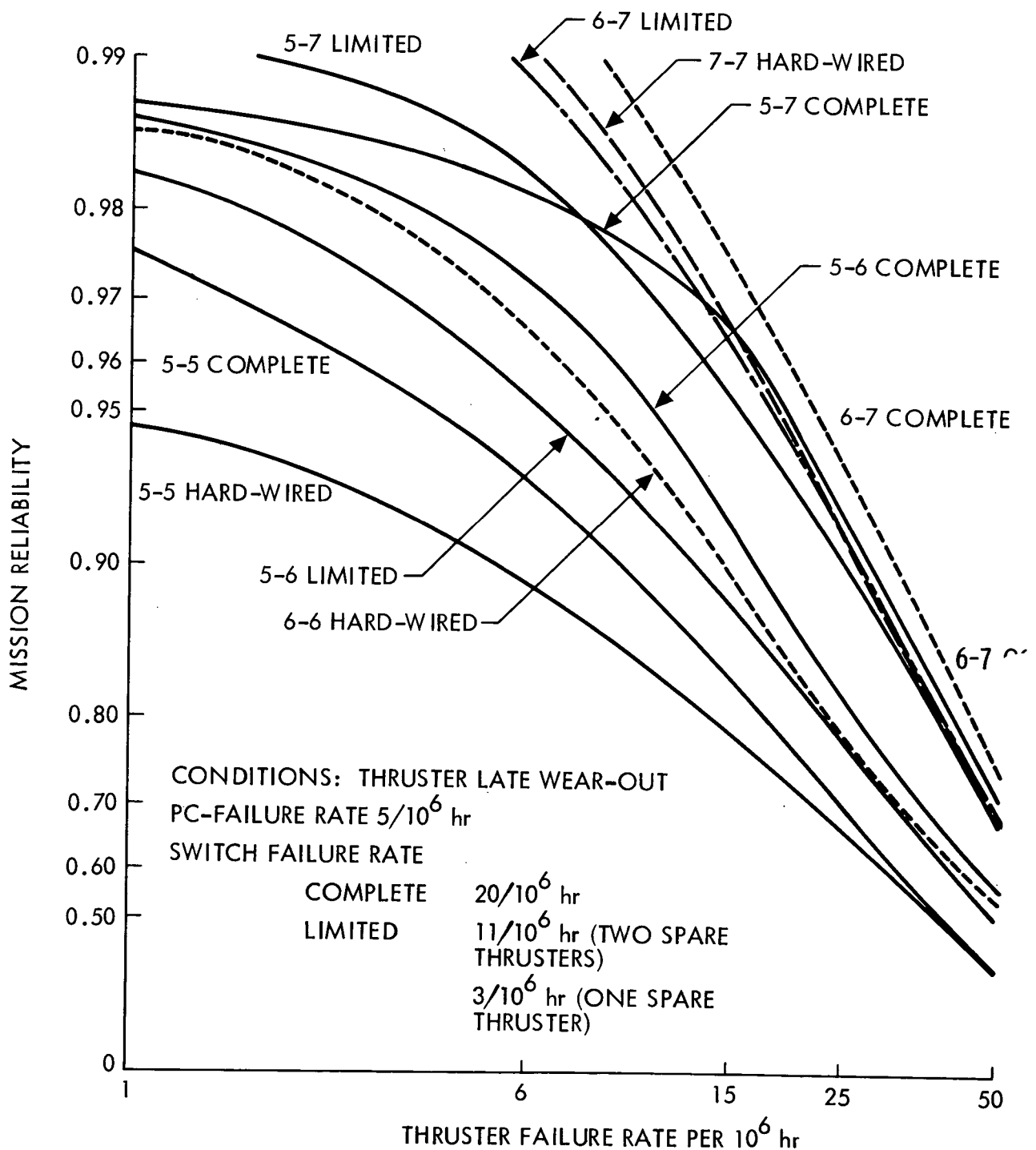


Fig. III-B-12. Encke Comet Mission Reliability Versus Thruster Failure Rate, Monte Carlo Simulation, Case 3

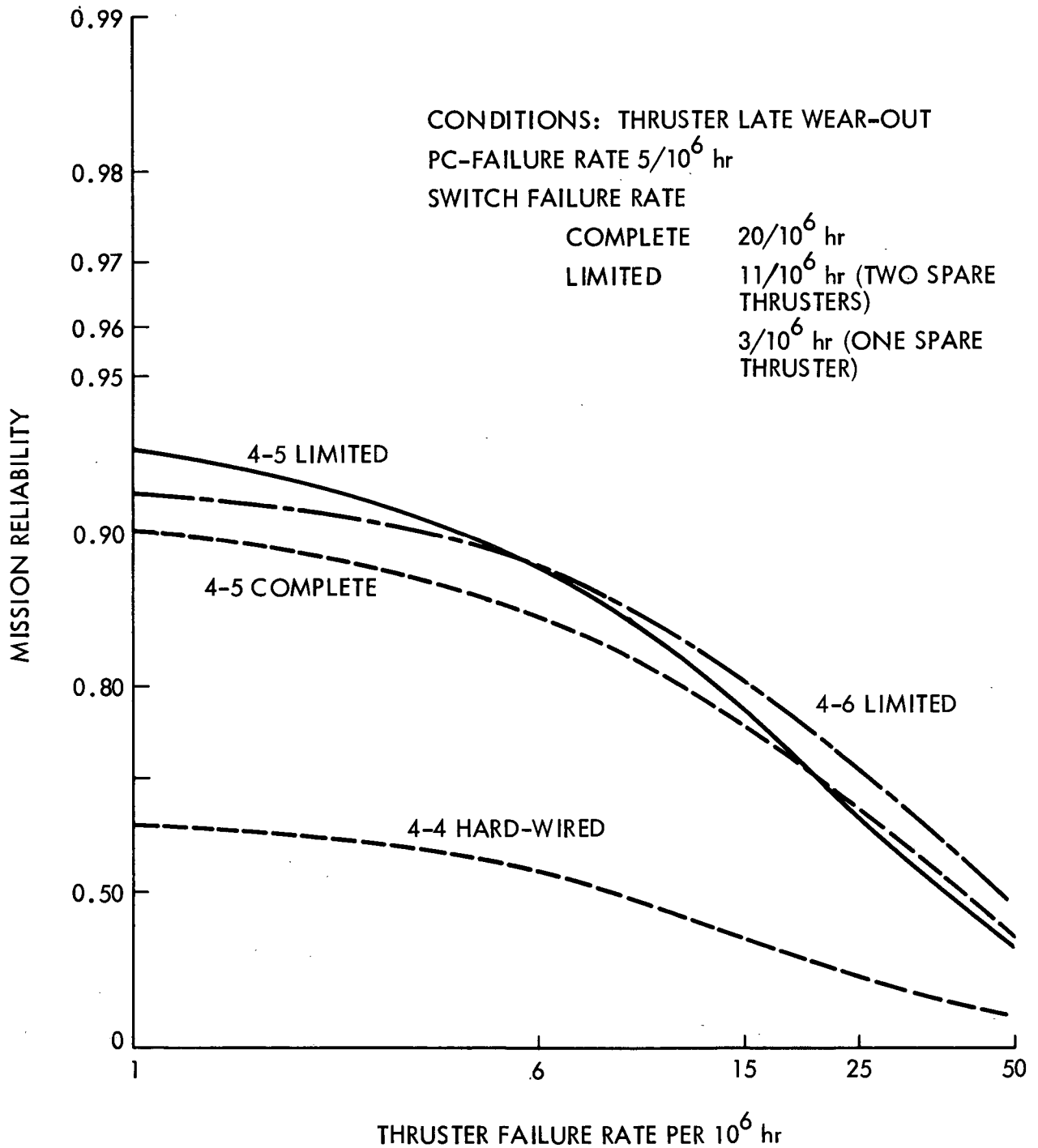


Fig. III-B-13. Encke Comet Mission Reliability Versus Thruster Random Failure Rate, New Thrust Subsystem Configurations, Case 3

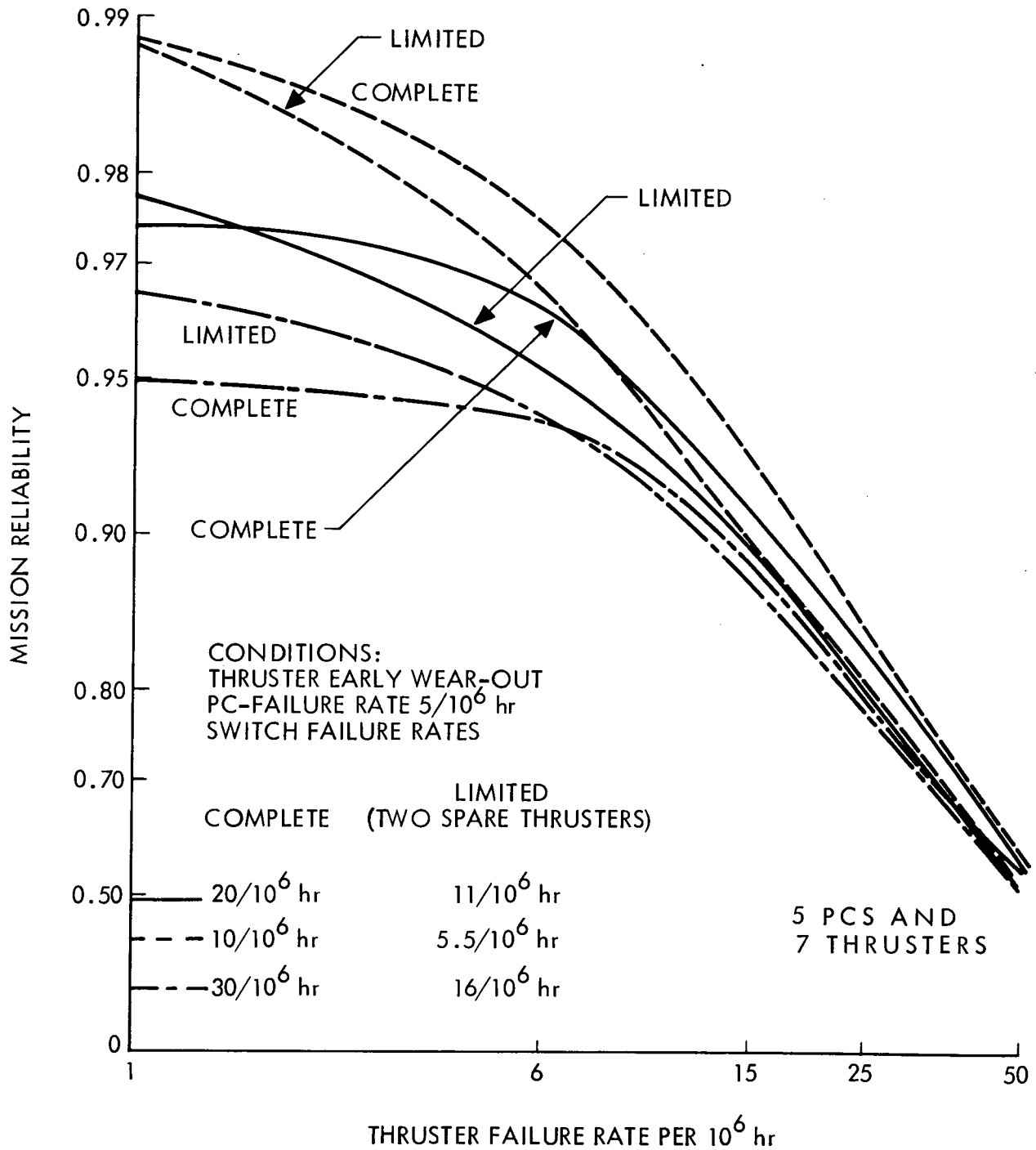
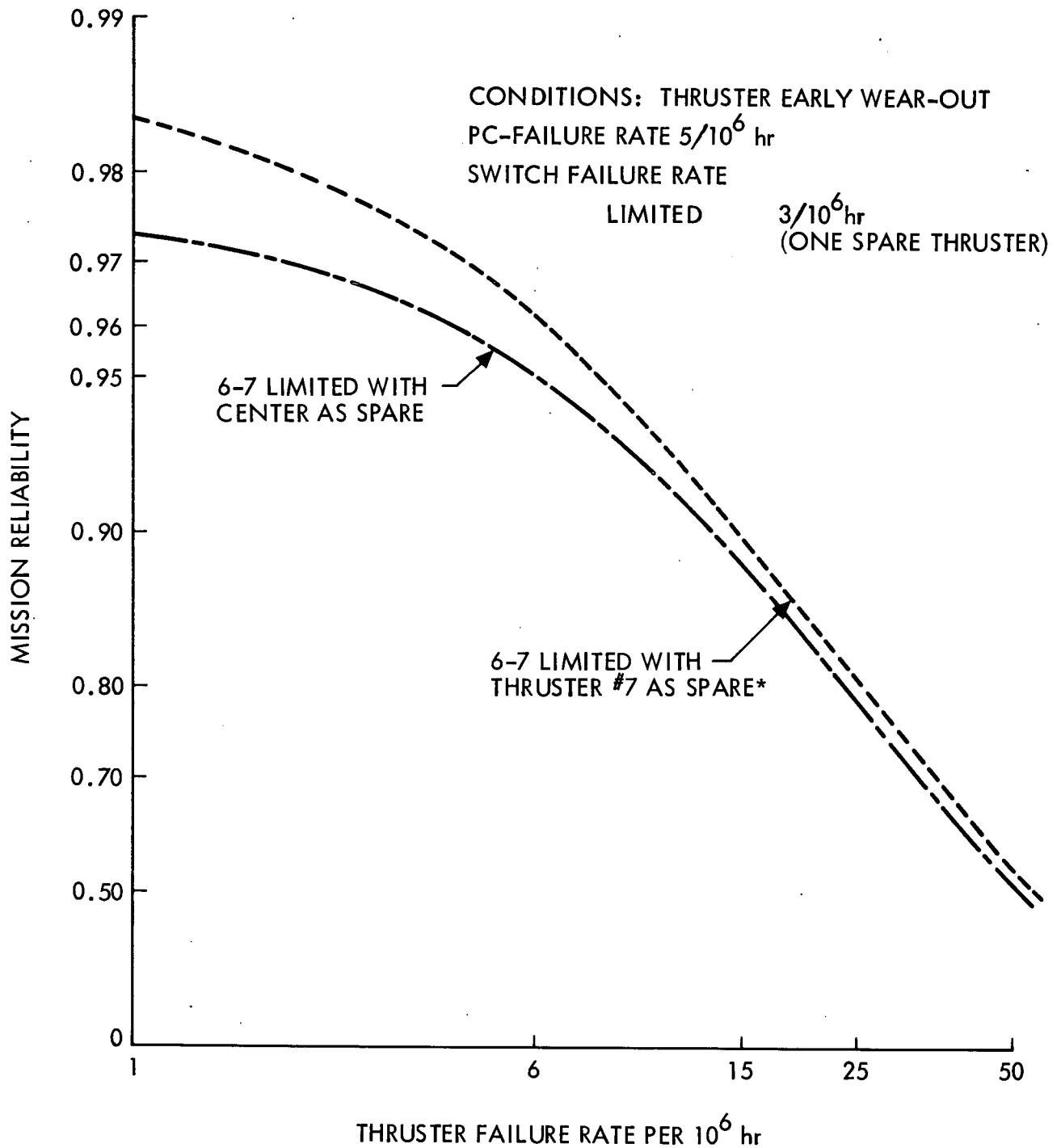


Fig. III-B-14. Encke Comet Mission Reliability Versus Thruster Random Failure Rate at Various Switch Failure Rates, Monte Carlo Simulation, Case 4



*SEE TABLE III-B-3.

Fig. III-B-15. Encke Comet Mission Reliability Versus Thruster Failure Rate, Monte Carlo Simulation, Location of a Spare Thruster, Case 5

- (2) The system with minimum mission reliability of cases considered is the one of four PCs hard-wired to four thrusters for all failure rates examined.
- (3) Thruster failure rates greater than $20/10^6$ hr yield unacceptable mission reliability, especially if the thruster mean lifetime is not greater than 10,000 hr.
- (4) Increasing the random failure rate of the PCs from $5/10^6$ hr to $10/10^6$ hr has no effect on the selection of the switching approach.
- (5) The complete switching cases were superior to hard-wired cases and to equivalent limited switching cases (same number of thrusters), except as noted in (6) below.
- (6) For the five-PC, seven-thruster system, the complete switching method becomes more reliable than the limited switching method as the thruster failure rate increases. At very low thruster failure rates, the limited switching is the more reliable. The crossover point depends on the thruster wear-out parameter; but it occurs on the graphs, when the thruster failure rate is between $1/10^6$ hr and $6/10^6$ hr.

When thrusters are more reliable, with a random failure rate of $6/10^6$ hr with late wear-out and a mean life at 12,000 hr, then the five PCs connected to seven thrusters via the limited switching method is more reliable than the complete switching connection method; this is because the higher switch failure rate for the complete switch connection begins to influence the reliability. On the other hand, with a thruster random failure rate higher than $1.5/10^6$ hr and early wear-out, or with a thruster random failure rate higher than $6/10^6$ hr and late wear-out, complete switching connection of the five PCs to the seven thrusters is more reliable than limited switching. Complete switching is also more reliable under these circumstances than

seven PCs hard-wired to seven thrusters. These results are not surprising because the connection flexibility offered by complete switching becomes more advantageous as thrusters fail more frequently.

- (7) Variations in the switch failure rate do not have a significant effect on the selection of the switching approach, as long as the same ratio between the failure rates for the complete and for the limited switching is maintained. As can be seen in Fig. III-B-14, the plots move up or down as the ratio of the failure rate decreases or increases about the estimated value. There is no major change on the crossover points, particularly those of the five-PC/seven-thruster complete switching connections, and the five-PC/seven-thruster limited switching connections.
- (8) In addition to displaying switch tradeoff results, Fig. III-B-10 through III-B-14 also show the effect of thrust-subsystem reliability on mission reliability, and, from this, acceptable thruster and PC failure rates can be allocated.
- (9) In limited switching systems, the choice of which thruster(s) should be the spare(s) is an important, not always obvious, decision. As a typical example, the 6-7 case was computed using two different choices for the spare thruster. The two cases are shown in Fig. III-B-15. The thruster numbering refers to Fig. III-B-6. The differences in reliability are due to the symmetry requirements necessary for attitude control. The symmetric case (center as spare) is the least reliable; this was not obvious before these calculations. If a limited switching case is chosen, the arrangements of spare thrusters should be studied with care.

4. Weight Analysis

Individual component weights are shown in Table III-B-4. Weights for the various PC/thruster combinations considered in this study are summarized in Table III-B-5. In all cases, connecting-cable weights are omitted.

Using these weights and the mission reliability data from the previous section, plots of the thrust subsystem weight versus mission reliability were originated. Four cases were plotted, two cases of thruster early wear-out at thruster random failure rates of $6/10^6$ and $20/10^6$ hr, and two cases of thruster late wear-out at thruster random-failure rates of $6/10^6$ hr and $20/10^6$ hr. The random failure rates were arbitrarily selected to show the relation of mission reliability to thrust subsystem weights at (a) a reasonable estimate of the random failure rate and at (b) a point more than twice this failure rate. The results are shown in Figs. III-B-16 through III-B-19. The four PC cases are not shown because of the extremely low mission reliability associated with these cases. The following comments can be made about the data presented in these figures:

- (a) Mission reliability increases with weight (additional spare units). However, there are some cases which do not follow this rule and are not recommended for the thrust subsystem. These are the cases that are not on the increasing reliability line.
- (b) In every figure except in Fig. III-B-18 (condition of late wear-out and $6/10^6$ hr random failure rate) the complete connection method improved the mission reliability.
- (c) In Fig. III-B-18, which shows somewhat optimistic thruster failure rates, the five PCs complete switching connection to seven thrusters is not better than the five PCs connected to seven thrusters with the limited switching method.
- (d) These weight curves will be used mainly as a tool for the spacecraft designer in deciding the thrust subsystem configuration for the mission and in weight tradeoffs for increased

Table III-B-4. Component Masses

Configurations		Weight, kg (lb)		
Number of PCs	Number of Thrusters	Hard-wired	Limited Switching	Complete Switching
4	4			
4	5	—		
4	6	—		
5	5	118 (260)		127.1 (280)
5	6	—	127.7 (281)	134.5 (296)
5	7	—	136.2 (299.5)	141.9 (312)
6	6	142 (312)	—	—
6	7	—	152.1 (333)	150.3 (352)
7	7	165.5 (364)	—	—

Table III-B-5. Thrust Subsystem Component Masses

Component	Mass, kg (lb)
30-cm thruster	7.3 (16)
PC	16.3 (36)
Switch to completely connect all thrusters	1.8 (4)
Switch to connect one spare thruster (limited)	0.45 (1)
Switch to connect two spare thrusters (limited)	0.68 (1.5)

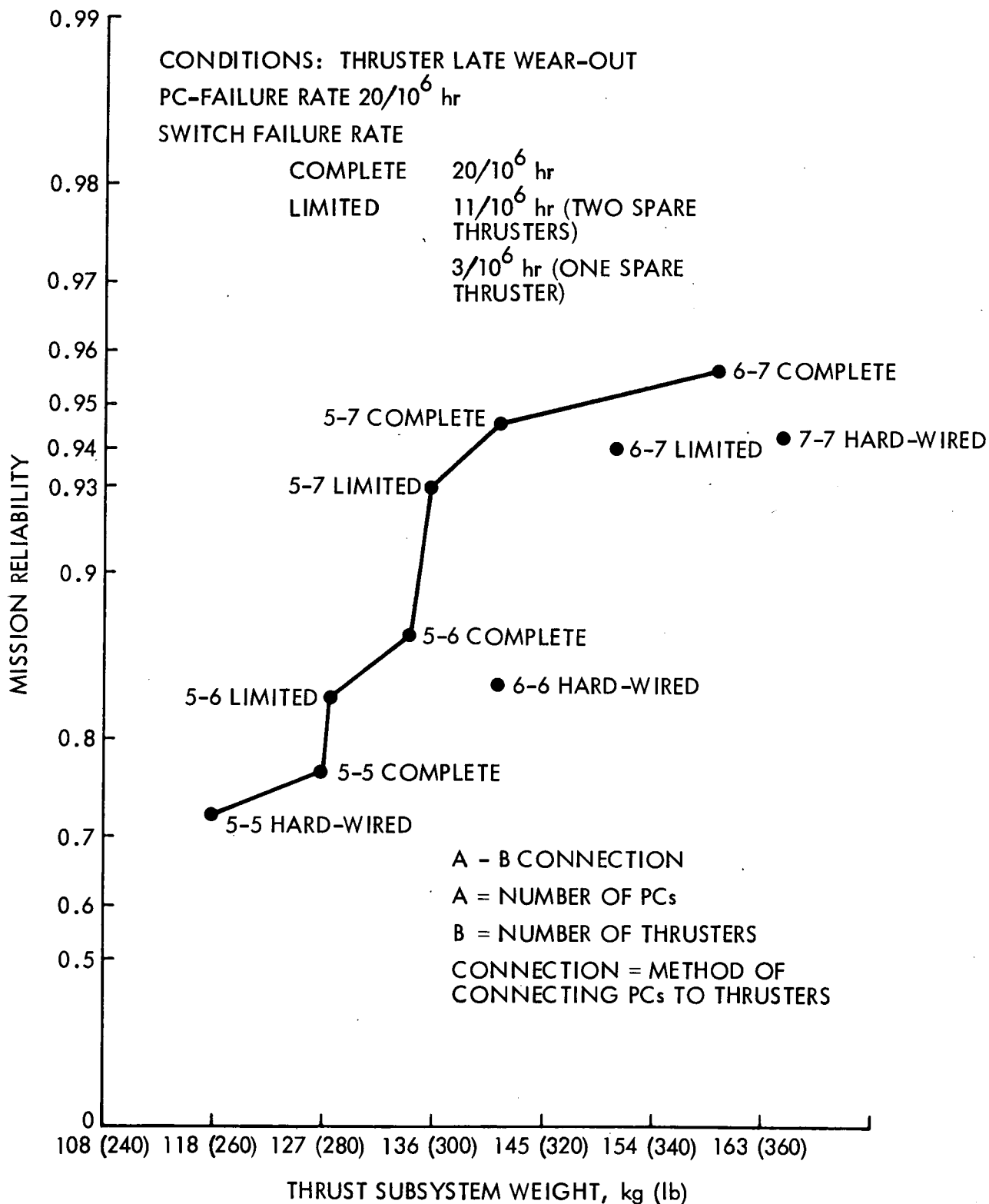


Fig. III-B-16. Encke Comet Mission Reliability Versus Thrust-Subsystem Weight

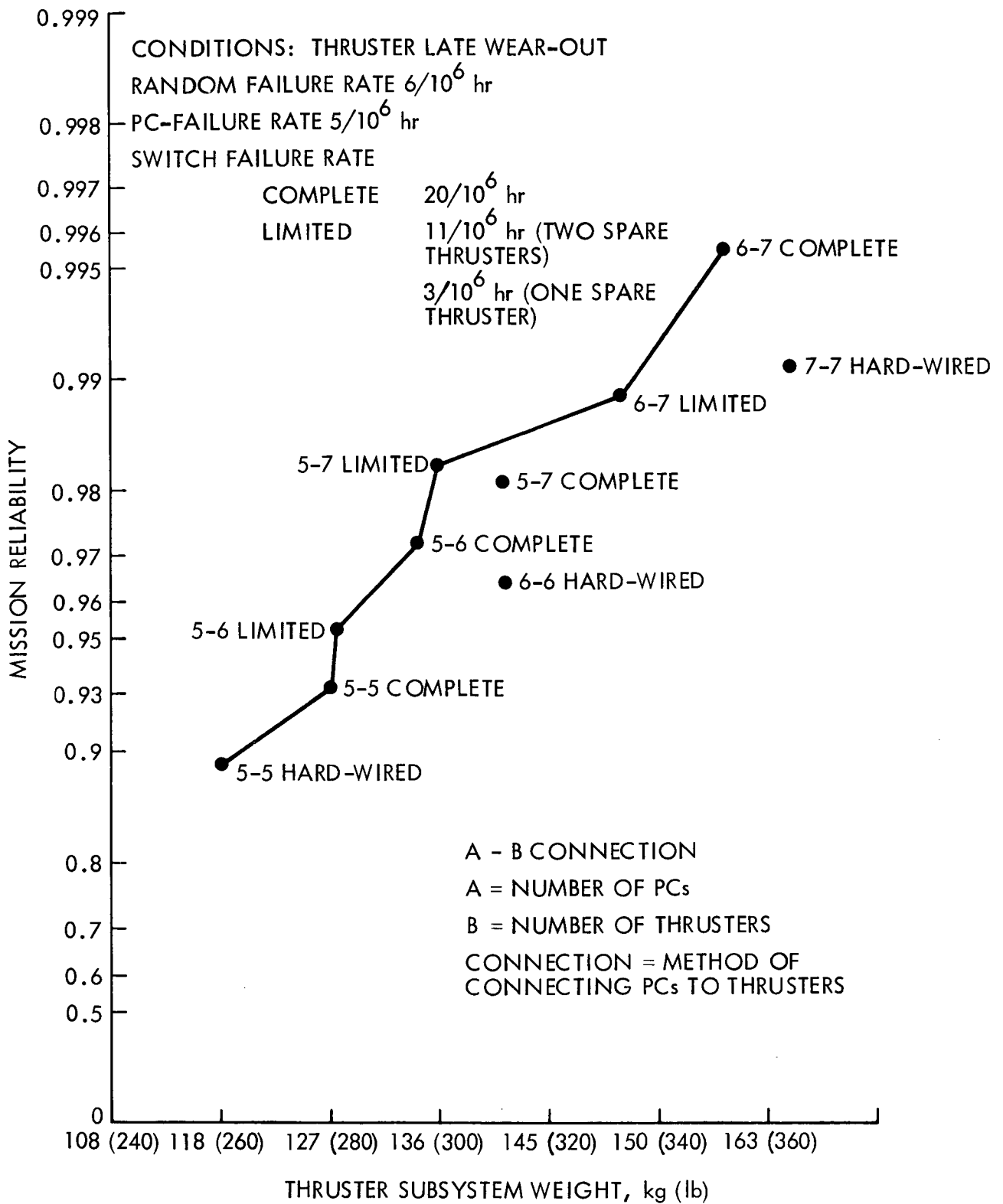


Fig. III-B-17. Encke Comet Mission Reliability Versus Thrust-Subsystem Weight

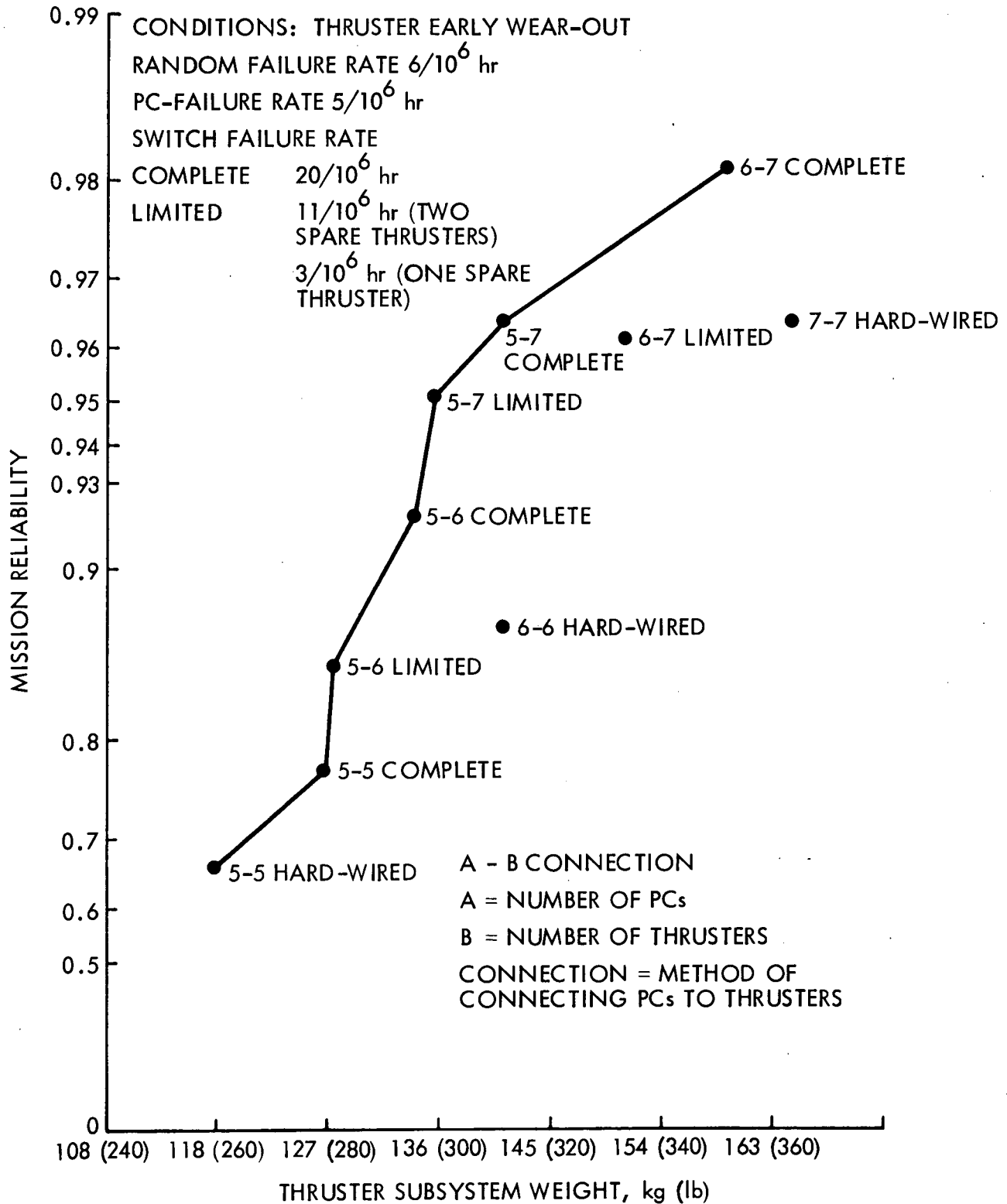


Fig. III-B-18. Encke Comet Mission Reliability Versus Thrust-Subsystem Weight

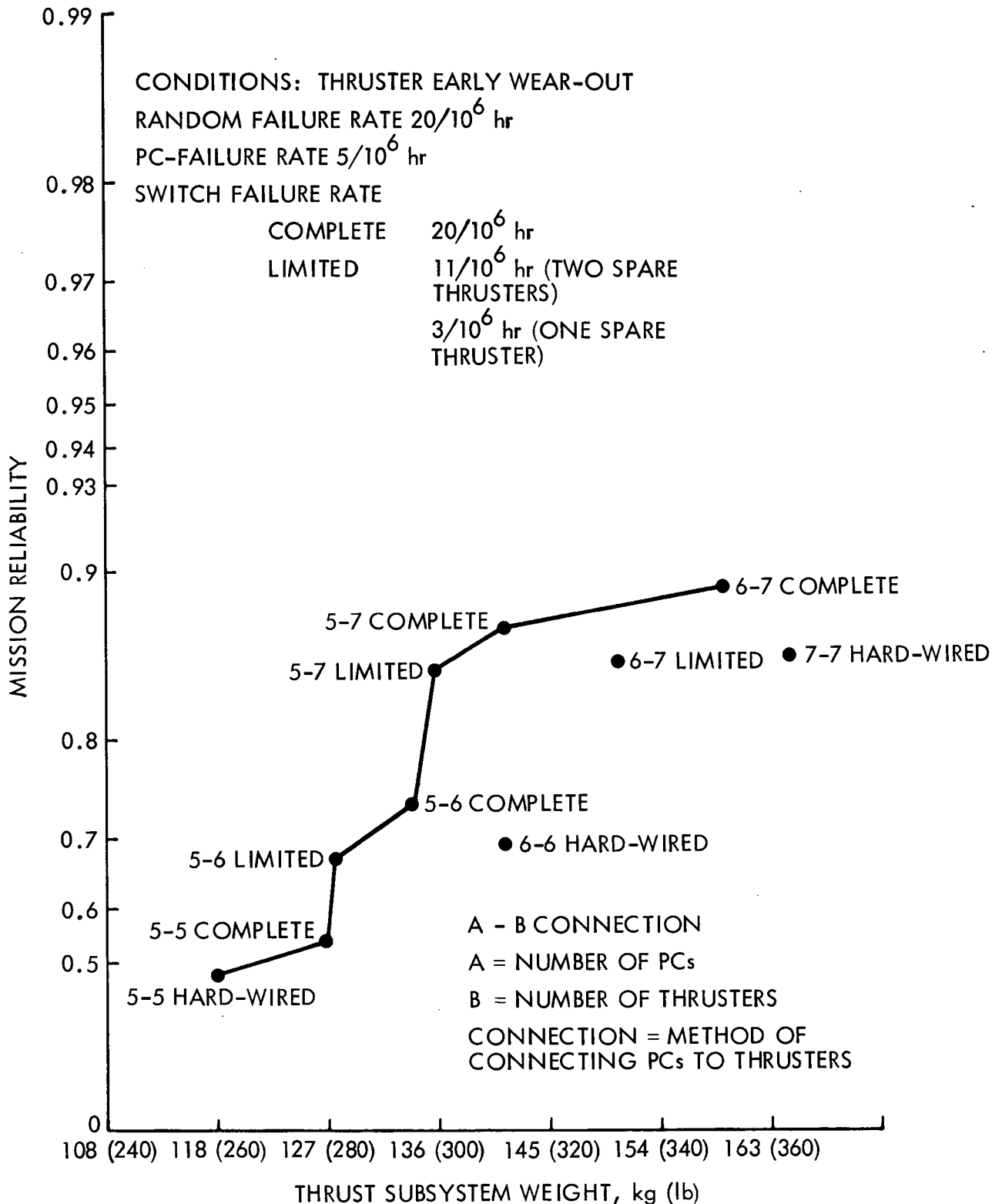


Fig. III-B-19. Encke Comet Mission Reliability Versus Thrust-Subsystem Weight

reliability. How much weight can be traded off will be his decision. The weight difference between the lightest and heaviest configuration studied is considerable, more than 45 kg. The requirements for the rest of the spacecraft need to be considered as well.

5. Conclusions

From the results of computed mission simulations and the results of the weight tradeoff, it is apparent that switching improves the mission reliability.

For the Encke Rendezvous Mission, the complete switching connection method has advantages over the limited switching connection, as is evident in the mission reliability data for the following cases:

- (a) Six PCs to seven thrusters for all thruster failure conditions.
- (b) Five PCs to seven thrusters for all thruster failure conditions except the late wear-out (12,000-hr mean life) and random failure rate of $6/10^6$ hr.

Based on this data, it is recommended that complete switching connection be used for the Encke mission because this higher reliability was obtained with a relatively low weight penalty. The flexibility of operating any PC with any thruster, provided by complete switching connections, can also conveniently be used to locate trouble in elements of the thrust subsystem during ground operations and even in flight.

C. SWITCHING MATRIX AND ROTARY SWITCH DESIGN AND ANALYSIS

The present thrust-subsystem design for an Encke rendezvous mission specifies seven 30-cm thrusters with six power conditioners (PCs) supplying the proper voltages and currents for operation of five out of the seven thrusters. A reliability tradeoff study (Section III-B) was made comparing several approaches for connection of PCs to thrusters, including hardwiring, partial, and complete switching. The results indicate that the highest mission reliability will be obtained by switching of any PC to any thruster. The switchgear requirements were initially based on the use of six hermetically sealed, individually mounted switches, similar to the units used on SEPST III. A preliminary part specification for the switch did not include design provisions for connection of the switches to the thrusters. It was determined from a review of this document that two features were needed to meet the switchgear requirements: (1) a new switch design to provide an improvement in high voltage/high current capability at reduced weight and volume, and (2) the integration of the switch into a matrix assembly providing both the mounting of the individual switches and the necessary splicing of the common outputs of the switches to the correct thruster input. A new switch and a switching matrix assembly were proposed. The design features of the switch and matrix assembly are discussed in the following paragraphs.

1. Rotary Switch Designa. Review of SEPST III Switch

At present, in laboratory tests of the SEPST III, the switching function is accomplished by a 10-deck, two circuits per deck, conventional wafer switch driven by a stepping motor. This switch is an engineering prototype assembled from two five-deck units previously used for 20-cm thruster tests (see Fig. III-C-1). The prototype switch configuration, constructed with readily available commercial parts, has several problem areas. It is difficult to make the long, narrow configuration for 10 decks rigid enough to prevent

Reproduced from
best available copy.

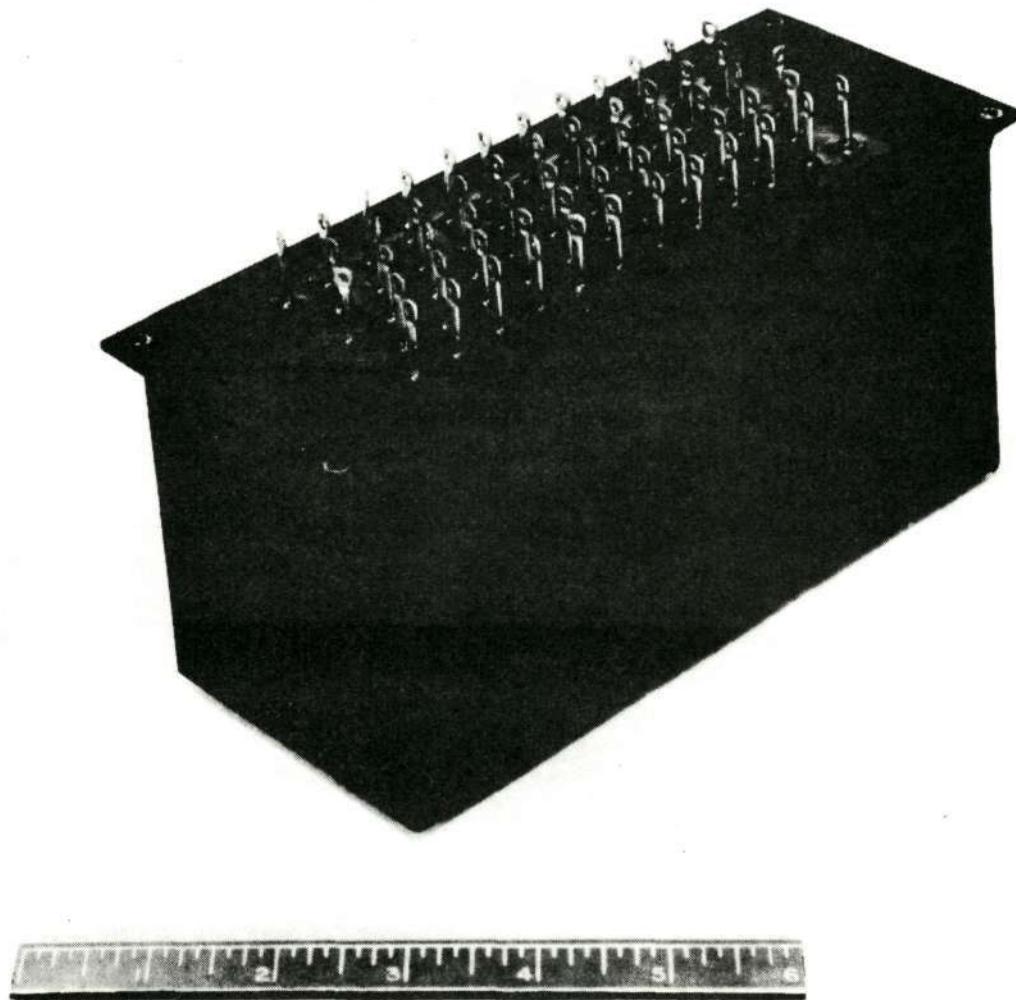


Fig. III-C-1. Photograph of Hermetically Sealed Five-Deck,
Ten-contact Switch

binding during the switching operation, and binding increases the torque output required of the stepping motor. The switch contacts themselves have sharp edges, which are undesirable from a high voltage gradient standpoint. The switch length also requires extra wire runs, which increase the weight over that for a flat switch.

The plan to hermetically seal the switch introduces another problem, that of loss of pressure over the lifetime of the mission, thus creating the possibility of arcing, if the pressure becomes critical. To reduce power losses, contact-current limitations require paralleling of several sets of contacts in the high current circuits.

b. Design Considerations

Compared to conventional applications, this switch has some rather unusual constraints:

- (1) The required voltages for a single thruster can be conveniently arranged into four groups. Group 1 consists of voltages at a nominal +1,400 V dc above ground. Group 2 comprises voltages within a few hundred volts of ground, while group 3 is a single voltage of -1,000 V dc. Group 4 is used to indicate the position of the switch for telemetering and control purposes. Two contacts in group 1 carry approximately 20 amp; all of the other contacts carry 5 amp or less. Wafer designs based on contact arrangements and ratings in the above groups allow reductions in contact spacing because of the voltage gradient control possible.
- (2) There is no requirement to switch with the load applied. Voltages in groups 1, 2, and 3 are not present on the switch contacts during switching. Group 4 voltages of about 5 V are required to indicate the position of the switch for control purposes.

- (3) There is no requirement for a large number of switching cycles or complete rotations. During the mission, the switch may be operated for a total of six complete cycles. Although many more cycles than this would be required for type approval and flight acceptance testing, the millions of cycles usually required are not necessary for this switch.
- (4) Reduction in weight is second only to reliability in importance. As a result of this constraint, any configuration which lends itself to weight reduction should be considered.
- (5) The switch should be repairable by replacement of faulty components.

c. Proposed Switch Design

Based on these constraints, and to overcome the disadvantages noted in 1-a above, a new switch design is proposed. Figure III-C-2 shows a typical four-circuit wafer, which consists of eight sets of contacts arranged in concentric rings. Four of the eight sets are bused together on the reverse side of the wafer. These contacts have a rounded geometry on the contact side and are spaced with .635 cm (.250 in.) of insulation between them to reduce the voltage gradient. Using an average gradient between contacts of 40 V/mil results in a maximum voltage stress of 10 kV, which is an adequate safety factor for the voltages employed. The number of group 1 voltages to be switched is such that the voltages can be assigned to one wafer pair and not be intermixed with the other groups of voltages, which enables closer spacing of the contacts. If the number of circuits in any group changes, alternate wafer arrangements are possible.

As can be seen in Fig. III-C-3, the rotor contacts are short sections which bridge between the bused input contacts and the thruster contacts. This design reduces exposure of the high voltage to the surrounding area, as contrasted to the knife edge rotor wiper configuration in the conventional wafer switch.

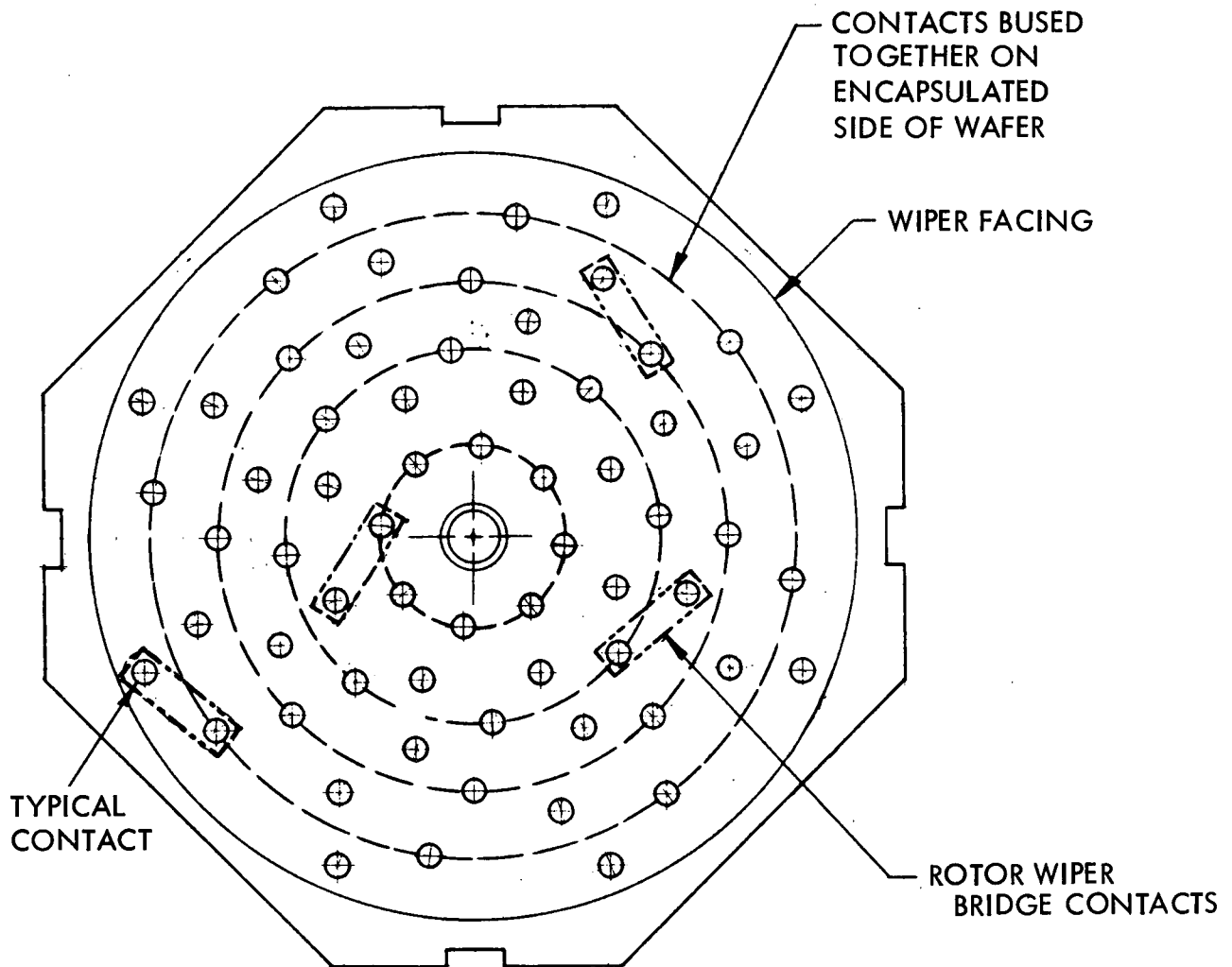


Fig. III-C-2. Typical Four-circuit Wafer

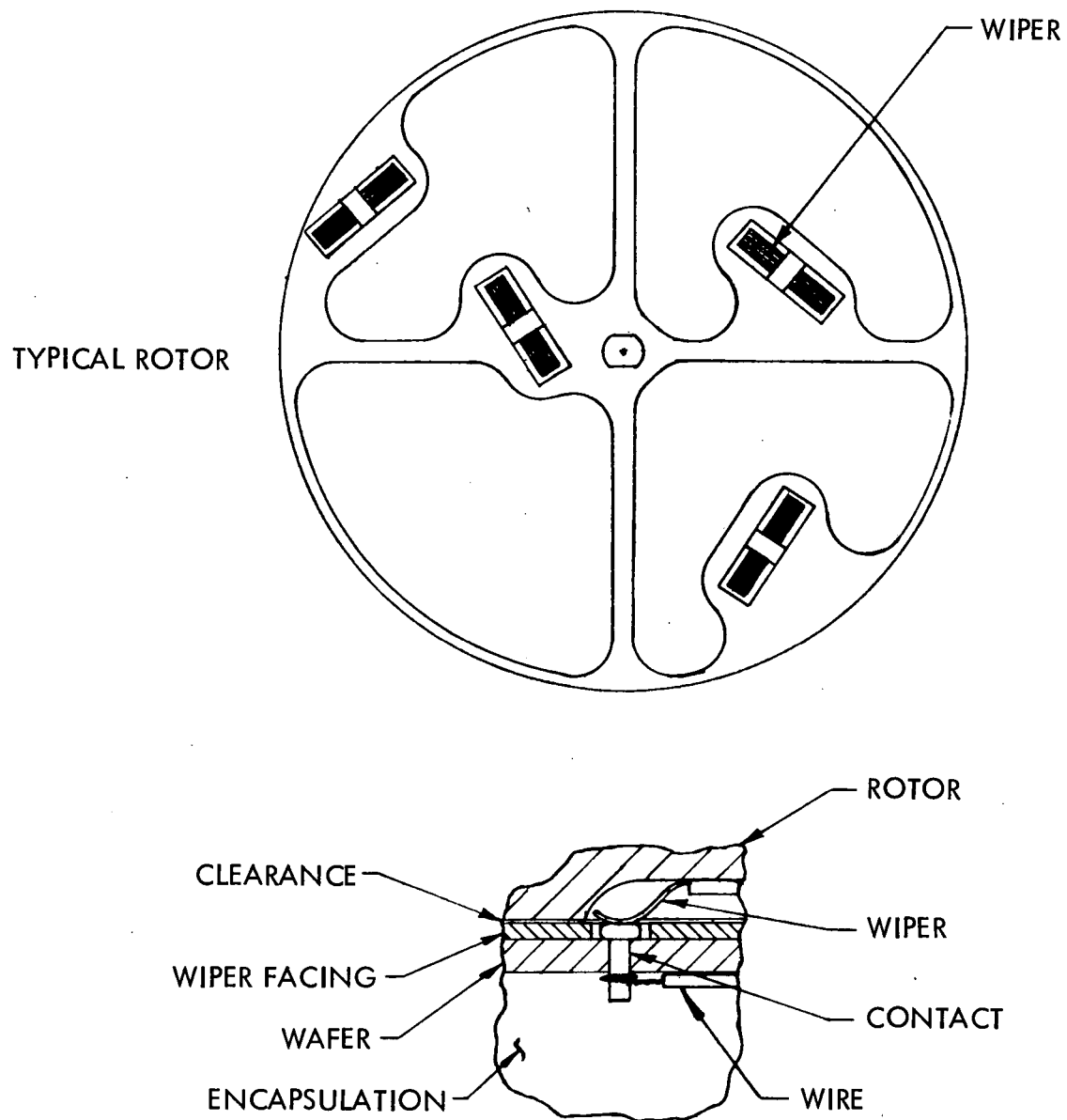


Fig. III-C-3. Wafer/Rotor Interface

Wires are attached to the contacts on the reverse side of the wafers, and two of the wafers are encapsulated back to back, as shown in Fig. III-C-4. Attachment of the input/output wiring directly to the contacts eliminates a series joint in the circuit and further isolates the voltages because the insulated wires can then exit the encapsulation material and be routed directly to the connection matrix. A total of five wafers is shown, four of which are encapsulated in pairs, and the fifth one encapsulated as a "half-wafer". Group 1 voltages are applied to the first wafer pair; group 2 voltages are applied to the second pair. The voltages in groups 3 and 4 would be on the half wafer. The shaft is insulated to prevent a possible breakdown path from the wafers to the shaft. The wafer pairs are supported by four support posts of sufficient rigidity, which are precision-machined to achieve good alignment. A hex recess is provided in the end of the shaft so that the torque required to rotate the switch may be measured. This torque measurement serves as a check on the switch assembly and alignment.

The mounting plate on which the motor is mounted could be integrated with the spacecraft structure. The short, cubical configuration lends itself to efficient packaging of the switching matrix assembly. It is planned to run the individual wires out of the wafer pairs to junction points or splices. Figure III-C-5 shows a top view of the switch with input wires on one side of the switch, and the output wires typically on the remaining three sides.

It is proposed that the mounting plate for alignment of support posts and at least one wafer pair with its associated contacts and wipers be fabricated as an engineering model to demonstrate this design. The contact resistances, especially under high current conditions, the torque required to rotate the switch, high voltage withstanding capability, and the estimated life can be obtained from tests of this model. Based on the torque requirement, the appropriate motor can then be sized and obtained for the switch. With this configuration, the weight can be estimated, and the packaging techniques evaluated for assembling and connecting six of the required switches. Tests would be made at sea level pressures and at high vacuum conditions to assure that effective leakdown of trapped air would occur to prevent operation of the switch in the critical pressure region.

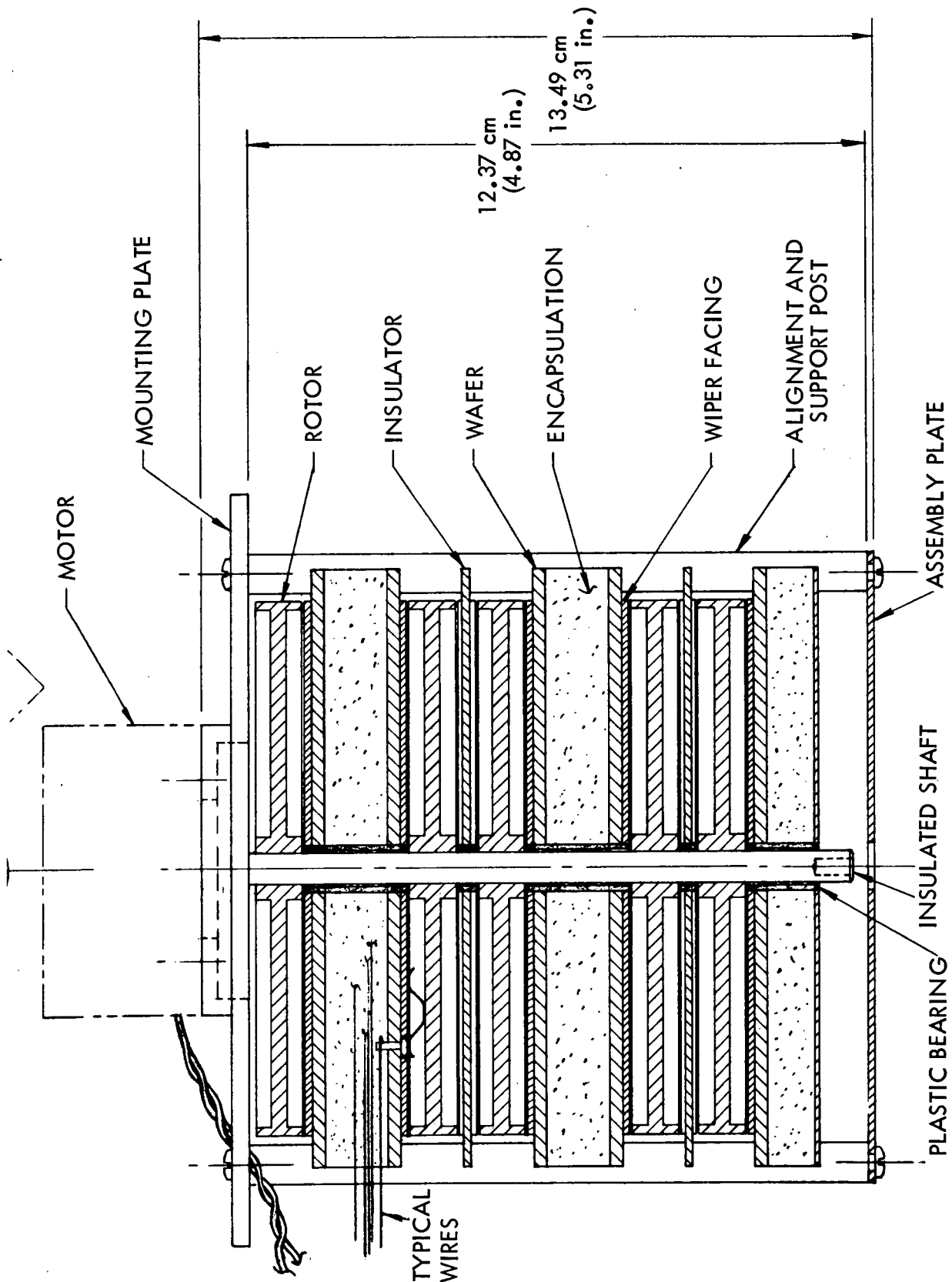


Fig. III-C-4. Switch Assembly

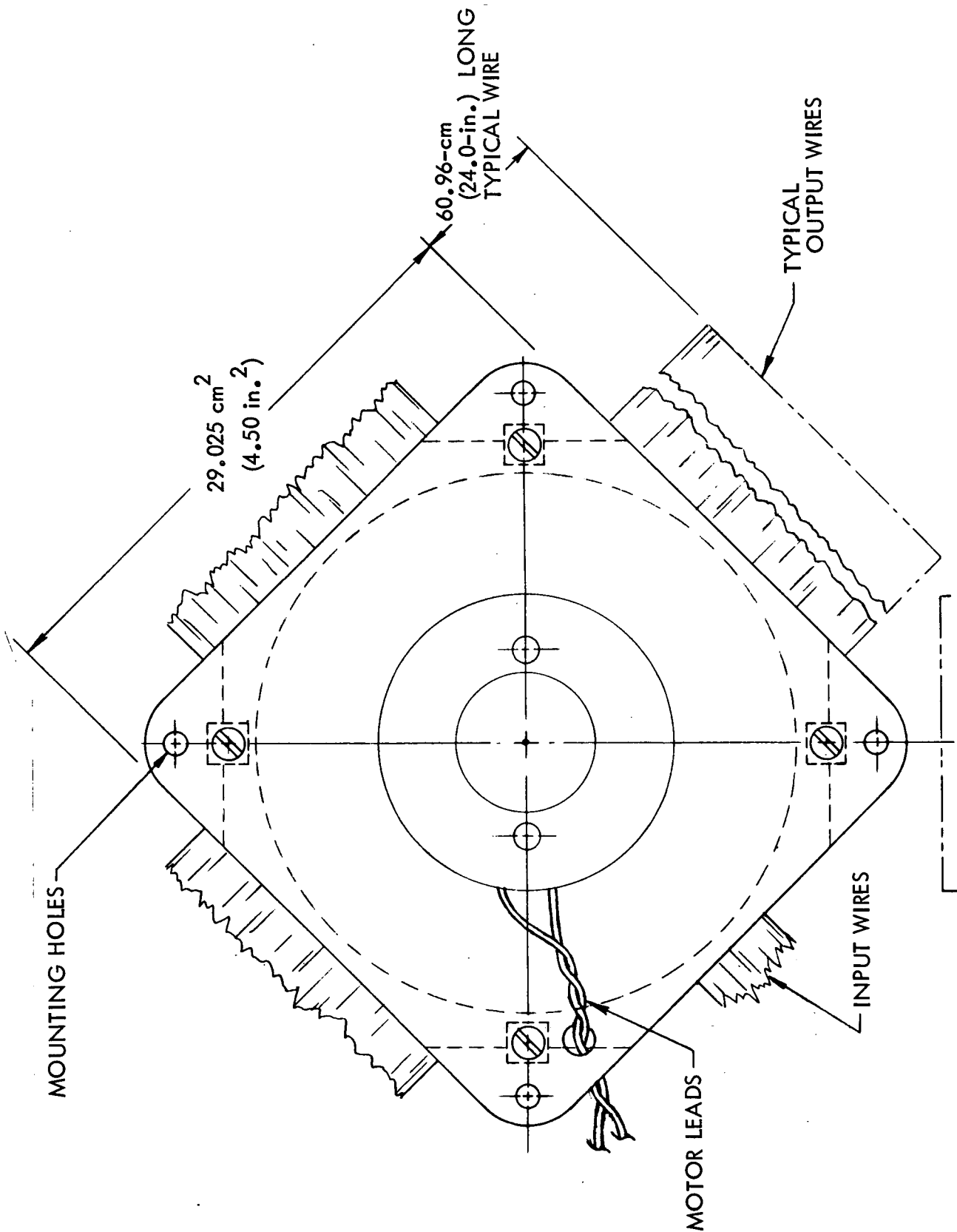


Fig. III-C-5. Switch, Top View

A preliminary draft of a procurement specification for the rotary stepping switch proposed in this section has been prepared (see Ref. III-C-1). Detail requirements are included. Assignment of current ratings and voltage groupings is on the basis of the described contact arrangement at this time and may be changed as future requirements are established. Wafer pairs may be replaced with newer designs, if necessary, without scrapping the whole unit.

2. Switching Matrix Assembly Design

a. Design Rationale

For purposes of the SEPST III facility tests, the outputs of the original switchgear were connected by terminations to terminal boards mounted at or near the systems test interfaces. This technique requires the use of substantial wire runs and multiple interconnection joints, especially where jumpers were "daisy-chained" to the thruster input connection. The terminal board does not provide adequate environmental protection for a spacecraft flight application; it tends to be heavy, and, in general, is not designed for the high voltage/high current application. In addition, the handling of shielding, ground returns, and twisted cable configurations for electromagnetic interference (EMI) protection is usually not considered in terminal board installations.

As discussed above, the initial approach to switchgear design used a hermetically sealed unit with feed-through terminals (Fig. III-C-1). In addition to the concern for probable high voltage breakdown, if leakage of the sealed unit occurred, there are also environmental constraints to be considered in the areas of reduction of EMI, operation at sea-level ambient conditions for test, and fabrication, assembly, and spacecraft-installation handling hazards. With the sealed-switch approach, the connection of the switch outputs must be made subsequent to installation of the switches on the spacecraft. Repair or replacement of defective components in the switch is not possible with a hermetically sealed enclosure.

The incorporation of the individual switches into a switching matrix assembly is therefore proposed. Such an assembly should provide the following capabilities:

- (1) A standard switch mounting interface.
- (2) Support for input/output wiring.
- (3) Clean electrical and mechanical interfaces to the SEP module structures and cabling subsystems.
- (4) Dust and contamination protection.
- (5) An effective EMI enclosure.
- (6) A method for connecting the various switch outputs to the identical output of the other switches and to the thruster inputs.
- (7) Ease of access for installation, maintenance, repair and/or replacement.
- (8) Suitable high voltage protection in accordance with specifications*.
- (9) Minimal weight and volume.

The connection requirements and design features of a proposed switching matrix assembly concept based on the proposed rotary switch are discussed in the following paragraphs.

b. Connection Requirements

The connection requirements for the switching matrix assembly are related to the Encke Rendezvous Mission requirements in terms of the total number of operating and spare thrusters required. It was determined during the reliability tradeoff study that six PCs and seven thrusters are required. This number provides one spare PC and two spare thrusters when five are operating, the maximum number which can operate on the solar array power available at 1 AU. It must be possible to connect the outputs of each PC to any one of the seven thrusters as selected on ground command or by the CCS.

*JPL Design Specification DM505139 (JPL internal document).

Six switches, one for each PC, are therefore needed. Appropriate logic to assure that two PCs are not connected to the same thruster would be supplied external to the switch.

The proposed switch has the total capacity of 20 outputs on 8 positions; however, this total capacity will not be required for the Encke mission. One switch position and four output connections of each of the remaining seven positions will be unused, based on PC/thruster electrical requirements, which results in 672 switch outputs being connected to 112 thruster inputs, for a total of 784 wires which must be spliced (or connected) to satisfy the switching requirements. The previously discussed problems of using terminal boards for the switch output connections are compounded by the large number of wires involved in this application. With these large quantities, designs which minimize the length of wire runs and reduce the overall envelope of the matrix of connections will have lighter-weight switching hardware. Another design constraint is that the high voltage connections in groups 1 and 3 will have no conductors in contact with the ambient vacuum environment.

A preliminary list of inputs/outputs which must be switched is given in Table III-C-1. Based on the switch voltage groupings, it is desirable to locate the same groups for all the switches physically close to each other and also close to the assembly electrical interfaces. Connections should be designed to facilitate assembly, installation, repair and/or rework procedures. Also, the possibility of removal and replacement of a complete switch should be considered during design. Because the switch will be provided with pigtailed leads, which exit the wafer encapsulation within a specific cross-section, the circuits are essentially pre-grouped for cabling and routing purposes.

In addition to the PC to thruster wiring which is to be connected in this assembly, the switch rotary solenoid power and the switch position data circuits are to be connected to the power and data system, respectively.

Table III-C-1. Circuit Grouping for Switching Matrix Assembly

Group	Circuit Designation	Voltage (approximate)	Current (maximum)	Wire Gage
1	(1) Arc + and Beam	+1400 V dc	19.2	12 SC ¹
	(2) Arc Return	+1400 V dc	17.0	12 SC
	(3) Cathode Keeper	+1400 V dc	1.0	22
	(4) Main Isolator	+1400 V dc	2.0	22
	(5) High Voltage Return	+1400 V dc	3.0	22
2	(1) Main Vaporizer Power	11 V ac	2.0	22
	(2) Main Vaporizer Return	11 V ac	2.0	22
	(3) Cathode Vaporizer Power	11 V ac	2.0	22
	(4) Cathode Vaporizer Return	11 V ac	2.0	22
	(5) Neutralizer Heater Power	50 V ac	0.9	22
	(6) Neutralizer Heater Return	50 V ac	0.9	22
	(7) Cathode Heater Power	50 V ac	0.9	22
	(8) Cathode Heater Return	50 V ac	0.9	22
	(9) Neutralizer Keeper (positive)	50 V dc	3.0	22
	(10) Neutralizer Keeper Return	50 V dc	3.0	22
3	(1) Accelerator	-1000 V dc	0.05	22
	(2) Spare	—	—	22
4	(1) Position (positive) (Position returns are wired directly to assembly connectors)	5 V dc	SIGNAL	26 SC

¹Single Conductor.²Twisted Triad.³Twisted Pair, Shielded and Jacketed.

c. Design Features of Proposed Switching Matrix Assembly

A conceptual sketch of a cut-away view of a proposed switching matrix assembly is shown in Fig. III-C-6. This assembly design was strongly influenced by electrical and mechanical interfaces with the cabling and structures subsystems and by the configuration for the proposed Encke rendezvous SEP module.

The assembly consists of a chassis measuring approximately 18 x 45 x 55 cm. The chassis mounts to the spacecraft PC compartment by means of support brackets on the compartment structure. Eight fasteners, which attach to the bottom of the chassis, are employed. The unit is not hermetically sealed and is designed to permit rapid leakdown of trapped air to prevent electrical breakdown, when power is applied to the circuits. For EMI protection, RF gaskets are placed at chassis penetration points and special finishes of the mounting surfaces are provided to ensure adequate grounding and shielding of the assembly. Within the chassis, provision is made for mounting six rotary stepping switches. Three switches are mounted in line along one end of the unit in proximity to the input interfaces from three of the PCs, whereas the others are located on the opposite end of the chassis near the other three PCs. The switches are mounted vertically on a hat section in the chassis. This mounting configuration is preferred to a cantilevered mounting from the chassis side wall because it makes the switch-axis parallel to the spacecraft-launch axis, which allows for a more rugged mounting to survive the launch shock and vibration. The chosen mounting pattern places the switches close together to improve utilization of the chassis volume, although this means that only two faces of the switches are available for input/output wires. Dimensional analysis of the spacing requirements for the output wires indicates that adequate area is provided on the side face of an encapsulated wafer pair so that the outputs can be grouped by thruster without any effect on the switch voltage or current capabilities.

To provide a clean interface with the thrust subsystem, all inputs and outputs of the assembly have been assigned to miniature quick-disconnect electrical connectors. Placement of the input and output connectors

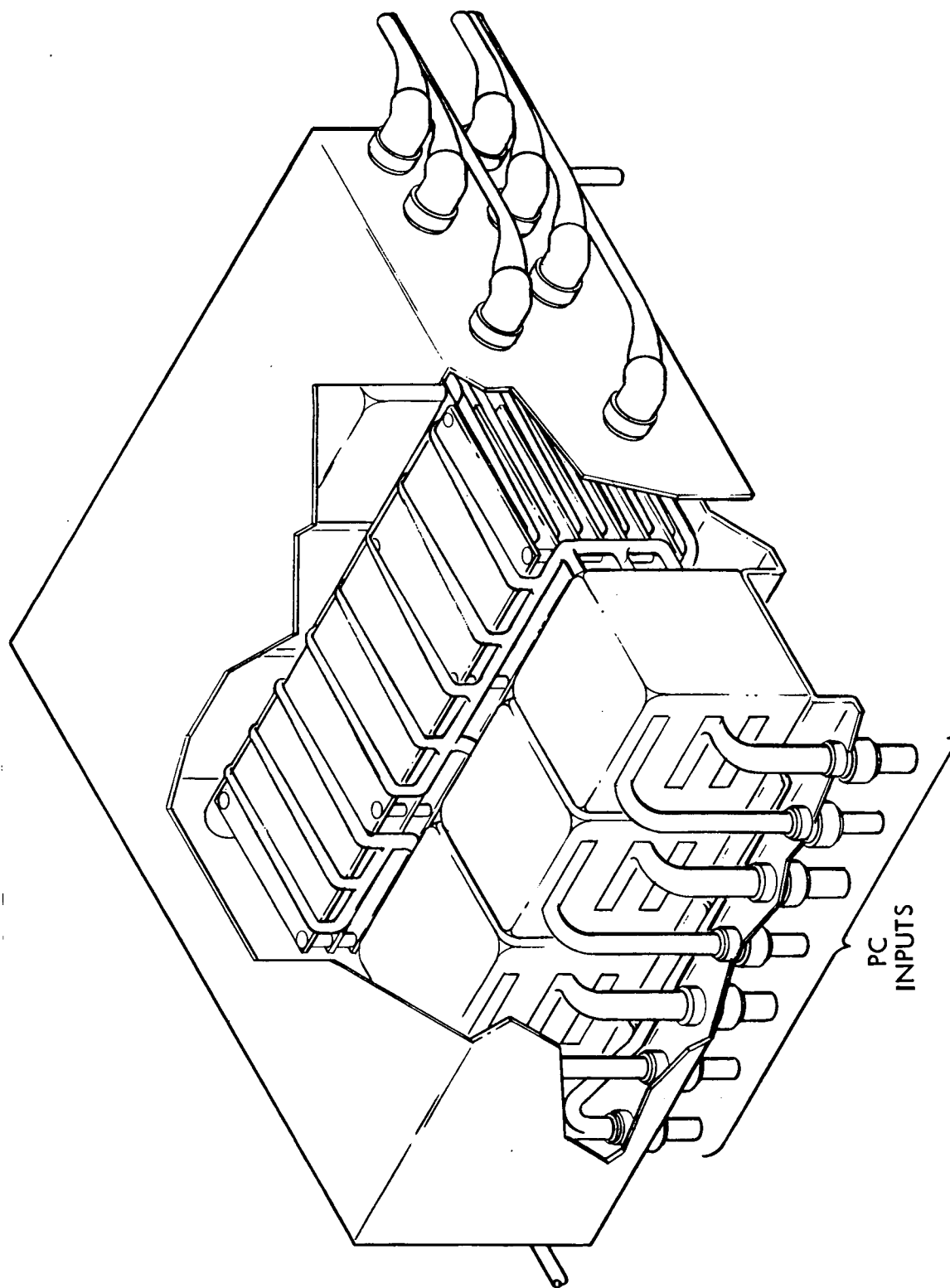


Fig. III-C-6. Cutaway View of Switching Matrix

on the unit is related to the SEP module configuration. In particular, the PC inputs to the assembly are located on the base of the chassis because this surface faces the PC compartment. The cable lengths from the individual PCs are thus shortened by placing the connectors centered on, and immediately below, the switch which handles each PC. Two connectors are used to separate the group 1 and group 2 circuits. The -1,000-V accelerator circuit is assigned to the center contact of the low voltage connector with six surrounding contacts spared. The routing of the input cables from these connectors to the switches continues the physical separation of the circuits into the switch wafers.

The output connectors which handle the thruster circuits have been placed on the assembly side walls. Again, configuration constraints resulted in the choice of this location. The cabling which handles the thruster circuits is supported in two troughs, which are suspended from the thruster array structure parallel with the sides of the assembly. The high voltage circuits are routed to seven connectors (one per thruster) on the side nearest the high voltage cable trough, and the low voltage outputs go to seven connectors on the opposite side, near the low voltage trough. This arrangement also provides easy access for mating and demating of the connectors in the event that the thruster array is removed from the spacecraft during assembly and test operations.

The connection of the switch outputs to the required thruster circuits is accomplished in the connection matrix indicated in the center of the assembly. All of the switch outputs are cabled and routed into this matrix. In general, the group 1 high voltage circuits will be routed to one end of the matrix, and the low voltage circuits (and -1,000 V accelerator circuit) will be routed to the other end. The 784 wires required are connected within the matrix.

At present, three approaches to making these connections are being considered. The first would use a laminated bus with special high voltage solder contacts along the bus board edge as needed. A stack of seven of these boards, mounted on edge, and having similar output contacts at the ends with

wires going to the thruster interface connectors, would comprise the connection matrix. A conceptual sketch of this approach is shown in Fig. III-C-7.

The second approach uses a crimped contact on the pigtailed switch output leads. Each contact would provide a removable (or replaceable) connection to an individually insulated bus block which has the capability of busing up to seven inputs to any one output. Hardware for implementing this approach is available commercially in a space-rated version. The blocks would be mounted on a support bracket in the envelope of the matrix, which would also provide cable routing and support.

A third approach would utilize a direct splice of the six switch output wires to the correct thruster circuit. Standard splice fabrication methods and processes would be applicable. Because of the number of wires and the need for some additional wire length to permit grouping of the wires for the crimp-splice operation, an orderly arrangement for positioning the splices would be needed. A proposed method of forming the matrix from the spliced contacts and simultaneously supporting and positioning the splices was designed. Figure III-C-8 shows a version of the hardware which serves to locate support and lock each splice into the matrix board. This approach, in comparison to the other two, has the best potential for reducing weight; but the hardware would not be as easy to repair or rework. All of these concepts need further study to establish weight, reliability, and high voltage/high current capability.

Additional wiring, which is incorporated in the assembly, includes the switch rotary power circuits and the switch position information circuits. The mounting of the switches on the hat sections provides a cable-routing space for the stepping-motor drive circuits, and the space at the bottom of the assembly between the switch mounting hat section and the connection matrix support allows routing of the position circuits without interfering with the PC/thruster circuits. Separate connectors, which mate to the PC-compartment cable harness, are provided for each of these two functions.

In summary, this design approach provides an integral unit, which has the capability of meeting thrust-subsystem switching requirements

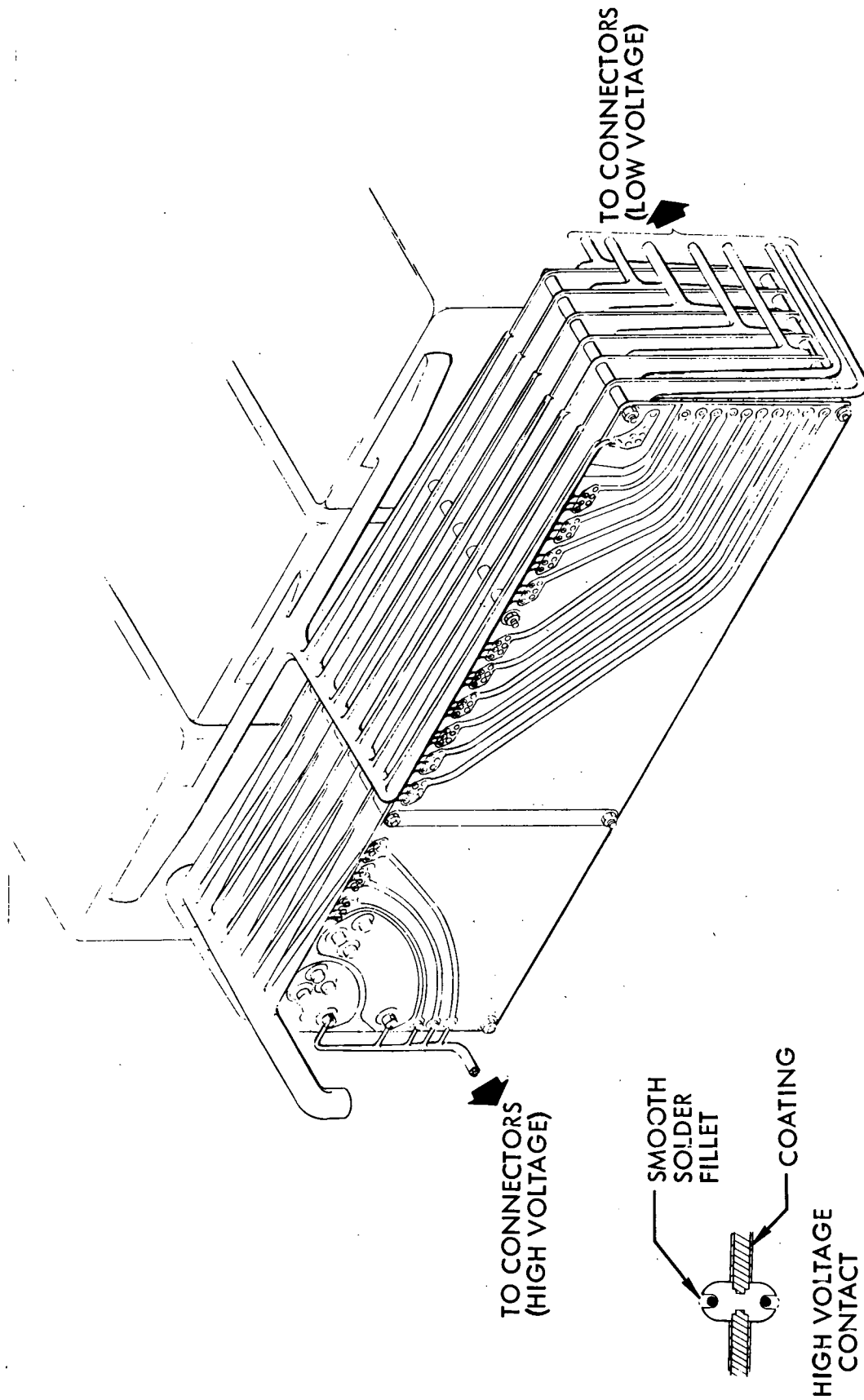


Fig. III-C-7. Edge-board Connection Concept

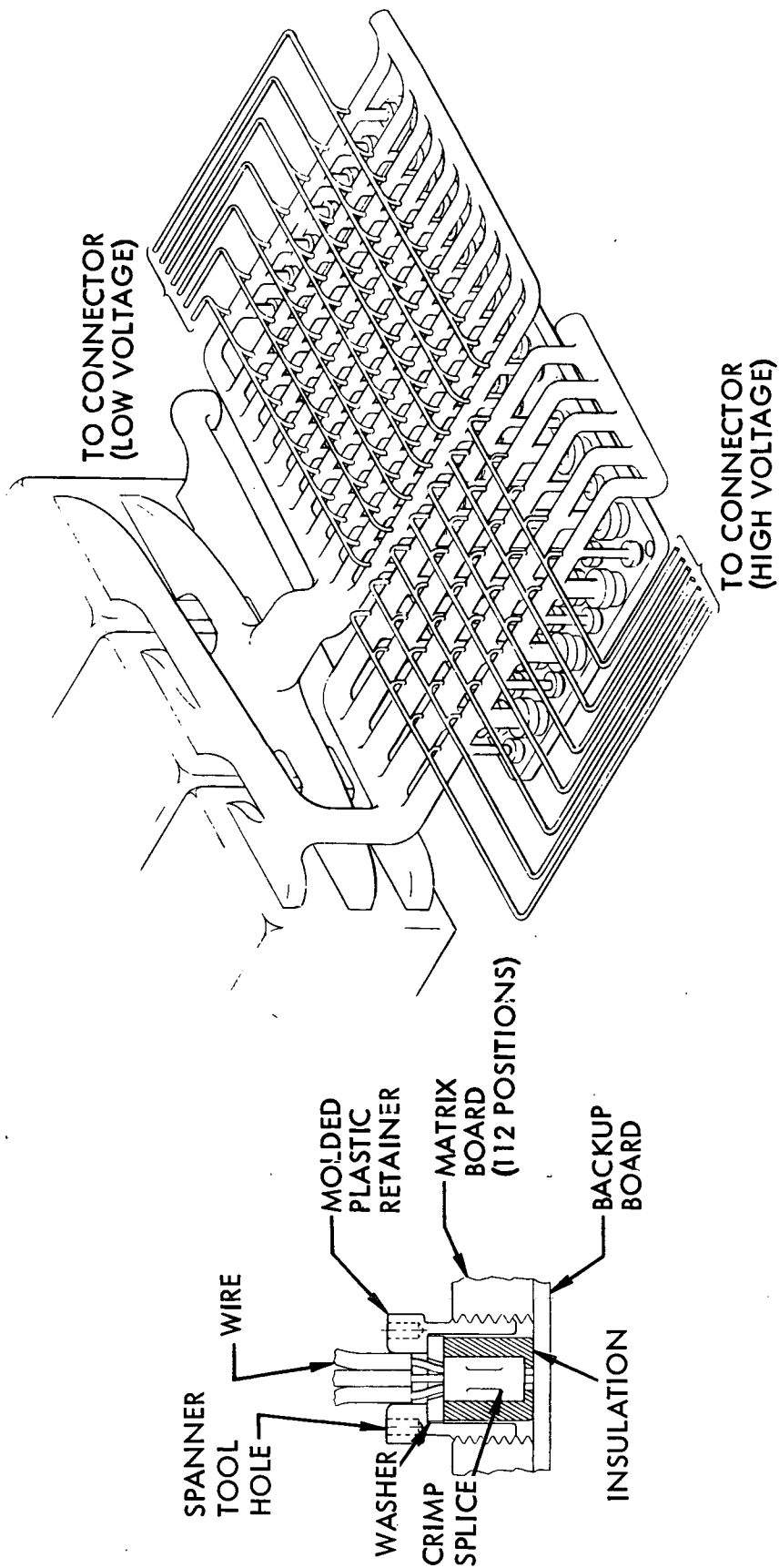


Fig. III-C-8. Crimp-splice Matrix Connection Concept

and which is compatible with the SEP module configuration. The use of connector interfaces provides good separation of high and low voltages and makes the unit maintainable. The design lends itself to on-the-bench assembly and check out and integrates easily with the spacecraft by installation of eight fasteners and mating of 28 input/output connectors. The configuration of the switch and this matrix assembly influence each other significantly, and reductions in the size and weight of the assembly chassis are dependent to a great extent on the design of the switch. Structural and electrical interface requirements for the assembly will, in turn, affect such switch design features as overall maximum height, pigtail length and exit direction, and mounting-plate hole pattern. It is proposed that a preliminary design of the switching matrix assembly be made to study the connection requirements and the dimensional aspects of integrating the six switches into a single assembly. An engineering breadboard of one section of each suggested bus (or splice) connection matrix should be fabricated for use in conjunction with the switch wafer electrical tests. Thus, the overall circuit resistance and high voltage capability could be evaluated as a system. The connection matrix models would aid in evaluating the assembly weight and in performing the necessary tradeoffs to select a matrix design.

3. Conclusions and Recommendations

- (a) Based on this study, the original design of the hermetically sealed SEPST III switch does not satisfy the optimum design constraints for this application.
- (b) A special design, as described, should be capable of meeting the requirements of smaller size, reduced weight, repairability, and reliability.
- (c) The fabrication of an engineering model of a switch wafer pair to demonstrate the design feasibility is recommended.
- (d) The described preliminary design for a switching matrix assembly can incorporate the rotary switch design and the required circuit connections.

- (e) Three design approaches to the connection matrix appear feasible.
- (f) The fabrication of engineering models of the three matrix concepts is recommended.

D. THRUSTER ARRAY THERMAL ANALYSIS

This section describes the results of a study of thruster-array thermal performance. Thruster operating temperature levels under various solar heating modes are analyzed for several candidate thermal arrangement schemes. Because of the lack of definitive design criteria and detailed thruster thermal characteristics, the present study offers only a qualitative discussion of several design alternatives. Potential thermal problems are identified for further detailed investigations.

1. Design Guidelines

A seven-thruster clustered array, consisting of 30-cm diameter ion thrusters and related gimbal devices is the baseline array configuration. Because of the nature of SEPSIT Encke rendezvous mission, it is planned to operate five thrusters at full power for a solar environment equal to or less than 1 AU. The peak of thermal loading occurs at spacecraft perihelion (.34 AU) where solar irradiance up to a 10-sun level may come in at any angle with respect to the thrust axis in a plane parallel to the shearplates of the PCs. The high irradiance solar heating, in addition to the maximum thruster power dissipation, estimated at 500 W per thruster, would cause the thruster to operate in a high temperature mode. To ensure proper thruster operation, the maximum temperature levels of all thrust-subsystem components have to be kept within the upper temperature limits through proper configuration arrangements and the application of thermal control devices.

On the other hand, at spacecraft aphelion (3.5 AU) only one thruster is operated at one-half power level, and the solar irradiance becomes less than one percent of the level at spacecraft perihelion. Thermal control measures are then required to keep all components above their lower temperature limits.

From a previous study (Ref. III-D-1), it was concluded that, for a clustered array, the most efficient way of rejecting thruster internal-heat dissipation is to radiate it through the back surfaces. However, the thermal

interaction between the thrusters and the remaining parts of the spacecraft must be minimized to protect the power conditioner units and to prevent overheating of mechanisms by the dissipation of thruster-heat. Before designing an improved thruster array/spacecraft integration plan, it was essential to investigate a limiting worst-case situation. For the worst case, it was assumed that the back surface of the thruster array was insulated with a super-insulation blanket. Such an arrangement isolates the thruster array for minimum thermal interface, but it increases the thruster operating temperature and is one of the major sources of overheating problems in inbound missions. However, an insulated mounting plate helps to keep all standby thrusters warmer at the spacecraft aphelion, when only one thruster is operating at a half-power level.

2. Preliminary Thermal Constraints

At the present time, most component thermal constraints are yet to be determined. In the following, the temperature limits were established in a preliminary fashion for evaluating various thermal arrangements of the clustered array.

a. Thruster Operating Upper Temperature Limits

For a solar environment equal or less than one AU, five of the thrusters are operated at full power level. To ensure proper thruster operation, the following thermal requirements have to be satisfied at all stages of the mission.

- (1) The controllability of cathode vaporizers have to be maintained. The combined thermal input from the controller electrical heater, cathode discharge power, and infrared radiation from other thruster components are to be regulated to keep the vaporizer at a set-point temperature (approximately 250°C) to produce the desired mercury flow-rate. Excessive environmental heating may raise the vaporizer temperature above the

set-point temperature even without the controller heater operating. Such a thermal runaway situation may result in the loss of thruster controllability.

- (2) The temperature level and gradients on the screen grid must be examined critically because thermal stresses along the thin grid induce buckling, which would induce an electrical short circuit.
- (3) The cathode operating temperature must be kept within a proper range to ensure the operating lifetime required for the mission.
- (4) The maximum allowable temperature of the thruster housing has to be kept below a limiting temperature. If permanent magnets are employed, the upper temperature limit of the housing is determined by the Curie temperature of the magnet. If electrical magnets are used, the temperature limit tolerable by the electrical insulator is $\approx 350^{\circ}\text{C}$.

b. Thruster Operating Lower Temperature Limits

When only one of the thrusters is operated at one-half of the power level, the cathode vaporizers of all six standby thrusters and the corresponding feedline assemblies have to be maintained above -39°C to prevent the liquid mercury from freezing and possibly penetrating the vaporizers.

c. Temperature Limits for Related Elements

The gimbal actuator units and the carriage translator actuator unit are to be maintained between 0°C and 125°C for proper functioning.

Thruster thermal design constraints depend strongly on the specific thruster internal design and performance. The configuration for the cathode-isolator-vaporizer assembly is a critical factor for vaporizer controllability and cathode thermal performance. Various proposed screen grid designs,

including dish-grid and rib-enforcement, not only determine the thermal gradients but also affect the grid stiffness for buckling considerations. Electrical insulating material and the type of magnets selected could conceivably change the temperature limits imposed on thruster housing. Before further detailed investigations are performed to establish such necessary design information, results of thermal analyses can be utilized only as a qualitative guide for design concepts. In the present investigation, emphasis was placed on the thermal evaluation of various arrangements of clustered array within the preliminary design guidelines. The applicabilities of different temperature control devices were also considered.

3. Approach

A design for a 30-cm thruster, developed at the NASA LeRC, was employed as the baseline thruster configuration (Fig. III-D-1). Because detailed thermal characteristics for the 30-cm thruster are not available at this time, the model employed in the present study is based on the extrapolation of the information obtained from a 20-cm ion thruster (Ref. III-D-1). Each thruster was represented by an eight-node thermal network. The entire array was simulated with an 86-node network. Thermal behavior of the thruster array is governed by the following parameters:

- (a) Operating conditions and environments.
- (b) Thermal-interface boundary conditions.
- (c) Surface characteristics.
- (d) Array-configuration geometry.
- (e) Effects of thermal-control devices.

In the present investigation, analyses were performed for the following conditions:

a. Operational Situations

Two limiting operational situations were studied. For the high temperature mode operation, five clustered thrusters (including the

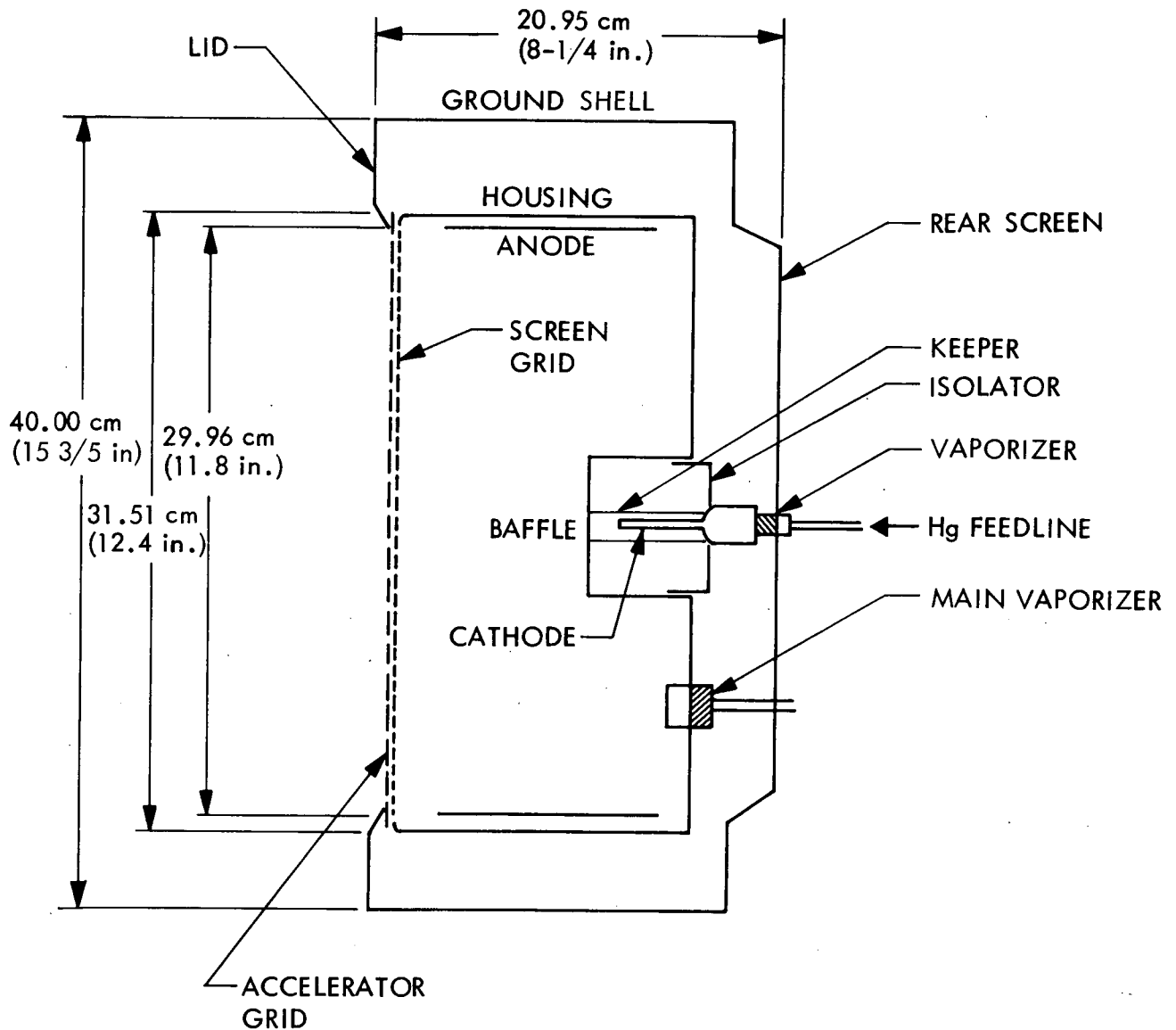


Fig. III-D-1. Baseline 30-cm Thruster

central one) are to be operated at full power level. Solar irradiance, varying from 1 to 10 sun levels, comes in either normal or parallel to the thrust axis and passes into grids and the thruster interior. For the low-temperature mode operation, only one thruster is operated at half power, when the spacecraft is at 3.5 AU aphelion. For a worst case consideration, it is assumed that solar heating is blocked completely by insulating materials.

b. Thermal Interface Boundary Conditions

As indicated in the preliminary design guideline, the back surface of the thruster array was assumed to be insulated to provide a complete thermal isolation of the thruster array from the rest of the spacecraft. However, such an arrangement also imposes a severe boundary condition on the high temperature mode of thrust operation.

c. Surface Characteristics

Infrared radiation is the principal mode of heat transfer between thruster components. High emittance coating can be used effectively to strengthen the radiation coupling between the thruster interior and the environment. However, the application of the high emittance coating (it is assumed $\epsilon = 0.8$) would be limited to the surfaces at the ground shells and the external side of the housing. Electron and ion bombardments at the interior cavity prevent such applications on the anode and the interior housing.

For surfaces exposed to high solar irradiance, it is advantageous to apply ion α / coating (such as OSR or white paints) for heat rejections. In this study, it was assumed that the ground surfaces* or the sun-shade surrounding the thruster array be painted with treated Z-93 white paint (with degraded α of 0.36). The surface characteristics of the lid, the grid, and the neutralizer, which are exposed to either direct primary beam ions or neutral particles, are expected to be seriously degraded by mercury ion bombardment and sputtered

*The thruster ground shell is either solid, as in the JPL 20-cm thruster, or perforated, as in the Hughes design.

molybdenum grid material. The contamination could result in a high α/ϵ ratio of approximately 4 (Refs. III-D-2, 3, and 4). The analytical results of this study are presented to demonstrate the thermal behavior of different thruster array arrangements under the conditions specified above.

4. Results and Discussions

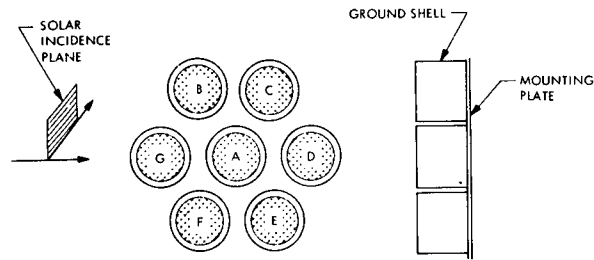
a. Baseline Configurations

Three configurations were investigated for the baseline seven-thruster array with the back surface of the mounting plate insulated. Component-temperature levels are shown in Fig. III-D-2 through III-D-6, for the conditions that five thrusters are operated at full-power level under various solar environments. It can be seen that, as long as the back surface of the mounting plate is insulated and no thermal control device is applied, the temperature responses of the array components are quite similar in all three configurations.

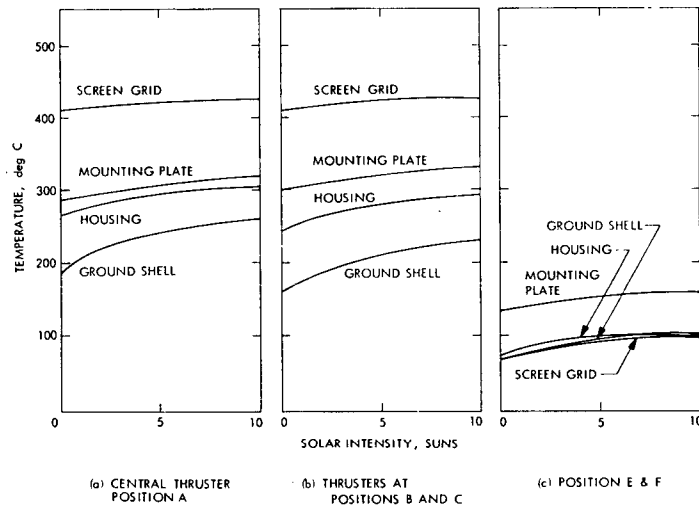
Although most component temperature limits are yet to be determined, the controllability of cathode vaporizers, which must be kept from heating above approximately 250°C, is a fundamental thermal constraint. For all five arrangements investigated, the predicted temperatures of the mounting plate with an insulated back exceed the set point temperature of the vaporizer, which means that major modifications of the baseline arrangements must be made to maintain the thruster controllability.

b. Modified Arrangement and Thermal Control Devices

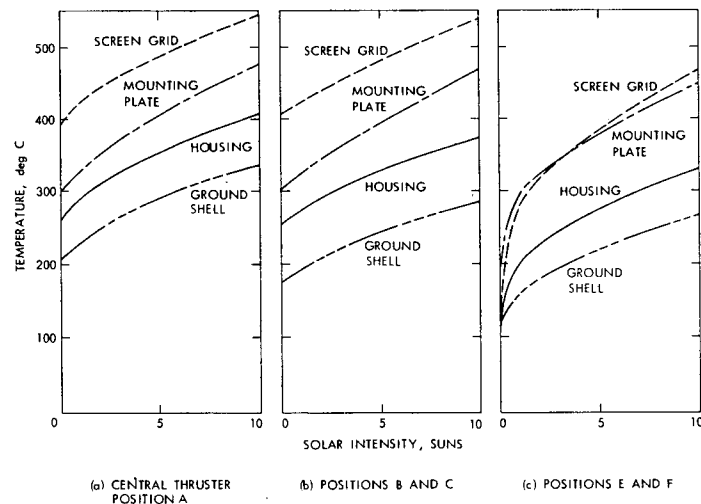
Previous analyses shows that, if the back surface of the thruster array is not allowed to radiate waste heat, the array configuration has to be modified to provide additional radiating surface and to accommodate the application of thermal control devices. The design of the perforated ground shell appears to be preferable to that of the solid, when thrusters are separated with baffle arrangements. In addition, the frame surface at both ends should be extended to shade the translator-actuator unit from direct solar irradiation and



(a) Configuration



(b) Solar Incidence Normal to Thrust Axis



(c) Solar Incidence Parallel to Thrust Axis

DESCRIPTION: NO SUNSHADE FRAME
 INSULATED MOUNTING PLATE 0.16 cm (1/16 in.) THICK ALUMINUM
 UNPERFORATED GROUND SHELL (Z93 WHITE PAINT)
 COATING $\alpha_{\text{DEGRADED}} = 0.36$
 OPERATING CONDITION: THRUSTERS: A, B, C, D, G OPERATING AT FULL POWER,
 E AND F STANDBY

Fig. III-D-2. Bare Thruster Array with Solid Ground Shells

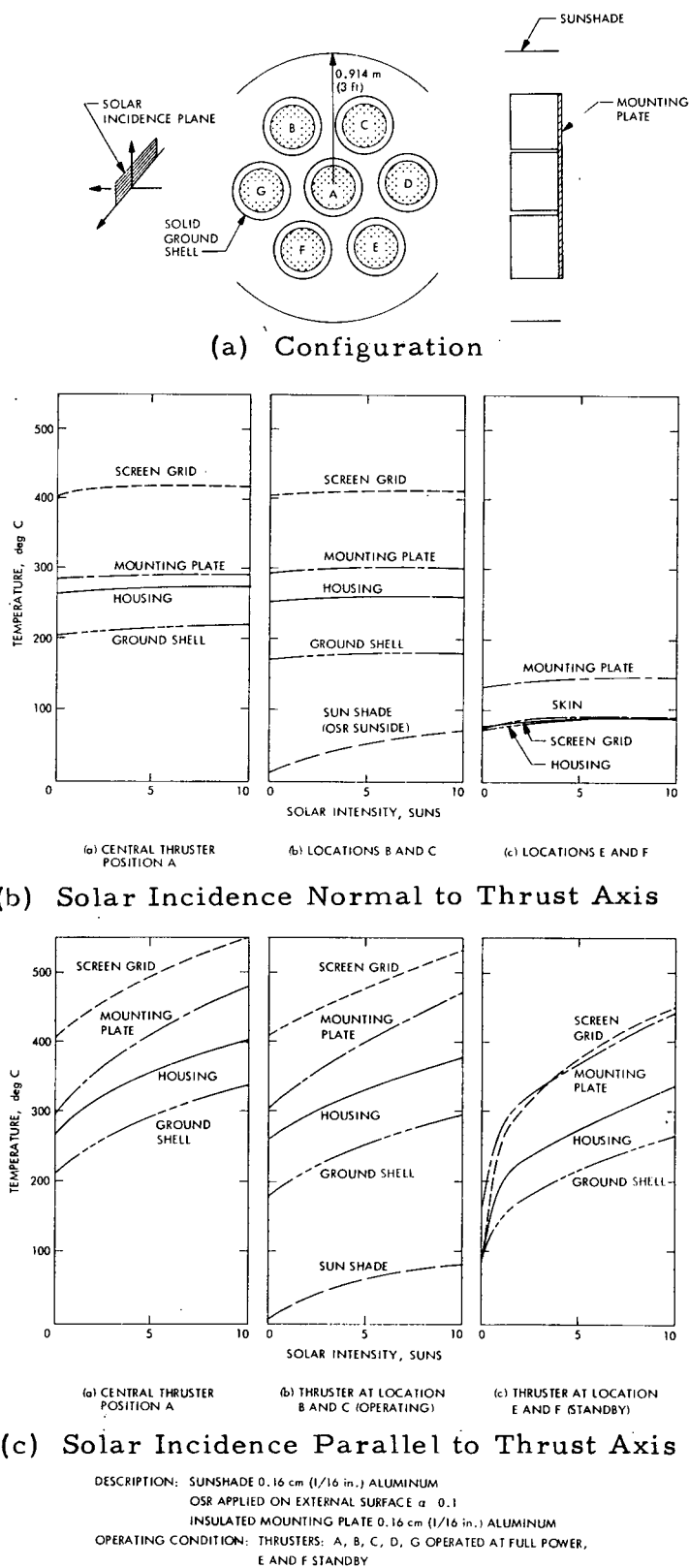
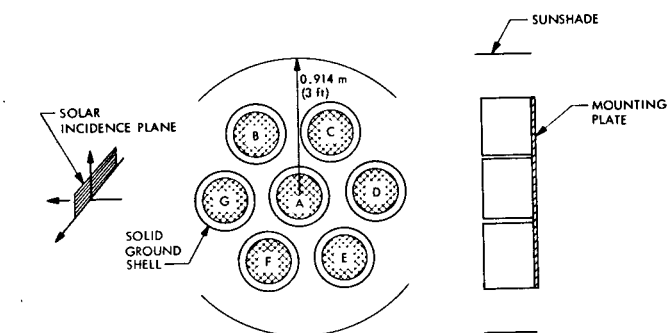
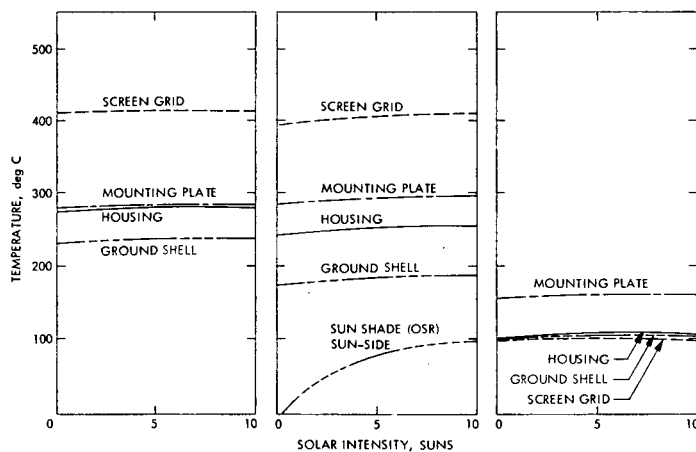


Fig. III-D-3. Sunshade Arrangement with Solid Ground Shell



(a) Configuration

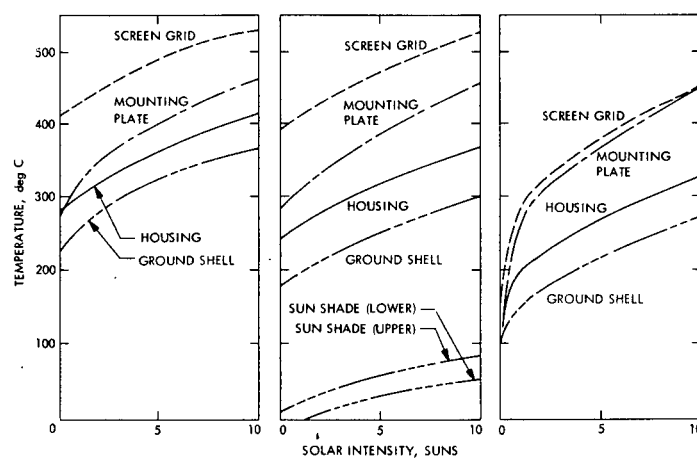


(a) CENTRAL THRUSTER
POSITION A

(b) POSITIONS B AND C

(c) POSITIONS E AND F

(b) Solar Incidence Normal to Thrust Axis



(a) CENTRAL THRUSTER
POSITION A

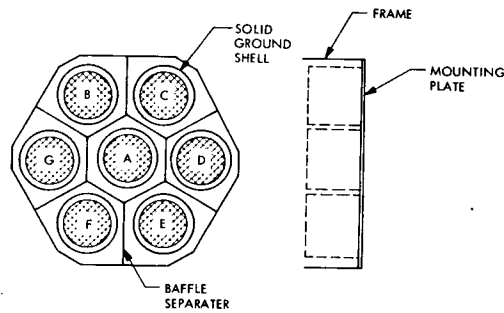
(b) POSITIONS B AND C

(c) POSITIONS E AND F

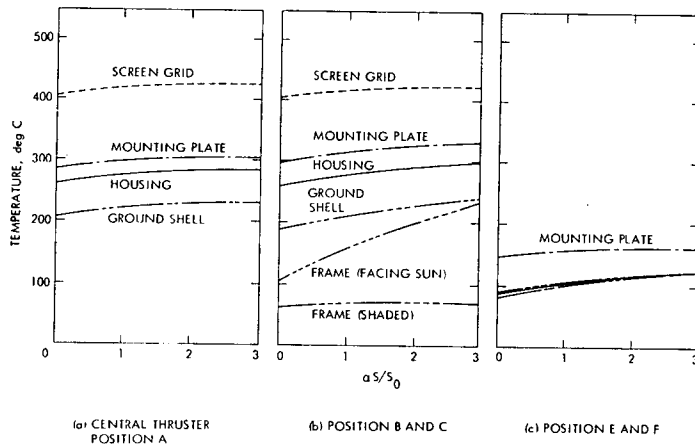
(c) Solar Incidence Parallel to Thrust Axis

DESCRIPTION: SUNSHADE 0.16 cm (1/16 in.) ALUMINUM
OSR APPLIED ON EXTERNAL SURFACE $\alpha=0.1$
INSULATED MOUNTING PLATE 0.16 cm (1/16 in.) ALUMINUM
OPERATING CONDITION: THRUSTERS: A, B, C, D, G OPERATED AT FULL POWER,
E AND F STANDBY

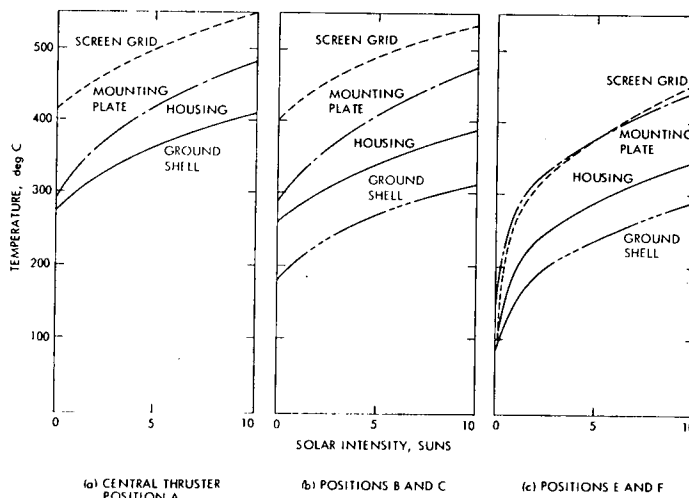
Fig. III-D-4. Sunshade Arrangement with Perforated Ground Shell



(a) Configuration



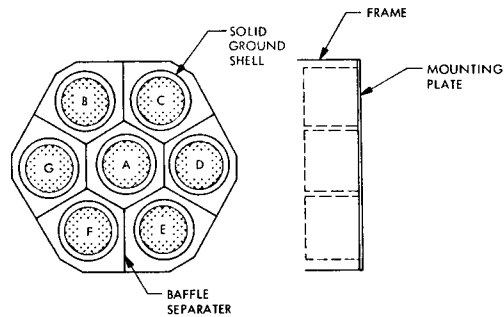
(b) Solar Incidence Normal to Thrust Axis



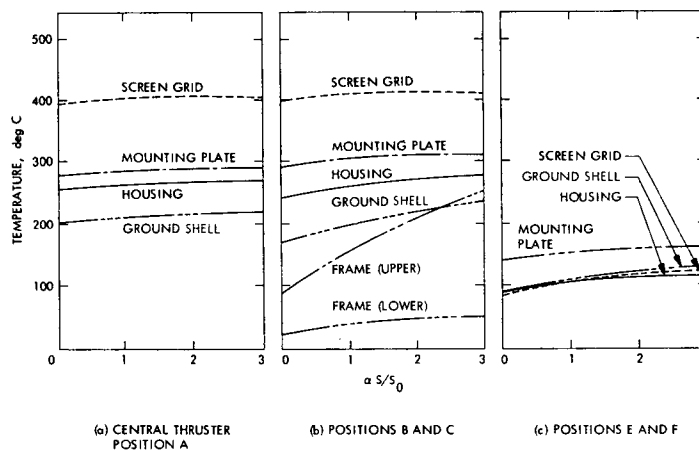
(c) Solar Incidence Parallel to Thrust Axis

DESCRIPTION: FRAME AND BAFFLE SEPARATOR 0.16-cm (1/16 in ALUMINUM)
INSULATED MOUNTING PLATE
OSR OR Z-93 WHITE PAINT APPLICATION ON FRAME
OPERATING CONDITION: THRUSTER A, B, C, D, G OPERATOR FULL POWER
E AND F STANDBY

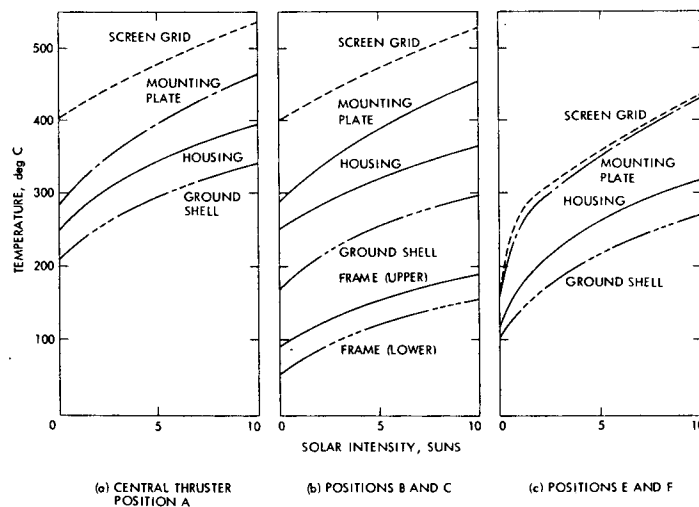
Fig. III-D-5. Thruster Array with Baffle Separator and Shading Frame with Solid Thruster Ground Shell



(a) Configuration



(b) Solar Incidence Normal to Thrust Axis



(c) Solar Incidence Parallel to Thrust Axis

DESCRIPTION: FRAME AND BAFFLE SEPARATOR 0.16-cm (1/16 in ALUMINUM)
 INSULATED MOUNTING PLATE
 OSR OR Z-93 WHITE PAINT APPLICATION ON FRAME
 OPERATING CONDITION: THRUSTER A, B, C, D, G OPERATOR FULL POWER
 E AND F STANDBY

Fig. III-D-6. Thruster Array with Baffle Separator and Shading Frame with a Perforated Thruster Ground Shell

and to baffle the gimbal actuator units from possible contamination by sputtered molybdenum grid material. The extended frame surfaces also provide an additional radiative area to reject excessive heat dissipation generated in the thruster. The modified configuration is shown in Fig. III-D-7. It is assumed that the supporting frame assembly is made of 0.16-cm (1/16-in.) thick aluminum. The thruster array behavior for inbound missions (five-thruster operation at full power level) is shown in Fig. III-D-8 (a) and (b). It is obvious that, when the back surface of the thruster array is insulated, the overheating problem can not be solved by increasing the side radiator area alone. This is mainly because of the poor thermal coupling between the thruster and the supporting-frame radiator. One possible way to lower the thruster operating temperature is by the application of a heat pipe. Figure III-D-9 (a) and (b) illustrate the lowering of thruster component temperature levels by the application of 1.27-cm (1/2-in.) diameter heat pipes, which conductively couple the mounting plate and the frame radiator. The figure shows that mounting plate temperature can be maintained at a level such that the cathode vaporizer temperature can be controlled. A comparable fluid loop arrangement would have a similar effect.

When the spacecraft is at 3.5 AU, only one thruster is operated at half-power level. During the thruster low-temperature mode, the high emittance coating on the frame surfaces becomes undesirable. A louver arrangement may be needed to adjust the apparent surface emittance to prevent the mercury feedline and vaporizers from freezing and to satisfy other low temperature constraints. Figure III-D-10 (a) and (b) demonstrates the dependency of thruster temperature behavior as a function of the apparent emittance from the frame surface or louver area. Without the heat pipe and louver arrangement, the lower frame temperature may become as cold as -120°C . The paint coating may start to peel off at -85°C . If heat-pipe and/or fluid-loop arrangements are to be utilized, the application of a louver system becomes even more desirable because the working fluid may freeze at low temperature. However, it may be feasible to select a non-condensing, gas-controllable heat pipe to accommodate the wide operating temperature range. The fluid-loop system may have to stand by during the entire low-temperature mode.

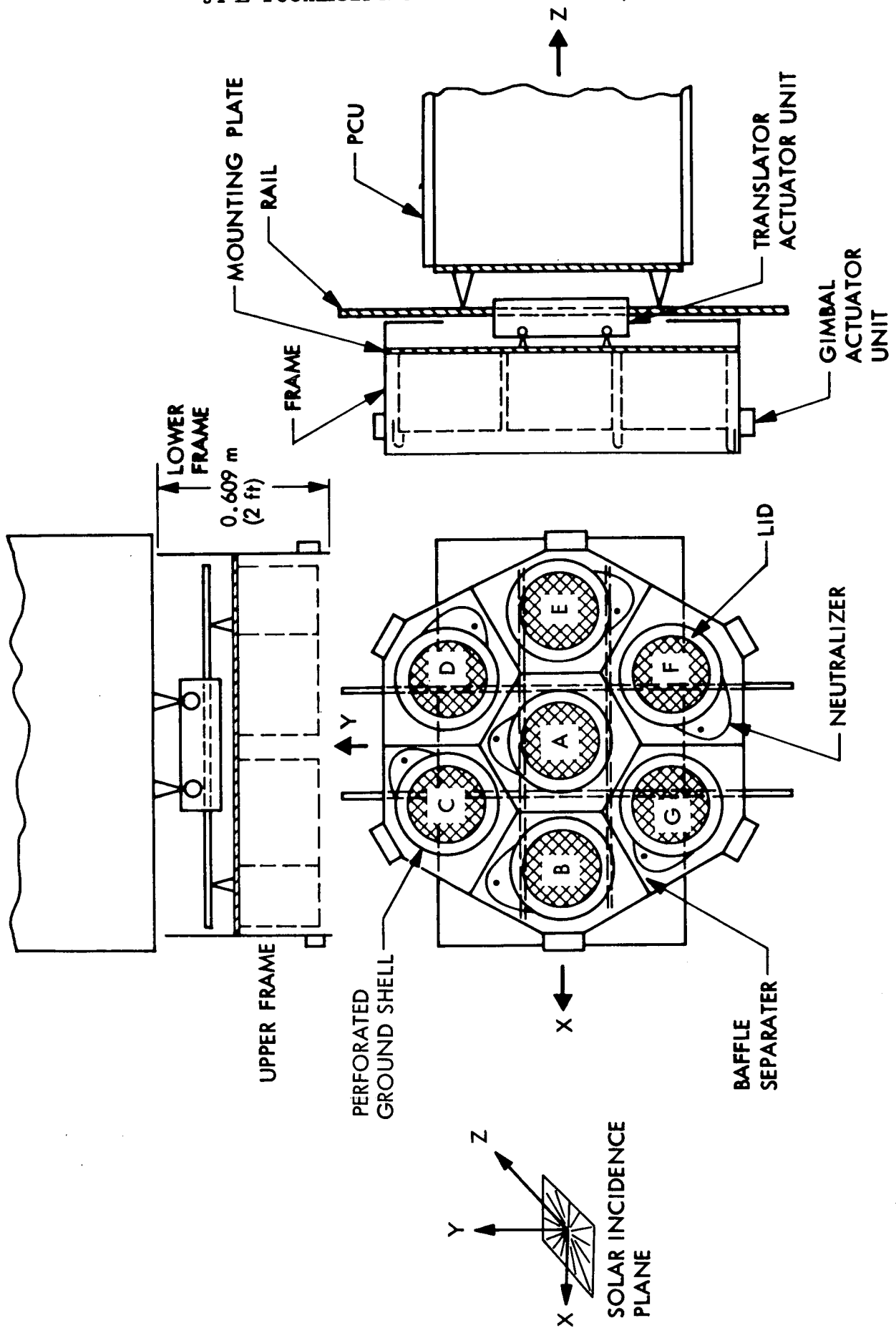
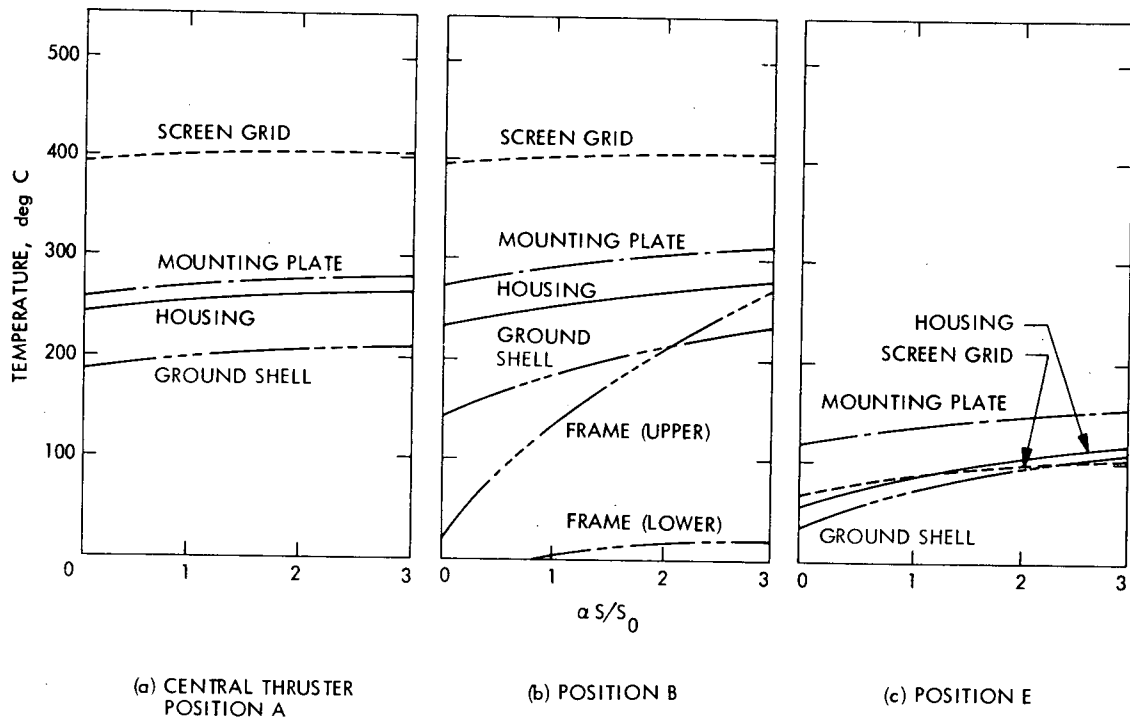
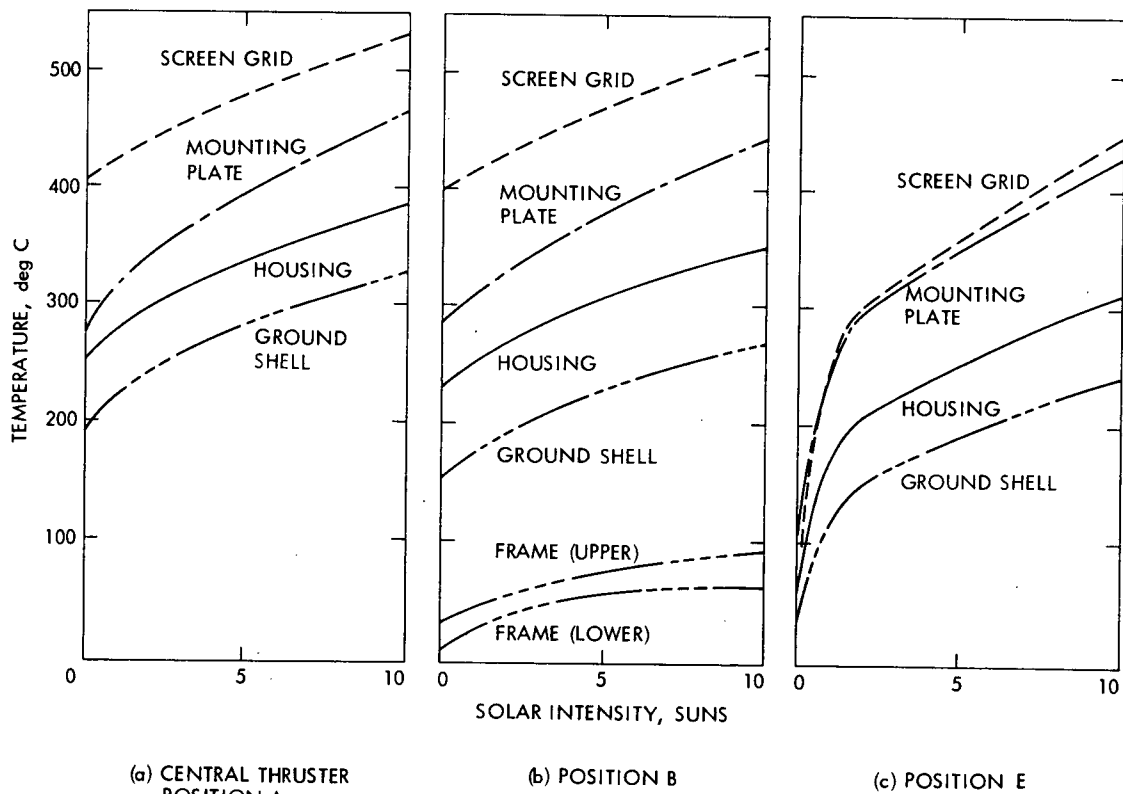


Fig. III-D-7. Basic Thruster-array Configuration

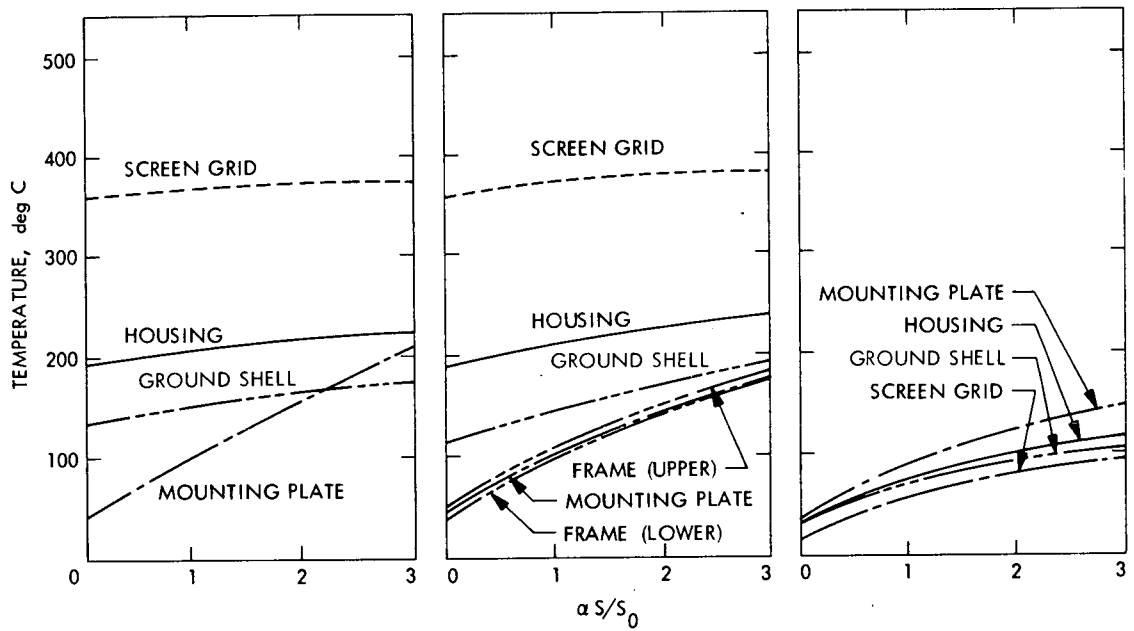


(a) Solar Incidence Normal to Thrust Axis



(b) Solar Incidence Parallel to Thrust Axis

Fig. III-D-8. Thrusters A, B, C, D, and G Operating at Full Power

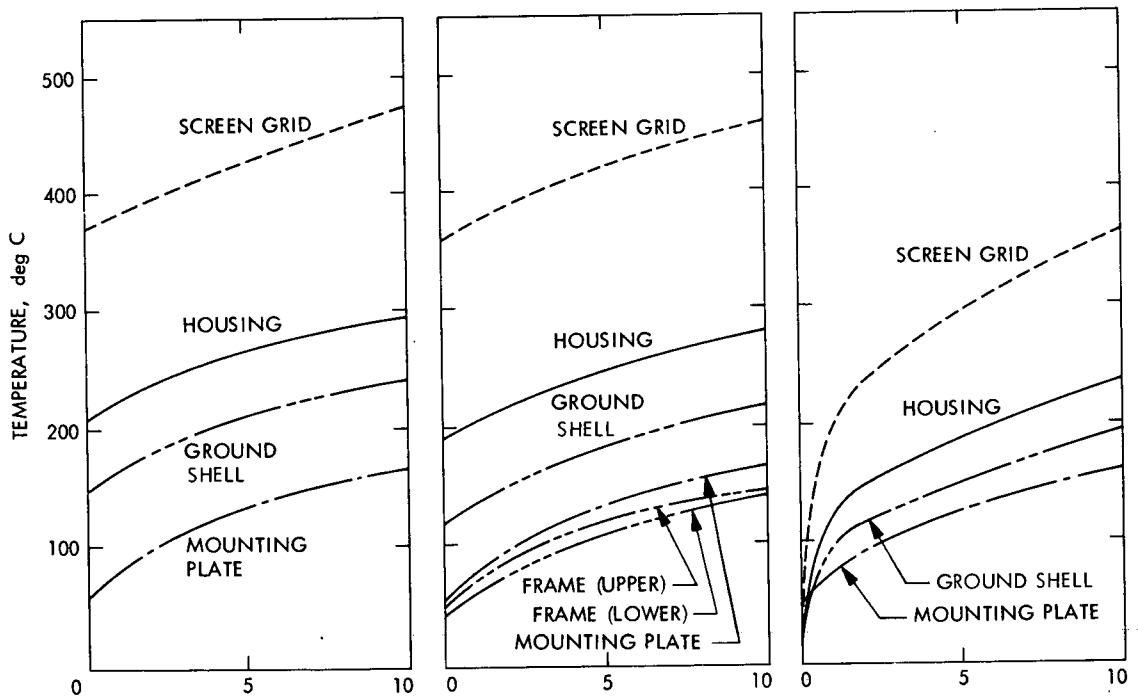


(a) CENTRAL THRUSTER
POSITION A

(b) POSITION B

(c) POSITION E

(a) Solar Incidence Normal to Thrust Axis



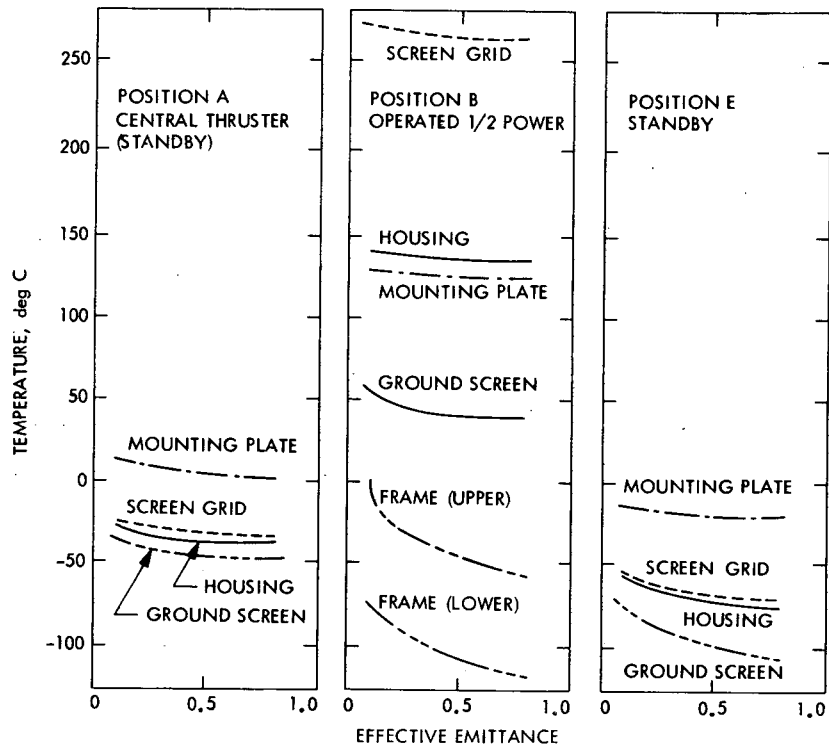
(a) CENTRAL THRUSTER
POSITION A

(b) POSITION B

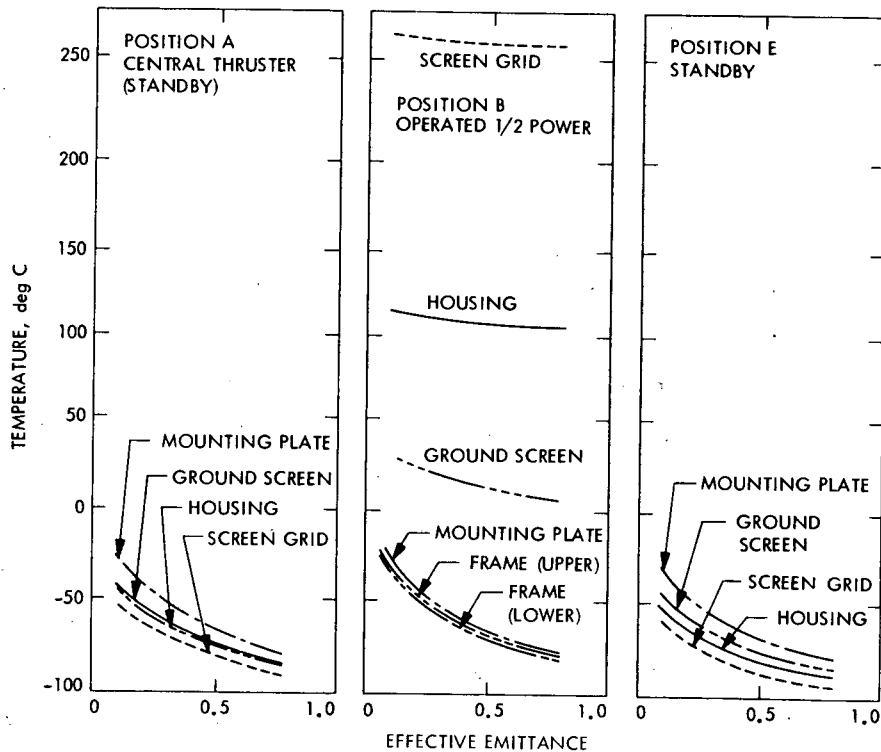
(c) POSITION E

(b) Solar Incidence Parallel to Thrust Axis

Fig. III-D-9. Thrusters A, B, C, D, and G Operating at Full Power, Heat Pipe Application



(a) Louver Applied



(b) Heat Pipe and Louver Applied

Fig. III-D-10. Thruster B Operated at One-half Power, No Solar Heating

5. Conclusions

- (1) When the mounting plate is insulated and has no additional thermal control devices, the thruster will overheat during full power operation even in a no-sun environment.
- (2) A radiator surface combined with a heat pipe/fluid loop is required to maintain thruster controllability in inbound missions, when the mounting plate is insulated. A louver configuration or system which can be jettisoned in an environment of high solar irradiance should be considered to accommodate the need of variable surface emittance for the extreme heat-load variation imposed by SEPSIT Encke mission.
- (3) The constraints associated with an insulated mounting plate appear to be undesirable because the application of a heat pipe/fluid loop would increase the weight and the uncertainties concerning performance reliability. Table III-D-1 gives an estimate of the additional weight requirements for several configurations discussed in the present investigation.
- (4) The following areas are crucial to the temperature control of the thruster subsystem and require further detailed investigations:
 - (a) Detailed experimental and analytical study of the thermal characteristics and the performance of the specified 30-cm diameter thruster.
 - (b) Establishment of definitive thermal constraints on all thrust-subsystem components.
 - (c) Experimental investigation of the thruster-array assembly under a realistic environment simulation, in particular, the effects of solar irradiance level and angle of incidence.
 - (d) Detailed investigation of thermal interactions between thruster array and related subsystem elements, such

Table III-D-1. Estimated Additional Weight for Thermal Control Arrangements

Components	Weight kg (lb)	Basic Array	Basic Array + Extended Sunshade	Basic Array + Sunshade + Heat Pipes	Basic Array + Fluid-Loop Assembly
Mounting Plate					
(a) 0.08 cm (1/32 in.) thick	5.0 (11)				
(b) 0.16 cm (1/16 in.)	10.4 (23)		x	x	
Frame 20.32 cm (8 in.) wide					
(a) 0.08 cm (1/32 in.)	2.3 (5)				
(b) 0.16 cm (1/16 in.)	4.5 (10)	x	x	x	
Sunshade 40.64 cm (1/16 in.)					
(a) 0.08 cm (1/32 in.)	4.5 (10)				
(b) 0.16 cm (1/16 in.)	9.0 (20)		x	x	
Baffle-Separator					
(a) 0.08 cm (1/32 in.)	1.6 (3.5)				
(b) 0.16 cm (1/16 in.)	3.2 (7)	x	x	x	
Fluid Loop Heat Exchanger					
(a) single layer	22.7 (50)				x
(b) double layer	40.8 (90)				
Pump Assembly	4.5 (10)				x
Heat Pipe	9.0 (20)			x	
Full Louver	10.0 (22)		x	x	x

as the power conditioning units and the control mechanisms. The investigation should aim at a feasible configuration with a proper integration scheme that would accommodate all the component thermal constraints and that would not require insulation of the mounting plate.

REFERENCES

- III-D-1. L. Wen, D. Crotty, and E. V. Pawlik, Ion Thruster Thermal Characteristics and Performance, AIAA Paper 72-476
- III-D-2. L. R. Kelley, et al, Damage of Thermal Control Coating Properties by Energetic Mercury Ion Bombardment, AIAA Paper 72-445.
- III-D-3. R. F. Kemp, et al, Effects of Electrostatic Rocket Material Incorporated on Solar Cells, AIAA 72-447.
- III-D-4. D. F. Hall, and H. Green, Erosive and Chemical Effects of Energetic Mercury Ions Bombarding Spacecraft Surface Material, AIAA Paper 72-446.

E. THRUST VECTOR CONTROL TRADEOFF STUDY

1. Introduction

In keeping with the major SEPSIT objective for FY'72 of establishing the functional specifications for the electric propulsion subsystem, a tradeoff study of the various thrust vector control (TVC) concepts was undertaken. The following four areas were selected for investigation:

- (1) JPL translator-gimballing concept.
- (2) TRW gimballing-twisting concept.
- (3) NASA-LeRC electrostatic gimballing concept.
- (4) NASA-LeRC electrostatic-mechanical gimballing concept.

The study was concentrated on the translator-gimballing and TRW gimballing-twisting designs because the other two designs are in the conceptual stage and will require new technology for implementation, whereas the concepts selected for study can be implemented by existing technology. Furthermore, the translator-gimballing design exists in actual hardware form and is currently being used in the SEPST program. No engineering model of the gimballing-twisting design has yet been built.

It may be argued that comparison between an actual piece of hardware and a mere concept is impossible and that such comparison invites inevitable bias. An attempt has been made to circumvent this problem by hypothesizing certain characteristics for the gimballing-twisting approach, thus providing a firmer basis for comparison. As an example, although no electronic circuitry for this scheme is available, an attempt has been made to approximate its complexity and general nature. On comparison with the existing translator-gimballing circuitry, the conclusion favors the gimballing-twisting approach on the basis of simplicity of design. However, modifications of the translator-gimballing design could reduce its electronics to a level compatible with that hypothesized for the gimballing twisting model.

Despite the attempt to establish a firm basis for comparison, one conclusion in favor of the translator-gimballing concept is inescapable, i.e.,

that building an engineering model of the gimbaling-twisting concept and bringing it up to the level of testing reached for the translator-gimbaling concept will be expensive and time consuming.

2. Conclusions

After detailed examination of the two concepts, a conclusion favoring the JPL design was reached. Tables III-E-1 through III-E-3 lists some of the pros and cons of the two designs. Substantial detail verifying these comments appears in subsequent sections. It should be remembered, however, that additional work needs to be done to flight-qualify either design.

3. Description of TVC Concepts

a. General Discussion

In the SEPSIT context, TVC refers to controlling the spacecraft attitude by adjusting the electric-propulsion thruster-array thrust vector. This adjustment produces a torque about the spacecraft mass center and the consequent response is a change in vehicle orientation. Figure III-E-1 is a conceptual version of the general spacecraft configuration. The solar arrays are denoted A, the spacecraft bus is B, and the thruster array is T. Axes x, y, z are the pitch, yaw, and roll axes, respectively. The vehicle is shown for an ideal situation where A is normal to the sun line and the thrust vector lies in the plane normal to the sun line. Such an attitude can not be maintained throughout the course of a mission as periodic reorientation of the thrust vector is required for guidance purposes. This study does not include the solution to this problem. Various schemes for doing this have suggested gimbaling the thruster array, gimbaling celestial sensors, or articulating the solar arrays or some combination of the three.

For the purpose of conducting the comparison between the translator-gimbaling and the gimbaling-twisting TVC concepts, the thrust vector reorientation problem need not be considered because it is believed that the problems encountered in solving the reorientation problem will be similar in nature for both concepts. As an example, if the thruster array gimbaling

Table III-E-1. Comparisons Based on the Basic TVC Attitude Control Function

	Translator-gimballing TVC Concept	Gimballing-twisting TVC Concept
Canting	No canting No thrust loss No higher thrust level No additional power Initial unbalance torque for unsymmetric thrust configuration compensated for by translation No thrust vector reorientation for unsymmetric thrust configuration No need to reorient thrust vector or solar arrays No celestial sensor bias No need to know mass center location exactly No gimballing required for mass center shifts Distance between mass center and thruster array not important Large roll or yaw torque requires large translation	Approximately 9° through mass center Approximate 1.2° thrust loss Higher thrust level required Higher power to provide higher thrust No unbalance torque for unsymmetric thrust configuration Thrust vector reorientation required for unsymmetric thrust configuration Possible lower solar power level due to reorienting thrust vector Celestial sensor bias required to establish new null position Mass center location needs to be known Gimballing required to compensate for mass center shifts Long separation between mass center and thruster array Large roll or yaw torque obtained with small gimbal angle
Lateral Thrust	No lateral thrust in roll or yaw control No need to compensate for lateral thrust	Lateral thrust in roll or yaw control Increased electronics complexity to compensate for lateral thrust
Cross Coupling	Third order coupling No pitch axis coupling	Second order coupling Coupling in all three axes
Failure Modes	Failure of a gimbal actuator not catastrophic No current redundancy for translator actuators. Possible redundancy using gimbal actuators	Failure of twist actuator is catastrophic. No redundancy provided No current redundancy for gimbal actuators
Other	Tail-wags-dog effect not a problem Heavier mechanism. However, has redundancy Feed-line and power-cable-line problems equivalent	Tail-wags-dog effect not a problem Lighter mechanism. Has no redundancy Feed-line and power-cable-line problems equivalent

Table III-E-2. Comparisons Based on the TVC Actuator Designs

Current Translator-gimballing Baseline Design	Gimballing-twisting Design
Requires 2 different designs, 6 gimbal actuators, 2 translator actuators	Requires single actuator design. Requires 3 JPL design gimbal actuators. No translator actuator designs
All concepts of the configuration built and life tested (proven design)	Design complete only, no hardware.
Uses ball bushings and rails (conventional)	Uses multiple flexible pivots (conventional)
May require bellows covers on rails for space environment	Flexure pivots can withstand space environment
Tortuous path feedline and power cable design - Larger motions (qualified design)	Tortuous path feedline and power cable design. Small motions involved
Simpler launch environment design. Stiffer system Single simple caging, low height	Complicated launch environment design inherently less stiff. Multiple caging, more height
Resultant motion straightforward	Uncertainty in resultant motion (cross-coupling)
Maximum redundancy a) Each engine gimbals independently b) Gimbal motion could provide backup for translational motion	No redundancy - motion for all engines fail/axis
More easily adaptable to changes in configuration (i.e., number of engines required)	Less adaptability
Few moving parts (fewer moving parts when caging is accounted for)	Few moving parts
Weight somewhat known based on hardware (some-what dependent on launch environment design)	Weight unknown - could be greater when caging (launch environment) accounted for

Table III-E-3. Comparisons Based on the TVC Electronic Design

Parameter	Translator-gimballing	Gimballing-twisting
Basic control problem	Same for both systems	Same for both systems
Gain change in pitch axis	Not required because only two motors gimballled at a time	May be required because all 6 motors on the perimeter are gimballled
Electronic control of cross axis coupling	Can probably be ignored in both systems (i.e., small translations or gimballing)	Can probably be ignored in both systems (i.e., small twist or gimballing)
Mode switching for pitch axis control	Sophisticated electronics required to choose which of 3 couples to use for control	No switching required because all engines gimballled by one actuator
Pitch axis gimbal skewing	Requires special circuitry to realign gimbal couple	No skewing inherent in this design - gimbals mechanically linked
Reliability	The increased parts count and electronic sophistication of the JPL design invites reliability problems. However, approximately one half of the electronics is unique to gimbal couples, therefore offering redundancy in case of a failure	Reliable because there is no more switching. However, there is no redundancy in case of an electronic or mechanical failure

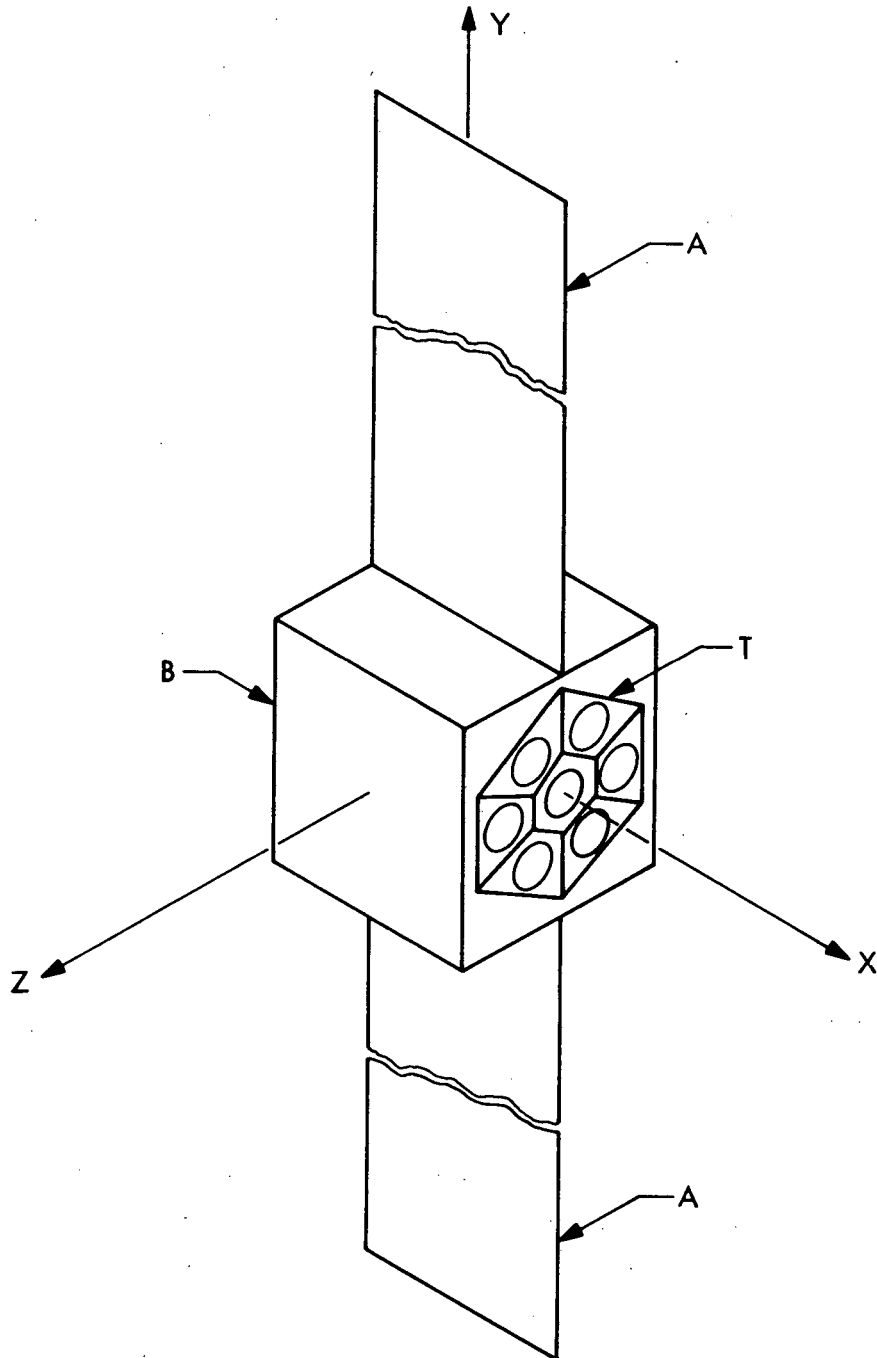


Fig. III-E-1. SEP Spacecraft

idea is adopted, the the scheme for implementing the idea could be identical for both designs.

The thruster array, T, consists of seven 30-cm thrusters arranged so that six of them are placed at 60-deg intervals about a center thruster (see Fig. III-E-2). The distance separating engine centers is d. The thrust profile for the Encke mission established that any number of thrusters from one to five may be operating for a given time during the mission. Thus, two of the seven thrusters serve as backups.

The attitude control function is provided only in part by TVC. A conventional N_2 gas system (ACS) is also available. For acquisition, gross maneuvers during encounter, and occasions when the ACS deadbands are exceeded, then a conventional N_2 gas system is used. There are no TVC deadbands. A hybrid attitude control mode is anticipated for the condition when only one thruster is operating. As will be demonstrated in this section, III-E-5, for this one thruster situation, pitch axis TVC is unattainable. Hence, the ACS pitch jets must be used in conjunction with the TVC roll and yaw control for three axis control.

b. TRW Gimballing-twisting TVC Concept

TRW has gone through several design iterations. The twisting-gimballing concept was presented to JPL personnel in May 1971. Discussions with TRW personnel in February 1972 revealed that no changes have been made since the presentation last year.

Figures III-E-3 and III-E-4 show the thruster array. Six thrusters arranged in a circular pattern are shown. In the following discussion, a seventh thruster at the center of the array has been hypothesized to conform with current SEP space vehicle design. Failure to provide a center thruster implies only one redundant thruster. All of the six outer thrusters are mounted to a gimbal ring in such a way that the thrust axis of each is canted to the pitch axis by an angle of 9 deg. The intent is to orient each thruster so that its

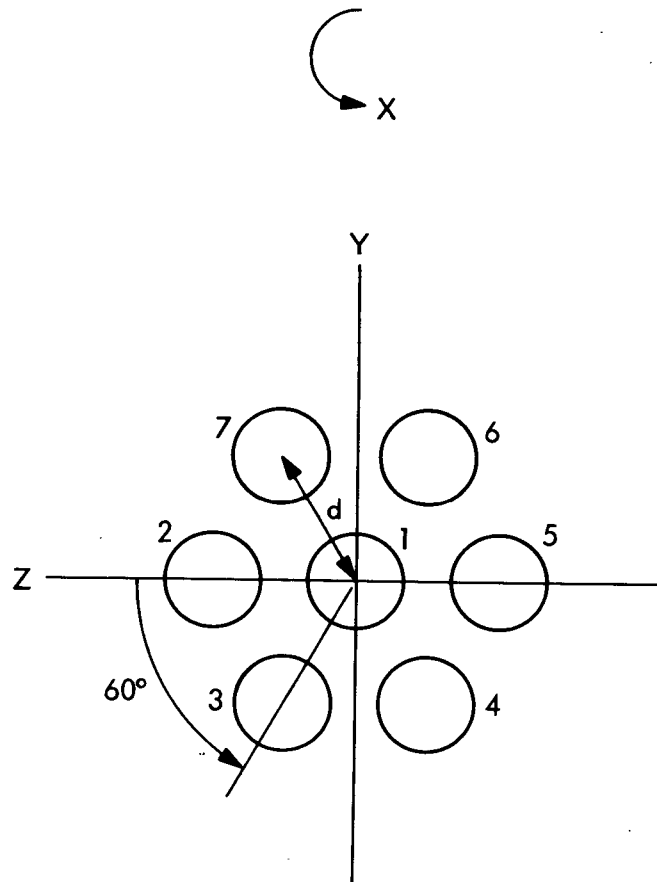


Fig. III-E-2. Thruster Array

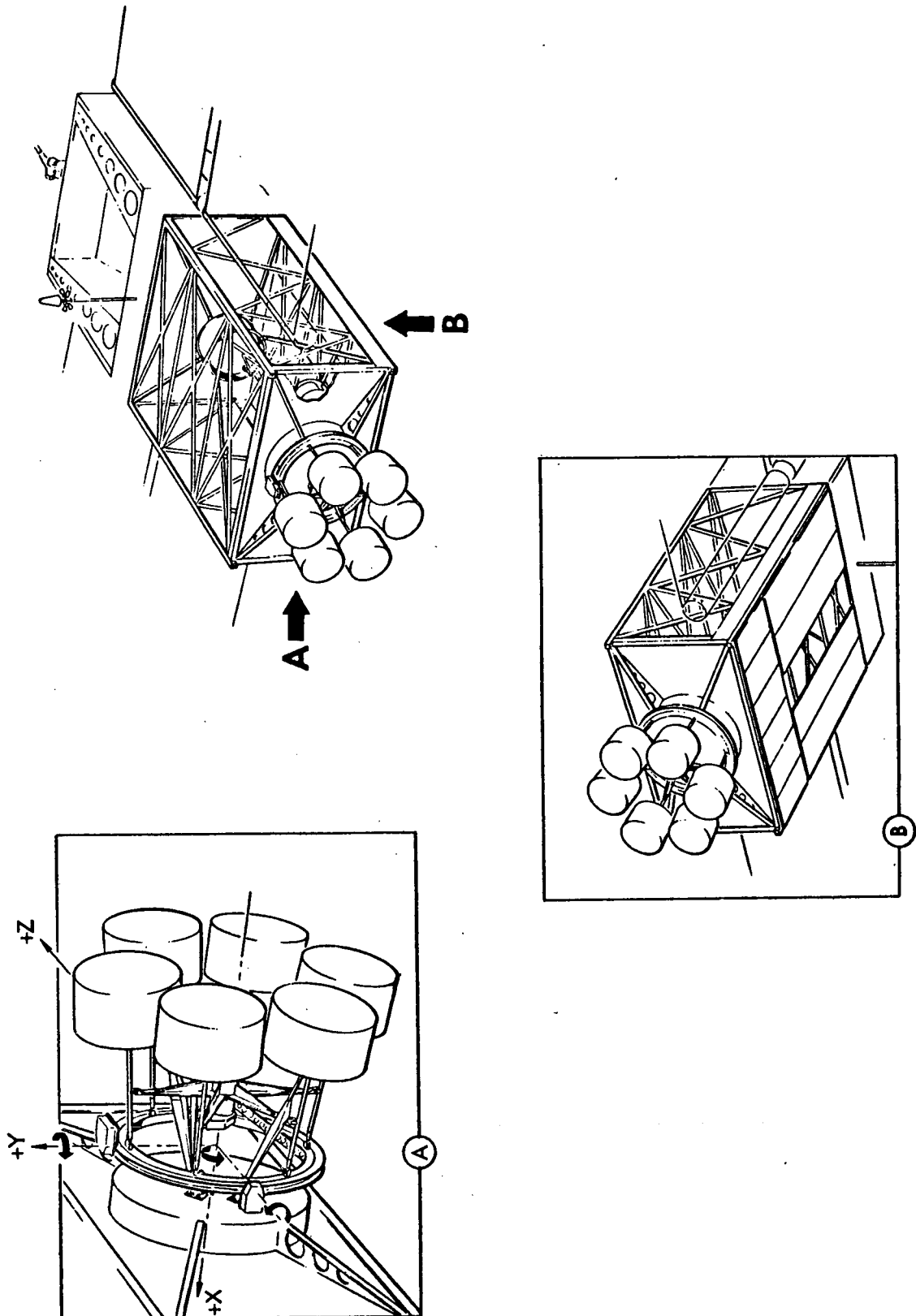


Fig. III-E-3. TRW Electric Propulsion Module

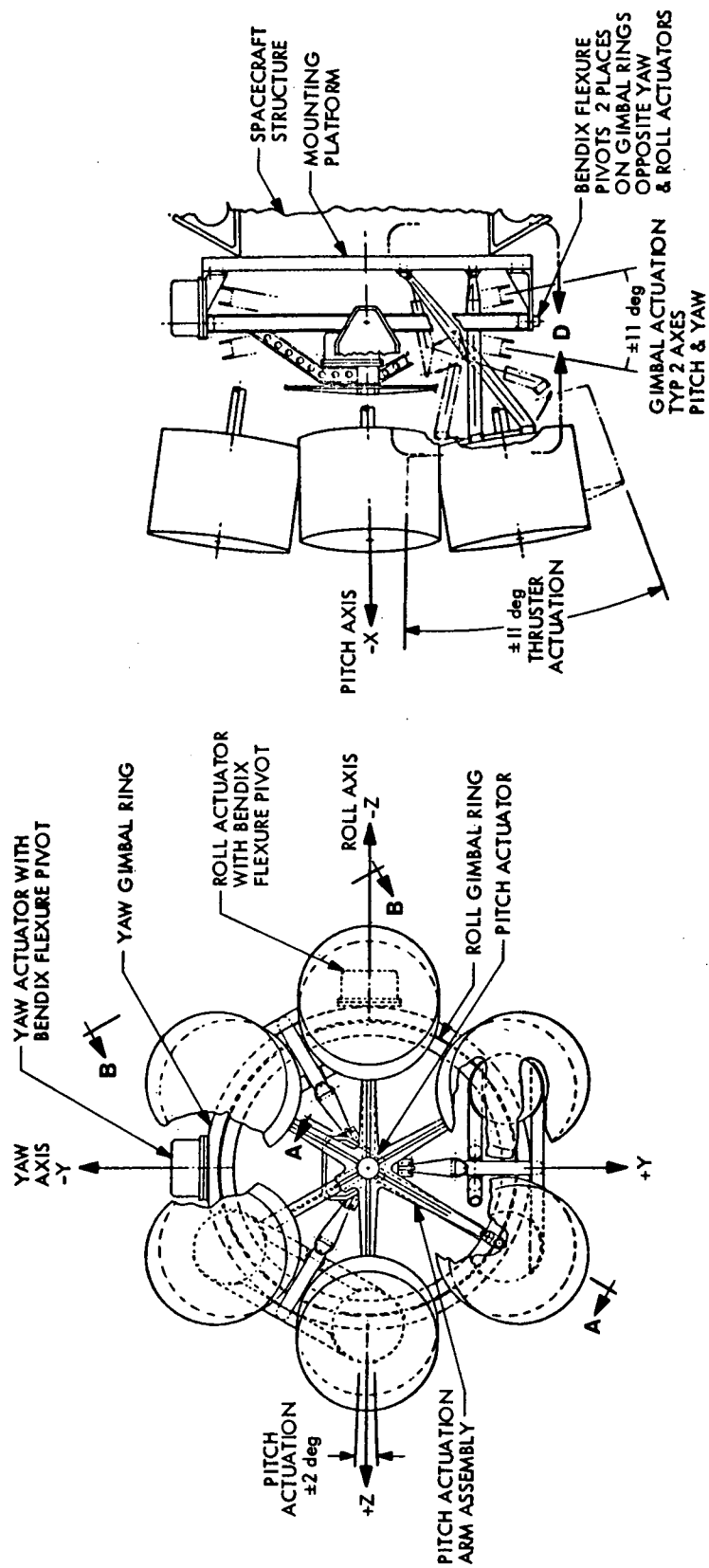


Fig. III-E-4. TRW Thrust Vector Control Actuator System and Retention Mechanism

thrust vector nominally points through the vehicle mass center. Hence, for unsymmetrical thrusting situations, no unbalance moment is exerted. The canting concept has the weaknesses that (1) the vehicle mass center must be known precisely, which is rarely the case, (2) the mass center must be far from the thruster array, and (3) canting through 9 deg means a 1.2% loss of thrust.

Figure III-E-3 shows six rods connecting the bases of the thrusters to an inner gimbal ring. Each rod is joined to the gimbal ring by means of two flexure pivots. Rigidly attached to the inner gimbal ring is a structure supporting the twist actuator whose output shaft parallels the pitch axis. It drives a six-pointed star-shaped structure, the arms of which are joined to the thruster support rods by means of double flexure pivot joints. Rotation of the twist actuator has the effect of reorienting the thrust vectors so that, for opposing pairs of thrusters, equal but oppositely directed force components tangential to the circle joining thruster centers are exerted on the vehicle (Fig. III-E-5). This system of forces has zero resultant force but non-zero moment about the CG and parallel to the pitch axis. Thus, pitch control is provided.

Roll and yaw control are achieved by more conventional means. Close scrutiny of Fig. III-E-3 shows both an outer and inner gimbal ring. The outer ring is driven by an actuator which is fixed to the spacecraft bus. The output axis of the actuator is parallel to the roll axis. In the absence of twist actuation or motion of the inner gimbal ring, outer gimbal ring rotation reorients the resultant thrust vector so that it no longer passes through the roll axis. Consequently, a roll moment is exerted on the vehicle.

Rigidly attached to the outer gimbal ring is an actuator, identical to the ones which drive the outer ring and provide twist, and which have an output axis parallel to the intersection of the outer gimbal ring plane and the pitch-yaw plane. For zero rotation of the outer ring, this axis is parallel to the yaw axis. If, furthermore, there is no twist, then rotation of the inner gimbal ring reorients the resultant thrust vector so that it no longer passes through the yaw axis. A yaw moment is thus produced.

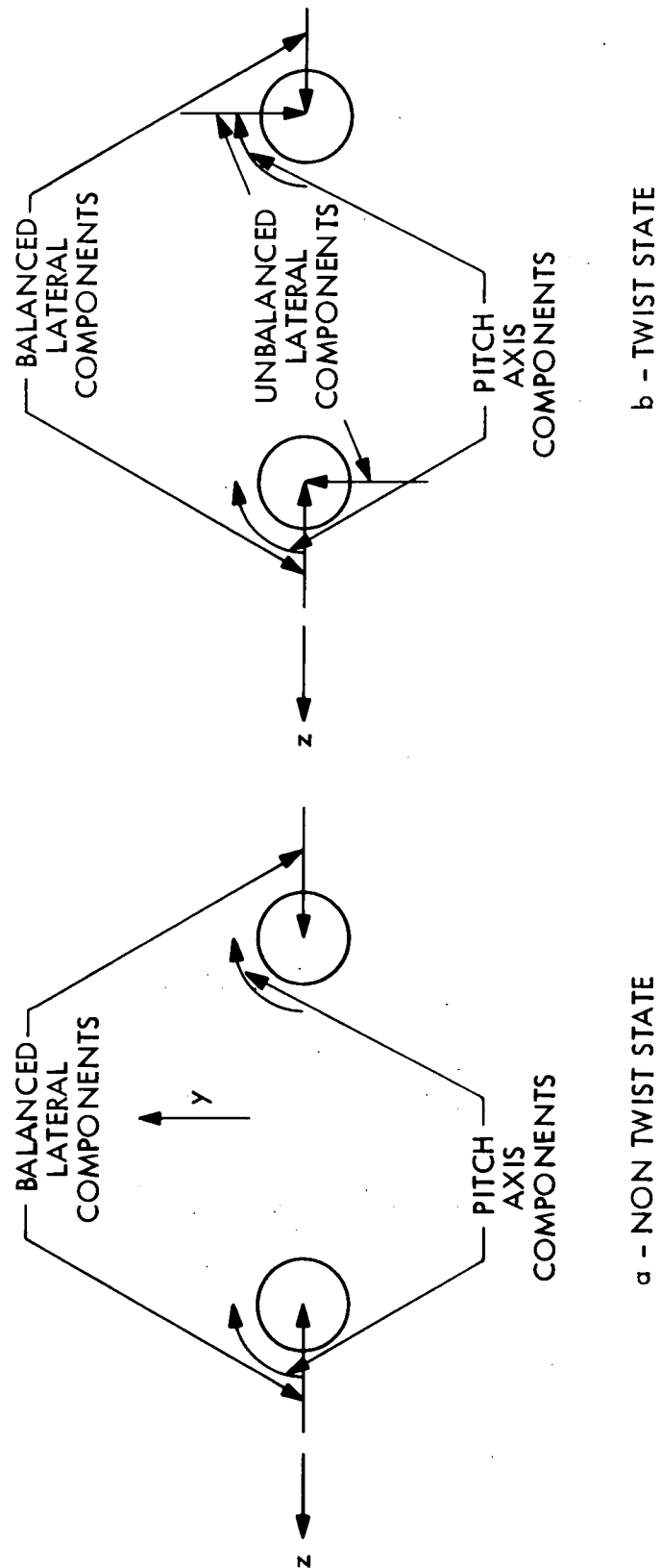


Fig. III-E-5. Pitch Control

It is seen that either twist, or outer gimbal or inner gimbal actuation produces either a pitch, or a roll, or a yaw motion. In the event that all three occur simultaneously, then for small twist and gimbal angles, the linearized attitude-moment equations show that independent three-axis control is achieved. For large angles, however, coupling occurs between the three axes; i.e., the effects of any one of the three types of actuation are felt as attitude moments in all three axes. This will be commented on in detail later.

The actuators for the twist-gimballing concept are identical to the gimbal actuators used for the JPL design; i.e., a stepper motor together with flexspline and/or conventional gear reduction is used.

c. JPL Translator-gimballing TVC Concept

Figure III-E-6 shows the thruster configuration for the JPL concept. Six outer thrusters are arranged symmetrically in a hexagonal frame about a center thruster. The plane of the frame is parallel to the roll-yaw plane. For the situation where no attitude control moments are required, the thrust direction for each thruster is parallel to the pitch axis.

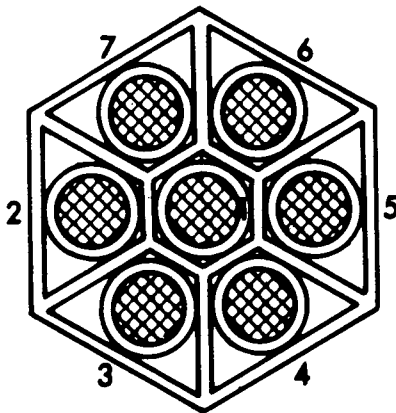


Fig. III-E-6. JPL Thruster Configuration

As the design currently stands, each outer thruster is provided with an actuator which permits it to rotate about an axis joining the

thruster center with the thruster center of the symmetrically placed thruster. For example, the two thrusters 2 and 5 can rotate about an axis parallel to the roll axis. The design is such that symmetrically placed thrusters rotate (or gimbal) by equal amounts, but in opposite directions. Each thruster then exerts a lateral thrust component on the vehicle. The lateral components for symmetrically placed engines will have zero resultant force. However, a non-zero couple is exerted on the vehicle about the pitch axis in a way analogous to that described for the twisting motion in the previous design. It is apparent that pitch control can be obtained with two thrusters, whereas there is no control over the number of thrusters participating in pitch control for the previous design. For that design, all operating outer thrusters contribute to pitch control. For the case when five thrusters operate, two pairs of outer thrusters may be used for pitch control. A negative feature of the JPL design is the electronic circuitry complexity required for switching gimbal actuator control from one pair of thrusters to another. Another drawback is that separate control over individual actuators increases electronics complexity. Figure III-E-7a shows the gimbal actuator. Stepper motors are used and motion is transmitted to the thruster by flexspline and conventional gear trains.

Roll and yaw control are obtained by translating the entire thruster array parallel to the yaw and roll axes, respectively. In translating parallel to the yaw axis, the resultant thrust vector remains parallel to the pitch axis and no longer passes through the roll axis. Consequently, a moment about the roll axis is generated. On the other hand, translation parallel to the roll axis dictates that the thrust vector no longer passes through the yaw axis and, hence, a moment about this axis is generated. Figure III-E-7b shows the translator actuator.

For the situation where simultaneous attitude control torques about the pitch, roll, and yaw axes are required, roll and yaw control are completely independent of each other. However, pitch and roll as well as pitch and yaw are coupled in a less severe manner than for the TRW design. In particular, coupling is a third order effect for the JPL concept and a second order effect for TRW. For small thruster gimbal angles, the linear equations show that independent three-axis control is achievable.

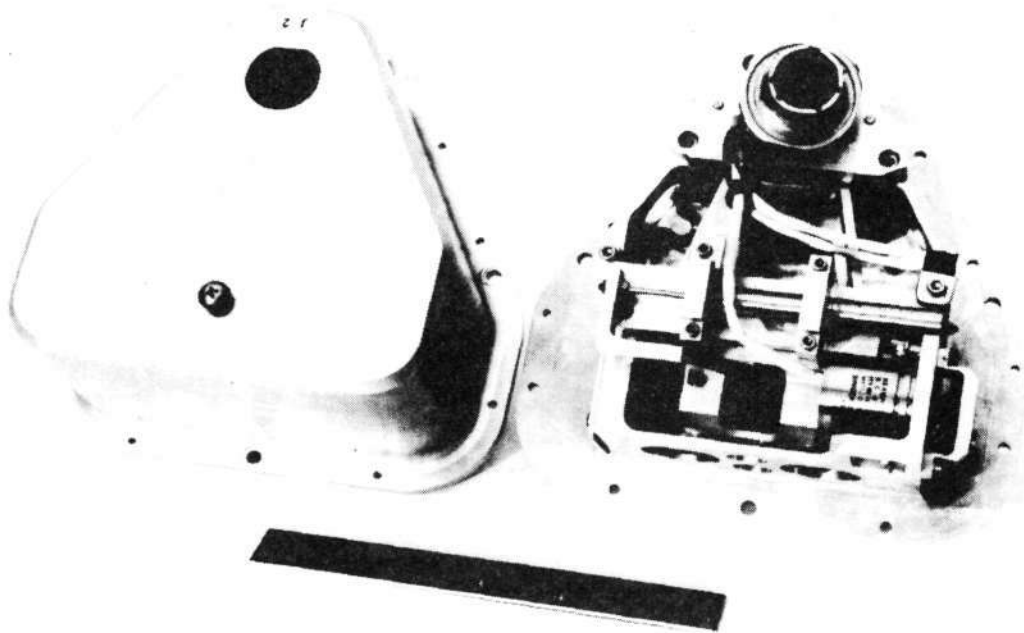


Fig. III-E-7a. Gimbal Actuator

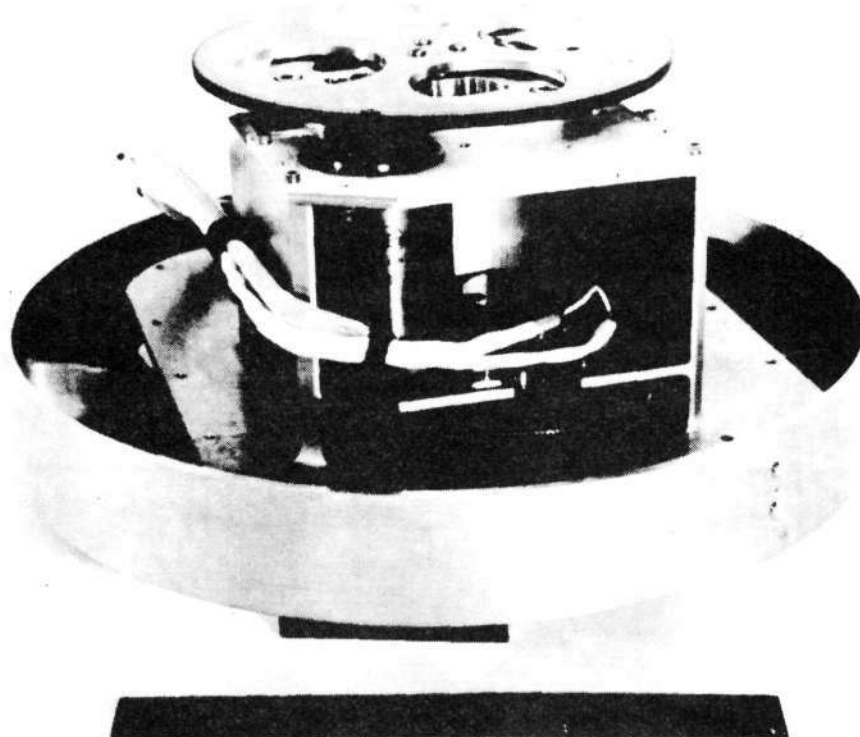


Fig. III-E-7b. Translator Actuator

Figure III-E-8 shows an artist's conception of the thruster array. For the translator control, the output motion of one actuator in the lower base is transmitted by gear reduction to a drum whose axis is fixed in the vehicle. Two bands have one end each fixed in the drum, are wrapped around it, and have the other ends attached to the lower base of the thruster array. When the stepper motor is activated, rotational motion of the output shaft is converted to translational motion of the lower base which is guided along steel rails fixed in the vehicle. Depending on whether the rails parallel the roll or yaw axis, translation parallel to the roll or yaw axis occurs. A second and similar actuator is mounted to the lower base and, through a scheme similar to that just described, translation motion is transmitted to the upper base at an orientation of 90 deg to that of the lower base. The upper base contains the thrusters.

Maximum stepper motor rate is 100 steps/sec and implies a maximum gimbal angle rate of 0.01 radians/sec and maximum translation rate of 0.0064 m/sec (0.021 ft/sec).

4. Detailed Comparison of Designs

a. Basic Attitude Control Function

1) Canting Effects. As mentioned, all except the center thruster on the gimbaling-twisting TVC design are canted at some small angle to insure that the thrust vector for each thruster nominally passes through the vehicle-mass center. The angle depends on the spacecraft configuration, and the 9-deg number quoted earlier is merely representative of a typical gimbaling-twisting TVC configuration. The thrust loss of 1.2% associated with canting can be significant for the type of long mission anticipated for the Encke rendezvous. This could mean that the thrusters may have to be designed to operate at a slightly higher thrust level than currently anticipated. The higher thrust level requires more power. On the other hand, there is no canting of the thrusters and no consequent thrust loss or higher power requirement on the translator-gimbaling TVC approach. It is apparent that the gimbaling-twisting TVC design demands a large separation of thruster array and spacecraft mass center. No such requirement is made of the translator-gimbaling TVC design.

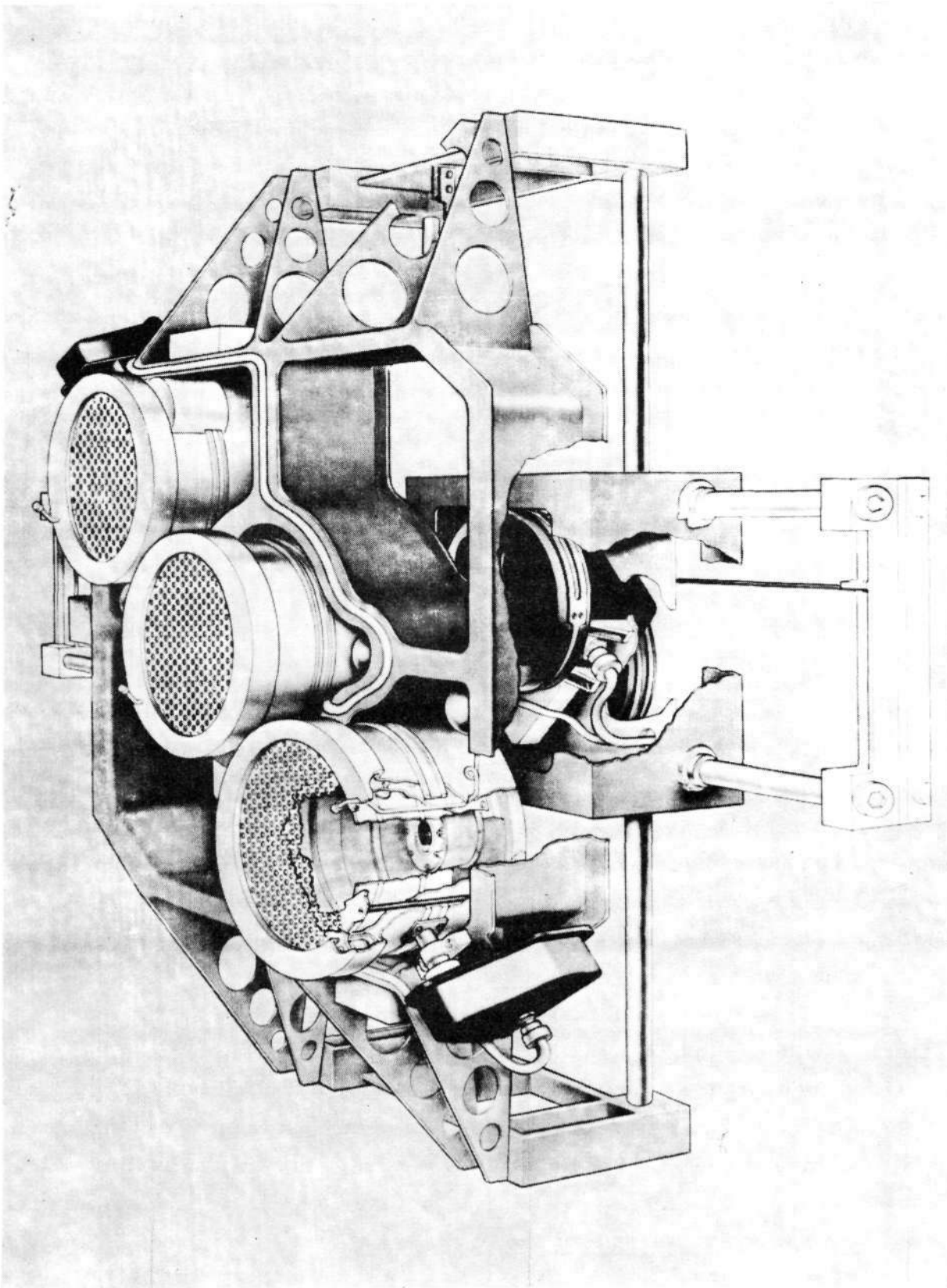


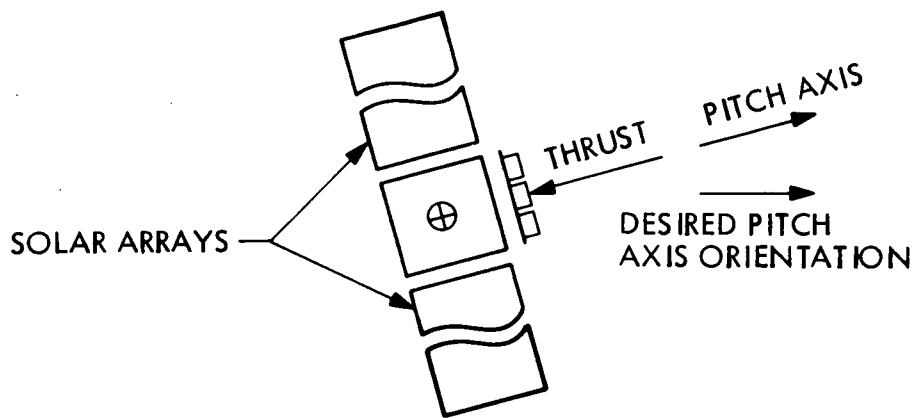
Fig. III-E-8. Thruster Array

The advantage of canting through the mass center is that regardless of how many engines are thrusting, there is no unbalance torque. However, for unsymmetric thrusting situations, thrust vector reorientation will be required for guidance purposes. For example, if three thrusters are required and all but thrusters 1, 2, 3 have failed, then the resultant thrust vector will deviate from that for a symmetric configuration, i.e., thrusters 1, 2, 5. Compensation must be provided for reorienting the spacecraft to maintain the appropriate trajectory and may result in some deviation of the solar arrays from the sun line and some power degradation. Furthermore, celestial sensors must be biased to establish this new orientation as the null configuration. No such difficulty arises for the translator-gimballing TVC design. Unsymmetric thrusting requires translating of the thruster array to a new location but no new spacecraft orientation. It should be observed for both the studied designs, and for the thruster failure mode case just cited, that pitch control through TVC is not possible, and the hybrid attitude mode must be switched on.

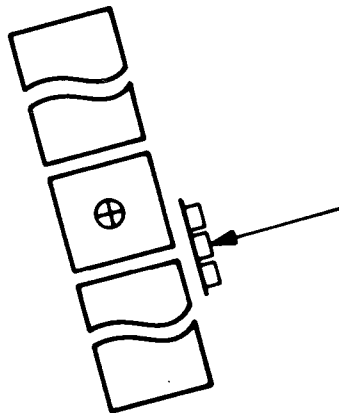
It should also be mentioned that the vehicle mass center location may not be precisely known. Furthermore, some variation of this location is anticipated during the course of the mission from such factors as depletion of mercury supply, and articulation of solar arrays or science instruments. For such mass center migration, the thruster on the gimballing-twisting array must be gimballed in roll and/or yaw to compensate for the resulting imbalance torque. The reorientation problem alluded to in the previous paragraph is again present.

In summary, mass center location is a critical factor in the gimballing-twisting design, whereas it is not a factor for the translator-gimballing design.

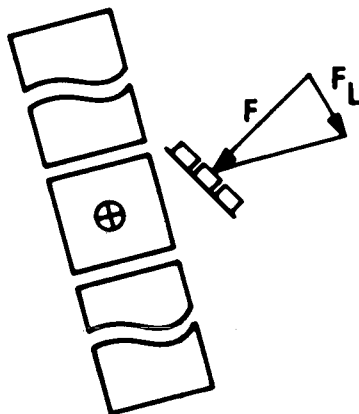
2) Lateral Thrust. For the cases where a roll and/or yaw torque is desired, lateral thrust is exerted on the spacecraft by TRW gimballing, whereas there is no lateral thrust for JPL translation. This can be understood by examining Fig. III-E-9. Figure III-E-9a shows the configuration to be corrected. Figures III-E-9b and 9c show how to accomplish this by the JPL and TRW schemes respectively. No lateral thrust component above that present



(a) Error State Prior to Reorientation



(b) JPL Reorientation Scheme



(c) TRW Reorientation Scheme

Fig. III-E-9. Reorientation Schemes

for the error state exists for the translator-gimballing design, whereas the additional lateral error force, F_L , exists for the gimballing-twisting concept. Over the course of a mission in excess of 900 days, such lateral errors could introduce guidance errors. TRW proposes a compensation scheme to solve the problem. Such additional complexity demands increased electronics complexity.

3) Cross Coupling. Examination of the nonlinear torque expressions in equations (26) and (32) developed for the TRW and JPL schemes respectively, indicates that second order coupling exists for the gimballing-twisting concept whereas only third order coupling exists for the translator-gimballing concept. Furthermore, for the gimballing-twisting design, yaw and roll gimballing is coupled into pitch axis control; pitch twisting, and roll gimballing is coupled into yaw axis control; and pitch twisting and yaw gimballing is coupled into roll control. On the other hand, for the translator gimballing design, there is no translation coupling into pitch axis control, only thruster gimballing coupling into yaw axis control, and only thruster gimballing coupling into roll axis control.

b. Actuators

At this point in time, the JPL design should be selected over the TRW design for two major reasons. The first is that the JPL design is a hardware-proven concept while the TRW design is still conceptual. All conceptual aspects of the JPL design have been built and are functional and life tested. The second reason is that the JPL design is more flexible in terms of adapting to spacecraft configuration changes, i.e., the number of thrusters required, gimbal angle increases, etc., and in terms of redundancy. The six separately gimballed engines allow for independent motion (one actuator failure fails only one thruster). Also, with proper programming, the gimbals could provide backup for a failed translator. If redundancy is not required, it is conceivable that, with simple linkage, the six gimbal actuators could be reduced easily to three gimbal actuators and, potentially, to one actuator. In terms of the mechanism, only the JPL design provides all of the functions of the TRW design while the reverse is not currently true.

c. Thrust Vector Control Electronics

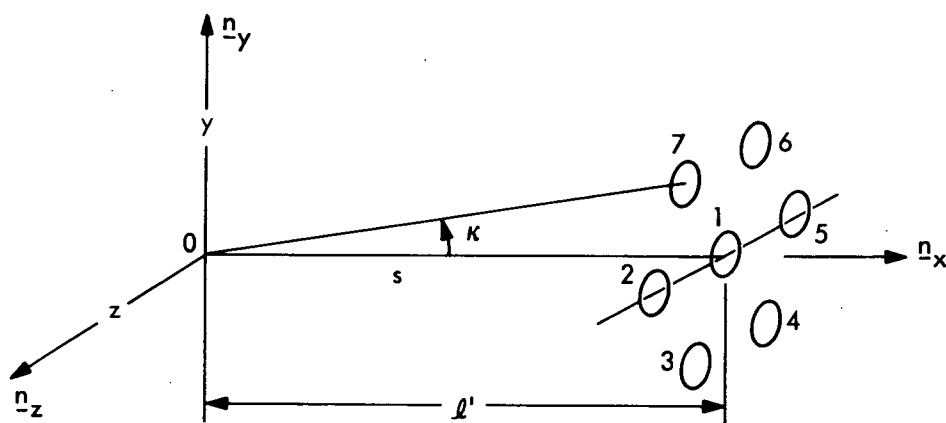
The basic control problem is essentially the same for both the JPL and the TRW mechanizations. Since TRW has proposed using the JPL actuators in their mechanization, the electronic circuits to drive the actuators will be identical for both systems. However, since TRW's proposal uses one actuator for pitch control and JPL's proposal uses six actuators for pitch control, the amount of circuitry and the amount of mode switching is less for the TRW proposal.

5. Analytical Expression for Total Thrust and Attitude Control Moment

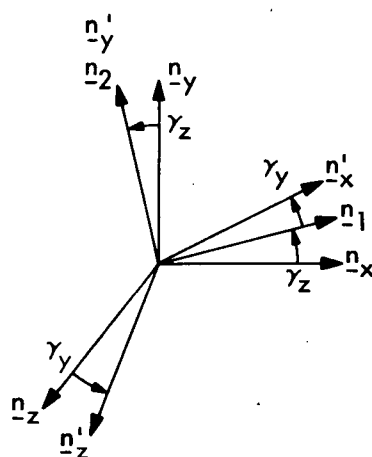
a. TRW Design

Figure III-E-10 shows the geometry for this design. The axes x , y , z in the perspective view of Fig. III-E-10 are the pitch, yaw and roll axes fixed in the spacecraft bus and emanating from the mass center D . The cant angle is κ . All thrusters except the center one are canted. The numbering scheme established in Fig. III-E-2 is adhered to here. The distance between thruster centers is d , while the distance from O to the thruster plane is s .

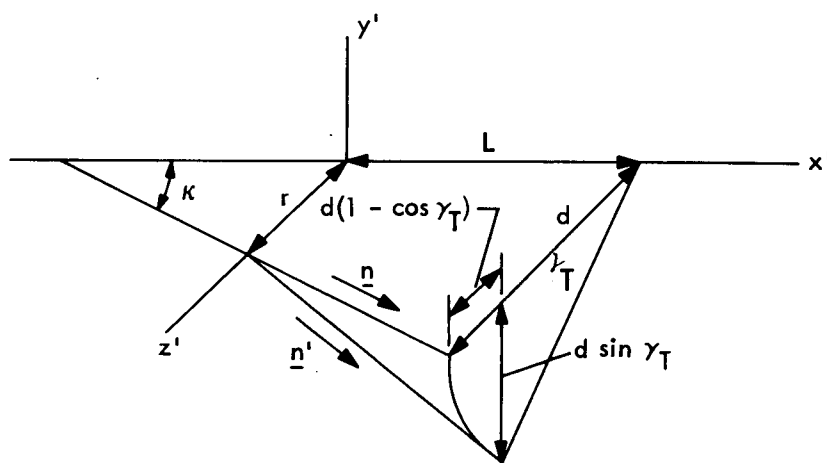
Denote unit vectors, fixed in the inner gimbal ring by \underline{n}'_x , \underline{n}'_y , \underline{n}'_z . Their relationship to \underline{n}_x , \underline{n}_y , \underline{n}_z is shown in Fig. III-E-10b. It is seen \underline{n}'_x , \underline{n}'_y , \underline{n}'_z is obtained by successive rotations through angles γ_z and γ_y about \underline{n}_z and about \underline{n}_2 . Unit vectors \underline{n}_1 , \underline{n}_2 , \underline{n}_3 form the intermediate set observed following the \underline{n}_z rotation. It can be shown that



(a)



(b)



(c)

Fig. III-E-10. Twist Geometry for TRW Design

$$\begin{bmatrix} \underline{n}'_x \\ \underline{n}'_y \\ \underline{n}'_z \end{bmatrix} = \begin{bmatrix} \cos \gamma_y \cos \gamma_z & \cos \gamma_y \sin \gamma_z & -\sin \gamma_y \\ -\sin \gamma_z & \cos \gamma_z & 0 \\ \sin \gamma_y \cos \gamma_z & \sin \gamma_y \sin \gamma_z & \cos \gamma_y \end{bmatrix} \begin{bmatrix} \underline{n}_x \\ \underline{n}_y \\ \underline{n}_z \end{bmatrix} \quad (1)$$

Angles γ_z and γ_y are the outer and inner gimbal angles, respectively.

A third kinematical variable is the twist angle γ_T . This is shown in Fig. III-E-10c. The distance between the center of the inner gimbal ring and the flexure pivot joint of the thruster is r . The distance from the thruster plane (for no twist) and the inner gimbal ring plane is L . Prior to twist, the thruster exhaust unit vector is \underline{n} while subsequent to twist, it is \underline{n}' . The diagram indicates what happens for thruster 2. The pictures are analogous for thrusters 3 thru 7. Observe that the point of application for the number 2 thrust vector is displaced by the amount $-d(1 - \cos \gamma_T)$ in the z' direction, and by the amount $-d \sin \gamma_T$ in the y' direction. A small change in the x' direction occurs as well. However, this is a second order effect. To be more precise, it may be shown that the change δ of distance between the inner gimbal ring plane and the thruster plane is

$$\delta = \frac{dr}{2L^2 + (d-r)^2} \gamma_T^2$$

Therefore, in the sequel, it will be assumed that upon twist, the thrust vectors continue to act on the original thruster plane.

The resultant thrust vector for the array is ascertained when the directions of the individual thrust vectors are known. Regardless of the amount of twist, the center thruster exhaust vector is always parallel to \underline{n}'_x . Hence, if the thrust magnitude is denoted F , then

$$\underline{F}^1 = -Fc_1 \underline{n}'_x \quad (2)$$

where \underline{F}^1 is the thrust vector for thruster number one, and c_1 is a constant which assumes the value of 1 or 0, depending on whether thruster 1 is operating or not. For thrusters 2 through 7, the expressions are more complex. Figure III-E-10c shows the thrust exhaust vector to be parallel to \underline{n}' for thruster 2, which can be written

$$\underline{n}' = \frac{L\underline{n}'_x - d \sin \gamma_T \underline{n}'_y + (d \cos \gamma_T - r) \underline{n}'_z}{(L^2 + d^2 + r^2 - 2rd \cos \gamma_T)^{1/2}} \quad (3)$$

Linearization of the twist angle implies

$$\underline{n} = \frac{L\underline{n}'_x - d\gamma_T \underline{n}'_y + (d - r) \underline{n}'_z}{(L^2 + d^2 + r^2 - 2rd)^{1/2}} \quad (4)$$

Hence, for thruster 2

$$\begin{aligned} \underline{F}^2 &= -Fc_2 \underline{n}' = - \frac{Fc_2}{[L^2 + (d - r)^2]^{1/2}} [L\underline{n}'_x - d\gamma_T \underline{n}'_y + (d - r) \underline{n}'_z] \\ &= -Fc_2 (f_{x\underline{n}'}^2 + f_{y\underline{n}'}^2 + f_{z\underline{n}'}^2) \end{aligned} \quad (5)$$

From symmetry, it may be argued that

$$\begin{aligned} \underline{F}^5 &= \frac{-Fc_5}{[L^2 + (d - r)^2]^{1/2}} [L\underline{n}'_x + d\gamma_T \underline{n}'_y - (d - r) \underline{n}'_z] \\ &= -Fc_5 (f_{x\underline{n}'}^5 + f_{y\underline{n}'}^5 + f_{z\underline{n}'}^5) \end{aligned} \quad (6)$$

An expression for \underline{F}^3 is

$$\underline{F}^3 = \frac{-Fc_3}{[L^2 + (d-r)^2]^{1/2}} \left[L\underline{n}''_x + d\gamma_T \underline{n}''_y + (d-r) \underline{n}''_z \right] \quad (7)$$

where

$$\begin{bmatrix} \underline{n}''_x \\ \underline{n}''_y \\ \underline{n}''_z \end{bmatrix} = \begin{bmatrix} 1 & 0 & 0 \\ 0 & 1/2 & \sqrt{3}/2 \\ 0 & -\sqrt{3}/2 & 1/2 \end{bmatrix} \begin{bmatrix} \underline{n}'_x \\ \underline{n}'_y \\ \underline{n}'_z \end{bmatrix} \quad (8)$$

That is, \underline{n}''_x , \underline{n}''_y , \underline{n}''_z are obtained from \underline{n}'_x , \underline{n}'_y , \underline{n}'_z by a 60-deg rotation about \underline{n}'_x . Consequently, the terms of \underline{n}'_x , \underline{n}'_y , \underline{n}'_z ,

$$\begin{aligned} \underline{F}^3 = \frac{Fc_3}{[L^2 + (d-r)^2]^{1/2}} & \left\{ L\underline{n}'_x - \frac{1}{2} [d\gamma_T + \sqrt{3}(d-r)] \underline{n}'_y \right. \\ & \left. - \frac{1}{2} [\sqrt{3}d\gamma_T - (d-r)] \underline{n}'_z \right\} = -Fc_3 \left(f_{x-x}^2 \underline{n}'_x + f_{y-y}^3 \underline{n}'_y + f_{z-z}^3 \underline{n}'_z \right) \quad (9) \end{aligned}$$

Similar arguments hold for determining \underline{F}^4 , \underline{F}^6 , and \underline{F}^7 and without further detail

$$\begin{aligned} \underline{F}^4 = - \frac{Fc_4}{[L^2 + (d-r)^2]^{1/2}} & \left\{ L\underline{n}'_x + \frac{1}{2} [d\gamma_T - (d-r)\sqrt{3}] \underline{n}'_y \right. \\ & \left. - \frac{1}{2} [\sqrt{3}d\gamma_T + (d-r)] \underline{n}'_z \right\} = -Fc_4 \left(f_{x-x}^2 \underline{n}'_x + f_{y-y}^4 \underline{n}'_y + f_{z-z}^4 \underline{n}'_z \right) \quad (10) \end{aligned}$$

$$\begin{aligned} \underline{F}^6 = & - \frac{Fc_6}{[L^2 + (d - r)^2]^{1/2}} \left\{ L\underline{n}'_x + \frac{1}{2} [d\gamma_T + \sqrt{3}(d - r)] \underline{n}'_y \right. \\ & \left. + \frac{1}{2} [\sqrt{3}d\gamma_T - (d - r)] \underline{n}'_z \right\} = - Fc_6 \left(f_{x-x}^2 \underline{n}'_x - f_{y-y}^3 \underline{n}'_y - f_{z-z}^3 \underline{n}'_z \right) \end{aligned} \quad (11)$$

$$\begin{aligned} \underline{F}^7 = & - \frac{Fc_7}{[L^2 + (d - r)^2]^{1/2}} \left\{ L\underline{n}'_x - \frac{1}{2} [d\gamma_T - (d - r)\sqrt{3}] \underline{n}'_y \right. \\ & \left. + \frac{1}{2} [\sqrt{3}d\gamma_T + (d - r)] \underline{n}'_z \right\} = - Fc_7 \left(f_{x-x}^2 \underline{n}'_x - f_{y-y}^4 \underline{n}'_y - f_{z-z}^4 \underline{n}'_z \right) \end{aligned} \quad (12)$$

Upon recognizing that

$$\cos \kappa = \frac{L}{[L^2 + (d - r)^2]^{1/2}}, \quad \sin \kappa = \frac{d - r}{[L^2 + (d - r)^2]^{1/2}} \quad (13)$$

it can be shown that the total thrust \underline{F} is

$$\begin{aligned} \underline{F} = \Sigma \underline{F}^i = & - F \left[< [c_1 + \cos \kappa (c_2 + c_5 + c_3 + c_6 + c_4 + c_7)] \cos \gamma_y \cos \gamma_z \right. \\ & - \left\{ \left(-c_2 + c_5 - \frac{c_3}{2} + \frac{c_6}{2} + \frac{c_4}{2} - \frac{c_7}{2} \right) \frac{d}{[L^2 + (d - r)^2]^{1/2}} \gamma_T \right. \\ & \left. + (-c_3 + c_6 + c_4 - c_7) \frac{\sqrt{3}}{2} \sin \kappa \right\} \sin \gamma_z \\ & \left. + \left\{ (-c_3 + c_6 - c_4 + c_7) \frac{\sqrt{3}}{2} \frac{d}{[L^2 + (d - r)^2]^{1/2}} \gamma_T \right. \right. \end{aligned}$$

$$\begin{aligned}
& + \left(c_2 - c_5 + \frac{c_3}{2} - \frac{c_6}{2} - \frac{c_4}{2} + \frac{c_7}{2} \right) \sin \kappa \left\{ \sin \gamma_y \cos \gamma_z > \frac{n_x}{\gamma_T} \right. \\
& + < \left[c_1 + \cos \kappa (c_2 + c_5 + c_3 + c_6 + c_4 + c_7) \right] \cos \gamma_y \sin \gamma_z \\
& + \left\{ \left(-c_2 + c_5 - \frac{c_3}{2} + \frac{c_6}{2} + \frac{c_4}{2} - \frac{c_7}{2} \right) \frac{d}{[L^2 + (d-r)^2]^{1/2}} \gamma_T \right. \\
& + \left. (-c_3 + c_6 + c_4 - c_7) \frac{\sqrt{3}}{2} \sin \kappa \right\} \cos \gamma_z \\
& + \left\{ (-c_3 + c_6 - c_4 + c_7) \frac{\sqrt{3}}{2} \frac{d}{[L^2 + (d-r)^2]^{1/2}} \gamma_T \right. \\
& + \left. \left(c_2 - c_5 + \frac{c_3}{2} - \frac{c_6}{2} - \frac{c_4}{2} + \frac{c_7}{2} \right) \sin \kappa \right\} \sin \gamma_y \sin \gamma_z > \frac{n_y}{\gamma_T} \\
& + < - \left[c_1 + \cos \kappa (c_2 + c_5 + c_3 + c_6 + c_4 + c_7) \right] \sin \gamma_y \\
& + \left\{ (-c_3 + c_6 - c_4 + c_7) \frac{\sqrt{3}}{2} \frac{d}{[L^2 + (d-r)^2]^{1/2}} \gamma_T \right. \\
& + \left. \left(c_2 - c_5 + \frac{c_3}{2} - \frac{c_6}{2} - \frac{c_4}{2} + \frac{c_7}{2} \right) \sin \kappa \right\} \cos \gamma_y > \frac{n_z}{\gamma_T} \left. \right] \quad (14)
\end{aligned}$$

Keep in mind that this expression is valid for small γ_T only. Accounting for nonlinear γ_T complicates the expression greatly.

If \underline{r}^i denotes the position vector of the point of application of \underline{F}^i with respect to 0, then the attitude moment exerted on the vehicle is

$$\underline{T} = \sum_{i=1}^7 \underline{r}^i \times \underline{F}^i \quad (15)$$

Observation of Fig. III-E-10 shows that

$$\begin{aligned} \underline{r}^1 &= (\ell' - L) \underline{n}_x + L \underline{n}'_x = \left(\frac{d}{\tan \kappa} - L \right) \underline{n}_x + L \underline{n}'_x \\ &= \left[\left(\frac{d}{\tan \kappa} - L \right) \cos \gamma_y \cos \gamma_z + L \right] \underline{n}'_x - \left(\frac{d}{\tan \kappa} - L \right) \sin \gamma_z \underline{n}'_y \\ &\quad + \left(\frac{d}{\tan \kappa} - L \right) \sin \gamma_y \cos \gamma_z \underline{n}_z = r^1_{x\underline{n}'_x} + r^1_{y\underline{n}'_y} + r^1_{z\underline{n}'_z} \end{aligned} \quad (16)$$

For thruster 2, the \underline{r}^2 vector is somewhat more complex

$$\begin{aligned} \underline{r}^2 &= (\ell' - L) \underline{n}_x + L \underline{n}'_x - d \sin \gamma_T \underline{n}'_y + d \cos \gamma_T \underline{n}'_z \\ &= \left[\left(\frac{d}{\tan \kappa} - L \right) \cos \gamma_y \cos \gamma_z + L \right] \underline{n}'_x \\ &\quad + \left[- \left(\frac{d}{\tan \kappa} - L \right) \sin \gamma_z - d \sin \gamma_T \right] \underline{n}'_y \\ &\quad + \left[\left(\frac{d}{\tan \kappa} - L \right) \sin \gamma_y \cos \gamma_z + d \cos \gamma_T \right] \underline{n}'_z = r^1_{x\underline{n}'_x} + \underline{n}'_x + r^2_{y\underline{n}'_y} + r^2_{z\underline{n}'_z} \end{aligned} \quad (17)$$

By symmetry arguments and rotations through appropriate multiples of 60 deg, as in the case for the force expressions, it is determined that

$$\begin{aligned}
 \underline{r}^3 &= \left[\left(\frac{d}{\tan \kappa} - L \right) \cos \gamma_y \cos \gamma_z + L \right] \underline{n}'_x \\
 &+ \left[- \left(\frac{d}{\tan \kappa} - L \right) \sin \gamma_z - \frac{d}{2} \sin \gamma_T - \frac{\sqrt{3}}{2} d \cos \gamma_T \right] \underline{n}'_y \\
 &+ \left[\left(\frac{d}{\tan \kappa} - L \right) \sin \gamma_y \cos \gamma_z - \frac{\sqrt{3}d}{2} \sin \gamma_T + \frac{d}{2} \cos \gamma_T \right] \underline{n}'_z \\
 &= r^1_{\underline{x}\underline{x}} \underline{n}'_x + r^3_{\underline{y}\underline{y}} \underline{n}'_y + r^3_{\underline{z}\underline{z}} \underline{n}'_z
 \end{aligned} \tag{18}$$

$$\begin{aligned}
 \underline{r}^4 &= \left[\left(\frac{d}{\tan \kappa} - L \right) \cos \gamma_y \cos \gamma_z + L \right] \underline{n}'_x \\
 &+ \left[- \left(\frac{d}{\tan \kappa} - L \right) \sin \gamma_z + \frac{d}{2} \sin \gamma_T - \frac{\sqrt{3}d}{2} \cos \gamma_T \right] \underline{n}'_y \\
 &+ \left[\left(\frac{d}{\tan \kappa} - L \right) \sin \gamma_y \cos \gamma_z - \frac{\sqrt{3}d}{2} \sin \gamma_T - \frac{d}{2} \cos \gamma_T \right] \underline{n}'_z \\
 &= r^1_{\underline{x}\underline{x}} \underline{n}'_x + r^4_{\underline{y}\underline{y}} \underline{n}'_y + r^4_{\underline{z}\underline{z}} \underline{n}'_z
 \end{aligned} \tag{19}$$

$$\begin{aligned}
 \underline{r}^5 &= \left[\left(\frac{d}{\tan \kappa} - L \right) \cos \gamma_y \cos \gamma_z + L \right] \underline{n}'_x \\
 &+ \left[- \left(\frac{d}{\tan \kappa} - L \right) \sin \gamma_z + d \sin \gamma_T \right] \underline{n}'_y \\
 &+ \left[\left(\frac{d}{\tan \kappa} - L \right) \sin \gamma_y \cos \gamma_z - d \cos \gamma_T \right] \underline{n}'_z = r^1_{\underline{x}\underline{x}} \underline{n}'_x + r^5_{\underline{y}\underline{y}} \underline{n}'_y + r^5_{\underline{z}\underline{z}} \underline{n}'_z
 \end{aligned} \tag{20}$$

$$\begin{aligned}
 \underline{r}^6 &= \left[\left(\frac{d}{\tan \kappa} - L \right) \cos \gamma_y \cos \gamma_z + L \right] \underline{n}'_x \\
 &+ \left[- \left(\frac{d}{\tan \kappa} - L \right) \sin \gamma_z + \frac{d}{2} \sin \gamma_T + \frac{\sqrt{3}}{2} d \cos \gamma_T \right] \underline{n}'_y \\
 &+ \left[\left(\frac{d}{\tan \kappa} - L \right) \sin \gamma_y \cos \gamma_z + \frac{\sqrt{3}}{2} d \sin \gamma_T - \frac{d}{2} \cos \gamma_T \right] \underline{n}'_z \\
 &= r^1_{x-x} \underline{n}'_x + r^6_{y-y} \underline{n}'_y + r^6_{z-z} \underline{n}'_z
 \end{aligned} \tag{21}$$

$$\begin{aligned}
 \underline{r}^7 &= \left[\left(\frac{d}{\tan \kappa} - L \right) \cos \gamma_y \cos \gamma_z + L \right] \underline{n}'_x \\
 &+ \left[- \left(\frac{d}{\tan \kappa} - L \right) \sin \gamma_z - \frac{d}{2} \sin \gamma_T + \frac{\sqrt{3}}{2} d \cos \gamma_T \right] \underline{n}'_y \\
 &+ \left[\left(\frac{d}{\tan \kappa} - L \right) \sin \gamma_y \cos \gamma_z + \frac{\sqrt{3}}{2} d \sin \gamma_T + \frac{d}{2} \cos \gamma_T \right] \underline{n}'_z \\
 &= r^1_{x-x} \underline{n}'_x + r^7_{y-y} \underline{n}'_y + r^7_{z-z} \underline{n}'_z
 \end{aligned} \tag{22}$$

If a_x , a_y , and a_z are defined as

$$\begin{aligned}
 a_x &= c_2 \left(r^2_{y-z} - r^2_{z-y} \right) + c_5 \left(- r^5_{y-z} + r^5_{z-y} \right) + c_3 \left(r^3_{y-z} - r^3_{z-y} \right) \\
 &+ c_6 \left(- r^6_{y-z} + r^6_{z-y} \right) + c_4 \left(r^4_{y-z} - r^4_{z-y} \right) + c_7 \left(- r^7_{y-z} + r^7_{z-y} \right)
 \end{aligned} \tag{23}$$

$$\begin{aligned}
a_y = & c_1 r_z^1 - c_2 \left(r_{xz}^1 r_z^2 - r_{zx}^2 r_x^2 \right) - c_5 \left(- r_{xz}^1 r_z^2 - r_{zx}^5 r_x^2 \right) - c_3 \left(r_{xz}^1 r_z^3 - r_{zx}^3 r_x^2 \right) \\
& - c_6 \left(- r_{xz}^1 r_z^3 - r_{zx}^6 r_x^2 \right) - c_4 \left(r_{xz}^1 r_z^4 - r_{zx}^4 r_x^2 \right) - c_7 \left(- r_{xz}^1 r_z^4 - r_{zx}^7 r_x^2 \right) \quad (24)
\end{aligned}$$

$$\begin{aligned}
a_z = & - c_1 r_y^1 + c_2 \left(r_{xy}^1 r_y^2 - r_{yx}^2 r_x^2 \right) + c_5 \left(- r_{xy}^1 r_y^2 - r_{yx}^5 r_x^2 \right) + c_3 \left(r_{xy}^1 r_y^3 - r_{yx}^3 r_x^2 \right) \\
& + c_6 \left(- r_{xy}^1 r_y^3 - r_{yx}^6 r_x^2 \right) + c_4 \left(r_{xy}^1 r_y^4 - r_{yx}^4 r_x^2 \right) + c_7 \left(- r_{xy}^1 r_y^4 - r_{yx}^7 r_x^2 \right) \quad (25)
\end{aligned}$$

Then the attitude control torque is

$$\begin{aligned}
\underline{T} = & - F \left[(a_x \cos \gamma_y \cos \gamma_z - a_y \sin \gamma_z + a_z \sin \gamma_y \cos \gamma_z) \underline{n}_x \right. \\
& + (a_x \cos \gamma_y \sin \gamma_z + a_y \cos \gamma_z + a_z \sin \gamma_y \sin \gamma_z) \underline{n}_y \\
& \left. + (- a_x \sin \gamma_y + a_z \cos \gamma_y) \underline{n}_z \right] \quad (26)
\end{aligned}$$

For consistency, $\sin \gamma_T$ and $\cos \gamma_T$ should appear as γ_T and 1 respectively in equation (26). This is due to the fact that the \underline{F}^i 's were expressed in terms of a linearized γ_T . Thus, equations (14) and (26) for force and torque are nonlinear in all variables except γ_T . The justification for doing this is that only small twist angles will be required for pitch control. However, large gimbal angles γ_y and γ_z may be experienced for cases of unsymmetric thrusting.

The expressions for \underline{F} and \underline{T} when γ_y , γ_z , and κ are small are also of interest. These are obtained from equations (14) and (26) and are

$$\begin{aligned}
\underline{F} = & -F < (c_1 + c_2 + c_5 + c_3 + c_6 + c_4 + c_7) \underline{n}_x \\
& + \left\{ (c_1 + c_2 + c_5 + c_3 + c_6 + c_4 + c_7) \gamma_z \right. \\
& + \left(-c_2 + c_5 - \frac{c_3}{2} + \frac{c_6}{2} + \frac{c_4}{2} - \frac{c_7}{2} \right) \frac{d\gamma_T}{[L^2 + (d-r)^2]^{1/2}} \\
& + (-c_3 + c_6 + c_4 - c_7) \frac{\sqrt{3}}{2} \kappa \left. \right\} \underline{n}_y \\
& + \left\{ -(c_1 + c_2 + c_5 + c_3 + c_6 + c_4 + c_7) \gamma_y \right. \\
& + (-c_3 + c_6 - c_4 + c_7) \frac{\sqrt{3}}{2} \cdot \frac{d\gamma_T}{[L^2 + (d-r)^2]^{1/2}} \\
& + \left(c_2 - c_5 + \frac{c_3}{2} - \frac{c_6}{2} - \frac{c_4}{2} + \frac{c_7}{2} \right) \kappa \left. \right\} \underline{n}_z >
\end{aligned} \tag{27}$$

and

$$\begin{aligned}
\underline{T} = & -F \left\{ (c_2 + c_5 + c_3 + c_6 + c_4 + c_7) \frac{d^2\gamma_T}{[L^2 + (d-r)^2]^{1/2}} \right. \\
& - \left[(c_2 - c_5) + \frac{1}{2}(c_3 - c_6) - \frac{1}{2}(c_4 - c_7) \right] d\gamma_z \\
& + (c_3 - c_6 + c_4 - c_7) \frac{\sqrt{3}}{2} d\gamma_y \left. \right\} \underline{n}_x \\
& - F < (c_1 + c_2 + c_5 + c_3 + c_6 + c_4 + c_7) \frac{Lr}{d-r} \gamma_y \\
& - (c_2 - c_5) \left(\frac{dL}{d-r} \kappa - d \right) + (c_3 - c_6) \left\{ \frac{dL}{2(d-r)} \left[\frac{\sqrt{3}d\gamma_T}{[L^2 + (d-r)^2]^{1/2}} \right. \right.
\end{aligned}$$

$$\begin{aligned}
& - \kappa \left[- \frac{\sqrt{3}}{2} d\gamma_T + \frac{d}{2} \right] + (c_4 - c_7) \left\{ \frac{dL}{2(d-r)} \left[\frac{\sqrt{3} d\gamma_T}{[L^2 + (d-r)^2]^{1/2}} \right. \right. \\
& \left. \left. - \kappa \right] - \frac{\sqrt{3}}{2} d\gamma_T - \frac{d}{2} > \underline{n}_y \right. \\
& - F < (c_1 + c_2 + c_5 + c_3 + c_6 + c_4 + c_7) \frac{Lr}{d-r} \gamma_z \\
& - (c_2 - c_5) \left\{ \frac{dL}{d-r} \frac{1}{[L^2 + (d-r)^2]^{1/2}} - 1 \right\} d\gamma_T \\
& - (c_3 - c_6) \left\{ \frac{dL}{2(d-r)} \left[\frac{d\gamma_T}{[L^2 + (d-r)^2]^{1/2}} + \sqrt{3}\kappa \right] - \frac{d\gamma_T}{2} - \frac{\sqrt{3}d}{2} \right. \\
& \left. + (c_4 - c_7) \left\{ \frac{dL}{2(d-r)} \left[\frac{d\gamma_T}{[L^2 + (d-r)^2]^{1/2}} - \sqrt{3}\kappa \right] - \frac{d\gamma_T}{2} + \frac{\sqrt{3}d}{2} > \underline{n}_z \right. \right. \\
& \hspace{15em} (28)
\end{aligned}$$

b. JPL Design

The thruster configuration is that shown in Figs. III-E-2 and 6. For the JPL design, the center thruster orientation with respect to the upper array base is invariant. Gimbal angles for thrusters 2 through 7 are denoted $\gamma_2, \gamma_3, \gamma_4, \gamma_5, \gamma_6, \gamma_7$, respectively. The individual thrust vectors are

$$\underline{F}^1 = -c_1 F \underline{n}_x$$

$$\underline{F}^2 = -c_2 F (\cos \gamma_2 \underline{n}_x + \sin \gamma_2 \underline{n}_y)$$

$$\underline{F}^3 = -c_3 F \left[\cos \gamma_3 \underline{n}_x + \sin \gamma_3 (\cos 60^\circ \underline{n}_y + \sin 60^\circ \underline{n}_z) \right]$$

$$\underline{F}^4 = -c_4 F \left[\cos \gamma_4 \underline{n}_x + \sin \gamma_4 (-\cos 60^\circ \underline{n}_y + \sin 60^\circ \underline{n}_z) \right]$$

$$\underline{F}^5 = -c_5 F (\cos \gamma_5 \underline{n}_x + \sin \gamma_5 \underline{n}_y)$$

$$\underline{F}^6 = -c_6 F \left[\cos \gamma_6 \underline{n}_x + \sin \gamma_6 (\cos 60^\circ \underline{n}_y + \sin 60^\circ \underline{n}_z) \right]$$

$$\underline{F}^7 = -c_7 F \left[\cos \gamma_7 \underline{n}_x + \sin \gamma_7 (-\cos 60^\circ \underline{n}_y + \sin 60^\circ \underline{n}_z) \right]$$

Hence, the total thrust is

$$\begin{aligned} \underline{F} &= \sum_{i=1}^6 \underline{F}^i = -F(c_1 + c_2 \cos \gamma_2 + c_5 \cos \gamma_5 + c_3 \cos \gamma_3 + c_6 \cos \gamma_6 \\ &\quad + c_4 \cos \gamma_4 + c_7 \cos \gamma_7) \underline{n}_x \\ &\quad - F \left(c_2 \sin \gamma_2 + c_5 \sin \gamma_5 + \frac{c_3}{2} \sin \gamma_3 + \frac{c_6}{2} \sin \gamma_6 \right. \\ &\quad \left. - \frac{c_4}{2} \sin \gamma_4 - \frac{c_7}{2} \sin \gamma_7 \right) \underline{n}_y \\ &\quad - F \frac{\sqrt{3}}{2} (c_3 \sin \gamma_3 + c_6 \sin \gamma_6 + c_4 \sin \gamma_4 + c_7 \sin \gamma_7) \underline{n}_z \end{aligned} \quad (30)$$

Let the separation distance between the center of mass and the thruster plane be a , and the y and z translation distances be t_y and t_z , respectively. Then the position vectors of the points of application of the thrust vectors are

$$\underline{r}^1 = a \underline{n}_x + t_y \underline{n}_y + t_z \underline{n}_z$$

$$\underline{r}^2 = a \underline{n}_x + t_y \underline{n}_y + (t_z + d) \underline{n}_z$$

$$\begin{aligned}
\underline{r}^3 &= a \underline{n}_x + \left(t_y - \frac{\sqrt{3}}{2} d \right) \underline{n}_y + \left(t_z + \frac{d}{2} \right) \underline{n}_z \\
\underline{r}^4 &= a \underline{n}_x + \left(t_y - \frac{\sqrt{3}}{2} d \right) \underline{n}_y + \left(t_z - \frac{d}{2} \right) \underline{n}_z \\
\underline{r}^5 &= a \underline{n}_x + t_y \underline{n}_y + (t_z - d) \underline{n}_z \\
\underline{r}^6 &= a \underline{n}_x + \left(t_y + \frac{\sqrt{3}}{2} d \right) \underline{n}_y + \left(t_z - \frac{d}{2} \right) \underline{n}_z \\
\underline{r}^7 &= a \underline{n}_x + \left(t_y + \frac{\sqrt{3}}{2} d \right) \underline{n}_y + \left(t_z + \frac{d}{2} \right) \underline{n}_z
\end{aligned} \tag{31}$$

Resultant torque is

$$\begin{aligned}
\underline{T} &= \sum_{i=1}^6 \underline{r}^i \times \underline{F}^i \\
&= F \left\{ c_2 (t_z + d) \sin \gamma_z + c_5 (t_z - d) \sin \gamma_5 \right. \\
&\quad - c_3 \left[\frac{\sqrt{3}}{2} \left(t_y - \frac{\sqrt{3}}{2} d \right) - \frac{1}{2} \left(t_z + \frac{d}{2} \right) \right] \sin \gamma_3 \\
&\quad - c_6 \left[\frac{\sqrt{3}}{2} \left(t_y + \frac{\sqrt{3}}{2} d \right) - \frac{1}{2} \left(t_z - \frac{d}{2} \right) \right] \sin \gamma_6 \\
&\quad - c_4 \left[\frac{\sqrt{3}}{2} \left(t_y - \frac{\sqrt{3}}{2} d \right) + \frac{1}{2} \left(t_z - \frac{d}{2} \right) \right] \sin \gamma_4 \\
&\quad \left. - c_7 \left[\frac{\sqrt{3}}{2} \left(t_y + \frac{\sqrt{3}}{2} d \right) + \frac{1}{2} \left(t_z + \frac{d}{2} \right) \right] \sin \gamma_7 \right\} \underline{n}_x
\end{aligned}$$

$$\begin{aligned}
& + F \left\{ -c_1 t_z - c_2 (t_z + d) \cos \gamma_2 - c_5 (t_z - d) \cos \gamma_5 \right. \\
& + c_3 \left[\frac{a\sqrt{3}}{2} \sin \gamma_3 - \cos \gamma_3 \left(t_z + \frac{d}{2} \right) \right] \\
& + c_6 \left[\frac{a\sqrt{3}}{2} \sin \gamma_6 - \cos \gamma_6 \left(t_z - \frac{d}{2} \right) \right] \\
& + c_4 \left[\frac{a\sqrt{3}}{2} \sin \gamma_4 - \cos \gamma_4 \left(t_z - \frac{d}{2} \right) \right] \\
& \left. + c_7 \left[\frac{a\sqrt{3}}{2} \sin \gamma_7 - \cos \gamma_7 \left(t_z + \frac{d}{2} \right) \right] \right\} \underline{n}_y \\
& + F \left\{ c_1 t_y - c_2 (a \sin \gamma_2 - t_y \cos \gamma_2) - c_5 (a \sin \gamma_5 - t_y \cos \gamma_5) \right. \\
& - c_3 \left[\frac{a \sin \gamma_3}{2} - \cos \gamma_3 \left(t_y - \frac{\sqrt{3}}{2} d \right) \right] - c_6 \left[\frac{a \sin \gamma_6}{2} - \cos \gamma_6 \left(t_y + \frac{\sqrt{3}}{2} d \right) \right] \\
& + c_4 \left[\frac{a}{2} \sin \gamma_4 + \cos \gamma_4 \left(t_y - \frac{\sqrt{3}}{2} d \right) \right] + c_7 \left[\frac{a}{2} \sin \gamma_7 \right. \\
& \left. \left. + \cos \gamma_7 \left(t_y + \frac{\sqrt{3}}{2} d \right) \right] \right\} \underline{n}_z \tag{32}
\end{aligned}$$

For small t_y , t_z , γ_i (neglect products of these variables), and for the case $\gamma_2 = -\gamma_5$, $\gamma_3 = -\gamma_6$, $\gamma_4 = -\gamma_7$,

$$\begin{aligned}
\underline{F} &= - (c_1 + c_2 + c_5 + c_3 + c_6 + c_4 + c_7) \underline{n}_x \\
& - F \left[(c_2 - c_5) \gamma_5 + \frac{1}{2} (c_3 - c_6) \gamma_3 - \frac{1}{2} (c_4 - c_7) \gamma_7 \right] \underline{n}_y \\
& - \frac{F\sqrt{3}}{2} \left[(c_3 - c_6) \gamma_3 + (c_4 - c_7) \gamma_7 \right] \underline{n}_z \tag{33}
\end{aligned}$$

$$\begin{aligned}
 \underline{T} = & F \left[(c_2 + c_5) d\gamma_2 + (c_3 + c_6) d\gamma_3 + (c_4 + c_7) d\gamma_4 \right] \underline{n_x} \\
 & + F(-c_1 - c_2 - c_5 - c_3 - c_6 - c_4 - c_7) t_z \underline{n_y} \\
 & + F(c_1 + c_2 + c_5 + c_3 + c_6 + c_4 + c_7) \underline{n_z}
 \end{aligned} \tag{34}$$

SECTION IV

SEP MODULE POWER SUBSYSTEM STUDIES

A. POWER SUBSYSTEM OPERATING VOLTAGE SELECTION

The purpose of this study is to select the optimum voltage range between 50 and 400 V for generating solar-array power, performing power conditioning within a SEP module, and distributing power to the engineering subsystems of the module and to a Mariner or Viking spacecraft. The selection process includes the following considerations:

- (1) Subsystem specific mass.
- (2) Subsystem efficiency.
- (3) Subsystem reliability.
- (4) Device limitations.
- (5) Maximum utilization of existing designs.

An upper limit of 400 V was established for the subsystem operating voltage because of the unavailability of JPL-approved components at higher power levels. The voltage ranges, based upon propulsion power conditioning designs in development, are: (1) 50-100 V, (b) 100-200 V, and (c) 200-400 V, respectively.

The potential advantages of operating at higher voltages, which results in reduced currents, higher efficiency, and lower weight were investigated. However, the advantages may be offset by technical problems in design, fabrication-qualification testing, safety and component limitations.

The above considerations were used in the analysis of the power subsystem elements (solar array, power conditioning, excluding propulsion, and distribution. The design characteristics of each of these power subsystem elements and the analyses performed leading to the selection of an operating voltage range are discussed in this section.

1. Power Subsystem Description

The block diagram of the SEP spacecraft power subsystem is shown in Figure IV-A-1. Power from the solar array is delivered to the power distribution module, to the thrust-subsystem power conditioners, and to the pre-regulator. The pre-regulator provides regulated power to the SEP module housekeeping power conditioners and to the payload-module power subsystem. The output voltage of the pre-regulator will be from 40 to 50 V for compatibility with the existing Mariner or Viking power subsystem designs. The SEP module housekeeping power inverter provides regulated alternating current to the engineering subsystems necessary for the operation of the thrusters. Spacecraft battery power will be delivered to the power distribution module for use by the pyrotechnic subsystem of the SEP module. The spacecraft battery and battery charger are located in the SEP module.

The maximum power point detector (MPPD), which is not included in this study, is utilized to determine the maximum solar-array power available at any time throughout the mission. This permits the use of maximum power for spacecraft thrust.

Most of the array power is utilized to provide power for propulsion. The payload module power requirements are expected to be approximately 675 W for Viking and 450 W for MVM 73. The SEP module housekeeping power requirements are estimated at about 150 W. Up to 15.5 kW will be available for propulsion based upon a total of 18% in uncertainty and degradation factors applied against an initial 20-kW solar-array capability and 200 W for distribution losses. Power required by the payload module subsystems and the SEP module subsystems is relatively constant compared to the expected power-versus-time demands of the electric propulsion subsystem, which are determined by the number of power conditioners in operation and the throttling range of each thruster. For an Encke rendezvous mission the power requirements are expected to be adjusted in small increments from 16 kW* to 1.6 kW**, depending on the mission profile and available solar power. A brief

*Five power conditioners each requiring 3.1 kW.

**50% power throttling.

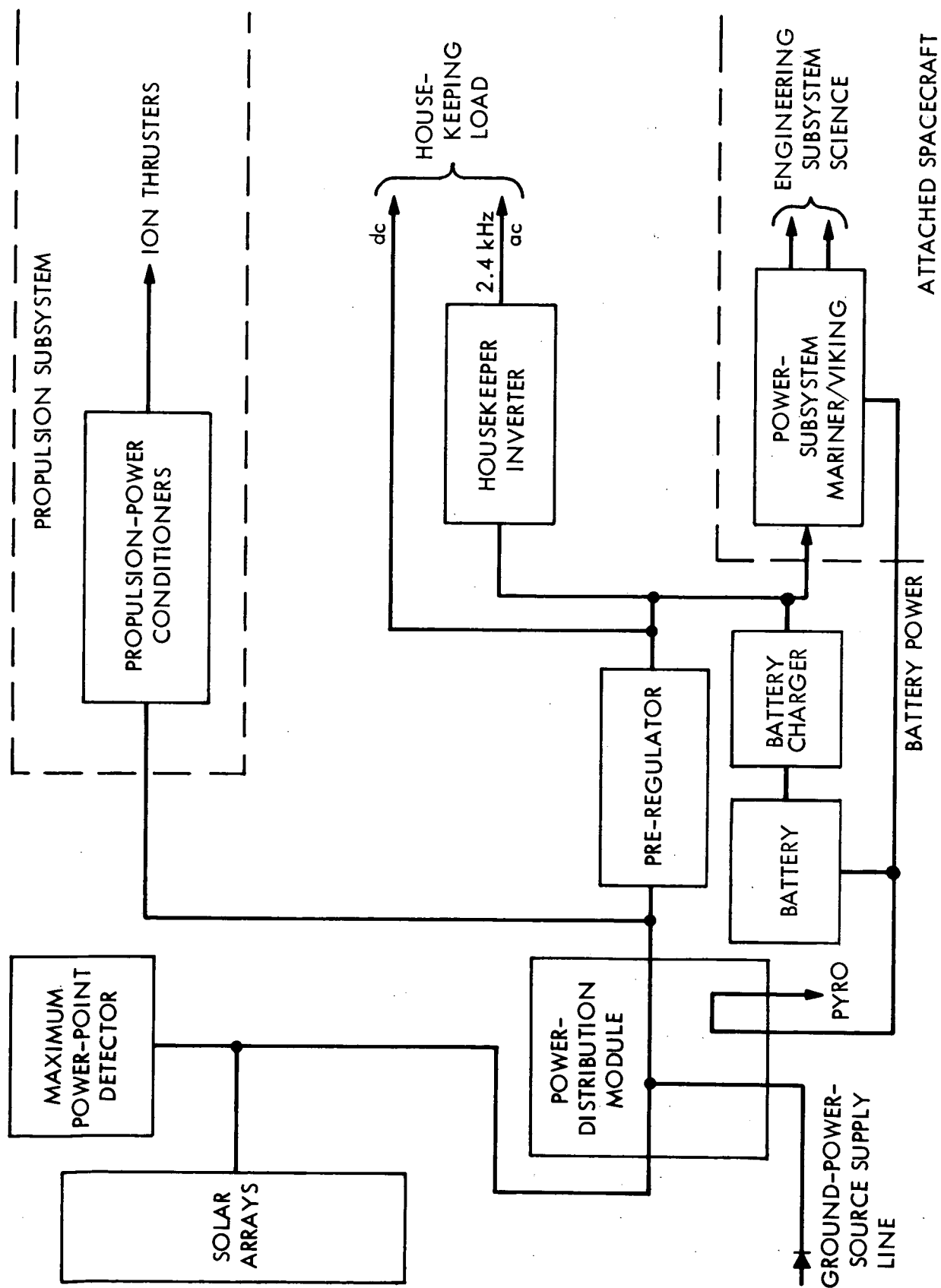


Fig. IV-A-1. SEP Module Power Subsystem with Mariner/Viking Spacecraft

description of the functional requirements and design characteristics of each element of the power subsystem follows:

a. Solar Array

The primary power source consists of two rollout solar arrays. The basic rollout array design, which has evolved from a JPL-sponsored development program, has a Kapton membrane which serves as a flexible substrate upon which the solar cells are mounted. The flexible substrate is rolled onto a drum in a manner similar to a window shade for storage during launch. Deployment of the substrate is achieved by an extensible motor driven boom, which also provides the required structure (aided by a loading edge member) to maintain the flexible substrate in a planar configuration, as shown in Fig. II-A-2. A rollout array has a nominal power-producing capability (at earth) of 107.6 W/m^2 (10 W/ft^2) at a temperature of 60°C and a solar intensity of 140 mW/cm^2 with the array normal to the sun. To generate 20 kW at 1 AU, a total area of 186 m^2 (2000 ft^2) is required. Two solar arrays, each having an area of 93 m^2 (1000 ft^2) will be used. Typical dimensions for each array are 4.3 by 22.8 m (14 ft wide by 75 ft long). The specific power density is expected to be approximately 66 W/kg (30 W/lb). Temperature, intensity and the sun angle of incidence combine to influence the power producing capability of the array. For operation at 5.0 AU, the solar intensity is about 3.5% of the near-earth value. The reduction in array temperature only partially offsets the reduction in intensity, so that the resultant power is only 5% of that available at earth.

For missions to 5.0 AU, the array voltage will vary over a range of 2 to 1. For example, if the array operating voltage at 1 AU is 50 V, it will increase to 100 V at 5.0 AU.

b. Power Distribution Module

The power distribution module receives all of the solar-array power which is then redistributed to: (1) the thrust subsystem where the power conditioners condition the power for use by the thrusters, and (2) to a

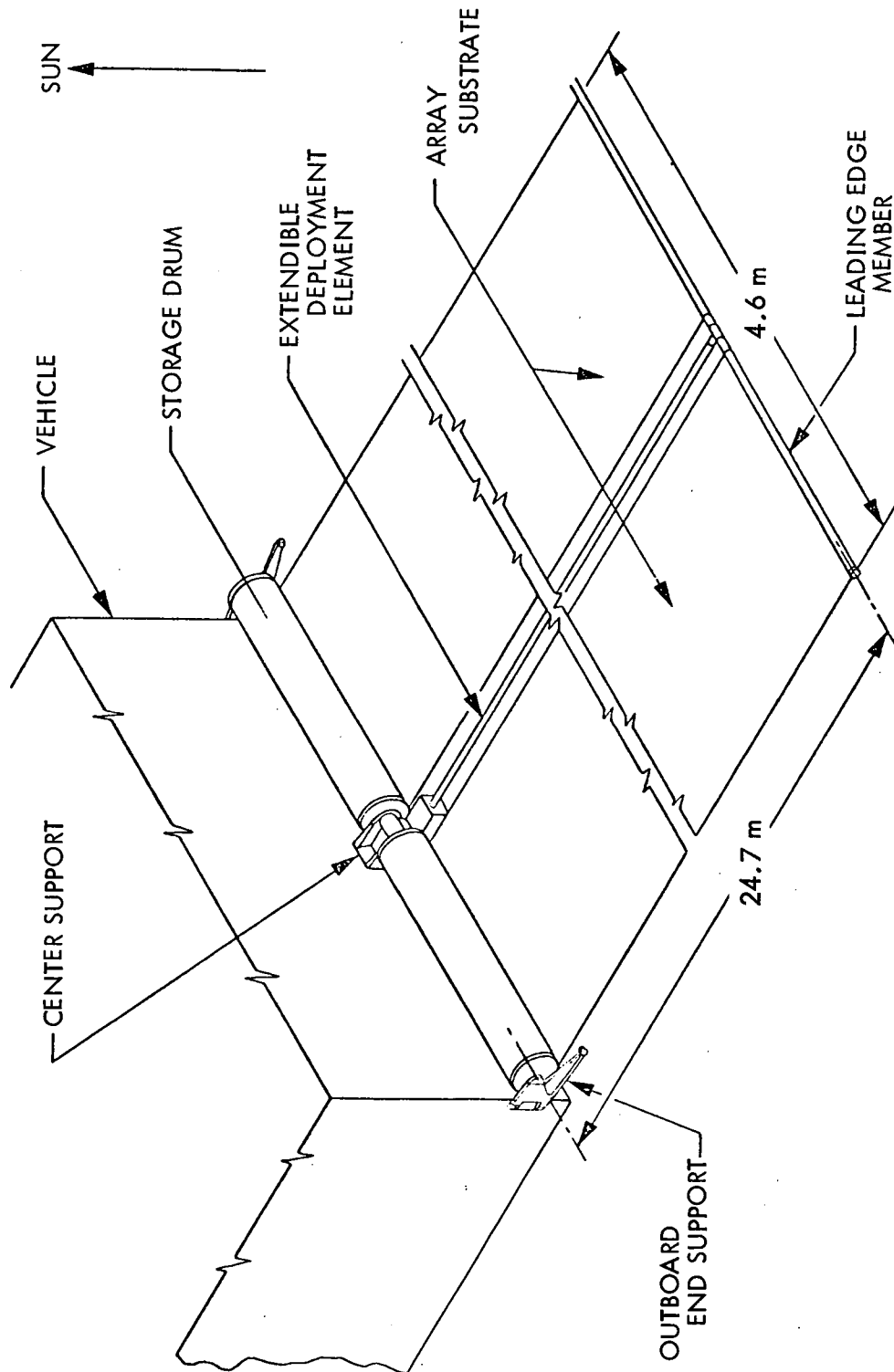


Fig. IV-A-2. Flexible Substrate in a Planar Configuration

pre-regulator to condition the power for the SEP module housekeeping dc loads, the SEP module housekeeping inverter to generate 2.4 kHz, and for the operation of the spacecraft engineering subsystems and science instruments, via the spacecraft power subsystem.

Ground power is supplied to the power distribution module for operation of the thrust subsystem and SEP module housekeeping subsystems during system tests. Battery power is supplied to the power distribution module for firing the solar-array release squibs after liftoff and for deploying the solar arrays.

The power-distribution module contains the bus bars and junction points of the power-subsystem power cables, in addition to the telemetry sensors required for evaluation of the power-subsystem performance.

c. Pre-regulator

The pre-regulator accepts power from the solar arrays and generates the necessary voltage for the SEP module housekeeping inverter and housekeeping dc loads, and the spacecraft. The pre-regulator output voltage must be compatible with the existing Mariner or Viking power subsystem to minimize design changes. An output voltage between 40 to 50V is required to ensure battery charging and proper operation of the Mariner or Viking booster regulator. In addition, the pre-regulator will be utilized as a filter between the thrust subsystem and the spacecraft to reduce noise and transients to the acceptable level that the spacecraft subsystems can tolerate.

d. Housekeeping Power Inverter

The housekeeping power inverter is driven by the pre-regulator and delivers 2.4 kHz, 50-V rms square wave. The 2.4 kHz was selected in order to use existing Mariner or Viking hardware.

2. Solar Array Study

a. Array Configuration

Each solar array is made up of two flexible substrates, one on each side of a deployment boom. The substrates are an assembly of sectors, individually fabricated and tested. It is planned that each sector be as similar in design as possible to allow replacement and interchangeability between substrates and between solar arrays. By adhering to this philosophy, the design, fabrication, assembly, test, repair and replacement of sub-components, and the number and size of spare elements will be held to a minimum. This could result in a substantial cost savings.

The conceptual designs for a 2.5-, 5.0- and 10-kW rollout solar panel of 50, 100, and 200 V*, respectively, (near earth at an operating temperature of 60°C) are basically the same. In each case, the interchangeability of parts has been the basis for selecting the number of cells in series parallel, and the power that each circuit or circuits will supply.

Two power distribution approaches were analyzed. In one, the total power from both rollout-solar arrays is distributed by a common bus to all loads, as shown in Figure IV-A-1. The alternate approach provides two electrically isolated array sections, one of which supplies power exclusively for propulsion and the other supplies power for SEP module housekeeping and all engineering subsystems of the spacecraft. The advantage of the latter approach is to isolate the relatively noisy thruster buses from the rest of the spacecraft. A requirement of this study was to determine the complexity of array-circuit design, if isolation between housekeeping power and thruster power was necessary. This isolation may be required to prevent transients originating within the thrust subsystem from affecting the housekeeping and other engineering subsystems. To accomplish this, a substrate is divided into different size circuits (each circuit consists of several sectors) with the power

*Minimum voltage of the voltage ranges examined.

leads brought back to the spacecraft where switching will take place. All substrates, for a given power array, are identical, although switching is limited to one solar panel of the array, and, whenever possible, to one substrate of a panel.

The various element weights and sizes with their resultant power-to-weight ratio, determined for this study, are shown in Table IV-A-1. This analysis was performed using the PSRUSA computer program developed during the 66-W/kg (30-W/lb) program (Ref. IV-A-1). During the 66-W/kg (30-W/lb) study, a 9-g launch acceleration was specified. This could be overly conservative for this study. Therefore, the effect of lowering the launch loads to 4.5 g are shown for illustration and indicate the potential increase in the power-to-weight ratio, which may be possible.

b. Electrical Design

The solar array is constructed of a number of electrically connected sectors. Each sector is comprised of 138 cells in series x 14 cells in parallel, interconnected as shown in Fig. IV-A-3. These sectors are electrically connected in series and parallel to achieve the required panel voltage and power. The use of this standard sector is in keeping with the philosophy of interchangeability.

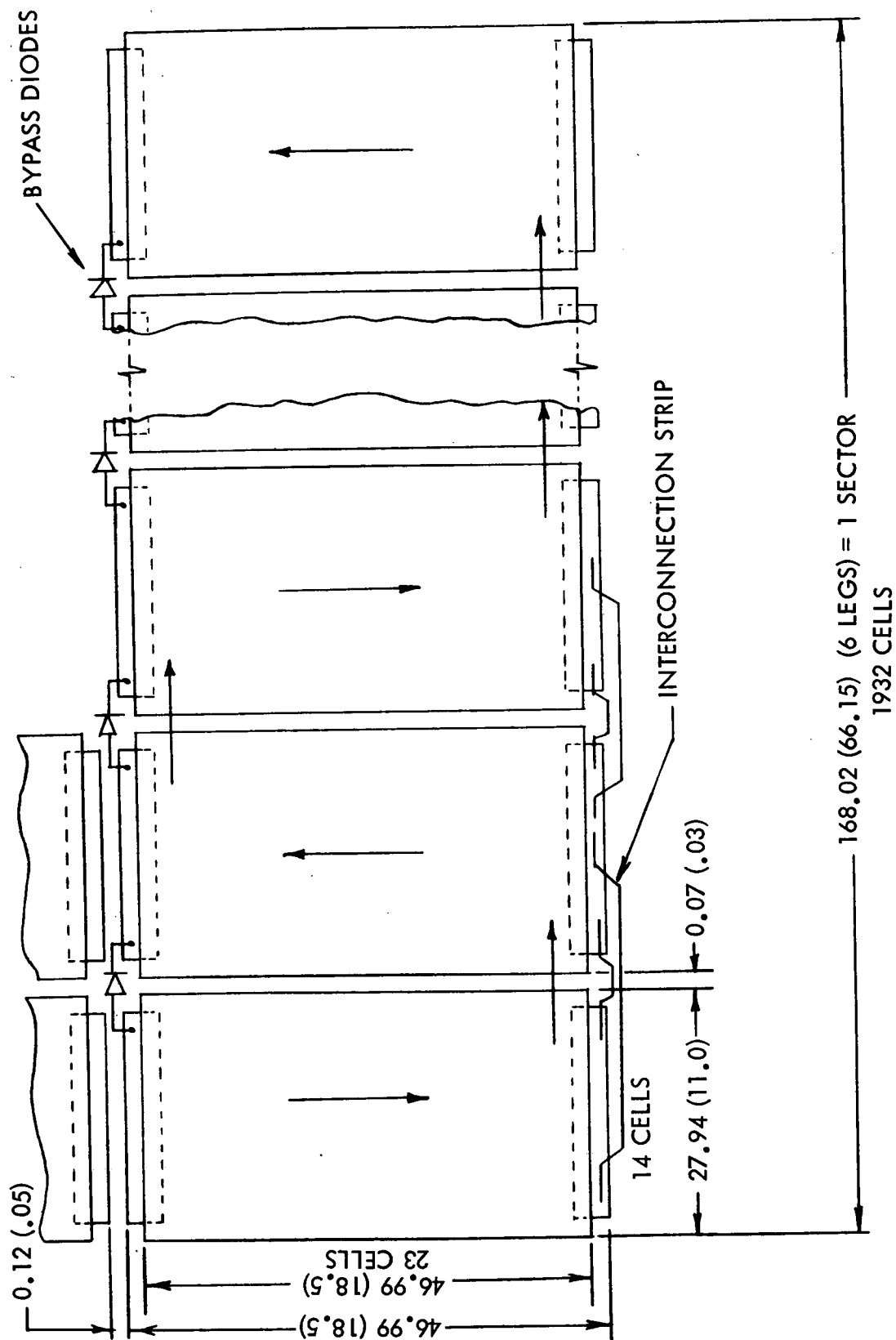
Open circuit failure protection of solar cells is assured by use of bypass diodes connected in parallel with each group of 46-series-connected solar cells. Isolation devices to compensate for short circuit failures are not employed; spacing between active elements will be chosen large enough to minimize the likelihood of this occurrence and to permit testing in air.

The electrical/mechanical design performed in this study is preliminary. The extrapolation of weight, area and watts per meter has been made, based upon the available data, from the 66-W/kg (30-W/lb) rollout solar array program. This program was to develop, fabricate and test a 23.2-m² (250-ft²), 2.5-kW rollout solar panel. Extrapolating the data of the 2.5-kW solar panel to the larger and higher power panel may result in some

Table IV-A-1. Solar Array Size, Weight and Power Estimates

Solar Panel Power	Launch Acceleration, 9 g												Launch Acceleration, 4.5 g											
	2.5 kW				5.0 kW				10.0 kW				2.5 kW				5.0 kW				10.0 kW			
	Volts	50	100	200	50	100	200	50	100	200	50	100	200	50	100	200	50	100	200	50	100	200		
Panel Area	m ²	24.447	24.193	23.943	48.895	48.385	47.887	97.789	96.771	95.773														
Panel Length	m	10.283	10.176	10.072	14.072	13.925	13.782	24.801	24.542	24.289														
Boom Diameter	cm	2.497	2.471	2.469	3.797	3.772	3.688	7.013	6.944	6.883														
Substrate Tension	kg/blanket	0.280	0.278	0.280	0.788	0.779	0.730	2.673	2.634	2.600														
Natural Frequency	Hz	0.040	0.040	0.040	0.040	0.040	0.040	0.040	0.040	0.040														
Actuator Width	m	0.112	0.111	0.111	0.170	0.169	0.165	0.314	0.312	0.308														
Panel Width	m	2.489	2.488	2.488	3.645	3.643	3.640	4.257	4.254	4.251														
Storage Drum Weight	kg	5.345	5.311	5.278	17.308	17.203	17.100	33.757	33.550	33.347														
End Cap Weight	kg	1.576	1.556	1.537	5.300	5.235	5.172	13.791	13.623	13.459														
Support Shaft Weight	kg	1.203	1.195	1.188	3.968	3.944	3.920	7.859	7.811	7.764														
Bearing Weight	kg	0.615	0.611	0.608	1.406	1.397	1.389	2.456	2.441	2.440														
Leading Edge Beam Weight	kg	0.386	0.384	0.385	1.880	1.871	1.825	4.771	4.734	4.702														
End Support Weight	kg	2.764	2.729	2.694	8.442	8.340	8.240	21.389	21.129	20.875														
Center Support Weight	kg	1.207	1.188	1.175	3.757	3.704	3.623	11.547	11.358	11.180														
Non-Structural Weight	kg	0.965	0.955	0.945	1.930	1.910	1.890	3.859	3.819	3.779														
Negator Weight	kg	0.327	0.326	0.327	0.548	0.545	0.527	1.010	1.002	0.996														
Boom Weight	kg	1.507	1.464	1.446	4.777	4.658	4.407	28.693	27.849	27.069														
Actuator Weight	kg	1.216	1.180	1.166	3.852	3.756	3.554	23.138	22.457	21.828														
Blanket Weight	kg	20.292	20.081	19.874	40.584	40.161	39.748	81.169	80.323	79.495														
Total Panel Weight	kg	37.404	36.980	36.621	93.752	92.725	91.396	233.437	230.096	226.919														
Watts Per kg/°	W/kg	13.751	13.909	14.046	10.973	11.094	11.256	8.813	8.942	9.067														

The above data are based on natural frequency 0.040 Hz, a conservative value. With natural frequency of 0.020 Hz and launch acceleration levels less than 4.5 g anticipated, a 10-kW array with specific power greater than 66 W/kg (30 W/lb) would be postulated.



NOTE:
DIMENSIONS IN cm (in.)

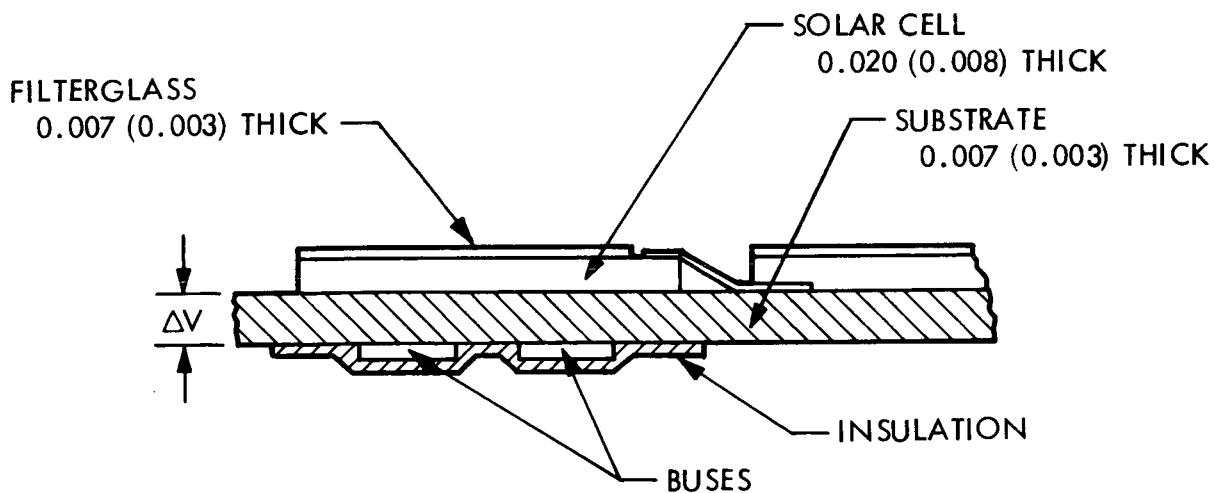
Fig. IV-A-3. Solar Cell Circuit Design for One Sector

inaccuracies. The data presented for the 5-kW and 10-kW electrical design are based on best estimates and a more detailed design effort will be required.

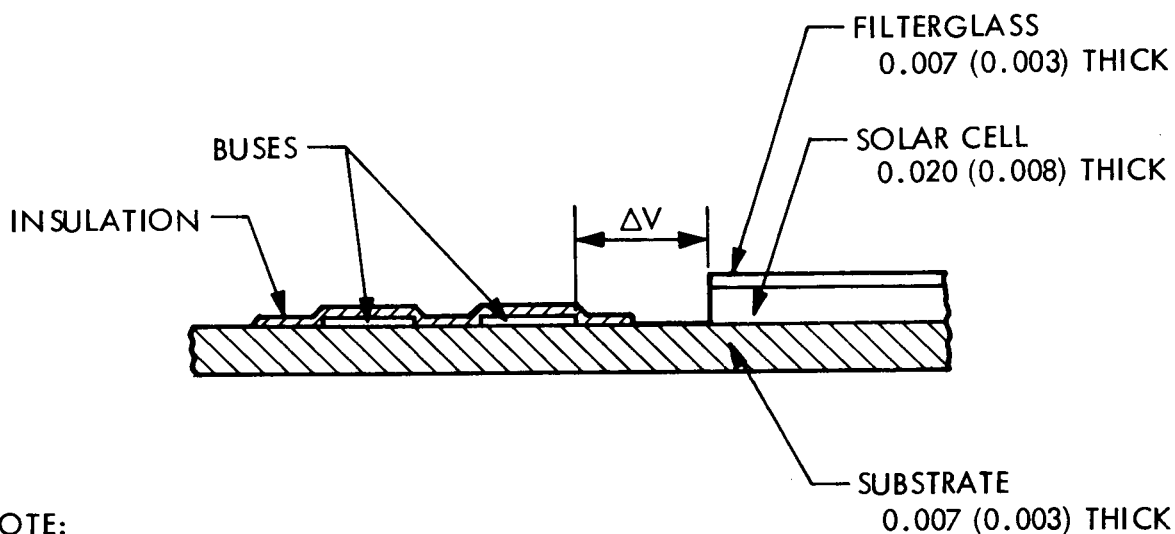
Table IV-A-1 shows the comparisons between the 2.5-kW solar panel and the extrapolation of this data to a 5-kW and 10-kW panel for the three (3) voltage ranges under investigation. A review of this table will show that no significant power-to-weight advantage in the solar array clearly exists over these voltage ranges. Other elements of the spacecraft, such as cabling, could be greatly affected by the proper choice of array voltage, and is discussed under the appropriate section. One parameter which does clearly influence the performance of the solar panel is the launch-acceleration level. Decreasing the launch loads from 9 to 4.5 g can result in an increase in the power-to-weight ratio of about 30%.

1) Bus Strip Locations. The design configuration of a roll-up array is influenced by the location of bus strips. Bus strips are used to sum the outputs of each power-producing section and to carry the power to terminals at the spacecraft solar-array interface. An option of locating the buses on the front or back of the array is shown in Fig. IV-A-4. Placing buses on the back of the array and beneath the solar cells imposes a severe insulation requirement on the array. Electrical breakdown would result in shorting between active elements and could cause array failure. The primary advantage is a reduction in array size. However, with the buses located on the front of the array, breakdown between active elements can occur only as a result of surface mechanisms. This fact allows a larger safety margin in dielectric design because of smaller electrical stresses, thereby reducing insulation requirements. For this reason, the front is the preferred location.

Permissible stress values for design spacing were established by consideration of the mechanisms of surface breakdown and the control of voltage gradients. The proposed level for the spacing of conductors is 10 to 50 V/.0025 cm (10 to 50 V/mil). These values are less than one-tenth of the measured breakdown levels in vacuum (Ref. IV-A-1), and thus the array can be designed with high dielectric reliability. Two other factors influenced the establishment of these limits: (1) atmospheric testing must be



(a) Back Side Positioning



NOTE:
DIMENSIONS IN cm (in.)

(b) Front Side Positioning

Fig. IV-A-4. Typical Locations of Electrical Bus Bars

permissible and (2) the critical spacing of conductors in fabrication must be minimized.

2) Power Distribution for Propulsion and Housekeeping.

Figures IV-A-5, 6, and 7 show the power available for the electrical thrusters and the power delivered to meet the requirements of housekeeping electronics. Each substrate of the solar array is designed with several independent circuits terminating at the spacecraft array interface. Each circuit has been sized to deliver a relatively uniform, minimum power level of 600 W* for housekeeping over the entire mission. The power not required for spacecraft housekeeping is used for thruster operation. The decrease in power available to the thrusters over the heliocentric distance from 1.0 AU to 3.0 AU can be seen in the figures. Tables IV-A-2, 3, and 4 list the estimated power (not including degradations and uncertainties) for each circuit, and the circuit numbers which are switched between the propulsion system and the housekeeping requirement. The three switching arrangements shown appear to be the simplest from a design, fabrication and substrate interchangeability standpoint. The electrical circuits on each substrate consist of a number of parallel connected sections which are also identical, allowing full interchangeability within an array of the same power rating. To provide the housekeeping power requirements a number of the array circuits will be assigned to the housekeeping bus. To maintain 600 W over the heliocentric distances of 1.0 to 3.0 AU, switching circuits to or from the housekeeping compartment have been considered in the event that separate housekeeping and thruster power compartments are required. Switching of the circuits from one compartment to the other will be done at the solar array/power distribution interface with the use of electronic switches. The complexity involved to provide the housekeeping from 20-, 10- and 5-kW array designs are described below. Circuit sizing was designed so that, to maintain the housekeeping power above 600 W, all switching could be accomplished on circuits of one solar panel.

For the 20-kW solar array as shown on Table IV-A-2, circuit 1 supplies all the power for housekeeping near earth. The remaining

*Assumed power requirement at beginning of the study. This level does not affect the final result.

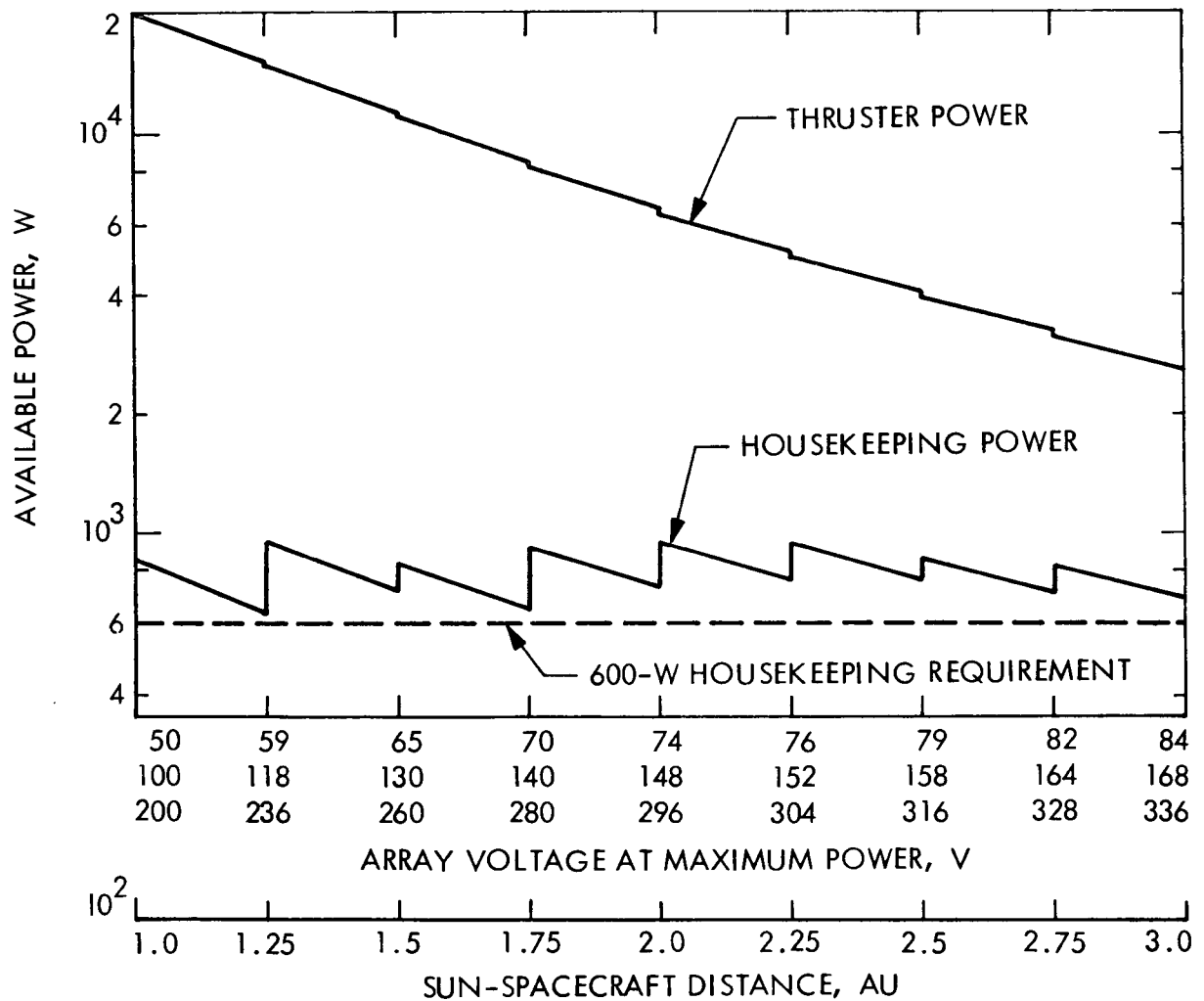


Fig. IV-A-5. Available Power, 20-kW Solar Array Configuration

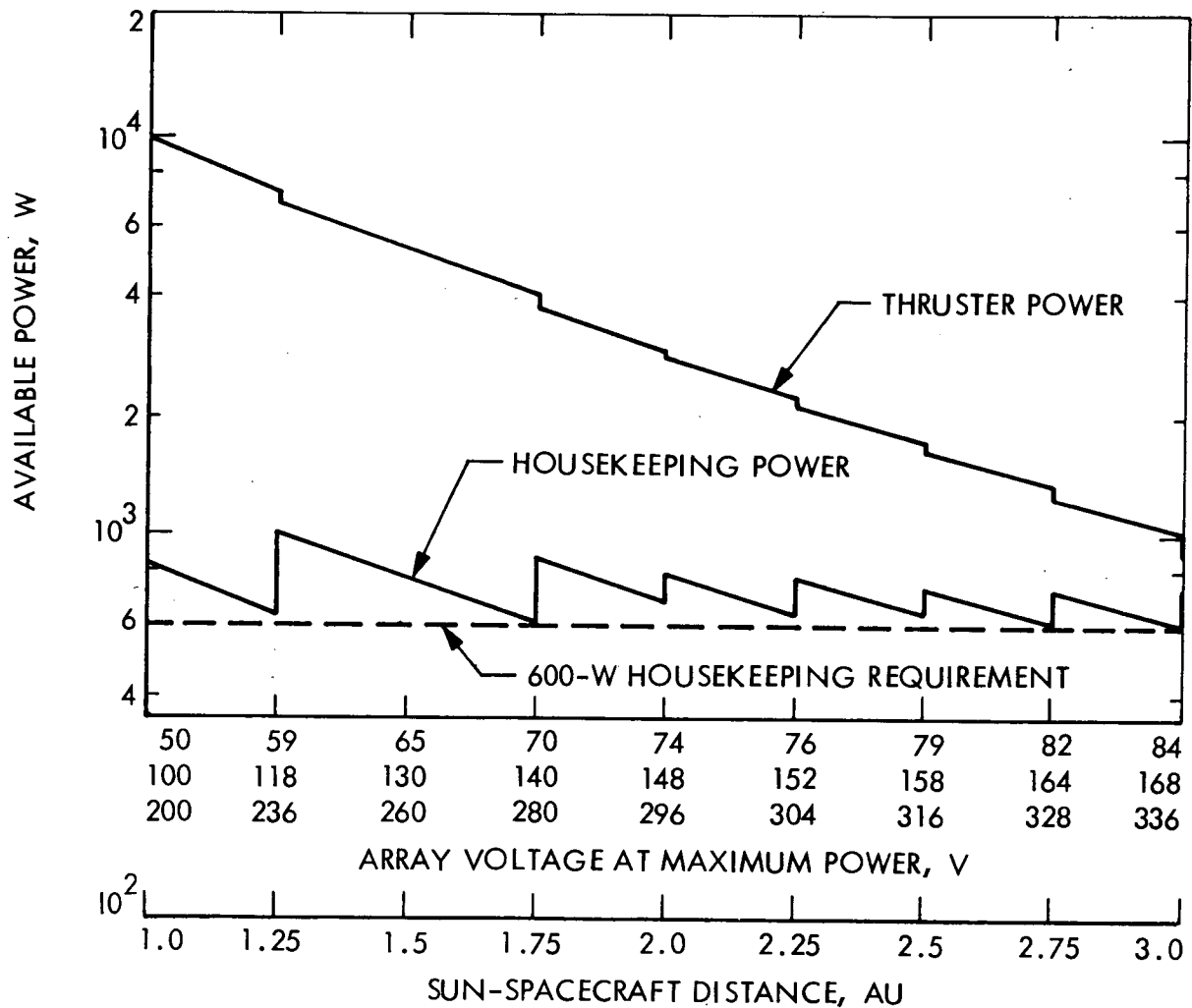


Fig. IV-A-6. Available Power, 10-kW Solar Array

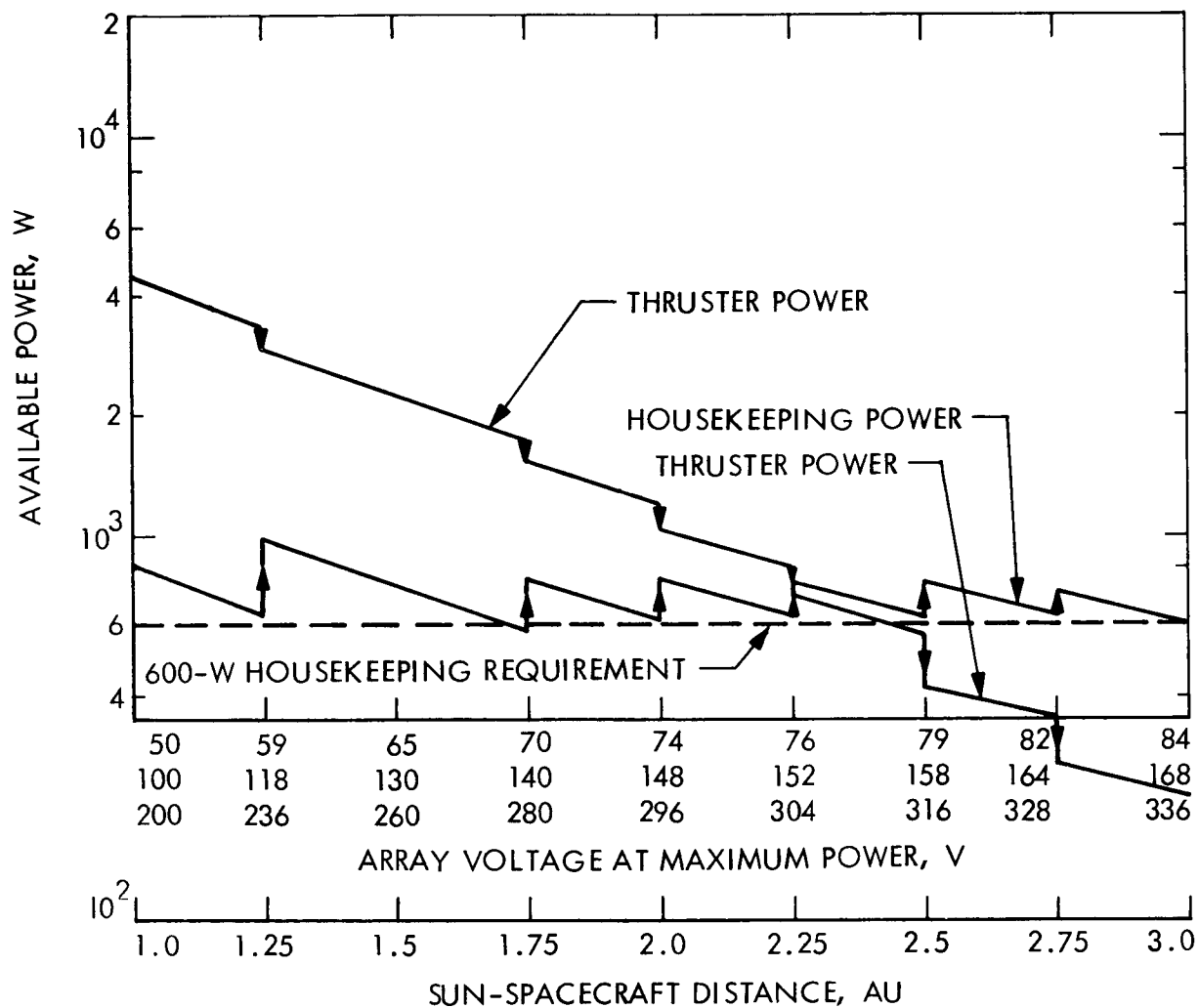


Fig. IV-A-7. Available Power, 5-kW Solar Array

Table IV-A-2. Circuit Switching and Estimated* Available Power for an Array of 20 kW

10 kW Per Panel - 2 Panels Per Spacecraft															
Circuit Number	Panel 1								Total Estimated* Power From Panel 1 W	Panel 1 Circuit Switching Circuit Numbers		Panel 1 Estimated* Available Power		Panels 1 and 2 Estimated* Array Power	
	Substrate 1				Substrate 2					House-keeping Circuit Number	Propulsion Circuit Number	House-keeping, W	Propulsion, W	House-keeping, W	Propulsion, W
	1	2	3	4	5	6	7	8							
Sun S/C Distance, AU	W	W	W	W	W	W	W	W	W						
1.0	857	1294	2594	647	647	2594	1294	857	10,748	1	2, 3, 4, 5, 6, 7 and 8	857	9,927	857	20,711
1.25	638	964	1928	482	482	1829	964	638	8,024	2	1, 3, 4, 5, 6, 7 and 8	638	7,386	638	15,410
1.5	480	726	1452	363	363	1452	726	480	6,042	1 and 4	2, 3, 5, 6, 7 and 8	726	5,316	726	11,358
1.75	370	556	1112	278	278	1112	556	370	4,632	1 and 2	3, 4, 5, 6, 7 and 8	926	3,706	926	8,338
2.0	291	440	880	220	220	880	440	291	3,662	1, 2 and 4	3, 5, 6, 7 and 8	731	2,931	731	6,593
2.25	234	354	708	177	177	708	354	234	2,946	1, 2, 4 and 5	3, 6, 7 and 8	765	2,181	765	5,127
2.5	191	288	576	144	144	576	288	191	2,398	2 and 3	1, 4, 5, 6, 7 and 8	864	1,534	864	3,932
2.75	158	238	476	119	119	476	238	158	1,982	2, 3 and 4	1, 5, 6, 7 and 8	714	1,268	714	3,250
3.0	131	198	396	99	99	396	198	131	1,648	2, 3 and 4		693	955	693	2,603

*Not including degradations and uncertainties.

Table IV-A-3. Circuit Switching and Estimated* Available Power for an Array of 10 kW

5.0 kW Per Panel - 2 Panels Per Spacecraft																
Circuit Number	Panel 1								Total Estimated* Power From Panel 1 W	Panel 1 Circuit Switching Circuit Numbers		Panel 1 Estimated* Available Power		Panels 1 and 2 Estimated* Array Power		
	Substrate 1				Substrate 2					House-keeping Circuit Number	Propulsion Circuit Number	House-keeping, W	Propul- sion, W	House-keeping, W	Propul- sion, W	
	1	2	3	4	5	6	7	8								
Sun S/C Distance, AU	W	W	W	W	W	W	W	W								
1.0	857	647	647	539	539	647	647	857	5,380	1	2,3,4,5,6,7 and 8	857	4,523	857		9,003
1.25	638	482	482	401	401	482	482	638	4,000	1 and 4	2,3,5,6,7 and 8	638	3,308	638		7,374
1.5	480	363	363	302	302	363	363	480	3,010	1 and 4	2,3,5,6,7 and 8	1,039	2,907	1,039		6,973
1.75	370	279	279	233	233	279	279	370	2,322	1 and 4	2,3,5,6,7 and 8	803	1,719	803		4,051
2.0	291	220	220	183	183	220	220	291	1,828	1,2 and 4	3,5,6,7 and 8	882	1,440	882		3,762
2.25	234	177	177	147	147	177	177	234	1,470	1,2 and 4	3,4,5,6 and 7	802	1,020	802		2,854
2.5	191	144	144	120	120	144	144	191	1,198	1,2,4 and 8	3,5,6 and 7	792	678	792		2,148
2.75	158	119	119	99	99	119	119	158	990	1,2,3,4 and 6	5,7 and 8	743	455	743		1,653
3.0	131	99	99	82	82	99	99	131	822	1,2,3,4,6 and 7	5 and 8	733	257	733		1,247
										1,2,3,4,6,7 and 8	5	609	213	609		1,035
												740	82	740		904

*Not including degradations and uncertainties.

Table IV-A-4. Circuit Switching and Estimated* Available Power for an Array of 5 kW

2.5 kW Per Panel - 2 Panels Per Spacecraft														
Circuit Number	Panel 1				Panel 2				Total Estimated* Power From Array	Circuit Switching Circuit Numbers		Estimated* Power Available		
	Substrate 1		Substrate 2		Substrate 1		Substrate 2			Housekeeping Circuit	Propulsion Circuit	Housekeeping, W	Propulsion, W	
	1	2	3	4	5	6	7	8						
Sun S/C Distance, AU	W	W	W	W	W	W	W	W	W					
1.0	857	485	857	485	857	485	857	485	5,368	1	2, 3, 4, 5, 6, 7 and 8	857	4,511	
1.25	638	361	638	361	638	361	638	361	3,996	1 and 2	3, 4, 5, 6, 7 and 8	638	3,358	
1.5	480	272	480	272	480	272	480	272	3,008	1 and 2	3, 4, 5, 6, 7 and 8	999	2,997	
1.75	370	210	370	210	370	210	370	210	2,320	1 and 2	3, 4, 5, 6, 7 and 8	752	2,256	
2.0	291	165	291	165	291	165	291	165	1,824	1, 2 and 4	3, 5, 6, 7 and 8	790	1,530	
2.25	234	132	234	132	234	132	234	132	1,464	1, 2, 4 and 6	3, 5, 7 and 8	786	1,038	
2.5	191	108	191	108	191	108	191	108	1,196	1, 2, 4, 6 and 8	3, 5 and 7	762	702	
2.75	158	89	158	89	158	89	158	89	988	1, 3, 5 and 7	2, 4, 6 and 8	623	573	
3.0	131	74	131	74	131	74	131	74	820	1, 2, 3, 5 and 7	4, 6 and 8	721	267	
										1, 2, 3, 4, 5, 6, 7 and 8	—	598	222	
												820	—	

*Not including degradations and uncertainties.

power from panel 1, circuits 2 through 8, are added to the power of panel 2, to be used for thruster operation. At 1.25 AU, circuit 2 supplies power for housekeeping. Circuit 1 is added to the thruster power. At 1.5 AU, circuits 1 and 4 are used for housekeeping, and circuit 2 is returned to the thruster power supply. Circuits 1 and 2 supply power for housekeeping from 1.75 to 2.0 AU; circuit 4 is returned to thruster power. At 2.0 AU, circuits 1, 2 and 4 are for housekeeping to about 2.25 AU, at which time circuit 5 is added to maintain the housekeeping power above 600 W. Then, at 2.5 AU, circuits 2 and 3 are used for housekeeping, and all others are applied to thruster power. At 2.75 AU, circuits 2, 3 and 4 supply housekeeping power. At 3.0 AU, with circuits 2, 3 and 4 functioning as housekeeping power, the available estimated power (not including degradation and uncertainties) is 693 W; thruster power is 2603 W.

For the 10-kW solar array, shown in Table IV-A-3, circuit 1 supplies all power for the housekeeping requirement up to 1.25 AU. From 1.25 AU to 1.75 AU, circuit 4 is added to maintain the housekeeping power above 600 W. At 1.75 AU, circuit 2 is added to circuits 1 and 4. When the spacecraft reaches 2.0 AU, circuit 4 is switched to thruster power and circuit 8 is added to circuits 1 and 2. At 2.25 AU, the power for housekeeping is supplied by circuits 1, 2, 4 and 8; then, at 2.25 AU, circuit 6 is switched to housekeeping, and circuit 8 is returned to thruster power. At 2.75 AU, circuit 7 is added to housekeeping power, followed by circuit 8 when the spacecraft reaches 3.0 AU. The estimated power (not including degradation and uncertainties) is then 740 W for housekeeping and 904 W for thruster power.

For the 5-kW solar array, it is necessary to switch circuits not only between substrates but also between panels to maintain a minimum power of 600 W for housekeeping electronics. Near earth, the total housekeeping power is supplied by circuit 1; as the spacecraft approaches 1.25 AU, circuit 2 is added. Circuits 1 and 2 supply sufficient power for housekeeping to a distance of about 1.7 AU, at which time circuit 4 is added. Then at 2.0 AU, circuit 6 is switched to housekeeping, leaving circuits 3, 5, 7 and 8 for thrusters. At 2.25 AU, circuits 1, 2, 4, 6 and 8 are used for housekeeping to a distance of 2.5 AU, at which time circuits 1, 3, 5 and 7 are

directed to housekeeping and 2, 4, 6 and 8 supply only 432 W of power to the thrusters. When the spacecraft is at 2.75 AU, 721 W of power is available for housekeeping from circuits 1, 2, 3, 5 and 7; circuits 4, 6 and 8 contribute 267 W to power the thrusters. At 3.0 AU all available power is switched to housekeeping.

c. Reliability

Two primary considerations with respect to the reliability of a solar array are (1) failures caused by open circuit and (2) short circuit conditions. The following information was obtained from a review of industry-published data (see Refs. IV-A-1, 2, and 3).

1) Open Circuit Cell Failures. Open circuit cell or wiring failures have a much greater degrading effect on the performance of high-voltage solar arrays than on that of low-voltage arrays, because the former requires a larger number of cells in series compared with the number in parallel. The larger number of cells in series increases the possibility of failure in a given cell string, and the smaller number in parallel reduces the capability of the array to compensate for failures by a shift of operating point on the I-V curve.

Figure IV-A-8 demonstrates this latter effect, which is critical for loads that are essentially constant-current in nature. If a load were operating at the maximum power point, as proposed for the SEP spacecraft, for a row of seven parallel cells, and one cell were to fail open, the I-V curve for the row would drop to 6/7 of its original current level. If the load is not able to also shift downward, then, instead of the row operating at its original +0.45 V, it will operate at -40 V, resulting in a considerable loss in power. This loss is not only inherently detrimental, it is also power which must be dissipated by the solar cells. The resultant heating of the cells and connections has been demonstrated to be potentially damaging (Ref. IV-A-2).

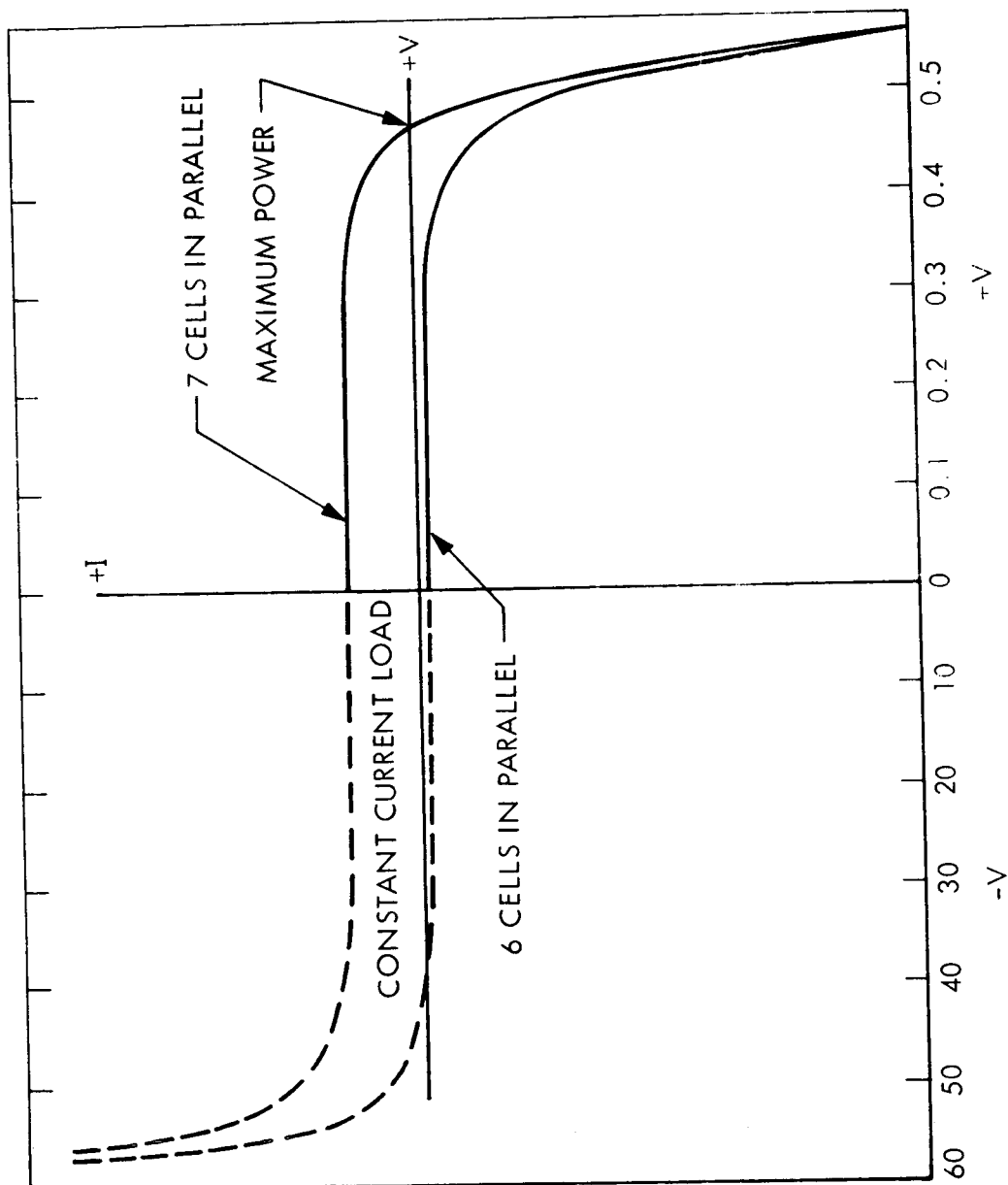


Fig. IV-A-8. Effect of Open-circuit Cell Failure and Back-biasing of Remaining Cells in Parallel

An effective means of solving this problem is to incorporate bypass diodes* in parallel with solar cell rows. These diodes provide an alternate path in the event that a failure occurs which results in back-biasing a portion of the array. The ratio of diodes to the rows to be used depends on the cell failure rate, ratio of number of cells in series to number in parallel, and the acceptable degradation in total array performance.

The assumed failure rate for cells in a flexible solar array is 3.0×10^{-8} /hr, or 0.001314 for a five-year mission, which is four times that expected for a rigid array (Ref. IV-A-3). This number can be considered accurate only within \pm one order of magnitude because of lack of flight experience with this type of array; however, the number indicates the effect on performance of varying the number of cells in parallel and the number of diodes used.

Figure IV-A-9 shows the effect of varying the number of cells in a parallel row while holding the number of rows per diode (constituting a bypass module) to one. Here the failure rate increases with increasing numbers because, as the number of cells in a parallel row increases, the possibility of failure also increases. This tendency of decreasing reliability with increasing parallel cells continues up to eight cells. Below this point, only one open circuit cell failure is necessary to back-bias the remaining parallel cells, but for eight or more in parallel, two cells must fail simultaneously before back-biasing occurs. The probability of the latter occurrence, which is low, is reflected in the figure.

Figure IV-A-10 illustrates the anticipated failure rate as a function of the number of series cells bypassed per diode. As expected, the probability of a failure within a given module increases with the number of cells in series bypassed. The curves also are presented as a function of cells in parallel, showing the same trend as in Fig. IV-A-9.

*A typical diode for this purpose is approximately 0.10 cm^2 and has a voltage drop of 1.1 V at 1 amp.

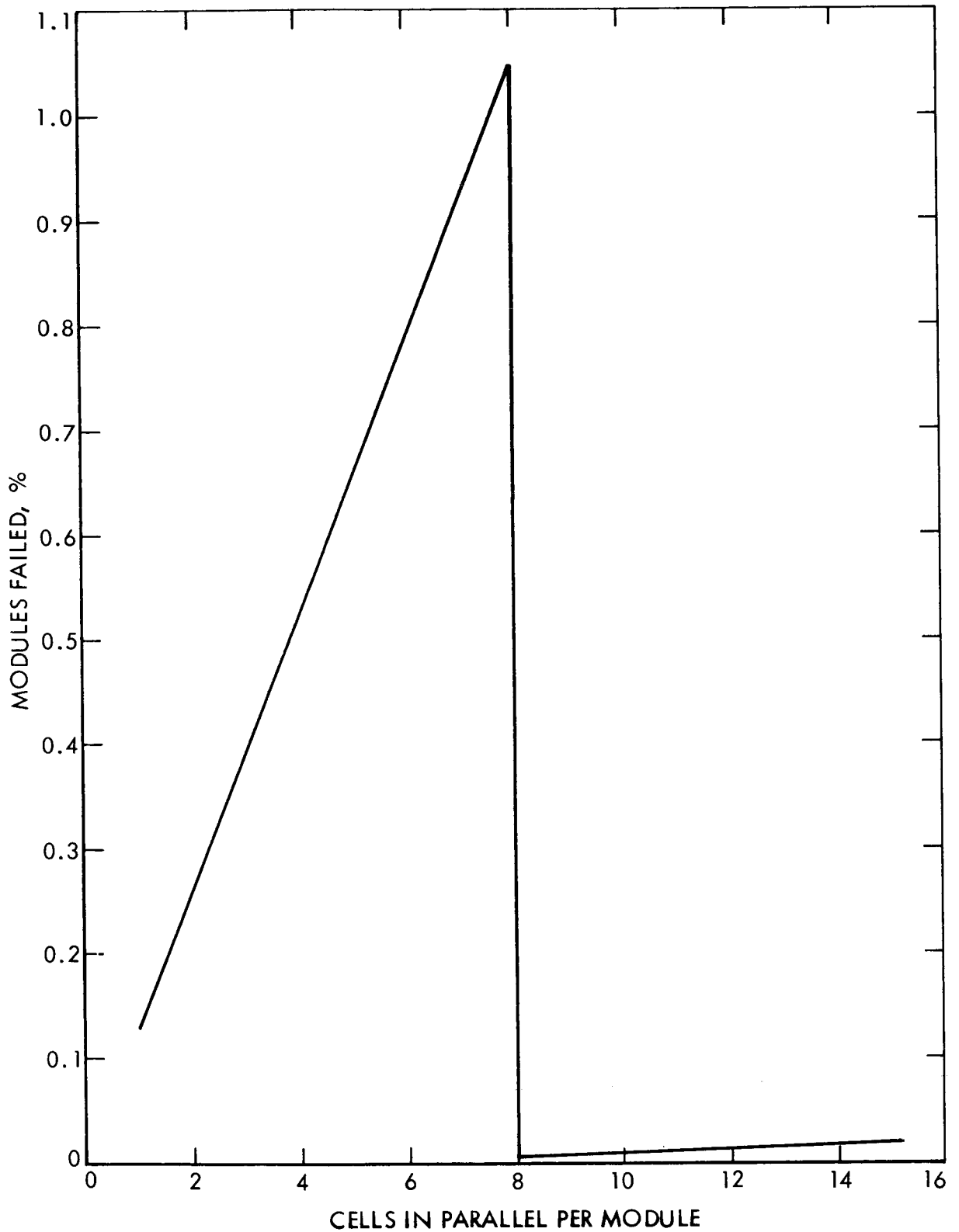


Fig. IV-A-9. Module Failure (Bypass) Rate as a Function of the Number of Cells in Parallel

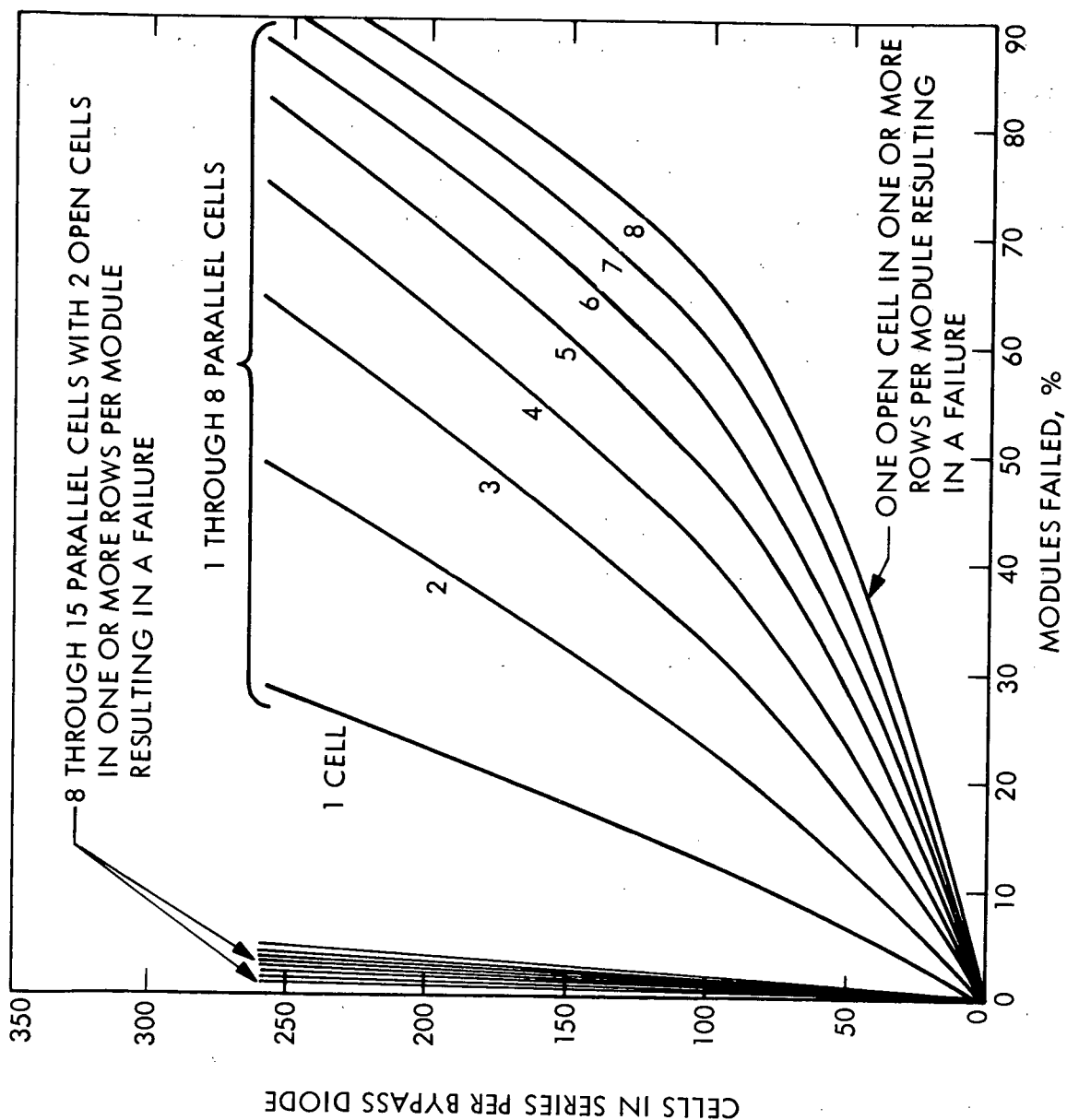


Fig. IV-A-10. Expected Percentage of Cell Module Failure Versus Cells in Series Per Bypass Diode After Five-year Operation in Space

The anticipated bypass module failure rate for a configuration using 14 cells in parallel per row is shown in Fig. IV-A-11. If it were decided to allow a failure rate of no more than 1%, there could be no more than 65 rows in a module which were connected in parallel with a bypass diode. The selected configuration has 46 parallel rows in series per module.

2) Short Circuit Failures. The risk of short circuit failures caused by cell short-circuiting to the buses or between blocks of cells is greatly reduced by utilizing a dielectric substrate. Other means also can be used to minimize this danger. Isolation devices can be placed between all blocks of cells and the main bus, and all array wiring and buses can be configured so that crossovers are minimized. Additionally, voltages ranging between 50 to 400 V minimize failures in this mode, whereas voltages approaching 600 to 1000 V are much less reliable.

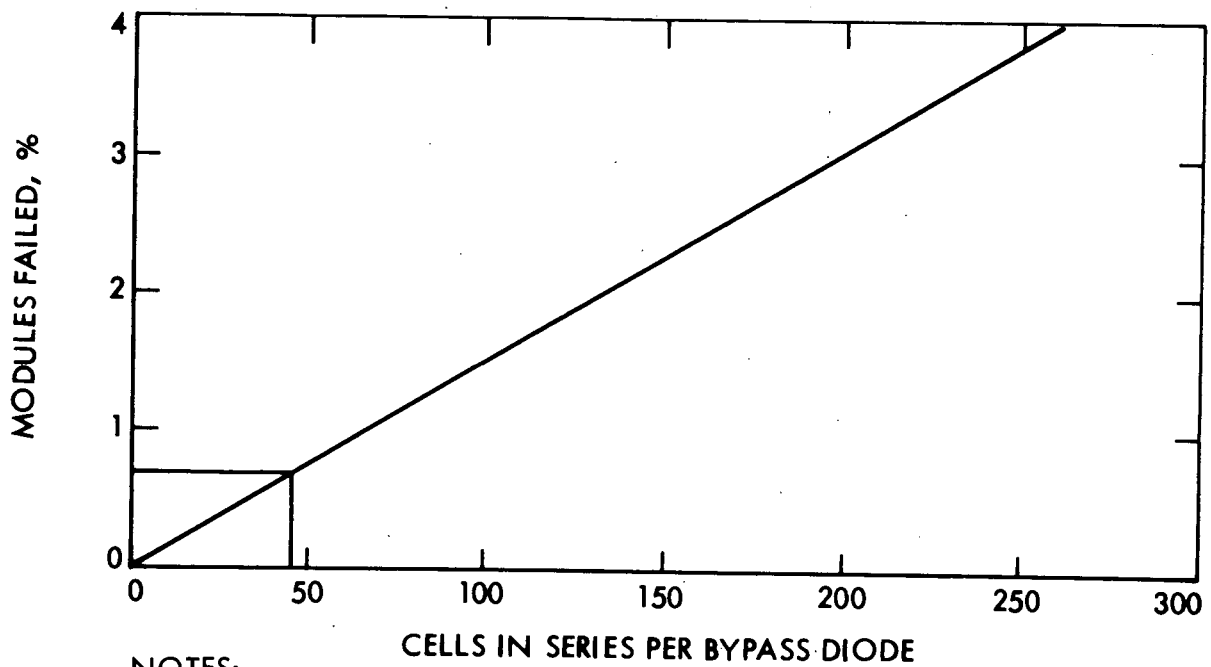
d. Testing

The basic testing philosophy and procedures are taken from past experience, recognizing the fact that knowledge and experience available in the development and testing of large flexible arrays is limited. Areas of concern for the arrays and their operating voltage are:

- (1) Facility limitations.
- (2) Array protection.
- (3) Higher voltage effects.
- (4) Critical tests.

1) Facility Limitations. A solar panel capable of producing up to 10 kW at either 50, 100 or 200 V requires special test constraints. Present pulsed xenon solar simulators will just accommodate a sector of a solar array approximately 0.61 x 2.28 m (2 x 7.5 ft), which means that individual sectors must be tested and then assembled into a full array.

Problems with size are also encountered in full solar-thermal-vacuum tests of the completed panel, which will be about 4.6 x 30.5 m



NOTES:

1. SELECTED DESIGN HAS 46 PARALLEL ROWS IN SERIES PER MODULE
2. 14 CELLS IN PARALLEL PER ROW

Fig. IV-A-11. Module Failure as a Function of the Number of Cells in Series per Bypass Diode After Five-year Operation in Space

(15 x 100 ft), when deployed. It is proposed that, under thermal vacuum conditions, all system functions be tested without deployment of the panels, as has been done in the past. The panel will be deployed following thermal-vacuum tests and partially illuminated to provide a qualitative performance check. Facility limitations may not allow the test and evaluation of a totally deployed panel.

2) Array Protection. The weight increase associated with array protection from non-flight loading conditions must be minimized. The array operates under less than 1 g conditions in space, but it must be assembled, handled, tested, transported, and stored under 1 g conditions. Deployment of the array for full array tests under ambient conditions requires added strength essential for protection in handling. Methods have already been developed during the 66 W/kg (30 W/lb) program for array deployment. These methods should be applicable to any large, lightweight arrays with minimal changes.

3) Higher Voltage Effects. The dielectric considerations which were applicable to the 66 W/kg (30 W/lb) program were evaluated for solar panels of 2.5, 5, and 10 kW and found to be acceptable. Application of this experience allows ambient testing of the arrays at 50 to 400 V.

4) Critical Tests. Critical testing of the solar panel, performed in an environment simulating mission conditions, should include high and low temperature soak, and thermal shock. In addition, launch loads, acoustic noise, random and sinusoidal vibration, and static acceleration tests are required.

e. Safety

1) "Safe" Current/Voltage Levels. Because the discomfort level for electric shock varies from person to person, the definition of a

safe-current voltage level for solar-cell groups is difficult. However, the following tentative guidelines can be established:

- (a) To minimize the danger of severe shock, the maximum current drawn by an individual should be less than 8 mamp.
- (b) The resistance measured between two electrodes placed on the skin varies from 500 to 5000 Ω . Normal dry-hand resistance is about 3,000 Ω .
- (c) Past experience with 2 x 2-cm, N on P cells indicates a wide variation in cell output under ambient (fluorescent) lighting. Short circuit values near 3 mamp/cell are realistic, although values which are a factor of ten lower have been experienced. The ambient voltage varies from 0.3 to 0.5 V/cell at open circuit.

Employing the above guidelines, basic cell groups sized from 3 in parallel by 100 in series to 14 in parallel by 50 in series may be handled with standard safety procedures.

2) Safety and Fabrication. The basic building block for the array segment will depend ultimately upon the required power level of the array to be fabricated and its operating voltage. The three voltages studied are:

- (a) 50 V, solar cells in series (138.0 x 14 cells in parallel).
- (b) 100 V, solar cells in series (276.0 x 14 cells in parallel).
- (c) 200 V, solar cells in series (552.0 x 14 cells in parallel).

A sector with 138.0 cells in series by 14 cells in parallel (Fig. IV-A-1) should be handled with care to avoid the possibility of electrical shock. As these

sectors are fabricated and interconnected, safety procedures related to an electrical shock hazard become increasingly necessary.

The point in fabrication at which the danger is highest is during the joining together of array segments to form the final array. Although methods such as ambient light filtering and shadowing have been considered, the possibility of severe shock hazard dictates that array sectors should be shorted and isolated from one another prior to the final step in the fabrication process.

3) Safety and Testing. Normal steady-state simulation to determine I-V performance at one solar constant would produce a much more severe hazard than ambient lighting. However, a pulsed xenon system allows large area tests at one solar constant without severe hazard to personnel. With a pulse length of less than 500 μ sec, the energy delivered by a sector during a single pulse at one solar constant is too small to cause bodily harm.

The physical short and isolation incorporated on the array during the final steps of fabrication must be removed with great care. The solar array will be designed for full panel tests in air; however, the high voltage hazard to personnel remains.

4) Safety Techniques. A number of secondary techniques and devices have been considered to enhance safety. These techniques, listed below, require the use of:

- (a) Standard cells to monitor the safe current level during fabrication.
- (b) Ambient light filtering in fabrication and testing areas.
- (c) Partial deployment and shadowing of the panels.
- (d) Partial illumination during full panel tests.

f. Areas for Development

Evaluation of a design to produce 2.5 kW using a 23.2 m^2 (250 ft^2) substrate revealed certain weaknesses, which must be corrected in future designs. These weaknesses were most evident in the fabrication of the array substrates; and centered around flatness, wrinkles, repair problems, and the need for modular assembly techniques. Thus, the following known problem areas require future mission-oriented development tests and analyses:

- (1) A fabrication process that will avoid wrinkling of the Kapton H-film substrate, which introduces bonding voids in the cell-to-substrate adhesive.
- (2) Array substrate designs and/or materials which will assure array flatness, within acceptable limits, when in the deployed state.
- (3) Modular assembly techniques to expedite array assembly, test and repair. Determination of the optimum modular dimensions based on the following: assembly, adaptability to solar simulators (pulsed xenon), comparison of adhesive bonded vs mechanical jointing of modules, and repair procedures.
- (4) Substrate stiffness as a function of temperature; testing is required to determine bending characteristics. This data is required to redesign the torque spring motors used to rewrap the substrates during retraction at low temperatures and to maintain the substrate natural frequency above 0.04 Hz. During testing of the 66-W/kg (30-W/lb) array, the torque spring motors were demonstrated to be marginal in size.

g. Conclusions

The preliminary analysis of the design and operational voltage for the 5-, 10-, and 20-kW array led to a number of conclusions: (1) From the estimated weight and watts per kilogram, it was concluded that a 200- to 400-V

array is more desirable than an array of 50 to 100 V. However, the most significant advantages accrue in other elements of the spacecraft, such as cabling. (2) All the arrays considered between 50 and 400 V can be built using conventional fabrication techniques. Standard technology can be employed until voltages reach 600 to 1000 V. (3) The layout of cells within cell-groups, cell sectors, and arrays can be chosen according to circuit needs and is little affected by environmental factors. (4) Because only a few cells are connected in parallel, the problem of open circuits is more serious in higher voltage arrays than in low voltage arrays. (5) To provide high reliability, open-circuit protection diodes are recommended for incorporation in this design. (6) To facilitate manufacturing, handling, and to minimize the potential of electrical shock, the array should be composed of smaller units manufactured separately and then be interconnected with other sectors at the end of the manufacturing process. (7) The complexity of an array having the capability of supplying power independently to both the housekeeping electrical bus and the thruster electrical bus was determined, but much more detailed investigations into the electronics of actually switching the electrical currents of the array to maintain a minimum 600-W of housekeeping power isolated from thruster power is required. The switching electronics could be the limiting element relative to maintaining an effective power-to-weight power system. (8) Voltages between 50 - 400 V do not pose any significant problem relative to space plasma. Space plasma is primarily a near-earth consideration and is not normally applicable to an interplanetary spacecraft. Also, the stated voltages are substantially below those at which power is believed to be affected, even in the most dense regions of the ionosphere.

3. Power Distribution Study

This study was conducted to determine the effects on the power distribution subsystem (PDS) of the operating voltage being considered for the SEP module. The power distribution subsystem was divided into four areas: (a) the cables* from the 20-kW solar array to the module, (b) the power distribution module, (c) the cables from the power distribution module to the propulsion

*A cable includes two or more pairs of wires (power and return).

subsystem power conditioners and (d) the cable from the power distribution module to the pre-regulator (see Fig. IV-A-12).

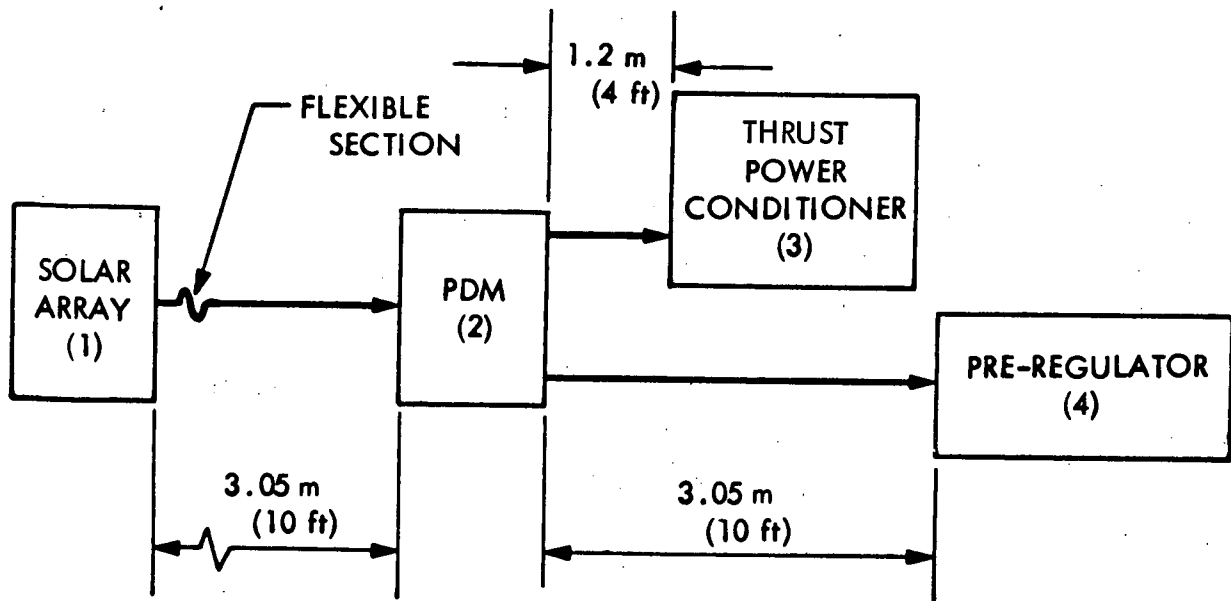


Fig. IV-A-12. Power Distribution Subsystem (PDM)

Two competing design goals, those of least weight and least power, were considered for each of the PDS elements. The analyses were based on worst-case current requirements associated with the lowest voltage of each of the three voltage ranges studied. Currents were calculated for a 20-kW solar array at each of the three voltage ranges. Design constraints established for the study included the following: current limitations on wire gages, current capacity of connectors, worst-case power requirements, and assigned cable lengths. The calculations provided a matrix of data from which the least power and least weight for the voltage ranges were determined.

a. Description of Power Distribution

1) Cables From Solar Array to Power Distribution Module.

To produce the 20-kW power, two arrays will be required. Each array consists of two substrates. Each of the two substrates is divided into four sections, which provide 600, 800, 1200, and 2400 W, respectively. For this study, it was assumed that each section is connected to the PDM by a single cable 3.05 m

(10 ft) long, resulting in a total of 16 cables. The interfaces of the solar array and PDM will have a comparable quantity of connector pin assignments.

2) PDM to Propulsion Power Conditioner Cables. It is assumed that the worst-case peak-input power requirements for each of the five power conditioners for the 30-cm thrusters are 4000 W; actually, the expected peak-input power is 3100 W. To properly size the input cables, the worst-case peak-power level was used. A central location for the PDM was assumed to provide equal minimum cable lengths 1.2 m (4 ft) between the PDM and each power conditioner.

3) Power Distribution Module to Pre-regulator Cables. The pre-regulator power requirements are about 700 W. This cable was therefore assumed to be identical in length to the 600-W cable between the solar array and the PDM, i.e., 3.05 m (10 ft).

4) Power Distribution Module. The power distribution module is an assembly approximately 18 x 20 x 35 cm (7 x 8 x 14 in.) that can be either a subassembly in a Mariner type chassis or a separate assembly. It has the capability of 32 connectors on a 4.4-cm (1.75-in.) matrix 10 cm (4 in.) high by 18 cm (8 in.) wide. The connectors for both input and output power are mounted on the face of the unit and pigtailed to a copper bus assembly. Lugs are used to splice the common voltage and ground from a connector. The lugs are bolted to the bus bars. The bus bars are capacitively coupled by a dielectric insulator. (Volume is allocated for transducers; weight is not included in the estimate and is not necessary for the tradeoff study.)

b. Design Constraints

The following assumptions were used in the PDS voltage tradeoff study:

- (1) Maximum voltage drop is 2% of the distributed voltage.
- (2) Cable temperature rise caused by current heating is not greater than 45°C above ambient*.

*JPL Specification VO-75-2009-1A (JPL internal document).

- (3) Maximum current in the wire is not to exceed the rated continuous limit. The maximum current in relation to wire gage is shown in Table IV-A-5.
- (4) Based on JPL experience, the use of 16-gage wire will be considered. All wire is 600-V rated and Teflon-insulated*.
- (5) Maximum current in connector contact is not to exceed the rated continuous duty limit (see Table IV-A-6).
- (6) Connector contacts and wire will not exceed 16 AWG or be smaller than 24 AWG. Connectors are miniature, quick disconnect, circular electrical connectors. Connector weights are not included in this estimate because of the multiplicity of insert arrangements and variation in the number of connector combinations possible.
- (7) A minimum of two conductor pairs are used in array power distribution circuit for reliability. Within any cable handling a specific power level, all conductors are the same AWG.

Table IV-A-5. Maximum Current in Relation to Wire Gage

Wire AWG	Maximum Current, amp
16	13.0
18	10.0
20	7.0
22	5.0
24	1.8

*JPL Specification ZPH-2239-0940 (JPL internal document).

Table IV -A -6. Maximum Current in Relation to Contact Size

Contact Size	Maximum Current, amp
16	13.0
20	7.5
22	5.0

c. Calculation Procedure

The approaches for power distribution subsystem design are: (1) the wiring weight is minimized at the expense of power loss, and (2) minimum power loss is sought at the expense of increased weight.

The following equations were used to determine the power losses and weights of the cables:

$$V_{\text{Drop, Max}} = 2\% \times \text{Lower Voltage, each voltage range} \quad (1)$$

$$I_{\text{Max (Total)}} = \frac{P}{E} \quad (2)$$

where

P = Power to be distributed

E = Voltage at lower end of voltage range

$$I_{\text{each Wire}} = \frac{V_{\text{Drop, Max}}}{R_{\text{Cable}}} \quad (3)$$

where

R_{Cable} = Equivalent resistance for wire gage and length

$$N = \frac{I_{\text{Max (Total)}}}{I_{\text{each wire}}} \quad (4)$$

where

N = Number wires required for a specific gage

Using equation (1), the maximum permissible voltage drop is determined from the lowest voltage of each voltage range. Equation (2) is used to determine the total current per cable for the delivered power at the voltage examined. From an assumed resistance value of wire gage which comes closest to carrying the current from equation (2), equation (3) is used to ascertain the current per wire. The current value per wire determined must fall within the current ratings for the specific wire gage and connector ratings. If it does not, the value of current per wire is determined by the lowest value of current per wire which satisfies all criteria simultaneously (voltage drop, wire temperature, and connector rating). In most cases, the JPL current limitations became an overriding constraint with the respect to the 2% maximum voltage drop requirement.

Equation (4) is used to calculate the number of wires (pairs of wires including power and return) necessary to carry the total current determined from equation (2). The power loss in each cable is determined from equation (5),

$$P_{\text{wire}} = (I_{\text{max}})^2 \times (R_{\text{awg}}) \times L \times N \quad (5)$$

where

$(R_{\text{avg}}) = \Omega/\text{m}$ of wire pairs,

L = the assigned cable length

N = the number of conductors from equation (4)

The power loss in the connector contacts was determined from the JPL-contact resistance data using the contact size selected for the specific wire gage. There are four contacts for each pair of wires. The connector losses were calculated with equation (6)

$$P_{\text{conn}} = (I_{\text{max}})^2 \times R_{\text{contact}} \times 4N \quad (6)$$

The total power loss for a cable including wires and connectors is

$$P_{\text{Total}} = P_{\text{Wire}} + P_{\text{Connector}} \quad (7)$$

Cable weights were calculated from the weight/meter data given in the JPL wire specifications, the number of conductors, and the length of the cable. In general, although connectors tend to add some weight to cables, the connector weights for the cables determined are not included.

d. Results

Tables IV-A-7 and 8 show the results of calculations to determine minimum weight and power loss, respectively. Each combination of the number of pairs of wire (# PRS) and wire size (AWG) result from minimizing weight (or power loss) for a particular power delivered and voltage combination.

Table IV-A-9 summarizes the analysis results. The only design which meets the SEPSIT allocations for a maximum power loss of 200 W and a cable weight of 4.27 kg (95 lb) is the least-power case for the 200- to 400-V range. Losses are 143 W, and weight is 8.77 m (19.5 lb).

Table IV-A-7. Least Weight Case

Solar Array to PDM Cables						
W	V	#PRS/AWG	Cable Loss W	Connector Loss W	Total Loss W	Cable Weight kg (lb)
600*	50	2 - 16	10.34	0.846	11.186	0.221 (0.488)
	100	2 - 22	8.64	0.600	9.240	0.086 (0.189)
	200	2 - 24	4.01	0.187	4.197	0.060 (0.132)
800	50	3 - 18	16.20	0.899	17.099	0.259 (0.571)
	100	2 - 22	15.35	0.600	15.950	0.086 (0.189)
	200	2 - 22	3.84	0.150	3.990	0.086 (0.189)
1200	50	9 - 18	21.91	0.960	22.870	0.431 (0.951)
	100	2 - 20	22.03	1.378	23.408	0.124 (0.273)
	200	2 - 22	8.64	0.600	9.240	0.086 (0.189)
2400	50	7 - 16	47.33	2.607	49.937	0.766 (1.688)
	100	2 - 16	41.42	2.281	43.701	0.221 (0.488)
	200	2 - 20	22.03	1.378	23.408	0.124 (0.273)
50-to 100-V panel total (1 each: 600-, 800-, 1200-, and 2400-W sections)					101.092	1.677 (3.698)
4 panels for total solar array					404.368	6.709 (14.792)
100-to 200-V panel total (same configuration)					92.299	0.517 (1.139)
4 panels for total solar array					369.196	2.066 (4.556)
200-to 400-V panel total (same configuration)					40.835	0.355 (0.783)
4 panels for total solar array					163.340	1.421 (3.132)
PDM to PC Cables						
4037	50	11 - 22	69.693	11.264	80.957	0.272 (0.6006)
	100	4 - 18	29.728	1.629	31.357	0.138 (0.3043)
	200	4 - 22	18.820	3.200	22.020	0.069 (0.1512)
For total of 5 PDU to PC cables			50-to 100-V range		404.785	1.362 (3.003)
			100-to 200-V range		156.785	0.690 (1.521)
			200-to 400-V range		110.100	0.343 (0.756)

*The pre-regulator cable losses and weight are assumed to be for one 600-W cable.

Table IV-A-8. Least Power Loss Case

Solar Array to PDM Cables						
W	V	#PRS/AWG	Cable Loss W	Connector Loss W	Total Loss W	Cable Weight kg (lb)
600*	50	3 - 18	9.11	0.400	9.510	0.259 (0.571)
	100	2 - 16	2.58	0.142	2.722	0.221 (0.488)
	200	2 - 16	0.65	0.036	0.686	0.221 (0.488)
800	50	3 - 16	12.25	0.675	12.925	0.328 (0.724)
	100	2 - 16	4.59	0.253	4.843	0.221 (0.488)
	200	3 - 24	1.15	0.159	1.309	0.221 (0.488)
1200	50	4 - 16	20.71	1.140	21.850	0.443 (0.977)
	100	7 - 24	10.03	0.819	10.849	0.210 (0.463)
	200	2 - 16	2.58	0.142	2.722	0.221 (0.488)
2400	50	15 - 20	46.85	2.933	49.783	0.929 (2.048)
	100	14 - 24	35.10	1.637	36.737	0.420 (0.927)
	200	2 - 16	10.34	0.564	10.904	0.221 (0.488)
50-to 100-V panel total (1 each: 600-, 800-, 1200-, and 2400-W sections)					94.068	1.959 (4.320)
4 panels for total solar array					376.272	7.838 (17.280)
100-to 200-V panel total (same configuration)					55.151	1.073 (2.366)
4 panels for total solar array					220.604	4.293 (9.464)
200-to 400-V panel total (same configuration)					15.621	0.885 (1.952)
4 panels for total solar array					62.484	3.542 (7.808)
PDM to PC Cables						
4037	50	45 - 24	49.437	5.767	55.204	0.541 (1.192)
	100	9 - 22	19.08	2.309	21.389	0.154 (0.3398)
	200	2 - 16	11.24	1.547	12.787	0.088 (0.1952)
For total of 5 PDU to PC Cables			50-to 100-V range		276.020	2.703 (5.960)
			100-to 200-V range		106.945	0.771 (1.700)
			200-to 400-V range		63.935	0.443 (0.976)

*The pre-regulator cable losses and weights are assumed to be for one 600-W cable.

Table IV-A-9. Power Loss and Cable Weights at Three Operating Voltage Ranges

Subsystem Element*	Design Point**	Voltage Range					
		50 to 100 V dc		100 to 200 V dc		200 to 400 V dc	
		Power Loss W	Weight kg (lb)	Power Loss W	Weight kg (lb)	Power Loss W	Weight kg (lb)
Solar-array Cable	LP	377	7.8 (17.3)	221	4.3 (9.5)	63	3.6 (8.0)
	LW	405	6.7 (14.8)	370	2.3 (5.0)	164	1.4 (3.0)
PDM (Estimate)	LP	72	5.4 (12)	28	4.9 (11)	20	4.5 (10)
	LW	52	4.9 (11)	18	4.5 (10)	14	4.5 (10)
Pre-regulator Cable	LP	10	0.3 (0.6)	3	0.2 (0.5)	1	0.2 (0.5)
	LW	12	0.2 (0.5)	10	0.09 (0.2)	5	0.09 (0.2)
PC Cables	LP	276	2.7 (5.9)	107	0.8 (1.7)	64	0.51 (1.0)
	LW	405	1.4 (3.0)	157	0.7 (1.5)	110	0.4 (0.8)
Totals	LP	735	16.2 (35.8)	349	10.28 (22.7)	143	8.8 (19.5)
	LW	874	13.3 (29.3)	555	7.56 (16.7)	293	6.4 (14.0)

*See Fig. IV-A-1.

**LP = Least-power design point.

LW = Least-weight design point.

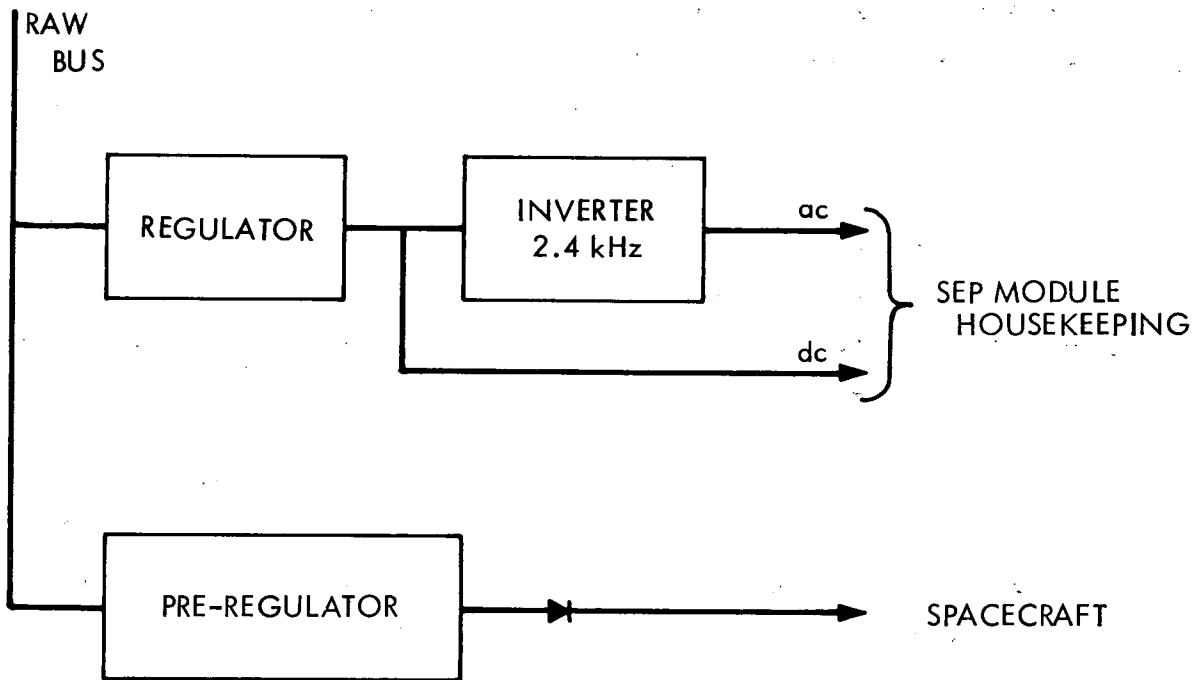
4. Pre-regulator and SEP Module Housekeeping Power Inverter Study

The design data for the pre-regulator and propulsion power inverter utilized in the study is summarized in Table IV-A-10. As can be seen, only the pre-regulator is affected by the choice of the array voltage.

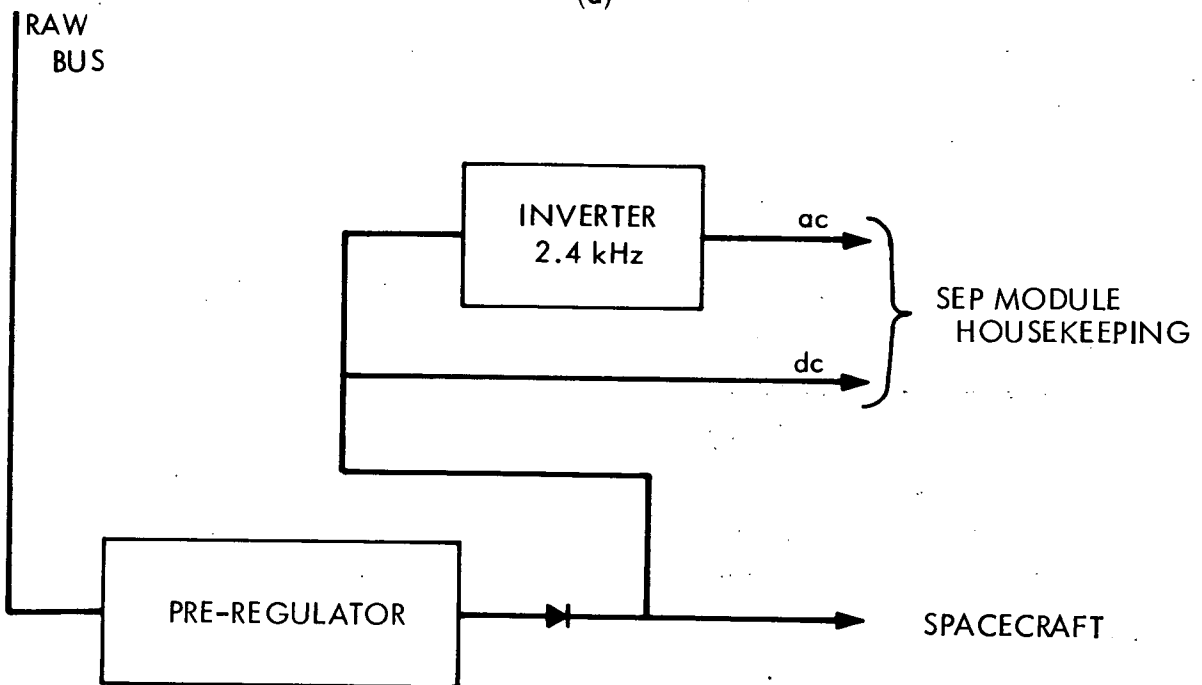
Table IV-A-10. Design Data for Pre-regulator and Propulsion Housekeeping Inverter

Power Conditioner	Input Voltage: Source/Range	Output Power (W)	Output Voltage (V)
Pre-regulator	Array: 1. 50-100 2. 100-200 3. 200-400	540 (Mariner) 775 (Viking)	45 V dc 50 V 50 V
Propulsion Housekeeping Power Inverter	Pre-regulator: 40-50 V dc	90	50 V rms

Regulated power supplied to the propulsion housekeeping subsystems can be generated by either of two approaches, shown in Fig. IV-A-13. In Fig. IV-A-13a, the housekeeping subsystems receive dc-regulated power from a separate dc regulator and regulated ac from an inverter supplied by that regulator. The pre-regulator shown supplies regulated dc power to the Mariner or to the Viking spacecraft power subsystem. Regulation of the output voltage of the pre-regulator is not closely controlled. In the second approach, the housekeeping subsystem receives regulated power from the same pre-regulator which supplies the spacecraft. The inverter operating from the output of the pre-regulator supplies regulated ac power to the propulsion housekeeping subsystem. To meet the regulation requirements of the propulsion housekeeping subsystems, the pre-regulator output voltage must be regulated to $\pm 1\%$. If the same efficiency is assumed for the regulator and the pre-regulator, no advantage in efficiency will be realized in either approach. However, the second approach was selected because it requires one less module.



(a)



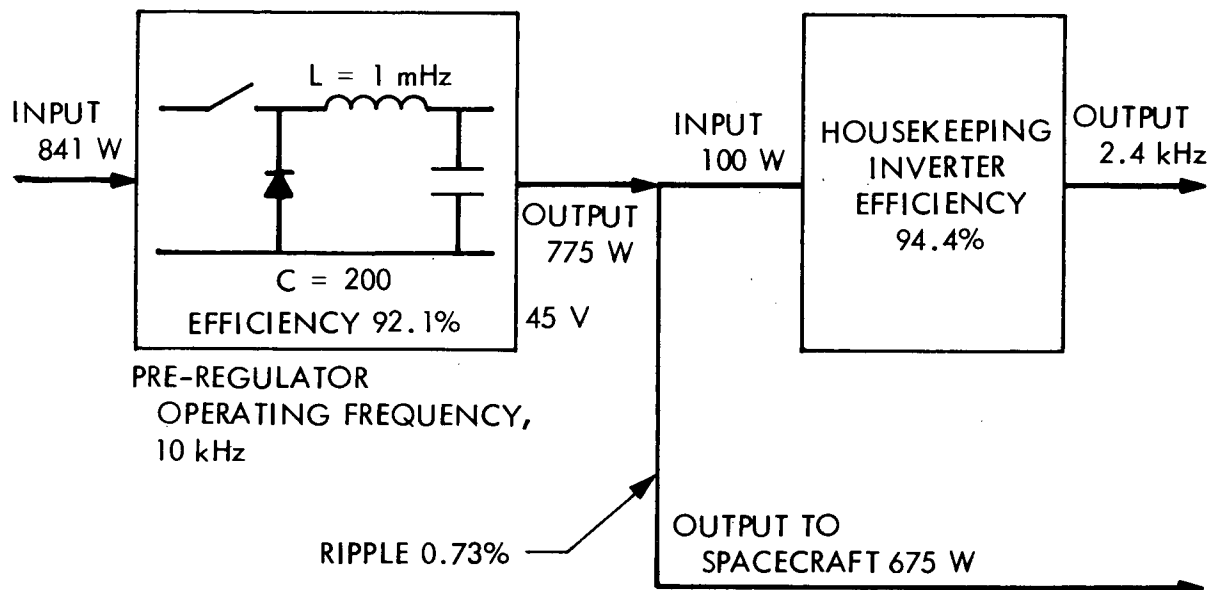
(b)

Fig. IV-A-13. Alternate Approaches for Delivering Regulated Power to Propulsion Housekeeping and Spacecraft

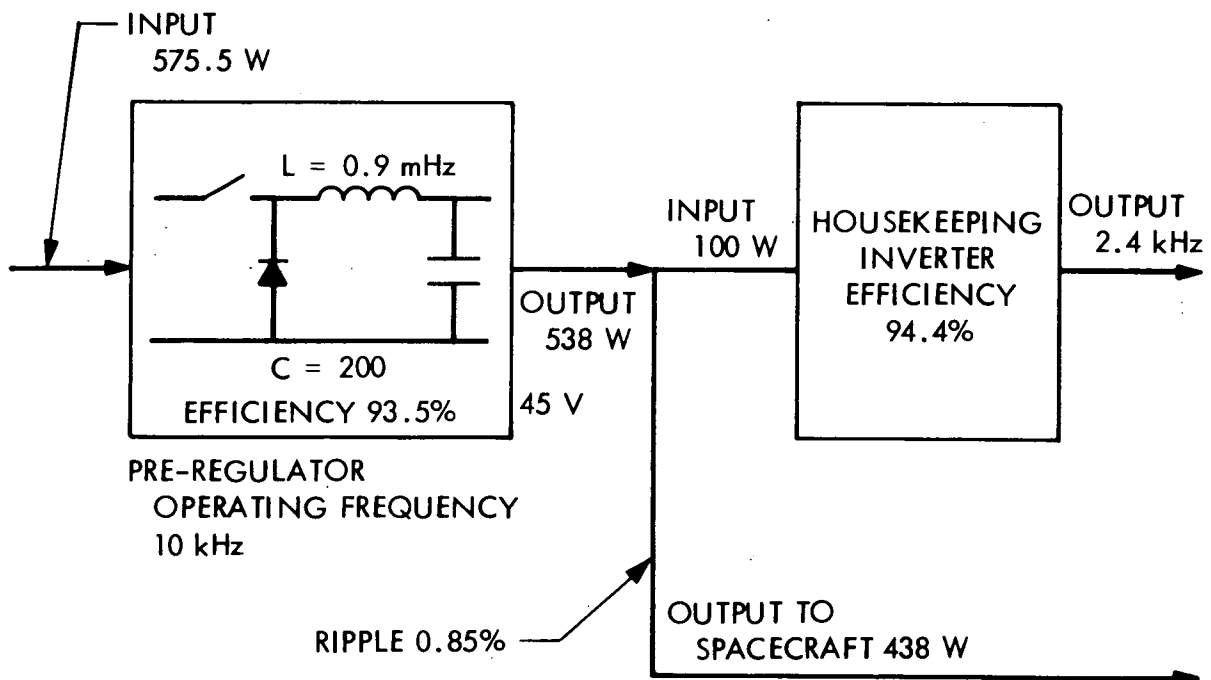
A pre-regulator was designed to supply regulator voltage between 40 to 50 V to satisfy both the Mariner or Viking power subsystem input voltage requirement. Thus, the solar array output voltage extreme range under consideration, 50 to 400 V, is always greater than the required output voltage, and a down switching regulator is the obvious choice. For the 50-to-100 V input range, the pre-regulator output will be 45 V, the maximum practical design value, allowing a 5-V drop across the module. For the two higher input voltage ranges (100 to 200 V and 200 to 400 V), the pre-regulator output voltage will be 50 V, the maximum allowable.

The pre-regulator design provides a maximum ripple of 1%, if a resistive load is assumed. Connecting the pre-regulator as designed to the input of Viking or MVM73 adds capacitance to its output filter, which means that either the ripple will be reduced or the pre-regulator filter capacitor can be reduced. The purpose of the analysis was to determine the losses that would result with a filter designed to limit ripple to a maximum of 1%. The filter choke was varied in an effort to reduce its size while still maintaining a maximum of 1% ripple. This study shows that no practical value exists in some cases in selecting choke sizes for a pre-regulator design that can handle both Viking and MV 73 or a pre-regulator design which can handle MVM73 only. Assuming the switching transistor can handle the current, the pre-regulator design for both the situations (both or MV 73 only) would be identical. The resistance of the choke was proportioned from a choke used in the Mariner design. The capacitor resistance is assumed to be $1\ \Omega$, based on manufacturer's data for a worst-case environment. Figures IV-A-14 through 16 show the filter design efficiencies and ripple calculations for the pre-regulator and housekeeping inverter for a common design to be used for both the Viking and Mariner spacecraft and for a design for a Mariner spacecraft only. The pre-regulator efficiencies for all three input voltages are summarized in Table IV-A-11.

The analyses performed have uncovered no major technical problems related to the pre-regulator design within a voltage range of 50 to 400 V; however, a breadboard design and testing is required to support the validity of the conclusions. Input filter design requirements must be reevaluated.

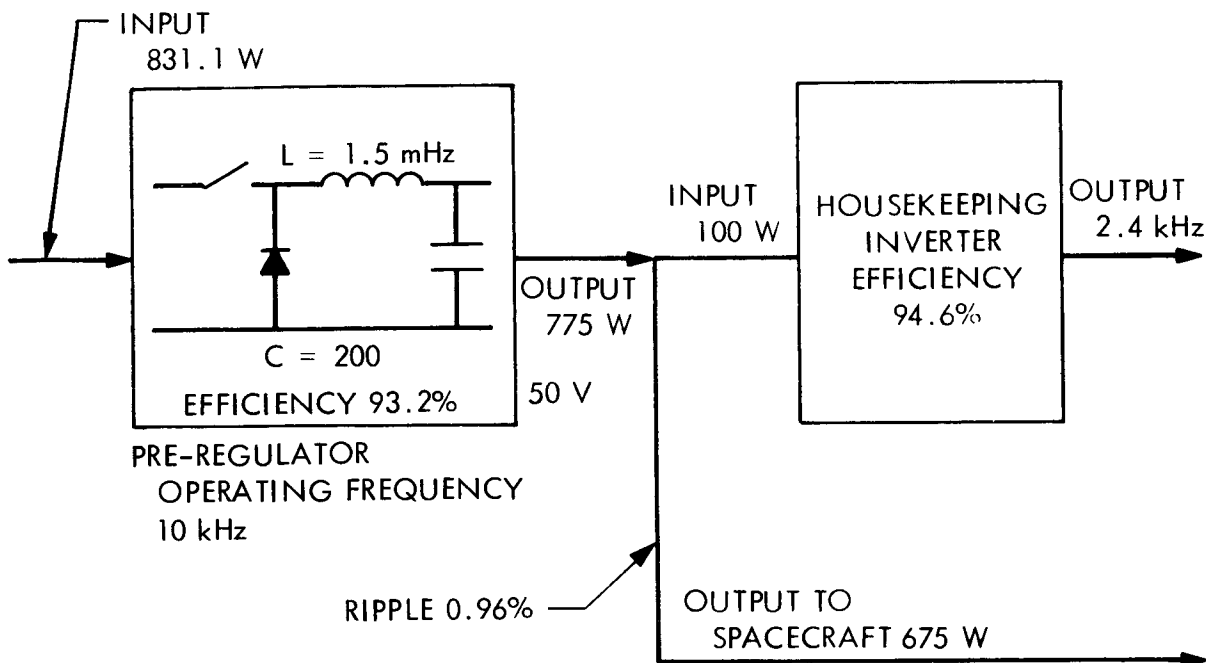


(a) For Use With Viking and MVM 73

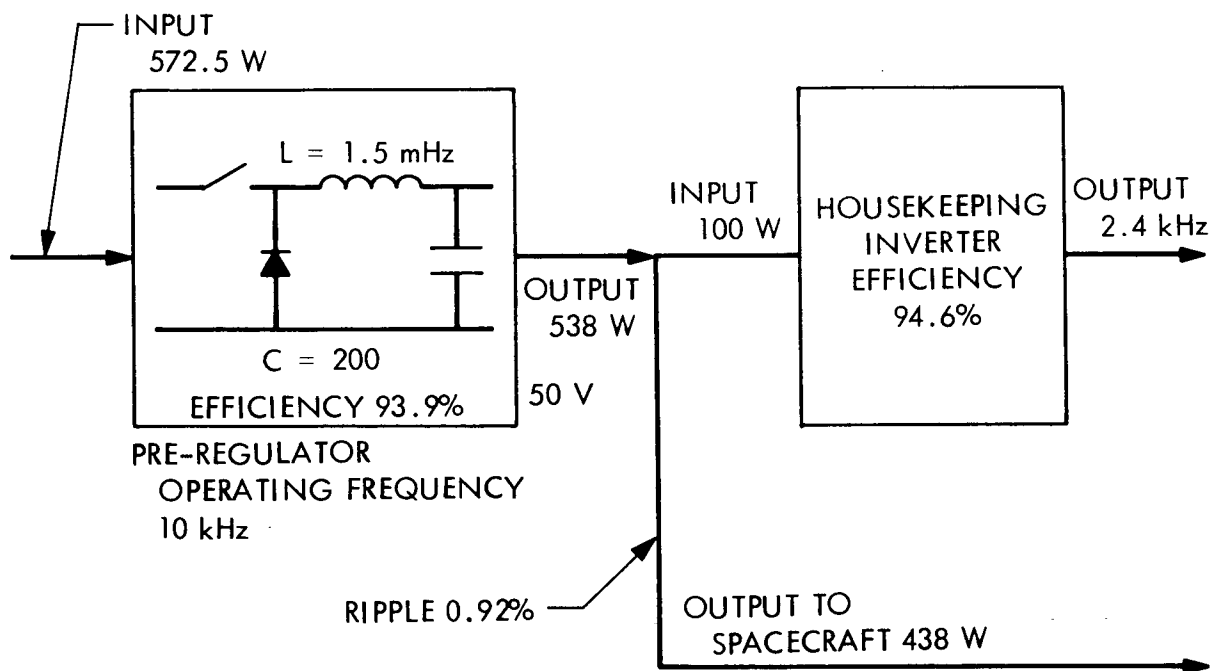


(b) For Use With MVM 73 Only

Fig. IV-A-14. Housekeeping Power Conditioning Units
(Input Voltage from 50 to 100 V)

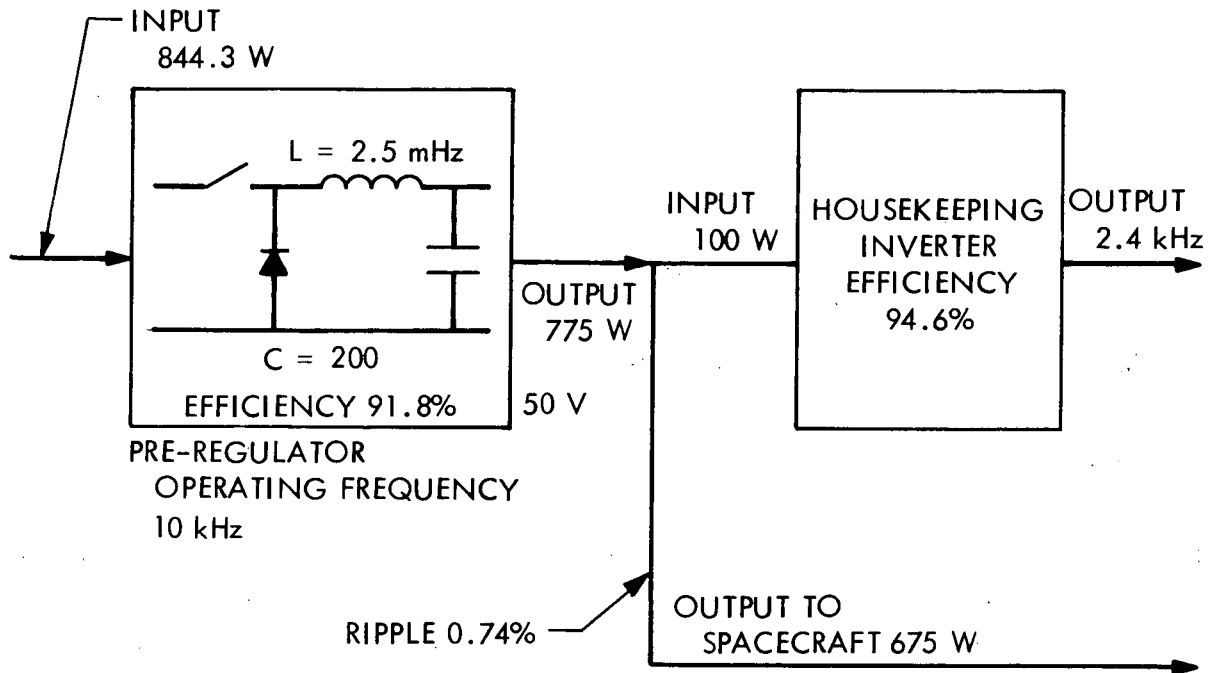


(a) For Use with Viking and MVM 73

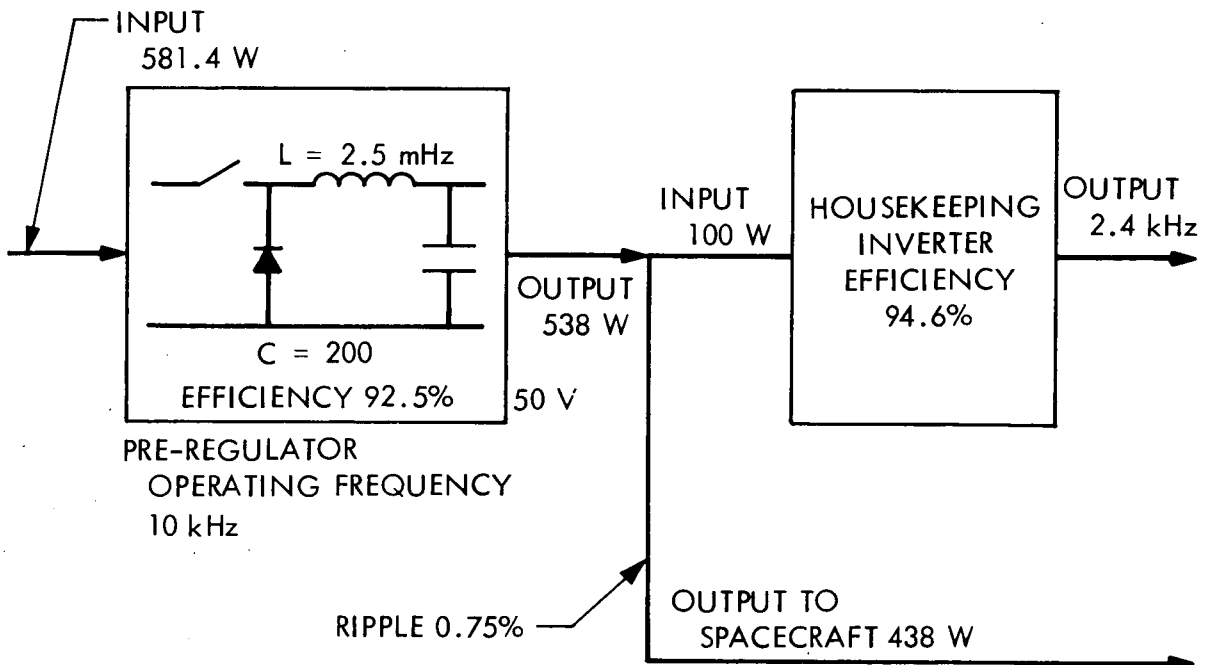


(b) For Use with MVM 73 Only

Fig. IV-A-15. Housekeeping Power Conditioning Units
(Input Voltage from 100 to 200 V)



(a) For Use with Viking and MVM 73



(b) For Use With MVM 73 Only

Fig. IV-A-16. Housekeeping Power Conditioning Units
(Input Voltage from 200 to 400 V)

Table IV-A-11. Summary of Efficiency Calculations for Pre-regulator

Spacecraft	Input, V	Pre-regulator Efficiency, %	Housekeeping Inverter Efficiency, %
Viking and MVM 73	50 to 100	92.1	94.4
MVM 73	50 to 100	93.5	94.4
Viking and MVM 73	100 to 200	93.2	94.6
MVM 73	100 to 200	93.9	94.6
Viking and MVM 73	200 to 400	91.8	94.6
MVM 73	200 to 400	92.5	94.6

High-power, high-voltage power transistors have only recently become available and must be proven and approved for space applications. The efficiencies shown in Table IV-A-11 indicate a small efficiency advantage for the pre-regulator in the 100- to 200-V input range. Because the pre-regulator processes less than 4% of the total array power, this small advantage insignificantly influences the selection of the optimum voltage range.

5. Results and Conclusions

a. Solar Array

- (1) A roll-out solar array with a voltage output between 50 to 200 V at 1 AU, and power levels up to 10 kW can be designed and built using conventional techniques, provided that additional development effort solves problems associated with array substrate fabrication, substrate stiffness and bending, and solar-cell module assembly techniques.
- (2) Array designs having output voltages of 50 to 400 V are relatively free from the effects of space plasma in planetary missions and are substantially below the voltages that are believed to be affected by the most dense regions of the ionosphere.

- (3) Calculation of the solar array design based on the General Electric Company solar array (2.5-kW model) have shown that the specific power density, W/kg, is greater at the highest voltage design of 200 to 400 V for all power levels. The data obtained is tabulated in Table IV-A-12.
- (4) A solar array design utilizing switching to maintain two electrically isolated array sections looks feasible. However, more detailed analysis in the number and type of switching circuits and interwiring should be performed before the approach can be recommended.

Table IV-A-12. Specific Power Density, 2.5-kW Solar Array

Power Output kW/panel	Launch Accel- eration \underline{g}	Voltage at 1 AU		
		50 V	100	200
		Power Density W/kg (W/lb)	Power Density W/kg/(W/lb)	Power Density W/kg (W/lb)
2.5	9.0	13.75 (30.32)	13.91 (30.66)	14.04 (30.96)
2.5	4.5	16.71 (36.84)	16.91 (37.27)	17.07 (37.64)
5.0	9.0	10.97 (24.19)	11.09 (24.46)	11.25 (24.81)
5.0	4.5	14.42 (31.80)	14.59 (32.16)	14.81 (32.65)
10.0	9.0	8.81 (19.43)	8.94 (19.71)	9.07 (19.99)
10.0	4.5	11.66 (25.70)	11.83 (26.09)	12.01 (26.47)

b. Power Distribution System

From the power distribution analyses it was determined that the least power loss and least weight are obtained within the design voltage range of 200 to 400 V. The data obtained are listed in Table IV-A-13.

Table IV-A-13. Least Weight and Power Loss

Voltage Range, V	Power Generated/ Distributed	Least-weight Design		Least-power-loss Design	
		Weight, kg (lb)	Losses, W	Weight, kg (lb)	Losses, W
50 to 100	20 kW/16 kW ↓	13.29 (29.3)	874.0	16.24 (35.8)	735.0
100 to 200		7.57 (16.7)	555.2	10.30 (22.7)	349.0
200 to 400		6.35 (14.0)	293	8.85 (19.5)	143.0

c. Pre-regulator and Propulsion Housekeeping

- (1) The pre-regulator efficiency calculations show that efficiency is somewhat higher within an input range of 100 to 200 V. However, the power processed by the pre-regulator is less than 4% of the total solar-array-power generated and processed and has little overall design impact.
- (2) The pre-regulator and inverter designs are considered to be essentially state of the art over the entire range of 50 to 400 V. The study assumed that high voltage transistors are available, but these devices must be procured and tested before acceptance. A breadboard power conditioner, using the high voltage transistor, is required to evaluate alternate designs and to verify performance characteristics with the Mariner (or Viking) power subsystem.

6. Recommendations

Based on the results summarized above, the 200- to 400-V range provides design advantages for the solar array and the power distribution system. The pre-regulator and propulsion-housekeeping power conditioning designs have the highest efficiency within the 100- to 200-V input voltage range.

The loss in efficiency at the 200- to 400-V input voltage range is approximately 2%. Considering that the power handled by the pre-regulator and propulsion-housekeeping power conditioner is approximately less than 4% of the power generated by the solar array and of the power distributed by the power subsystem, the power losses incurred by operating the housekeeping-power conditioners at 200 to 400 V are negligible. For these reasons, it is recommended that 200 to 400 V be selected for the unregulated bus voltage of the SEP module power subsystem.

REFERENCES

- IV-A-1. J. V. Coyner, Jr. and R. G. Ross, Jr., Parametric Study of the Performance Characteristics and Weight Variations of the Large-Area Roll Up Solar Arrays, JPL Technical Report, TR 32-1502, December 15, 1970.
- IV-A-2. F. A. Blake and K. L. Hanson, "The 'Hot Spot' Failure Mode for Solar Arrays", IEEE Intersociety Energy Conversion Engineering Conference Record, pp. 575-581, 1969.
- IV-A-3. W. Knauer et al, High Voltage Array Study, NASA CR 72675, prepared by Hughes Research Laboratories for Lewis Research Center under contract NAS 3-11535, May 1970.

B. SOLAR ARRAY STUDIES

1. Dynamic Interactions With Attitude Control

a. Summary

A tradeoff study was initiated to evaluate a best solar array for an electric propulsion Encke mission from an attitude control point of view. The study was intended to examine, in detail, the flexible solar array/attitude control interaction problem for both the thrust vector control (TVC) and the reaction control system (RCS) modes of operation. The effects of attitude control system non-linearities were also to be evaluated.

At this time, the linear TVC model is complete and has been subjected to exhaustive stability analysis. A digital computer simulation program was constructed for the model and shows the time history of control. It was decided that inclusion of the non-linearities in the TVC model not only was not feasible, but that, because of earlier simulation work, was not necessary.

Work is continuing on the RCS model and results are expected shortly. However, it is felt that the basic conclusions for the TVC model will be applicable to the RCS model. The remainder of this study is concerned with the TVC model.

The stability study is parametric in nature. The parameters are solar-array aspect ratio, first natural frequency, and solar-array rotation angle (about the yaw axis). In addition, the celestial sensor gain factors were also varied in the study. First natural frequencies varied from approximately 0.014 to 0.06 Hz. Actually, the first six modes of solar array vibration were included. Aspect ratios of 7.38, 5.40, and 4.11 were considered. Solar-array rotation angles of 0, 30, and 60 deg were allowed.

Such anomalous behavior as unequal tension in solar array blankets was not considered in this study. The effects of this as well as those

of higher than the sixth mode of vibration should be determined in later studies. Frequency sensitivity studies are also recommended to indicate how accurately natural frequencies need to be known.

The stability analysis takes the form of an eigenvalue analysis; i.e., for a given spacecraft (the aspect ratio, natural frequency, rotation angle, spacecraft inertia properties, etc.), the roots of the characteristic equation for the configuration were determined. For six modes of vibration, the number of roots is 30. The appearance of any root with a positive real part implies instability. The presence of all distinct roots each with a negative real part guarantees attitude stability. The response character of a given configuration was then ascertained with a digital computer simulation program for the system's equations of motion. Results of some of these simulations are included in this report.

b. Major Conclusions

The four major conclusions reached are (a) that solar arrays with large aspect ratio are more attractive than those with small aspect ratio, (b) that solar arrays with higher natural frequencies are more likely to be stable than those with lower natural frequencies, (c) that lowest array frequency is not always the criterion for stability, and (d) that array tip deflections are so small that large stresses at the base of the arrays do not develop. The second of these statements was expected. However, the conclusion (a) seems somewhat surprising at first. Intuition would probably lead one to suspect that a small aspect ratio (a short solar array) would be more stable because an array with a low aspect ratio would seem to be stiffer in the roll and pitch axes. However, from the dynamics analysis, it is the yaw axis which is most sensitive to solar-array flexibility, and small aspect ratio has the effect of stiffening in the yaw axis.

At this point in the study of the solar-array attitude-control interaction problem, the 3.657 or 4.267-m (12-or 14-ft) wide array should be recommended for the Encke rendezvous mission. This is in keeping with the

concept of the 4.267-m (14-ft) wide array currently being designed, which has an aspect ratio of 5.57, slightly larger than the 5.40 value adhered to in the interaction study. Conceivably, an array with lowest natural frequency of 0.015 Hz could be used. However, additional analysis is required to confirm this.

The study points out vividly the necessity and usefulness of a design tool such as the computer program, SEWART. This coupled three-axis eigenvalue program can determine, in microseconds, if a configuration is likely to be stable. The term likely is appropriate in that the SEWART program examines the linear equations, which only approximate the actual spacecraft configuration. However, such linear models generally tell a good deal about the actual model. The alternatives to using an eigenvalue problem are the root locus analysis, which can not evaluate coupled three-axis stability criteria, or the simulation analysis. However, simulation analysis can often lead to erroneous results. Clearly, for the flexible configuration, a simulation of 1000 sec in real time would indicate a stable configuration. Only after 1500 sec does the instability make itself apparent.

Comparisons of the results for rigid models with those for flexible models show the need for including the flexible characteristics of the arrays in the design of the attitude control system. In many instances, the rigid models are stable whereas the flexible ones are not. In rare instances, the opposite is true.

c. Attitude Control Analysis

It has been determined in earlier work (Ref. IV-B-1) that the pitch, yaw, and roll equations of motion for the solar electric spacecraft are

$$I_{xx}\ddot{\theta}_x + I_{xy}\ddot{\theta}_y + I_{xz}\ddot{\theta}_z - (\delta_{1x}\ddot{\eta}_1 + \dots + \delta_{Nx}\ddot{\eta}_N) = -2\sqrt{2} p_y^{3*0} F\alpha_x + T_{Dx} \quad (1)$$

$$\begin{aligned}
 & I_y \ddot{\theta}_y + I_{yz} \ddot{\theta}_z + I_{yx} \ddot{\theta}_x + \bar{K}_3 \ddot{t}_z - (\delta_{1y} \ddot{\eta}_1 + \dots + \delta_{Ny} \ddot{\eta}_N) \\
 & = -\frac{3(M - \bar{m})}{M} Ft_z - \frac{3F}{M} (\Delta_{1z} \eta_1 + \dots + \Delta_{Nz} \eta_N) + T_{Dy}
 \end{aligned} \tag{2}$$

$$\begin{aligned}
 & I_z \ddot{\theta}_z + I_{zx} \ddot{\theta}_x + I_{zy} \ddot{\theta}_y - K_3 \ddot{t}_y - (\delta_{1z} \ddot{\eta}_1 + \dots + \delta_{Nz} \ddot{\eta}_N) \\
 & = \frac{3(M - m)}{M} Ft_y + \frac{3F}{M} (\Delta_{1y} \eta_1 + \dots + \Delta_{Ny} \eta_N) + T_{D3}
 \end{aligned} \tag{3}$$

The symbols have the following definitions:

I_x, I_y, I_z - spacecraft pitch, yaw, roll moments of inertia

I_{xy}, I_{yz}, I_{zx} - spacecraft products of inertia, $I_{xy} = I_{yz}$, etc.

$\theta_x, \theta_y, \theta_z$ - pitch, yaw, roll Euler angles

δ_{ij}, Δ_{ij} - rigid-elastic coupling terms, $i = 1, \dots, N$, and $j = x, y, z$,

and N is the number of modes considered (see Ref. IV-B-2 for more detail)

η_i - modal coordinates, $i = 1, \dots, N$

p_y^{3*0} - y axis offset of outer thruster from center of thruster array
(assumed equal to z axis offset)

F - thrust level of one thruster

α_x - thruster gimbal angle

T_{Di} - disturbance torque, $i = x, y, z$

M - total spacecraft mass

m - mass of thruster array and translating mechanism

\bar{m} - mass of thruster array only

t_i - thruster array translation in i th direction, $i = y, z$

\bar{K}_3 - product of m and distance 1.52 m (10 ft) between spacecraft mass center and thruster array

K_3 - product of \bar{m} and distance 1.52 m (10 ft) between spacecraft mass center and thruster array

From the control block diagram (Fig. IV-B-1) it can be determined that expressions for the translating and gimbaling rates, and the first and second derivatives respectively of the sensor and feedback circuit voltages are:

$$\dot{t}_z = K_{my} K_{Vy} (V_{sy} - V_{Fy}) \quad (4)$$

$$\dot{t}_y = K_{mz} K_{Vz} (-V_{sz} - V_{Fz}) \quad (5)$$

$$\dot{\alpha}_x = K_{ml} K_{Vx} (V_{sz} - V_{Fz}) \quad (6)$$

$$\dot{V}_{sx} = \frac{1}{\tau_{sx}} (K_{sx} \theta_x - V_{sx}) \quad (7)$$

$$\dot{V}_{sy} = \frac{1}{\tau_{sy}} (K_{sy} \theta_y - V_{sy}) \quad (8)$$

$$\dot{V}_{sz} = \frac{1}{\tau_{sz}} (K_{sz} \theta_z - V_{sz}) \quad (9)$$

$$\begin{aligned} \ddot{V}_{Fx} = & \frac{K_{Fx} K_{1x} K_{Vx}}{\tau_{1x}} \dot{V}_{sx} + \frac{K_{Fx} K_{1x} K_{Vx}}{\tau_{1x} \tau_{2x}} (1 + K_{2x}) V_{sx} \\ & - \left(\frac{K_{Fx} K_{1x} K_{Vx}}{\tau_{1x}} + \frac{\tau_{1x} + \tau_{2x}}{\tau_{1x} \tau_{2x}} \right) \dot{V}_{Fx} \\ & - \left[K_{Fx} K_{1x} K_{Vx} (1 + K_{2x}) + 1 \right] \frac{V_{Fx}}{\tau_{1x} \tau_{2x}} \end{aligned} \quad (10)$$

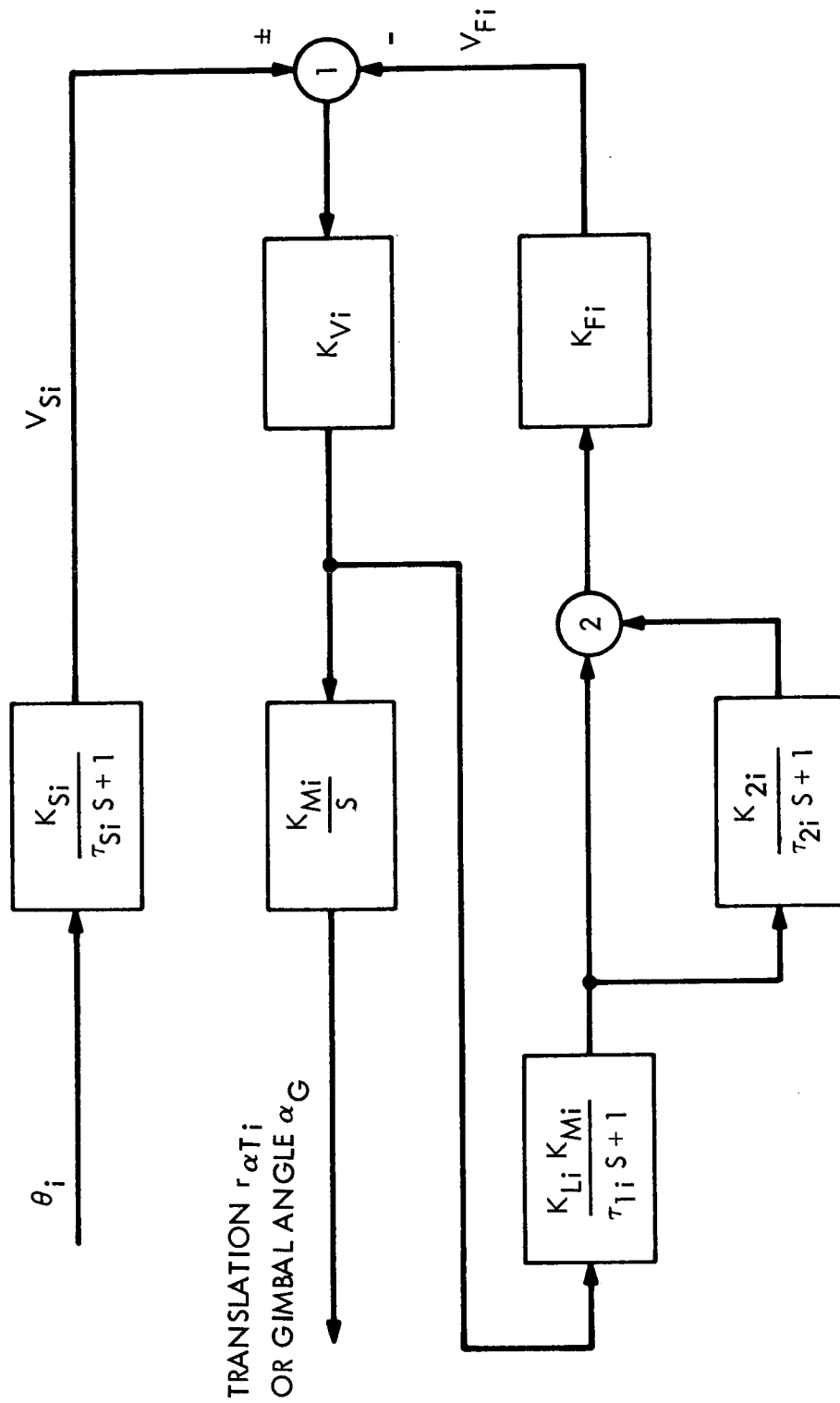


Fig. IV-B-1. Control System Block Diagram

$$\begin{aligned}
\ddot{V}_{Fy} = & \frac{K_{Fy} K_{ly} K_{Vy}}{\tau_{ly}} \dot{V}_{sy} + \frac{K_{Fy} K_{ly} K_{Vy}}{\tau_{ly} \tau_{2y}} (1 + K_{2y}) V_{sy} \\
& - \left(\frac{K_{Fy} K_{ly} K_{Vy}}{\tau_{ly}} + \frac{\tau_{ly} + \tau_{2y}}{\tau_{ly} \tau_{2y}} \right) \dot{V}_{Fy} \\
& - \left[K_{Fy} K_{ly} K_{Vy} (1 + K_{2y}) + 1 \right] \frac{V_{Fy}}{\tau_{ly} \tau_{2y}}
\end{aligned} \tag{11}$$

$$\begin{aligned}
\ddot{V}_{Fz} = & - \frac{K_{Fz} K_{lz} K_{Vz}}{\tau_{lz}} \dot{V}_{sz} - \frac{K_{Fz} K_{lz} K_{Vz}}{\tau_{lz} \tau_{2z}} (1 + K_{2z}) V_{sz} \\
& - \left(\frac{K_{Fz} K_{lz} K_{Vz}}{\tau_{lz}} + \frac{\tau_{lz} + \tau_{2z}}{\tau_{lz} \tau_{2z}} \right) \dot{V}_{Fz} \\
& - \left[K_{Fz} K_{lz} K_{Vz} (1 + K_{2z}) + 1 \right] \frac{V_{Fz}}{\tau_{lz} \tau_{2z}}
\end{aligned} \tag{12}$$

New parameters introduced here are:

K_{si} - sensor gain parameters, $i = x, y, z$

K_{mi} - stepper motor gain parameters, $i = x, y, z$

K_{Vi} - voltage controlled oscillator gain parameters, $i = x, y, z$

K_{li}, K_{2i} - gain parameters associated with the feedback circuits,
 $i = x, y, z$

V_{si} - sensor voltage, $i = x, y, z$

V_{Fi} - feedback voltage, $i = x, y, z$

τ_{si} - sensor time constants, $i = x, y, z$

τ_{li}, τ_{2i} - time constants associated with feedback circuits, $i = x, y, z$

A complete set of equations for describing the vehicle attitude motion is available upon the addition of the appendage equation

$$\ddot{\eta}_i + 2\zeta_i\sigma_i\dot{\eta}_i + \sigma_i^2\eta_i = \delta_{ix}\ddot{\theta}_x + \delta_{iy}\ddot{\theta}_y + \delta_{iz}\ddot{\theta}_z - \frac{1}{M}(\Delta_{iy}\ddot{t}_y + \Delta_{iz}\ddot{t}_z) \quad (13)$$

where ζ_i and σ_i are the damping factor and natural frequency, respectively, associated with the i th mode.

To facilitate programming the equations for the stability and simulation analyses, it is convenient to redefine the variables as

$$\begin{aligned} \theta_x &= y_1 & \theta_y &= y_2 & \theta_z &= y_3 \\ v_{Fx} &= y_4 & v_{Fy} &= y_5 & v_{Fz} &= y_6 \\ \eta_1 &= y_7 & \dots & , & \eta_N &= y_{N+6} \\ \alpha_x &= y_{N+7}, & t_y &= y_{N+8}, & t_z &= y_{N+9} \\ v_{sx} &= y_{N+10}, & v_{sy} &= y_{N+11}, & v_{sz} &= y_{N+12} \\ \dot{v}_{Fx} &= y_{N+13}, & \dot{v}_{Fy} &= y_{N+14}, & \dot{v}_{Fz} &= y_{N+15} \\ \dot{\theta}_x &= y_{N+16}, & \dot{\theta}_y &= y_{N+17}, & \dot{\theta}_z &= y_{N+18} \\ \dot{\eta}_1 &= y_{N+19}, & \dots & , & \dot{\eta}_N &= y_{2N+18} \end{aligned} \quad (14)$$

In matrix form, the attitude equations are

$$A\dot{y} = By + T \quad (15)$$

where

$$y = [y_1, \dots, y_{2N+18}]^T, \quad T = \left[0, \dots, 0, \frac{T_{D1}}{I_1}, \frac{T_{D2}}{I_2}, \frac{T_{D3}}{I_3}, 0, 0, 0, 0, 0, 0\right]^T \quad (16)$$

and A and B are constant matrices of coefficients obtained from eqs (1) through (13), and T is the column matrix of disturbance torques. To be more precise,

$$A = \begin{bmatrix} I & O \\ O & C \end{bmatrix} \quad (17)$$

where I is the identity matrix, O is the zero matrix, and C is an $(N+3) \times (N+3)$ matrix of coefficients of second derivative terms in eqs (1) through (13). Pre-multiplication of both sides of eq (15) by the inverse of A

$$A^{-1} = \begin{bmatrix} I & O \\ O & C^{-1} \end{bmatrix} \quad (18)$$

produces

$$\dot{y} = A^{-1}By + A^{-1}T \quad (19)$$

Denote

$$D = A^{-1}B \quad (20)$$

then, eq (19) becomes

$$\dot{y} = Dy + A^{-1}T \quad (21)$$

Stability of the linear system

$$\dot{y} = Dy \quad (22)$$

is guaranteed if the roots of the characteristic equation

$$|D - sI| = 0 \quad (23)$$

are distinct and have negative real parts. A digital computer program, Solar Electric with Array Articulation (SEWART), was generated for the purpose of calculating the roots of eq (23). At present, the program can handle up to 50th order systems. This means that up to 16 modes of array vibration can be accommodated. The current study includes only the first six modes, since all modes above the sixth are of higher order. The resulting system of equations is of order 30. Thus, for a given configuration, if all 30 roots are distinct and have negative real parts, the attitude motion is asymptotically stable.

The simulation program, Solar Electric Spacecraft Simulation (SESSIM), integrates the equations of motion, eqs (21). In general, the program assumes initial conditions on y_1, \dots, y_{30} as well as disturbance torques T_{Di} ($i = x, y, z$). The disturbance torques are determined by the amount of mass center offset assumed. Both solar torques and torque from thruster offset are present.

d. Structural Analysis

The output data from a structural analysis of the solar arrays, carried out at JPL, is contained in Ref. IV-B-3. A computer program entitled, "Modal Analysis of Spacecraft with Rollup Solar Arrays", was written for the purpose of determining structural data. The model for the array is drawn in Fig. IV-B-2. Blankets A and B constitute one solar array while blankets C

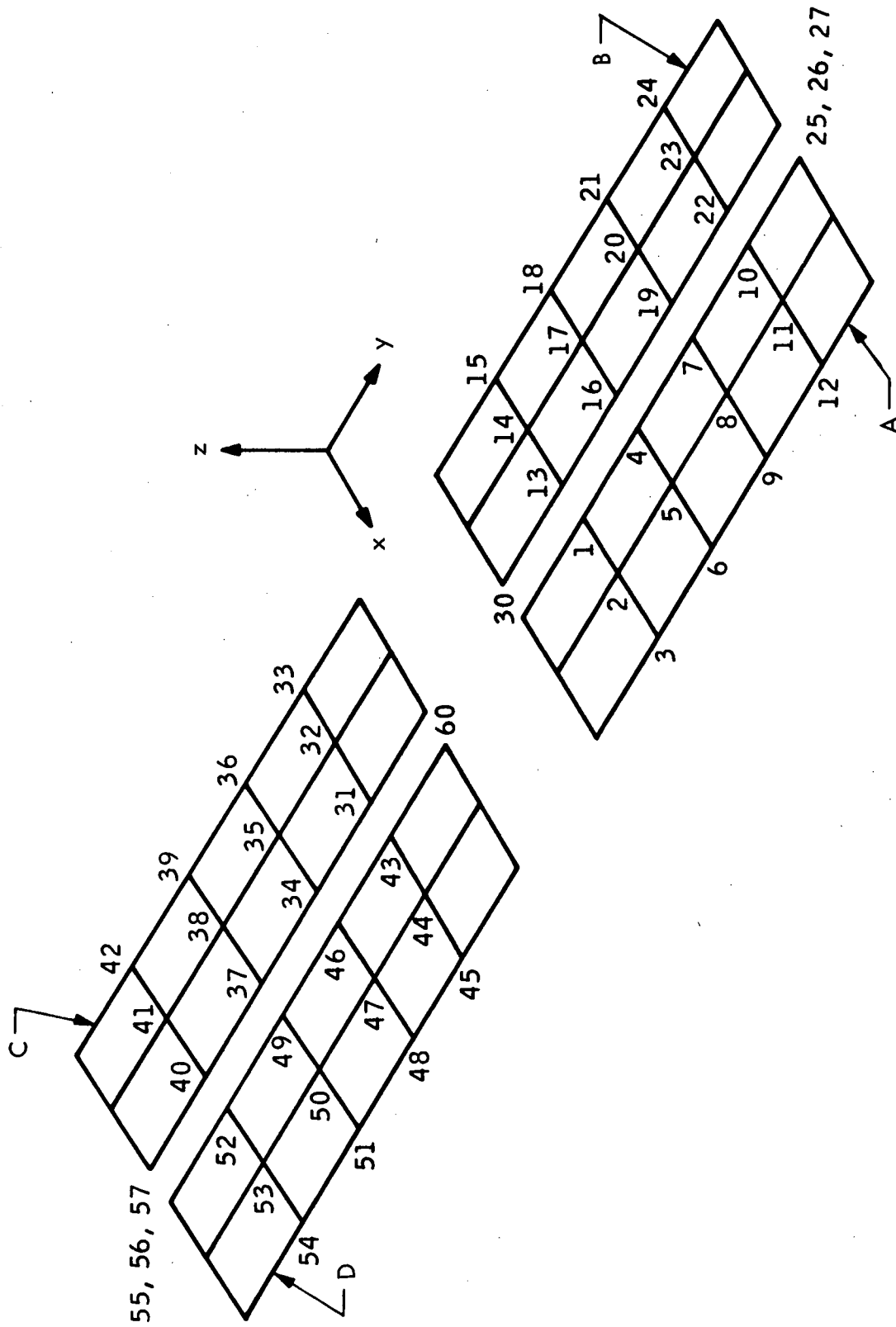


Fig. IV-B-2. Solar Array Model

and D constitute the other. Not shown are the spacecraft bus between the arrays, the rollout mechanism in which the array is housed during launch, the booms separating blankets A and B and blankets C and D, and the leading edge members.

Each blanket is subdivided into 10 elements. Finite-elements structural analysis techniques are then applied to the 40 elements comprising the array (Ref. IV-B-3). Each number on the array is a node and corresponds to an actual coordinate of displacement. Nodes 1 through 12, 13 through 24, 31 through 42, 43 through 54, and 26 and 56 correspond to displacements normal to the array surface (or z axis). Nodes 25 and 55 correspond to rotational displacements about the yaw (y) axis and nodes 27, 30, 57 and 60 correspond to rotations about the roll axis.

Data for a 20-kW array were evaluated and consist of mode frequencies, mode shapes, rigid-elastic coupling terms, and total spacecraft mass and inertia data. Samples of these kind of data were generated by the JPL program and appear in Tables IV-B-1 through IV-B-4. Input data to the program include stiffness of the boom (EI), tension in the blankets (T), length of the array (LARY), width of the array (WARY), inertias of the bus (IXX, IYY, IZZ), weight of the rollup drum (WDRM), weight of the leading edge member (WLEM), weight of the blanket (WBLK), weight of the boom (WBOM), and rotation angles of the arrays (ARL and ARR).

Three sizes of array were considered (see Fig. IV-B-3). Their dimensions are 3.65 x 26.97 m (12 x 88.5 ft), 4.26 x 23.03 m (14 x 75.6 ft), and 4.87 x 20.02 m (16 x 65.7 ft). These correspond to aspect ratios of 7.38, 5.40, and 4.11 respectively. Array rotation angles of 0, 30, and 60 deg were considered (see Fig. IV-B-4). First mode natural frequencies of approximately 0.014, 0.03, and 0.06 Hz were assumed for the arrays. Table IV-B-5 lists these various configurations in a more compact manner. Numbers 1A through 9C are assigned to the 27 cases. Structural data for all but 2A, 2B, 2C, 3A, 3B, 3C and 9C are ascertained.

Table IV-B-1. Mode Frequencies For 20-kW Array, Aspect Ratio = 7.38
Lowest Natural Frequency = 0.03 Hz

1	2	3	4	5	6	7	8	9	10
.02962	.02962	.02965	.03208	.03612	.03907	.06153	.06153	.06158	.06158
11	12	13	14	15	16	17	18	19	20
.08496	.09533	.09152	.09152	.12909	.12909	.12922	.12922	.14756	.14841
21	22	23	24	25	25	27	28	29	30
.15268	.15268	.15269	.15266	.16104	.16104	.19135	.19135	.19135	.19135
31	32	33	34	35	36	37	38	39	40
.20765	.20755	.20735	.20735	.21899	.21902	.23898	.23899	.25291	.25291
41	42	43	44	45	46	47	48	49	50
.25291	.25291	.29089	.29089	.29119	.29119	.29263	.29313	.30779	.30779
51	52	53	54	55	56	57	58	59	60
.32695	.32695	.32695	.32695	.38739	.39022	1.36509	1.36757	3.60853	3.61016

JPL Technical Memorandum 33-583, Vol. III

Table IV-B-2. First Six Hybrid Elastic Modes and Frequencies (Hz),
20-kW Array, Aspect Ratio = 7.38

	.02962	.02962	.02965	.03206	.03612	.03907
	1	2	3	4	5	6
1	-.301	.000	.122	-.128	.000	.000
2	-.161	.001	.121	-.128	-.000	-.000
3	-.321	.001	.120	-.128	-.000	-.000
4	-.002	.000	.232	-.248	.000	.000
5	-.307	.001	.231	-.248	-.000	-.000
6	-.612	.003	.230	-.248	-.000	-.000
7	-.002	.000	.320	-.345	.000	.000
8	-.424	.002	.319	-.345	-.000	-.000
9	-.846	.004	.317	-.345	-.000	-.000
10	-.002	.000	.378	-.410	.000	.000
11	-.501	.002	.377	-.410	-.000	.000
12	-1.001	.004	.375	-.410	-.000	-.000
13	.000	.000	.122	-.128	.000	.000
14	.160	-.001	.122	-.128	.000	.000
15	.320	-.001	.123	-.128	-.000	-.000
16	.000	.000	.232	-.248	.000	.000
17	.305	-.001	.233	-.248	.000	.000
18	.610	-.003	.234	-.248	-.000	-.000
19	.000	.000	.320	-.345	.000	.000
20	.422	-.002	.321	-.345	.000	.000
21	.844	-.004	.323	-.345	-.000	-.000
22	-.000	.000	.378	-.410	.000	.000
23	.499	-.002	.380	-.410	.000	.000
24	.998	-.004	.382	-.410	-.000	-.000
25	.177	-.001	.001	-.000	.000	.000
26	-.001	.000	.401	-.436	.000	.000
27	-.000	.000	.007	-.007	.000	.000
28	-.000	.000	.120	-.130	.000	.000
29	-.000	.000	.005	-.005	.000	.000
30	-.000	-.000	-.000	-.000	.005	.005
31	.000	-.001	-.121	-.128	-.000	-.000
32	-.000	-.160	-.121	-.128	-.000	.000
33	-.001	-.320	-.121	-.128	.000	.000
34	.001	-.001	-.232	-.248	-.000	-.000
35	-.001	-.305	-.231	-.248	-.000	.000
36	-.002	-.611	-.232	-.248	-.000	.000
37	.001	-.001	-.320	-.345	-.000	-.000
38	-.001	-.423	-.320	-.345	-.000	.000
39	-.003	-.845	-.320	-.345	-.000	.000
40	.001	-.001	-.378	-.410	-.000	-.000
41	-.001	-.500	-.373	-.410	-.000	-.000
42	-.003	-1.000	-.378	-.410	-.000	-.000
43	.000	.001	-.121	-.128	.000	-.000
44	.001	.160	-.121	-.128	.000	-.000
45	.002	.320	-.122	-.128	.000	.000
46	.001	.001	-.232	-.248	.000	-.000
47	.002	.305	-.232	-.248	.000	-.000
48	.003	.611	-.232	-.248	.000	.000
49	.001	.001	-.320	-.345	.000	-.000
50	.003	.423	-.320	-.345	.000	-.000
51	.005	.845	-.320	-.345	.000	.000
52	.001	.001	-.378	-.410	.000	-.000
53	.003	.500	-.378	-.410	.000	-.000
54	.005	.999	-.379	-.410	.000	.000
55	.001	.177	-.000	-.000	.000	.000
56	.001	-.000	-.401	-.436	-.000	-.000
57	.000	-.000	-.007	-.007	-.000	-.000
58	.000	-.000	-.120	-.130	-.000	-.000
59	.000	-.000	-.005	-.005	-.000	-.000
60	-.000	-.000	.000	-.000	.005	-.005

Table IV-B-3. Rigid Elastic Coupling Terms for First Six Modes,
20-kW Array, Aspect Ratio = 7.38

	1	2	3	4	5	6
1	.00	.00	.00	.67	7.22	.00
2	.00	.00	.00	.03	-7.28	.00
3	.00	.00	.00	210.03	.02	.00
4	.00	.00	-3.57	.01	.00	.00
5	.00	.00	.00	.00	.00	214.38
6	-3.57	.00	.00	.00	.00	.00
7	.00	.00	.00	.00	.00	.00
8	.00	.00	.00	.00	.00	.00
9	.00	.00	.00	.00	.00	.00
10	.00	.00	.00	.00	.00	.00
11	.00	.00	.00	-27.41	.00	.00
12	.00	.00	.88	.00	.00	.00
13	.00	.00	.00	.00	2.42	.00
14	.00	.00	.00	.00	-2.39	.00
15	.00	.00	.00	.00	.00	.00
16	.00	.00	.00	.00	.00	.00
17	.00	.00	.00	.00	.00	.00
18	.00	.00	.00	.00	.00	.00
19	.00	.00	.00	15.79	.00	.00
20	.00	.00	1.02	.00	.00	.00
21	.00	.00	.00	.03	.00	.00
22	.00	.00	.00	.00	.01	.00
23	.00	.00	.00	.04	.00	.00
24	.00	.00	.00	.04	.00	.00
25	.00	.00	.00	.00	-1.39	.00
26	.00	.00	.00	.00	-1.40	.00
27	.00	.00	.00	.01	.00	.00
28	.00	.00	.00	.02	.00	.00
29	.00	.00	.00	.01	.00	.00
30	.00	.00	.00	.01	.01	.00

Table IV-B-4. Mass-Inertia Properties, 20-kW Array,
Aspect Ratio = 7.38

	1	2	3	4	5	6
1	75.155	.000	.000	.000	.000	.000
2	.000	75.155	.000	.000	.000	.000
3	.000	.000	75.155	.000	.000	.000
4	.000	.000	.000	45924.009	.000	.000
5	.000	.000	.000	.000	1555.939	.000
6	.000	.000	.000	.000	.000	47346.789

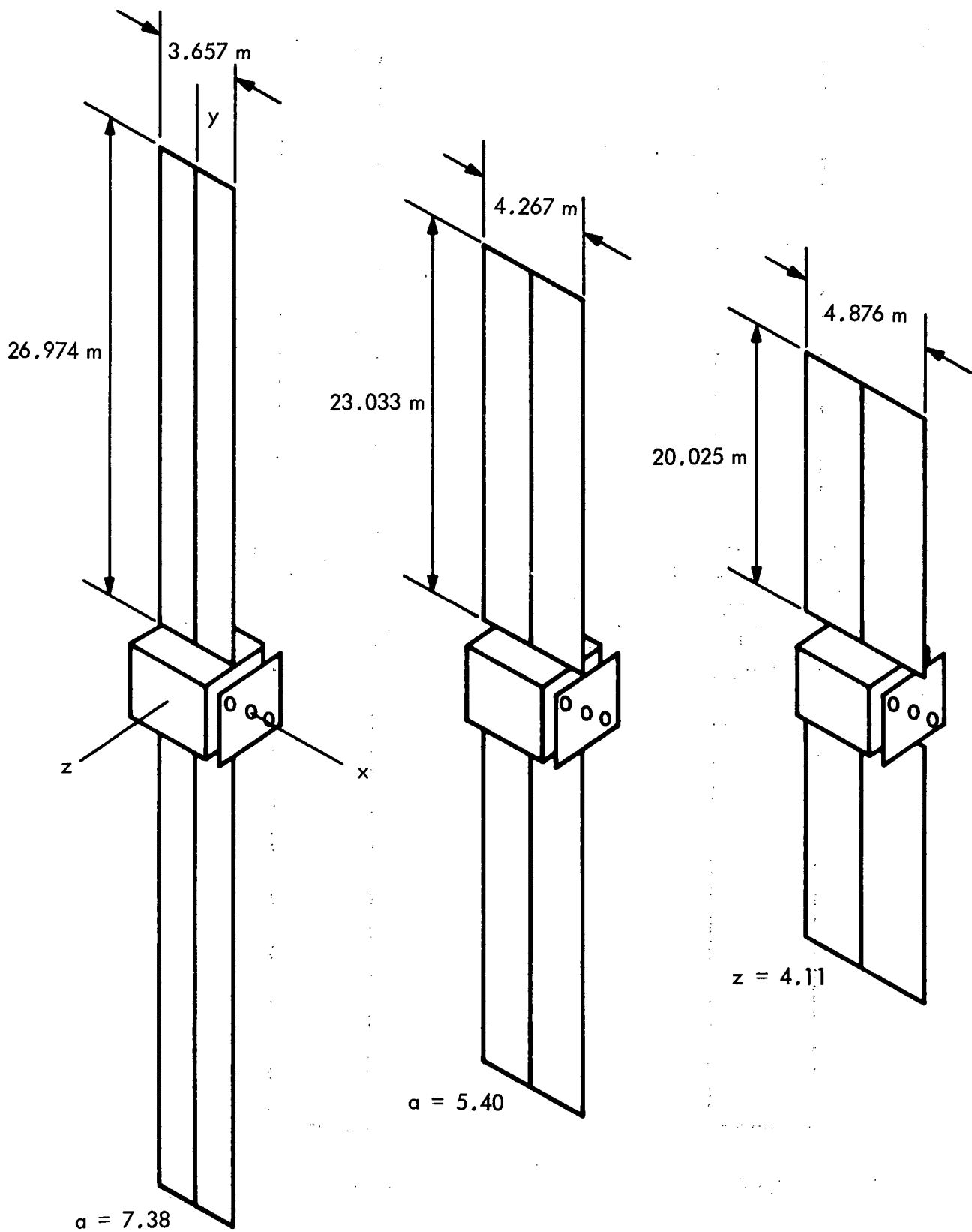


Fig. IV-B-3. Array Configurations Considered in Study

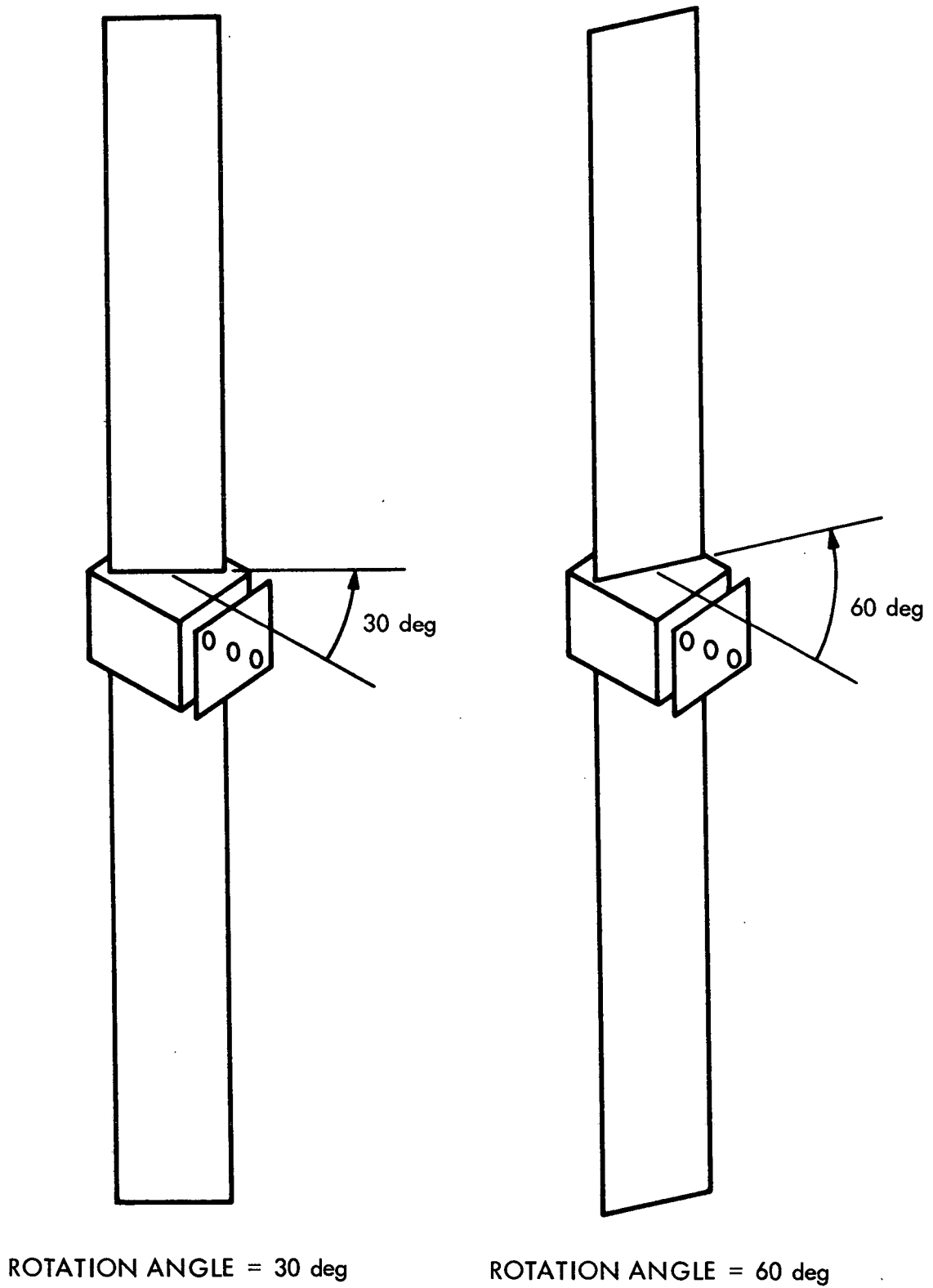


Fig. IV-B-4. Array Rotation Configurations

Table IV-B-5. Solar Array Configurations

Case	Rotation Angle	First Mode Natural Frequency Hz	Aspect Ratio
1A	0.0°	0.01366	7.38
2A	0.0°	-	5.40
3A	0.0°	-	4.11
4A	0.0°	0.02962	7.38
5A	0.0°	0.03050	5.40
6A	0.0°	0.02894	4.11
7A	0.0°	0.05782	7.38
8A	0.0°	0.05720	5.40
9A	0.0°	0.05644	4.11
1B	30.0°	0.01366	7.38
2B	30.0°	-	5.40
3B	30.0°	-	4.11
4B	30.0°	0.02962	7.38
5B	30.0°	0.03050	5.40
6B	30.0°	0.02894	4.11
7B	30.0°	0.05782	7.38
8B	30.0°	0.05720	5.40
9B	30.0°	0.05644	4.11
1C	60.0°	0.01366	7.38
2C	60.0°	-	5.40
3C	60.0°	-	4.11
4C	60.0°	0.02962	7.38
5C	60.0°	0.03050	5.40
6C	60.0°	0.02894	4.11
7C	60.0°	0.05782	7.38
8C	60.0°	0.05720	5.40
9C	60.0°	-	4.11

The mode shapes for a particular array configuration are illustrated in Figs. IV-B-5 through IV-B-12. Mode type 1 is an antisymmetric bending mode which might be excited by pitch axis rotation. Mode type 2 is a symmetric bending mode which would be excited by roll axis translation. Mode type 3 is an antisymmetric in-plane bending mode where both arrays rotate as a unit. Roll axis rotation excites this mode. Mode type 4 is a symmetric in-plane bending mode excited by pitch axis translation. Mode type 5 is an antisymmetric torsional mode. Fig. IV-B-10 shows a symmetric torsional mode excited by yaw axis rotation. Figs. IV-B-11 and 12 show array deflections for typical higher order modes, the 8th and 30th modes in particular.

e. Input Data to SESSIM and SEWART

Each of the cases in Table IV-B-5 requires 88 input data numbers before a conclusion regarding stability can be made. Many of these numbers are identical for all cases. For example, for all cases

$$K_{1x} = K_{1y} = K_{1z} = 1 \text{ V sec/pulse}$$

$$K_{2y} = 8.5 \text{ (dimensionless)}$$

$$K_{fy} = 0.6 \text{ (dimensionless)}$$

$$K_{my} = K_{mz} = .000064 \text{ m/pulse (0.00021 ft/pulse)}$$

$$K_{mx} = 0.000097 \text{ rad/pulse}$$

$$K_{vx} = K_{vy} = K_{vz} = 50.0 \text{ pulses/V sec}$$

$$T_{1x} = T_{1z} = 500.0 \text{ sec}$$

$$T_{1y} = 250.0 \text{ sec}$$

$$T_{2x} = T_{2z} = 500.0 \text{ sec}$$

$$T_{2y} = 250.0 \text{ sec}$$

$$T_{sx} = T_{sy} = T_{sz} = 1.0 \text{ sec}$$

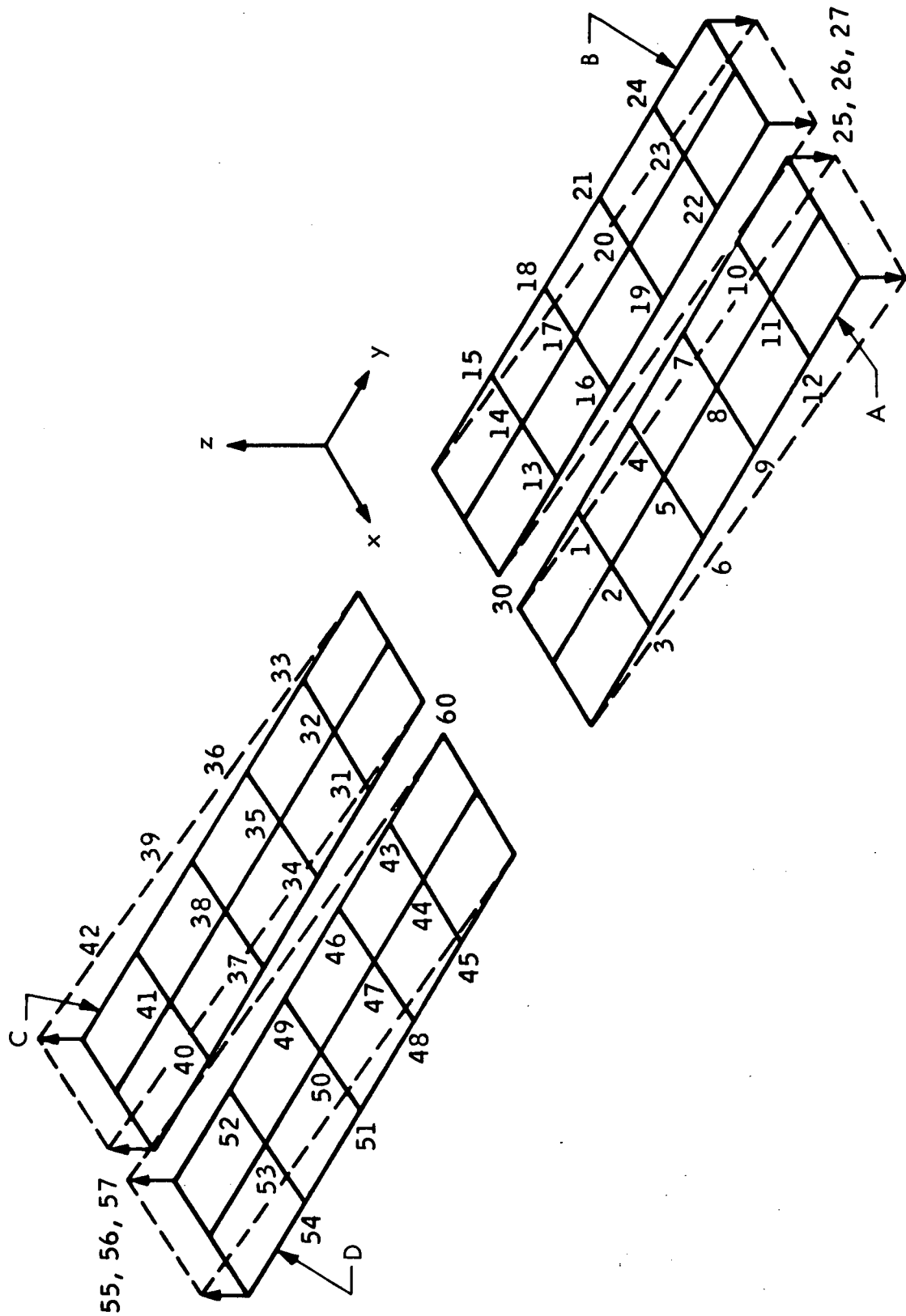


Fig. IV-B-5. Mode Type 1

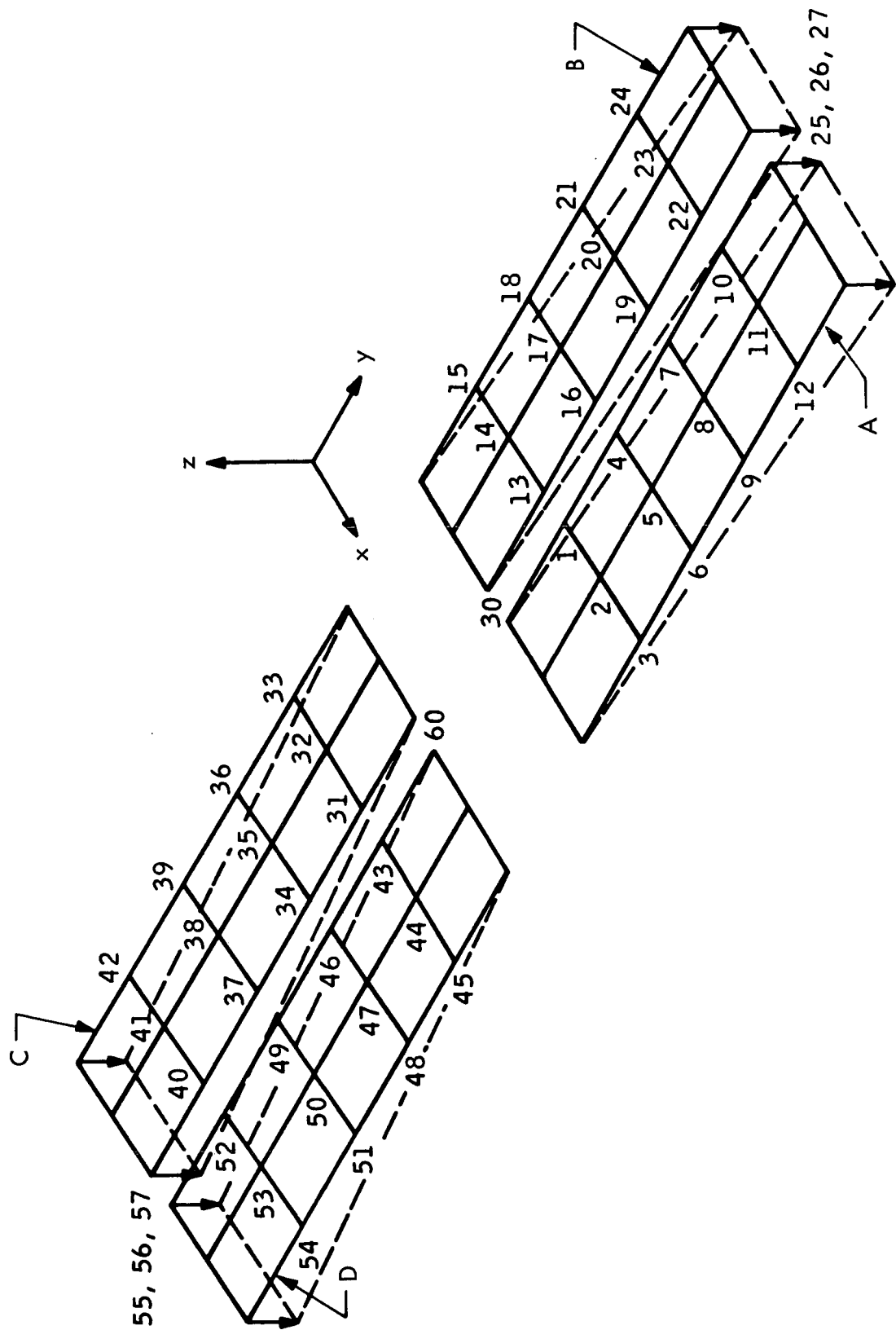


Fig. IV-B-6. Mode Type 2

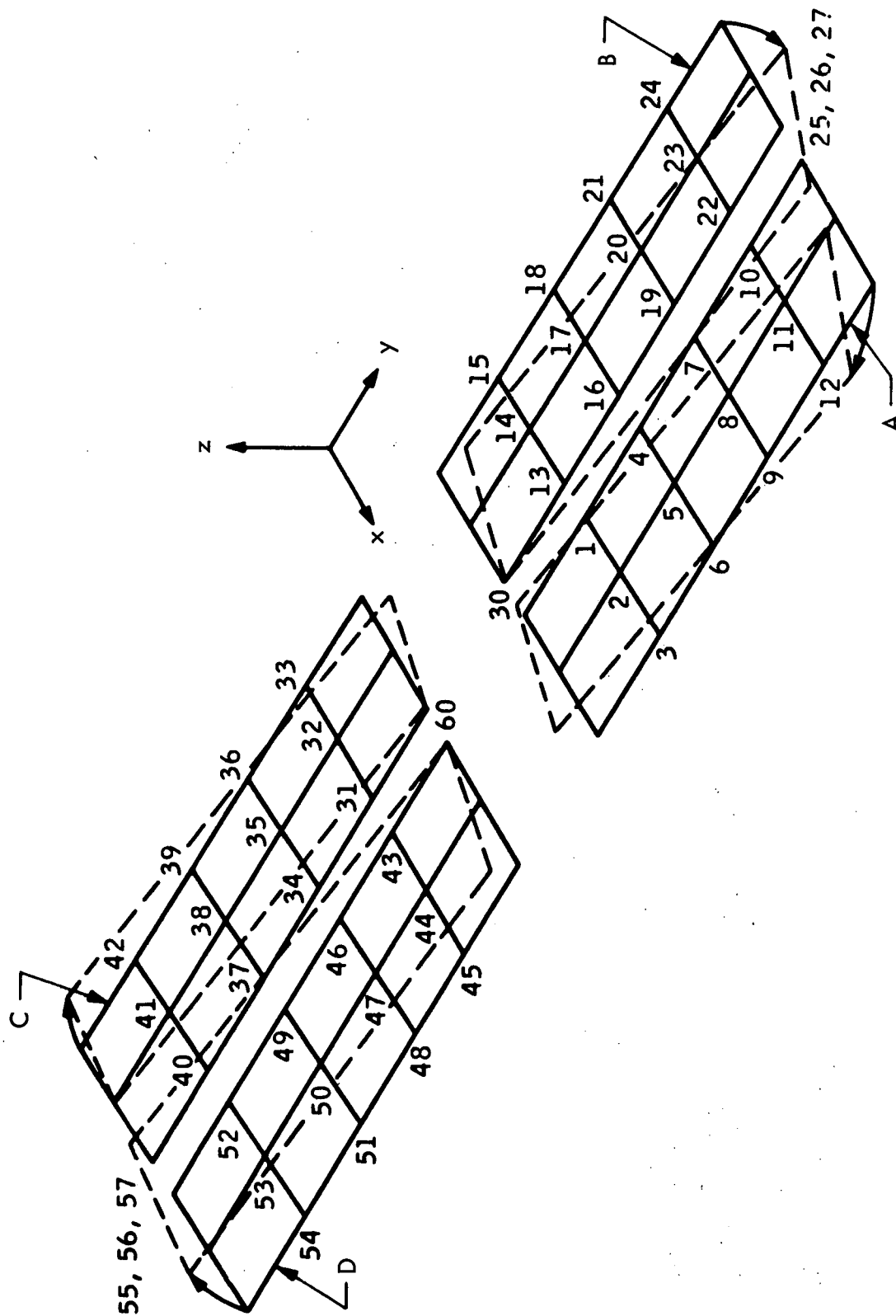


Fig. IV-B-7. Mode Type 3

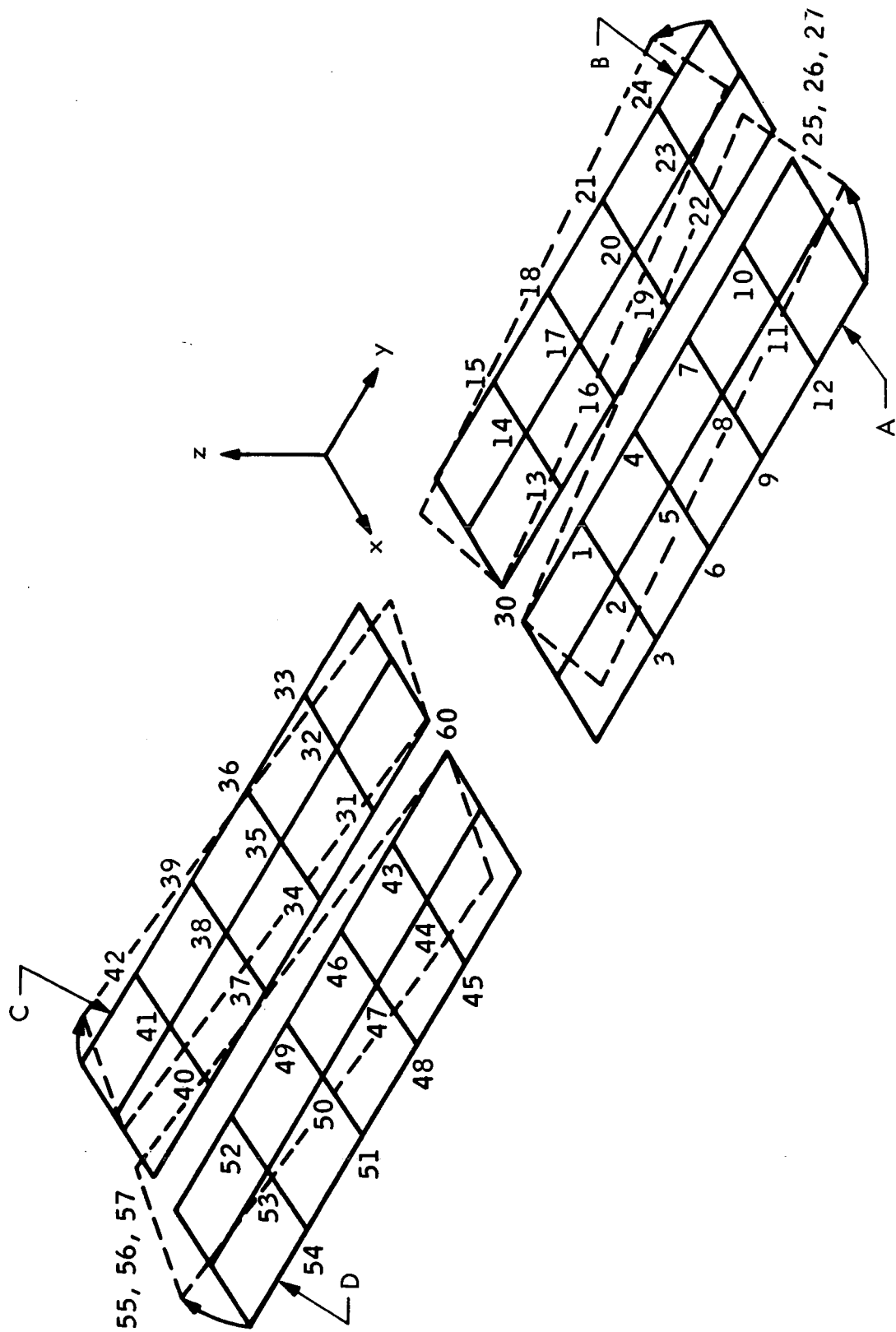


Fig. IV-B-8. Mode Type 4

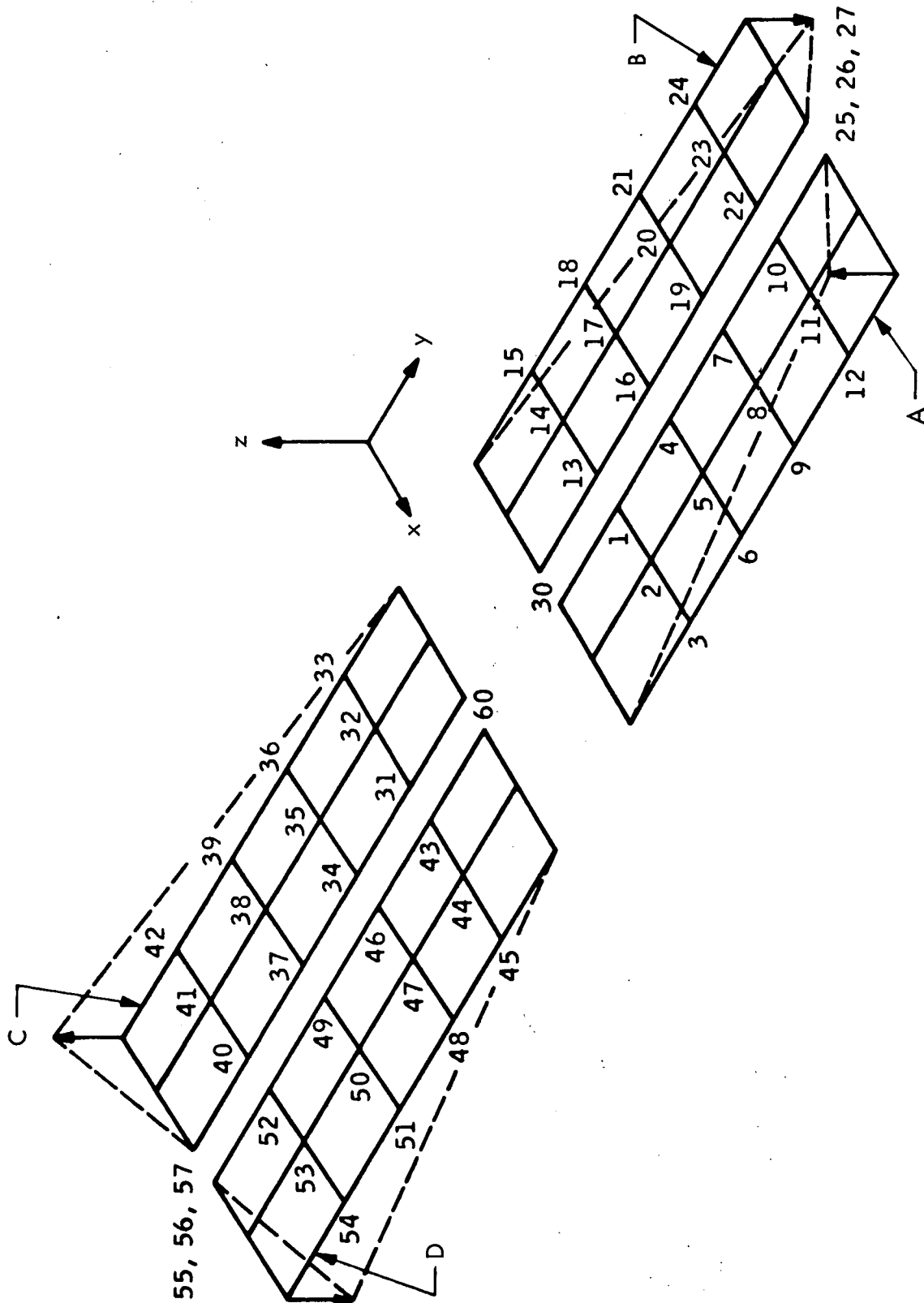


Fig. IV-B-9. Mode Type 5

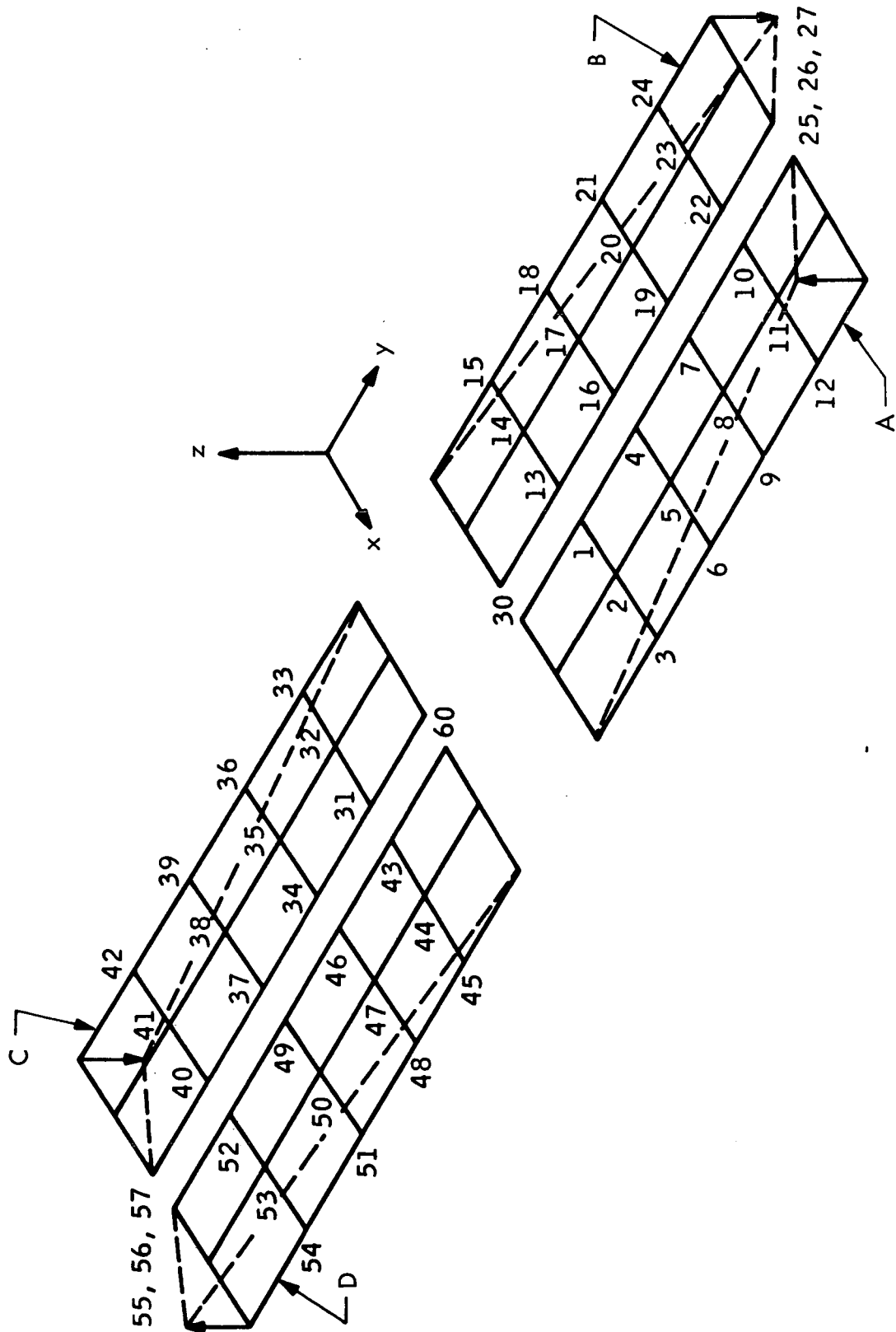


Fig. IV-B-10. Mode Type 6

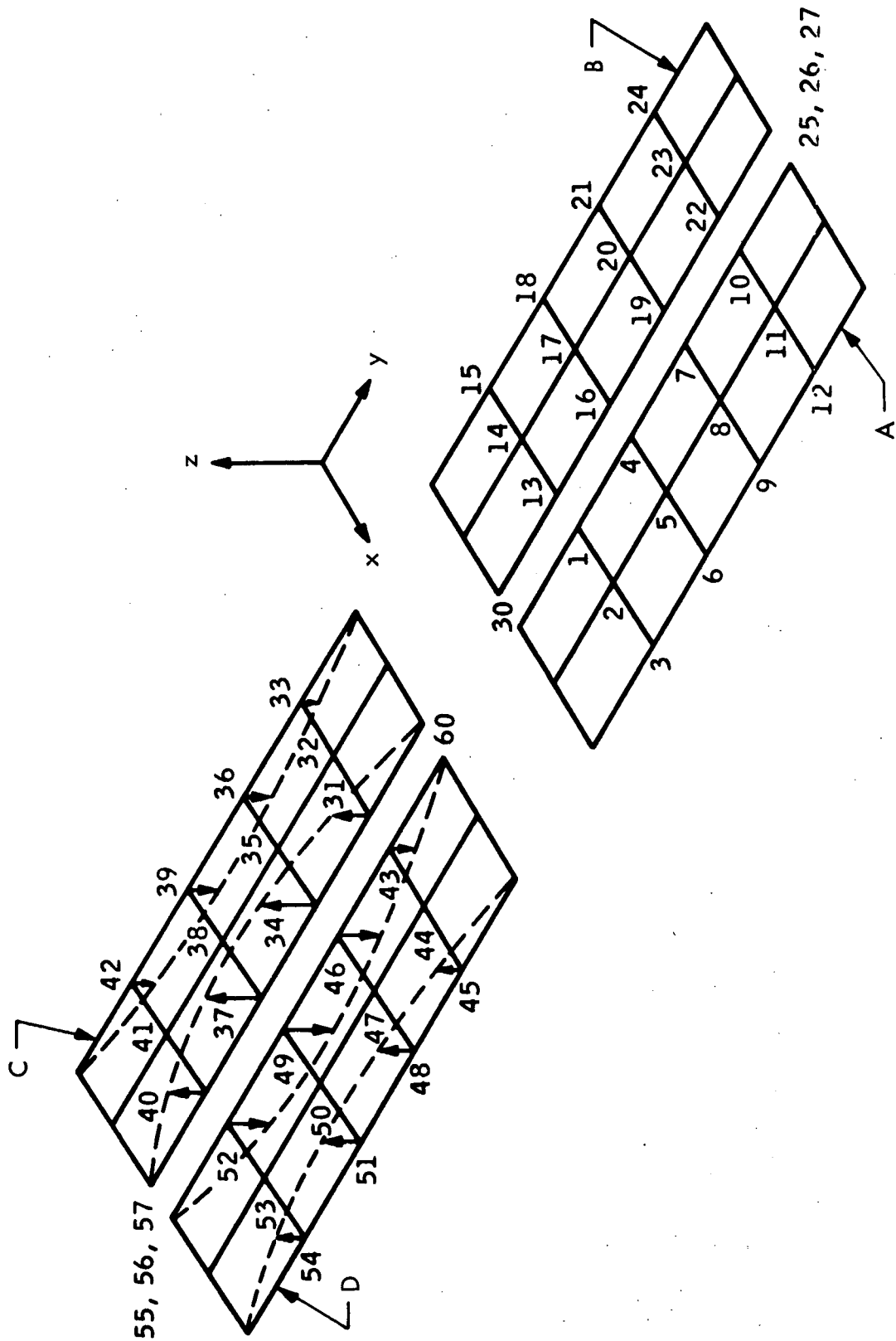


Fig. IV-B-11. Mode Type 7

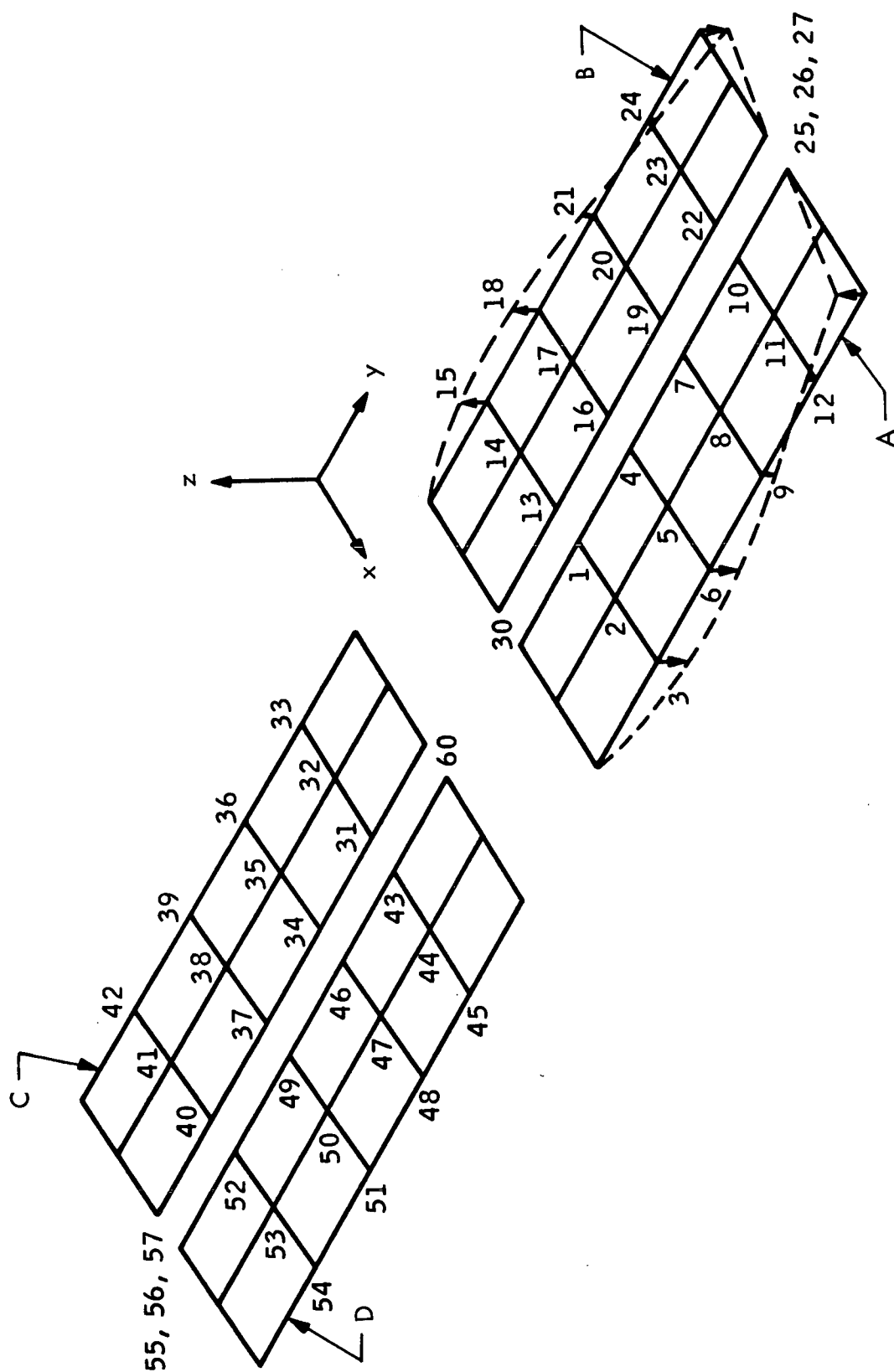


Fig. IV-B-12. Mode Type 8

$$m = 54.388 \text{ kg (3.727 slugs)}$$

$$\bar{m} = 45.326 \text{ kg (3.106 slugs)}$$

$$K_3 = 165.88 \text{ kg-m (37.27 slug ft)}$$

$$\bar{K}_3 = 138.24 \text{ kg-m (31.06 slug ft)}$$

$$F = .009072 \text{ kg (0.02 lb)}$$

$$P_y^{3*0} = 0.2335 \text{ m (0.7661 ft)}$$

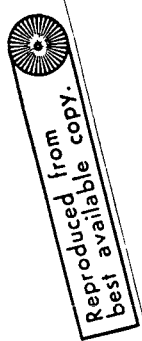
This leaves 62 items to be specified for a given case. These are listed in Table IV-B-6. Omitted values of δ_{ij} and Δ_{ij} are zero.

f. Results of Stability Analysis

The 27 cases (except those where no structural data are available), itemized in Table IV-B-5 have been subjected, by means of program SEWART, to a stability analysis. The results of the analysis are listed in Tables IV-B-7 to 9. Stability data are tabulated as a function of K_{si} the celestial sensor gain for axis i ($i=x, y, z$). It was determined from an earlier rigid spacecraft model analysis that stability for all configurations could be guaranteed for celestial sensor gains of $K_{sx} = 295 \text{ V/radian}$, $K_{sy} = 100 \text{ V/radian}$, and $K_{sz} = 250 \text{ V/radian}$. These were used as nominal values and a sensitivity study about these values was conducted for the non-rigid model. Each column of Tables IV-B-7 through 9 is further subdivided into two columns. The first column states the stability character for the rigid model whereas the second states the stability character for the non-rigid model. Symbols S and U denote stable and unstable, respectively. Each table shows the changing stability pattern with variation of K_{sx} , K_{sy} , or K_{sz} .

As expected, for the nominal case defined above, the rigid model configuration is always stable regardless of panel size, natural frequency, or rotation angle. However, when the flexible character of the panels is introduced, the nominal set of K_{si} values is no longer stable as indicated for

Table IV-B-6. Computer Input Data



CASE	K_{zx}	K_{2z}	K_{fx}	K_{fz}	K_{sx}	K_{sy}	K_{sz}	M	I_x	I_y	I_z	I_{xy}	I_{yz}	I_{zx}	σ_1	σ_2	σ_3	σ_4	σ_5	σ_6	ζ_1	ζ_2	ζ_3	ζ_4	ζ_5	ζ_6	δ_{1x}	δ_{1y}	δ_{1z}	δ_{2x}
1A	8.8	8.8	0.140	0.261	295	250	250	73.354	37659.858	1556.305	39078.322	0	0	0	0.01366	0.01461	0.02111	0.02262	0.02798	0.02798	0.005	0.005	0.5	0.5	0.005	0.005	-192.23	-	-	-
2A	-	-	-	-	-	-	-	-	-	-	-	-	-	-	-	-	-	-	-	-	-	-	-	-	-	-	-	-	-	-
3A	-	-	-	-	-	-	-	-	-	-	-	-	-	-	-	-	-	-	-	-	-	-	-	-	-	-	-	-	-	-
4A	9.1	9.1	0.123	0.227	295	250	250	75.155	45934.009	1555.999	47346.789	0	0	0	0.02962	0.02962	0.02965	0.03206	0.03612	0.03907	0.005	0.005	0.005	0.005	0.5	0.5	-0.67	7.22	0.03	0.03
5A	8.6	8.6	0.156	0.293	295	250	250	74.907	29798.114	1625.521	31285.996	0	0	0	0.03050	0.03231	0.03231	0.03279	0.03757	0.04034	0.005	0.005	0.005	0.005	0.5	0.5	170.07	-	-	-
6A	8.3	8.3	0.170	0.322	295	250	250	75.528	22570.684	1716.309	24152.637	0	0	0	0.02894	0.03099	0.03641	0.03641	0.03646	0.03898	0.005	0.005	0.005	0.005	0.5	0.5	-148.73	-	-	-
7A	10.0	10.0	0.074	0.127	295	250	250	80.807	70485.468	1557.931	71931.637	0	0	0	0.05782	0.05782	0.05841	0.06438	0.06690	0.07428	0.005	0.005	0.005	0.005	0.5	0.5	0.03	-7.06	-	-
8A	8.0	8.0	0.134	0.224	295	250	250	78.012	40271.753	1629.166	41285.837	0	0	0	0.05720	0.05720	0.05800	0.06309	0.06820	0.07433	0.005	0.005	0.005	0.005	0.5	0.5	-0.05	8.41	-	-
9A	8.5	8.5	0.159	0.299	295	250	250	77.578	28006.309	1722.055	29616.957	0	0	0	0.05644	0.05651	0.05651	0.06100	0.06702	0.07237	0.005	0.005	0.005	0.005	0.5	0.5	-184.52	-0.04	0.69	0.69
1B	8.8	8.8	0.140	0.261	295	250	250	73.354	37701.970	1556.305	39036.202	0	0	0	0.01366	0.01461	0.02111	0.02262	0.02798	0.02798	0.005	0.005	0.5	0.5	0.005	0.005	-166.48	-	96.12	-
2B	-	-	-	-	-	-	-	-	-	-	-	-	-	-	-	-	-	-	-	-	-	-	-	-	-	-	-	-	-	-
3B	-	-	-	-	-	-	-	-	-	-	-	-	-	-	-	-	-	-	-	-	-	-	-	-	-	-	-	-	-	-
4B	9.1	9.1	0.123	0.227	295	250	250	75.155	45967.205	1555.999	47303.591	0	0	0	0.02962	0.02962	0.02965	0.03206	0.03612	0.03907	0.005	0.005	0.005	0.005	0.5	0.5	-0.41	7.52	0.24	-0.05
5B	8.6	8.6	0.156	0.293	295	250	250	74.907	29857.585	1625.521	31226.524	0	0	0	0.03005	0.03231	0.03231	0.03279	0.03757	0.04034	0.005	0.005	0.005	0.005	0.5	0.5	147.28	-	-85.03	-0.01
6B	8.3	8.3	0.170	0.322	295	250	250	75.528	22653.672	1716.309	24066.647	0	0	0	0.02894	0.03099	0.03641	0.03641	0.03646	0.03898	0.005	0.005	0.005	0.005	0.5	0.5	138.80	-	-74.36	-0.01
7B	10.0	10.0	0.074	0.127	295	250	250	80.807	70534.482	1557.931	71882.509	0	0	0	0.05782	0.05782	0.05841	0.0648	0.06690	0.07428	0.005	0.005	0.005	0.005	0.5	0.5	0.13	-7.12	-0.06	-
8B	8.0	8.0	0.134	0.224	295	250	250	78.012	40337.771	1629.166	41719.81	0	0	0	0.05720	0.05720	0.05800	0.06309	0.06820	0.07433	0.005	0.005	0.005	0.005	0.5	0.5	-0.05	8.41	-	-
9B	8.5	8.5	0.159	0.299	295	250	250	77.578	28006.469	1722.005	29566.791	0	0	0	0.05644	0.05651	0.05651	0.06100	0.06702	0.07237	0.005	0.005	0.005	0.005	0.5	0.5	142.48	-0.02	-2.20	-0.31
1C	8.8	8.8	0.140	0.261	295	250	250	73.354	37786.202	1556.305	38951.972	0	0	0	0.01366	0.01461	0.02111	0.02262	0.02798	0.02798	0.005	0.005	0.5	0.5	0.005	0.005	96.12	-	-110.46	0.03
2C	-	-	-	-	-	-	-	-	-	-	-	-	-	-	-	-	-	-	-	-	-	-	-	-	-	-	-	-	-	-
3C	-	-	-	-	-	-	-	-	-	-	-	-	-	-	-	-	-	-	-	-	-	-	-	-	-	-	-	-	-	-
4C	9.1	9.1	0.123	0.227	295	250	250	75.155	46053.590	1555.999	47217.203	0	0	0	0.02962	0.02962	0.02965	0.03206	0.03612	0.03907	0.005	0.005	0.005	0.005	0.5	0.5	-0.21	-7.37	-0.30	-0.01
5C	8.6	8.6	0.156	0.293	295	250	250	74.907	29976.525	1625.521	31107.586	0	0	0	0.03004	0.03050	0.03231	0.3279	0.03757	0.04034	0.005	0.005	0.005	0.005	0.5	0.5	85.03	-	-147.28	-0.01
6C	8.3	8.3	0.170	0.322	295	250	250	75.528	22819.647	1716.309	23903.674	0	0	0	0.02894	0.03099	0.03641	0.03641	0.03646	0.03898	0.005	0.005	0.005	0.005	0.5	0.5	-74.36	-	125.80	-0.01
7C	10.0	10.0	0.074	0.127	295	250	250	80.807	70632.507	1557.931	71784.48	0	0	0	0.05782	0.05782	0.05841	0.3438	0.06690	0.07428	0.005	0.005	0.005	0.005	0.5	0.5	0.02	-7.23	-0.03	-
8C	8.0	8.0	0.134	0.224	295	250	250	78.012	40409.812	1629.166	41587.768	0	0	0	0.05720	0.05720	0.05800	0.36309	0.06820	0.07433	0.005	0.005	0.005	0.005	0.5	0.5	-	8.41	-	-
9C	-	-	-	-	-	-	-	-	-	-	-	-	-	-	-	-	-	-	-	-	-	-	-	-	-	-	-	-	-	-

Table IV-B-6. Computer Input Data (Contd)

CASE	δ_{2y}	δ_{2z}	δ_{3x}	δ_{3y}	δ_{3z}	δ_{4x}	δ_{4y}	δ_{4z}	δ_{5x}	δ_{5y}	δ_{5z}	δ_{6x}	δ_{6y}	δ_{6z}	Δ_{1x}	Δ_{1y}	Δ_{1z}	Δ_{2x}	Δ_{2y}	Δ_{2z}	Δ_{3x}	Δ_{3y}	Δ_{3z}	Δ_{4x}	Δ_{4y}	Δ_{4z}	Δ_{5x}	Δ_{5y}	Δ_{5z}	Δ_{6x}	Δ_{6y}	Δ_{6z}
1A	-	-	-	-	-194.15	-	-	-	-	7.19	-	-	7.26	-	-	-	-	-	-	-3.25	-	-	-	-3.3	-	-	-	-	-	-	-	-
2A	-	-	-	-	-	-	-	-	-	-	-	-	-	-	-	-	-	-	-	-	-	-	-	-	-	-	-	-	-	-	-	
3A	-	-	-	-	-	-	-	-	-	-	-	-	-	-	-	-	-	-	-	-	-	-	-	-	-	-	-	-	-	-	-	
4A	-7.28	-	210.03	0.02	-	0.01	-	-	-	-	214.38	-	-	-	-	-	-	-	-	-	-	-	-	-	-	-3.57	-	-	-	-3.57	-	
5A	-8.13	-	0.01	8.82	-	-	-	-	-	-	172.83	-	-	-	-	-	-	-	-	-	-	-	-	-	-	-3.41	-	-	-	-3.41	-	
6A	-	-	-	9.70	-0.1	-0.01	9.85	-	-	0.01	150.65	-	-	-	-	-	-	-	-	-3.32	-	-	-	-	-	4.17	-	-	-	4.34	-	
7A	-	-	258.72	-	-	-	-	-	-	-	-265.58	-	-	-	-	-	-	-	-	-	-	-	-	-	-	-3.78	-	-	-	3.83	-	
8A	8.79	-	196.43	-	-	-	-	-	-	-	-200.91	-	-	-	-	-	-	-	-	-	-	-	-	-	-	3.61	-	-	-	3.59	-	
9A	-4.88	-	0.27	-13.14	-	0.01	-	-	-	7.24	-	-	-7.22	-	-	-	-	-1.63	-2.82	-	-	-	-	-	2.86	-1.65	-	-	-	-	-	
1B	-	-	-97.07	-	-168.14	-	-	-	-	-	-	-	-	-	-	-	-	-	-	-	-	-	-	-	-	-	-	-	-	-	-	
2B	-	-	-	-	-	-	-	-	-	-	-	-	-	-	-	-	-	-	-	-	-	-	-	-	-	-	-	-	-	-	-	
3B	-	-	-	-	-	-	-	-	-	-	-	-	-	-	-	-	-	-	-	-	-	-	-	-	-	-	-	-	-	-	-	
4B	-6.97	0.03	-181.89	-0.02	105.02	0.01	-	-	-107.19	-	-185.66	-	-	-	-	-	-	-	-	-	-	-	-	-	-1.78	-3.09	-	-	-	-3.09	1.79	
5B	-8.15	0.01	-	8.80	-	-	-	-	86.41	-	149.67	-	-	-	-	-	-	-	-	-	-	-	-	-	-1.71	-2.96	-	-	-	-2.93	1.69	
6B	-	0.01	-0.01	-9.58	-0.02	-	9.57	-	75.32	-	130.46	-	-	-	-	-	-	-	-	-	-	-	-	-	-	-2.85	-	-	-	-2.85	1.64	
7B	-7.53	-	224.05	-	-129.36	-0.01	-	-	-132.79	-	-230.00	-	-	-	-	-	-	-	-	-	-	-	-	-	-	3.61	-	-	-	-3.75	2.17	
8B	-8.79	-0.01	170.11	98.21	-	-	-	-	100.46	-	173.99	-	-	-	-	-	-	-	-	-	-	-	-	-	-	1.89	-	-	-	3.31	-1.91	
9B	-9.80	0.8	-0.04	-10.02	0.02	-	-	-	-83.9	-	-145.32	-	-	-	-	-	-	-	-	-	-	-	-	-	-1.80	-3.12	-	-	-	3.11	-1.79	
1C	-	-0.05	168.14	-	97.07	-	-	-	-	7.19	-	-	-	7.26	-	-	-	-	-	-	-	-	-	-	-	-	-	-	-	-	-	-
2C	-	-	-	-	-	-	-	-	-	-	-	-	-	-	-	-	-	-	-	-	-	-	-	-	-	-	-	-	-	-	-	
3C	-	-	-	-	-	-	-	-	-	-	-	-	-	-	-	-	-	-	-	-	-	-	-	-	-	-	-	-	-	-	-	
4C	7.14	-0.01	105.02	0.01	-181.89	0.01	-	-	-185.66	-	-107.19	-	-	-	-	-	-	-	-	-	-	-	-	-	-	-	-	-	-	-	-	-
5C	-7.65	0.01	-	9.23	-	-	-	-	149.67	-	86.41	-	-	-	-	-	-	-	-	-	-	-	-	-	-	-1.78	-	-	-	-1.79	3.09	
6C	-	0.01	0.06	-9.84	0.04	-	9.71	0.01	-	-	-75.32	-	-	-	-	-	-	-	-	-	-	-	-	-	-	1.71	-	-	-	-1.69	-	
7C	-7.43	-	129.36	-	-224.05	230.0	-	-	130.46	-	-	-	-	-	-	-	-	-	-	-	-	-	-	-	-	-	-	-	-	-1.64	2.85	
8C	8.57	-	98.21	-	-170.11	-	-	-	-173.99	-	-100.46	-	-	-	-	-	-	-	-	-	-	-	-	-	-	-	-	-	-	2.17	-3.75	
9C	-	-	-	-	-	-	-	-	-	-	-	-	-	-	-	-	-	-	-	-	-	-	-	-	-	-	-	-	-	-1.91	3.31	

Table IV-B-7. $K_{sy} = 100$, $K_{sz} = 250$

Case/ K_{sx} (Volts/radian)	295	450	600	650	700	750
1A	S S	S S	S S	S S	U U	U U
2A	- -	- -	- -	- -	- -	- -
3A	- -	- -	- -	- -	- -	- -
4A	S S	S S	S S	S S	U U	U U
5A	S S	S S	S S	U U	U U	U U
6A	S S	S S	U U	U U	U U	U U
7A	S S	S S	U U	U U	U U	U U
8A	S S	S S	S S	S S	U U	U U
9A	S S	S S	U U	U U	U U	U U
1B	S S	S S	S S	S S	U U	U U
2B	- -	- -	- -	- -	- -	- -
3B	- -	- -	- -	- -	- -	- -
4B	S S	S S	S S	S S	U U	U U
5B	S S	S S	S S	U U	U U	U U
6B	S S	S S	U U	U U	U U	U U
7B	S S	S S	U U	U U	U U	U U
8B	S S	S S	S S	S S	U U	U U
9B	S S	S S	U S	U U	U U	U U
1C	S U	S U	S U	S S	U U	U U
2C	- -	- -	- -	- -	- -	- -
3C	- -	- -	- -	- -	- -	- -
4C	S S	S S	S S	S S	U U	U U
5C	S S	S S	S S	U U	U U	U U
6C	S S	S S	U U	U U	U U	U U
7C	S S	S S	U U	U U	U U	U U
8C	S S	S S	S S	S S	U U	U U
9C	- -	- -	- -	- -	U U	- -

Table IV-B-8. $K_{sz} = 250$, $K_{sx} = 295$

Case/ K_{sy} (Volts/radian)	50	100	125	200	300	400	500	1000
1A	S S	S S	S S	S U	S U	U -	U -	U -
2A	- -	- -	- -	- -	- -	- -	- -	- -
3A	- -	- -	- -	- -	- -	- -	- -	- -
4A	S S	S S	S S	S U	S U	U -	U -	U -
5A	S S	S S	S U	S U	S U	S -	U -	U -
6A	S S	S S	S U	S U	S U	S -	U -	U -
7A	S S	S S	S S	S S	S U	U -	U -	U -
8A	S S	S S	S S	S S	S U	S -	U -	U -
9A	S S	S S	S S	S U	S U	S -	U -	U -
1B	S S	S S	S S	S U	S U	U -	U -	U -
2B	- -	- -	- -	- -	- -	- -	- -	- -
3B	- -	- -	- -	- -	- -	- -	- -	- -
4B	S S	S S	S S	S U	S U	U -	U -	U -
5B	S S	S S	S U	S U	S U	S -	U -	U -
6B	S S	S S	S U	S U	S U	S -	U -	U -
7B	S S	S S	S S	S S	S U	U -	U -	U -
8B	S S	S S	S S	S S	S U	S -	U -	U -
9B	S S	S S	S S	S U	S U	S -	U -	U -
1C	S U	S U	S U	S U	S U	U -	U -	U -
2C	- -	- -	- -	- -	- -	- -	- -	- -
3C	- -	- -	- -	- -	- -	- -	- -	- -
4C	S S	S S	S S	S U	S U	U -	U -	U -
5C	S S	S S	S U	S U	S U	S -	U -	U -
6C	S S	S S	S U	S U	S U	S -	U -	U -
7C	S S	S S	S S	S S	S U	U -	U -	U -
8C	S S	S S	S S	S S	S U	S -	U -	U -
9C	- -	- -	- -	- -	- -	- -	- -	- -

Table IV-B-9. $K_{sy} = 100$, $K_{sx} = 295$

Case/ K_{sz} (Volts/radian)	250	500	600	750
1A	S S	S S	S S	U U
2A	- -	- -	- -	- -
3A	- -	- -	- -	- -
4A	S S	S S	S S	U U
5A	S S	S S	U U	U U
6A	S S	S S	U U	U U
7A	S S	U U	U U	U U
8A	S S	S S	U U	U U
9A	S S	S S	U U	U U
1B	S S	S S	S S	U U
2B	- -	- -	- -	- -
3B	- -	- -	- -	- -
4B	S S	S S	S S	U U
5B	S S	S S	U U	U U
6B	S S	S S	U U	U U
7B	S S	U U	U U	U U
8B	S S	S S	U U	U U
9B	S S	S S	U U	U U
1C	S U	S U	S U	U U
2C	- -	- -	- -	- -
3C	- -	- -	- -	- -
4C	S S	S S	S U	U U
5C	S S	S U	U U	U U
6C	S S	S U	U U	U U
7C	S S	U U	U U	U U
8C	S S	S S	U U	U U
9C	- -	- -	- -	- -

case 1C. Here, for the case of 60-deg panel rotation, lowest array natural frequency, and largest aspect ratio, the flexible spacecraft model shows instability.

Increasing K_{sx} generally exacerbates the stability situation. For example, increasing K_{sx} from 295 V/radian to 600 V/radian shows an increased number of unstable cases for either the rigid or non-rigid models. Oddly enough, comparison of the case 9B data for $K_{sx} = 600$ shows the rigid case to be unstable and the case for the flexible body to be stable. In effect, this result implies that flexibility enhances stability. This kind of behavior is observed for the pitch axis only. As K_{sx} is further increased, the number of stable configurations decreases until for $K_{sx} = 700$, all configurations, both rigid and non-rigid, are unstable. Except for the anomalous case already referred to, it seems as if flexibility of the arrays has no effect on pitch attitude stability; i.e., for a given value of K_{sx} , each configuration whether rigid or non-rigid displays identical stability character. It should be mentioned, except for array rotation cases, that pitch axis rotation should excite out-of-plane bending modes (types 1 and 2).

Yaw axis rotation, except for array rotation configurations, should excite twisting modes (types 5 and 6). Table IV-B-8 shows the effect of K_{sy} variations on attitude stability. Flexibility has a clearly deleterious effect over the stability predicted for the rigid body model. For example, increasing K_{sx} from 100 to 125 has no effect on the rigid model. All configurations are stable. However, for the non-rigid model, the number of unstable cases increased from 1 to 6. No clear pattern emerges regarding the array rotation. Instabilities for each of the configurations for 0-, 30-, and 60-deg rotation increase by two when K_{sy} increases from 100 to 125.

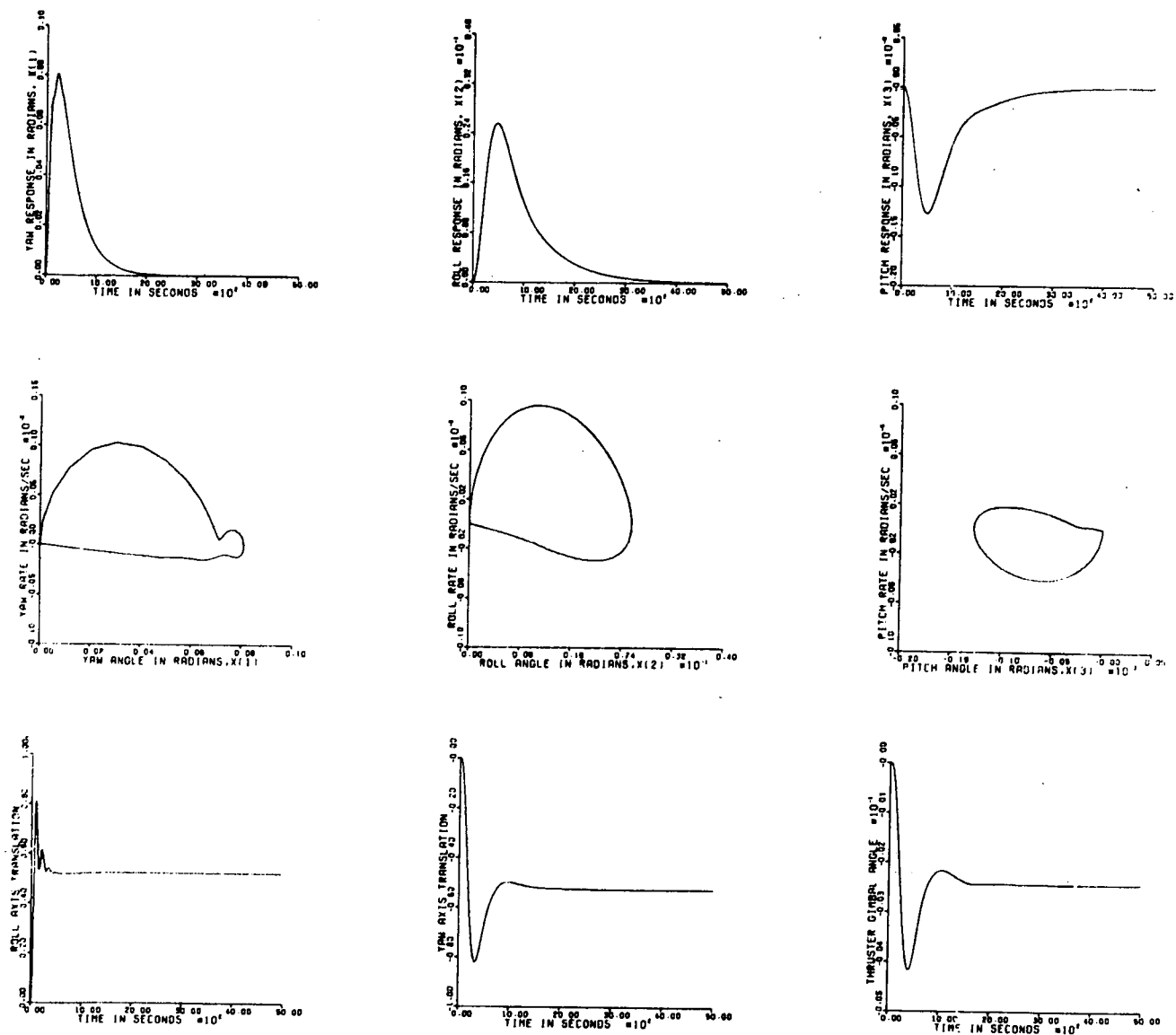
If the behavior for $K_{sy} = 125$ and zero rotation angle is observed, it is seen that fewer instabilities occur for the stiffer array. That is, the $\sigma \cong 0.03$ -Hz cases show more instabilities than the $\sigma \cong 0.06$ -Hz cases. Also, it appears as if arrays with larger aspect ratios are more acceptable than arrays with small aspect ratios. This is demonstrated by cases 4A, 5A, and 6A for $K_{sx} = 125$ where the pattern is S, U, U. Thus, the wider the array, the more likely it is to cause instability.

As K_{sy} increases, the effects of flexibility are felt more strongly. It is seen for $K_{sy} = 300$ that none of the non-rigid cases is stable. However, all of the rigid model cases are stable. In fact, the sensor gain factor must be increased to 400 before any instabilities for the rigid model occur. Raising its value to 500 destroys stability for all cases. No data is listed for $K_{sy} = 400, 500, \text{ or } 1000$ for the non-rigid model. It was felt that increasing it beyond 300 would not be likely to stabilize the model.

Roll-axis rotation should excite in-plane bending modes of types 3 or 4. These modes have a different damping factor from mode types 1, 2, 5, or 6. It is $\zeta = 0.5$. For the torsional or out-of-plane bending modes, ζ is assumed to be 0.005. Despite the high damping factor, stability is influenced strongly by flexibility, as it was for the yaw axis. For example (see Table IV-B-9), both rigid and non-rigid models display similar stability characteristics for a gain factor of 250 V/radian (except for case 1C). For $K_{sz} = 500$, only three new instabilities appear for the rigid model whereas five appear for the non-rigid model. Further increase in K_{sz} shows rapid deterioration of stability until both models are unacceptable for $K_{sy} = 750$. Trends similar to those observed for the yaw axis regarding aspect ratio and frequency are noted.

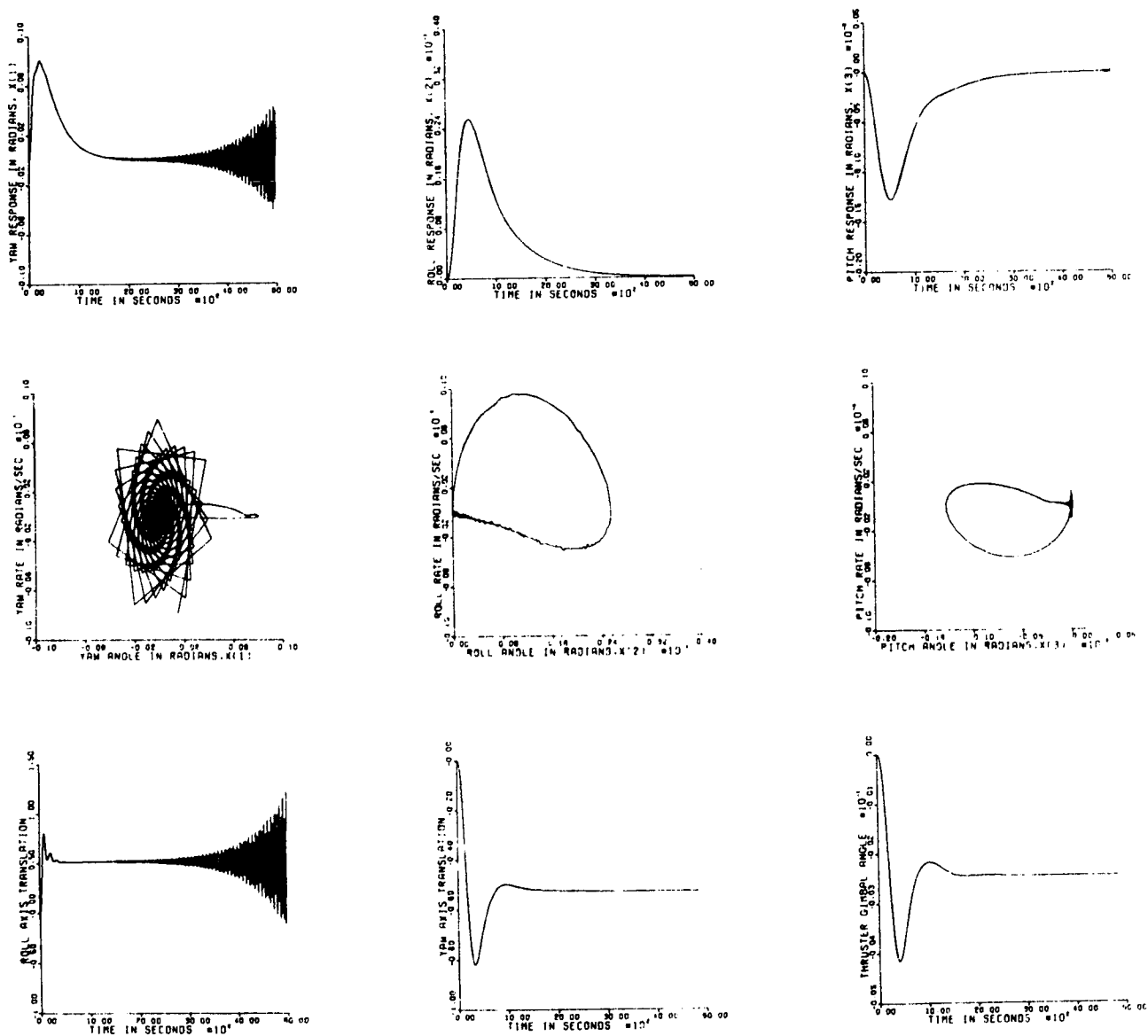
g. Simulation Studies

The simulation program SESSIM was run for several cases. The results are displayed in Figs. IV-B-13 through 21, and are referred to as cases a to i. Each figure contains six plots. The top row of plots shows the response curves for yaw, roll, and pitch angles, respectively. The second row shows phase plots for these three axes. In many cases (for example Fig. IV-B-17), the print resolution is not good enough to show the actual phase plots. These anomalous cases are easily recognized by the fact that, at the abscissa crossover points, the phase curve is not normal to the abscissa, as it must be, except for singular points. The third row of graphs shows the time histories of roll axis translation (which controls the yaw axis), yaw axis translation (which controls the roll axis), and thruster gimbal angle.



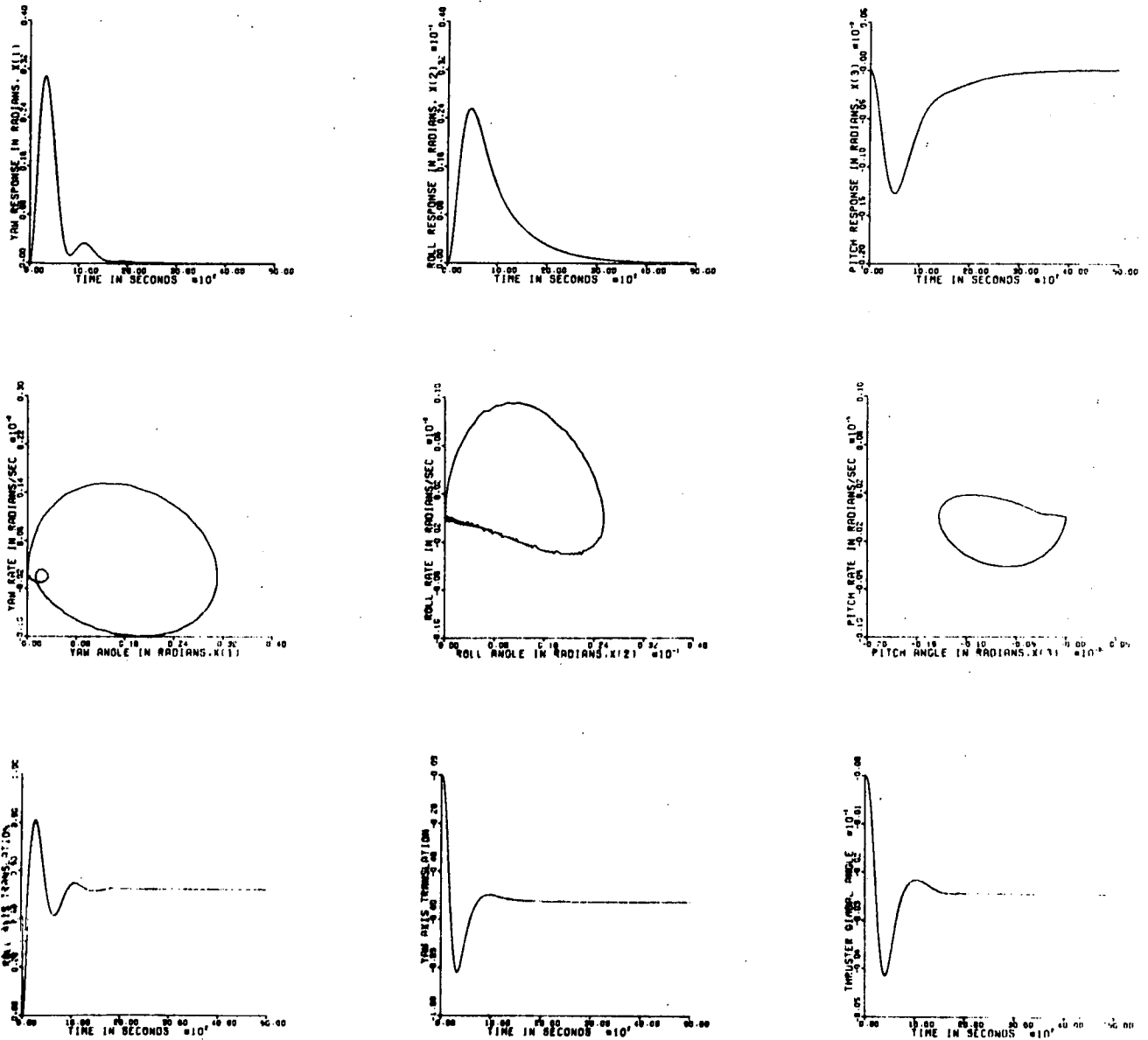
Stable Rigid Model, $K_{si} = 300, 250, 295$ V/rad,
Rotation Angle = 0° , Aspect Ratio = 7.38

Fig. IV-B-13. Simulation Analysis, Case a



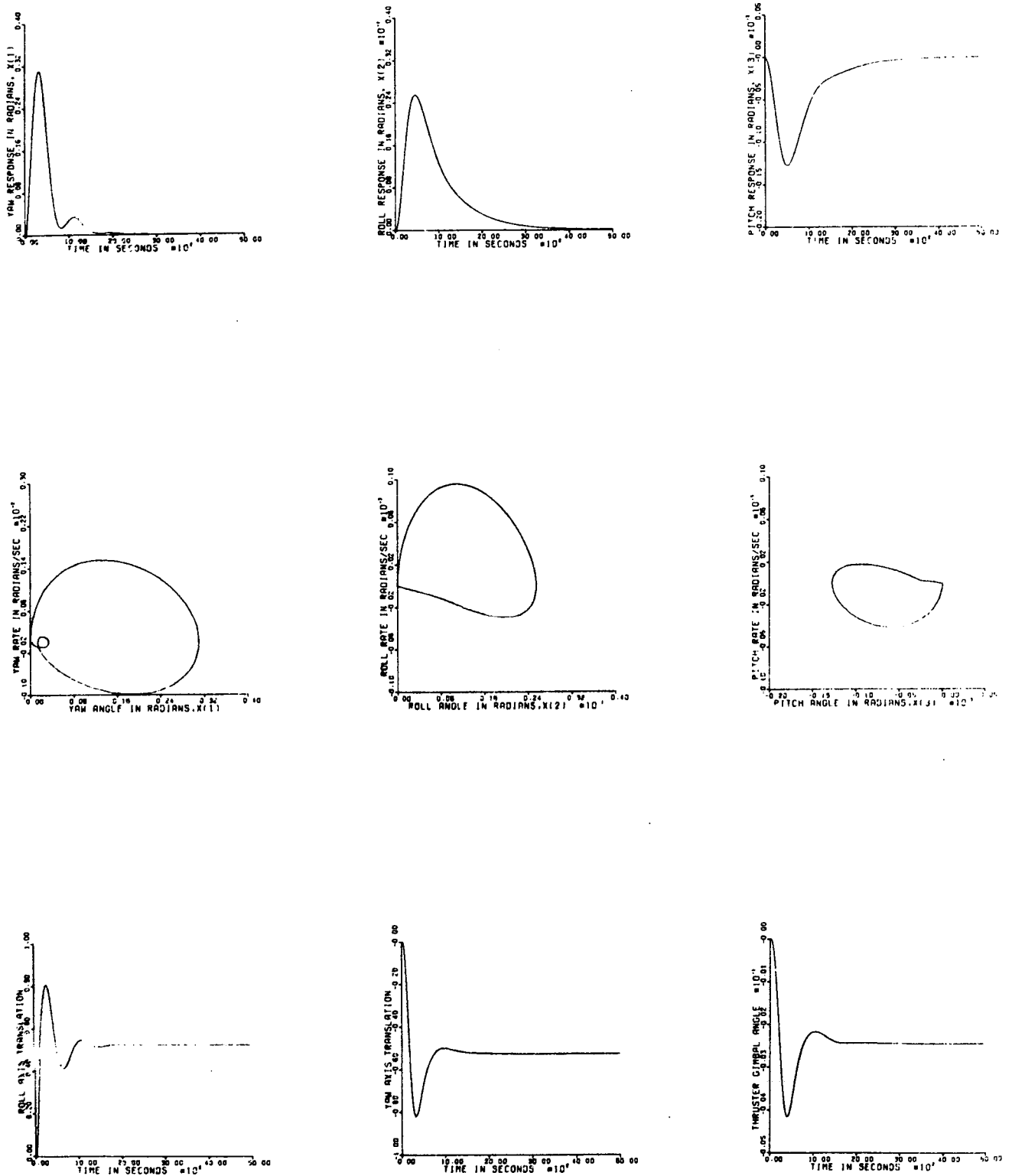
Unstable Flexible Model, $K_{si} = 300, 250, 295$ V/rad,
 $\sigma_1 = 0.01366$ Hz, $\sigma_2 = 0.01461$ Hz, $\sigma_3 = 0.02111$ Hz,
 $\sigma_4 = 0.02262$ Hz, $\sigma_5 = 0.02798$ Hz, $\sigma_6 = 0.02798$ Hz,
 Rotation Angle = 0°, Aspect Ratio = 7.38

Fig. IV-B-14. Simulation Analysis, Case b



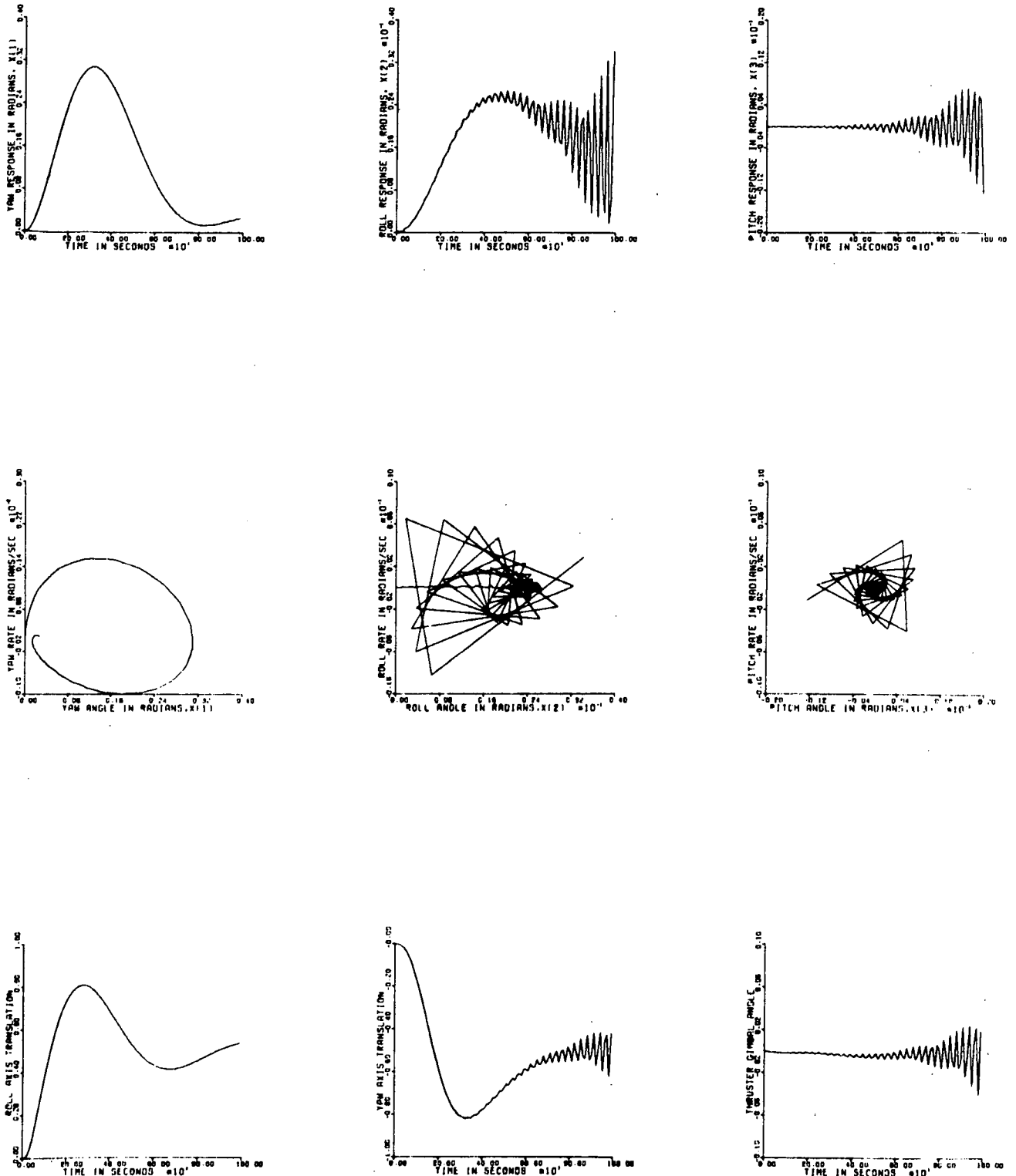
Stable Flexible Model, $K_{si} = 100, 250, 295$ V/rad,
 $\sigma_1 = 0.01366$ Hz, $\sigma_2 = 0.01461$ Hz, $\sigma_3 = 0.02111$ Hz,
 $\sigma_4 = 0.02262$ Hz, $\sigma_5 = 0.02798$ Hz, $\sigma_6 = 0.02798$ Hz,
 Rotation Angle = 0° , Aspect Ratio = 7.38

Fig. IV-B-15. Simulation Analysis, Case c



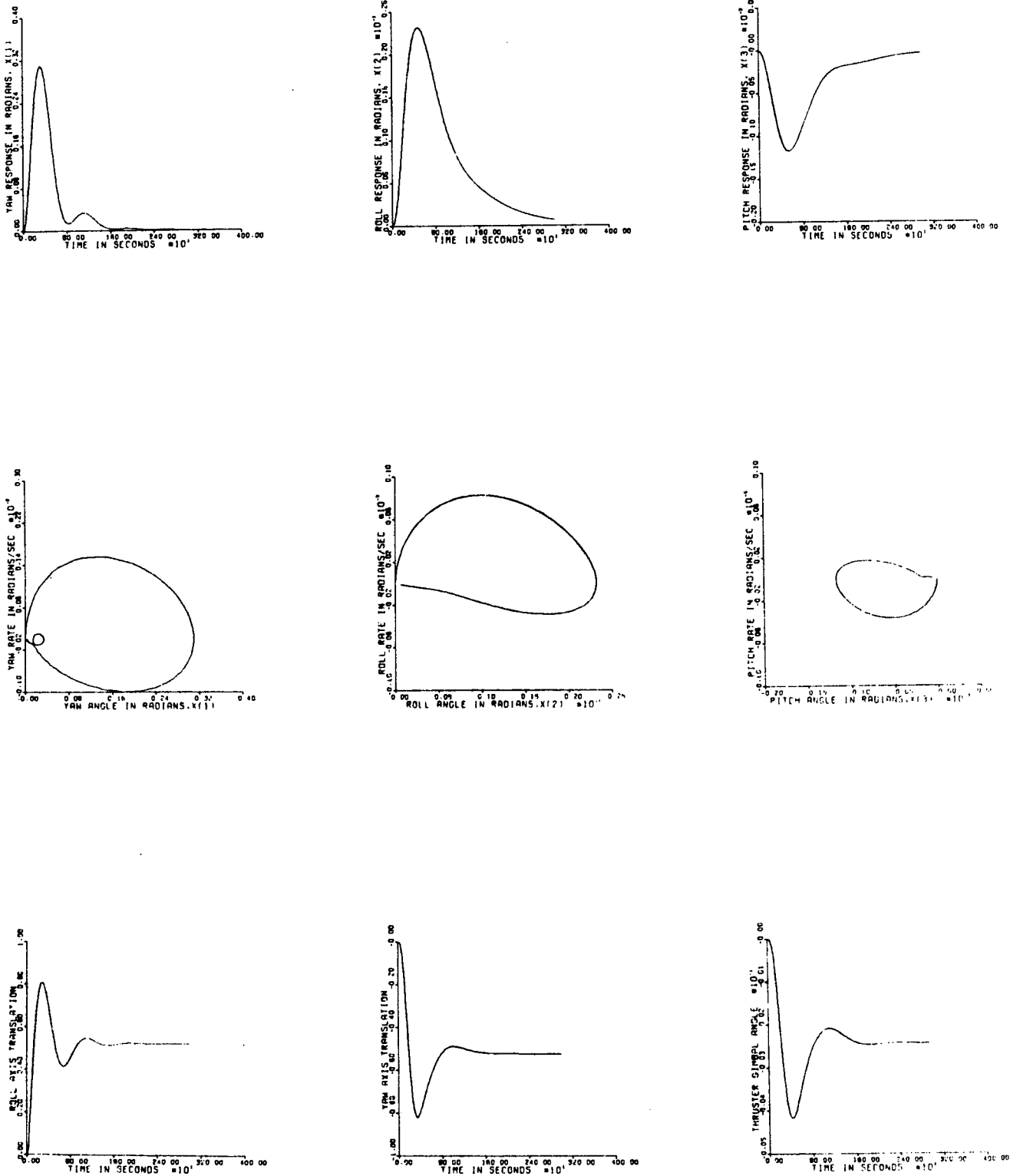
Stable Rigid Model, $K_{si} = 100, 250, 295$ V/rad,
Rotation Angle = 0° , Aspect Ratio = 7.38

Fig. IV-B-16. Simulation Analysis, Case d



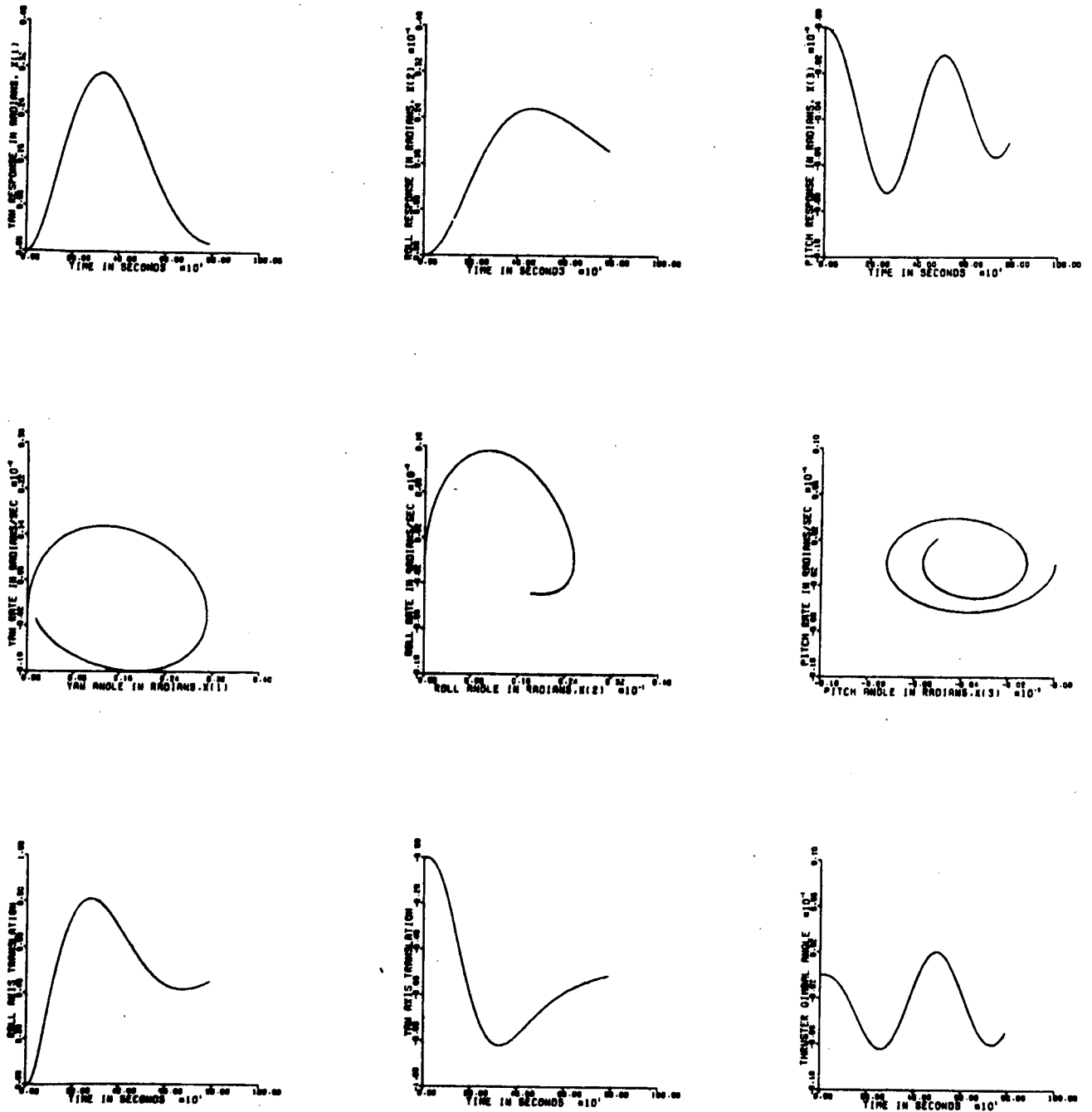
Unstable Flexible Model, $K_{si} = 100, 250, 295$ V/rad,
 $\sigma_1 = 0.01366$ Hz, $\sigma_2 = 0.01461$ Hz, $\sigma_3 = 0.02111$ Hz,
 $\sigma_4 = 0.02262$ Hz, $\sigma_5 = 0.02798$ Hz, $\sigma_6 = 0.02798$ Hz,
 Rotation Angle = 60° , Aspect Ratio = 7.38

Fig. IV-B-17. Simulation Analysis, Case e



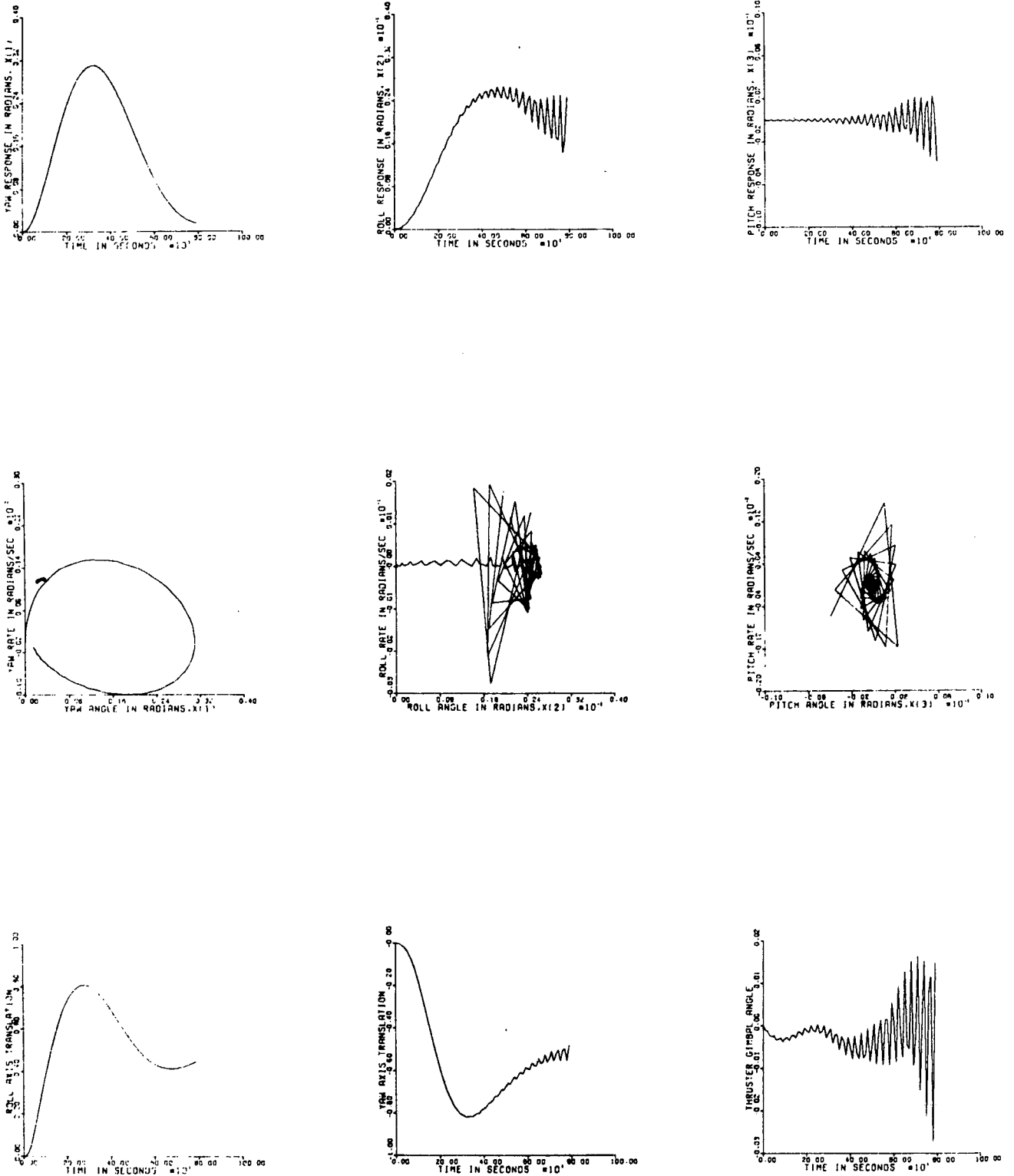
Stable Flexible Model, $K_{Si} = 100, 250, 295$ V/rad
 $\sigma_1 = 0.02962$ Hz, $\sigma_2 = 0.02962$ Hz, $\sigma_3 = 0.02965$ Hz,
 $\sigma_4 = 0.03206$ Hz, $\sigma_5 = 0.03612$ Hz, $\sigma_6 = 0.03907$ Hz,
 Rotation Angle = 0° , Aspect Ratio = 7.38

Fig. IV-B-18. Simulation Analysis, Case f



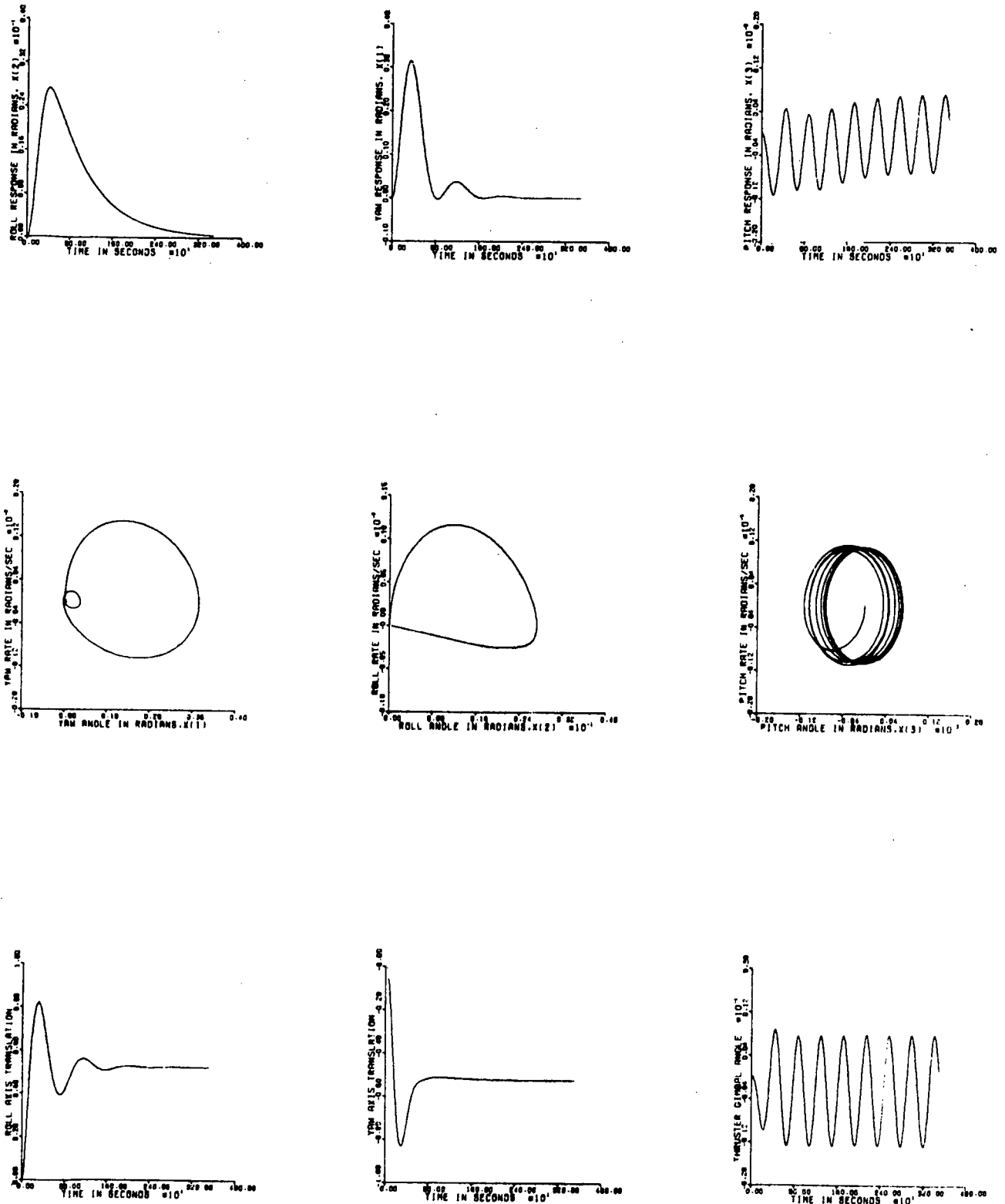
Stable Rigid Model, $K_{si} = 100, 250, 600$ V/rad,
Rotation Angle = 60° , Aspect Ratio = 7.38

Fig. IV-B-19. Simulation Analysis, Case g



Unstable Flexible Model, $K_{si} = 100, 250, 600$ V/rad,
 $\sigma_1 = 0.01366$ Hz, $\sigma_2 = 0.01461$ Hz, $\sigma_3 = 0.02111$ Hz,
 $\sigma_4 = 0.02798$ Hz, $\sigma_5 = 0.02798$ Hz, $\sigma_6 = 0.02798$ Hz,
 Rotation Angle = 60° , Aspect Ratio = 7.38

Fig. IV-B-20. Simulation Analysis, Case h



Unstable Rigid Model, $K_{si} = 100, 250, 600$ V/rad,
Rotation Angle = 30° , Aspect Ratio = 4.11

Fig. IV-B-21. Simulation Analysis, Case i

The initial conditions for all configurations are $y = 0$. However, an initial mass center offset of 15.24 cm (6 in.) in roll, pitch, and yaw is assumed. This implies that, initially, there are thruster disturbance torques in roll and yaw. The mass center offset implies a non-zero solar torque in pitch and roll because center of pressure and mass center are not coincident. For a stable configuration, it is expected that the errors should be driven to zero and that the translator should move approximately 15.24 cm (6 in.) parallel to the roll and yaw axes. Further, the gimbal angles for the gimballed thrusters should reach some steady value in accordance with the solar torque.

The first simulation results of Fig. IV-B-13 are for a rigid model case. This means that the solar arrays are assumed to be completely rigid. The input data are $K_{sx} = 295.0$, $K_{sy} = 300.0$, $K_{sz} = 250.0$, solar-array rotation angle = 0 deg, and aspect ratio = 7.38. These data match those of cases 1A, or 4A, or 7A in Table IV-B-8. In any case, the eigenvalue analysis indicates that this spacecraft configuration is stable. This conclusion is borne out by the simulation results. The initial mass center offset gives rise to attitude perturbations which reach their maxima at approximately 250, 500, and 500 sec for the yaw, roll, and pitch axes, respectively. The roll axis translation curve shows the translator displacing through a maximum of .2438 m (0.8 ft) before settling down eventually to approximately .1524 m (0.5 ft) after about 400 sec. Maximum yaw axis excursion for the translator is .2438 m (0.8 ft) along the negative axis. Time to settle down to a steady state .1524-m (0.5-ft) value is 1500 sec. To control against the steady-state solar torque, the gimballed thrusters rotate to a maximum value of 0.0042 radian and then settle down to a steady state value of 0.0025 radian or 0.14 deg.

Figure IV-B-14 shows, dramatically, the effect of flexibility on the attitude motion. The configuration shown is identical to the above except that the first six modes of flexible motion are included. Also the softest array is considered; i.e., lowest natural frequency is 0.01366 Hz. The eigenvalue analysis indicated (Table IV-B-8, case 1A) that the attitude motion is unstable. Initially, a simulation run of 1500 sec of real time was made. Figure IV-B-14 indicates apparent stability up to 1500 sec. The yaw, roll, and pitch response

curves are identical to those for the rigid case. After 1500 seconds the instability becomes obvious. The first six modes to which the frequencies listed on Fig. IV-B-14 correspond are, sequentially, two out-of-plane bending modes, two in-plane bending modes, and two torsion modes. The torsion modes are excited by yaw-axis rotation, and it is these modes which cause the instability of Fig. IV-B-14. It is interesting to note that these are not the lowest frequency modes. The frequency associated with both modes is 0.02798 Hz. Coupling of the structural dynamics with the rigid body dynamics modifies the frequencies associated with the various modes. In particular, it can be shown that the modified frequencies associated with modes 5 and 6 are approximately 0.0285 Hz. The period corresponding to this value is approximately 35.1 sec. The relatively high frequency oscillation of Fig. IV-B-14 has this period. This confirms that it is the torsional mode which induces instability. Notice that no instability is observed for the roll or pitch axes.

Figure IV-B-15 shows how the instability of the previous case can be eliminated by a simple change in the control system electronics. In particular, the system gain is changed by reducing the yaw axis sun sensor gain from 300 to 100 V/radian. As expected, no appreciable change occurs for the roll or pitch axis responses. However, the yaw axis response damps out after nearly 3000 sec in contrast to the unstable behavior for the previous case. However, it should be noted that despite the fact that the disturbance torques are the same for this and the previous cases, the maximum initial yaw-angle excursion is considerably greater in the stable case than for the unstable case (compare Figs. IV-B-14 and IV-B-15).

If the last configuration is changed to a rigid model, the results are nearly identical to those of the non-rigid model (compare Figs. IV-B-15 and IV-B-16). In other words, for this configuration, flexibility has very little effect on the attitude response.

Rotation of the solar arrays about their boom axis can induce unstable behavior. For example, if the arrays for case d are rotated through

60 deg about the yaw axis, unstable motion is predicted by the eigenvalue analysis (see Table IV-B-8, case 1C). An out-of-plane bending mode causes the instability. The rotation angle of 60 deg explains why the array bending mode couples into both the yaw and pitch responses. This case reinforces the notion that stability is very dependent upon configuration. Thus, although the zero-rotation configuration for this array is stable (Fig. IV-B-15), the rotated array case is not (Fig. IV-B-17).

Case f (Fig. IV-B-18) gives an indication of how sensitive the control is to array stiffening. The plots should be compared to those in Fig. IV-B-15. Lowest natural frequencies are 0.01366 Hz and 0.02962 Hz for the softer and stiffer arrays respectively; i.e., lowest natural frequency has more than doubled. However, for both cases, attitude motion is stable and nearly identical. As expected, the array oscillations are felt a little more strongly for the soft array than for the stiff one (compare roll-axis phase plots in Figs IV-B-15 and IV-B-17). Thus, control is not very sensitive to changes in array natural frequency for the cases examined. This conclusion should not be generalized to extend to any configuration.

Figures IV-B-19 and IV-B-20 demonstrate again the possible negative effect of flexibility on attitude motion. Cases g and h are array-rotation cases where the rotation angle is 60 deg. In Fig. IV-B-19, the vehicle is assumed to be rigid. The eigenvalue analysis predicts stability (see Table IV-B-7). This is indeed the type of behavior illustrated in Fig. IV-B-19. Yaw motion has nearly damped out after 800 sec, and roll and pitch motion appear to be decreasing in amplitude. On the other hand, the eigenvalue study determined that, if the panels are considered flexible, then the motion is unstable. Figure IV-B-20 bears this out. Yaw motion is not affected by flexibility. However, the roll and pitch motions are upset by the array bending modes.

Finally the anomalous case where flexibility enhances stability was examined (see Table IV-B-7, case 9B $K_{sx} = 600$). Here, instability and

stability were predicted for the rigid and flexible models respectively. A simulation run for 800 sec showed no appreciable difference between the two cases and as such, only one series of graphs is shown to represent both cases (Fig. IV-B-21). The attitude motion appears to be stable. This conflicts with the eigenvalue analysis for the rigid model. However, it should be remembered that the results up to 800 sec only are known. Recall that for case b, the instability did not manifest itself until approximately 1500 sec. Thus, the simulation program probably should be run longer to demonstrate the instability. The root which gives rise to unstable motion has a real part equal approximately to 10^{-5} whereas the unstable root for case b has a root with real part approximately 10^{-2} . One would therefore expect the instability for case h to develop only after a very long time (several thousand sec). High computer costs preclude running SESSIM long enough to see the instability. Confidence gained from the analysis of case b indicates that there is no need to run the simulation program until the instability develops.

Solar-array tip deflections were calculated for case c. Results are shown in Fig. IV-B-22. The top row of graphs shows the deflections for nodes 26 and 56 in feet. Maximum deflections occur at approximately 40 sec and are approximately 0.0006 m (0.002 ft). The torsion modes oscillate at higher frequency, and tip deflections from these modes at the array corners are shown in the middle row of Fig. IV-B-22. Maximum deflections are approximately 0.003 m (0.01 ft). For the in-plane bending-mode, deflections at nodes 26 and 56 are plotted in the bottom row of Fig. IV-B-22. Maximum deflections of 0.0012 m (0.004 ft) occur. None of the modes gives rise to deflections sufficiently high to cause excessively high stress levels in the arrays.

2. Structural Interface With SEP Module

A total solar cell area on the order of 186 m^2 ($2,000 \text{ ft}^2$) is necessary to meet the high power requirement of the Encke mission. Because of

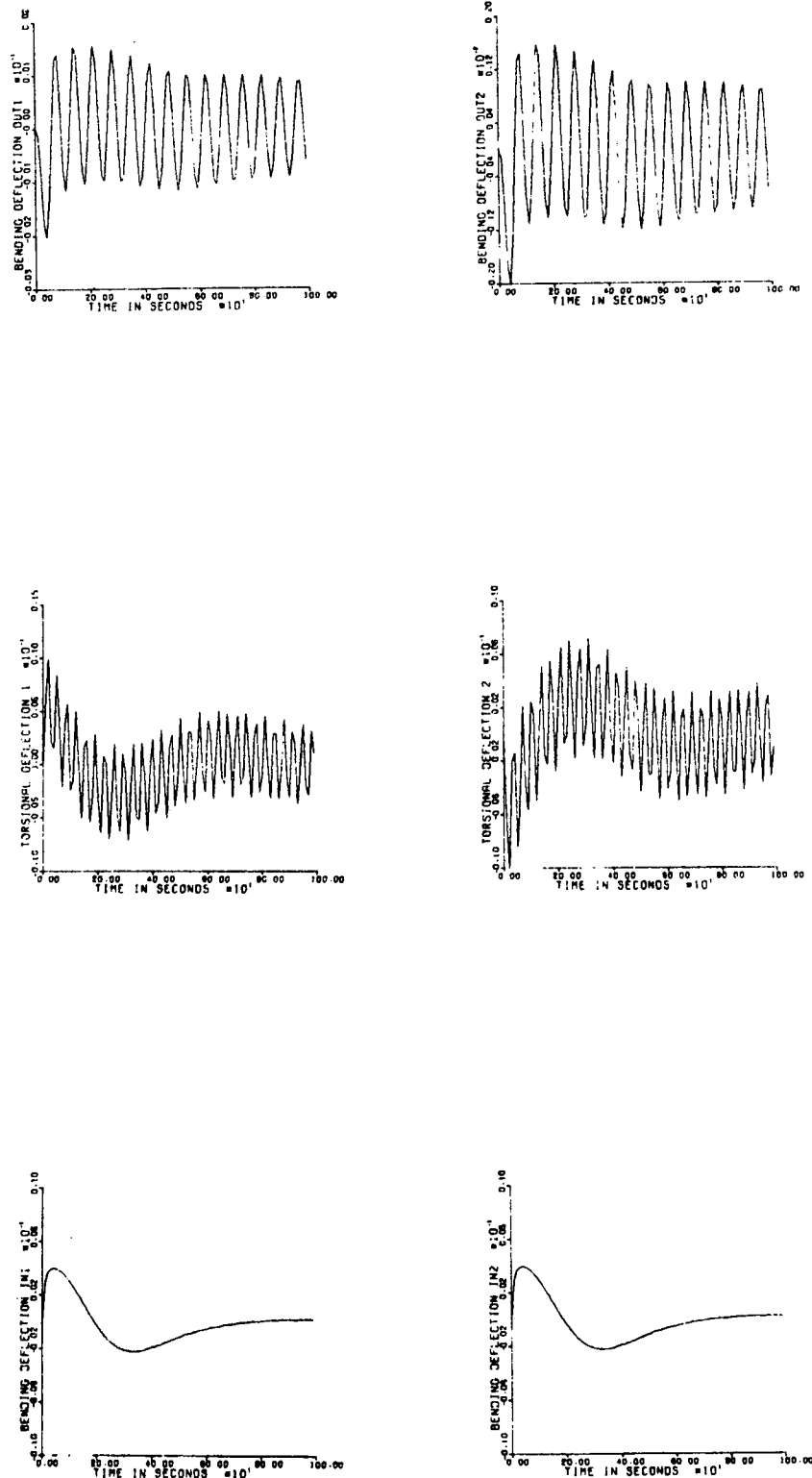


Fig. IV-B-22. Simulation Analysis, Solar Array Tip Deflections

weight and other considerations as described in Ref. IV-B-4, the lightweight rollup solar array concept developed by the General Electric Company for JPL was selected for the Encke mission. The General Electric concept is shown in Fig. IV-A-2 and is described in detail in Ref. IV-B-5. Two of these GE panels, each 4.3 m wide by 23.8 m long (14 by 78 ft) are used on the Encke spacecraft.

The ease and manner with which these large panels integrate with the spacecraft structure can have a significant impact on spacecraft configuration and total mass. For this reason, a study was undertaken to identify and explore the requirements of the structural integration of the solar array with the spacecraft structure. The interaction between array and spacecraft during large-displacement, low-frequency, spacecraft launch-vibration modes was of particular interest.

a. Solar-Array Structural Interface Requirements

Because the solar array is essentially an add-on subsystem, the spacecraft structural interface design is primarily based on meeting the structural support requirements of the panels. Accordingly, these requirements must be understood before the spacecraft interface can be examined.

The basic structure of the rollup solar panel consists of a pair of cylindrical storage drums, on which the two solar-cell blanket halves are wrapped during launch, and an extendible boom which deploys the blankets following launch. The two storage drums are cantilevered from a center support structure on individual sets of preloaded bearings. The center support is the primary structural tie to the spacecraft and is, generally, attached to an orientation drive mechanism.

In the stowed condition during launch, the outboard ends of the drums are also supported by movable arms attached to the spacecraft structure. These outboard-end supports carry only lateral loads, loads perpendicular to

the axis of the drum; however, they also (1) prevent the drums from unwinding during launch, and (2) support the outboard end of the leading edge member during launch.

Before panel deployment, the outboard end supports are released by firing electroexplosive devices. They then swing clear of the drums and the leading edge member. In the released state, the center support is the only attachment between the array and the spacecraft structure.

Because flight loads are negligible, the solar array/spacecraft structural interface design is primarily aimed at meeting the launch-load support requirements, as follows:

- (1) The interface structure must support the solar array in a preestablished position with respect to the spacecraft and must maintain structural integrity throughout the launch environment. The stiffness of the interface structure must be high enough to avoid a solar array/spacecraft natural frequency which would couple excessively with low-frequency launch-vehicle excitation.
- (2) The stiffness of the entire spacecraft structure connecting the outboard-end supports and center support must be significantly stiffer than the solar-panel drum-center support assembly. This is necessary because the GE rollup solar panel design attaches to the spacecraft at three points, in a statically indeterminate manner. With the statically indeterminate support arrangement, the distribution and magnitude of the launch loads on the solar panel are a function of the spacecraft interface support stiffness. The GE rollup solar array was designed to attach to a very rigid spacecraft structure.
- (3) Low-frequency spacecraft deflection must not lead to excessive relative movement between the solar-panel outboard-end support and center-support spacecraft

interfaces. This is necessary because, with the statically indeterminate support arrangement, relative movement between the spacecraft attachment points applies loads to the solar array.

- (4) The solar array support structure should be lightweight and should integrate well into the overall spacecraft design.

Though the support stiffness and relative motion requirements [see (2) and (3)] are not too difficult to meet for the 2.5-m (8-ft) wide GE prototype panel, they become more significant as the width of the panel increases. Meeting the requirements for the 4.3-m (14-ft) wide baseline SEPSIT solar panel could significantly impact the spacecraft configuration and total mass. The following study was thus undertaken to critically evaluate the impact of the solar-array requirements on the spacecraft design.

b. Structural Analysis Approach

To evaluate the impact of the solar-array support requirements on the spacecraft design, a dynamic analysis of the combined solar array/spacecraft structural system was undertaken. Accurate representation of the solar-array support stiffness and calculation of low-frequency spacecraft deflections required a reasonably detailed analytical model of the entire spacecraft, including the solar array. Because the solar-panel interface forces and deflections were of primary interest, the dynamic properties of the solar array had to be accurately modeled. In particular, previous dynamic studies of the stowed solar panel (Ref. IV-B-6) determined that the solar-cell blankets must be treated as separate spring-mass systems with a high degree of damping. The dynamic response of the blankets on the solar array drums was found to be a combination of highly damped resonances extending between about 25 and 100 Hz. In this region, the blankets have an amplification factor (Q) of between 2 and 3.

The solar panel model used in the study is shown in Fig. IV-B-23. Because the drums are much stiffer than their support-bearing

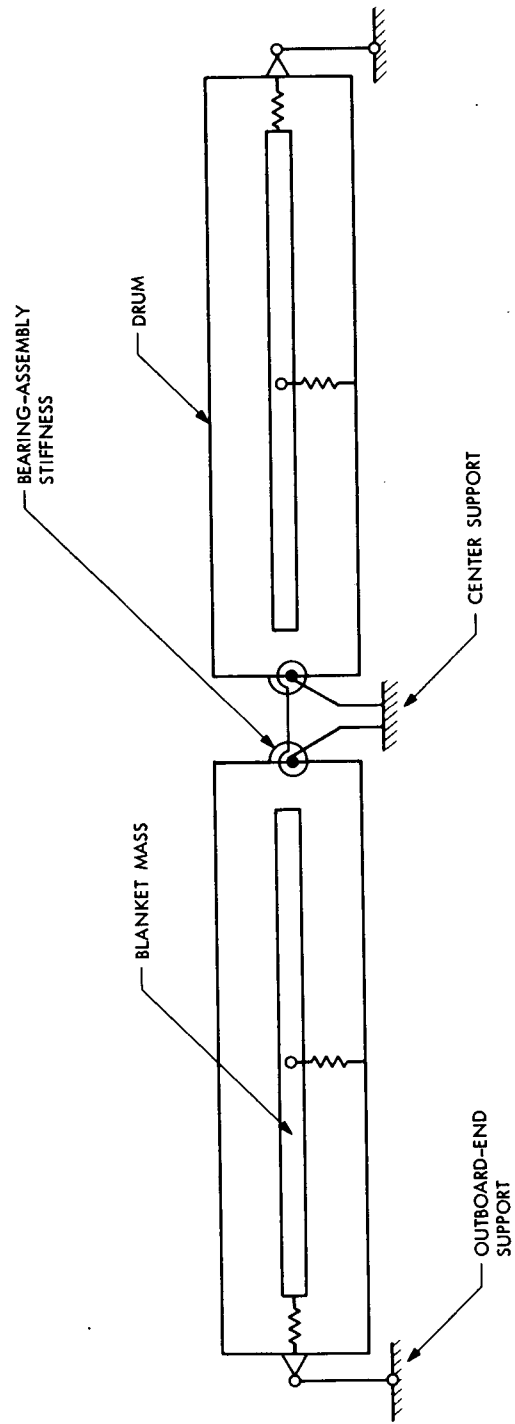


Fig. IV-B-23. Rollup Solar-Panel Structural Model

assemblies at the center support, the drums are modeled as rigid bars connected to the center support by torsion springs. The deflection between the drums and the center support was used as a measure of the critical stress at the base of the drums. The blankets were also modeled as rigid bars and were allowed to translate in two degrees of freedom with respect to the drums. However, no relative rotation was allowed. The springs connecting the blankets to the drums were sized to give the desired natural frequency to the blankets in both the longitudinal and the transverse directions.

To complete the spacecraft, two of the above solar-panel models were connected by a planar representation of the SEPSIT Option 3, Configuration 1, spacecraft. The planar representation, considered sufficient for the current study, reduced the size of the computational problem to 34 degrees of freedom. A schematic representation of the model is indicated in Fig. IV-B-24. As indicated, the primary structure of the spacecraft was idealized using seven beam elements with infinite axial stiffness. The solar-array support members were all idealized as pinned-end, axial members except for the main center support tube, which was modeled as a beam. The effect of the width of the primary spacecraft structure on the motion of the solar-panel member attachments was properly accounted for by using multipoint constraints to define the true attachment motions in terms of the idealized truss coordinates. Similar methods were used to define the motion of the solar-array blankets with respect to the drums. The mass distribution was modeled by a combination of lumped masses and consistent mass elements.

Though the model shown in Fig. IV-B-24 is representative of the current SEPSIT spacecraft configuration, it was designed to incorporate two other solar-array support configurations: one with the upper outboard-end supports removed, and a second with all outboard-end supports removed. This was done because the three-point, statically indeterminate support arrangement is largely responsible for the complexity of the solar array/spacecraft structural interface. It was apparent that, if required, the removal of at least one of the solar-panel outboard-end supports would make the panel support statistically determinate and thus would eliminate the previously described support

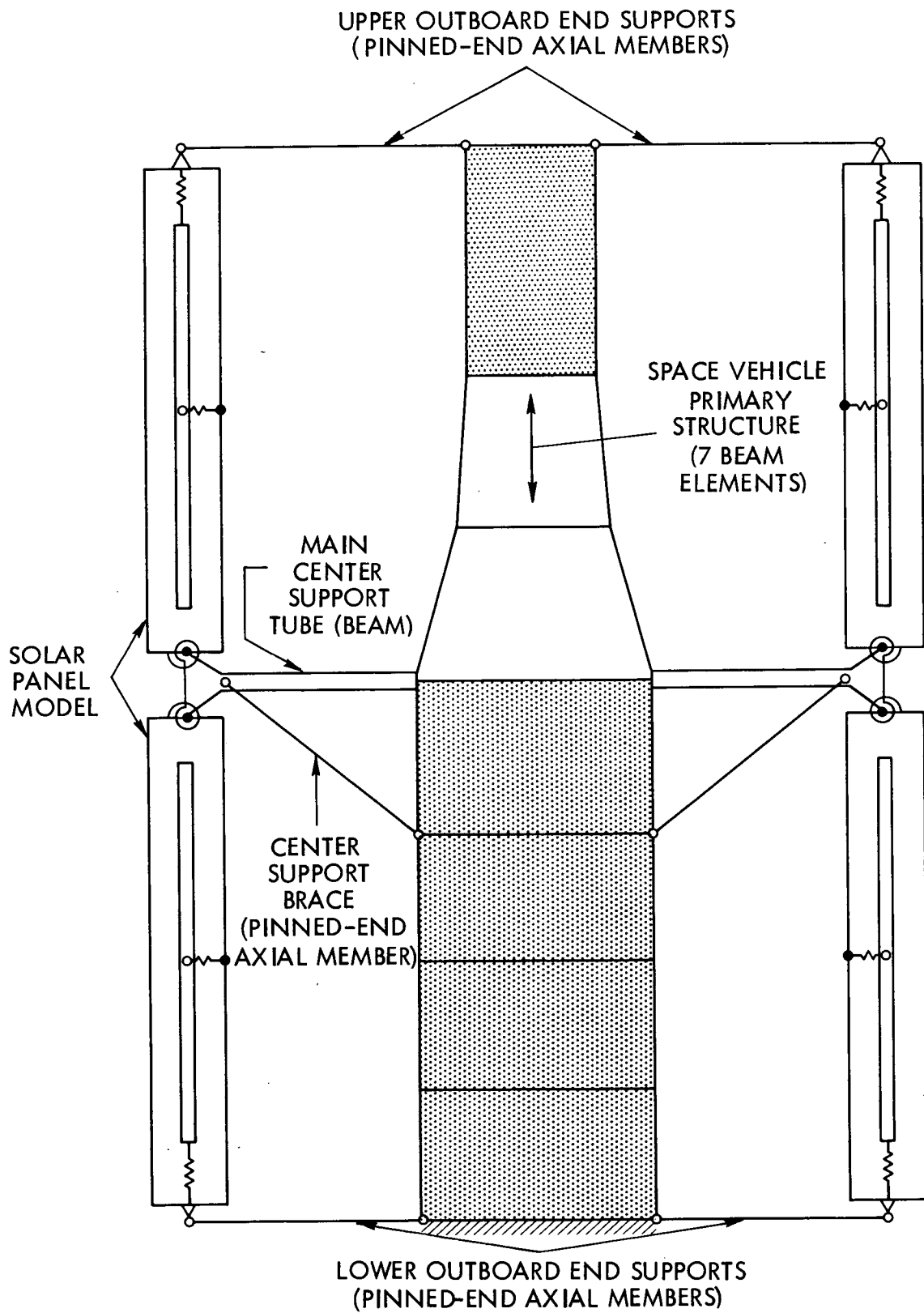


Fig. IV-B-24. SEPSIT Spacecraft Structural Model

stiffness and support relative motion requirements. Removal of an outboard-end support would also eliminate the spacecraft structure required for its support and would thereby reduce spacecraft weight. However, some additional weight would be required elsewhere to strengthen the drum-bearing assemblies and to provide an alternate means of locking the drums and leading edge member during launch. The feasibility of removing the end supports is enhanced by the fact that the mass associated with the solar-cell blankets has been found to be coupled to the drums in a highly damped manner. The high damping results in considerably lower loads than were assumed in the original design.

After the above composite model was made, the first 20 natural frequencies and vibration modes were calculated for the cantilevered spacecraft with and without outboard-end supports. The rigid-elastic coupling terms which indicate the degree of coupling between the spacecraft modes and the launch vehicle interface motions were also calculated. Subsequently, each mode was scaled to indicate its expected launch vibration level based on its effective mass and degree of coupling to the launch vehicle excitation. After the modes were appropriately scaled, the modal deflections were used to calculate the critical stresses in the solar array-drum-bearing assemblies.

c. Solar Array/Spacecraft Structural-Analysis Results

During the course of the study, analyses were made using various solar cell blanket natural frequencies, and solar-array drum-bearing assembly and support member stiffnesses. Each case was analyzed using three spacecraft configurations: (1) all outboard-end supports present, (2) upper outboard-end supports removed, and (3) both upper and lower supports removed.

Figure IV-B-25 summarizes the spacecraft mode shapes with frequencies less than about 40 Hz. Modes A, C, D, and E are the first four modes with all outboard-end supports present. Removal of the upper outboard-end supports results in two additional modes, B and F. When the lower outboard-end supports are also removed, modes B and F are replaced by four modes, G, H, I, and J.

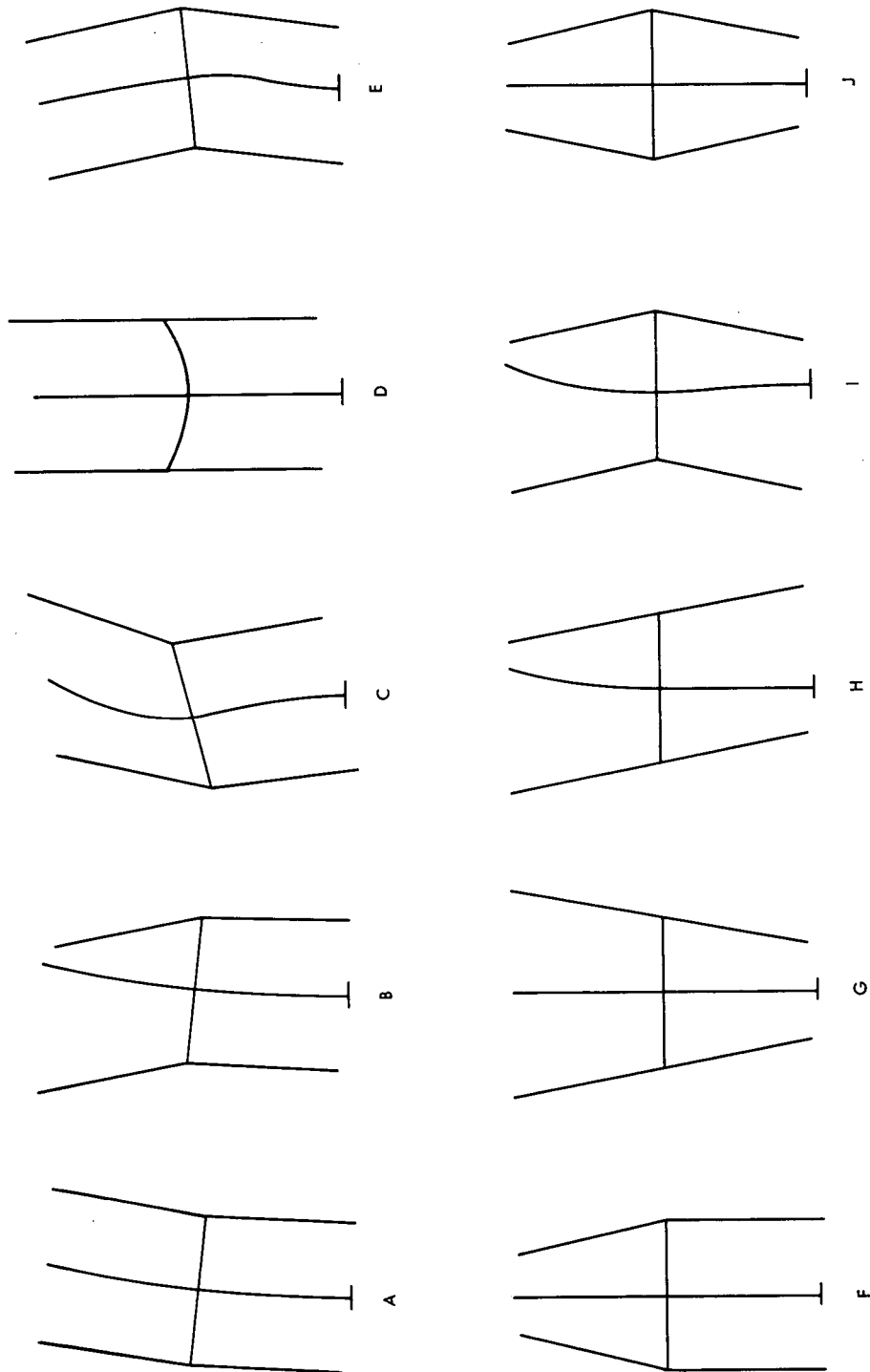


Fig. IV-B-25. SEPSIT Spacecraft Mode Shapes

The natural frequencies and solar panel stresses associated with these modes are presented in Table IV-B-10 for three solar panel configurations designated 50L, 50H, and 30H. The number prefix of the designation refers to the natural frequency of the solar-cell blanket, which is tuned to 50 Hz and 30 Hz, respectively, for the 50X and 30X configurations. The suffixed letters, H and L, denote a high bearing-assembly stiffness of 2700 kN-m/rad and a low bearing assembly stiffness of 54 kN-m/rad, respectively. The low bearing-assembly stiffness corresponds to the measured stiffness of the GE prototype solar array.

As noted in Table IV-B-10, the results indicate that none of the solar panel configurations is in danger of failing, when all outboard-end supports are used. However, more detailed results indicate that relative motions on the order of 1 cm can be expected between the tips of the solar-panel drums and the outboard end-support attachments at the spacecraft. The outboard-end supports must be capable of accommodating this relative motion. Though the pinned members used in the model have this capability, the prototype design is supported by tapered plugs which would disengage during such motion. Some minor reconfiguration of the outboard-end-support attachment to the drum is therefore suggested.

The data in Table IV-B-10 also indicate that one or both of the outboard-end supports can be removed, providing the solar-panel drum-bearing assembly is sufficiently stiffened. With the current bearing assembly design, the first mode of the cantilevered drum occurs at about 4 Hz and couples extensively with the first mode of the spacecraft. At this low frequency, the solar cell blanket and drum move in unison and with very low damping. This leads to unacceptably high stresses at the root of the drum assembly.

When the cantilevered drum resonance is increased to about 20 Hz, the drum structure uncouples from the solar cell blanket to some degree, and the relative motion between the blanket and the drum leads to considerable damping. At this frequency, the drum resonance is uncoupled from the spacecraft first mode and is coupled instead to the much diminished spacecraft

Table IV-B-10. SEPSIT Spacecraft Natural Frequency and Ratio of Bearing-assembly Stress to Failure Stress for Three Solar-panel Configurations

Outboard End Supports	Mode Type	Frequency, Hz			Stress Ratio		
		Configuration			Configuration		
		50L	50H	30H	50L	50H	30H
Both	A	6.17	6.87	6.86	.13	.14	.14
	C	21.73	24.56	22.65	.05	.04	.04
	D	34.56	35.00	26.80	.01	.00	.00
	E	38.22	39.04	29.97	.01	.01	.01
Lower Only	A	3.84	6.54	6.53	2.30	.03	.03
	B	6.75	17.45	16.62	.25	.09	.09
	F	3.90	20.21	18.62	.00	.00	.00
	C	22.24	25.96	23.22	.04	.05	.05
	D	34.56	35.02	26.81	.01	.00	.00
	E	38.38	39.39	30.03	.01	.01	.01
None	A	3.69	6.41	6.40	1.77	.04	.04
	G	3.72	8.62	8.51	.00	.00	.00
	H	6.76	8.73	8.63	.25	.08	.08
	I	4.04	20.13	18.96	1.77	.06	.06
	J	4.07	26.29	22.69	.00	.00	.00
	C	22.33	28.83	24.41	.04	.06	.05
	D	34.56	35.03	26.81	.01	.00	.00
	E	38.83	41.15	34.78	.01	.02	.02

second mode. Thus, although an alternate method of locking the drums and leading edge member during launch is required, the elimination of the outboard-end supports appears feasible. Though both the upper and lower outboard-end supports could be removed, removal of just the upper supports has certain advantages. A primary advantage is that the lower supports prevent solar-panel resonances such as modes G and H in Fig. IV-B-25. These modes create high moments in the center support structure.

d. Conclusion

Before the current study, it was apparent that the solar-panel structural interface requirements could have a significant impact on the configuration and total mass of the spacecraft. Study of the interface requirements indicated that the statically indeterminate support arrangement of the solar array is sensitive to large-displacement, low-frequency, spacecraft motion. However, the above study also indicates that the General Electric rollup solar-array concept is compatible with the motion amplitudes expected for the SEPSIT spacecraft design. The study also indicates that removal of the solar-array outboard-end supports is feasible, providing the solar-array drum-bearing assembly stiffness is increased. If the outboard-end supports are retained, some minor reconfiguration of the outboard end-support drum attachment is recommended.

3. Solar Array Temperature Analysis

During the Encke Rendezvous Mission, the solar irradiance to which the spacecraft is exposed (i.e., the rate of solar energy incident upon a surface per unit projected area) varies in proportion to the inverse square of its heliocentric distance. The expected spacecraft aphelion and perihelion are 3.5 AU and .34 AU, respectively. As a result, the solar irradiance varies by more than two orders of magnitude over the mission lifetime. The spacecraft element most directly affected by this variation is the rollup solar array.

If the array conversion efficiency were constant, the derivable electrical power would be proportional to the solar energy collected which, in

turn, is proportional to the irradiance. However, the actual relationship is not that simple. It has been shown (Ref. IV-B-7) that conversion efficiency for maximum power output can be accurately expressed as a separable product of two functions: (1) the effective relative irradiance and, (2) the solar cell temperature. As evidenced by the analysis which follows, cell temperature itself is highly dependent on the irradiance.

Because of the strong relationship which exists between conversion efficiency and temperature for most practical temperature ranges, no accurate prediction of available electrical power can be made without a precise knowledge of solar-array temperature level and distribution. Furthermore, the expected temperature extremes must be known so that the array can be designed and built to accommodate them.

a. Temperature Control

If only soft-solder-interconnect technology is used for the construction of the rollup array, the maximum permissible solar-cell blanket temperature should be 140°C because of reliability considerations. The simplest temperature control scheme is to rotate the array about its longitudinal axis, when necessary, so that the cells are exposed to solar rays at something less than normal incidence. This has the same effect as a reduction in the solar irradiance. However, this scheme succeeds only when all cells are exposed to the same solar angle of incidence regardless of the array's angle of rotation. Therefore, the plan works for perfectly flat blankets, but not as well for non-flat blankets unless the required angle of rotation is not very large. By the nature of its construction, the SEPSIT rollup array blankets are inherently non-flat. Temperature non-uniformities are, consequently, unavoidable. One of the major goals of this study was to determine the relationship between the degree of flatness and the resulting temperature non-uniformity as a function of heliocentric distance. This information can be useful in determining blanket flatness requirements and may lead to the investigation of array designs which are less sensitive to temperature level and distribution.

It is not planned nor deemed desirable to limit the blanket low temperature extreme. Indeed, one of the characteristics of the silicon solar cell is that its efficiency generally improves as its temperature decreases for a fixed solar irradiation. Considering that spacecraft electrical power is at a premium at aphelion (when the solar irradiance is at its lowest value) it is advantageous to have the array operate at as low a temperature as is practical and possible.

b. Thermal Analysis

The thermal analysis of the solar array is complicated by the fact that the SEPSIT cell-blanket contour can not be predicted with great certainty. However, prior JPL experience with rollup arrays strongly indicates that the blanket contour, neglecting geometrical edge effects along the drum and along the leading edge member, can be approximated by the one-dimensional edge-curl model shown in Fig. IV-B-26. The cross section through a row of cells is considered a circular arc; whereas, the cross section through a column of cells is a straight line*.

If thermal edge effects are neglected, the temperature along a column of cells is constant. The relationship between the temperature of cell column i and the temperatures of the other cell columns are given by the steady-state heat balance for column i , that is:

$$q_1 + q_2 + q_3 = q_4 + q_5 \quad (1)$$

where q_1 = solar flux absorbed by direct solar incidence

q_2 = solar flux absorbed as a result of reflections from other cell columns

q_3 = infrared flux absorbed due to thermal emission from other cell columns

*The thermal analysis is independent of the actual placement of cells on the blanket. The term "row of cells" or "column of cells" is used more to describe a locus of points on the blanket than actual cell locations.

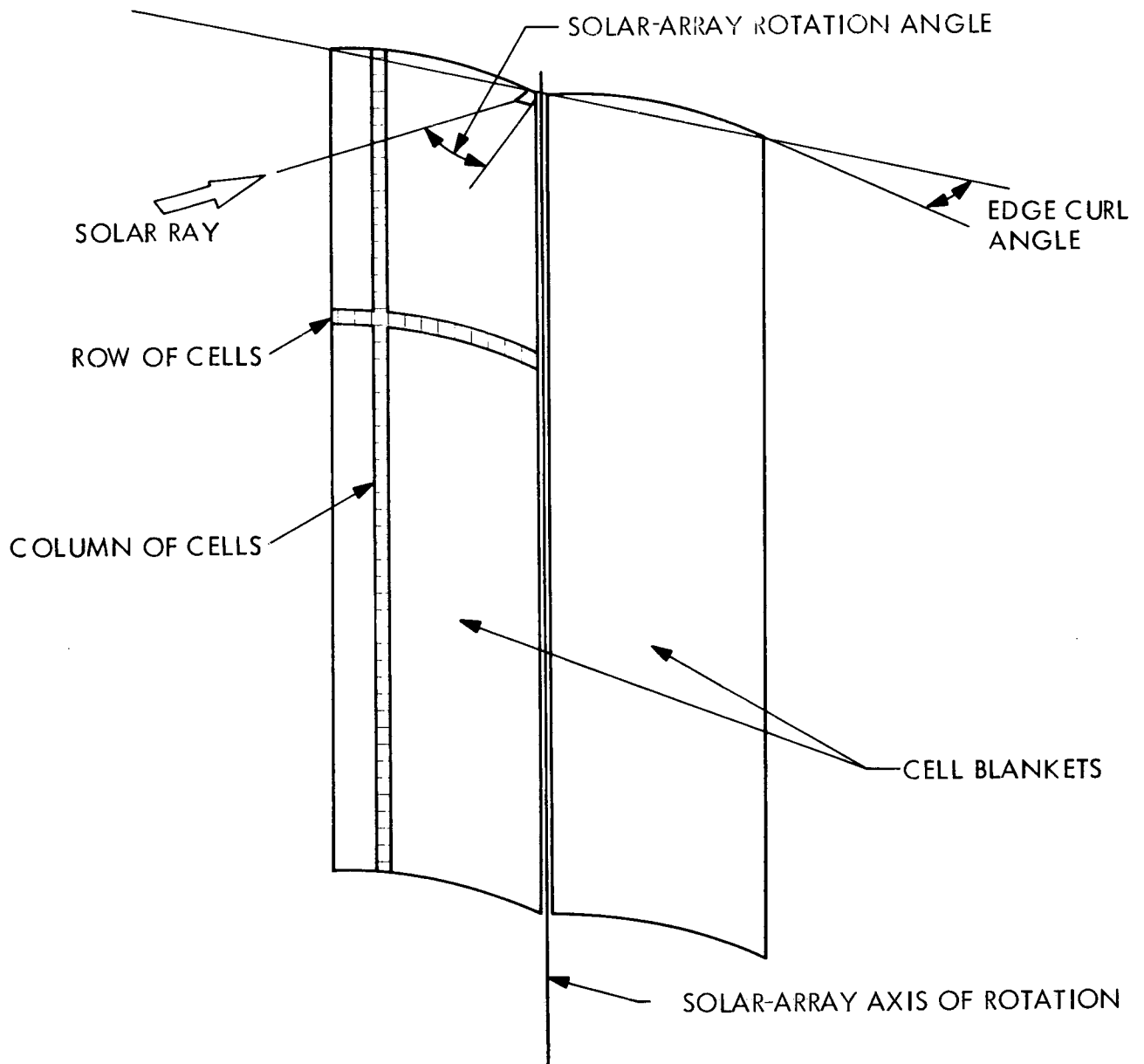


Fig. IV-B-26. Thermal Model of Solar Array

q_4 = infrared flux emitted by front (cell/coverglass) and back (substrate) sides of cells in column i

and q_5 = electrical power per unit area of column i extracted by spacecraft electrical load.

The above expression is a conservative assumption because it neglects the conductive coupling which exists between cells by virtue of the electrical connections and the cell substrate.

The mathematical equivalent of Equation (1) is:

$$\begin{aligned} \alpha S \max(\cos \theta_i, 0) + \sum_{j=1}^N \alpha \rho G_{j,i} S \max(\cos \theta_j, 0) + \sum_{j=1}^N \epsilon(t_i) \epsilon(t_j) F_{j,i} \sigma T_j^4 \\ = [\epsilon(t_i) + \epsilon_s(t_i)] \sigma T_i^4 + (P/A)_0 R_i \Psi(R_i) \Phi(t_i) \end{aligned} \quad (2)$$

where T = absolute temperature, K

t = temperature, °C

α = solar absorptance of cell/coverglass

ρ = solar reflectance of cell/coverglass = $1 - \alpha$

ϵ = emittance of cell/coverglass, function of t

ϵ_s = back side (cell substrate) emittance, function of t

$F_{j,i}$ = infrared form factor from column j to column i

$G_{j,i}$ = solar form factor from column j to column i

σ = Stefan-Boltzmann constant

S = local value of solar irradiance

θ = angle between cell area normal and a solar ray

R = effective relative irradiance = $\frac{S}{S_{\oplus}} \max(\cos \theta, 0) \frac{1-r(\theta)}{1-r(0)}$

r = effective reflectance of coverglass (estimated by the Fresnel formulas and Snell's law for fused silica), function of θ

Ψ = cell relative efficiency, function of R

Φ = cell relative efficiency, function of t

$(P/A)_0$ = solar cell electrical power output per unit area for $R=1$ and $t = 60^\circ\text{C}$

N = number of cell columns

and subscripts i , j , and \oplus denote column i , column j , and earth, respectively.

Equation (2), in reality, represents a system of non-linear, simultaneous equations because the index i can run from 1 through N . It should be noted, however, that the equations become uncoupled if q_2 and q_3 (the second and third terms, respectively) vanish, as they do when the blankets are flat. To determine the effect of these terms, solutions were obtained with q_2 omitted and with q_2 included with $G_{j,i}$ matrices spanning the range of fully specular to fully diffuse solar reflections. The test was then repeated with q_3 omitted. For edge curl angles of 10 deg or less, the net effect of q_2 and q_3 amounted to only a few degrees centigrade. On the basis of this information, subsequent calculations were simplified considerably by omitting these terms.

For the purpose of this analysis, the pertinent thermophysical and electrical properties of Mariner Mars 71 cell/filters were assumed. These data (Ref. IV-B-7) are regarded as representative for the type of cell/filter which may ultimately be selected. The General Electric, 66-W/kg (30-W/lb) rollup-array prototype, for example, utilized an 8-mil, N/P, 2-ohm cm cell with an unfiltered, 4-mil coverglass. A flight version would probably use a coverglass equipped with a number 415 blue filter. Except for the thickness of its components, the Mariner Mars 71 cell/filter combination is identical.

A Kapton panel-blanket substrate is used in the thermal model. Cells are bonded onto the substrate with GE SMRD-745 adhesive. Test data

indicates that the emittance for this substrate/adhesive combination can be estimated by

$$\epsilon_s(t) = .74 - \frac{.02}{123}(t-27)$$

The results of the analysis are summarized in Figs. IV-B-27 and 28. As shown in Fig. IV-B-27, solar-array rotation is not required at heliocentric less than 140°C. But for lesser heliocentric distances, the required angle of rotation rapidly increases to 73.4 deg at perihelion (.34 AU). IV-B-28 illustrates the effect of edge curl angle and spacecraft heliocentric distance on the estimated maximum temperature deviation between cells*. Edge curl effects do not become significant until the solar array is rotated. Thus, only the results for heliocentric distances of less than .635 AU are shown. At greater distances, temperature deviations amount to less than 2°C for edge curl angles of up to 10 deg.

c. Conclusions

Rotation of the solar array can be used successfully to achieve temperature control provided the blankets can be kept fairly flat or can be made to withstand large temperature deviations. It should be remembered, however, that even with an edge curl angle of 10 deg, the solar array will experience large temperature deviations only at heliocentric distances less than .635 AU, well past the point of Encke rendezvous.

*For solar-array rotation angles greater than the edge curl angle, the temperature extremes occur along the edges of the blanket (cell columns 1 and N).

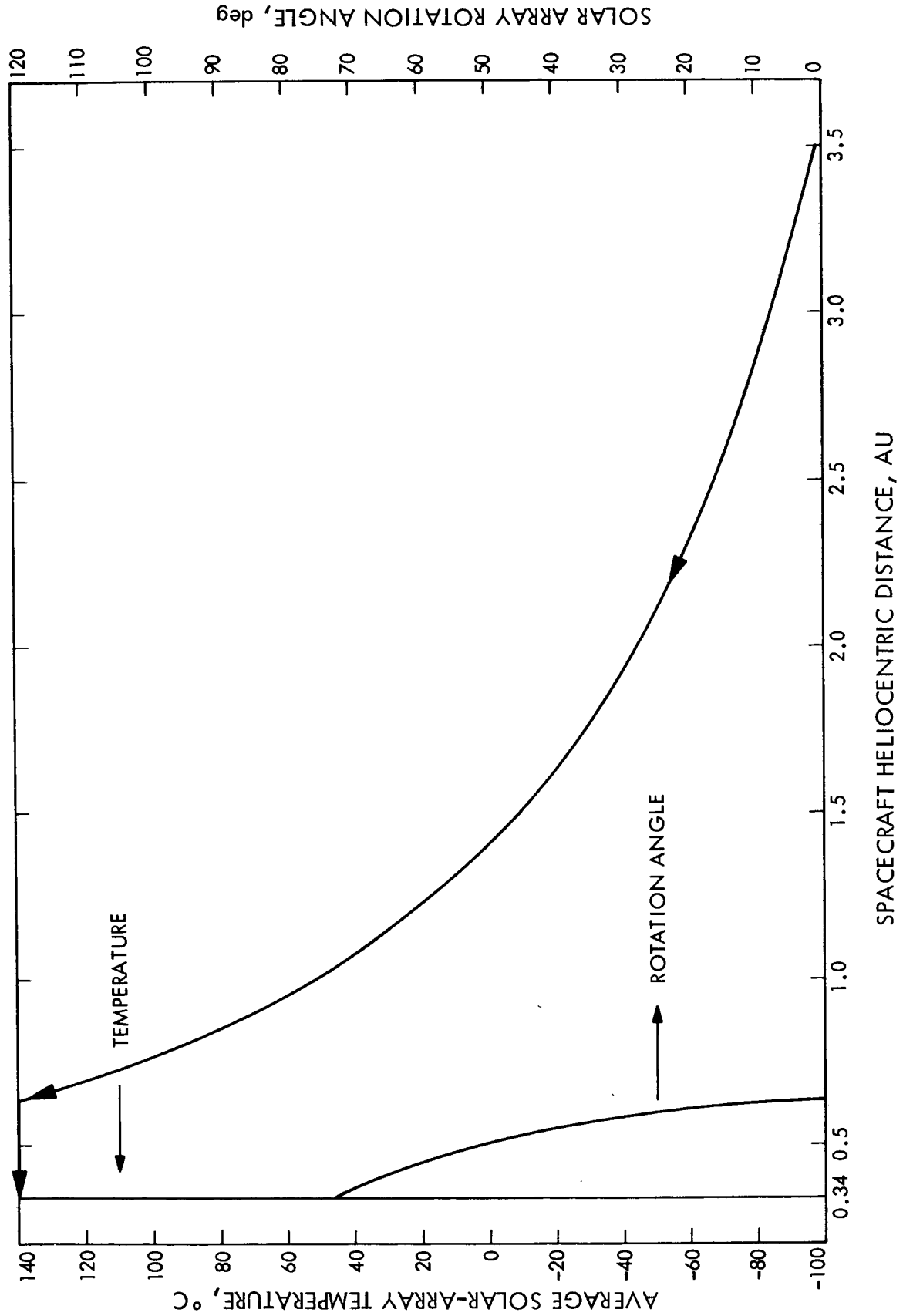


Fig. IV-B-27. Solar-array Sensitivity to Heliocentric Distance

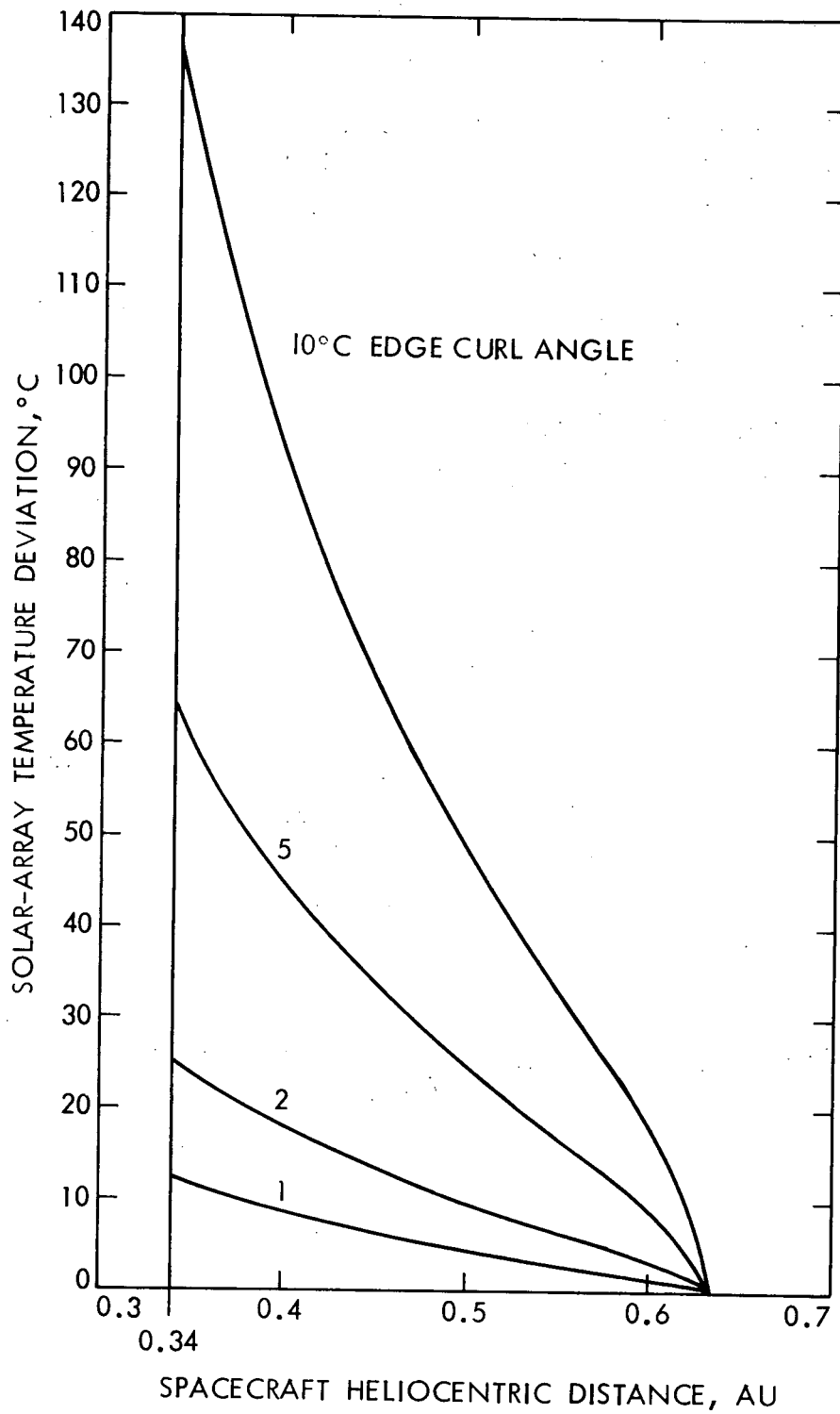


Fig. IV-B-28. Effect of Edge Curl on Solar-array Temperature

REFERENCES

- IV-B-1. Likins, P. W., Dynamics and Control of Flexible Space Vehicles, JPL TR 32-1329, Rev. 1, January 15, 1970.
- IV-B-2. Marsh, E. L., The Attitude Control of a Flexible Solar Electric Spacecraft, AIAA Paper No. 70-1140, presented at AIAA 8th Electric Propulsion Conference, Stanford, California, August 31 - September 2, 1970.
- IV-B-3. Ross, R. G., Unpublished notes on the structural analysis of a solar electric spacecraft.
- IV-B-4. Solar Electric Multimission Spacecraft (SEMMS) Phase A Final Report, Spacecraft Subsystem Analyses, Doc. 617-4, Jet Propulsion Laboratory, Pasadena, California, March 17, 1972 (JPL internal document).
- IV-B-5. Hasbach, W. A., and Ross, R. G., Jr., Summary Report on the Development, Design and Test of a 66 W/kg (30 W/lb) Rollup Solar Array, Technical Report 32-1562, Jet Propulsion Laboratory, Pasadena, California, September 15, 1972.
- IV-B-6. Final Report, Design and Development of a 30 Watts per Pound, 250 Square Foot Roll-Up Solar Array, Document 70SD4286. Prepared for the Jet Propulsion Laboratory by the Missiles and Space Division, General Electric Co., Philadelphia, Pa., Dec. 1, 1970.
- IV-B-7. R. G. Ross, et al, Measured Performance of Silicon Solar Cell Assemblies Designed for Use at High Solar Intensities, JPL Technical Memorandum, TM 33-473, March 15, 1971.

C. MAXIMUM POWER POINT DETECTOR CONCEPT SURVEY

The purpose of this memorandum is to summarize the results of a preliminary study of maximum power utilization methods for planetary spacecraft using an ion thruster propulsion system and a solar array as the primary energy source. The problems which arise from operating the solar array at or near the maximum power point, are discussed. The two basic methods of maximum power point operation and the advantages and disadvantages of each are presented, and recommendations for further development are made.

1. Maximum Power Point Operating Problem

A block diagram of a typical power system with ion thruster power conditioning circuitry and spacecraft engineering subsystem is shown in Fig. IV-C-1. Regulated power required by the ion thrusters is generated by the propulsion power conditioner. In a typical mission, a number of thrusters may be utilized, and each thruster requires approximately 2.5 kW of power. If a power conditioner efficiency of 90% is assumed, the total array power required can be high by many kilowatts, much higher than required by power systems developed in the past. This unusually high power level creates a unique problem that is not present in the lower power systems. Usually a power system contains an energy storage element, such as a battery, to provide power when the loads exceed the available array power. A battery large enough to provide kilowatts for any period of time is too bulky to be desirable. In a typical spacecraft, the battery will be designed to support only the housekeeping spacecraft loads. For this reason, the array maximum power can not be exceeded or an instability problem will occur. This instability problem can be explained with the aid of Fig. IV-C-2. Load line curve (1) of Fig. IV-C-2 is a typical converter input characteristic with three possible operating points on the corresponding solar array curve. Point C is the desirable operating point on the regulating portion of the curve where the converter acts as a constant power load. Point B is an unstable operating point which can result in the converter operating at point A on the nonregulating portion of the converter curve. If the converter input power is increased to load line curve (2), points B and C come together at

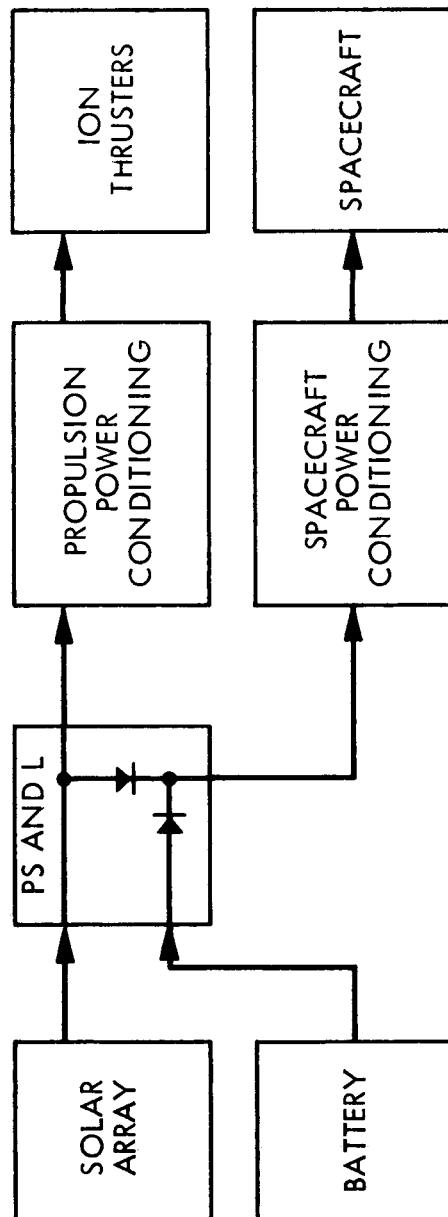


Fig. IV-C-1. Block Diagram of a Solar Electric Propulsion Spacecraft

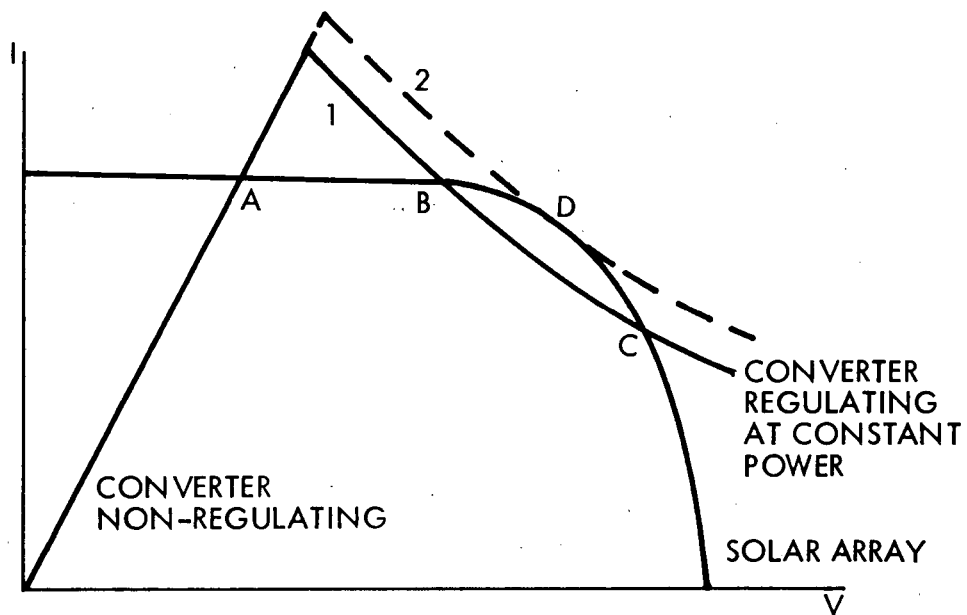


Fig. IV-C-2. Solar Array - Converting Operating Points

point D, the maximum power point of the array. Any further increase in power from curve (2) will cause the converter to snap to point A, which would be the nonregulating operating point. The system power demand would then need to be reduced to allow a desirable operating point on the solar array (I-V) curve.

The above discussion leads to the conclusion that active electronic systems are needed to operate at or near the solar array maximum power point. To operate at the maximum power point, the active system can be a closed loop system where a device is employed within the power system, to track the array maximum power and constantly adjust the power system characteristics. Such a system must utilize a variable load in conjunction with the converter constant load to adjust for system fluctuations. The alternative approach that allows operation near the maximum power point is an open loop system that either (1) measures the maximum power of an array section and computes the total array power, (2) utilizes a reference array to predict the characteristics of the solar array, or (3) utilizes impedance measurements to predict the maximum power utilization.

2. Closed-loop Systems

Maximum power point trackers (MPPT) fall into a general category of adaptive control systems. The MPPT is more precisely known as an extremum regulator. The extremum regulator differs from a normal regulator, which compares a controlled parameter (voltage or current) to a fixed reference. The extremum regulator continuously searches for the extremum position of the controlled parameter (power, in this case) and maintains the system at that point.

There are two system configurations which can be considered for this application: a series tracker, Fig. IV-C-3, and a parallel tracker, Fig. IV-C-4. Both MPPT concepts in Figs. IV-C-3 and 4 can be expanded into the functional block diagram in Fig. IV-C-5 to provide a basic understanding of MPPT design principles. The block labeled "T" is a transducer which measures either the deviation of solar array power from the maximum power

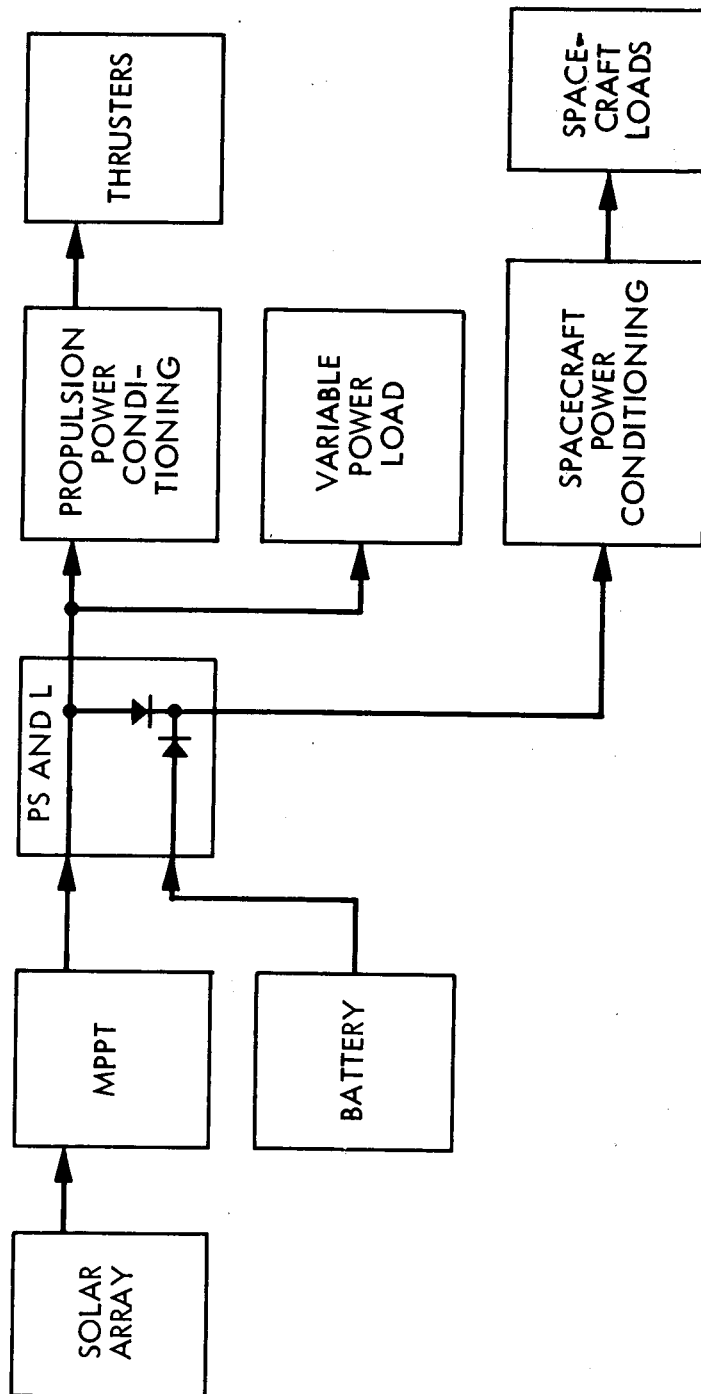


Fig. IV-C-3. Series MPPT Configuration

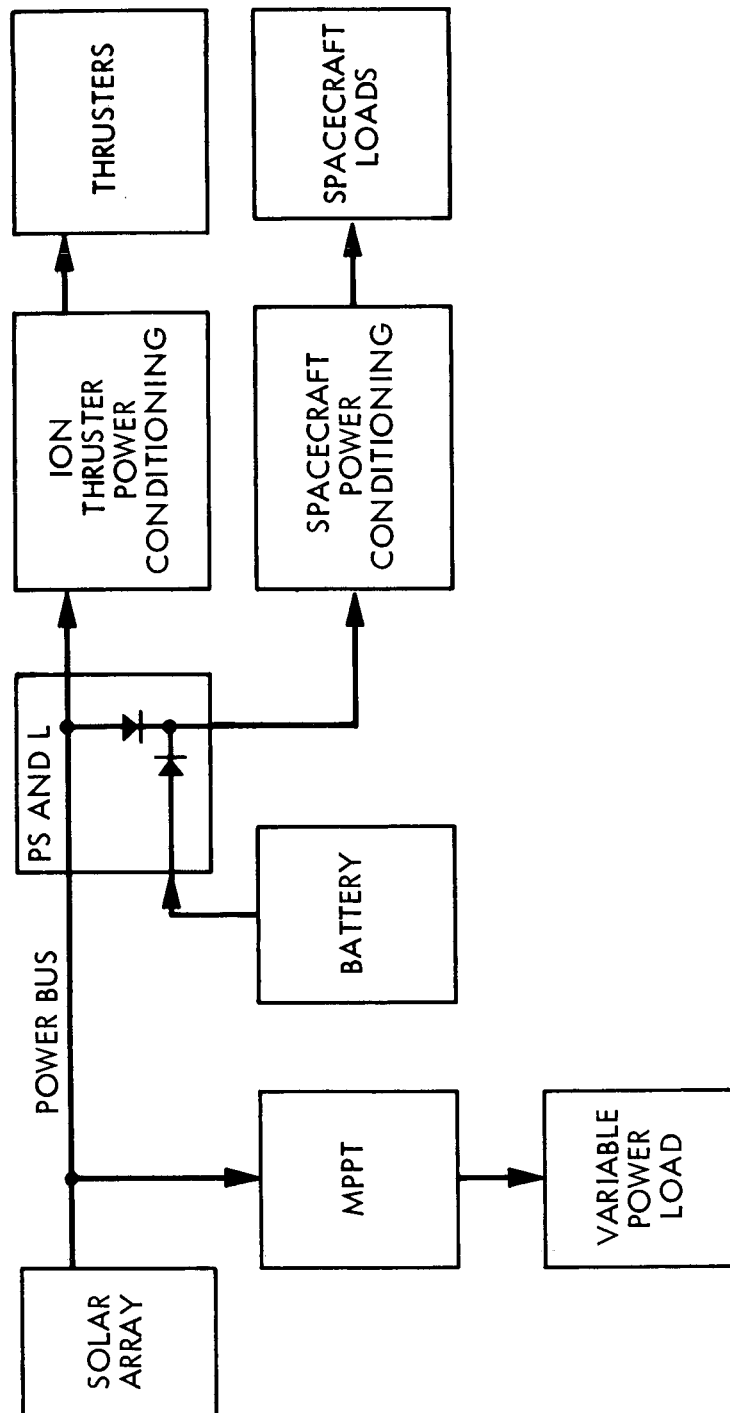


Fig. IV-C-4. Parallel MPPT Configuration

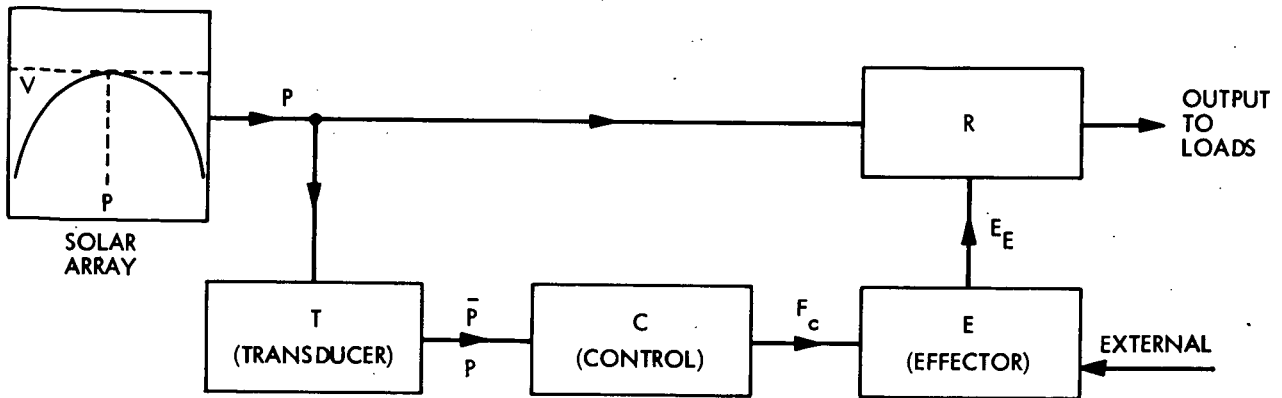


Fig. IV-C-5. Extremum Regulator Functional Block Diagram

point or the derivative of power with respect to voltage. The output of T is called the search error signal. Block C is a control device which reverses the search direction. The control device must also determine either the time or sign of the search reversal, or produce an output proportional to the search error signal, depending on the type of system. Block E , the effector, produces the automatic search signal from either a small external continuous perturbation signal or directly from the feedback properties of the control loop. The effector must provide a constant output, about which the search signal oscillates, that corresponds to the extremum position. The effector is therefore an integrator. Block R is the regulator unit. This regulator is a pulse-width modulator. The regulator duty cycle is varied by the effector output so that the load impedance is matched to the array impedance and maximum power is thereby transferred. The accuracy of the extremum regulator depends primarily on the amplitude of the search oscillation. This amplitude is a function of transducer sensitivity and time delays within the control loop. System noise, in turn, determines the minimum allowable search oscillation amplitude. For this reason, extremum regulators are usually low frequency devices. Previously designed systems have tracked the maximum power within 1%.

The most desirable feature of the tracker is operating-point stability. In the series tracker, power detecting problems are reduced since system noise is isolated from the power detecting transducer by the series configuration. Also, since the total system power is controlled by the series tracker, the maximum power point can always be recovered after load transients, assuming that the variable load power remains greater than zero. This condition is not true for the parallel tracker. The parallel tracker is susceptible to the stability problem previously discussed (Fig. IV-C-2). Heavy load transients may cause the parallel tracker system to lock-up at point A or B of Fig. IV-C-2, since the power delivered to the thruster power conditioning is not controlled by the tracker. A parallel tracker system requirement, therefore, is that the system response time must be fast enough to prevent the instability under all load transient and system noise conditions. This requirement could be quite severe since the extremum regulator is typically a low frequency device as previously discussed.

The main disadvantage of the series tracker is that the total array power must flow through the tracker. A pulse-width modulated regulator is typically 90% efficient; therefore, 10% of the power will be dissipated by the series tracker. This amount of power creates a severe thermal problem which requires heavy heat sinks and large electronic components. The series tracker design does not appear feasible for this reason. Also the 10% power loss compares unfavorably with open-loop systems which could probably predict the maximum power point within 10% with smaller less dissipative circuitry.

The size of the parallel tracker depends primarily upon the power margin. The power margin can be defined as the difference between the maximum array power and the power consumed by the thruster and spacecraft power conditioning. The variable power load must then equal the power margin to allow the maximum power point operation. The minimum allowable power margin is determined as follows:

$$\text{Power Margin (Min)} = \text{Transient Power} + \text{Noise Power} + \text{Tracking Error}$$

where,

Transient Power = the maximum system instantaneous step load change

Noise Power = the maximum instantaneous power from system noise

Tracking Error = maximum error of the power tracking system

The power margin caused by transients and noise is estimated to be 2%. If the tracking error is 1%, then the variable power load must be 480 W minimum at beginning of life for a 16-kW array. If it is assumed that a variable power load of 1 kW is reasonable, this load is quite large; and there is no useful load on the spacecraft which could be employed. Therefore a dummy load must be used. This load could possibly cause thermal problems if it were constantly drawing power. A solution of this problem would be to track the maximum power just long enough to obtain a reading and adjust the system accordingly.

In summary, the series tracker has been determined unfeasible because of its thermal problem and excessive power loss. Further analysis of the parallel tracker instability problem is required to determine the feasibility of the parallel tracker. Its main advantage is accurate continuous tracking of the maximum power point. The parallel tracker approach will be compared to open-loop systems later.

3. Open-loop Systems

Open-loop systems measure one or more array parameters and determine or predict the array maximum power point from this data. Three types of open-loop systems are discussed here: array section measurements, reference array measurements, and source-to-load impedance comparison. Other methods such as array temperature and illumination measurements were reviewed and appeared to be too indirect for this application.

a. Array Section Measurements

One method of maximum power point detection is to measure the power of each array section and add the results. This method is presently being considered at JPL. A brief description of this method follows. The solar array to be measured is divided into a number of sections. Each section is normally connected to the solar array through an isolation diode. A transistor load is connected to one section at a time, and the load is increased until the maximum power point of that section is traversed. The maximum power is measured with a peak detector and recorded. The load is stepped through each section, and the process is repeated. As each section is loaded, its power is removed from the solar array by the isolation diode. The spacecraft power demands must therefore be reduced by the corresponding power contribution of each section prior to loading so that the remaining array power is not exceeded.

If the section maximum power points do not occur at the same voltage, they can not be directly added to determine the total array maximum power because each array section is forced to operate at the same voltage during actual system operation. Each section must then be remeasured to determine its power at the established operating voltage of the array. The maximum power-point voltage is primarily a function of temperature. Therefore, if large temperature gradients across the array are presented during the power measurements, then inaccuracies in the summation process are possible.

b. Reference Array

A second method of predicting the array characteristics is to place test cells at representative positions within each array section. The cells are connected to form a reference array which is electrically isolated from the actual array. The reference array can then be scanned to determine the maximum power point. The accuracy of the system depends mainly on the ability of the reference array to simulate actual array conditions. The size and location of the reference array sections are therefore very critical. The array cost is the primary factor which limits the size. The cost is estimated

at \$350/W. Therefore, to be practical, the array size is limited to the 50-W range which is 0.25% of the actual array size. The electronic circuitry required to measure the maximum power point of a 50-W reference array can be quite simple and lightweight. A peak power detector and a scanning circuit are basically all that is required.

c. Impedance Comparison

A third method of maximum power prediction is accomplished by the load impedance to the solar array impedance. The array power can be expressed as:

$$P_A = VI \quad (1)$$

and

$$\frac{dP_A}{dV} = \frac{VdI}{dV} + I \frac{dV}{dV} \quad (2)$$

at the maximum power point:

$$\frac{dP_A}{dV} = 0 \quad (3)$$

Therefore,

$$V dI + I dV = 0$$

Or,

$$\frac{V}{I} = -\frac{dV}{dI} \quad (4)$$

Equation (4) states that the load resistance determined by the dc operating point is equal to the dynamic resistance, or slope, of the solar

array at the maximum power point. It can be concluded that the load impedance to array impedance ratio is an index of the power mismatch. The degree of mismatch is dependent upon the shape of the solar array current-voltage (I-V) curve. If the array I-V characteristics were linear, then the power mismatch could be calculated within the accuracy of the impedance measuring devices. Unfortunately, this is not the case. Instead, the solar array characteristic may vary from the curve of Fig. IV-C-2 to almost a straight line. Some additional information about the array characteristic, such as end points, is therefore needed to determine the shape of the I-V curve. Possibly, the array open circuit voltage and short circuit current data from the transducers already on the spacecraft would provide sufficient accuracy.

The technique for measuring the solar array dynamic resistance is shown in Fig. IV-C-6. A small perturbing signal e_{ac} is introduced onto the array through the transformer T. If the reactance of C is much less than the load resistance R_L at the perturbing frequency, then the solar array is, in effect, directly across the secondary of T. If e_{ac} is constant in amplitude, then $1/r_a$, the solar array conductance, is proportional to i_s . Therefore, i_s can be measured to determine the array dynamic resistance r_a .

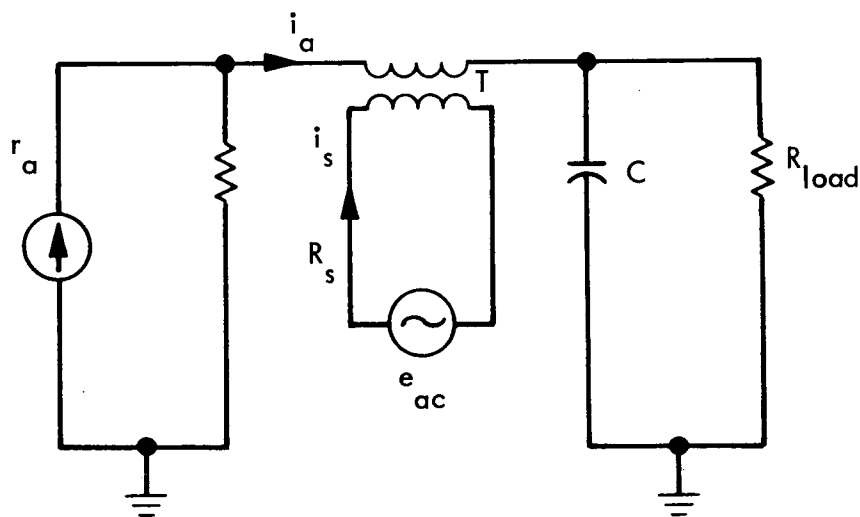


Fig. IV-C-6. Solar Array Dynamic Resistance Measurement

d. Comparison of Open-loop Systems

In this section, the various open-loop measuring techniques are examined and the advantages and disadvantages presented in the system operation are discussed. The array section measurement system is probably the most accurate of the three systems if the temperature of each section is the same. The system accuracy then depends upon the sweep rate and the sensitivity of the power measuring circuitry. This system is the most complex of the three and must dissipate the array section power (up to 1.5 kW) for short periods of time. The necessity of reducing the power demands of the system during the maximum power measurement is also a disadvantage, but not a serious one, if the maximum power measurements are infrequent.

The accuracy of the reference array system is questionable. The reference array maximum power can be calibrated to the actual array maximum power at the beginning of the mission. However, degradation caused by space irradiation is unknown, and damage from micrometeorites, etc., will always remain uncertain. The main advantage of this system is that the circuitry involved can be lightweight and the design is simple.

The main advantage of the impedance comparator system is that it presents an actual array measurement which provides an index of power mismatch while the system is operating. A disadvantage is that the accuracy depends upon some outside knowledge of the array I-V characteristics which may be difficult to predict. It appears that the development of the actual hardware will also present some difficulties. The capacitor C of Fig. IV-C-6 must be quite large and withstand an array voltage of up to 400 V. Also, system noise may affect the accuracy of the dynamic resistance measurement.

In summary, further investigation of the reference array and impedance comparison system accuracies is required to determine the feasibility of the systems. The array section measurement system appears to be the most accurate of the three. However, this system is much more complex than the other two and is larger in size and weight. The reference array system is the least complex and smallest in size and weight.

4. Comparison of Closed-loop and Open-loop Systems

The main advantage of the closed-loop system is the continuous accurate tracking of the maximum power point. However, the application of a maximum power point tracker design to an outer planetary spacecraft presents a number of problems. The solar array power output continuously varies with time and requires variable tracker characteristics and reference inputs. To accomplish this requirement, complex circuitry must be employed in conjunction with continuous power dissipating elements to force the operation of the system at the maximum power point. Another disadvantage is the susceptibility of the tracker design to the anticipated high noise and transients present on the power lines from the thruster subsystem.

The array section measurement system compares closely with the tracker accuracy if the solar array section temperatures are all the same. This system is equally as complex as the parallel tracker and also has the disadvantage of system power reduction during operation. The system must dissipate approximately 1.5 kW of array section power. Therefore, it probably will require larger and heavier components than the parallel tracker, depending upon the time required for measurement.

The reference array and impedance comparison systems are much less complex and are much lighter than the parallel tracker. Again, further investigation of the accuracies of these two systems is necessary to determine their feasibility.

5. Recommendations for Further Development

The various types of systems are listed in Table IV-C-1 with their advantages and disadvantages. Unfortunately, not one single system uniquely provides a solution to the power tracking problem. As previously stated, the direct array measurement system is presently being developed. Further development of the other systems is required before it can be concluded which

Table IV-C-1. Summary of Open-loop and Closed-loop Systems

Method	Type	Advantages	Disadvantages
Series Tracker	Closed loop	Continuous accurate tracking of the maximum power point	Thermal problem and excessive power losses require dummy load and complex circuitry
Parallel Tracker	Closed loop	Continuous accurate tracking of the maximum power point	Requires complex circuitry, dummy load, and has operating point stability problem
Reference Array	Open loop	Simplicity and light weight	Accuracy is difficult to determine
Impedance Comparison	Open loop	Provides power mismatch index	Accuracy is difficult to determine; may have component problems
Direct Array Measurement	Open loop	Provides actual array measurement	Power reduction is required, circuitry is complex, and array section temperatures must be the same

system is best for this application. It is recommended that further development of the reference array, impedance comparator, and parallel tracker systems be made.

Additional information may be obtained from Refs. IV-C-1 through 13.

REFERENCES

- IV-C-1. Iv. I. Ostrovski, Extremum Regulation, Automation and Remote Control, 18, 9, p. 900, 1957.
- IV-C-2. I. S. Morosanov, Methods of Extremum Control, Automation and Remote Control, 18, 11, p. 1077, 1957.
- IV-C-3. J. H. Wescott, An Exposition of Adaptive Control, 1962.
- IV-C-4. A. Dumont, Development of an Advanced Control Circuit for Satellite Power Systems, First Progress Report, ESTEC Contract No. 616/6851, 1969.
- IV-C-5. Walter Hasbach, JPL Photovoltaics Group, personal conference.
- IV-C-6. Hughes Aircraft Co., Report No. P65-125, "Non Dissipative Solar Array Optimum Charge Regulator," First Quarterly Report, NASA Contract NAS 5-9210, October 1965.
- IV-C-7. Engelhardt, R. A., "Optimized Solar-Array-Battery-Space Power System," IEEE, Twelfth East Coast Conference on Aerospace and Navigational Electronics, October 1965.
- IV-C-8. Paulkovich, John, "Slope Detection as a Method of Determining the Peak Power Point of Solar Arrays," Goddard Space Flight Center, X-636-64-282, October 1964.
- IV-C-9. Boehringer, Andreas F., "Self Adapting dc Converter for Solar Spacecraft Power Supply," IEEE Transactions on Aerospace and Electronic Systems, Vol. AES-4, No. 1, January 1968.
- IV-C-10. Gulton Industries, Report No. 1906, Final Report for Optimum Charging System Study Program, NASA Contract No. NAS-5-3785, August 1, 1966.
- IV-C-11. Radio Corporation of America, AED R-3221, "Advanced Voltage Regulator Techniques as Applied to Maximum Power Point Tracking for the NIMBUS Meteorological Satellite," Final Report, NASA Contract No. NAS-5-3248, October 1967.

REFERENCES (Contd)

- IV-C-12. Knauer, Paul, "Automatic Impedance Matching in dc Circuits," IEEE Trans. on Aerospace and Electronic Systems, Vol. AES-2, No. 6, November 1966.
- IV-C-13. Hartman, David A., "Adaptive Power Conditioning for Solar Cell Arrays," IEEE Trans. on Aerospace and Electronic Systems, Vol. AES-2, No. 6, November 1966.

SECTION V

SEP MODULE SUPPORT SUBSYSTEMS STUDIES

A. DATA HANDLING

The synthesis of a data system which can support a SEP module for interplanetary missions is described in this section. The two objectives of the study were:

- (1) To determine the command, control, and sequencing requirements of a SEP thrust subsystem, including the response times required, parameters to be measured, failures to be handled (both transient and permanent), parameters to be controlled, data storage, and data transmission.
- (2) To evaluate the various hardware implementations in relation to: complexity, cost effectiveness in satisfying the requirements, reliability, noise tolerance [electromagnetic interference (EMI) and radio frequency interference (RFI)], and weight; and, from the evaluation, to arrive at a preferred data system configuration.

Mercury-ion thrusters are different from chemical thrusters in that there are several parameters which must be monitored continuously, some parameters which need to be monitored at short intervals (\approx sec), and others which need to be measured at longer intervals (\approx min). In addition, there are reference signals which must be controlled according to the thrust level requirements of the mission and the power available from the solar arrays. These measurements and control parameters interact far too rapidly to allow control from an earth-based station, especially on a mission such as the Encke Rendezvous, wherein the two-way light time can be as much as about 80 min. Thus, some on-board control system, which utilizes the thrust subsystem measurements and control parameters to control the thrusters and to obtain the desired operation of the thrust subsystem, must be employed

In addition to command and control of the thrust subsystem, the SEP module data system has other functions. Among these are:

- (1) Control of the power subsystem.
- (2) Control of the thermal control subsystem.
- (3) Control of the thrust vector control.
- (4) Collection of data from the power subsystem.
- (5) Collection of data from the thermal control subsystem.
- (6) Collection of data from the thrust vector control.
- (7) Conditioning and formatting of collected data for telemetry.
- (8) Receipt of and execution of commands from the earth control station.
- (9) Communication with the main spacecraft.

These requirements are similar to those imposed on the data subsystems of earlier spacecraft. The closed-loop process control is, however, a completely new requirement for unmanned spacecraft.

1. SEP Module Data System Requirements

One observation made early in the study is that there are two rather distinctly different work loads on the data system: (a) a continuing routine of sampling and checking of limits on telemetry data and; (b) command and control to establish new modes of operation and/or changes in the SEP module status. The first of these is a simple, predictable, repetitive operation, which involves analog to digital conversion, comparisons against fixed limit values or fixed ratios, and generation of an alert signal (interrupt) when something is not as it should be. The second function is more complex and involves decision-making and the effecting of changes in the spacecraft status in accordance with some pre-established plan of action which is dependent upon spacecraft status. The first function is predominantly a communication and information gathering activity, whereas the second is an information processing activity.

Figure V-A-1 is a block diagram showing the components of the thrust subsystem in the SEP module. The data system interfaces with: (a) the

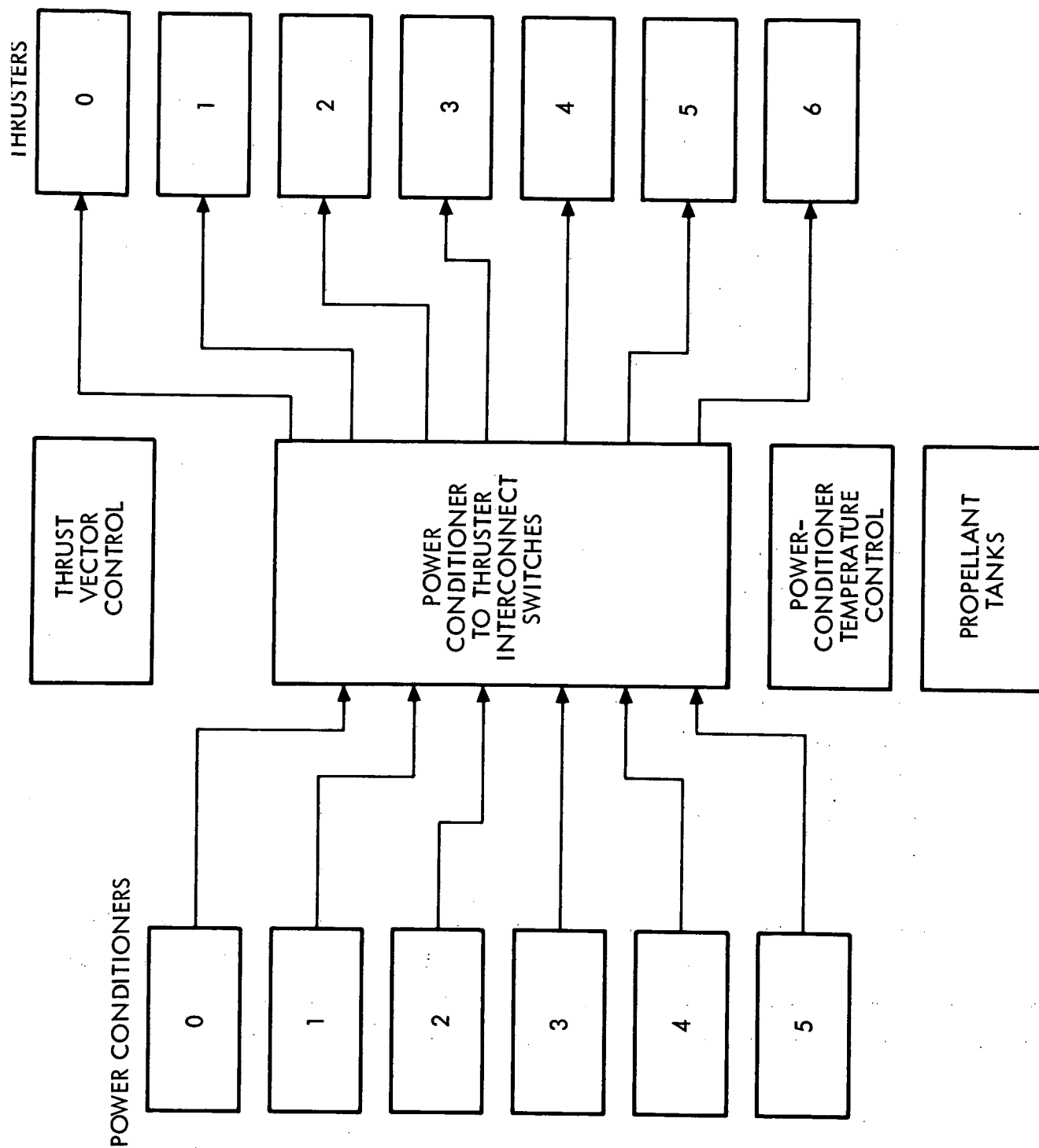


Fig. V-A-1. Thrust Subsystem Components

power conditioners (PCs); (b) the PC-to-thruster interconnect switches (SW); (c) propellant tanks; (d) the thrust vector control (TVC) and; (e) the power conditioner temperature control. Some of the commands required by these elements are listed in Table V-A-1. Thus far, 68 commands have been identified. As the project progresses, other commands will be added and some may be deleted. The types of codes used are: analog (A), coded (C), and discrete (D). Type (C) is a group of position weighted digits which represents a meaningful pattern to a user. Type (D) is a single bit or position-weighted bits, each of which represents the state of any dichotomy, e.g., raise-lower, turn-on turn-off, to which the user can respond. The binary code for each of the signals is yet to be determined, and, for that reason the binary code column has been omitted from the table as shown here. Additionally, commands for the power housekeeping power conditioner, the main spacecraft power preregulator, and for the main spacecraft are also to be determined.

Table V-A-2 lists the data signals required by the data subsystems. Thus far, 144 measurements have been identified. It is probable that, as the project progresses, some measurements will be added and some may be deleted. The types of measurements are:

- (a) A.1, 0-to 100-mV signal.
- (b) A.6, 500-to 600-mV signal.
- (c) A1.5, ± 1.5 -V signal.
- (d) A3, 0-to +3-V signal.
- (e) C, coded data.
- (f) D, discrete (status).

The datum code (binary) has been omitted in this table because the code is yet to be determined. The housekeeping module for the power subsystem, the main spacecraft preregulator, and the main spacecraft have been omitted from the table because the required measurements have not yet been defined.

Figure V-A-2 is a block diagram of the power subsystem in the SEP module. The data system interfaces with (a) solar arrays, (b) main

Table V-A-1. SEP Thrust Subsystem Commands

Identifier	Type	Effects Produced by the Command, Conditions, Initiating the Command and/or Code Descriptions	Response Time Required	Short Term Rate of Repetition
Power Conditioner				
BEAM REF	A	Set beam current reference value This command establishes the thruster beam current and hence the operating power level of the thruster connected to this power conditioner. The signal has a 10-bit resolution	10 sec	1/min
ION REF	A	Set ionizer arc current reference value This command establishes the ionizer arc power and affects the mass utilization efficiency of the thruster connected to the power conditioner. The signal has a 10-bit resolution	10 sec	1/min
OFF-1	D	Off 1. This command turns off the main vaporizer power and leaves the other power supplies unaffected		
OFF-2	D	Off 2. This command turns off the entire power conditioner	10 sec	1/min
OFF-3	D	Off 3. This command turns off the screen and accelerator power supplies and leaves the others unaffected. This signal is needed for the operation of the maximum power point determination circuits (MPPD) and routine. Because of the speed of response needed, this signal may come direct from the MPPD	1 msec	1/min
ON-1	D	On 1. This command turns on the group 1 power supplies and initiates thruster preheating	1 sec	4/min
ON-2	D	On 2. This command turns on the group 2 power supplies and thus initiates the heating of the main vaporizer, cathode vaporizer and neutralizer	30 sec	1/min
ON-3	D	On 3. This command turns on the remaining power supplies and thrust is initiated in the thruster connected to this power conditioner	30 sec	1/min
STORTMP-0	D	Maintain temperature above -45°C on PC-0	5 min	1/hr
OPRTMP-0	D	Maintain temperature above 0°C on PC-0	5 min	1/hr
STORTMP-1 through 5	D	Same as STORTMP-0, except for PCs 1 through 5, respectively	As for PC-0	
OPRTMP-1 through 5	D	Same as OPRTMP-0, except for PCs 1 through 5, respectively	As for PC-0	

Table V-A-1. SEP Thrust Subsystem Commands (Contd)

Identifier	Type	Effects Produced by the Command, Conditions, Initiating the Command and/or Code Descriptions	Response Time Required	Short Term Rate of Repetition
Propellant Tankage and Delivery				
OPEN V-0	D	Open valve. This command allows the propellant to flow to the thrust subsystem from tank 0	1 min	1/hr
CLOSE V-0	D	Close valve. This command stops the flow of propellant to the thrust subsystem from tank 0. Command identifiers will be repeated for additional tanks as needed	1 min	1/hr
Power Conditioner to Thruster Switching Matrix				
STEP-0	D	This command causes the switch to advance to the next thruster position thus connecting PC-0 to the next higher numbered thruster	1 min	5 steps in 30 sec
STEP-1 through STEP-5	D	Same as STEP-0, except for PCs 1, 2, 3, 4, and 5, respectively	As for Step 0, 1 through 5, respectively	As for Step 0, 1 through 5, respectively
Solar Arrays				
EXTEN-0 EXTEN-1	D	Extend array. (One command for each half of the array.) This command causes the solar array to be extended as long as it is on or until limit switches stop the extension	1 sec 1 sec	1/wk 1/wk
RETR-0	D	Retract array. (One command for each half of the array.) This command causes the solar array to be retracted as long as it is on or until limit switches stop the retraction	1 sec 1 sec	1/wk 1/wk
ROT POS	D	Rotate array positive This command causes the solar array to rotate in the positive direction relative to the spacecraft as long as it is on or until limit switches stop the rotation	1 sec	1/wk
ROT NEG	D	Rotate the array negative This command causes the solar array to rotate in the negative direction relative to the spacecraft as long as it is on or until limit switches stop the rotation	1 sec	1/wk

Table V-A-2. Thrust Subsystem Measurements

Identifier	Type	Nature of Measurement and/or System Use	Response Time Required	Sampling Rate
Power Conditioner				
ARC CNT 0	D	Arcing count This signal lasts for a period of one minute and indicates that more than ten arcing trip and recovery cycles have occurred in the preceding one-minute period	30 sec	15 sec
ACCL CUR-0	A3	Accelerator current This signal is upper-threshold monitored at 200% of normal current with a sampling rate not less than once per second (in addition to the normal value scan)	1 sec	1 sec
BEAM CUR-0	A3	Beam current This signal is double threshold monitored at $\pm 3\%$ of full scale against the beam current reference signal at a sampling rate not less than once per second (in addition to the normal value scan)	1 sec	1 sec
CATH CUR-0	A3	Cathode heater current	30 sec	15 sec
	D	In addition to the normal scan, there is a discrete digital "on-off" status signal available		
CAT KPR I-0	A3	<u>Cathode Keeper Current</u>	1 min	15 sec
CAT VAPI-0	A3	Cathode vaporizer current	1 min	15 sec
ION ARC I-0	A3	Ionizer arc current	1 min	15 sec
MAG I-0	A3	Ionizer stabilization magnet current This signal is single threshold monitored at about 70% of its normal operating level with a sampling rate not less than once per second	1 sec	1 sec
MN VAPI-0	A3	Main vaporizer current	1 min	15 sec
NEUT B I-0	A3	Neutralizer bias current Changes in neutralizer implementation may make this signal come from another subsystem or module	1 min	15 sec
NEUT HT I-0	A3	Neutralizer heater current	1 min	15 sec
NEUT KPR I	A3	Neutralizer keeper current	1 min	15 sec
PC OFF-0	D	PC-off status	1 sec	1 sec
PC TEMA-0	A. 6	PC-panel temperature. There are four resistance thermometers on each of the PCs	15 min	1 min
PC TEMB-0	A. 6			
PC TEMC-0	A. 6			
PC TEMD-0	A. 6			
ACCLE-0	A3	Accelerator voltage	1 min	15 sec
BEAM E-0	A3	Beam (screen) voltage	1 min	15 sec
CAT KPRE-0	A3	<u>Cathode keeper voltage</u>	1 min	15 sec
ION ARCE-0	A3	Ionizer arc voltage This signal may be lower threshold monitored with a sampling rate not less than once per second (in addition to the normal value scan)	1 min	15 sec
NEUT BE-0	A3	Neutralizer bias voltage Changes in the neutralizer implementation may cause this signal to come from another module or subsystem	1 min	15 sec

Table V-A-2. Thrust Subsystem Measurements (Contd)

Identifier	Type	Nature of Measurement and/or System Use	Response Time Required	Sampling Rate
Power Conditioner (Contd)				
NEUT KPRE	A3	Neutralizer keeper voltage Changes in the neutralizer implementation may cause this signal to come from another module or subsystem	1 min	15 sec
PCTC ON-0	D	PC-0 thermal control on	5 min	15 sec
PCTC ON-1 through 5	D	Same as PCTC ON-0, except for PCs 1 through 5, respectively	As for PCTC ON-0	As for PC ON-0
Propellant Tankage and Delivery				
VILV CL-0	D	Valve closed on tank 0	1 min	15 sec
TNK PRS-0	A.1	Pressure on tank 0	1 min	15 sec
TNK TEM-0	A.6	Temperature of tank 0 Datum identifiers will be repeated as needed for additional tanks	1 min	15 sec
Power Conditioner to Thruster Switch Matrix				
SW POS-0	C	Switch position The selector switch associated with this PC (PC-0) is in position N. This is a coded digital signal (3 or 4 bits) and is in TBD (serial, parallel) form	1 min	15 sec
SW POS-1 through 5	C	Same as SW POS-0, except for PCs 1 through 5, respectively	As for SW POS-0	As for SW POS-0
Solar Arrays				
SANGLE	A3	Solar array angle	1 sec*	1 sec*
SA EXT-0	A3	Solar array extension	1 sec*	1 sec*
SA EXT-1	A3	This signal may appear for each half of the array		
POS LIM	D	Array is at positive rotation limit	1 sec*	1 sec*
NEG LIM	D	Array is at negative rotation limit	1 sec*	1 sec*
EXT LIM-0	D	Array is fully extended	1 sec*	1 sec*
EXT LIM-1	D	This signal may appear for each half of the array		
RET LIM-0	D	Array is fully retracted	1 sec*	1 sec*
RET LIM-1	D	This signal may appear for each half of the array		
SA CUR	A3	Array current	1 hr	1 hr
SA VOL	A3	Array voltage	1 hr	1 hr
SATEM-0	A.6	Solar array temperature	15 min	15 sec
SATEM-N	A.6	Temperatures may be measured at several points on the arrays		

*These responses and sampling rates are needed only while the array is in motion. One hour is adequate otherwise.

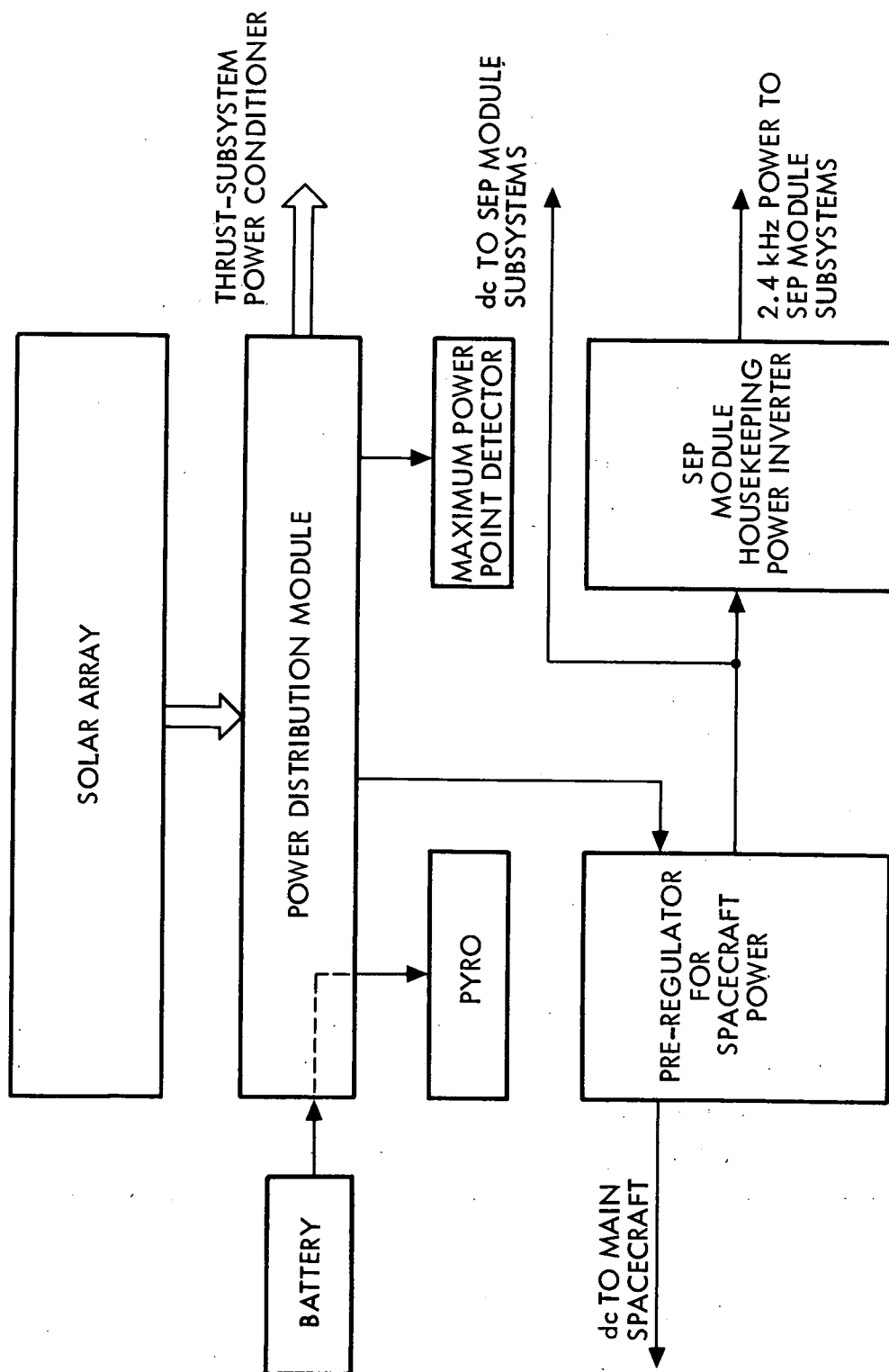


Fig. V-A-2. SEP Module Power Subsystem Components

spacecraft power preregulator, (c) the module housekeeping PC and, (d) the maximum power point detector. Thus far, 8 commands are identified and 12 measurements established (see Tables V-A-1 and 2).

Requirements for thruster subsystem software were examined. Ten functional subroutines were developed by the SEPST program. These routines are detailed in Table V-A-3. In addition to the thrust subsystem, software requirements of other SEP module subsystems were also examined, and the memory needed for these functions was estimated. Anticipated routines of this nature are also detailed in Table V-A-3.

Tentative onboard versus ground-control priorities for the various routines were made. As thruster reliability information becomes more firm and the mission navigation tolerances of thrust loss-time (coast time) are better known, these priorities can be firmly established. At this time, the trend is toward putting more and more autonomy into the spacecraft, thus requiring more of the control routines to be on board. Table V-A-4 compares a nearly autonomous SEP module, which can detect and isolate thrust-subsystem faults and reconfigure as needed to continue thrusting, with a ground-control-dependent configuration, in which any non-trivial fault results in thrust subsystem partial or total shutdown, until the next ground station can analyze the error and send corrective commands to the spacecraft.

2. Data System Candidates

Figure V-A-3 illustrates the subsystems of a typical Mariner-class ballistic trajectory spacecraft, and shows their data-path connections. In this traditional configuration, closed-loop control is not possible because the data collection device, the FDS, has no direct means of communication with the device which exercises command and control, the CCS. Therefore, this configuration is not able to provide one of the essential features required by the SEP module.

Figure V-A-4 shows the traditional data system modified and applied to the SEP module. The modification is indicated by the dashed lines

Table V-A-3. Subsystem Software

Thrust Subsystem	
Identifier	Description/Purpose
FSR-1	Starting of a PC/thruster set This routine takes care of starting the specified PC/thruster set. The routine may be started by a ground command or by a signal generated within the data subsystem by the action of another routine
FSR-2	Monitors the performance of a set This routine monitors the thruster operation and, if an out of tolerance condition is encountered, the FSR initiates corrective action
FSR-3	Thrust level control This routine adjusts the thrust level in accordance with the flight plan and available power from the solar arrays
FSR-4	Dummy-load checkout This routine is used when it is found that a PC/thruster set has failed in some way. The use of the routine is to isolate the failure to either the thruster or the PC
FSR-5	Used by ground command to put together a specific PC/thruster set as designated in the command
FSR-6	Used by either ground command or by the thrust level control routine (FSR3) and forms a designated number of PC/thruster sets from the available usable PCs and thrusters
FSR-7	Power margin measurement This routine works in cooperation with the MPPD to determine the total operating power margin (the difference between the power available from the solar array versus the power presently in use by the entire spacecraft)
FSR-8	Operation at reduced thrust This routine handles situations of unexpected undervoltage which cause the PCs to trip off. If the undervoltage was caused by a continuing reduction of available power from the solar array, this routine overrides the power profile and operates at reduced thrust (reduced power)
FSR-9	Adjustment of solar-array power margin This routine overrides the power profile routine and operates the thrusters with minimal acceptable power margin regardless of the planned thrust level
FSR-10	Definition of peak power This routine is a subroutine to FSR7 and is the routine which actually determines the solar array maximum available power
General Housekeeping	
SCHED	Scheduler (executive) This routine is responsible for the scheduling and allocation of resources of the CCS among the various users
ERR-1	Error routine This routine is needed to allow the CCS to recover from errors which may arise in the operation of the CCS or other subsystems

Table V-A-3. Subsystem Software (Contd)

General Housekeeping (Contd)	
Identifier	Description/Purpose
INT	<p>Interrupt processor</p> <p>This routine handles the various "flag" and "alert" conditions which arise in the operations of the SEP module</p>
ECNT	<p>Event counter routine</p> <p>This is a utility routine which is used by other routines. (A utility routine is one which is freely available to be called upon by other routines in the course of their operations)</p>
BITASY	<p>Bit assembly</p> <p>The command decoder function of the CCS assembles commands from the modulation-demodulation subsystem data stream bit by bit through the action of this routine</p>
TIME	<p>Timer</p> <p>This is a utility routine used by other routines</p>
MILSEC	<p>One hundred (100) count per second clock</p> <p>This is a utility routine which is used by other routines</p>
SECOND	<p>One count per second clock</p> <p>This is a utility routine which is used by other routines</p>
MINUTE	<p>One count per minute clock</p> <p>This is a utility routine which is used by other routines</p>
HOURL	<p>One count per hour clock</p> <p>This is a utility routine which is used by other routines</p>
MUL	<p>Multiply</p> <p>This is a utility routine which is used by other routines</p>
ERR-2	<p>Error control</p> <p>Commands from ground control are subject to transmission link noise and are sent with redundant information. This routine uses that redundant information to check for errors in transmission and in some cases to make corrections in the received data</p>
SUP	<p>This routine (or set of routines) is also used by the support equipment for SEP module checkout and other launch phase activity</p>
FDSCON	<p>Master flight data subsystem (FDS) control</p> <p>This routine controls the operations of the FDS and parameter limit settings for the monitoring of the thruster subsystem and other subsystems</p>
COMDEC	<p>Command decode</p> <p>There are two main routines in this category, command initiate and command sync, which are used to process the data received from ground control and distribute the resultant commands to the various destinations in the SEP module</p>

Table V-A-3. Subsystem Software (Contd)

General Housekeeping (Contd)	
Identifier	Description/Purpose
BLKLD	FDS load from block data This routine enables the memories of the FDS to be loaded in blocks of variable length and variable starting points, and it is used to alter scan sequences and parameter limits in the FDS
BLKLD	CCS load from block data This routine allows the CCS memories to be loaded in blocks of variable length and with variable starting points, and it is used to alter the CCS stored programs in flight
TMOUT	Telemetry output routine This routine allows the data stored in the CCS memories to be transmitted (without altering the contents of the memory) to ground control
OUTPUT	Output routine This routine handles all output from the CCS to the various users
FMEMRD	FDS memory readout This routine allows the contents of the FDS memories to be read non-destructively for the purpose of content verification or retransmission over the CCS telemetry link to ground control
PWRCON	Power subsystem control This routine or set of routines (to be determined) controls the power utilization in the attachable module so as to maximize the probability of mission success
CHECK	Hardware quality confirmation This set of routines is used to exercise the CCS and other SEP module subsystems to establish the facts of functionality or non-functionality in each of the areas thus tested
ERR-3	Undervoltage routine This routine is responsible for the recovery of the CCS from undervoltage on the primary power bus. It is conceivable that this routine will never be used, but, if it is needed, there is no way to load it into the CCS memory, if the spacecraft is tumbling or in some other state of emergency. Therefore, it must be loaded at launch or some other time previous to the emergency
ARCCNT	Arc count This routine (which might be hardwired) counts the number of times arcing occurs between the screen and accelerator grids of a thruster. Corrective action may be taken or not depending on the frequency of occurrence of such arcing. Such arcing may be very frequent (several times per minute)
TVCON	Thrust vector control This routine is the software interface with the TVC-ACS subsystem pair

Table V-A-4. Comparison of an Autonomous SEP Module with a Ground-Dependent Module

Routine	Word Counts			
	Highly Autonomous		Ground Dependent	
	Count	Variance	Count	Variance
FSR 1, 2, 4	896	40	896	40
FSR 3	100	20	60	30
FSR 5, 6	871	70	150	40
FSR 7	74	4	25	4
FSR 8	151	7	50	10
FSR 9	120	24	40	10
FSR 10	32	2	32	2
Scheduler	600	120	600	120
Error	150	30	150	30
Interrupt Part of FSR 8	—	—	—	—
Event Counter	50	10	50	10
Bit Assembly	200	30	200	30
Timer	80	16	20	16
100 PPS Clock	80	16	80	16
1 PPS Clock	60	12	60	12
1 PPM Clock	60	12	60	12
1 PPH Clock	60	12	60	12
Multiply	50	2	50	2
Divide	45	2	45	2
Sign	20	2	20	2
Error Control	100	20	100	20
FDS Control	250	40	250	40
Command Decode	200	40	200	40
FDS Load from Block	100	10	100	10
CCS Load from Block				
Telemetry Output	50	10	50	10
Output				
FDS Memory Readout	50	10	50	10
Power Subsystem Control	150	30	150	30
Undervoltage Recovery	150	30	150	30
Arc Count	25	5	25	5
Other (Contingency)	920	180	760	150
Total	5594	251 rss	4543	222 rss
90% Confidence	5600	±750	4500	±660

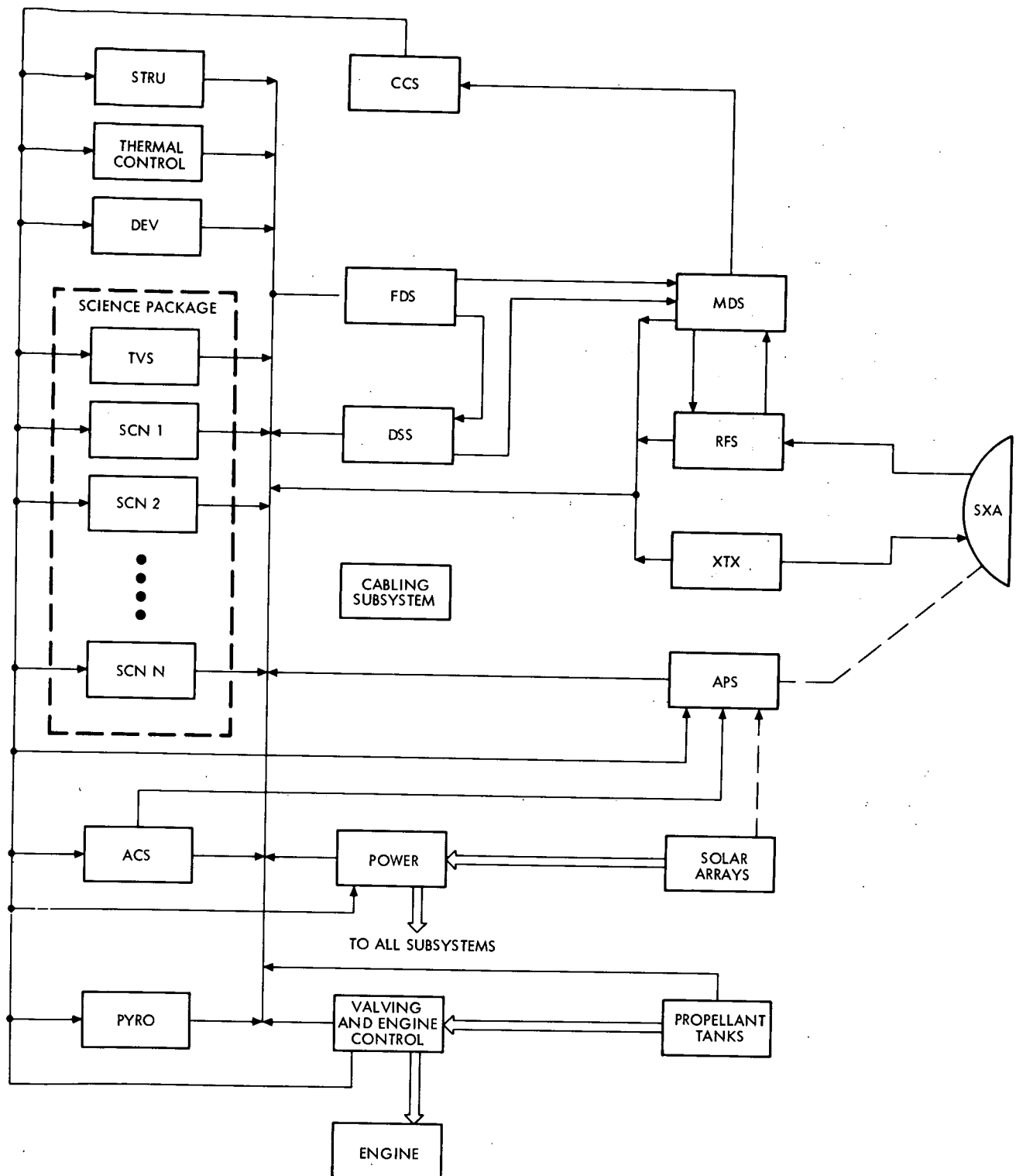


Fig. V-A-3. Typical Ballistic-Trajectory, Unmanned Spacecraft
(Based on MVM 73 and Viking Orbiter 75)

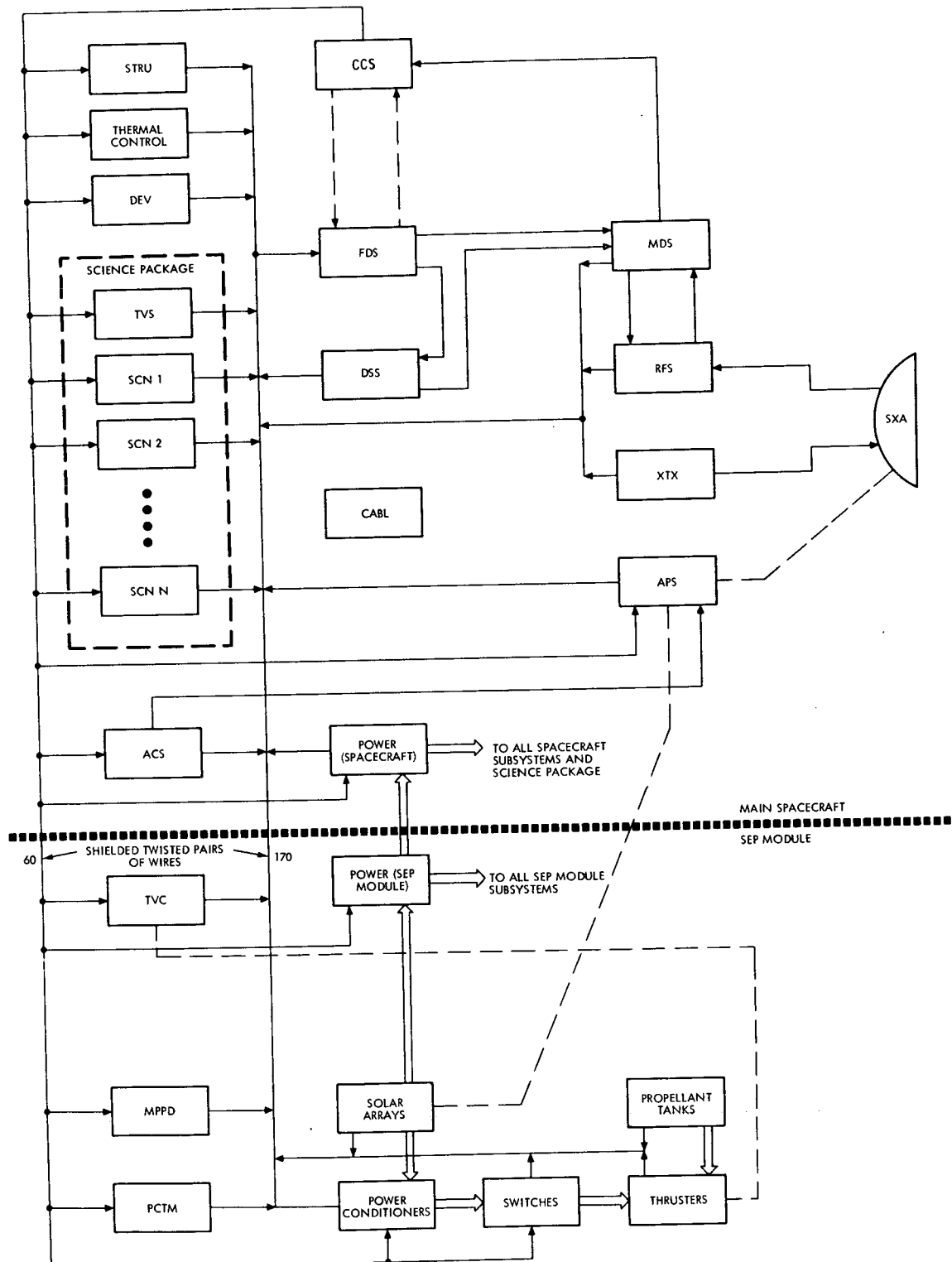


Fig. V-A-4. SEP Spacecraft with CCS and FDS Interface Lines Between the Spacecraft and the SEP Module

between the FDS and the CCS. It can be seen that, for the interface between the main spacecraft and the SEP module alone (neglecting all of the main spacecraft subsystems), the FDS must handle 170 or more inputs, and the CCS must provide 60 or more command outputs.

Figure V-A-5 shows the data system further modified by the addition of the multiplexer-converter and data bus interface. This modification results in a reduction in the number of lines to eight each for the FDS and the CCS, and a reduction in the number of connector pins in the interface to a total of about 400 pins. The actual benefit is far greater than this, however, because the case depicted in Fig. V-A-4 has no redundancy, but that shown in Fig. V-A-5 has a full dual redundancy.

In selecting the preferred data system, these and other hardware configurations were examined in the light of the study objectives. Software requirements of the thrust subsystem were examined to a level of detail sufficient to gain confidence in the ability of each configuration to meet system performance requirements or to eliminate the configuration from further consideration. Hardware-software tradeoffs were made; subsystem configurations were established; and cost, weight, functional effectiveness, noise tolerance, and reliability estimates were made. These activities led to the conclusion that a Viking Orbiter 75 CCS with a modified-function FDS (mini FDS) in the SEP module was the preferred implementation when minimum impact of the SEP module on the main spacecraft is desired. This preferred configuration is shown in Fig. V-A-6.

3. Preferred Data System Characteristics

a. Operational Characteristics

As an aid to understanding the preferred data system configuration, several typical operations will be described. A detailed functional block diagram of the preferred system is shown in Fig. V-A-7.

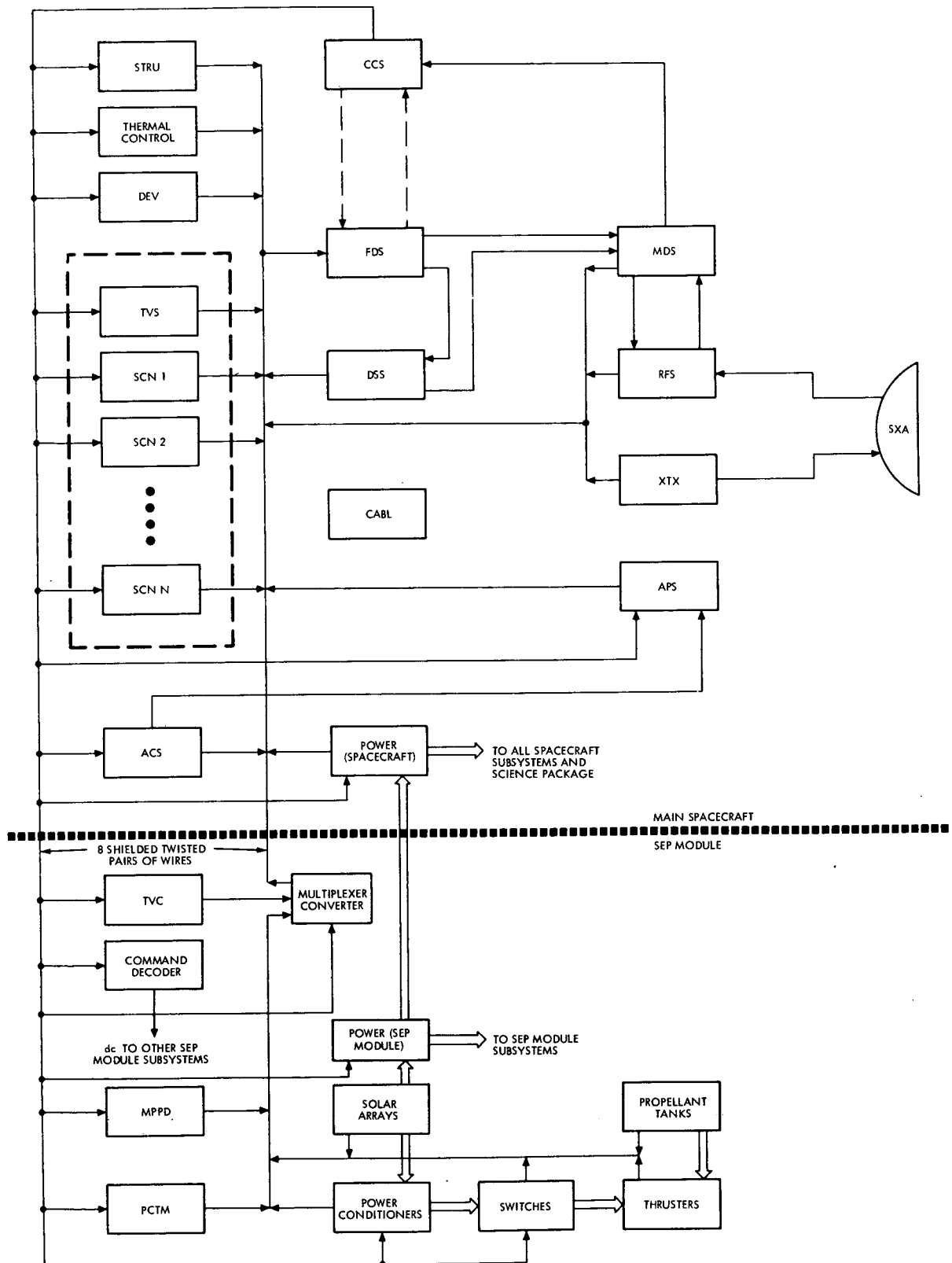


Fig. V-A-5. Candidate SEP Spacecraft Showing Effects of Signal Conversion and Multiplexing on the SEP Module

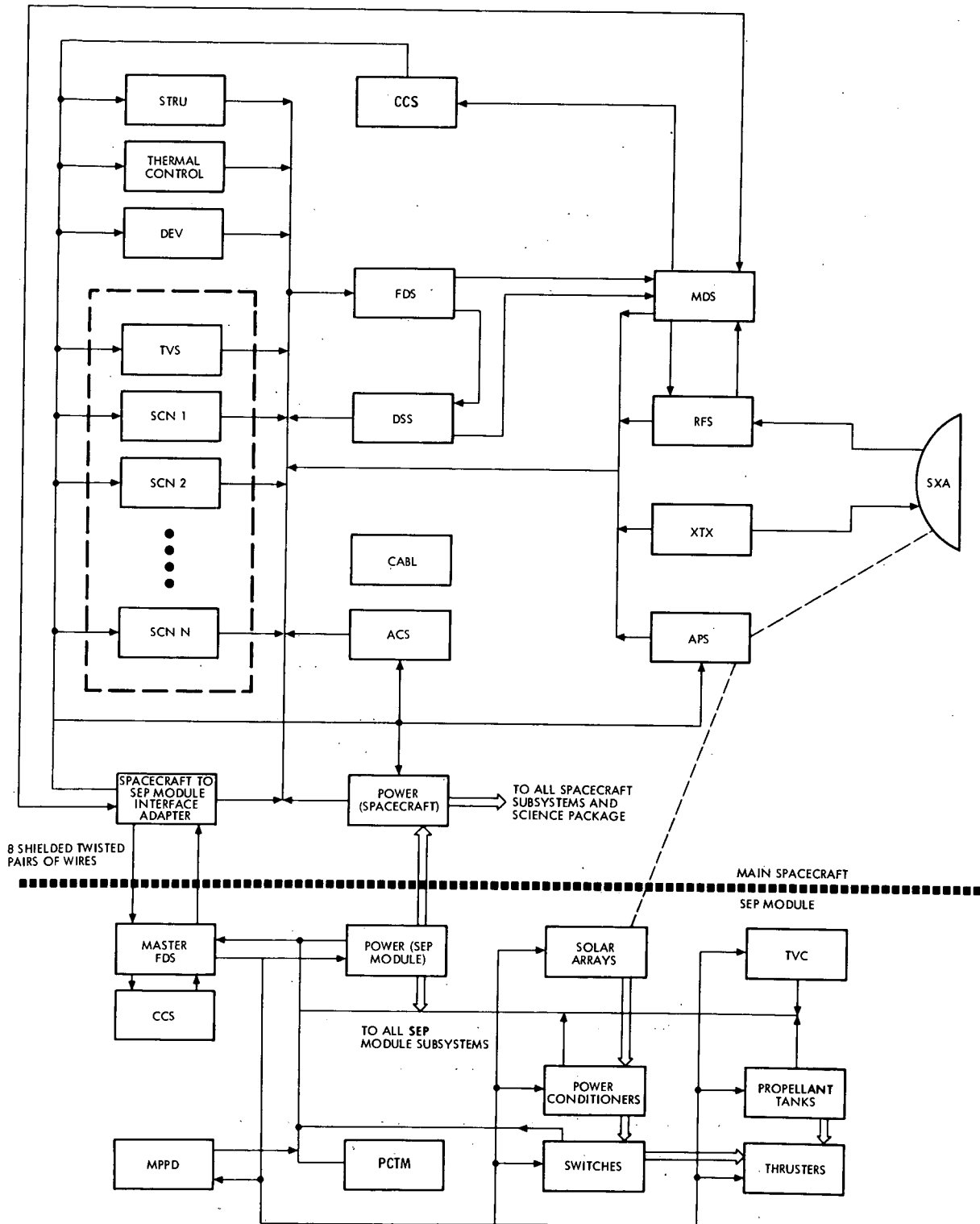


Fig. V-A-6. Candidate SEP Spacecraft Showing Preferred Data System Configuration

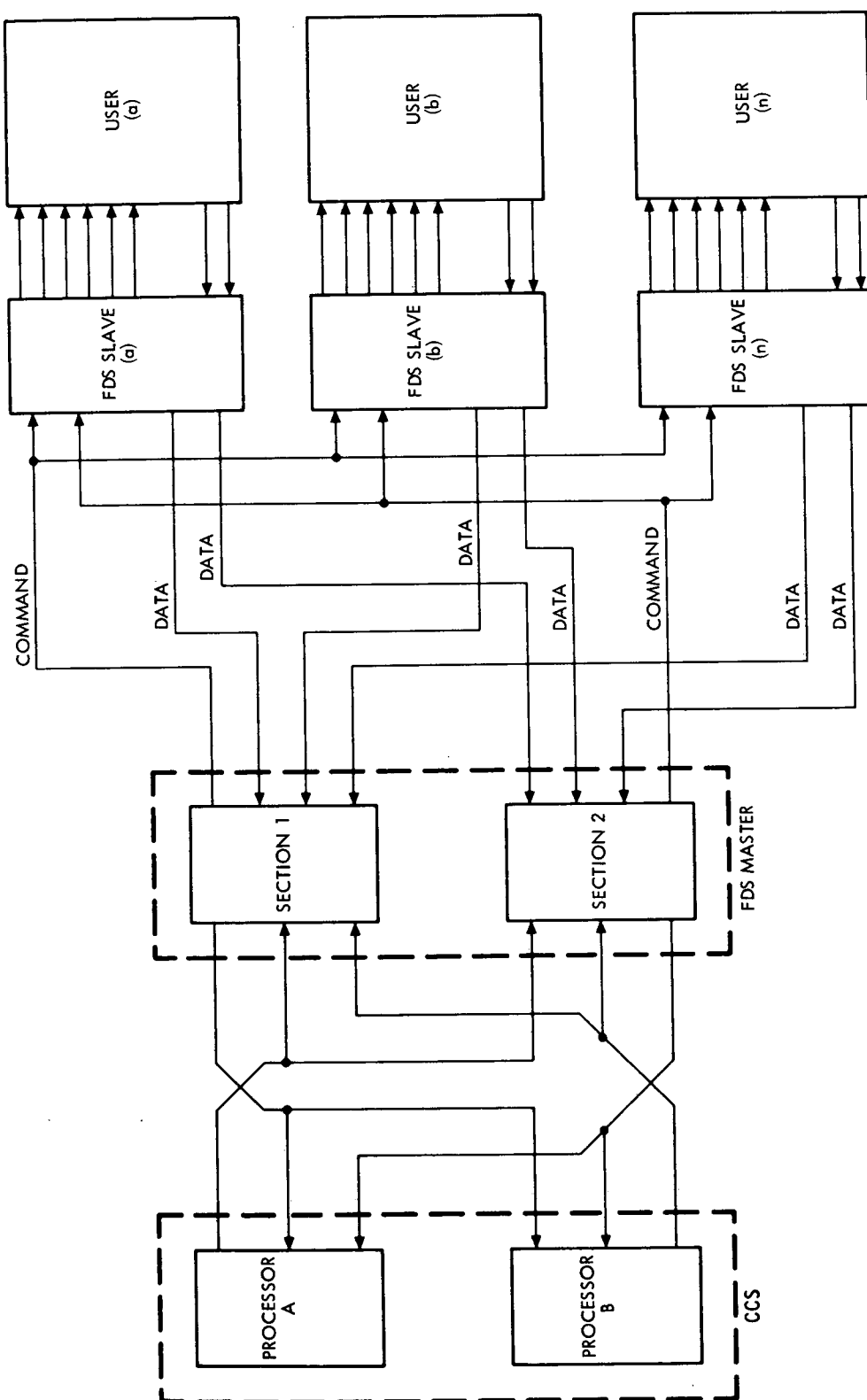


Fig. V-A-7. Preferred Data Subsystem

The first function of the SEP module data subsystem to be examined is telemetry scanning. It is assumed that the CCS processors A and B are dormant (in "wait" state).

In the FDS master, there is a clock chain, address counter, memory units, and other logic. For this particular operation, the clock (timing chain) advances and initiates the following cycle of action:

- (1) A coded command (on an idle command bus), which contains a user selection code, and a measurement request code is generated.
- (2) All of the users receive this coded command. The user code is checked and, if the user is the correct one, it enables the measurement, which has been requested.
- (3) If this is an analog measurement, a conversion to digital form is executed, and the result is returned on a data line to the FDS master. If this measurement is of status (i.e., on-off, high-low or any other dichotomy measurement), a coded status word (containing several status measurements) is returned to the FDS master. Digital coded information is returned to the FDS master as digital coded information with only a parallel to serial conversion, if needed.
- (4) The returned data is checked by the FDS master against information contained in its memory. For example, a returned status word is compared with a memory word representing expected status and, if equal, everything is correct. If an inequality is found, the FDS master generates an alert (interrupt) signal to the CCS so that the CCS can then take action to correct the situation.
- (5) The clock advances to the next measurement address, and the cycle repeats from (1).

This scan cycle follows a fixed format with a fixed period of time between measurements. This fixed mode of FDS operation takes approximately 15% of the available FDS time (worst case).

Another function of the FDS which fits into this same sequence of fixed operations is the "refreshing" of data, which is subject to alteration by system noise, etc. The sequence for this is:

- (1) A coded command containing the user selection code, the datum identifier, and the value of the datum (from the FDS memory) is generated.
- (2) The users which are selected (group selection codes may be used) enable the acceptance of the value of the datum, and this becomes the value from which the user operates.
- (3) The FDS clock advances and the next cycle is initiated.

These "refresher" operations represent about 5% of the operating time of the FDS (worst case).

The remaining 80% of the time is available for the CCS to use the FDS for non-routine operations. One possible way to do this is to have basic periods of 5 msec between measurements or refresh operations, 1 msec for the measurement or refresh, leaving 4 msec available for non-routine commands and operations.

In the following discussion, it is assumed that the CCS is not dormant. If the CCS should want to change a beam current reference level on a thruster power conditioner, two main ways are available:

- (1) The CCS generates a coded command to the FDS master to change the data in its refresh memory (and in its appropriate compare memory, if this parameter change will cause a change in a monitored variable) and allows the fixed format refresh cycle to execute the change.

- (2) The CCS generates a coded command, which will be passed by the FDS master directly to the command bus. This will result in an "out of tolerance" alert to the CCS, when the FDS next gets around to that user, unless the CCS also generates commands to the FDS to update its memory. It is also true that the new value will be lost, if and when the datum is "refreshed" by the FDS.

The first of these two methods is obviously the preferred one, unless response time is critical. The first method responds in less than 2 sec; the second can respond in 2 msec.

In cases when there is no effect on a limit-monitored or refreshed value, the CCS can generate commands which go directly through the FDS master to the command bus. If the command requires a response, the response will come back to the CCS via the data line of the users slave unit.

Thus far, it appears that the slave units are indeed slaves, that they speak only when spoken to and do only as commanded. However, should the slave have some data of importance, such as a change of state caused by noise, or a component failure, or a situation wherein the user may be the MDS of the main spacecraft with a coded command from earth, there must be some way to make the CCS aware of this. The method employed is as follows: The user sends a continuous low (logical 1) signal to the FDS on its data line. If such a condition is detected by the FDS master, when the FDS master has not addressed the unit, this is taken as an interrupt or alert condition. The CCS is interrupted; and the FDS master sends an acknowledge command to the slave unit, which then sends its data across the data line to the master and, thence, to the CCS for action.

The foregoing characteristic can be used for error detection in the system. As an example, the following assumptions are made: a decoder fails in a slave and responds erroneously to the selection code for another slave. Further, any time a decoder responds, it generates an alert level on

its data line. In this case, then, both the desired user will generate an alert and an unselected user will generate an alert. The alert is detected as an error, and the command can be aborted by a null command sent. The remedy for this situation is to use an alternate selection code or the second command bus. All user selection decoders are implemented to respond to more than one code. A failure of one code in a slave so that its selection code becomes congruent with that of another slave still leaves the unfailed slave with another useable selection code on that same command bus plus selection codes on the redundant command bus.

b. FDS Master to FDS Slave Interface

The arrows on Fig. V-A-7 indicate the direction of signal flow. Two redundant command buses are indicated, and signal flow directions are shown as opposite. The intention of this is to indicate that, in the actual layout of the cable, these buses should be routed in such a way that, if physical damage which opens a line should occur to both sets of buses in the same location in the spacecraft, each user will still be left with one useable command bus. By having the command buses make a full loop, it is possible to make an integrity check on the bus and to confirm that data sent to the bus is actually getting to the users. This latter function can also be done by the data lines as indicated in the previous discussion.

Separate data lines are used for each slave to avoid the potential problems of one user seizing a data line and making it unavailable to other users, which might happen in a bused-data arrangement. As with the command buses, it is desirable to run these data lines over different paths to minimize effects of physical damage.

Figure V-A-8 shows one possible bus receiver, which is able to handle large common mode (ground offset, noise, and transient) signals without generating errors in the received data and without loading the line significantly.

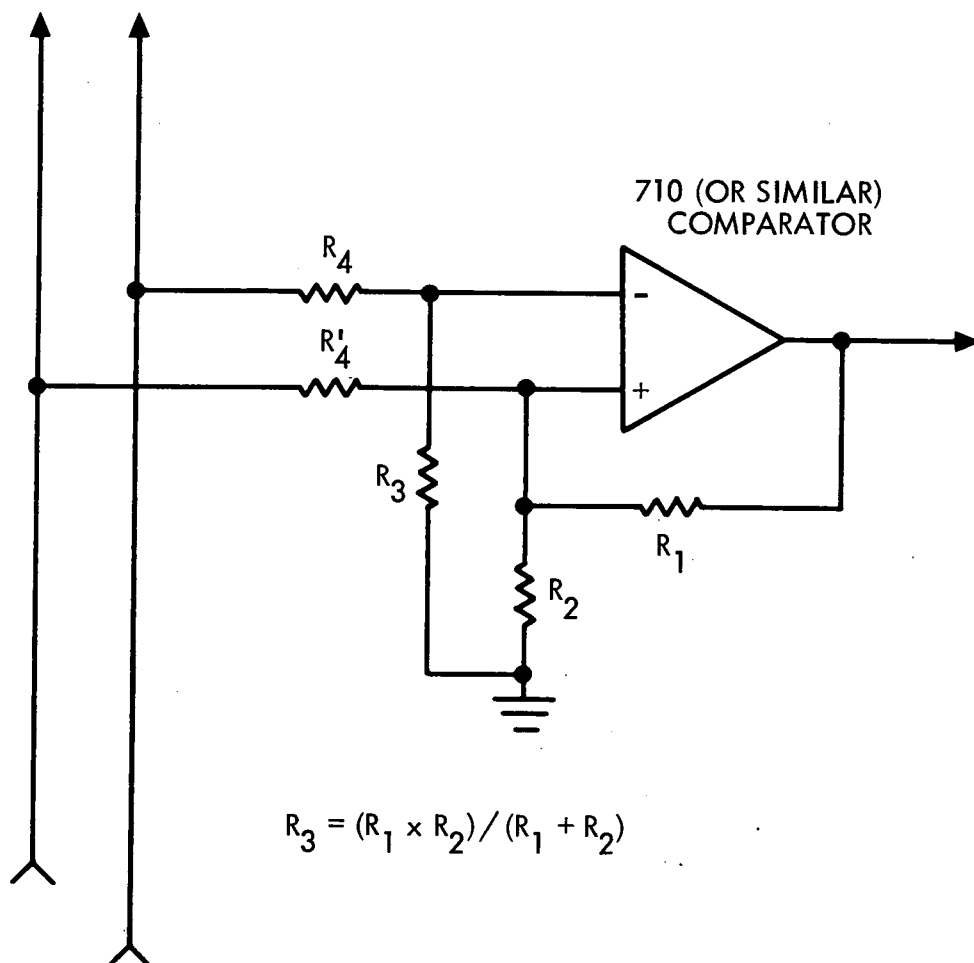


Fig. V-A-8. Typical Bus Receiver

Each interface command bus comprises three lines:

- (1) Clock, a continuous pulse stream for the purpose of synchronizing the users to the master FDS and CCS.
- (2) Strobe or synch, which comes on at beginning of command.
- (3) Information, a non return to zero (NRZ) pulse train which conveys the command intelligence.

Each FDS master/slave interface data path comprises one line. Data is inputted to the FDS master in NRZ form. If a unit which has not been addressed by the master energizes its data line, the FDS takes it as an alert or interrupt condition, which is acted upon in accord with interrupt handling procedures. Very critical items (catastrophic, if done at the wrong time or in wrong sequence) can be arranged to generate an interrupt, when such things as decoder failures occur. The priority level of such an interrupt could be such that it aborts the command being sent out by the FDS. Decoders will be implemented redundantly and will have two or more user codes assigned to each user with a code structure that minimizes the possibility of false decoding (3 out of 7 code, for example).

The only information passed between the FDS master and FDS slave is bit-serial coded information. Consequently, the FDS slave has several functions:

- (1) Receive and decode commands.
- (2) If needed by the user, convert coded information to discrete commands.
- (3) If needed by the user, transmit coded information to the user with serial to parallel conversion and/or rate change.
- (4) If needed by the user, convert coded information to analog commands.
- (5) If needed by the user, relay discrete digital data to the FDS master as coded data.

- (6) If needed by the user, relay coded digital data to the FDS master in proper bit-serial speed and NRZ format.
- (7) If needed by the user, convert analog data to digital form and relay to the FDS master in proper bit-serial speed and form.

Figure V-A-9 shows the composition of the FDS slave. The blocks 1 through 5 will always be present in varying degrees. The other blocks are user-dependent and may be totally absent in some cases.

It is intended that the FDS slave be physically very close to the user, certainly in the same bay and, preferably, part of the user module. In this way, the total spacecraft weight and cabling complexity are greatly reduced. The greater simplicity of hardware, which is achieved through this technique, leads to improved data system reliability, in comparison with a more divorced function of CCS and FDS in which, for example, each power conditioner would have as many as 49 wires attached to it. Of these wires, as many as 26 would go directly to the CCS output unit and 23 would go to the FDS. Hence, for power conditioners alone, the CCS might have 156 wires and the FDS, 132 wires. The cabling and connector problems represented by these wires are almost incomprehensible.

The FDS master performs the following functions:

- (1) Transmits commands from the CCS to the desired slave.
- (2) Receives information from slave units and, if the information is measurement data, compares it against limits or status information in the FDS memory and alerts the CCS to out-of-tolerance conditions; if the information is command information (as, for example, from the main spacecraft MDS), holds the information and generates an interrupt (alert) to the CCS.
- (3) Refreshes commands to users on a regular basis to minimize the deleterious effects of noise in the system.

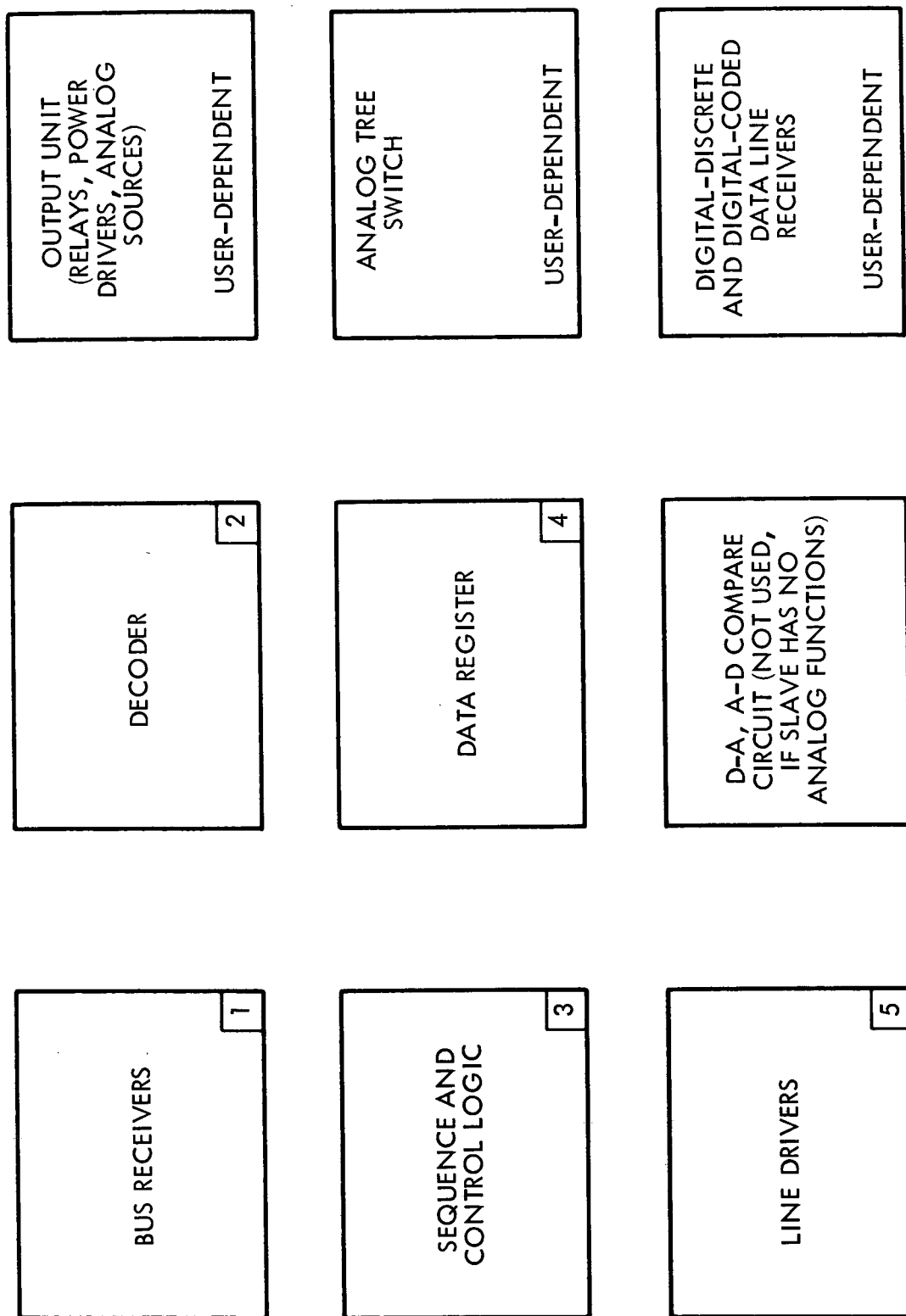


Fig. V-A-9. FDS Slave, Basic Components

- (4) Scans the users and requests measurement or status information on a regular fixed-format basis.
- (5) Transmits engineering data of the attachable module to the FDS of the main spacecraft for storage or transmission to ground.
- (6) Makes measurement data available to the CCS on demand or by out-of-tolerance criteria.
- (7) Allows broadcast commands to multiple similar function users, e.g., on the thrust subsystem power conditioners, where these broadcast commands can be useful. Some of these commands are:
 - (a) Off 2, allows all thrusters to be turned off at one time.
 - (b) Reference setting, allows all reference (beam current and ionizer arc current) to be set to a common value; useful on start up when the references are set for minimum.
 - (c) Off 3 (if implemented), allows all PCs to have beam power cut off at one time, which is useful in handling the effects of power surges and impending solar array voltage collapse.

c. Characteristics of Command Signals at FDS Slave-to-User Interface

- 1) Analog Commands. Analog commands will be transmitted to users as a differential pair which, if referenced, is referenced to signal ground at the sending end.

The common mode signal caused by ground offset, noise, and transients combined should be less than 1-V peak magnitude. The range of the signal should be ± 1.5 V or 0 to +3 V. The receiver differential impedance should be at least 20,000 Ω at any frequency less than 5,000 Hz. The impedance

to ground from either line of the differential pair should be at least $10,000\ \Omega$ at any frequency less than 5,000 Hz.

The resolution of the analog signal will be as required by the user but will not exceed 12 bits plus sign. Accuracy of the analog signal will be related to resolution but will not be better than 0.25% of full scale $\pm 1/2$ least significant bit of the resolution. Analog commands will be monotonic within $\pm 1/4$ least significant bit for resolutions up to and including 8 bits, and within $\pm 1/2$ least significant bit for higher resolution.

These are new requirements on the FDS and are not yet implemented. The frequency of change of an analog command should be sufficiently great to allow for the requirements of the subsystems without imposing an extraordinary load on the processor. The analog command slewing rate is limited by power and weight considerations and should be kept to easily achievable values. Changes in analog command will occur as a direct shortest path change from one voltage level to another without first going to a rest level. Overshoot and ringing on analog commands should not exceed 3% of the change and should stabilize to within $1/2\%$ of the new value in 10 msec. Typical analog receivers are shown in Figs. V-A-10 and 11.

2) Discrete Digital Commands. In general, discrete digital commands are expected to handle some power. The exact implementation will be dependent upon the power and speed requirements of the user. If inductive loads such as relay coils, solenoids, motors, or the like, are to be driven, some "spike" suppression scheme, as shown in Fig. V-A-12 will be required. Figure V-A-13 shows three typical drivers.

3) Coded Digital Commands. Coded digital commands are user-dependent and may go to the user in either a bit-parallel or a bit-serial form. The rate is also user-dependent, but FDS clock rate is preferred. The signal levels are standard transistor-transistor logic (TTL) levels. The logic circuits used are Texas Instruments 54L or equivalent. The normal wiring rules, which apply to these circuits, are used with these exceptions:

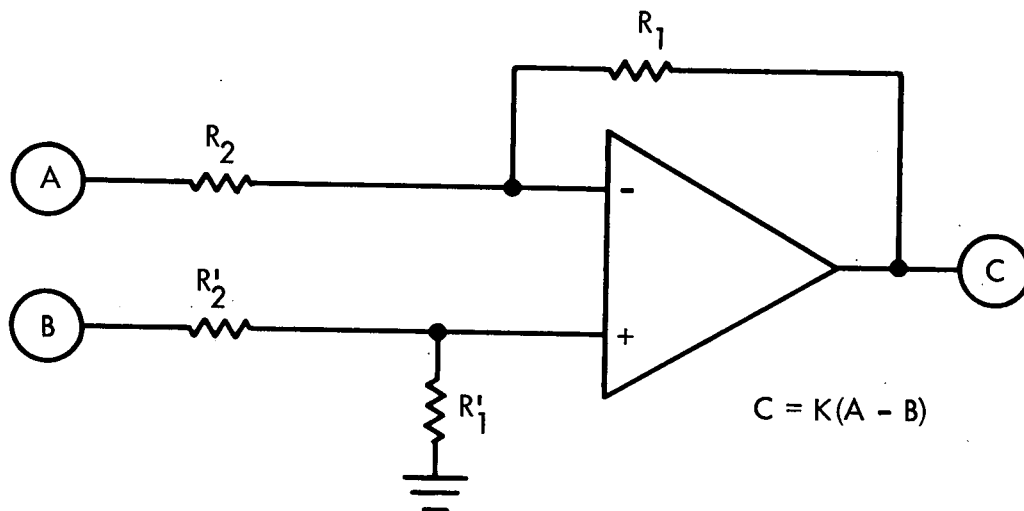


Fig. V-A-10. Analog Receiver with Common Mode Suppression

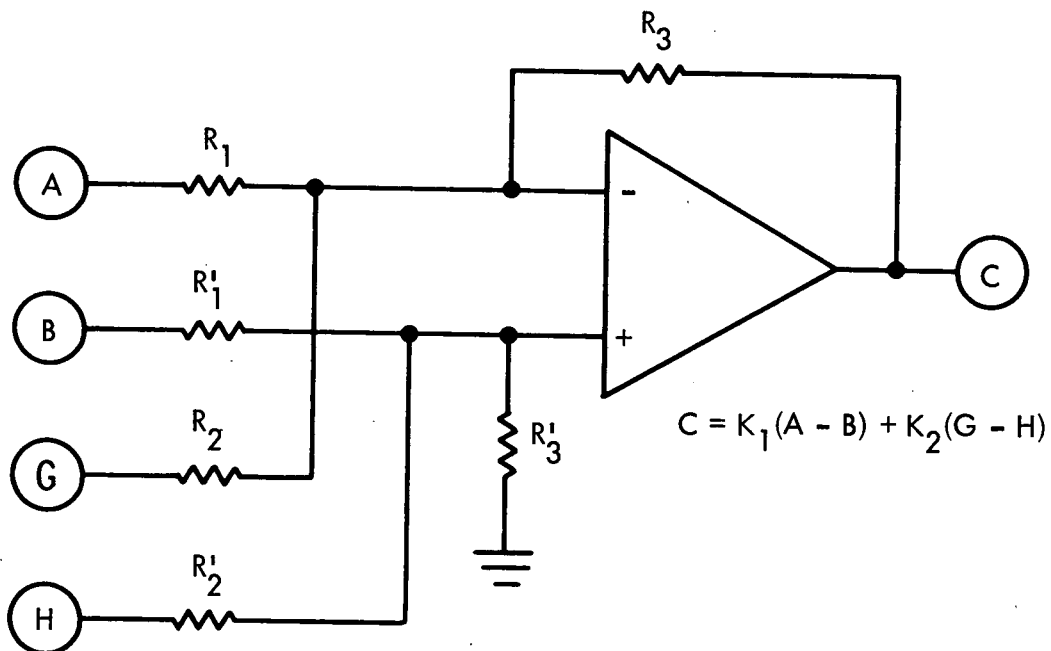


Fig. V-A-11. Differential Analog Summing Amplifier with Common Mode Suppression

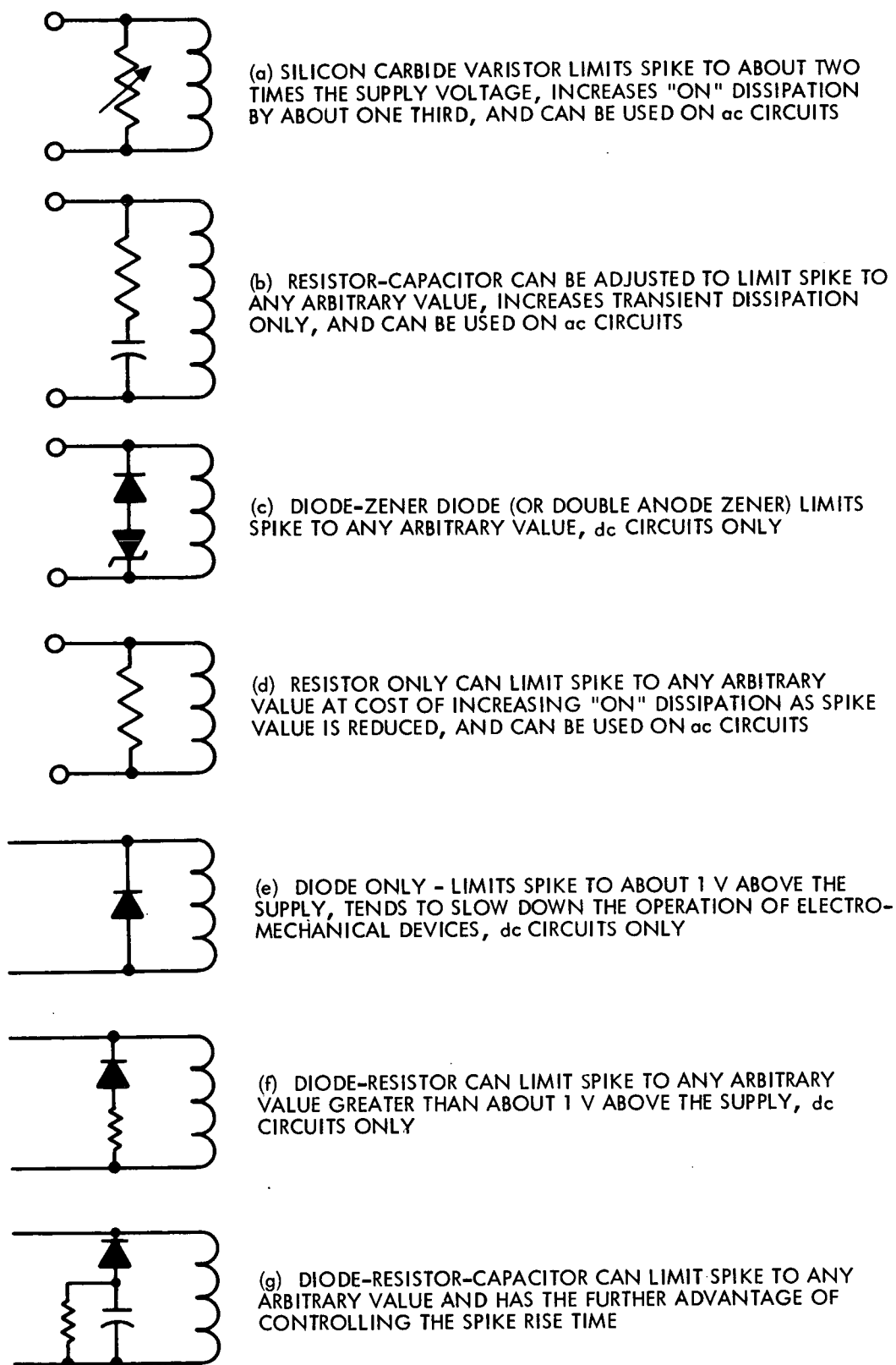
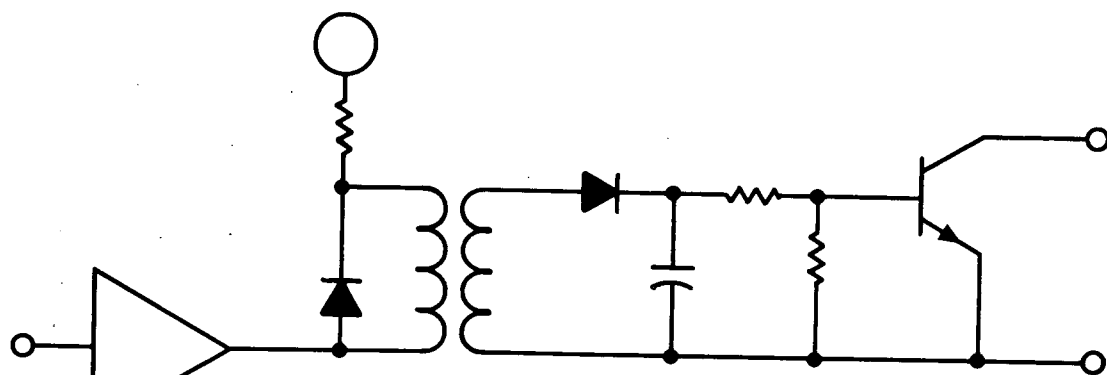
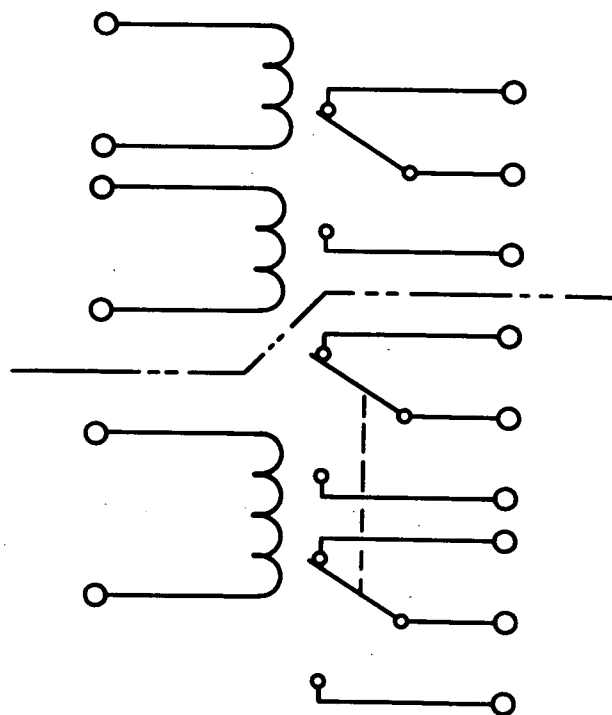


Fig. V-A-12. Methods of Inductive Spike Suppression



(a) TRANSFORMER-ISOLATED TRANSISTOR DRIVER



(b) LATCHING RELAY
(RELAY DRIVER NOT SHOWN)

(c) PULSED RELAY
(RELAY DRIVER NOT SHOWN)

Fig. V-A-13. Typical Interface Output Circuits

- (a) Twisted pair wire is used for lengths between transmitter and receiver which are longer than specified, and the wire is referenced at both the sending and receiving end. The twisted pair is terminated with a resistor of appropriate value to prevent ringing. For longer lines (length to be determined), the twisted pair is terminated on a differential line receiver with a proper resistor to prevent reflections and ringing and is referenced at the sending end only. These rules are for use within one common signal reference module only, but for no more than one bay, and for connection to modules outside the common signal reference volume, or other bays sending and receiving circuits such as those used between the FDS master and FDS slave.
- (b) Peak data rates should be chosen so that they do not exceed the data bandwidth of the data system (words per second times bits per word). The average data rate over any one-minute interval should be within the data bandwidth of the data system (processor-load dependent). Peak noise transient and ground offset combined are controlled to values which cause little interference with the operation of the data system.

d. Characteristics of Data Signals at the User to FDS Slave Interface

1) Analog Signals. Unless otherwise stated, each datum is scanned about once per minute. Analog data are normalized to ± 1.5 -V or 0-to 3-V ranges. The precision of conversion on all analog signals is seven bits. Accuracy of conversion of high level analog signals is $1/2\%$ of reading plus $1/2\%$ of full scale. Temperature measurements are made with resistance

thermometers, which have a range from 500 to 600 Ω over the temperature range of interest. The accuracy of temperature conversion is 3%. Other transducers may cover the range of 0-to 100-mV, and the accuracy of conversion for these is 3%. The high and low limit of all analog signals may be checked on each scan. Program alert (interrupt) signals are generated by out-of-limit conditions. Analog signal source impedances are controlled to acceptable maximum values. Analog data will be taken from the user as a differential pair, which is referenced to ground at the sending end. The common-mode signal caused by ground offset, noise, and transients combined should be less than 1-V peak magnitude.

2) Discrete Digital Data (Status). In general, discrete signals are represented by switch closures to ground. Typical switches are shown in Fig. V-A-13. Discrete signals should change no more frequently than once per minute except in instances where more rapid operation is essential to mission success.

3) Coded Digital Data. In general, coded signals are represented by switch closures of a type similar to those defined under 2) above or by TI 54L series logic elements. Data may be either in a bit-parallel or bit-serial form. The peak data rate should not exceed the data bandwidth of the data system. The average data rate over any 1-min period should also be within the data bandwidth of the data system. The wiring rules are the same as discussed previously.

e. Electromagnetic and Radio Frequency Interference

A major point of susceptibility of any system to exogenous interference is in the potential differences and grounding system currents among the units comprising the system. In this configuration, the most vulnerable elements, namely, interconnecting cables and interface circuits, are minimized and can be designed to accept very large ground offsets with no deleterious effects on the information transfer. (If transformer coupling is used, several hundred volts could be tolerated.) Steps should be taken to prevent

endogenous interference. The thrust subsystem has some 72 switching power supplies, of which 60 may be operating at any one time. These supplies operate with switching frequencies of 5 to 10 kHz. The thrusters are subject to arcing and consequent reflected transients on the power bus. Arcing causes the beam supplies to shut down, thus unloading the array suddenly. The main logic power distribution is a 50-V rms square wave at 2.4 kHz. Work is being done to minimize these sources of interference. The features which tend to make this data subsystem resistant to exogenous interference tend also to make it resistant to endogenous interference. Input filters on the 2.4-kHz power line, which effectively terminate the line for the high frequency components (series resistor and capacitor across the line), can reduce high frequency radiation and conducted noise from this source.

f. Grounding Requirements

The requirements for grounding and referencing of the circuits in the data subsystem are given in Ref. V-A-1.

4. Areas Requiring Further Study

Because of limitations imposed by time, available equipment, and manpower, a number of areas were superficially examined, postponed, or otherwise not fully included in this study. However, the following subjects were considered to the extent that further investigation will have no serious impact on the conclusions of the study up to this point.

a. Main Spacecraft Interface

The data subsystem of the SEP module must rely upon the main spacecraft for commands and data from ground for the provision of a path for the transmission of engineering data to earth. Consequently the SEP module data subsystem must interface with the modulation-demodulation subsystem (MDS) and the FDS of the main spacecraft. It may also be necessary to interface with the central computer and sequencer (CC&S) of the main spacecraft.

In the implementation of the data subsystem which is recommended by this report, allowance has been made for these interfaces, and they can be handled with a minimum of difficulty.

b. Power Subsystem Interface

The SEP module produces all of the power for both the SEP module and the main spacecraft. The interfaces between the data system and the power subsystem are not yet completely defined. However, they will be implemented to permit easy handling.

c. Thrust Vector Control or Attitude Control Subsystem Interface

This pair of subsystems must interface between the main spacecraft and the SEP module because the gas-operated attitude control system (ACS) is in the main spacecraft and the thruster-related TVC is in the SEP module. Some assumptions were made about the nature of the interaction with the data system and allowances made for interfacing to this subsystem pair.

Because software is subject to logical errors in much the same way as hardware, some attention was given to error conditions which might arise in the course of spacecraft operation, and methods of handling these errors were devised. Both software and hardware methods will be used. Interrupt assignments have not yet been made. Such assignments are heavily dependent upon the requirements of the subsystems with which the data system is interfaced. The requirements of the thrust subsystem are known and can be easily handled by the recommended implementation.

In a process control application such as this, resource allocation and scheduling are a major activity, and the routines entrusted with this activity should be the most thoroughly tested and perfected part of the software. To date, however, a minimum effort has been expended in this area because its

nature and approximate magnitude are known. The main effort has been in areas less known and understood. Some of the functions which this routine must perform are:

- (1) Schedule the users in accordance with their priority assignment.
- (2) Control the distribution of load between the processors (the proposed system has dual processors for reliability).
- (3) Control and handle all input and output.
- (4) Sequence the execution of routines according to priority and user-need.

Memory maps are not available because the programming is incomplete. No instruction-set optimization has been attempted, although it might be possible to reduce memory requirements by 10 to 20%, if the CCS is modified. The current implemented instructions are satisfactory, and this area will probably not be examined further.

Improvement of data system reliability is an important area. Presently available data indicates that reliability for the Encke mission is about 80%. No effort has yet been made to determine how pessimistic this estimate is or what can be done to improve the data system. It appears that the memory unit is the greatest contributor to system unreliability. It is likely that the "self-sparing" capability of many memories has not been considered in assessing the reliability.

5. Summary and Recommendations

- (a) Data subsystem failure analysis and reliability are continuing, as are the analyses of transient and hard failures in other subsystems for which the data subsystem has command and control responsibility. This is a vital effort and should be continued.

- (b) CCS and FDS loading study programs are initiated and further work is needed to optimize the load tradeoff between these pieces of hardware.
- (c) The control parameters and measurements needed on the thrust subsystem are isolated and most of the programming needed to control the thrust subsystem is completed. Further programming is needed to optimize the handling of the thrust subsystem, minimize storage requirements, take care of other subsystem needs, and handle the housekeeping tasks.
- (d) The presently recommended data system configuration has these physical characteristics:
 - (1) Weight: CCS, depending on memory requirements, 20.41 to 24.95 kg (45 to 55 lb). FDS, 9.07 kg (20 lb).
 - (2) Volume: CCS and FDS together will take about one and one-half bays.
 - (3) Power: The total 2.4-kHz power will average about 45 W.
 - (4) Cost: not yet accurately determined.
 - (5) Reliability: total data system reliability for the 1000 day Encke mission (950 days to encounter plus post encounter operations), about 80%. Further study and design refinement can improve this considerably.
 - (6) Noise tolerance: not yet well defined.
- (e) Data and program storage requirements are estimated and require further refinement. The degree of autonomy and "self correcting" capability must be decided before programming can be completed. (See Table V-A-4 for a comparison of the data storage requirements for a high degree of autonomy and self correcting ability with a situation in which any non-trivial failure results in shut-down and reliance on ground control to correct operations.) No estimate has been made

of the impact of either mode of operation on the probability of mission success. Such an estimate requires thrust subsystem operational information (failure modes and frequencies of failure), which is not yet available.

REFERENCES

- V-A-1. Functional Requirement: Viking Orbiter 1975 Electrical Grounding and Interfacing, JPL Specification VO75-3-260 (JPL internal document).

B. TELECOMMUNICATIONS/SEP INTERACTION STUDIES

1. Spacecraft Ion Beam Noise Effects

The magnitude of the noise interference in uplink signal reception caused by the operation of an ion engine on board a spacecraft is discussed in this section. The discussion is limited to noise generated by the exhaust beam as a result of ion-electron collisions, or "Bremsstrahlung radiation." Degradation is estimated in terms of the uplink received signal-to-noise ratio and the increase in antenna noise temperature. This activity represents one phase of the SEPSIT program to determine the interaction of a solar electric propulsion system with other spacecraft subsystems.

Under ideal conditions, the spacecraft antenna is pointing away from the ion beam axis, and, thus, there is little chance for ion-noise interference. If the antenna is movable, however, there is a possibility that the antenna might point into the exhaust beam during certain portions of the mission. Therefore, a worst-case spacecraft antenna/ion beam configuration is assumed, in which the antenna is located in the exit plane of the ion engine exhaust, at a distance R_a from the beam axis, and pointing in the direction $\phi = \pi/2$, $\theta = \psi$ (see Fig. V-B-1). R_0 is the beam radius and α the beam divergence angle. The geometry of this worst-case configuration simplifies the mathematics and provides an upper limit to other, perhaps more realistic, cases.

The incident noise power to the antenna from the ion beam is obtained by integrating the Bremsstrahlung radiation, weighted by the antenna gain pattern over the volume of the exhaust plume.

a. Radiative Properties of the Exhaust Beam

The exhaust of an ion-propulsion engine consists of a diverging beam of ions, which are neutralized outside of the engine by injected electrons. These electrons have a certain thermal velocity, and thus suffer Coulomb

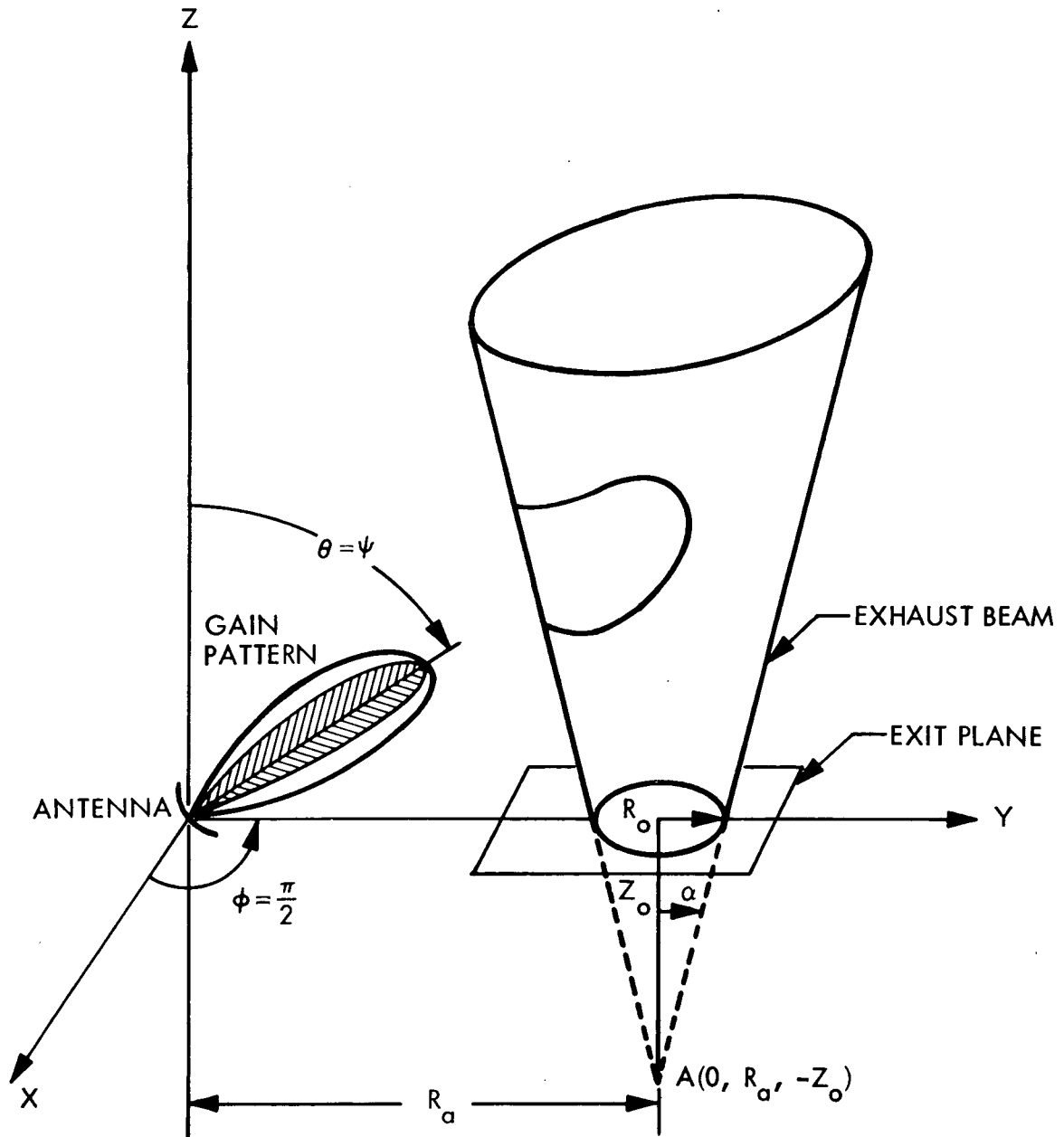


Fig. V-B-1. Spacecraft Antenna/Exhaust Beam Configuration

collisions with neighboring ions which produce Bremsstrahlung radiation. A numerical expression for the radiated spectral power density is given by Heald (see Ref. V-B-1) as

$$S_b = \frac{3.2 \times 10^{-47} G_a n^2 \exp(-h\omega/eT)}{\sqrt{T}} \text{ W/cm}^3/\text{Hz} \quad (1)$$

where n is the electron density in particles/cm³, T is the electron temperature in electron-volts, and G_a is the "Gaunt factor" (typically between 1 and 10), which accounts for the collective effects of ion-electron interactions for varying collision impact parameters. At microwave frequencies, the noise spectrum is essentially "white" and independent of frequency.

To find the power radiated by the ion beam, spatial variations of the electron density and temperature must be assumed throughout the volume of the beam. A truncated conical beam with a uniform core, i.e., no transverse variation, and a decreasing axial dependence is assumed in the work that follows. Approximate variations for $n(z)$ and $T(z)$ have been investigated by Sellen (Ref. V-B-2) for a constant current, conservative energy flow; the normalized dependence is

$$\frac{n(z)}{n_0} = \frac{1}{\left(1 + \frac{z}{z_0}\right)^2}, \quad \frac{T(z)}{T_0} = \frac{1}{\left(1 + \frac{z}{z_0}\right)^{\frac{4}{3}}} \quad (2)$$

where n_0 and T_0 are the exit plane ($z = 0$) values and z_0 is the distance from the apex of the cone to the x - y exit plane. The axial dependence of $S(z)$ is thus

$$S_b(z) = \frac{S_0}{\left(1 + \frac{z}{z_0}\right)^{\frac{10}{3}}} \quad (3)$$

where S_0 is the exit plane value of S_b .

b. Antenna Noise Temperature

The energy radiated from a source may be expressed in terms of its brightness, b , in units of power/area/steradian/Hz. A brightness temperature T_b associated with this radiation is found by equating it to the equivalent Planck radiation from a black body at a temperature T_b . In the limit $hf \ll k T_b$, the radiation from a black body is

$$b = \frac{2k T_b}{\lambda^2} \quad (4)$$

For the case considered here, which assumes isotropic radiation, the brightness of the ion beam is given by $S_b(r, \theta, \phi)/4\pi$ where r , θ , and ϕ are the spherical coordinates shown in Fig. V-B-2. A single integration over the line-of-sight produces the brightness temperature $T_b(\theta, \phi)$.

$$T_b(\theta, \phi) = \frac{\lambda^2}{2k} \int_{r_1(\theta, \phi)}^{r_2(\theta, \phi)} \frac{S_b(r, \theta, \phi) dr}{4\pi} \quad (5)$$

The above expression neglects absorption because the optical depth is much larger than the beam dimension. The limits $r_1(\theta, \phi)$ and $r_2(\theta, \phi)$ in the integral are determined in the next section. However, $S_b(z)$ may be expressed in spherical coordinates, since $z = r \cos \theta$:

$$S_b(r, \theta, \phi) = \frac{S_0}{\left(1 + \frac{r \cos \theta}{z_0}\right)^{\frac{10}{3}}} \quad (6)$$

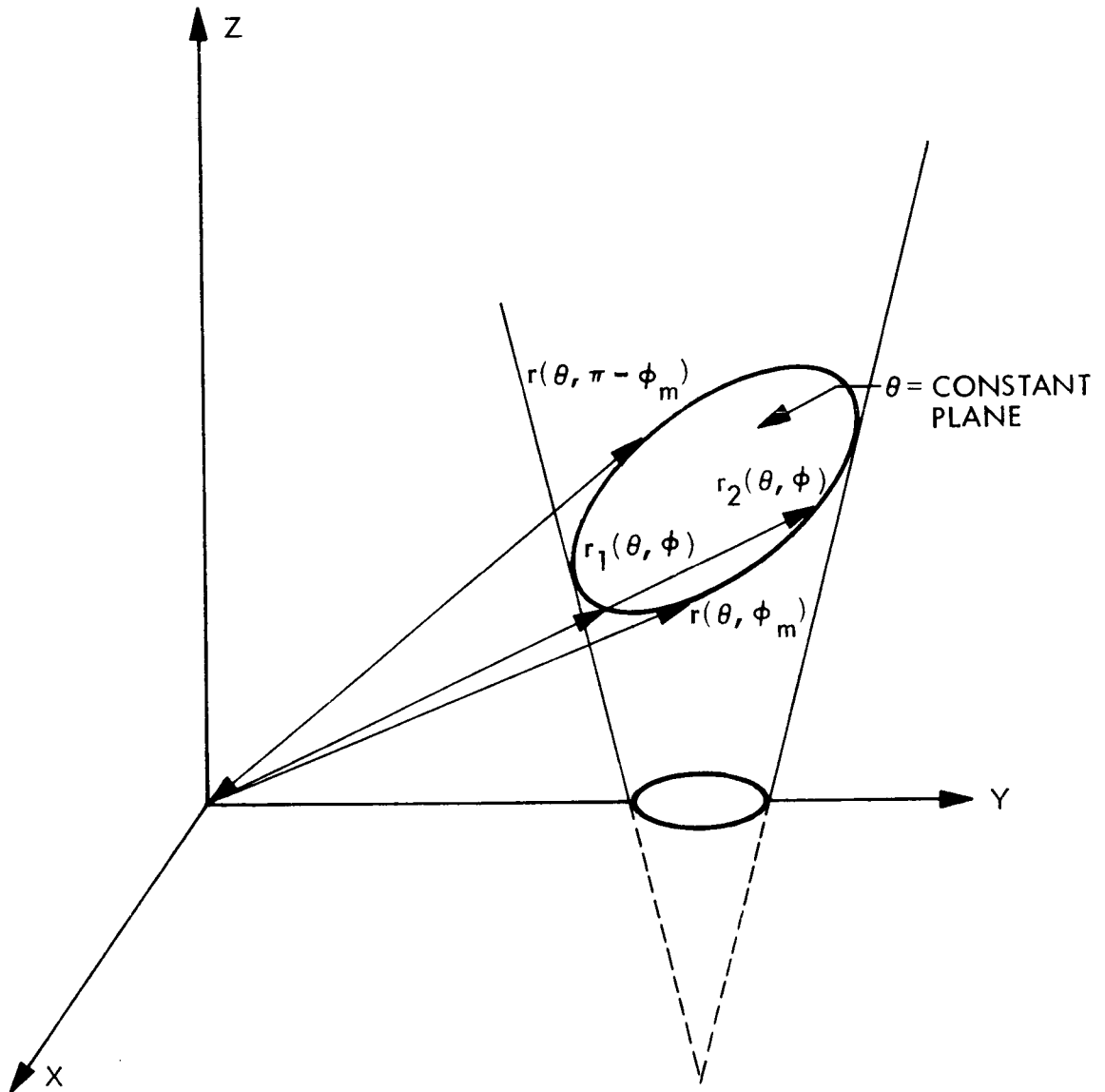


Fig. V-B-2. Integration Limits of Conical Beam

The brightness temperature can then be integrated directly, to give

$$T_b(\theta, \phi) = \frac{3S_0 \lambda^2 z_0}{56\pi k \cos \theta} \left[t_1(\theta, \phi) - t_2(\theta, \phi) \right] \quad (7)$$

where

$$t_i(\theta, \phi) = \left[1 + \frac{r_i(\theta, \phi) \cos \theta}{z_0} \right]^{-\frac{7}{3}}, \quad i = 1, 2 \quad (8)$$

The antenna noise temperature is a measure of the total received power from the radiating source. To obtain this power, the Bremsstrahlung radiation, or its equivalent brightness temperature, weighted by the antenna gain pattern, is integrated. The general form of the antenna noise temperature T_a is therefore given by the equation

$$T_a = \frac{\iint T_b(\theta, \phi) G(\theta, \phi) d\Omega}{\iint G(\theta, \phi) d\Omega} \quad (9)$$

where $G(\theta, \phi)$ is the gain pattern and $d\Omega$ is an element of solid angle. The received noise power then is $N = k T_a B$, where B is the bandwidth of the receiver.

c. Conical Beam Limits of Integration

These limits of integration for the brightness temperature are found by writing the equation of the cone in spherical coordinates.

The equation, in rectangular coordinates, of a right cylindrical cone with half angle α , axis parallel to the z direction, and apex located at $(0, R_a, -z_0)$ is

$$x^2 + (y - R_a)^2 = m^2(z + z_0)^2 \quad (10)$$

where $m = \tan \alpha = R_0/z_0$ (see Fig. V-B-2). The equation of the cone transformed into spherical coordinates, and solved explicitly for $r(\theta, \phi)$ is:

$$r(\theta, \phi) = \frac{R_a \sin \theta \sin \phi + m^2 z_0 \cos \theta}{\sin^2 \theta - m^2 \cos^2 \theta} \pm \quad (11)$$

$$\frac{\sqrt{(R_a \sin \theta \sin \phi + m^2 z_0 \cos \theta)^2 - (\sin^2 \theta - m^2 \cos^2 \theta) (R_a^2 - R_0^2)}}{\sin^2 \theta - m^2 \cos^2 \theta}$$

The limits of integration are $r_1(\theta, \phi)$ and $r_2(\theta, \phi)$, with the plus and minus signs, respectively, are shown in Fig. V-B-2.

The domain of ϕ for a given value of θ in the range $\alpha < \theta \leq \frac{\pi}{2}$ is $\phi_m \leq \phi \leq \pi - \phi_m$, where ϕ_m is determined by setting the square-root expression in $r(\theta, \phi)$ equal to zero:

$$\sin \phi_m = \frac{\sqrt{(\sin^2 \theta - m^2 \cos^2 \theta) (R_a^2 - R_0^2) - M^2 z_0 \cos^2 \theta}}{R_a \cos \theta} \quad (12)$$

The source of radiation is now defined by $T_b(\theta, \phi)$ everywhere in the volume of the ion beam, and zero outside this volume.

d. Antenna Gain Pattern

The antenna gain pattern $G(\theta, \phi)$ is assumed in this treatment to be symmetric and pointing in the $\theta = \psi$, $\phi = \pi/2$ direction. For simplicity, the pattern is assumed to have no side lobes. The shape of the pattern is taken to be a simple cosine distribution with a half-power beamwidth of θ_3 as given below:

$$G(\theta, \phi) = \cos \left[\frac{\pi}{3} \frac{(\phi - \theta)}{\theta_3} \right] \cos \left[\frac{\pi}{3} \frac{(\frac{\pi}{2} - \phi)}{\theta_3} \right]$$

$$\text{if } \left| \frac{\psi - \theta}{\theta_3} \right| \leq 1.5 \quad \text{and} \quad \left| \frac{\pi - \phi}{\theta_3} \right| \leq 1.5 \quad (13)$$

and $G(\theta, \phi) = 0$ otherwise.

The limits of integration for the antenna-noise-temperature integral are given by the intersection of the domains given by the cone boundary and the antenna gain pattern.

Noise generated by the exhaust beam may then be compared to the received uplink signal level, to obtain the signal-to-noise ratio. The received signal power is

$$S = P_{\text{inc}} A_{\text{eff}} \quad (14)$$

where A_{eff} is the effective aperture area of the antenna and P_{inc} is the incident power density. For an antenna that is always pointing towards the point of transmission, perfectly matched and lossless, the maximum effective area is given by

$$A_{\text{eff}} = \frac{\lambda^2}{\iint G(\theta, \phi) d\Omega} \quad (15)$$

The signal-to-noise ratio is thus

$$\frac{S}{N} = \frac{P_{inc} \lambda^2}{kB \iint T_b(\theta, \phi) G(\theta, \phi) d\Omega} \quad (16)$$

where B is the receiver bandwidth.

e. Discussion of Results

Two effects of ion-beam induced noise may be calculated: (1) the increase in antenna noise temperature caused by the exhaust beam, and (2) the uplink signal-to-noise ratio, when all other noise contributions are zero.

The expression for the antenna noise temperature was evaluated on the UNIVAC 1108 computer. Results of the antenna noise temperature versus antenna pointing angle are shown in Fig. V-B-3 for several half-power beamwidths. The brightness temperature $T_b(\psi, \frac{\pi}{2})$ is also plotted for reference. The peak in T_a for each value of θ_3 corresponds to pointing angles, ψ , in which the gain pattern is partially blocked by the engine, which is exterior to the beam volume. A case with an assumed isotropic pattern, i.e., $G(\theta, \phi) = 1$, is also shown; the low value of T_a for this case is due to the large field-of-view and thus lower gain of the antenna in the direction of the plume. A peak antenna noise temperature of about 0.2°K (about -200 dBm/Hz) was found. A spacecraft receiver might typically have a noise temperature of 500°K (or -170 dBm/Hz), a margin of 30 dB above the ion-noise.

Although the ion noise signal increases for narrow antenna beam patterns, the effective aperture area is also larger so that received signals are greater than for broader patterns. Thus, to find the signal-to-noise ratio for the worst case, comparisons of S/N for various antenna beamwidths must be made.

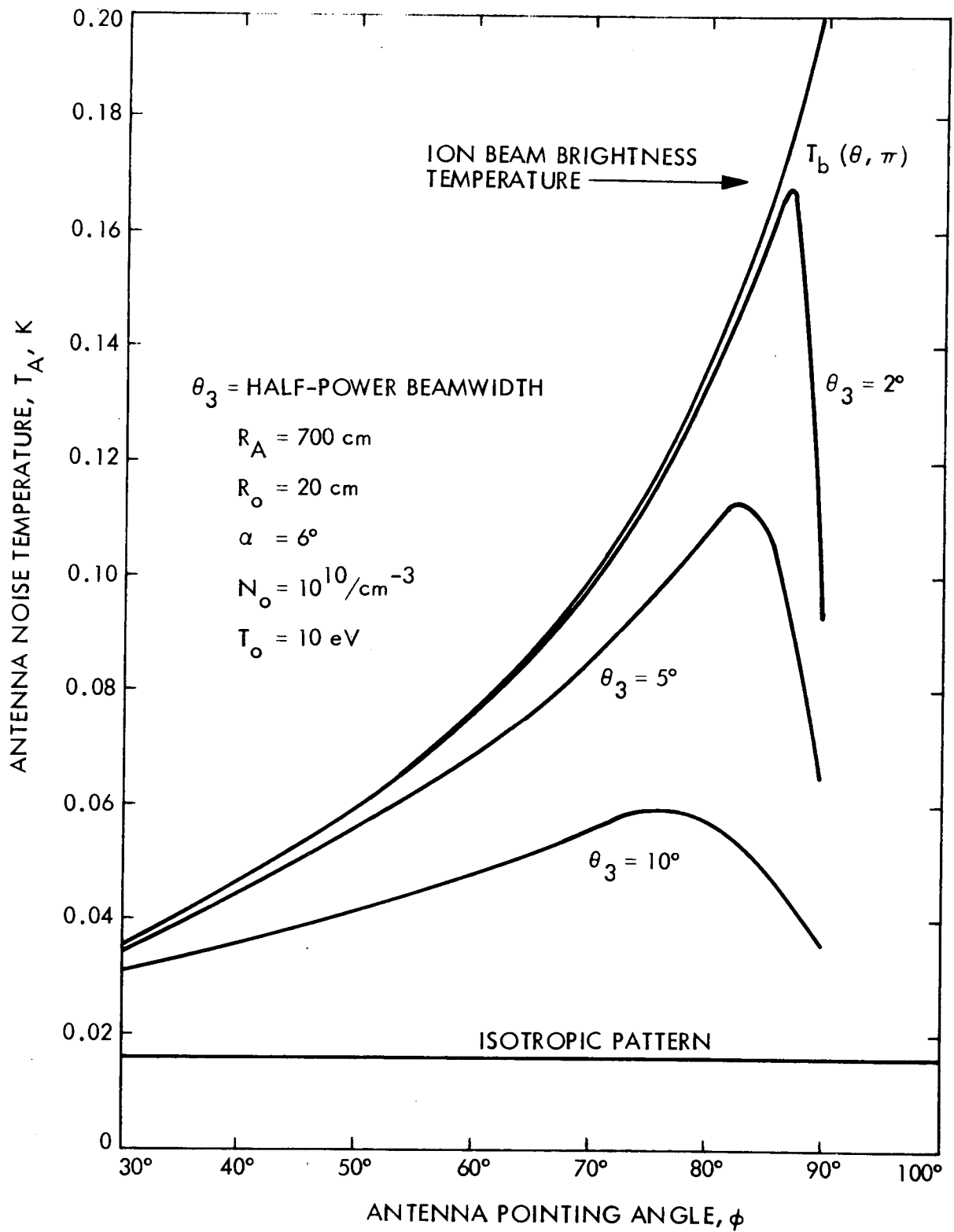


Fig. V-B-3. Results of Antenna Noise vs Antenna Pointing Angle

Consider a typical uplink ranging signal transmitted by a 26-m antenna (52 dB gain) at 10 kW with 12 dB ranging suppression, at 2 GHz with a 1 MHz bandwidth. Rather than determining the S/N at various distances, the critical distance R_{cr} (in AU) at which the uplink signal equals the exhaust beam noise will be determined.

The critical range is shown in Fig. V-B-4 for several beam-widths and the isotropic case. The shortest critical range occurs for an isotropic or low-gain antenna, which, for the spacecraft parameters indicated on the figure, is 4 AU.

The effect of the exhaust beam divergence angle α and the antenna distance to the beam axis is shown in Fig. V-B-5 for an isotropic antenna. As the exhaust-beam divergence-angle decreases, the characteristic length z_0 increases, indicating a decreased ion density and temperature drop-off and thus larger noise contributions.

It can be concluded that operating an ion engine ordinarily introduces much less degradation than receiver noise.

2. Effects of Dispersive Media on Coherent Communications

Unlike a ballistic spacecraft, a SEP spacecraft accelerates continuously throughout a mission. During that time, most of the subsystems function and must be monitored. This requirement for prolonged communications places greater demands on the SEP than on ballistic communication subsystems.

In the Encke mission, the additive white Gaussian noise channel must be used rather than the usual deep space communication channel. Further, in two cases, one mission-dependent and one mission-independent, the signal itself is randomly disturbed in both amplitude and phase by its passage through a plasma. In one instance, the solar corona occults the spacecraft twice during the mission, causing a communications blackout. However, with a better

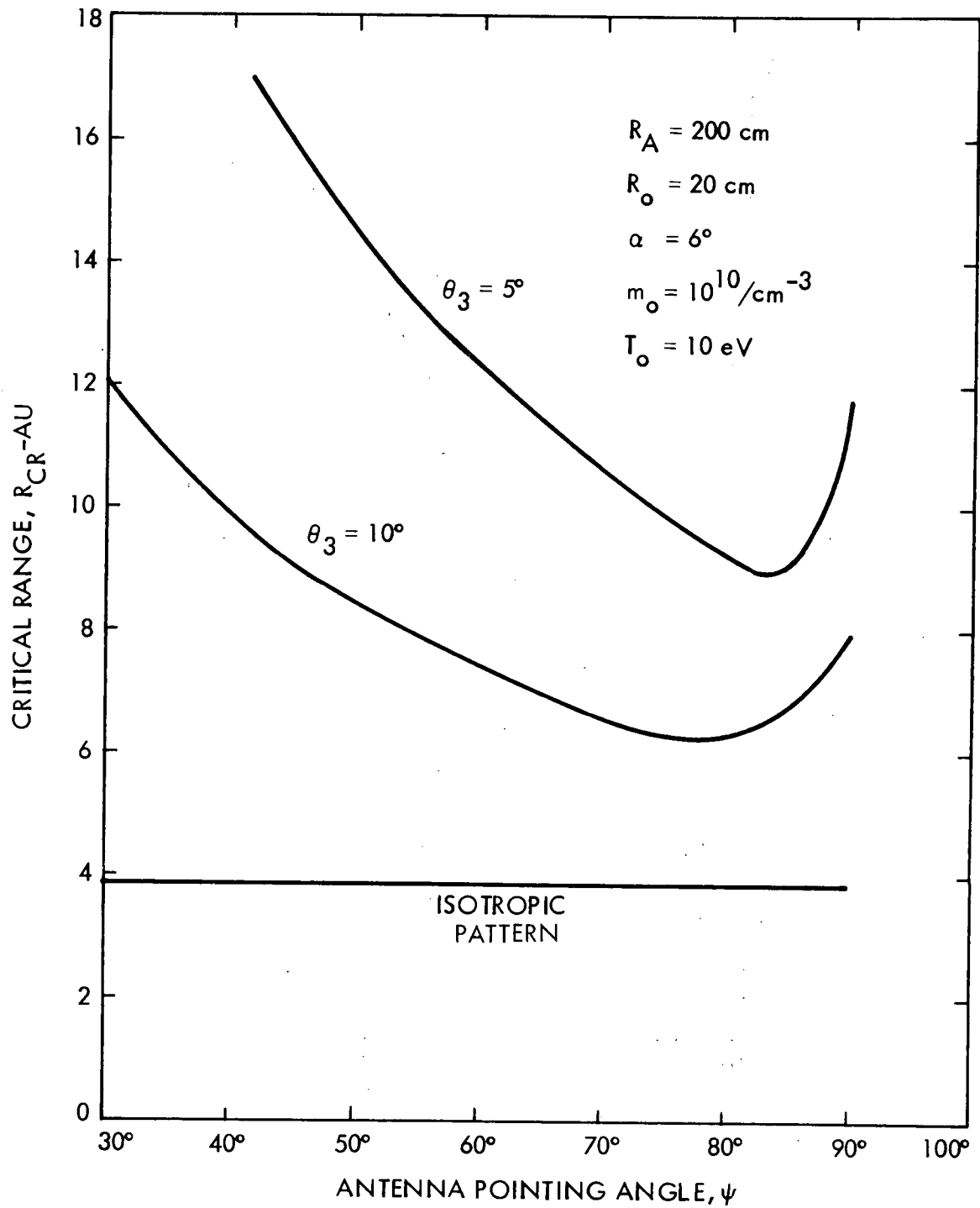


Fig. V-B-4. Critical Ranges

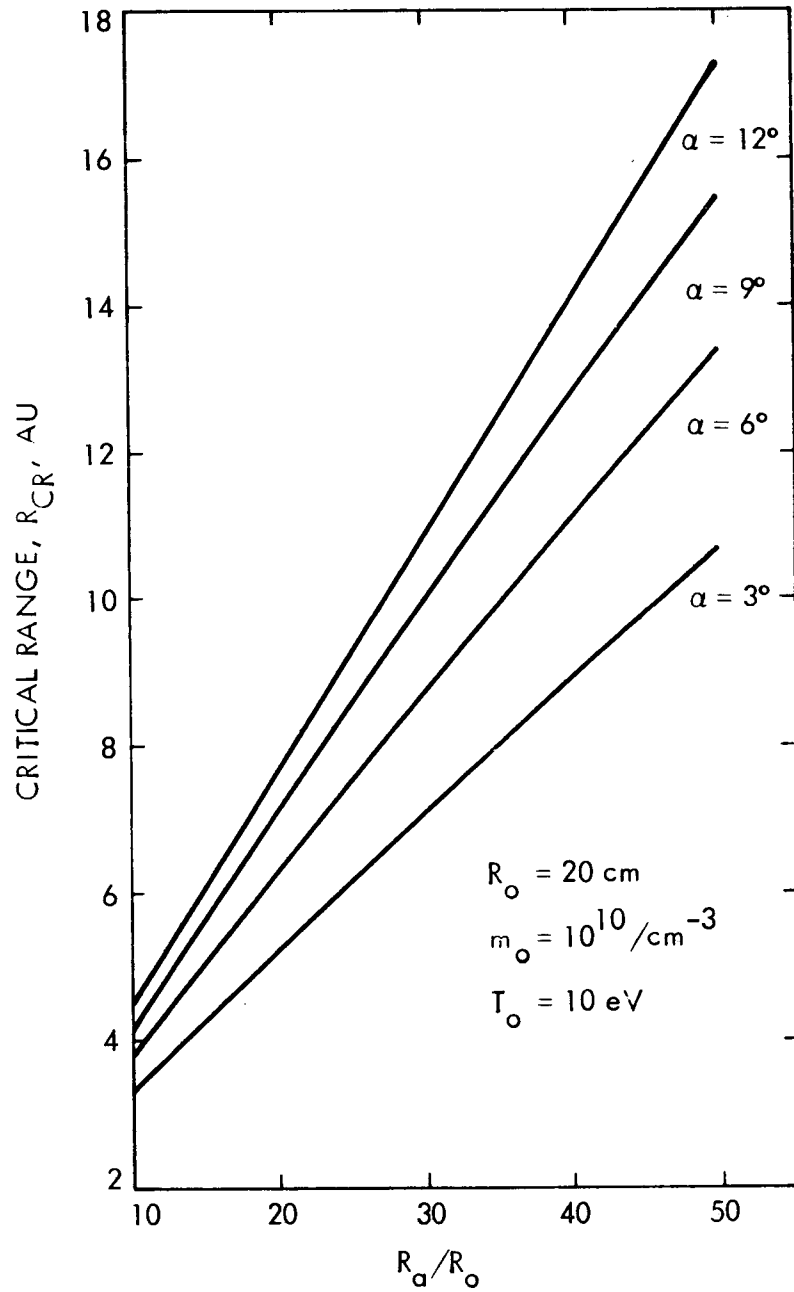


Fig. V-B-5. Critical Range vs Normalized Spacecraft Antenna Distance to Beam Radius

understanding of the blackout phenomenon, it should be possible to design the communication subsystems so that the blackout period is shortened. In the other instance, plasma interference may be the ion beam of the SEP thrusters. Further study is needed to determine whether or not the ion beam will adversely affect communications, and, if it will, to understand the extent and effects of the interference.

The problem of communicating through this media can be broken down into various areas for analysis. First, the interaction between the medium and the signal must be characterized by a communication channel model with input-output characteristics determined by the given signal and medium. Then, the performance of the various system functions such as carrier tracking, ranging, command, telemetry, etc., can be analyzed. For this analysis, a general model covering a broad class of channels of interest is postulated. When the specific channel models (such as the ion beam and solar corona channels) are completed, the parameters of these models can then be applied to the results of this analysis.

Presently, the configuration used for deep space communication uses phase-locked loop (PLL) receivers for carrier tracking and coherent demodulation. The performance of the tracking loop affects all communication subsystem functions. For example, one- and two-way doppler measurements and ranging, which are required for navigation and orbit determination, are highly dependent on the PLL performance. Similarly, the phase jitter of the tracking PLL degrades the telemetry and command performance because of imperfect coherent demodulation. For these reasons, the first step in predicting coherent communications performance through dispersive media must be a thorough analysis of the PLL.

a. Channel Model and PLL Equations

To analyze the carrier tracking ability of the PLL receiver, it is assumed that a signal is transmitted having the form:

$$s(t) = \sqrt{2} S \sin \omega t = \sqrt{2} S \sin (\omega_0 t + \Omega_0 t)$$

where ω_0 is the loop quiescent frequency and Ω_0 is the transmitted frequency offset. The received signal is assumed to be

$$\begin{aligned} r(t) = & \sqrt{2} A \sin \omega t + \sqrt{2} x_s(t) \sin \omega t \\ & + \sqrt{2} x_c(t) \cos \omega t + n'(t) \end{aligned} \quad (17)$$

The term $x_s(t)$ is a zero mean random process referred to as the in-phase fading component, and $x_c(t)$ is also a zero mean random process referred to as the quadrature component. The term $n'(t)$ is additive white Gaussian noise of spectral density $N_0/2$. It should be noted that the terms $x_s(t) \sin \omega t$ and $x_c(t) \cos \omega t$ are due to the signal passing through the dispersive media. In modeling the dispersive media as a communication channel, it is necessary, under the above received signal assumption, that the statistics of x_s and x_c be specified.

The most common channel which arises in a vast number of physical situations is the case where x_s and x_c are stationary Gaussian random processes with equal variances. The received signal may be written in the following form:

$$r(t) = \sqrt{2} A \sin \omega t + \sqrt{2} a(t) \sin [\omega t + \xi(t)] + n'(t)$$

where

$$a(t) = \sqrt{x_s^2 + x_c^2(t)}$$

$$\xi(t) = \tan^{-1} \left[\frac{x_c(t)}{x_s(t)} \right]$$

For this case, it can be shown that $a(t)$ has a Rayleigh distribution and $\xi(t)$ has a uniform distribution. This analysis will investigate the cases where $x_s(t)$ and $x_c(t)$ are stationary Gaussian random processes, and, in particular, the case where they have equal variances.

The PLL is shown in Fig. V-B-6. The loop filter, $F(p)$, has the form:

$$F(p) = F_o + \sum_{k=1}^n \frac{1 - F_k}{1 + \tau_k p} \quad (18)$$

The two loops of interest are the first and second order loops for which

$$F(p) = 1 \text{ for first order loop}$$

and

$$F(p) = \frac{1 + \tau_2 p}{1 + \tau_1 p} \text{ for second order loop} \quad (18a)$$

(i.e., $F_o = F_1 = \tau_2 / \tau_1$)

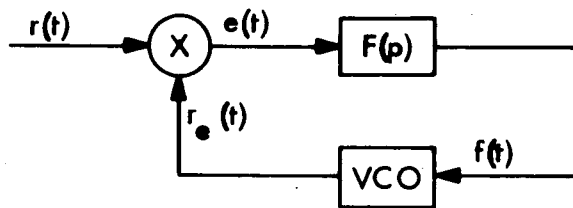


Fig. V-B-6. Phase-locked Loop

The voltage control oscillator (VCO) output has the following output and input-output properties:

$$r_e(t) = \sqrt{2} K_1 \cos [\omega_o t + \hat{\theta}(t)] \quad (19)$$

where

$$\frac{d}{dt} [\omega_o t + \hat{\theta}(t)] = \omega_o + K_{vco} f(t)$$

$$\text{i.e., } \frac{d\hat{\theta}(t)}{dt} = K_{vco} f(t)$$

To derive the equation of loop operation, $r(t)$ and $r_e(t)$ are written as follows:

$$\begin{aligned} r(t) &= \sqrt{2} \cdot \sqrt{[A + x_s(t)]^2 + x_c^2(t)} \sin [\omega t + \delta(t)] \\ &\quad + \sqrt{2} [n_s(t) \sin \omega_o t + n_c(t) \cos \omega_o t] \\ &= \sqrt{2} \cdot \sqrt{[A + x_s(t)]^2 + x_c^2(t)} \sin \Phi(t) \\ &\quad + \sqrt{2} [n_s(t) \sin \omega_o t + n_c(t) \cos \omega_o t] \end{aligned} \quad (20)$$

where

$$\Phi(t) = \omega t + \delta(t) = \omega_o t + \Omega_o t + \delta(t)$$

$$\delta(t) = \tan^{-1} \left[\frac{x_c(t)}{A + x_s(t)} \right]$$

and $n'(t)$ has been expanded as a narrow-band Gaussian random process.

The distribution of $\sqrt{[A + x_s(t)]^2 + x_c(t)^2}$ is Rician in the equal variance case, giving rise to the term Rician fading channel.

$$r_e(t) = \sqrt{2} K_1 \cos \hat{\Phi}(t) \quad (21)$$

where

$$\hat{\Phi}(t) = \omega_o t + \hat{\theta}(t)$$

Thus, the error voltage into the loop filter is:

$$e(t) = K_1 K_m \sqrt{(A+x_s)^2 + x_c^2} \sin(\Phi - \hat{\Phi}) + K_1 K_m n(t) \quad (22)$$

where K_m is the multiplier constant, and $n(t)$ is shown by Lindsey and Viterbi (see Refs. V-B-3 and 4) to be approximately white Gaussian noise of spectral density $N_o/2$. Note that the 2ω terms have been dropped since they are not passed by the loop. The output of the loop filter is thus represented as,

$$f(t) = F(p) e(t) \quad (23)$$

From (19) and (22), the VCO relationship can now be written as,

$$\dot{\hat{\Phi}} = \omega_o + KF(p) \left[\sqrt{(A + x_s)^2 + x_c^2} \sin(\Phi - \hat{\Phi}) + n(t) \right] \quad (24)$$

where

$$K = K_1 K_m K_{vco}$$

The loop phase tracking error is defined as

$$\phi \triangleq \Phi - \hat{\Phi} . \quad (25)$$

By differentiation and substitution for Φ and $\hat{\Phi}$ from (20) and (24) respectively, the loop equation of operation becomes,

$$\dot{\phi} = \Omega_o + \dot{\delta} - KF(p) \left[\sqrt{(A + x_s)^2 + x_c^2} \sin \phi + n \right] \quad (26)$$

where it is understood that $\dot{\phi}$, ϕ , $\dot{\delta}$, x_s , x_c , and n are functions of time. It is frequently advantageous to normalize x_c , x_s , and n to the constant A . Thus, the loop equation becomes,

$$\dot{\phi} = \Omega_o + \dot{\delta} - AKF(p) \left[\sqrt{(1 + x_{s1})^2 + x_{c1}^2} \sin \phi + n_1 \right] \quad (27)$$

where

$$x_{s1} \triangleq \frac{x_s}{A} ; x_{c1} \triangleq \frac{x_c}{A} ; n_1 \triangleq \frac{n}{A}$$

and

$$\delta \triangleq \tan^{-1} \left[\frac{x_c}{A + x_s} \right] = \tan^{-1} \left[\frac{x_{c1}}{1 + x_{s1}} \right]$$

Figure V-B-7 shows the geometric configuration of the various signals and their phase angles. When the loop is tracking, the phase error ϕ should be as small as possible for optimum coherent demodulation.

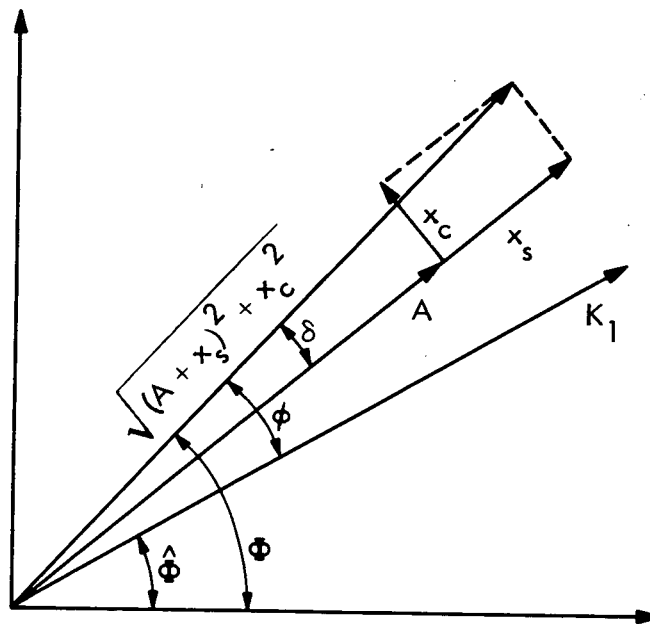


Fig. V-B-7. Geometric Configuration of Signals and Phase Angles

Since the random processes x_c and x_s are zero mean and Gaussian, it is convenient for analytical purposes to assume that they have rational spectra. (If their spectra are not rational, then techniques exist for approximating them by processes with rational spectra.) In this case, x_c and x_s are assumed to be generated by passing white Gaussian noise through filters of the form shown in Fig. V-B-8.

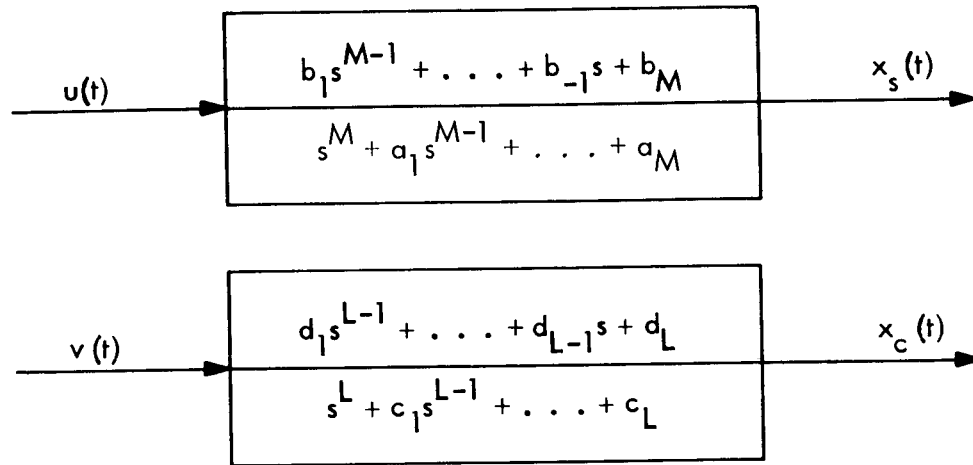


Fig. V-B-8. White Gaussian Noise Filters

Using this form for the generating filters, the following state equations can be written (see Ref. V-B-5):

$$\dot{\underline{x}} = A\underline{x} + Bu \quad (28)$$

$$\dot{\underline{z}} = C\underline{z} + Dv$$

where

$$\underline{x} = \begin{bmatrix} x_1 \\ \vdots \\ x_M \end{bmatrix} ; \quad \underline{z} = \begin{bmatrix} z_1 \\ \vdots \\ z_L \end{bmatrix}$$

$$A = \begin{bmatrix} -a_1 & 1 & 0 & \dots & 0 \\ -a_2 & 0 & 1 & 0 & \dots & 0 \\ \vdots & \vdots & \vdots & \ddots & \vdots & \vdots \\ -a_M & 0 & \dots & \dots & 1 & 0 \end{bmatrix} \quad B = \begin{bmatrix} b_1 \\ \vdots \\ b_M \end{bmatrix}$$

$$C = \begin{bmatrix} -c_1 & 1 & 0 & \dots & 0 \\ -c_2 & 0 & 1 & 0 & \dots & 0 \\ & & \ddots & \ddots & \ddots & \vdots \\ -c_L & 0 & \dots & \dots & 1 & 0 \end{bmatrix} \quad D = \begin{bmatrix} d_1 \\ \vdots \\ d_L \end{bmatrix}$$

and

$$x_s = x_1$$

$$x_c = z_1$$

Thus, (27) describes the phase error process in terms of the driving functions which are white noise and functions of components in (28). The primary goal is to find the steady-state probability density function, $p(\phi)$. The techniques for solving such a problem usually depend on a linearization of (27) or the use of Fokker-Planck techniques (Refs. V-B-3 and 4). Using these techniques to obtain $p(\phi)$ in this case involves difficulty with the highly nonlinear nature of the amplitude $\sqrt{(1 + x_{s1})^2 + x_{c1}^2}$ and $\dot{\delta}$, which can be written as,

$$\dot{\delta} = \dot{x}_{c1} \left[\frac{1 + x_{s1}}{(1 + x_{s1})^2 + x_{c1}^2} \right] - \dot{x}_{s1} \left[\frac{x_{c1}}{(1 + x_{s1})^2 + x_{c1}^2} \right] \quad (29)$$

A greater problem than the nonlinearity is the fact that in $\dot{\delta}$ the derivatives of state components are multiplying state components. For any kind of reasonable analytic solutions to the problem, certain simplifying assumptions must be made. Such assumptions depend on three factors: (1) the bandwidth, W_s , of

x_{c1} , and x_{s1} , compared to the bandwidth of the loop, W_L ; (2) signal-to-noise ratio*, $\rho \triangleq \frac{2A^2}{N_o W_L}$; and (3) the ratio of power in the specular component (A^2) to that in the fading components, that is,

$$\gamma^2 \triangleq \frac{A^2}{2\sigma_{x_s}^2} = \frac{A^2}{2\sigma_{x_c}^2} \quad (30)$$

Four Rician cases are presented, each based on one of the following assumptions:

- (1) Case A: $W_s \ll W_L$ (i.e., slow fading)
- (2) Case B: $W_s \gg W_L$ (i.e., fast fading)
- (3) Case C: ρ and γ^2 , relatively large
- (4) Case D: γ^2 , relatively large

Naturally, the closer the real channel is to one of these assumptions, the better the analysis for that channel.

1) Case A: $W_s \ll W_L$. When the fading components x_s and x_c change slowly with time, the phase angle of the received signal can be tracked by the loop, provided the loop bandwidth is large compared to the spectral bandwidth of the fading components. In terms of equation (27), the assumption leads to the approximation that $\dot{\delta} \approx 0$ and $\sqrt{1 + x_{s1}^2 + x_c^2}$ is roughly

*It should be noted here that the signal-to-noise ratio ρ , as defined above, should be treated as a parameter and not as the total signal power (which includes x_c and x_s) to additive noise ratio. Also, the total power into the channel, namely S^2 , need not equal the total power out because of the reflection or absorption which may take place in the channel.

constant over a relatively long period of loop operation. A similar type argument is used by Yuen (Ref. V-B-6) treating a double-loop tracking system.

Essentially, what this amounts to is calculating $p(\phi | \sqrt{(1 + x_s)^2 + x_{c_1}^2})$. Then, the amplitude can be integrated out using the Rician distribution to $p(\phi)$. Formally, the bandwidth assumption permits the following approximation:

$$p[\phi(t) | x_{s_1}(\xi), x_{c_1}(\xi), t_0 \leq \xi \leq t] \approx p[\phi(t) | x_{s_1}(t), x_{c_1}(t)]$$

With this approximation, $p(\phi | x_{s_1}, x_{c_1})$ can be found using (27) and the Fokker-Planck equation. For example, for a first-order loop and $\Omega_0 = 0$, the solution (Refs. V-B-3 and 4) is:

$$p(\phi | x_{s_1}, x_{c_1}) = \frac{\exp(\alpha \cos \phi)}{2\pi I_0(\alpha)} \quad -\pi \leq \phi \leq \pi$$

where

$$\alpha = \frac{4A}{KN_0} \sqrt{(1 + x_{s_1})^2 + x_{c_1}^2} \quad (31)$$

$$= \rho \sqrt{(1 + x_{s_1})^2 + x_{c_1}^2}$$

and

$$\rho = \frac{4A}{KN_0} \quad (\text{SNR for 1st order loop})$$

Since x_{s_1} and x_{c_1} are independent Gaussian processes, the solution for $p(\phi)$ can be solved in two ways. The first method uses the Gaussian densities for x_{s_1} and x_{c_1} , that is,

$$\begin{aligned}
 p(\phi) &= \iint_{-\infty}^{\infty} p(\phi | x_{s_1}, x_{c_1}) p(x_{s_1}, x_{c_1}) dx_{s_1}, dx_{c_1} \\
 &= \iint_{-\infty}^{\infty} p(\phi | x_{s_1}, x_{c_1}) p(x_{s_1}) p(x_{c_1}) dx_{s_1}, dx_{c_1} \\
 &= \iint_{-\infty}^{\infty} \left[\frac{\exp(\rho \sqrt{(1+x_{s_1})^2 + x_{c_1}^2} \cos \phi)}{2\pi I_0(\rho \sqrt{(1+x_{s_1})^2 + x_{c_1}^2})} \right] \left[\frac{\gamma}{\sqrt{\pi}} \exp(-\gamma^2 x_{s_1}^2) \right] \\
 &\quad \left[\frac{\gamma}{\sqrt{\pi}} \exp(-\gamma^2 x_{c_1}^2) \right] dx_{s_1} dx_{c_1} \tag{32}
 \end{aligned}$$

This integral can be evaluated on a computer. However, the following approach is more suited to numerical solution. The amplitude,

$\alpha' = \sqrt{(1+x_{s_1})^2 + x_{c_1}^2}$, has a Rician distribution. Then

$$\begin{aligned}
p(\phi) &= \int_0^{\infty} p(\phi, \alpha') p(\alpha') d\alpha' \\
&= \int_0^{\infty} \left[\frac{\exp(\rho \alpha' \cos \phi)}{2\pi I_0(\rho \alpha')} \right] \left[2\gamma^2 \alpha' \exp\{-\gamma^2(\alpha'^2 + 1)\} I_0(\gamma^2 \alpha') \right] d\alpha' \\
p(\phi) &= \frac{\gamma^2}{\pi} e^{-\gamma^2} \int_0^{\infty} \alpha' \exp\left[-\gamma^2 \alpha'^2 + \rho \alpha' \cos \phi\right] \frac{I_0(2\gamma^2 \alpha')}{I_0(\rho \alpha')} d\alpha' \quad (33)
\end{aligned}$$

Similar expressions can be derived for the second-order loop and the cases where $\Omega_0 \neq 0$.

Figure V-B-9 shows $p(\phi)$ for the case when all transmitted power is received through the dispersive media. That is, the specular power plus dispersive power is the same for each case in Fig. V-B-9. Only the distribution of power between specular and dispersive components is changed as is shown by the parameter γ^2 . It can be seen from the curves that, for the very slow fading case, the loop performance is not degraded significantly from the case when nearly all received power is in the specular component, to the case when nearly all power is in the dispersive components.

2) Case B: $W_s \gg W_L$. For the fast fading case, the fading components look like additive white noise to the loop. The process $\sqrt{2} \left[x_s(t) \sin \omega_0 t + x_c(t) \cos \omega_0 t \right]$ is a narrow band Gaussian random process which could be considered as white noise of spectral density N_{01} if it is flat over the loop bandwidth and $W_s \gg W_L$. The equivalent noise is then just $N_{0'} = N_0 + N_{01}$, which may then be used in known phase-locked loop results for $p(\phi)$.

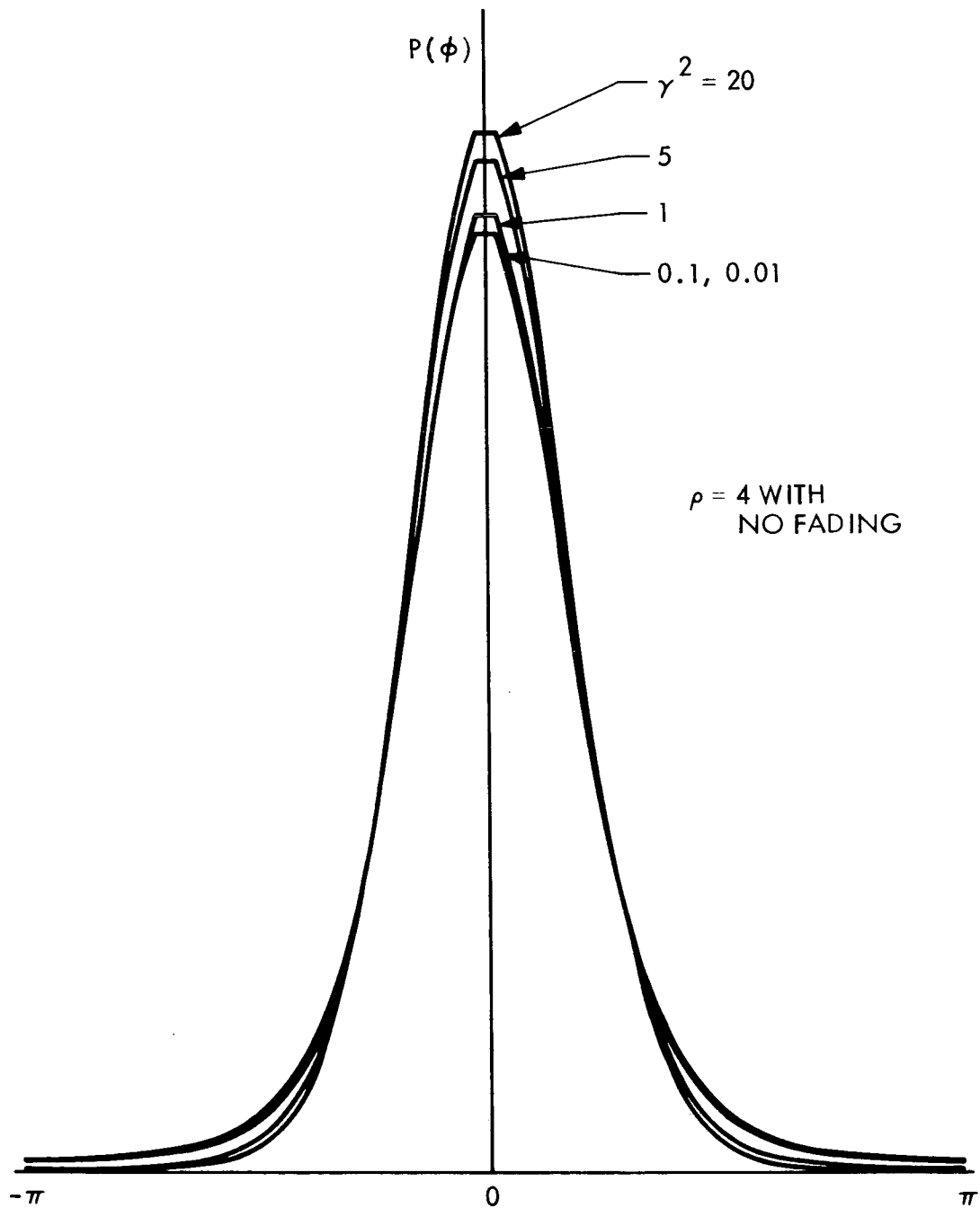


Fig. V-B-9. Slow Fading (Received Signal Power the Same in Each Case)

3) Case C: ρ and γ^2 Relatively Large. When both ρ and γ^2 are large, a linearization of (27) can be made and the resulting linear equations produce a Gaussian $p(\phi)$. Under the above assumption, the linearization produces the following approximations:

$$\dot{\phi} \approx \dot{x}_{c_1} \quad (34)$$

$$\sin \phi \approx \phi$$

$$\sqrt{(1 + x_{s_1}^2 + x_{c_1}^2)} \approx 1$$

Thus, (27) becomes

$$\dot{\phi} = \Omega_0 + \dot{x}_{c_1} - AKF(p) [\phi + n_1] \quad (35)$$

With $F(p)$ in the form of (2) an appropriate state variable is

$$\dot{y}_i = \frac{y_i}{\tau_i} - \frac{(1 - F_1) AK [\phi + n_1]}{\tau_i} \quad (36)$$

Now using (35), (36), and (28), we get the following linear state equations:

$$\begin{aligned} \dot{w} = & -AKF_0 + \sum_{i=1}^N y_i + (-c_1 \frac{z_1}{A} + \frac{z_2}{A}) \\ & - AKF_0 n_1 + d_1 \frac{v}{A} \end{aligned} \quad (37)$$

$$\begin{aligned}\dot{y}_1 &= -\frac{y_1}{\tau_1} - \frac{(1 - F_1) AK [\phi + n_1]}{\tau_1} \\ &\vdots \\ \dot{y}_N &= -\frac{y_N}{\tau_N} - \frac{(1 - F_N) AK [\phi + n_1]}{\tau_N}\end{aligned}$$

$$\frac{1}{A} \dot{\underline{z}} = \frac{1}{A} C \underline{z} + \frac{1}{A} D \underline{v}$$

where

$$w = \phi - \frac{\Omega_0}{AKF_0}$$

$$\frac{1}{A} z_1 = x_{c1}$$

These equations represent a complete set of simultaneous differential equations and could be written in matrix notation in the form

$$\dot{\underline{x}} = A \underline{x} + B \underline{u}$$

where A and B are constant matrices, \underline{x} is the state vector, and the components of \underline{u} are white noise.

The resulting probability density for \underline{x} is a joint Gaussian density. The covariance matrix for the state vector can be found by matrix techniques (see Ref. V-B-7, for example). In principle, any order loop and any rational spectra for the fading components can be used to find $p(\phi)$ for the strong specular component case.

As an example of the above technique, a basic situation was worked out in detail, namely a first-order loop and x_c given by

$$\dot{x}_c = -c_1 x_c + d_1 v \quad (38)$$

where v is white noise of unity spectral density and c_1 and d_1 are arbitrary constants. To give (38) more physical meaning, note that

$$\sigma_{x_c}^2 = \frac{d_1^2}{2c_1}$$

The transfer function of the filter corresponding to (38) is

$$\frac{d_1}{s + c_1} = \frac{d_1/c_1}{1 + \frac{s}{c_1}}$$

If the filter is normalized so that the transfer function is unity at $s = 0$, then the bandwidth of the x_c process can be defined as

$$W_s = \frac{\sigma_{x_c}^2}{\left(\frac{d_1}{c_1}\right)^2} = \frac{c_1}{2}$$

Dividing (38) by A , (38) can be written as

$$\dot{x}_{c_1} = -2W_s x_{c_1} + v_1 \quad (39)$$

where

v_1 is white noise with spectral density

$$\frac{4\sigma_{x_c}^2 W_s}{A^2} = \frac{2W_s}{\gamma^2}$$

Thus, for this simple model and first-order loop (i.e., $F_0 = 1$), (37) becomes

$$\begin{bmatrix} \dot{w} \\ \dot{x}_{c1} \end{bmatrix} = \begin{bmatrix} -2W_L & -2W_s \\ 0 & -2W_s \end{bmatrix} + \begin{bmatrix} -2W_L & 1 \\ 0 & 1 \end{bmatrix} \begin{bmatrix} u_1 \\ v_1 \end{bmatrix} \quad (40)$$

or in matrix notation

$$\dot{\underline{s}} = G \underline{s} + H \underline{n}$$

where

$$W_L = \frac{AK}{2} \text{ (First-order loop bandwidth)}$$

and

$$E(\underline{n} \underline{n}^T) = \begin{bmatrix} \frac{N_0}{2A^2} & 0 \\ 0 & \frac{2W_s}{\gamma^2} \end{bmatrix} = \begin{bmatrix} \frac{1}{\rho W_L} & 0 \\ 0 & \frac{2W_s}{\gamma^2} \end{bmatrix}$$

The details of finding the covariance matrix of \underline{s} will be omitted here, but they are straightforward matrix manipulations. The variance of ϕ is found to be

$$\sigma_{\phi}^2 = \sigma_w^2 = \frac{1}{\rho} + \frac{W_s}{2\gamma^2 (W_L + W_s)} \quad (41)$$

and (34), the mean, is just

$$\bar{\phi} = \frac{\Omega_0}{AK} = \frac{\Omega_0}{2W_L} \quad (42)$$

While this is a somewhat simple case, it does give insight into the effect of the interference on $p(\phi)$. The limiting cases (holding $\sigma_{x_c}^2$ constant) are

$$\begin{aligned} W_s \rightarrow 0 \quad \sigma_{\phi}^2 &= \frac{1}{\rho} \\ W_s \rightarrow \infty \quad \sigma_{\phi}^2 &= \frac{1}{\rho} + \frac{1}{2\gamma^2} \end{aligned} \quad (43)$$

Thus, for slow fading, the fading terms can be ignored because the variance for this case is the same as for a first-order loop with no interference. In the very fast fading case, the loop tracks only the specular term; thus, the loop phase error variance is increased by the presence of the fading terms by $\frac{1}{2\gamma^2}$.

It should be noted here that, whereas the above fading model of (38) is a simple one, it is usually difficult to characterize the process x_c by any more than the variance and bandwidth. Thus, (38) is probably a good representation for x_c in most cases.

4) Case D: γ^2 Relatively Large. The analysis in Case C can be improved upon in the low ρ case by using a nonlinear analysis technique while keeping the fading terms linearized. The technique will be illustrated for the first-order loop and $\Omega_0 = 0$ case, and it can be readily extended to the second-order loop and $\Omega_0 \neq 0$ cases.

Again the approximations in (34) hold, except that the $\sin \phi$ term will be retained. Thus the loop equations (for $\Omega_0 = 0$) become

$$\begin{aligned}\dot{\phi} &= -2W_s x_{c1} + v_1 - 2W_L [\sin \phi + n_1] \\ \dot{x}_{c1} &= -2W_s x_{c1} + v_1\end{aligned}\tag{44}$$

The steady-state modulo- 2π probability density, $p(\phi)$, can be solved in principle using the generalized Fokker-Planck equation as derived by Pawula (see Ref. V-B-8). Essentially, his work shows that the first equation in (44) can be written as

$$\dot{\phi} = -2W_s E(x_{c1} | \phi) + v_1 - 2W_L [\sin \phi + n_1]\tag{45}$$

If $E(x_{c1} | \phi)$ were known, then $p(\phi)$ could be solved for by using standard Fokker-Planck techniques. While $E(x_{c1} | \phi)$ is not known, Lindsey (Ref. V-B-3) has shown techniques for approximating it once the general functional form has been established by experimental or other considerations. Thus, equations (44) were simulated on a computer with the result that

$$E(x_{c1} | \phi) \approx \beta \sin \phi\tag{46}$$

where β is a constant and will be evaluated by using Lindsey's technique which is an application of the orthogonality principle (Ref. V-B-9). The orthogonality principle states that to minimize

$$E_{\phi} \{ [E(x_{c_1} | \phi) - \beta \sin \phi]^2 \}$$

then the following must hold true

$$E_{\phi} \{ [E(x_{c_1} | \phi) - \beta \sin \phi] \sin \phi \} = 0$$

This implies that

$$\beta = \frac{E_{\phi} \left[\frac{E(x_{c_1} | \phi) \sin \phi}{E_{\phi} \sin^2 \phi} \right]}{E_{\phi} \sin^2 \phi}$$

The numerator is

$$\begin{aligned} &= \int \left[\int x_{c_1} p(x_{c_1} | \phi) dx_{c_1} \right] \sin \phi p(\phi) d\phi \\ &= \iint x_{c_1} \sin \phi p(x_{c_1}, \phi) dx_{c_1} d\phi \\ &= E(x_{c_1} \sin \phi) \end{aligned}$$

Thus, the approximation for β is

$$\beta = \frac{E(x_{c_1} \sin \phi)}{E(\sin^2 \phi)} \quad (47)$$

This, of course, in itself is not available without knowing beforehand the joint statistics on x_{c_1} and ϕ which is, in essence, the desired result. However, good results can be obtained by using the linear analysis of Case C to evaluate the expectations in (47). The linear analysis shows that

$$\sigma_{\phi}^2 = \frac{1}{\rho} + \frac{1}{2\gamma^2} \left(\frac{W_s}{W_L + W_s} \right)$$

$$\sigma_{x_{c_1}}^2 = \frac{1}{2\gamma^2}$$

$$E(x_{c_1} | \phi) = \frac{1}{2\gamma^2} \left(\frac{W_s}{W_L + W_s} \right) \quad (48)$$

From this and the use of some helpful equalities in Ref. V-B-3, the expectations in (47) are given by

$$E(\sin^2 \phi) = \frac{1}{2} - \frac{1}{2} \exp \left\{ -2 \left[\frac{1}{\rho} + \frac{1}{2\gamma^2} \left(\frac{W_s}{W_L + W_s} \right) \right] \right\}$$

$$E(x_{c_1} \sin \phi) = \frac{1}{2\gamma^2} \left[\frac{W_s}{W_L + W_s} \right] \exp \left\{ -\frac{1}{2} \left[\frac{1}{\rho} + \frac{1}{\gamma^2} \left(\frac{W_s}{W_L + W_s} \right) \right] \right\} \quad (49)$$

Thus, $E(x_{c_1} | \phi)$ is approximated by (46) where β is given by (47) and (49).

Now the mod- 2π density for ϕ can be determined using (45) and the Fokker-Planck technique outlined in Refs. V-B-3 and 4, and $p(\phi)$ can be written as

$$p(\phi) = C_0 \exp [-U_0(\phi)] \quad (50)$$

where C_0 is the normalizing constant

$$V_0(\phi) = -\int^{\phi} \frac{2K_0(x)}{K_{00}} dx$$

$$K_0(\phi) \triangleq \lim_{\Delta t \rightarrow 0} \frac{E[\Delta\phi|\phi]}{\Delta t}$$

$$K_{00} \triangleq \lim_{\Delta t \rightarrow 0} \frac{E[(\Delta\phi)^2|\phi]}{\Delta t}$$

In this case, it can be shown from (45) that

$$K_0(\phi) = -2W_s E(x_{c_1}|\phi) - 2W_L \sin \phi \quad (51)$$

$$K_{00} = \frac{4W_L}{\rho} + \frac{2W_s}{\gamma^2}$$

Using (51) along with (46), (50) becomes

$$p(\phi) = \frac{\exp(\alpha \cos \phi)}{2\pi I_0(\alpha)} ; \quad -\pi \leq \phi \leq \pi \quad (52)$$

where

$$\alpha = \frac{\beta W_s + W_L}{\frac{W_L}{\rho} + \frac{W_s}{2\gamma^2}}$$

$$\beta = \frac{\epsilon}{\gamma^2} \left\{ \frac{\exp \left\{ -\frac{1}{2} \left[\frac{1}{\rho} + \frac{\epsilon}{2\gamma^2} \right] \right\}}{1 - \exp \left\{ -2 \left[\frac{1}{\rho} + \frac{\epsilon}{2\gamma^2} \right] \right\}} \right\}$$

$$\epsilon = \frac{W_s}{W_L + W_s}$$

Again, a look at the limiting cases for W_s is enlightening

$$\begin{aligned} W_s \rightarrow 0 : \quad \alpha &= \rho \\ W_s \rightarrow \infty : \quad \alpha &= 2 \left\{ \frac{\exp \left\{ -\frac{1}{2} \left[\frac{1}{\rho} + \frac{1}{2\gamma^2} \right] \right\}}{1 - \exp \left\{ -2 \left[\frac{1}{\rho} + \frac{1}{2\gamma^2} \right] \right\}} \right\} \end{aligned}$$

The first case is identical to the first-order loop result with no interference. It can be noted that the second result agrees with Case C if ρ and γ^2 are large. In this case, the asymptotic behavior of α is

$$\alpha = \frac{1}{\frac{1}{\rho} + \frac{1}{2\gamma^2}}$$

This is just $1/\sigma_\phi^2$ in the limiting linear case from equation (43).

b. Conclusions

This analysis has shown some approaches to the solution of $p(\phi)$ for a phase-locked loop whose input signal has passed through a Rician channel. From $p(\phi)$, the phase variance, a more useful parameter to the system analyst, can be computed. Emphasis has been placed on the first-order loop, but the techniques are directly applicable to second-order loops. The

case for low γ^2 (including $\gamma^2 = 0$ or Rayleigh channel), for other than slow fading, has not been included but is presently being worked on.

The results given here depend primarily on the variance and bandwidth of the fading components. For this to be a meaningful study, these parameters must be obtained for the ion beam and solar corona channels by modeling the plasma radiowave interaction. This modeling may show situations in which the Rician or Rayleigh channels are inappropriate. In these cases, the models and equations presented here would have to be modified, but the general techniques of analysis would remain the same.

REFERENCES

- V-B-1. Heald, M. A. and C. B. Wharton. Plasma Diagnostics with Microwaves, New York, Wiley, 1965, p. 254.
- V-B-2. Sellen, G. M., Jr., H. S. Ogawa, and R. K. Cole. "Factors in the Electrostatic Equilibrium Between a Plasma Thrust Beam and Ambient Space Plasma", Presented at the AIAA 8th Electric Propulsion Conference, Stanford, California, August 31 - September 2, 1970. AIAA Paper No. 70-1142.
- V-B-3. W. C. Lindsey, Synchronization Systems in Communication and Control, Prentice-Hall, Englewood Cliffs, N. J., 1972.
- V-B-4. A. J. Viterbi, Principles of Coherent Communication, McGraw-Hill, New York, 1966.
- V-B-5. C. A. Desoer, A Second Course on Linear Systems, Van Nostrand Reinhold, New York, 1970.
- V-B-6. J. H. Yuen, Analysis of a Double Loop Tracking System, JPL Report 900-480, June 19, 1971 (JPL internal document).
- V-B-7. N. E. Nahi, Estimation Theory and Applications, John Wiley and Sons, New York, 1969.
- V-B-8. R. F. Pawula, "Generalizations and Extensions of the Fokker-Planck-Kolmogorov Equations," I.E.E.E. Transactions on Information Theory, Vol. IT-13, No. 1, January, 1967.
- V-B-9. A. Papoulis, Probability, Random Variables, and Stochastic Processes, McGraw Hill, New York, 1965.